Timescales of Migmatization, Metamorphism, and Deformation in a Collapsed Orogenic Plateau

A DISSERTATION
SUBMITTED TO THE FACULTY OF THE GRADUATE SCHOOL
OF THE UNIVERSITY OF MINNESOTA
BY

STACIA MICHELLE GORDON

IN PARTIAL FULFILLMENT OF THE REQUIREMENTS
FOR THE DEGREE OF
DOCTOR OF PHILOSOPHY

Donna L. Whitney, Co-Advisor
Christian Teyssier, Co-Advisor

January 2009

ACKNOWLEDGMENTS

Many thanks are due to my two advisors, Donna Whitney and Christian Teyssier, for their continuous support over the last four and a half years. They have answered countless questions over the years and have always given me the freedom to pursue projects and opportunities. I thank them for helping me in making the transition from graduate student to independent researcher. I hope that we will continue to work together, and I look forward to future projects.

Many thanks are also due to my pseudo-advisors at other universities: Sam Bowring (MIT), Marty Grove (UCLA-Stanford), and Bob Miller (San Jose State). Without their support in both the laboratory and the field, this project would not have been possible. In addition, thank you to the TIMS lab group at MIT, including Jahan Ramezani, Noah McLean, and Matt Rioux, for showing me around the lab and also keeping me in high spirits throughout the countless lab hours. Also, thank you to Matt for introducing me to the beauty of Oman. Axel Schmitt at UCLA was also essential in lab analyses, and thank you for spending so many hours setting up the ion probe.

I thank the members of my written, oral, and final examining committee for discussions and for taking the time to read through my work. Members of these committees, in addition to my advisors, include David Kohlstedt, Larry Edwards, and Martin Saar. Also, thank you to Marc Hirschmann for interesting discussions at Hard Rock Lunch and introduction to the LEPR database.

The STAMP group, including past and present members, has been very important in creating discussions about the different chapters of this thesis. In particular, from STAMP and from the department, I wish to thank: Annia Fayon, Ellery Frahm, Eric

Goergen, Rory McFadden, Nick Seaton, Seth Kruckenberg, Peter Davis, Graham Baird, Leonardo Cruz, Lindsay Iredale, Anna Courtier, Anna Henderson, Andreas Mulch, Ryan Kerrigan, and Fawna Korhonen. Megan Kelly, thank you for your friendship and keeping me smiling in the last few months of writing this dissertation! Thank you to Sharon Kressler; you are an underappreciated and invaluable resource in the department. Thank you for your friendship and your help!

I acknowledge my funding sources, including the University of Minnesota Graduate School, the Department of Geology and Geophysics, Geological Society of America, and the National Science Foundation.

Finally, I wish to express many thanks to my friends and family. Thank you to my parents and my brother. Without your support, this dissertation would not have been possible!

ABSTRACT

Migmatites play an important role in the evolution of mountain systems by inducing rheological contrasts and focusing strain. In modern orogenic plateaux, investigations have suggested that a layer of partially molten crust is located in the mid- to lower crust. To understand the role of partially molten crust in orogenic systems, it is important to determine how much of the crust was partially molten for how long, and to link the conditions, timing, and consequences of partial melting to tectonic processes at different crustal levels during construction and collapse of orogens. The Skagit Gneiss, in the high-grade core of the North Cascade continental magmatic arc of Washington, USA and BC, and the Valhalla complex, in the Shuswap metamorphic core complex of southeastern British Columbia, Canada, both contain abundant migmatites and represent the western and eastern margins, respectively, of a proposed orogenic plateau that was once present in western North America during the Late Mesozoic-Early Cenozoic.

In the Valhalla complex, samples of migmatite were collected from the dome core to the bounding detachment fault for conventional, *in situ*, and depth profiling ion microprobe analyses. The conventional and *in situ* analyses of stromatic migmatites and leucosomes crystallized in boudin necks yield concordant U-Pb zircon ages that cluster near 60 Ma, interpreted as the timing of melt crystallization. Monazite Th-Pb ages range from 57-49 Ma. Patchy zoning and the range of dates suggest that the monazite was recrystallized under fluid-mediated conditions. To better understand the late history recorded in the monazite, depth profiling U-Pb ages were obtained from the outermost rims of zircons and yield a consistent age of 51 Ma. Oxygen isotopic measurements of the unpolished crystal faces systemically yield heavier $\delta^{18}O$ (up to 9.0 ‰) relative to

interior compositions (down to 5.5 ‰). Furthermore, Ti concentrations of unpolished crystal faces and grain interiors yield temperatures of ~650 ºC. The depth profiling zircon results and the conventional Th-Pb monazite results indicate that deformation- and fluid-mediated recrystallization of zircon and monazite occurred at high-*T* conditions as late as 51 Ma. The Ar cooling ages overlap with the youngest monazite and zircon results and cluster from 51 to 49 Ma. The geochronometric, geochemical and trace element results from the Valhalla complex, combined with field, structural, and petrologic data from this and previous studies of the Omineca domes, show that a large region of orogenic crust in this part of the Cordillera was partially molten in the early Tertiary. Rapid cooling is associated with extension and exhumation of migmatites in the domes.

In the Skagit Gneiss, monazite and zircon were dated using the U-Pb TIMS method from migmatites in 3 localities. Zircons from the mesosome of the westernmost locality commonly yield Cretaceous dates, with younger dates clustering at 61 Ma. Leucosomes yield zircon with concordant dates that range from 68 to 47 Ma, interpreted as representing the timing of melt crystallization. In comparison, monazite reveal bimodal results, with one group clustering near 48 Ma and a second set of older dates from 69 to 65 Ma. The latter monazite dates are consistently older than the zircons from the same leucosome, consistent with the possibility that the older monazites record the timing of prograde to possibly peak metamorphism. The Eocene zircon and monazite dates are at the young end of the age spectrum for the North Cascades arc system and overlap with the timing of transtensional basin formation, suggesting that partial melting was an active process during at least the initial stages of extension and exhumation of the high-grade rocks. In addition, in the Skagit Gneiss, a detailed study of part of the eastern

bounding strike-slip fault zone suggests that a dynamic system was present between the high-grade Skagit rocks, the fault, and the adjacent basin. A step-over zone in the strike-slip fault may have developed during transpression and allowed part of the basin to be incorporated into the high-grade core and undergo metamorphism and deformation with the Skagit Gneiss.

Although ~ 300 km separate the North Cascades from the Shuswap metamorphic core complex today, the two regions share many similarities: 1) both areas expose deformed high-grade gneiss that underwent isothermal decompression; 2) both areas contain abundant deformed migmatites that crystallized at similar times; and 3) Ar cooling ages from the two regions are similar. In both the Skagit Gneiss and the Valhalla complex, the partially molten crust played a significant role in the decompression and exhumation of the terranes. The similarities in *P*-*T*-t-d between the two regions strongly indicate that the North Cascades and the Omineca belt were dynamically linked and that the two areas represent the collapsed margins of an orogenic plateau. The migmatites in both areas are evidence of the layer of partially molten crust that once flowed beneath the proposed plateau. The data from the two areas suggest that partial melting must play a major role in the tectonic evolution of orogenic systems that contain abundant melt (e.g., Himalaya-Tibet; Andes-Altiplano-Puna; Cordillera).

TABLE OF CONTENTS

LIST OF FIGURES

Chapter 1

Chapter 2

Chapter 3

Chapter 4

Chapter 5

LIST OF TABLES

Chapter 6

Chapter 1: Introduction to the Thesis

CRUSTAL MELTING AND THE EVOLUTION OF AN OROGENIC PLATEAU

Convergent plate boundaries are characterized by crustal shortening and thickening and by the formation of orogenic plateaux. Eventually orogens will extend, gravitationally collapse, and flow under their own weight (Coney & Harms, 1984; Dewey, 1988; Rey *et al*., 2001; Vanderhaeghe & Teyssier, 2001a, b). Many studies have suggested that during orogenic evolution, the crust becomes rheologically layered with a thin, rigid upper layer overlying a channel of low viscosity, partially molten crust (e.g., Goetze & Evans, 1979; Brace & Kohlstedt, 1980; Block & Royden, 1990; Wernicke, 1990; Kruse *et al*., 1991; Bird, 1991; Wdowinski & Axen, 1992; Clark & Royden, 2000; Vanderhaeghe & Teyssier, 2001b). The thermally weakened layer may decouple the upper and lower crust, has the ability to smooth topography through lateral channel flow, and plays a fundamental part in the distribution of strain and heat during orogenesis (Bird, 1991; Nelson *et al*., 1996; Vanderhaeghe & Teyssier, 2001a, b; Teyssier *et al.,* 2005). Moreover, the flow of this thick, weak, partially molten crust has a significant mechanical role in the collapse of orogens.

Metamorphic core complexes (MCC) and gneiss domes located within collapsed orogenic belts expose a significant quantity of former partially molten material in the form of migmatites (Whitney *et al*., 2004a). Commonly, the core rocks of domes and MCCs have been exhumed from the mid- to lower crust through a combination of vertical and lateral crustal flow, which is commonly accompanied by partial melting and upper crustal extension. Understanding the timescales of partial melting, melt crystallization, deformation, and exhumation is essential for interpreting the rheologic, thermal and mechanical transition of an orogen from contractional crustal thickening to extension and

collapse. Furthermore, the timing and rates of crustal processes can provide information on the behavior of partially molten crust and reveal details about the coupling/decoupling of shallow and deep processes.

In this study, I have investigated two areas of the North American Cordillera: the exhumed North Cascades arc, north-central Washington; and the Valhalla complex, southeastern British Columbia (Fig. 1). The Valhalla complex is part of a north-south trending series of gneiss domes exposed in the Shuswap MCC. The North Cascades arc and the Valhalla complex are connected in the elementary sense of an arc and backarc system. In addition, it has been proposed that the exhumed arc and the Shuswap MCC may have been part of a broad orogenic plateau (Whitney *et al*., 2004b), with these terrains representing the western and eastern edge of the plateau, respectively.

The primary goals of this research are to study the role of partial melting in orogeny by examining the geologic record in a collapsed orogenic plateau system, and in addition, to understand the role of partial melting in the deep parts of continental magmatic arcs and in the hinterland of the orogen within gneiss domes. The results from this study will contribute to ongoing investigations of modern orogenic plateaux (e.g., the Altiplano-Puna plateau) in allowing predictions of what will happen to a plateau once it is unstable and begins to extend and collapse. Furthermore, this study addresses the link between partial melting, deformation, metamorphism, extension, fluid migration, and exhumation during orogenesis, and seeks to decipher how these processes evolve during thickening of the crust and during extension and collapse of the thickened crust. A combination of U-Pb geochronology, a technique that provides the timescales of these processes, with structural and microstructural analyses, geothermobarometry, stable

isotope measurements, and field mapping has provided significant information that has allowed me to address the goals of understanding the role of partial melting and other processes during orogenesis, and in particular, during the potential collapse of a plateau.

Each chapter, after this initial introduction, is written as a separate scientific paper. The second chapter, *Timescales of Migmatization, Melt Crystallization, and Cooling in a Cordilleran Gneiss Dome: Valhalla Complex, Southeastern British Columbia*, was published in Tectonics in 2008 (Gordon *et al.,* 2008). This work focuses on the Valhalla complex and uses U-Pb geochronology on zircon and monazite to understand the timing of melt crystallization and metamorphism in the gneiss dome. Argon thermochronology results are described and yield information on the timing of cooling in the gneiss dome. The results from the Valhalla complex combined with similar results from studies of the migmatites in other domes of the Shuswap MCC suggest that a large region of orogenic crust may have been partially molten during the early Tertiary. Furthermore, these results indicate that there was a localization of exhumation at the boundary between the flowing crust of the hinterland (the region containing the series of gneiss domes) and the rigid, colder crust of the Rocky Mountain foreland.

The third chapter, *Fluid-rock Interaction in Orogenic Crust Tracked by Zircon Depth Profiling*, has been submitted to Geology and is a paper that addresses fluid-rock interaction during crystallization and cooling of deep orogenic crust. The paper describes the use of a novel combination of techniques including U-Pb geochronology, $\delta^{18}O$ measurements, and Ti in zircon thermometry to investigate the relationship between timing, temperature, and geochemical environment in the mid- to lower-crust. The techniques are all applied to a single accessory mineral, zircon, and the high-spatial

resolution of the ion microprobe permits investigation of both the natural zircon rims and subsequently, the polished interior of the zircons. The combination of techniques is a powerful approach to investigating fluid-rock interaction and can be applied to a variety of terrains in which fluids have been present and altered the zircon crystals.

The fourth chapter, *Time-temperature-fluid Evolution of Migmatite Dome Crystallization: Coupled U-Pb Age, Ti Thermometry, and O Isotopic Ion Microprobe Depth Profiling of Zircon and Monazite*, has been submitted to Chemical Geology and is a paper that uses the techniques described in Chapter 3 to address the fluid evolution of the Valhalla complex. The U-Pb zircon and monazite results from the second chapter, described above, left some questions unanswered from the Valhalla complex in regards to the high-temperature fluid history. Using the combination of ion microprobe techniques, the age, temperature and chemistry results indicate that fluid infiltration driven by amphibolite-facies metamorphic devolatization and/or igneous crystallization persisted at deep crustal levels until just before the time that the rocks were rapidly exhumed to upper crustal levels. In addition, the thermometry results reveal that the Valhalla complex remained at high-temperature and that the U-Pb zircon rim results overlap with argon cooling ages, indicating rapid cooling. The collective results suggest that within gneiss domes, partial melting, metamorphism, deformation, fluid-rock interaction, extension and exhumation are all intimately connected and all need to be addressed in order to understand the evolution of a gneiss dome and other similar high-temperature terrains.

The fifth chapter, *High-precision Dating of Migmatites in an Exhumed Continental Arc*, focuses on understanding the role of partial melting and its link to other crustal-scale processes within the Skagit Gneiss, part of the North Cascades continental

magmatic arc. This chapter will soon be submitted to Lithos. The North Cascades is an ideal place to study continental arc processes because > 40 km of structural depth is exposed, from the high-grade migmatites to basins that lie adjacent to the core and that received detritus during exhumation of the core. A variety of leucosome samples (e.g., pegmatitic/fine-grained; layer-parallel/discordant) and the host-gneisses were collected for high-precision chemical abrasion-thermal ionization mass spectrometry (CA-TIMS) analyses from three outcrops in the Skagit Gneiss. The results reveal that within each outcrop, a narrow range of crystallization ages are recorded; however, each individual outcrop yields a distinct set of dates, some Late Cretaceous and some Eocene dates. Collectively, the zircon and monazite geochronology indicates that partial melting occurred during Late Cretaceous metamorphism and Eocene transtension and exhumation, suggesting that the crust must have been relatively weak for a significant period of time during Late Cretaceous to Eocene time. In addition, the similarity in U-Pb zircon and monazite ages in the migmatites to Ar cooling ages and basin formation ages suggests coupling between flow of the middle crust and brittle extension and basin formation.

The sixth chapter, *Metamorphism and Deformation of a Basement-Cover System Along a Strike-slip Fault Zone, Ross Lake Fault, North Cascades, USA*, will be submitted to the Journal of Metamorphic Geology and focuses on understanding the exhumation of a crystalline core domain of a continental magmatic arc along a oblique strike-slip boundary. The Ross Lake fault zone forms the eastern boundary of the Skagit Gneiss and separates high-grade orthogneiss from low-grade Methow basin. The *P*-*T*-d conditions recorded by rocks on either side of the fault vary along the length of the fault. For

example, in one area of the fault zone, thermobarometry results yield high-grade conditions of 8-10 kbar at 650 – 750 ºC from rocks of Methow affinity whereas in other areas of the fault zone, the Methow rocks have only achieved lower-amphibolite-facies to greenschist-facies conditions. We suggest that an overlapping step-over zone developed in the Ross Lake fault zone and facilitated the burial and exhumation of a slice of the Methow basin. Oblique slip on the Ross Lake fault and the step-over in a transtensional regime combined with buoyant vertical flow of migmatitic gneiss exhumed the high-grade Skagit Gneiss and the adjacent tectonic slice of metamorphosed Methow basin.

The seventh and final chapter discusses the evidence from this study for the existence and collapse of an orogenic plateau in which the North Cascades arc represents part of the western margin of the plateau, and the Valhalla Complex, part of the eastern margin.

REFERENCES

Bird, P., 1991. Lateral extrusion of lower crust from under high topography, in the isostatic limit. *Journal of Geophysical Research*, **96**, 10275-10286.

Block, L. & Royden, L.H., 1990. Core complex geometries and regional scale flow in the lower crust. *Tectonics*, **9,** 557-567.

Brace, W.F. & Kohlstedt, D.L., 1980. Limits on lithospheric stress imposed by laboratory experiments. *Journal of Geophysical Research*, **85**, 6248-6252.

Clark, M.K. & Royden, L.H., 2000. Topographic ooze: Building the eastern margin of Tibet by lower crustal flow. *Geology*, **28**, 703-706.

Coney, P.J. & Harms, T.A., 1984. Cordilleran metamorphic core complexes: Cenozoic extensional relics of Mesozoic compression. *Geology*, **12**, 550-554.

Dewey, J.F., 1988. Extensional collapse of orogens. *Tectonics*, **7**, 1123-1139.

Goetze, C. & Evans, B., 1979. Stress and temperature in the bending lithosphere as constrained by experimental rock mechanics, *Geophys. J. R. Astr. Soc.*, **59**, 463-478.

Gordon, S.M., Whitney, D.L., Teyssier, C., Grove, M. & Dunlap, W.J., 2008. Timescales of migmatization, melt crystallization, and cooling in a Cordilleran gneiss dome: Valhalla complex, southeastern British Columbia. *Tectonics*, **27**, TC4010, doi:10.1029/2007TC002103.

Kruse, S., McNutt, M.K., Phipps-Morgan, J., Royden, L. & Wernicke, B.P., 1991. Lithospheric extension near Lake Mead, Nevada: A model for ductile flow in the lower crust. *Journal of Geophysical Research*, **96**, 4435-4456.

Nelson, K.D., Wenjin Zhao, Brown, L.D., Kuo, J., Jinkai Che, Xianwen Liu, Klemperer, S.L., Makovsky, Y., Meissner, R., Mechie, J., Kind, R., Wenzel, F., Ni, J., Nabelek, J., Chen Leshou, Handong Tan, Wenbo Wei, Jones, A.G., Booker, J., Unsworth, M., Kidd, W.S.F., Hauck, M., Alsdorf, D., Ross, A., Cogan, M., Changde Wu, Sandvol, E. & Edwards, M., 1996. Partially molten middle crust beneath southern Tibet: Synthesis of project INDEPTH results. *Science*, **274**, 1684-1688.

Rey, P., Vanderhaeghe, O. & Teyssier, C., 2001. Gravitational collapse of the continental crust: definition, regimes and modes. *Tectonophysics*, **342**, 435-449.

Teyssier, C., Ferré, E.C., Whitney, D.L., Norlander, B., Vanderhaeghe, O. & Parkinson, D., 2005. Flow of partially molten crust and origin of detachments during collapse of the Cordilleran orogen. *In*: Bruhn, D. & Burlini, L. (eds). *High-strain zones: Structure*

and physical properties, Geological Society, London, Special Publications, **245**, 39-64.

Vanderhaeghe, O. & Teyssier, C. 2001a. Crustal-scale rheological transitions during late-orogenic collapse. *Tectonophysics*, **335**, 211-228.

Vanderhaeghe, O. & Teyssier, C., 2001b. Partial melting and flow of orogens. *Tectonophysics*, **342**, 451-472.

Wdowinski, S. & Axen, G.J., 1992. Isostatic rebound due to tectonic denudation: A viscous flow model of a layered lithosphere. *Tectonics*, **11**, 303-315.

Wernicke, B.P., 1990. The fluid crustal layer and its implications for continental dynamics, *In:* Salisbury, M.H. & Fountain, D.M. (eds.). *Exposed cross sections of the continental crust*, Kluwer Academic Publishers, Dordrecht, Netherlands, pp. 509-544.

Whitney, D.L., Teyssier, C. & Fayon, A.K., 2004a. Isothermal decompression, partial melting and exhumation of deep continental crust. *In:* Grocott, J., McCaffrey, K.J.W., Taylor, G. & Tikoff, B. (eds). *Vertical Coupling and Decoupling in the Lithosphere*, Geological Society, London, Special Publications, **227**, 313-326.

Whitney, D.L., Paterson, S.R., Schmidt, K.L., Glazner, A.F. & Kopf, C.F., 2004b. Growth and demise of continental arcs and orogenic plateaux in the North American Cordillera: from Baja to British Columbia. *In*: Grocott, J., McCaffrey, K.J.W., Taylor, G. & Tikoff, B. (eds). *Vertical Coupling and Decoupling in the Lithosphere*, Geological Society, London, Special Publications, **227**, 167-176.

Figure 1.1: DEM image of the North American Cordillera with the location of the two field areas highlighted by the boxes: the North Cascades and the Shuswap metamorphic core complex, including the Valhalla complex.

Chapter 2: Timescales of Migmatization, Melt Crystallization, and Cooling in a Cordilleran Gneiss Dome: the Valhalla Complex, Southeastern British Columbia

Stacia Gordon*, Donna Whitney*, Christian Teyssier*, Marty Grove, W. Jim Dunlap***

*Department of Geology and Geophysics, University of Minnesota, Minneapolis, MN 55455
**Department of Earth and Space Sciences, University of California, Los Angeles, CA 90095

This chapter has already been published and is included as part of this dissertation **with permission from *Tectonics*, 27, TC4010, doi:10.1029/2007TC002103, 2008,**

ABSTRACT

Integration of *in situ* and conventional ion microprobe U-Th-Pb zircon and monazite geochronology with $^{40}Ar/^{39}Ar$ hornblende, biotite, and muscovite thermochronology provides a temporal record of metamorphism, partial melting, fluids, and cooling of exhumed mid- to lower crustal rocks. The Valhalla complex, SE British Columbia, is one of a series of elongate gneiss domes within the Omineca belt of the Canadian Cordillera. We have performed U-Th-Pb and $^{40}Ar/^{39}Ar$ age measurements on migmatitic gneisses from a range of structural levels and settings within the Valhalla complex in an effort to better document the timing of migmatization and exhumation. Stromatic migmatites and leucosomes crystallized in boudin necks yield concordant U-Pb zircon ages that cluster near 60 Ma, and Th-Pb monazite ages of ca. 60-50 Ma. *In situ* analyses of monazite in samples that contain <10% leucosome yield a bimodal distribution at 70-65 Ma and 62-57 Ma. The younger ages are similar to migmatite zircon ages. $^{40}Ar/^{39}Ar$ analyses from the same rocks document cooling at 51-49 Ma. These new data, combined with field, structural, and petrologic data from this and previous studies of the Omineca domes indicate that a large region (thousands of km^2) of orogenic crust may have been partially molten during the early Tertiary (>60-50 Ma). However, the combined data also suggest that melt crystallization (ca. 60 Ma) in the Valhalla complex occurred rapidly and before the other domes within the Omineca belt. Cooling at 49 Ma throughout the Omineca is associated with regional extension and exhumation of migmatites in the domes. The presence of abundant migmatites and the similarity in timing of melt crystallization and cooling in domes along the 400 km-long Omineca belt is consistent with localization of

exhumation at the boundary between the flowing crust of the hinterland and the rigid, colder crust of the Rocky Mountain foreland.

INTRODUCTION

Convergent plate boundaries are characterized by the shortening and thickening of crust, which may be accompanied by significant deformation, metamorphism and partial melting. Many rock mechanic, geodynamic, and tectonic studies suggest that the thickened crust that develops is rheologically layered with a thin, rigid upper crust overlying a weak ductile lower layer that can flow [e.g., *Goetze and Evans*, 1979; *Brace and Kohlstedt*, 1980; *Block and Royden*, 1990; *Wernicke*, 1990; *Kruse et al*., 1991; *Bird*, 1991; *Wdowinski and Axen*, 1992; *Clark and Royden*, 2000; *Vanderhaeghe and Teyssier*, 2001b]. Partial melting within the ductile lower crust can enhance tectonic strain rates due to melt-induced weakening and strain localization [*Hollister and Crawford*, 1986; *Dell'Angelo et al*., 1987; *Hollister*, 1993; *Handy et al.,* 2001]. Partial melting also may play a fundamental role in the distribution of heat during orogenesis [*Raia and Spera*, 1997] and in facilitating crustal differentiation [*Lambert and Heier*, 1968; *Vanderhaeghe and Teyssier*, 2001a]. Therefore, it is important to investigate deeply exhumed orogens in order to understand the role of partial melting in crustal dynamics and to determine the kinematics and timing of melt-present deformation and crustal flow.

Deeply exhumed rocks from thickened crust may be exposed within metamorphic core complexes (MCC) and gneiss domes, both characteristic features of collapsed orogenic belts [*Coney*, 1980; *Armstrong*, 1982; *Coney and Harms*, 1984]. The cores of MCCs and gneiss domes may contain migmatitic rocks that are evidence of a former partially molten crust [*Whitney et al.*, 2004a]. The migmatites are characteristically exhumed from mid- to lower crustal levels through a combination of vertical and lateral crustal flow, and commonly accompanied, and perhaps driven by, partial melting and

upper crustal extension. A classic example of migmatitic domes in metamorphic core complexes is the Omineca belt of southeastern British Columbia [e.g., *Monger et al*., 1972]. The Omineca belt represents the crystalline hinterland of the foreland fold and thrust belt, and contains the Shuswap MCC (*Monger et al.,* 1982). A succession of Eocene detachment faults form a series of elongate gneiss domes within the Shuswap MCC (Fig. 1). The domes, including the Valhalla complex, the Thor-Odin dome, and the Frenchman Cap dome, contain migmatitic cores and midcrustal detachments that were exhumed during extension of the rigid upper crust. Previous studies of the Shuswap MCC have investigated the exposed migmatites and noted their importance in the evolution of the domes [e.g., the Thor-Odin dome; *Vanderhaeghe and Teyssier*, 1997; *Vanderhaeghe et al.*, 1999a, b; *Vanderhaeghe and Teyssier*, 2001b; *Norlander et al*., 2002; *Vanderhaeghe et al*., 2003; *Teyssier et al*., 2005; *Hinchey et al*., 2006].

Previous investigations of the Valhalla complex have focused on the metamorphic, structural, and geochronological history of the paragneisses and mantling granitoids exposed within the Valhalla and Passmore domes (Fig. 2) [*Carr et al.*, 1987; *Parrish et al.*, 1988; *Heaman and Parrish*, 1991; *Carr,* 1992; *Parrish*, 1995; *Spear and Parrish*, 1996; *Schaubs and Carr*, 1998; *Schaubs et al.,* 2002; *Ducea et al.*, 2003; *Spear*, 2004; *Carr and Simony*, 2006]. Here we report new results that bear upon the timing of migmatite crystallization at different structural levels of the Valhalla complex, and relate migmatite textures to the tectonic evolution of the migmatitic Valhalla and Passmore domes and the Shuswap core complex. Analyses of U-Th-Pb zircon and monazite and $^{40}Ar/^{39}Ar$ hornblende, muscovite, and biotite isotopic compositions have been performed on the metatexites (migmatites with 10-50% leucosome) and migmatitic biotite gneisses

(<10% leucosome) exposed in the Valhalla complex. Our geochronologic and thermochronometric results document the timescales of melt crystallization and cooling of the complex. Based upon these results, we evaluate the significance of abundant melt in Valhalla and discuss the tectonic evolution of the complex in the framework of the Omineca belt and of this part of the North American Cordillera.

TECTONIC EVOLUTION OF THE OMINECA BELT

Near the 49th parallel, the tectonic history along the eastern boundary of the North American Cordillera is characterized by two main phases: 1) Mesozoic convergence that resulted in Jurassic and Cretaceous batholith emplacement, thrusting, folding and crustal thickening; and 2) Paleocene-Eocene extension and orogenic collapse involving tectonic denudation and regional plutonism [*Armstrong*, 1982; *Monger et al*., 1982; *Archibald et al.*, 1983; *Brown and Read*, 1983; *Okulitch*, 1984; *Brown et al*., 1986; *Parrish et al*., 1988; *Carr,* 1992; *Teyssier et al.*, 2005]. Mesozoic convergence resulted in the accretion of numerous allocthonous terranes onto the western margin of the North American craton [*Coney et al.,* 1980]. These terranes were thrust eastward over sedimentary sequences that had previously accumulated along the North American paleomargin, likely forming a 50-60 km thick crustal welt [*Coney and Harms*, 1984; *Brown et al*., 1986; *Price*, 1986]. Thickening, burial of sediments, and later thermal relaxation resulted in widespread high-temperature metamorphism and crustal melting [*Brown et al*., 1986; *Sevigny et al*., 1989; *Carr*, 1992; *Nyman et al*., 1995; *Vanderhaeghe and Teyssier*, 1997] that may have culminated in the development of an orogenic plateau during the Late Cretaceous-Early Cenozoic [e.g., *Coney and Harms*, 1984; *England and Thompson*, 1986; *Wolfe et al.*,

1998; *Whitney et al*., 2004b]. The second tectonic phase of extension and collapse was coeval with regional transtension to the west in the continental arc and possibly with ridge subduction along the plate boundary [*Morris et al.*, 2000; *Haeussler et al.*, 2003; *Paterson et al.*, 2004; *Rusmore et al.*, 2005]. Some of the extension may be related to transtensional events and strike-slip faulting [*Parrish et al.*, 1995; *Struik and Anderson*, 2003].

The Omineca belt represents the buried paleomargin, the exhumed hinterland of the Cordillera [*Monger et al*., 1972; *Coney*, 1980; *Crittenden et al*., 1980], and the eastern margin of the proposed orogenic plateau [*Whitney et al*., 2004b]. The belt exposes the easternmost upper amphibolite- to granulite-facies metamorphic and plutonic rocks in a north-south trending series of elongate gneiss domes (Fig. 1) [*Monger et al*., 1982; *Parrish et al*., 1988]. The domes are located in the immediate footwall of the eastern detachment of the Shuswap MCC. Results of previous geochronometric investigations demonstrated that early Tertiary exhumation of gneiss domes in the Omineca core complexes was coeval along the entire belt [*Parrish and Wheeler*, 1983; *Parrish and Armstrong*, 1987; *Carr*, 1991; *Parkinson*, 1991, 1992; *Parrish*, 1995; *Crowley*, 1997a, 1997b; *Johnston*, 1998].

THE VALHALLA COMPLEX

Geologic Overview

The Valhalla complex contains high-temperature migmatitic metasedimentary and plutonic rocks that are exposed in two domes, the Valhalla dome in the north and the Passmore dome in the south (Fig. 2A) [*Reesor*, 1965; *Carr et al*., 1987]. Both domes are

defined by outward dipping low angle (< 35º) foliation and lithologic contacts (Fig. 2B) [*Carr et al*., 1987]. Structurally, the Valhalla complex is dominated by a pervasive east-west lineation with kinematic indicators that show top-to-the-east movement [*Parrish*, 1984; *Parrish et al*., 1985; *Carr*, 1985, 1986]. A pronounced strain gradient recognized within the core of the Valhalla and Passmore domes is associated with the Gwillim Creek shear zone (GCSZ) [*Parrish et al*., 1985; *Carr et al*., 1987; *Schaubs and Carr*, 1998]. This shear zone has been imaged as a major reflector in Lithoprobe profiles [*Cook et al*., 1988; *Parrish et al*., 1985], and has been interpreted as a thrust fault that is part of a larger thrust system that accommodated east-west shortening of the foreland belt during Late Cretaceous and Paleocene time [*Parrish et al*., 1988; *Brown et al*., 1992; *Varsek and Cook*, 1994; *Carr and Simony*, 2006]. Previous tectonic models for the high-temperature cooling of the Valhalla complex have proposed that the complex was thrust along the GCSZ onto a cold footwall, and this was followed by a lower temperature cooling history induced by extensional faulting [*Parrish et al.,* 1988; *Parrish,* 1995; *Spear and Parrish*, 1996; *Schaubs et al*., 2002; *Spear*, 2004; *Carr and Simony*, 2006]. Furthermore, Valhalla has been interpreted to expose a higher structural level than the other domes in the Shuswap MCC [*Parrish*, 1995].

The Valhalla complex is bounded on all sides by east-directed Eocene faults/shear zones (Fig. 2): at the eastern margin, the brittle/ductile Slocan Lake fault was active from 54 to 45 Ma and is a north-striking, low-angle fault that separates the high-temperature core rocks from the ca. 169 Ma Nelson batholith [*Carr et al*., 1987; *Parrish et al*., 1988]. To the north, west, and south, the ductile Valkyr shear zone bounds and arches over the complex [*Carr et al*., 1987]. This amphibolite facies shear zone is ~2 km thick and was

active from 59 to 54 Ma [*Carr*, 1986; *Carr et al*., 1987; *Parrish et al*., 1988]. Both the arched profile of the Valkyr shear zone and the fact that both bounding faults are east-directed and coeval suggests that the Valkyr shear zone and the Slocan Lake fault are part of a single extensional fault zone [*Parrish*, 1984; *Carr et al.*, 1987, *Parrish et al.*, 1988], analogous to the Columbia River detachment along the eastern margin of the Shuswap complex in the Thor-Odin dome region, interpreted as a rolling hinge detachment zone [*Teyssier et al*., 2005].

The Valhalla complex consists of arched sheets that match the shape of the overlying Valkyr and underlying GCSZ (Fig. 2B). The sheets are composed of three main bodies (from lowest to highest structural level) [*Reesor*, 1965; *Carr et al.,* 1987]: 1) the granodioritic, K-feldspar megacrystic Mulvey orthogneiss, 2) a metasedimentary unit consisting of mixed gneisses (biotite and quartzofeldspathic gneiss) with significant bodies of leucosome and lesser amounts of calc-silicate, amphibolite, and quartzite; this unit records maximum *P-T* conditions of 820 ± 30 ºC and 8 ± 1 kbar in garnet-sillimanite-K-feldspar gneiss [*Spear and Parrish*, 1996], and 3) two sheet-like leucocratic granitoid bodies, including the Airy quartz monzonite and the Ladybird leucogranite.

Previous geochronometric investigations of the Valhalla complex have focused on dating the metamorphism of metasedimentary rocks, the crystallization of the orthogneiss in the core of the dome, and the crystallization of the mantling granitoids (Table 1). U-Pb zircon/monazite [*Parrish et al*., 1988; *Heaman and Parrish,* 1991; *Parrish,* 1995; *Spear and Parrish,* 1996] and Sm-Nd garnet [*Ducea et al*., 2003] analyses of Valhalla paragneiss, including rocks in the GCSZ, document Late Cretaceous to early Tertiary metamorphism (85-60 Ma). These data have been interpreted to indicate Late Cretaceous

prograde metamorphism (85-65 Ma) and early Tertiary peak metamorphism (60 Ma) [*Spear*, 2004]. U-Pb and Pb-Pb zircon dates for the orthogneiss in the core of the Valhalla dome range from 116-89 Ma and are older than the dates obtained from metasedimentary rocks [*Parrish,* 1984; *Carr et al*., 1987; *Heaman and Parrish,* 1991; *Parrish,* 1995, *Spear and Parrish,* 1996]. The mantling Airy quartz monzonite and the Ladybird leucogranite yield ages that overlap with the inferred timing of peak metamorphism: ca. 64-57 Ma (U-Pb zircon) [*Parrish*, 1984; *Parrish and Roddick*, 1985; *Parrish et al*., 1988], similar to ages from late, cross-cutting pegmatite and aplite in the complex [*Parrish et al*., 1988; *Parrish*, 1995; *Spear and Parrish*, 1996]. Previous thermochronology data indicate that denudation-related cooling of the Valhalla complex occurred between 58-47 Ma (Table 1) [*Wanless et al*., 1978, 1979; *Parrish*, 1984; *Heaman and Parrish*, 1991; *Parrish et al*., 1988]. The argon ages are, however, limited to the core orthogneiss and mantling leucogranite bodies. No argon ages have previously been reported from the mixed gneiss unit.

Valhalla Migmatites

Previous investigations have presented evidence for partial melting within the mixed gneiss unit of the Valhalla complex and have noted the Airy and Ladybird granitoid bodies [*Reesor,* 1965; *Spear and Parrish*, 1996; *Schaubs and Carr*, 1998]. Leucosomes that we interpret as crystallized melt are typically associated with extensional structures and occur in fine-scale layers within the paragneiss of the mixed gneiss unit (Fig. 3A). Leucogranite dikes and sills permeate the mixed gneiss and orthogneiss units (Fig. 4A) and are prominent in ductile fold structures in the mixed

gneiss unit (Fig. 4B), and in layers, lenses, and small magma bodies within the eastern Slocan Lake fault zone (Fig. 4C).

We infer that this migmatization and leucogranite injection likely represent a widespread partial melting episode in the Valhalla complex. An anatectic origin for the migmatites is supported by the *P*-*T* conditions that are above the solidus for dehydration reactions in quartzofeldspathic rocks, the presence of igneous textures in some leucosomes (e.g., euhedral grains, granophyric intergrowths of orthoclase and quartz, Fig. 3B), and outcrop-scale textures that suggest a fluid behavior of the leucosomes (e.g., melt intermingling with the Mulvey orthogneiss, Fig. 4A; and concentration of leucosome in boudinaged necks of paragneiss, Fig. 4D).

Melting may have occurred during prograde heating and subsequent decompression, as the crust underwent dehydration-melting reactions. Evidence for high-temperature (isothermal?) decompression in the Passmore dome is the symplectitic corona texture in pods of gedrite-cordierite gneiss. Al_2SiO_5 polymorphs are surrounded by symplectitic rims of sapphirine + spinel + corundum + cordierite + anorthite [*Marshall and Simandl*, 2006], similar to textures reported for the Thor-Odin dome [*Duncan*, 1984, *Norlander et al*., 2002]. These assemblages are consistent with the high-*T* metamorphic conditions documented by *Spear and Parrish* [1996] for high-grade gneiss in the region. Similar textures in gedrite-cordierite lenses in the Thor-Odin dome have been interpreted to indicate near-isothermal decompression [*Norlander et al.*, 2002].

The great abundance of migmatite and leucogranite exposed in the Valhalla complex (Fig. 3 and 4) indicate that partial melting was important in the tectonic evolution of the region, and therefore it is essential to know the timescale of partial

melting and the effect of melt on the exhumation of the complex. Previous investigations noted the presence of migmatites in the development of tectonic models (e.g., *Spear*, 2004) but have not known the timing of melt crystallization; therefore, the deformation and exhumation history of Valhalla has been incomplete because of the lack of migmatite ages. Models for the exhumation history of the complex must take into account the thermo-mechanical effects of partial melting and the geodynamic consequences of large melt fractions in actively deforming orogenic crust. In addition, the previous argon thermochronology is spatially limited; therefore we lack a sufficient understanding of the cooling pattern for the complex. Moreover, previous workers have proposed that metamorphism of Valhalla was older than that of other domes in the Omineca belt, although the Omineca domes cooled at the same time. This and other aspects of the thermal and tectonic history of the region need to be addressed.

Previous studies of the Valhalla complex therefore leave unresolved important questions about the tectonic evolution of the complex, its relationship to the rest of the Omineca belt, and the timing and mechanisms of flow of partially molten crust during Cordilleran orogenesis. Although the orthogneiss and leucogranites have been the focus of several studies, the migmatites that dominate the Valhalla and Passmore domes have not previously been dated. Because the leucosome fractions occur in a variety of structural sites (e.g., boudin necks), ages of migmatite crystallization can be linked to the deformation history and therefore the tectonic evolution of the complex. Other dome studies have documented a close association of the partial melting and cooling histories [e.g., *Vanderhaeghe et al*., 2003]. Therefore, the combination of U-Th-Pb and $^{40}Ar/^{39}Ar$ geochronology is essential for determining the thermal evolution of the Valhalla

complex. In the following sections, we describe the samples, methods, and results of a U-Pb and $^{40}Ar/^{39}Ar$ study of the Valhalla migmatites and associated rocks.

METHODOLOGY

U-Th-Pb Geochronology

In order to ascertain the duration of partial melting and its relationship to the metamorphic history in the Valhalla complex, *in situ* Th-Pb monazite and U-Pb zircon geochronometry were applied to the migmatitic rocks. Documenting the timing of partial melting of rocks such as migmatites that may have contained precursor zircon and monazite can be a difficult task. Zircon is very refractory during most metamorphic reactions, including reactions that generate melt [*Harrison and Watson*, 1983; *Watson*, 1996] because it exhibits very sluggish U, Th, and Pb diffusion [*Cherniak and Watson*, 2000]. Monazite is similarly problematic for determining the timing of migmatization because it also is highly retentive of radiogenic Pb [*Cherniak et al.,* 2004]. This enables monazite to record multiple thermal events in high-grade metamorphic settings [*Townsend et al*., 2000; *Catlos et al*., 2002; *Nyström and Kriegsman,* 2003; *Vance et al*., 2003]. Because precursor zircon and monazite tend to dominantly record different events in high-grade metamorphic settings (detrital provenance of igneous protolith versus prograde metamorphic events, respectively), combined consideration of the results from both phases offers the soundest basis for evaluating the timing of migmatization.

Ten samples were selected from the Valhalla and Passmore domes on the basis of their potential to yield geochronometric information as a function of structural level, degree of migmatization, and proximity to the detachment (Table 2). Of the ten samples,

five samples with 10 – 50% leucosome were chosen to document the crystallization of partial melt and fluid history; two leucosomes crystallized in boudin necks, two samples of migmatitic quartzofeldspathic gneisses, and a migmatitic paragneiss. In addition, two metapelitic gneiss samples and two samples of garnet-bearing biotite gneiss from between the dome core and the detachment were chosen for *in situ* analyses. One of these samples contains cm- to mm-scale leucocratic layers. The other three occur as ~ 0.5 to 1 m inclusions or pods within metatexite and diatexite; therefore, the samples containing <10% leucosome reveal evidence for both the metamorphic and the partial melting history of the complex. Finally, a sample from the Ladybird unit was collected for analysis to compare the monazite age of the mantling granitoid with the crystallization age of the migmatites.

Samples were analyzed using conventional sectioned and polished grain mounts and through *in situ* analysis of polished 30 μm sections. To produce the grain mounts, samples were crushed and processed using standard density and magnetic methods to concentrate monazite and zircon. The accessory minerals were hand selected, potted in epoxy along with standards, sectioned, polished, and ultrasonically cleaned. Zircon grain mounts were rinsed in 1 *N* HCl to reduce surficial common Pb contamination. For the *in situ* method, monazite grains were located in thin sections, imaged with backscatter (BSE)/cathodoluminescence (CL) techniques. Regions of interest were trimmed with a wafering saw, mounted with prepolished standards, and potted in epoxy following the protocols outlined in the work of *Catlos et al.* [2002]. All epoxy mounts were coated in Au. Features revealed within the BSE and CL imaging of monazite and zircon in Figures 5, 6, and 7 show spatial variation in chemical composition within a single crystal that

potentially correlate with the growth evolution of the crystal. Consequently, we used this imagery to guide selection of analysis sites in both grain and *in situ* ion microprobe age measurements.

For all samples, multiple-spot, single-grain Th-Pb and U-Pb ages were measured using the CAMECA ims1270 ion microprobe facility at the University of California, Los Angeles, following the analytical methods described by *Catlos et al*. [2002] for monazite and *Schmitt et al.* [2003] for zircon. Generally, a 10-15 nA primary O^- ion beam was focused to a ~ 20 x 30 μm spot using aperture-defined illumination. The instrument was tuned to achieve a mass resolving power of ~4500, using a 50 eV energy window and a mechanical "field" that blocked ions derived from the crater walls. The Th-Pb monazite ages were determined relative to the monazite standard 554 [45 ± 1 Ma; *Harrison et al.,* 1999] and the U-Pb zircon ages were determined relative to the zircon age standard AS3 [1099 ± 1 Ma; *Paces and Miller*, 1993]. The Pb/U and Pb/Th relative sensitivity factors were determined to 2-3% using a calibration approach described in *Harrison et al*. [1995]. Flooding of the sample surface with O_2 (3 x 10^{-5} Torr) was performed to increase Pb+ and UO+ ion yields from zircon.

Measured ion intensities were reduced with in-house software written by C.D. Coath (ZIPS v2.4) and further interpreted in ISOPLOT v3 [*Ludwig*, 2003] to obtain weighted average domain ages and $^{206}Pb/^{238}U$ - $^{207}Pb/^{235}U$ concordia diagrams (Fig. 8). For the monazite, Th-Pb dates were plotted on relative probability diagrams in ISOPLOT to determine the major populations of mineral age domains with the criteria that the mean square weighted deviation (MSWD) be maintained below 2.5 for the resulting age distribution (Fig. 9). The weighted average domain ages are calculated to describe the

results but do not necessarily represent discrete igneous or metamorphic events. Errors for the resulting weighted average ages of mineral age domains are reported as ± 2σ. Complete isotopic data from Th-Pb monazite and U-Pb zircon analyses are listed in Tables 3 and 4, respectively.

$^{40}Ar/^{39}Ar$ Thermochronology

To further elucidate the cooling history of the complex, we measured $^{40}Ar/^{39}Ar$ cooling ages for biotite, muscovite, and hornblende. As with monazite and zircon, pure mineral separates (~99%) were prepared using standard density and magnetic techniques. Nine samples were chosen for analysis based on the abundance and quality of the analyzed phases in the samples (six biotite, one muscovite, and three hornblende; see Table 5). The samples were chosen to represent a variety of structural locations, from the core of the Passmore dome to directly beneath the Slocan Lake detachment (Fig. 2A). Four of the samples were also dated by the U-Th-Pb method. Samples for hornblende and biotite were collected within ca. 15 m of each other at any given locality. Note that the hornblende samples share the same prefix in the sample number as nearby biotite samples (e.g., GL-6.1 was from an outcrop near GL-4.1 and GL-12).

Conventional step-heating was conducted at ANU using a double-vacuum, resistance furnace. Argon was purified in an all-metal extraction line and analyzed with a VG1200S mass spectrometer. The heating schedule is shown with the results in Table 6. All ages are calculated with the decay constants recommended by *Steiger and Jäger* [1977]. Errors are reported at the 1σ confidence level. The $^{40}Ar/^{39}Ar$ results are presented as conventional age spectra. Preferred ages shown represent integrated weighted mean

ages calculated for selected portions of each age spectrum (Figs. 10, 11). A preferred age is defined for this investigation as a large part of an age spectrum composed of contiguous increments in which the majority are within 1σ uncertainty in age of neighbouring steps within the subset. The initial low-temperature increasing steps (typically the first 3-5) were not used in calculating the preferred ages. Similarly, the final high-temperature steps were commonly ignored due to elevated furnace blanks at very high temperature (~1350-1450 °C). K/Ca plots are determined from the Ca-derived ^{37}Ar and K-derived ^{39}Ar; we note that the flattest parts of the age spectra generally correspond to relatively high and nearly constant K/Ca values. The results are shown in Figure 10 for hornblende and muscovite, Figure 11 for biotite, and listed in Table 6.

RESULTS

Zircon U-Pb and Monazite Th-Pb Geochronology

Detachment zone and mantling leucogranites

Sample Rt6-4 was collected from the Slocan Lake fault zone along the eastern margin of the complex. It is a tonalitic leucosome that crystallized within a boudin neck. The boudin consists of a ~0.5 m quartzofeldspathic lens rimmed by biotite selvages (see Fig. 4C for stromatic migmatites from the same locality). The outcrop from which this sample was collected consists of > 50% leucocratic material and has been extensively deformed, as indicated by its mylonitic fabric. The sample is from the mixed gneiss unit, and we interpret the locality as the site of abundant leucosome ponding below the Slocan Lake fault zone. The matrix of this sample consists mainly of sericitized plagioclase and recrystallized quartz, with lesser amounts of titanite and biotite defining a weak foliation

(Fig. 3C). Both zircon and monazite are strongly associated with biotite-rich domains. The zircon grains are typically fractured, and, unlike most other migmatitic samples from the complex, they do not exhibit obvious evidence of inheritance in BSE images (Fig. 5A). Seventeen spots on thirteen grains yield a weighted average ^{238}U-^{206}Pb zircon age domain of 60.3 ± 2.0 Ma (MSWD: 2.40; Fig. 5A; 8A). In contrast, the monazite grains yield a younger weighted average Th-Pb age (52.9 ± 1.5 Ma; MSWD: 0.61) from twenty-three spots on seventeen grains (Fig. 9A). The younger monazite age in comparison to the zircon ages is expected as zircon has been shown to be more robust to thermal resetting, and monazite can be more susceptible to thermal and fluid events [*Harrison and Watson*, 1983; *Watson*, 1996; *Teufel and Heinrich*, 1997; *Harlov et al.*, 2006].

Sample ML-7 is representative of the deformed leucogranite that mantles the high-grade core rocks of the Valhalla complex, and was collected ~ 7 km west of the Valhalla dome core (Fig. 2A). The unit contains ~ 1 m long inclusions of amphibolite, calc-silicate, and biotite gneiss, suggesting that the leucogranite invaded part of the mixed gneiss unit. The leucogranite consists of porphyroclasts of quartz and plagioclase that are enveloped by finer-grained recrystallized material of the same composition. Based on the lack of hornblende and presence of monazite, we infer that sample ML-7 is part of the Ladybird leucogranite. The sample also contains minor biotite. Fourteen single-spot analyses reveal a weighted average Th-Pb monazite age domain of 50.8 ± 2.3 Ma (MSWD: 0.25; Fig. 9A).

Migmatites (10 – 50% leucosome)

Four migmatite samples from the mixed gneiss unit with variable leucosome content (10 – 30%) were collected from sites defining a north-south traverse across the complex (Fig. 2A). Sample EL-19 is a migmatitic quartzofeldspathic gneiss collected for *in situ* analysis from the mixed gneiss unit ~ 1 km north of the core of the Valhalla dome. The gneiss is exposed ~ 50 m west of the core orthogneiss and ~1 km northwest of the GCSZ. On a hand-sample scale, the sample has thin (cm- to mm-) leucocratic layers rimmed by biotite selvages and consists of ~20% leucosome. Between the leucosomes, the mesosome consists of interlayered biotite and quartzofeldspathic material. Recrystallized quartz and sericitized plagioclase dominate the matrix, and biotite forms a weak foliation. The monazite grains from this sample are typically ~20-25 μm in size and were analyzed from both biotite and quartzofeldspathic layers of the neosome and mesosome. The grains do not show much evidence for zoning but appear to have corroded edges and some contain cracks. The monazite grains are located: 1) along the edge or within biotite grains or 2) included within quartz grains, commonly along cracks within the grains. A single Th-Pb weighted average age of 54.0 ± 3.6 Ma (MSWD: 1.80) was determined from 16 single-spot monazite analyses performed on 12 grains (Fig. 9B).

Two km west of the Valhalla dome, a migmatitic quartzofeldspathic gneiss with ~30% leucosome (GL-4.1) was collected for Th-Pb monazite analysis from the mantling gneiss (Fig. 2A, 4E). The stromatic migmatite is located ~1 km from the orthogneiss and southwest of the GCSZ. This location, ~ 2 km southwest of the core of the Valhalla dome, contains abundant diatexite (high-melt fraction migmatite) and metatexite. GL-4.1 is a metatexite located ~ 10 m from the diatexite. The deformed matrix of this sample consists mainly of quartz, plagioclase and apatite defining the leucosome with layers of

biotite defining the foliation and melanosome. Both monazite and zircon are abundant accessory phases and are principally located as biotite inclusions in the melanosome as evidenced by numerous radiation haloes surrounding the accessory minerals. Reconnaissance analysis leads us to conclude that zircon is largely inherited from the protolith. In contrast, fourteen single-spot analyses on ten monazite crystals show three weighted average Th-Pb age domains of 54.7 ± 3.1 Ma (MSWD: 1.80), 51.9 ± 1.5 (MSWD: 0.68) and 49.7 ± 1.6 (MSWD: 1.02; Fig. 9B). Furthermore, one of the grains that yielded a 54.7 Ma age also produced an older age of 61.7 ± 2.2 Ma. The latter is very similar to the monazite results from the biotite gneiss samples and the zircon results from the leucosomes that crystallized in boudin necks (Rt6-4 and AC-1.2).

HR-7.1, a garnet-bearing migmatitic paragneiss, is comprised of ~ 10% leucosome and was collected from between the Valhalla and Passmore domes in the mixed gneiss unit in order to understand the north-south trend in migmatite crystallization across the complex. The gneiss consists mainly of quartz with subgrain development, seriticized plagioclase, and K-feldspar. The sample also contains lesser amounts of biotite, garnet, muscovite, sillimanite, apatite, zircon and monazite. Microstructures such as a checkerboard extinction pattern in the quartz and interstitial quartz and plagioclase growth suggest high-temperature deformation and partial melting. The monazites yield a range of Th-Pb ages from 73 to 48 Ma with multiple ages clustering near ca. 58 Ma (Fig. 9B). The entire sample of HR-7.1 was crushed, and the monazite grains were analyzed in a standard grain mount; therefore, monazite from leucosomes and mesosomes were mixed together, and this probably explains the wide distribution in ages. In thin section, the monazite is located in a variety of textural settings such as inclusions within garnet,

biotite, quartz, and along boundaries between K-feldspar grains. The garnet contains cracks; however, the monazite does not occur along these cracks. Thus, perhaps the older monazite ages represent monazite included in garnet that was armored from thermal or fluid resetting.

Leucosome from a boudin neck (AC-1.2) was collected in the Passmore dome. The sample was located in the western limb of the GCSZ, in a lesser-deformed part of the shear zone (Fig. 2A). Similar to Rt6-4, the Slocan Lake boudin neck, the boudins adjacent to AC-1.2 also contain abundant leucosome of the same composition. The leucosome is granitic in composition: quartz + plagioclase + K-feldspar + biotite + hornblende + titanite + zircon ± muscovite ± monazite. Sericite is abundant, as are myrmekitic textures. Zircons yield a weighted mean ^{238}U-^{206}Pb result of 60.2 ± 3.0 Ma (MSWD: 2.80; Figs. 5B, 8B). In thin section, the zircons were all included within quartz and plagioclase grains. We were only able to obtain two monazite grains from the crushed sample. The two grains yielded Th-Pb ages of 56.5 ± 2.0 Ma and 51.7 ± 1.9 Ma, which are similar to results from migmatite samples with 10 – 50% leucosome.

Biotite gneiss and metapelite (<10% leucosome)

Four metasedimentary samples with <10% leucosome were collected and analyzed to understand the relationship of the metamorphic history to partial melting. Three of the four samples were collected ~2 km southwest of the GCSZ in the Valhalla dome core (Fig. 2A). This area contains abundant metatexite (migmatite with 10-50% leucosome) and diatexite (high-melt fraction migmatite), including some migmatite with > 75 % leucosome [*Schaubs and Carr*, 1998; this study]. The biotite gneiss and

metapelitic rocks in this region are included within and invaded by granitic leucosomes and dikes. The fourth sample, from the western limb of the GCSZ in the Passmore dome, is used for comparison of the domes.

In the mixed gneiss unit, GL-2.1, a garnet-sillimanite metapelite was obtained from ~ 2 km southwest of the Valhalla dome core for *in situ* Th-Pb monazite analyses. The metapelite was found as a pod within migmatitic (~30% leucosome) quartzofeldspathic gneiss. The sample consists of thick biotite/sillimanite layers that define foliation and exhibit mm-scale folds. The matrix also consists of minor plagiocase and K-feldspar and accessory garnet, corundum, apatite, zircon and monazite. The garnets have a corona of plagioclase and chlorite ± biotite. BSE images of the monazite grains reveal that monazite inclusions in biotite are large (~35 μm) and zoned, whereas monazite inclusions in garnet are commonly small (~15 μm). Monazite is not abundant in this sample; therefore, only five individual spot analyses on three grains were obtained. These analyses yield a Th-Pb weighted average domain age of 59.9 ± 4.2 Ma (MSWD: 0.092; Fig. 6A, 9C).

Sample GL-12 represents a garnet-bearing biotite gneiss that was collected ~ 2 km southwest of the core of the Valhalla dome. The gneiss occurs as a 1 m long raft in diatexite from the same locality as sample GL-4.1 (Fig. 4F). The gneiss is medium-grained with a matrix consisting of quartz, plagioclase, biotite, garnet, apatite, monazite, zircon ± epidote. Biotite defines a strong foliation in the rock. BSE images of GL-12 show that monazite grains are typically ~15-20 μm, have patchy zoning (Fig. 6B, C) and corroded edges, and occur within garnets and biotite, commonly near or along cracks. The compositional zones of each crystal could not be analyzed because of the shape and

small size of the grains in comparison to the spot size. However, the results are bimodal, and a total of seven *in situ* analyses yield one weighted mean Th-Pb age of 70.0 ± 4.5 Ma (MSWD: 0.22). The second age population consisted of four monazite ages that ranged from 65.6 Ma to 59.5 Ma (Fig. 6B,C; 9C). The age domains do not correlate in any clear fashion with the textural location of the monazite (inclusions in garnet vs. biotite), suggesting that garnet may not always armor inclusions from thermal resetting.

Sample DL-1.1, a garnet-bearing biotite gneiss, was collected from ~ 4 km southwest of the Valhalla core, south of GL-4.1 and GL-12 (Fig. 2A). The gneiss was selected for analysis because it contains cm- to mm-scale leucosomes. The sample is a fine- to medium-grained rock containing mainly quartz exhibiting subgrain development, plagioclase, and biotite. Individual garnet crystals are elongate parallel to the foliation defined by biotite. Monazite and zircon occur in both mesosome and leucosome. BSE images show that the size of the monazite grains is bimodal: one population is ~35 μm in size and the other is ~15 μm (Fig. 6 D,E,F). The grains are located both within and bordering garnet grains (Fig. 7A). Furthermore, monazite was also analyzed from the biotite matrix and leucocratic layers. Twenty-one single-spot analyses on fourteen monazite grains reveal two *in situ* Th-Pb weighted mean ages of 65.8 ± 3.8 Ma (MSWD: 0.89) and 57.4 ± 4.2 Ma (MSWD: 1.60; Fig. 6D,E,F; 7A, 9C). Like other gneiss samples, the age domains are not correlated with the monazite location or with spot location (core vs. rim).

To the south, in the core of the Passmore dome, sample AC-20.1 is a garnet-sillimanite-K-feldspar metapelite. Like AC-1.2, the metapelite was collected from the western limb of the GCSZ, in a low strain part of the shear zone. As in many locations

throughout the complex, the metapelite was found as a ~ 0.5 m pod within migmatitic (~20% leucosome) quartzofeldspathic gneiss. The matrix of the sample consists of abundant biotite, quartz, plagioclase, sillimanite, and cordierite, and accessory apatite, zircon, and monazite (Fig. 7B). Thick biotite and sillimanite layers define foliation and are folded on the mm-scale. This sample was analyzed with the *in situ* technique to compare ages of matrix monazite vs. monazite inclusions in garnet. The monazite grains are typically small (~25 μm) with patchy zoning and irregular/cracked edges. A Th-Pb monazite age of 64.5 ± 2.4 Ma (MSWD: 1.05) was determined from sixteen single-spots on ten grains while twenty-one spots on fifteen grains yield a second weighted average domain age of 60.1 ± 2.4 (MSWD: 1.40; Fig. 7B, 9C). The single-spot ages show no correlation based on location (i.e., garnet versus matrix). In some cases, the monazite ages are similar to the ages found in the matrix, while in other cases the monazite yield younger ages. The younger monazite inclusion ages seem to be located along cracks within the crystal (e.g., Fig. 7B). Previous studies have shown that cracks within the garnet may allow a fluid phase to alter the Th-Pb system of monazite, resetting the monazite age and revealing that garnet does not always shield its inclusions from isotopic disturbances [e.g., *DeWolf et al.*, 1993; *Montel et al.*, 2000; *Carson et al.,* 2004].

^{40}Ar/^{39}Ar Analyses

Three hornblende-bearing samples along a north-south traverse through the complex were analyzed: one sample from ~ 2 km southwest of the Valhalla dome, one from the GCSZ in the Passmore dome and one from between the two domes (Fig. 2A). The step-heating analyses for hornblende from all three samples yields discordant and

irregular age spectra (Fig. 10 A,B,C). Hornblende from the amphibolite GL-6.1 appears to be the most reliable and yields a $^{40}Ar/^{39}Ar$ total gas age of 55.5 ± 0.9 Ma and a preferred age of 54.3 ± 0.4 Ma (Fig. 10A). Inverse isochron analysis of the data for GL-6.1 yields a similar model age with a near atmospheric intercept. Hornblende from an amphibolite located between the two domes is more problematic. Sample HR-4.1 yields a total gas age of 89.3 ± 0.5 Ma (Fig. 10B). Because the K/Ca ratio for this sample is low (~ 0.035), the radiogenic argon component could easily be overwhelmed by excess ^{40}Ar. Hornblende from an amphibolite collected from the GCSZ in the Passmore dome core, AC-1.3, yields a total gas age of 79.4 ± 0.8 Ma (Fig. 10C). The youngest steps of the spectrum are combined for a preferred age of 60.3 ± 0.5 Ma. Like HR-4.1, the Passmore amphibolite also shows a low K/Ca ratio of ~0.13 and a $^{40}Ar/^{36}Ar$ intercept ratio of 602.0 ± 73.0 that probably indicates excess ^{40}Ar.

Sample PR-2.1, was collected from ~ 1 km structurally above the GCSZ in the Passmore dome. The rock is not as intensely deformed as rocks from within the shear zone. The garnet-bearing metapelite contains a two-mica assemblage with muscovite, biotite, quartz, plagioclase, sillimanite, and lesser amounts of garnet, titanite, zircon and monazite. The age spectrum yielded by the muscovite is somewhat irregular and yielded a total gas and preferred age of 53.8 ± 1.6 Ma and 54.7 ± 1.1 Ma, respectively (Fig. 10D). Isochron analysis is not useful due to the large error on the $^{40}Ar/^{36}Ar$ intercept. The discordance of the results led us to discount them.

Sample VP-2.1, a medium- to coarse-grained leucogranite, was collected within ~1 km of the Valkyr shear zone on the western side of the complex (Fig. 2A). The sample contains quartz with subgrain development, myrmekitic plagioclase that has been

extensively sericitized, and lesser amounts of biotite, sphene and zircon. Furthermore, the leucogranite has micro-shear zones where recrystallization is focused. The biotite from this sample reveals a discordant spectrum, which yields a total gas age of 53.1 ± 1.0 Ma, and a preferred age of 53.1 ± 0.3 Ma (Fig. 11A).

Sample GL-4.1, the migmatitic quartzofeldspathic gneiss from ~ 2 km west of the Valhalla dome core, yields consistent integrated, preferred, and isochron ages of 50.9 ± 0.4 Ma, 50.6 ± 0.2 Ma, and 51.0 ± 0.2 Ma, respectively (Fig. 11B). The migmatitic paragneiss from between the Valhalla and Passmore domes, sample HR-7.1, has a preferred age of 49.1 ± 0.4 Ma with ~60% of the gas released from these steps (Fig. 11C).

Two biotite-bearing samples from the Passmore dome were analyzed: 1) sample PR-2.1, a garnet-bearing paragneiss that has a preferred age of 48.6 ± 0.5 Ma (Fig. 11D); and 2) sample AC-1.2, a leucosome crystallized in a boudin neck located in the western limb of the GCSZ, which yields an older total gas age of 52.5 ± 0.6 Ma (Fig. 11E). A preferred age of 51.4 ± 0.4 Ma was calculated from the data for AC-1.2. After the eighth step, the steps have a very low K/Ca ratio, suggesting that feldspar inclusions may have contaminated this sample.

The youngest age revealed from a biotite separate is from a leucosome crystallized in a boudin neck (Rt6-4) along the eastern bounding Slocan Lake fault. The biotite from the mylonitic migmatite yields a preferred age of 48.2 ± 0.5 Ma with 96% of the gas released (Fig. 11F). The sample also yields similar integrated and isochron ages: 48.2 ± 0.6 Ma and 48.5 ± 0.2 Ma, respectively.

TIMING OF MIGMATIZATION

Combined with the results of previous investigations (Table 1), the U-Pb monazite and zircon geochronology results presented above indicate that the Valhalla complex records a protracted thermal history from the Late Cretaceous to the Eocene (Fig. 12) [*Carr et al*., 1987; *Parrish et al*., 1988; *Heaman and Parrish*, 1991; *Parrish*, 1995; *Spear and Parrish*, 1996; *Ducea et al.*, 2003; *Spear*, 2004]. *In situ* monazite analyses for three of the four metasedimentary samples with <10% leucosome reveal a bimodal age distribution of ca. 70-65 Ma and 62-57 Ma (Fig. 6, 9). The older age group is consistent with previous single crystal monazite and zircon TIMS results of paragneiss from the cores of the Valhalla and Passmore domes [*Heaman and Parrish*, 1991; *Spear and Parrish*, 1996]. The previously documented Late Cretaceous ages, combined with the 70-65 Ma ages from this investigation, indicate the timing of prograde metamorphism during regional convergent tectonics, crustal thickening, and subsequent thermal relaxation. Geochronometric results from paragneiss of the mixed gneiss unit suggest that the Valhalla complex subsequently achieved near peak metamorphic conditions of 820 ºC and 8 kbar at ca. 60 Ma [*Spear*, 2004]. The present study is consistent with this interpretation: all four metapelite and biotite gneiss samples have monazite ages of 62-57 Ma (Fig. 6, 9).

U-Pb zircon dating of migmatitic samples with variable leucosome (10 - 50%) content from throughout the complex reveals that crystallization of migmatites occurred at or soon after peak metamorphism at ca. 60 Ma (Fig. 5, 8), suggesting a rapid high-temperature cooling event, possibly driven by upward flow of buoyant melt. Previous zircon TIMS analyses from a highly sheared and mylonitized pegmatite and from the

Airy and Ladybird units yielded ca. 60 Ma ages [*Carr et al.,* 19987; *Parrish et al.,* 1988; *Spear and Parrish*, 1996], consistent with the boudin neck zircon ages. Furthermore, the younger age grouping (62-57 Ma) from the metapelite and biotite gneiss samples analyzed in this study is also similar to the zircon ages. In comparison, monazite from metatexite, the boudin neck samples, and from the Ladybird leucogranite range from ca. 60 Ma to 50 Ma. Previous monazite analyses (61-52 Ma) [*Parrish*, 1995] of texturally late granitic bodies (veins in the core orthogneiss, slightly deformed pegmatite and aplite samples) yielded similar ages to the monazite analyzed in this study.

The preponderance of new and previously obtained U-Th-Pb zircon and monazite results centered around ~60 Ma [*Parrish*, 1984; *Carr et al.*, 1987; *Parrish et al.*, 1988; this study] indicate that prograde regional metamorphism, anatexis, and crystallization of the Airy and Ladybird granitoids peaked at this time. Furthermore, because deformation and migmatite crystallization is recorded at the structurally highest position in the Slocan Lake fault zone and at the deepest position as represented by the western limb of the Passmore GCSZ, it seems that the entire complex experienced a major tectonothermal event at ca. 60 Ma and that melt crystallization was coeval at all structural levels. The geochronometric results suggest that partial melting was a major component of the tectonic evolution of the Valhalla complex until relatively late (~ 60 Ma).

The fact that Th-Pb monazite ages are as young as ca. 50 Ma may indicate protracted anatectic conditions (i.e., 60-50 Ma or ca. 10 m.y.). Melt crystallization from ca. 60 to 50 Ma would be consistent with migmatite crystallization ages reported from other Omineca domes, which also expose abundant migmatite [*Vanderhaeghe et al.,* 1999b; *Crowley et al.*, 2001; *Hinchey et al.,* 2006; *Kruckenberg et al.,* ms]. For example,

zircon rims from Thor-Odin migmatite and magmatic zircons from pegmatite and aplite that cut the host gneiss of the Frenchman Cap dome have ages of ca. 56-52 Ma [*Vanderhaeghe et al.,* 1999b; *Hinchey et al*., 2006] and ca. 58-49.5 Ma [*Crowley et al*., 2001], respectively. Monazite results from the mantling migmatitic gneisses and leucogranites range from ca. 60-53 Ma [*Carr*, 1992; *Teyssier et al.,* 2005]. Furthermore, zircon and monazite in migmatites of the Okanogan dome, at the southern end of the Omineca belt in Washington (USA), yield U-Pb ages of 61-49 Ma [*Kruckenberg et al*., ms].

In spite of this overlap in age with the other domes, the spread in monazite Th-Pb ages from the Valhalla complex down to 50 Ma might simply reflect loss of radiogenic Pb. Although recent experimental data indicate that Pb loss from monazite is unlikely to have occurred via diffusion [*Cherniak et al.*, 2004], Pb loss via fluid-mediated recrystallization is a real possibility. Experimental and field-based investigations of monazite have shown that monazite is prone to recrystallization in fluid-rich environments, such as ductile shear zones [e.g., *Hawkins and Bowring*, 1997; *Teufel and Heinrich*, 1997; *Ayers et al.*, 1999; *Townsend et al.,* 2000; *Cherniak et al.*, 2004*; Ayers et al.*, 2006; *Harlov et al.*, 2006]. In the case of the Valhalla complex, many of the monazite grains reveal patchy zoning (e.g., Fig. 6). The textures observed in the grains have been interpreted by others to indicate fluid-mediated recrystallization in monazite [e.g., *Townsend et al.*, 2000]. This phenomena has been recognized within other regions of the Omineca belt. For example, *Crowley and Ghent* [1999] have documented the presence of Tertiary age domains that they attributed to fluids that disturbed the U-Pb isotope system and dissolved Proterozoic monazite in the Frenchman Cap dome.

The migmatites of Valhalla are bounded by the Valkyr shear zone/Slocan Lake fault system. Since the Valkyr shear zone and the Slocan Lake fault were active during the Paleocene and Eocene [*Carr et al.*, 1987], it is likely that they facilitated significant high-temperature fluid flow as crystallizing migmatites and mantling leucogranites released fluids. Deformation would have enhanced fluid flow, thus also contributing to dynamic recrystallization of monazite.

COOLING AND EXHUMATION

What emerges from the geochronometric investigations of the Omineca belt is that the domes experienced Late Cretaceous to Early Tertiary high-grade metamorphism, significant partial melting in the Paleocene, and cooling in the Early Tertiary following crystallization of the melt at ca. 60 Ma (Fig. 13). Our 51-48 Ma biotite $^{40}Ar/^{39}Ar$ ages combined with previous ca. 52-47 Ma muscovite K-Ar ages [*Wanless et al.,* 1978, 1979; *Parrish*, 1995] require that the Valhalla complex was exhumed through ca. 350 ºC at this time (Fig. 11). Although the muscovite and hornblende ages from this study are somewhat older, excess ^{40}Ar complicates their interpretation (Fig. 10). The most reliable results from hornblende GL-6.1 indicate that lower amphibolite facies conditions persisted to ca. 55.5 Ma, similar to previous hornblende results [*Wanless et al*., 1978, 1979; *Parrish*, 1995]. In any case, our $^{40}Ar/^{39}Ar$ results are consistent with the Eocene cooling history documented by previous K-Ar results on hornblende, muscovite and biotite from the core orthogneiss body and the Ladybird leucogranite [*Wanless et al*., 1978, 1979; *Parrish*, 1984; *Parrish et al.*, 1988; *Heaman and Parrish*, 1991]. Moreover,

thermochronometric studies from Thor-Odin and Frenchman Cap yield ages of ca. 49.5 to 48 Ma for $^{40}Ar/^{39}Ar$ muscovite and biotite [*Vanderhaeghe et al*., 2003].

Models for the exhumation of the high-grade rocks exposed in Valhalla need to consider the evidence for large volumes of partially molten crust and leucogranite that crystallized at ca. 60 Ma, isothermal decompression recorded in symplectitic textures (including replacement of kyanite by cordierite and sillimanite) [*Marshall and Simandl*, 2006], argon cooling ages, and thermal and diffusion modeling that indicates an early (by ca. 60 Ma), rapid cooling rate in excess of 100 ºC/m.y. [*Spear*, 2004]. Here we consider three models proposed for the exhumation of the Valhalla migmatites and associated rocks: 1) thrusting accompanied by erosion and/or tectonic denudation; 2) channel flow accompanied by erosion and/or tectonic denudation; or 3) extension, accompanied by vertical flow of partially molten crust (Fig. 14).

Previously, the high temperature (older than ca. 60 Ma) cooling of the Valhalla complex has been viewed in terms of being driven by thrusting of the complex onto a footwall with a lower ambient temperature. This model is based on geochronology, thermal and diffusion modeling, and mapping of a thrust zone (Fig. 14A) [*Parrish et al.*, 1988; *Parrish*, 1995; *Spear and Parrish*, 1996; *Schaubs et al*., 2002; *Spear,* 2004; *Carr and Simony*, 2006]. The thrust model holds that a 30 km thick coherent crystalline thrust sheet was translated eastward along the Gwillim Creek shear zone, rapidly cooling the high-grade rocks exposed in the complex. Previous investigations have suggested that the Gwillim Creek shear zone is linked to regional thrusting in the foreland fold and thrust belt [*Parrish et al*., 1988; *Brown et al.*, 1992; *Varsek and Cook*, 1994; *Carr and Simony*, 2006]. *Spear* [2004] suggested that the presence of melt may have enhanced the thrusting

of the complex, noting that the crystallization ages at ca. 60 Ma are coeval with the end of deformation in the Gwillim Creek shear zone. Subsequently, previous studies suggest that final cooling of the complex took place at a slower cooling rate and was driven by extensional faulting beginning at ca. 55 Ma [*Parrish et al.*, 1988; *Parrish*, 1995; *Spear and Parrish*, 1996; *Schaubs et al*., 2002; *Spear,* 2004; *Carr and Simony*, 2006; this study].

Lateral flow of partially molten crust through a channel may also account for some of the observations seen in the Valhalla complex (Fig. 14B). The Gwillim Creek shear zone would serve as the base of a partially molten channel. Lateral flow must be accompanied by focused denudation to allow for material to be extruded from the mid- to lower-crust. The extrusion and erosion could have produced the decompression, cooling, and exhumation of the Valhalla complex if extrusion were rapid. *Carr and Simony* [2006] proposed that channel flow may have developed within the infrastructure of the thrust sheet that moved along the Gwillim Creek shear zone, but argued that crustal flow was not the main orogenic process in Valhalla.

The arching and continuous nature of the Slocan Lake fault and the Valkyr shear zone suggests that the two faults are one continuous rolling hinge detachment fault that may have played a major role in the exhumation of the Valhalla complex (Fig. 14C). A rolling hinge detachment zone allows exhumation of ductile footwall rocks as high-angle normal faults sequentially form, rotate, and become inactive [*Buck*, 1988, 1991]. The Slocan Lake-Valkyr shear zone system is very similar to the detachment system invoked by *Teyssier et al*. [2005] to explain the rapid decompression, melting, and exhumation of the Thor-Odin dome. In both domes, there is a slight west to east younging in biotite

cooling ages, and this is consistent with a rolling hinge detachment zone geometry. Furthermore, beginning of movement along the rolling hinge detachment in the Paleocene could have driven the upward flow of high-grade migmatites, creating the decompression textures preserved in the gedrite-cordierite rocks, generating melt, and producing the high cooling rates suggested by *Spear* [2004]. With upward flow, cooling and crystallization of the migmatites would progress downward. The late crystallization releases fluids that may have participated in the recrystallization of monazite. In this model, the Gwillim Creek shear zone is a relic thrust or possibly an high-grade extensional shear zone located within the partially molten crust.

Both the thrusting and channel flow models require syn-thrusting extension of the upper crust and/or very rapid, localized erosion to produce the isothermal decompression textures preserved in the gedrite-cordierite rocks. Based on argon thermochronology, extension and denudation did not occur until ca. 53 Ma; therefore, these upper-crustal processes could not have coupled with the thrusting to induce decompression.

To the north of the Valhalla complex, the Thor-Odin dome exposes abundant metatexite and diatexite in the core of the dome. Exhumation models for Thor-Odin have suggested a model in which extension driven by a rolling hinge detachment and accompanied by upward flow of a partially molten crust exhumed the diatexitic core of the dome [*Vanderhaeghe et al.*, 1999a,b, 2003; *Norlander et al.*, 2002; *Teyssier et al.*, 2005]. Based on the similar geology and proximity of the Valhalla and Thor-Odin domes in the Omineca belt, we suggest that extension associated with a rolling hinge detachment also best explains the metamorphic, geochronologic, and structural features of the Valhalla complex.

The eastern bounding detachment systems of the Omineca core complexes have similar tectonic and thermal histories. For example, both the Slocan Lake fault (Valhalla) and the Columbia River fault (Thor-Odin, Frenchman Cap) had melt pool below them and cooled through biotite closure of Ar diffusion at 50-48 Ma [*Vanderhaeghe et al*., 2003; this study]. In addition, kinematic indicators for all three domes show top-to-the-east sense of shear near the eastern detachments. Field studies and geochronologic results suggest that the eastern bounding detachment systems for the Omineca domes served as a major thermal boundary between the rigid, cold crust of the Rocky Mountain foreland and the partially molten crust of the hot hinterland. Lithoprobe profiles [*Cook et al.*, 1988] through Passmore dome have imaged the Slocan Lake fault and have revealed that the fault extends down to near the base of the crust, further supporting that the Slocan Lake fault formed a major thermal and mechanical boundary. The slightly older $^{40}Ar/^{39}Ar$ biotite results from the Valhalla complex suggest that the Valkyr shear zone-Slocan Lake fault may in fact represent the breakaway of the detachment system.

Within the north-south trending series of Omineca domes, the Slocan Lake fault is offset from the other eastern detachment, the Columbia River fault, that forms the eastern boundary for the Thor-Odin, Frenchman Cap, and Okanogan-Kettle domes (Fig. 1). Minor differences in the tectonic and thermal histories of Valhalla relative to the other domes of the Omineca belt may well be a consequence of its easterly position and resulting proximity to the cold crust of the Rocky Mountain foreland. For example, while the available geochronology indicates that migmatization, peak grade metamorphism, and leucogranite crystallization within the Valhalla complex peaked at ca. 60 Ma, it continued to later times in the domes situated further west. We infer that that the more westerly

domes were better insulated from the cold crust of the Rocky Mountain foreland. Such a relationship may be indicated by the lack of diatexite in the core of the Valhalla complex and its occurrence within the cores of the more westerly domes. Perhaps, as the detachment that serves as the boundary between the flowing crust and cold foreland stepped to the west (i.e., the present locality of the Columbia River fault), the system was able to access hotter, deeper, and better insulated crust. Thus the rocks exposed in the Valhalla complex are at a higher structural level than the core rocks of the other Omineca domes (Fig. 14C) [*Parrish*, 1995; this study].

CONCLUSIONS

New and previously obtained U-Pb zircon results for the Valhalla complex centered around ~60 Ma indicate that prograde regional metamorphism, anatexis, and crystallization of mantling leucogranite all peaked at this time. Although the overall duration of partial melting cannot be confidently determined, the pervasive occurrence of leucosomes, leucogranite, and other granitic bodies, and their close association with deformation features throughout the complex at all structural levels, indicate that melt likely played a prominent role in the Paleocene tectonic evolution of the Valhalla complex. The evidence for high-temperature decompression and the understanding of the timescales of melt crystallization and extension suggest that vertical flow of melt combined with a rolling hinge detachment probably drove the decompression, partial melting, exhumation, and rapid cooling of the Valhalla complex. Although the Thor-Odin and Frenchman Cap domes to the north expose somewhat different structural levels and appear to have experienced slightly different histories, we believe that a large region

(thousands of km^2) of orogenic crust along the eastern margin of the southern British Columbian segment of the Cordillera was likely partially molten in the Early Tertiary (ca. 60-50 Ma) and then cooled at ca. 51-48 Ma. We speculate that the upward flow, cooling, and crystallization of partially molten crust that now forms the core and the mantling gneisses of the Omineca domes marks the end of Cordilleran orogenesis, and may indicate that continental orogeny ends when the transfer of heat during lateral and vertical crustal flow results in the widespread crystallization of the partially molten crust.

ACKNOWLEDGMENTS. This research was supported by the NSF grant EAR-0409776, the Department of Geology and Geophysics at the University of Minnesota, and a GSA student research grant. We thank Axel Schmitt for assistance in carrying out ion microprobe measurements. The ion microprobe facility at UCLA is partly supported by a grant from the Instrumentation and Facilities Program, Division of Earth Sciences, National Science Foundation. We thank the Australian Institute of Nuclear Science and Engineering and the Australian Nuclear Technology Organization for facilitating irradiation of minerals. The paper benefited from constructive reviews from Mike Wells and Randy Parrish. We also thank A. Fayon, G. Baird, E. Goergen, F. Korhonen, R. McFadden, and S. Kruckenberg for assistance in the field and laboratory.

REFERENCES

Archibald, D.A., J.K. Glover, R.A. Price, E. Farrar, and D.M. Carmichael (1983), Geochronology and tectonic implications of magmatism and metamorphism, southern Kootenay arc and neighboring regions, southeastern British Columbia. Part I: Jurassic to mid-Cretaceous, *Can. J. Earth Sci.*, *20*, 1891-1913.

Armstrong, R.L. (1982), Cordilleran metamorphic core complexes – From Arizona to southern Canada, *Annu. Rev. Earth Planet. Sci.*, *10*, 129-154.

Armstrong, R.L., and P.L. Ward (1991), Evolving geographic patterns of Cenozoic magmatism in the North American Cordillera; the temporal and spatial association of magmatism and metamorphic core, *J. Geophys. Res.*, *96*, 13201-13224.

Ayers, J.C., C. Miller, B. Gorisch, and J. Milleman (1999), Textural development of monazite during high-grade metamorphism: hydrothermal growth kinetics, with implications for U-Th-Pb geochronology, *Am. Mineral., 84*, 1766-1780.

Ayers, J.C., M. Loflin, C.F. Miller, M.D. Barton, and C.D. Coath (2006), In situ oxygen isotope analysis of monazite as a monitor of fluid infiltration during contact metamorphism: Birch Creek Pluton aureole, White Mountains, eastern California, *Geology, 34*, 653-656.

Bird, P. (1991), Lateral extrusion of lower crust from under high topography, in the isostatic limit, *J. Geophys. Res.*, *96*, 10275-10286.

Block, L., and L.H. Royden (1990), Core complex geometries and regional scale flow in the lower crust, *Tectonics*, *9*, 557-567.

Brace, W.F., and D.L. Kohlstedt (1980), Limits on lithospheric stress imposed by laboratory experiments, *J. Geophys. Res.*, *85*, 6248-6252.

Brown, R.L., and P.B. Read (1983), Shuswap terrane of British Columbia: A Mesozoic "core complex," *Geology*, *11*, 164-168.

Brown, R.L., J.M. Journeay, L.S. Lane, D.C. Murphy, and C.J. Rees (1986), Obduction, backfolding and piggyback thrusting in the metamorphic hinterland of the southeastern Canadian Cordillera, *J. Struct. Geol.*, *8*, 255-268.

Brown, R.L., S.D. Carr, B.J. Johnson, V.J. Coleman, F.A. Cook, and J.L. Varsek (1992), The Monashee decollement of the southern Canadian Cordillera: A crustal scale shear zone linking the Rocky Mountain foreland to the lower crust beneath accreted terranes, in *Thrust tectonics*, *Special Publication,* edited by K.R. McClay, pp. 357-364, Geol. Soc-Lon.

Buck, W.R. (1988), Flexural rotation of normal faults, *Tectonics, 7*, 959-973.

Buck, W.R. (1991), Mode of continental lithospheric extension, *J. Geophys. Res., 96*, 20161-20178.

Carr, S.D. (1985), Ductile shearing and brittle faulting in Valhalla gneiss complex, southeastern British Columbia, *Geol. Surv. Can. Pap.*, *85-1A*, 89-96.

Carr, S.D. (1986) The Valkyr shear zone and the Slocan Lake fault zone: Eocene structures that bound the Valhalla gneiss complex, southeastern British Columbia, M.S. thesis, 106 pp., Carleton University, Ottawa.

Carr, S.D. (1991), U-Pb zircon and titanite ages of three Mesozoic igneous rocks south of the Thor-Odin-Pinnacles area, southern Omineca Belt, British Columbia, *Can. J. Earth Sci., 28*, 1877-1882.

Carr, S.D (1992), Tectonic setting and U-Pb geochronology of the early Tertiary Ladybird leucogranite suite, Thor-Odin-Pinnacles area, southern Omineca belt, British Colombia, *Tectonics*, *11*, 258-278.

Carr, S.D., and P.S. Simony (2006), Ductile thrusting versus channel flow in the southeastern Canadian Cordillera: evolution of a coherent crystalline thrust sheet, in *Channel flow, Extrusion, and Exhumation in Continental Collision Zones, Special Publications*, vol. 268, edited by R.D. Law, M.P. Searle and L. Godin, pp. 561-587, Geol. Soc.-Lon.

Carr, S.D., R.R. Parrish, and R.L. Brown (1987), Eocene structural development of the Valhalla complex, southeastern British Columbia, *Tectonics*, *6*, 175-196.

Carson, C.J., R.G. Berman, R.A. Stern, M. Sanborn-Barrie, T. Skulski, and H.A.I. Sandeman (2004), Age constraints on the Paleoproterozoic tectonometamorphic history of the Committee Bay region, western Churchill Province, Canada: evidence from zircon and in situ monazite SHRIMP geochronology, *Can. J. Earth Sci., 41*, 1049-1076.

Catlos, E.J., L.D. Gilley, and T.M. Harrison (2002), Interpretation of monazite ages obtained via in situ analysis, *Chem. Geol.*, *188*, 193-215.

Cherniak, D.J., and E.B. Watson (2000), Pb diffusion in zircon, *Chem. Geol.*, *172*, 5-24.

Cherniak, D.J., E.B. Watson, M. Grove, and T.M. Harrison (2004), Pb diffusion in monazite: A combined RBS/SIMS study, *Geochim. Cosmochim. Acta*, *68*, 829-840.

Clark, M.K., and L.H. Royden (2000), Topographic ooze: Building the eastern margin of Tibet by lower crustal flow, *Geology*, *28*, 703-706.

Coney, P.J (1980), Cordilleran metamorphic core complexes; an overview, in *Cordilleran metamorphic core complexes: Boulder, Colorado*, vol. 153, edited by M.D. Crittenden, P.J. Coney, and G.H. Davis, pp. 7-34, Geol. Soc. Am. Memoir.

Coney, P.J., and T.A. Harms (1984), Cordilleran metamorphic core complexes: Cenozoic extensional relics of Mesozoic compression, *Geology*, *12*, 550-554.

Coney, P.J., D.L. Jones, and J.W.H. Monger (1980), Cordilleran suspect terranes, *Nature*, *288*, 329-333.

Cook, F.A., P.S. Simony, K.C. Coflin, A.G. Green, B. Milkereit, R.A. Price, R. Parrish, C. Patenaude, P.L. Gordy, and R.L. Brown (1988), Lithoprobe southern Canadian Cordilleran transect: Rocky Mountain thrust belt to Valhalla gneiss complex, *Geophys. J. R. Astron. Soc.*, *89*, 91-98.

Crittenden, M.D., P.J. Coney, G.H. Davis (1980), Cordilleran metamorphic core complexes, *Geol. Soc. Am. Memoir*, *153*, 496.

Crowley, J. (1997a), U-Pb geochronologic constraints on the cover sequence of the Monashee complex, Canadian Cordillera: Paleoproterozoic deposition on basement, *Can. J. Earth Sci., 34*, 1008-1022.

Crowley, J. (1997b), U-Pb geochronology in Frenchman Cap dome of the Monashee Complex, Southern Canadian Cordillera: Early Tertiary tectonic overprint of a Proterozoic history, Ph.D. thesis, 219 pp., Carleton University, Ottawa.

Crowley, J.L., and E.D. Ghent (1999), An electron microprobe study of the U-Th-Pb systematics of metamorphosed monazite: the role of Pb diffusion versus overgrowth and recrystallization, *Chem. Geol.*, *157*, 285-302.

Crowley, J.L., R.L. Brown, and R.R. Parrish (2001), Diachronous deformation and a strain gradient beneath the Selkirk allochthon, northern Monashee complex, southeastern Canadian Cordillera, *J. Struct. Geol.*, *23*, 1103-1121.

Dell'Angelo, L.N., J. Tullis, and R.A. Yund (1987), Transition from dislocation creep to melt-enhanced diffusion creep in fine-grained granitic aggregates, *Tectonophysics*, *139*, 325-332.

DeWolf, C.P., N. Belshaw, and R.K. O'Nions (1993), A metamorphic history from micron-scale $^{207}Pb/^{206}Pb$ chronometry of Archean monazite, *Earth Planet. Sci. Lett., 120*, 207-220.

Dilek, Y., and E.M. Moores (1999), A Tibetan model for the Early Tertiary western United States, *J. Geol. Soc.-Lon.*, *156*, 929-941.

Ducea, M.N., J. Ganguly, E.J. Rosenberg, P.J. Patchett, W. Cheng, and C. Isachsen (2003), Sm-Nd dating of spatially controlled domains of garnet single crystals: a new method of high-temperature thermochronology, *Earth Planet. Sci. Lett.*, *213*, 31-42.

Duncan, I.J. (1984), Structural evolution of the Thor-Odin gneiss dome, *Tectonophysics*, *101*, 87-130.

England, P.C., and A.B. Thompson (1986), Some thermal and tectonic models for crustal melting in continental collision zones, in *Collision Tectonics*, vol. 19, edited by M.P. Coward and A.C. Ries, pp. 83-94, Geol. Soc.-Lon.

Goetze, C., and B. Evans (1979), Stress and temperature in the bending lithosphere as constrained by experimental rock mechanics, *Geophys. J. R. astr. Soc.*, *59*, 463-478.

Haeussler, P.J., D.C. Bradley, R.E. Wells, and M.L. Miller (2003), Life and death of the Resurrection plate: evidence for its existence and subduction in the northeastern Pacific in Paleocene-Eocene time, *Geol. Soc. Am. Bull.*, *115*, 867-880.

Handy, M.R., A. Mulch, M. Rosenau, and C.L. Rosenberg (2001), The role of fault zones and melts as agents of weakening, hardening and differentiation of the continental crust: a synthesis, in *The Nature and Tectonic Significance of Fault Zone Weakening*, vol. 186, edited by R.E. Holdworth, R.A. Strachan, J.F. Magloughlin and R.J. Knipe, pp. 305-332, Geol. Soc.-Lon.

Harlov, D.E., R. Wirth, and C.J. Hetherington (2006), Replacement of monazite by a huttonite component: nature and experiment, *Geochim. Cosmochim. Ac., 70*(18S), A231.

Harrison, T.M., and E.B. Watson (1983), Kinetics of zircon dissolution and zirconium diffusion in granitic melts of variable water content, *Contrib. Mineral. Petrol.*, *84*, 67-72.

Harrison, T.M., K.D. McKeegan, and P. Le Fort (1995), Detection of inherited monazite in the Manaslu leucogranite by $^{208}Pb/^{232}Th$ ion microprobe dating: Crystallization age and tectonic significance, *Earth Planet. Sci. Lett.*, *133*, 271-282.

Harrison, T.M., M. Grove, K.D. McKeegan, C.D. Coath, O.M. Lovera, and P. Le Fort (1999), Origin and episodic emplacement of the Manaslu Intrusive Complex, Central Himalaya, *J. Petrol.*, *40*, 3-19.

Hawkins, D.P., and S.A. Bowring (1997), U-Pb systematics of monazite and xenotime: case studies from the Paleoproterozoic of the Grand Canyon, Arizona, *Contrib. Mineral. Petrol., 127*, 87-103.

Heaman, L., and R.R. Parrish (1991), U-Pb geochronology of accessory minerals, in *Short course handbook on applications of radiogenic isotope systems to problems in geology*, edited by L. Heaman and J.N. Ludden, pp. 59-100, Mineralogical Association of Canada, Toronto.

Hinchey, A.M., S.D. Carr, P.D. McNeill, and N. Rayner (2006), Paleocene-Eocene high-grade metamorphism, anatexis, and deformation in the Thor-Odin dome, Monashee complex, southeastern British Columbia, *Can. J. Earth Sci.*, *43*, 1341-1365.

Hollister, L.S. (1993), The role of melt in the uplift and exhumation of orogenic belts, *Chem. Geology*, *108*, 31-48.

Hollister, L.S., and M.L. Crawford (1986), Melt-enhanced deformation: A major tectonic process, *Geology*, *14*, 558-561.

Kretz, R. (1983), Symbols for rock-forming minerals, *Am. Mineral.*, *68*, 277-279.

Kruckenberg, S.C., D.L. Whitney, C. Teyssier, M. Fanning, and W.J. Dunlap (in review), Paleocene-Eocene migmatite crystallization, extension, and exhumation in the hinterland of the northern Cordillera: Okanogan dome, Washington USA, *Geol. Soc. Am. Bull.*

Kruse, S., M.K. McNutt, J. Phipps-Morgan, L. Royden, and B.P. Wernicke (1991), Lithospheric extension near Lake Mead, Nevada: A model for ductile flow in the lower crust, *J. Geophys. Res.*, *96*, 4435-4456.

Johnston, D.H. (1998), Structural and thermal evolution of northwest Thor-Odin dome, Monashee complex, southeast British Columbia, Ph.D. thesis, 321 pp., University of New Brunswick, Fredericton, New Brunswick.

Lambert, I.B., and K.S. Heier (1968), Geochemical investigations of deep-seated rocks in the Australian Shield, *Lithos*, *1*, 30-53.

Lorencak, M., D. Seward, O. Vanderhaeghe, C. Teyssier, and J.P. Burg (2001), Low-temperature cooling history of the Shuswap metamorphic core complex, British Columbia: Constraints from apatite and zircon fission-track ages, *Can. J. Earth Sci.*, *38*, 1615-1625.

Ludwig, K.R. (2003), Isoplot/Ex, v3.00, *Berkeley Geochronology Center Special Publication, 4*, 70.

Marshall, D., and G. Simandl (2006), Phase relations and metamorphism in the sapphirine bearing granulites of the Valhalla complex, Slocan Valley, BC, *GAC/MAC Annual Meeting Abstracts Program*, *31*, 96.

Monger, J.W.H., J.G. Souther, and H. Gabrielse (1972), Evolution of the Canadian Cordillera; a plate-tectonic model, *Am. J. Sci.*, *272*, 577-602.

Monger, J.W.H., R.A. Price, and D.J. Tempelman-Kluit (1982), Tectonic accretion and plutonic welts in the Canadian Cordillera, *Geology*, *10*, 70-75.

Montel, J.-M., J. Kornprobst, and D. Vielzeuf (2000), Preservation of old U-Th-Pb ages in shielded monazite: example from the Beni Bousera Hercynian kinzigites (Morocco), *J. Met. Geol., 18,* 335-342.

Morris, G.A., P.B. Larson, and P.R. Hooper (2000), 'Subduction style' magmatism in a non-subduction setting: the Colville Igneous Complex, NE Washington state, USA, *J. Petrol.*, *41*, 43-67.

Norlander, B.N., D.L. Whitney, C. Teyssier, and O. Vanderhaeghe (2002), Partial melting and decompression of the Thor-Odin dome, Shuswap metamorphic core complex, Canadian Cordillera, *Lithos*, *61*, 103-125.

Nyman, M.W., D.R.M. Pattison, and E.D. Ghent (1995), Melt extraction during formation of K-feldspar-sillimanite migmatites, west of Revelstoke, British Columbia, *J. Petrol.*, *36*, 351-372.

Nyström, A.I., and L.M. Kriegsman (2003), Prograde and retrograde reactions, garnet zoning patterns, and accessory phase behaviour in SW Finland migmatites, with implications for geochronology, in *Geochronology: Linking the Isotopic Record with Petrology and Textures, Special Publications,* vol. 220, edited by D. Vance, W. Müller and I.M. Villa, pp. 213-230, Geol. Soc.-Lon.

Okulitch, A.V. (1984), The role of the Shuswap metamorphic complex in Cordilleran tectonism: A review, *Can. J. Earth Sci.*, *21*, 1171-1193.

Paces, J.B., and J.D. Miller (1993), Precise U-Pb age of Duluth Complex and related mafic intrusions, northeastern Minnesota: geochronological insights into physical, petrogenetic, paleomagnetic, and tectonomagmatic processes associated with the 1.1 Ga midcontinent rift system, *J. Geophys. Res.*, *98*, 13997-14013.

Parkinson, D.L. (1991), Age and isotopic character of Early Proterozoic basement gneisses in the southern Monashee Complex, southeastern British Columbia, *Can. J. Earth Sci.*, *28*, 1159-1168.

Parkinson, D.L. (1992), Age and tectonic evolution of the southern Monashee complex, southeastern British Columbia: A window into the deep crust, Ph.D. thesis, 197 pp., Univ. of California, Santa Barbara.

Parrish, R.R. (1984), Slocan Lake fault: a low angle fault zone bounding the Valhalla gneiss complex, Nelson map area, southern British Columbia, *Geol. Surv. Can. Pap., 84-1A*, 323-330.

Parrish, R.R. (1990), U-Pb dating of monazite and its application to geological problems, *Can. J. Earth Sci., 27*, 1431-1450.

Parrish, R.R. (1995), Thermal evolution of the southeastern Canadian Cordillera, *Can. J. Earth Sci.*, *32*, 1618-1642.

Parrish, R.R., and J.O. Wheeler (1983), An U-Pb zircon age for the Kuskanax batholith, southeast British Columbia, *Can. J. Earth Sci., 20*, 1751-1756.

Parrish, R.R., and J.C. Roddick (1985), Geochronology and isotope geology for the geologist and explorationist, Geological Association of Canada, Cordilleran section, *Short Course 4*, 71 pp., Vancouver, British Columbia.

Parrish, R.R., and R.L. Armstrong (1987), The ca. 162 Ma Galena Bay stock and its relationship to the Columbia River fault zone, southeast British Columbia, in *Radiogenic age and isotopic studies: Report 1*, vol. 87-2, pp. 25-32, Geol. Surv. Can. Paper.

Parrish, R., S.D. Carr, and R.L. Brown (1985), Valhalla gneiss complex, southeast British Columbia: 1984 fieldwork, *Geol. Surv. Can. Pap.*, *85-1A*, 81-87.

Parrish, R.R., S.D. Carr, and D.L. Parkinson (1988), Eocene extensional tectonics and geochronology of the southern Omineca belt, British Colombia and Washington, *Tectonics*, *7*, 181-212.

Paterson, S.R., R.B. Miller, H. Alsleben, D.L. Whitney, P.M. Valley, and H. Hurlow (2004), Driving mechanisms for > 40 km of exhumation during contraction and extension in a continental arc, Cascades core, Washington, *Tectonics*, *23*, TC3005.

Price, R.A. (1986), The southeastern Canadian Cordillera: Thrust faulting, tectonic wedging and delamination of the lithosphere, *J. Struct. Geol.*, *8*, 238-254.

Raia, F., and F.J. Spera (1997), Simulations of crustal anatexis: Implications for the growth and differentiation of the continental crust, *J. Geophys. Res.*, *102*, 22629-22648.

Reesor, J.E. (1965), Structural evolution and plutonism in Valhalla gneiss complex, British Columbia, *Geol. Surv. Can. Bull.*, *129*, 128 pp.

Rusmore, M.E., G.J. Woodsworth, and G.E. Gehrels (2005), Two-stage exhumation of midcrustal arc rocks, Coast Mountains, British Columbia, *Tectonics*, *24*, TC5013.

Schaubs, P., and S. Carr (1998), Geology of metasedimentary rocks and late Cretaceous deformation history, in the Northern Valhalla complex, British Columbia, *Can. J. Earth Sci.*, *38*, 1018-1036.

Schaubs, P.M., S.D. Carr, and R.G. Berman (2002), Structural and metamorphic constraints on ca. 70 Ma deformation of the northern Valhalla complex, British Columbia: Implications for the tectonic evolution of the southern Omineca belt, *J. Struct. Geol.*, *24*, 1195-1214.

Schmitt, A.K., M. Grove, T.M. Harrison, O.M. Lovera, J. Hulen, and M. Waters (2003), The Geysers – Cobb Mountain Magma System, California (Part 1): U-Pb zircon ages of volcanic rocks, conditions of zircon crystallization and magma residence times, *Geochim. Cosmochim. Acta*, *67*, 3423-3442.

Sevigny, J.H., R.R. Parrish, and E.D. Ghent (1989), Petrogenesis of peraluminous granites, Monashee Mountains, southeastern Canadian Cordillera, *J. Petrol.*, *30*, 557-581.

Spear, F.S. (2004), Fast cooling and exhumation of the Valhalla metamorphic core complex, southeastern British Columbia, *Int. Geol. Rev.*, *46*, 193-209.

Spear, F.S., and R.R. Parrish (1996), Petrology and cooling rates of the Valhalla Complex, British Columbia, Canada, *J. Petrol.*, *37*, 733-765.

Spell, T.L., and I. McDougall (2003), Characterization and calibration of $^{40}Ar/^{39}Ar$ dating standards, *Chem. Geol., Isotope Geoscience Section, 198*, 189-211.

Steiger, R., and E. Jaeger (1977), Subcommission on geochronology: Convention on the use of decay constants in geo and cosmochronology, *Earth Planet. Sci. Lett.*, *36*, 359-362.

Struik, B., and R.G. Anderson (2003), Paleogene pull-apart core- and rind-complexes, Canadian Cordillera, *Geol. Soc. Amer. Abstracts with Programs*, *35*, 473.

Teufel, S., and W. Heinrich (1997), Partial resetting of the U-Pb isotope system in monazite through hydrothermal experiments: An SEM and U-Pb isotope study, *Chem. Geol., 137*, 273-281.

Teyssier, C., E.C. Ferré, D.L. Whitney, B. Norlander, O. Vanderhaeghe, and D. Parkinson (2005), Flow of partially molten crust and origin of detachments during collapse of the Cordilleran orogen, in *High-strain zones: Structure and physical properties*, *Special Publications*, vol. 245, edited by D. Bruhn and L. Burlini, pp. 39-64, Geol. Soc.-Lon.

Townsend, K.J., C.F. Miller, J.L. D'Andrea, J.C. Ayers, T.M. Harrison, and C.D. Coath (2000), Low temperature replacement of monazite in the Iretaba granite, southern Nevada: geochronological implications, *Chem. Geol.*, *172*, 95-112.

Vance, D., W. Müller, and I.M. Villa (2003), Geochronology: linking the isotopic record with petrology and textures – an introduction, in *Geochronology: Linking the Isotopic Record with Petrology and Textures, Special Publications,* vol. 220, edited by D. Vance, W. Müller and I.M. Villa, pp. 1-24, Geol. Soc.-Lon..

Vanderhaeghe, O., and C. Teyssier (1997), Formation of the Shuswap metamorphic complex during late-orogenic collapse of the Canadian Cordillera: role of ductile thinning and partial melting of the mid- to lower crust, *Geodin. Acta*, *10*, 41-58.

Vanderhaeghe, O., and C. Teyssier (2001a), Crustal-scale rheological transitions during late-orogenic collapse, *Tectonophysics*, *335*, 211-228.

Vanderhaeghe, O., and C. Teyssier (2001b), Partial melting and flow of orogens, *Tectonophysics*, *342*, 451-472.

Vanderhaeghe, O., J.-P. Burg, and C. Teyssier (1999a), Exhumation of migmatites in two collapsed orogens: Canadian Cordillera and French Varscides, in *Exhumation processes: normal faulting, ductile flow and erosion*, edited by U. Ring, M.T. Brandon, G.S. Lister and S.D. Willet, pp. 181-204, Geol. Soc.-Lon.

Vanderhaeghe, O., C. Teyssier, and R. Wysoczanski (1999b), Structural and geochronological constraints on the role of partial melting during the formation of the Shuswap metamorphic core complex at the latitude of the Thor-Odin Dome, British Columbia, *Can. J. Earth Sci., 36*, 917-943.

Vanderhaeghe, O., C. Teyssier, I. McDougall, and W.J. Dunlap (2003), Cooling and exhumation of the Shuswap metamorphic core complex constrained by $^{40}Ar/^{39}Ar$ thermochronology, *GSA Bull.*, *115*, 200-216.

Varsek, J.L., and F.A. Cook (1994), Three-dimensional crustal structure of the Eastern Cordillera, southwestern Canada and northwestern United States, *Geol. Soc. Am. Bull.*, *106*, 803-823.

Wanless, R.K., R.D. Stevens, G.R. Lachance, and R.N. Delabio (1978), Age determinations and geological studies, K-Ar isotopic ages, report 13, *Geol. Surv. Can. Pap.*, *77-2*.

Wanless, R.K., R.D. Stevens, G.R., Lachance, and R.N. Delabio (1979), Age determinations and geological studies, K-Ar isotopic ages, report 14, *Geol. Surv. Can. Pap.*, *79-2*.

Watson, E.B. (1996), Surface enrichment and trace-element uptake during crystal growth, *Geochim. Cosmochim. Acta*, *60*, 5013-5020.

Wdowinski, S., and G.J. Axen (1992), Isostatic rebound due to tectonic denudation: A viscous flow model of a layered lithosphere, *Tectonics*, *11*, 303-315.

Wernicke, B.P. (1990), The fluid crustal layer and its implications for continental dynamics, in *Exposed cross sections of the continental crust*, edited by M.H. Salisbury and D.M. Fountain, pp. 509-544, Kluwer Academic Publishers, Dordrecht, Netherlands.

Wheeler, J.O., and P. McFeely (1991), Tectonic Assemblage Map of the Canadian Cordillera and Adjacent Parts of the United States of America, Geological Survey of Canada, Map 1712A.

Whitney, D.L., C. Teyssier, and A.K. Fayon (2004a), Isothermal decompression, partial melting and exhumation of deep continental crust, in *Vertical Coupling and Decoupling in the Lithosphere, Special Publications*, vol. 227, edited by J. Grocott, K.J.W. McCaffrey, G. Taylor and B. Tikoff, pp. 313-326, Geol. Soc.-Lon.

Whitney, D.L., S.R. Paterson, K.L. Schmidt, A.F. Glazner, and C.F. Kopf (2004b), Growth and demise of continental arcs and orogenic plateaux in the North American Cordillera: from Baja to British Columbia, in *Vertical Coupling and Decoupling in the Lithosphere, Special Publications*, vol. 227, edited by J. Grocott, K.J.W. McCaffrey, G. Taylor and B. Tikoff, pp. 167-176, Geol. Soc.-Lon.

Wolfe, J.A., C.E. Forest, and P. Molnar (1998), Paleobotanical evidence of Eocene and Oligocene paleolatitudes in midlatitude western North America, *Geol. Soc. Am. Bull.*, *110*, 664-678.

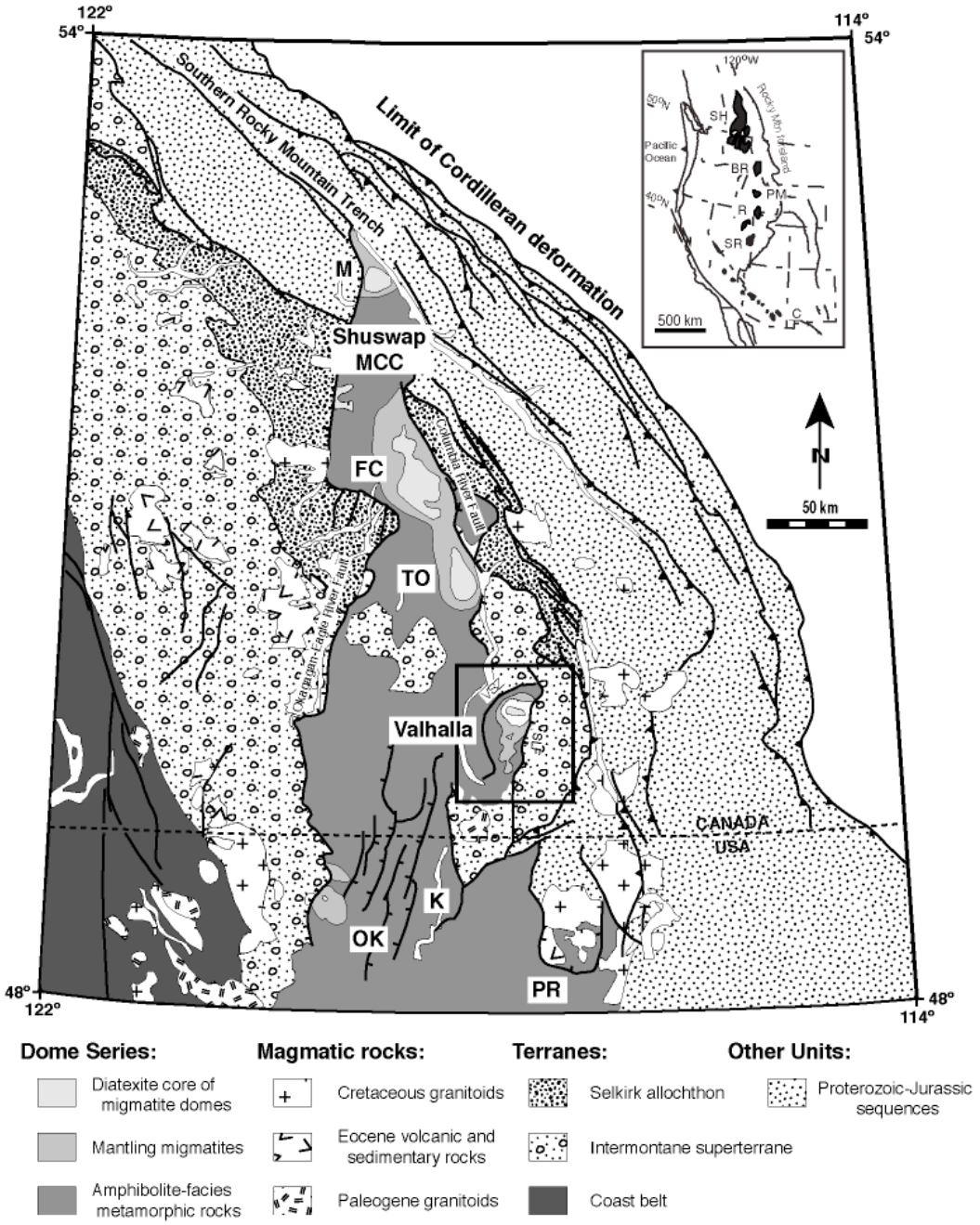

Figure 2.1: Simplified geological map of the Canadian Cordillera and the Omineca belt; FC, Frenchman Cap dome; TO, Thor-Odin dome; Ok, Okanagon dome; K, Kettle dome; PR, Priest River dome (modified after *Wheeler and McFeely* [1991] and *Vanderhaeghe et al*. [2003a]). Inset shows the location of the Omineca belt in regards to the other Cordilleran core complexes; SH, Shuswap MCC; BR, Bitterroot MCC; PM, Pioneer MCC; R, Ruby MCC; SR, Snake River MCC; C, Catalina MCC (modified after *Coney* [1980], *Armstrong and Ward* [1991], and *Vanderhaeghe et al.* [1999a].

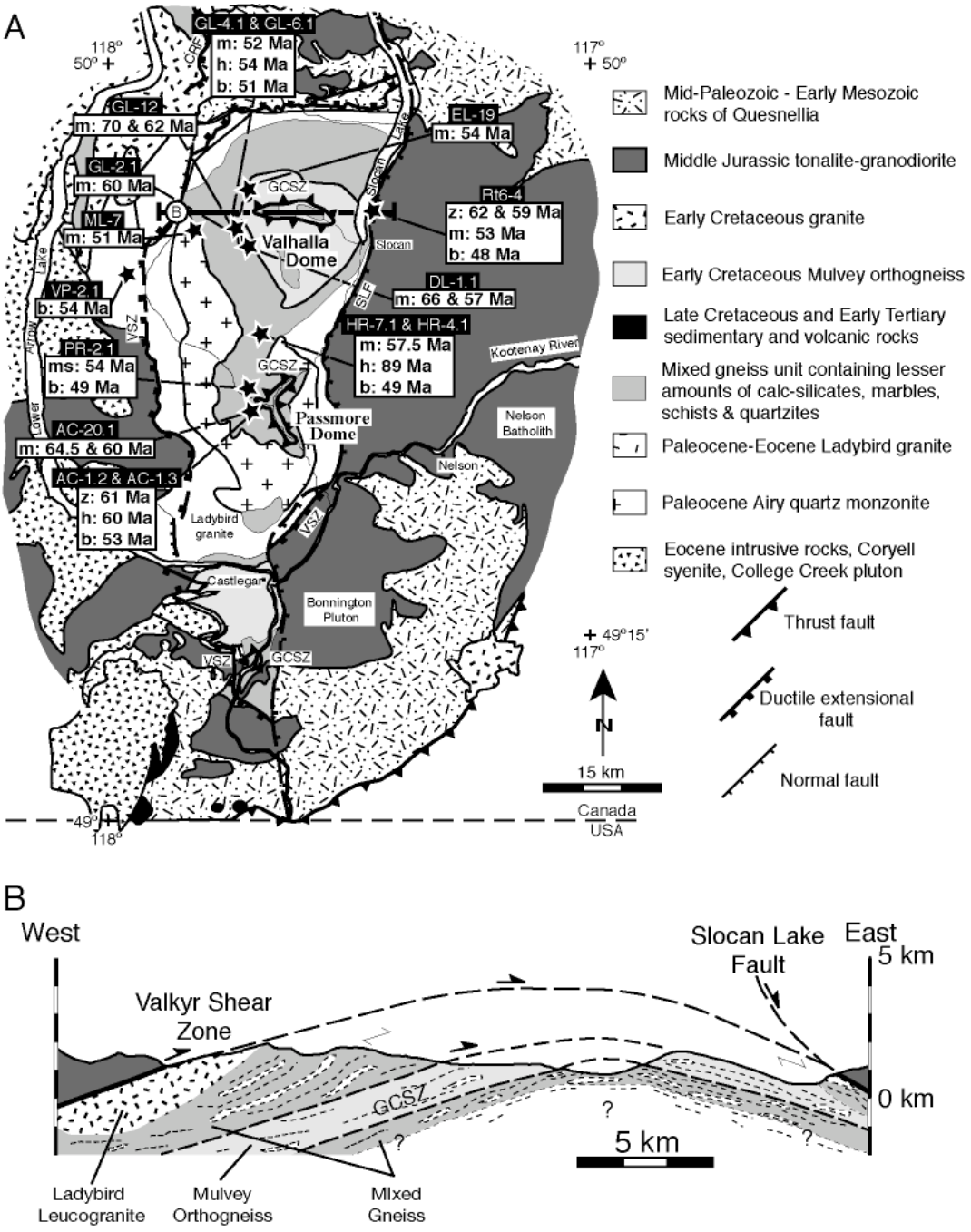

Figure 2.2: (A) Simplified geologic map of the Valhalla complex, showing main lithological units, structural elements, sample locations and results of isotopic analyses. GCSZ, Gwillim Creek shear zone; SLF, Slocan Lake fault; VSZ, Valkyr shear zone (modified after *Schaubs et al*. [2002]). z: zircon; m: monazite; h: hornblende; ms: muscovite; b: biotite. (B) Simplified cross-section through the Valhalla dome of the complex. The cross-section shows the outward dipping low angle foliation and lithologic contacts of the three main units: leucogranite, mixed gneiss, and orthogneiss. The dashed in the cross section represent the general foliation.

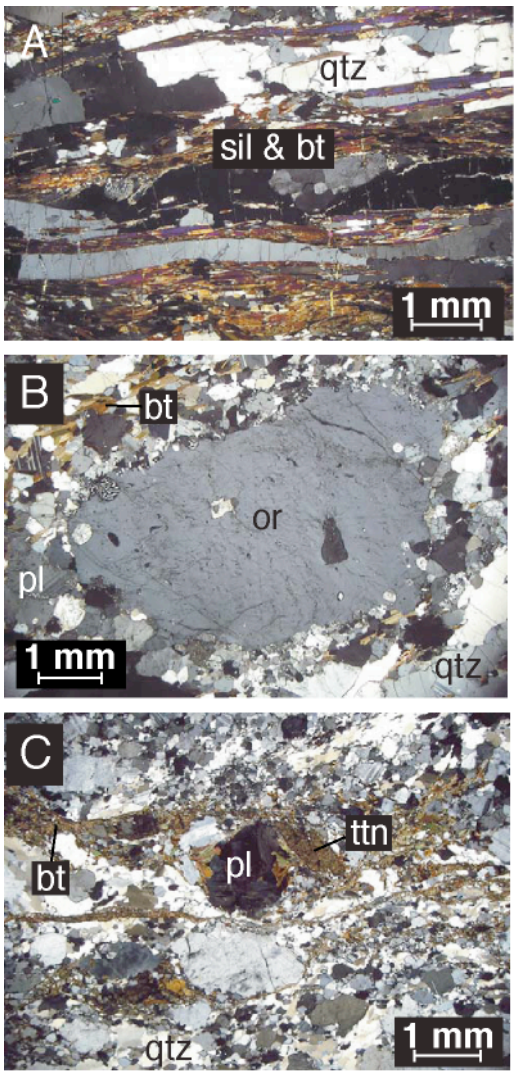

Figure 2.3: Photomicrographs of leucosome from the Valhalla complex: (A) quartz ribbons in a paragneiss from the GCSZ of Passmore. Note the leucosome is rimmed by sillimanite and biotite selvages; (B) granophyric intergrowths at the boundary between quartz and orthoclase in a migmatitic quartzofeldspathic gneiss from the mixed gneiss unit; and (C) mylonitic leucosome exposed along the Slocan Lake fault that has been deformed by movement along the fault. Mineral abbreviations from *Kretz* [1983].

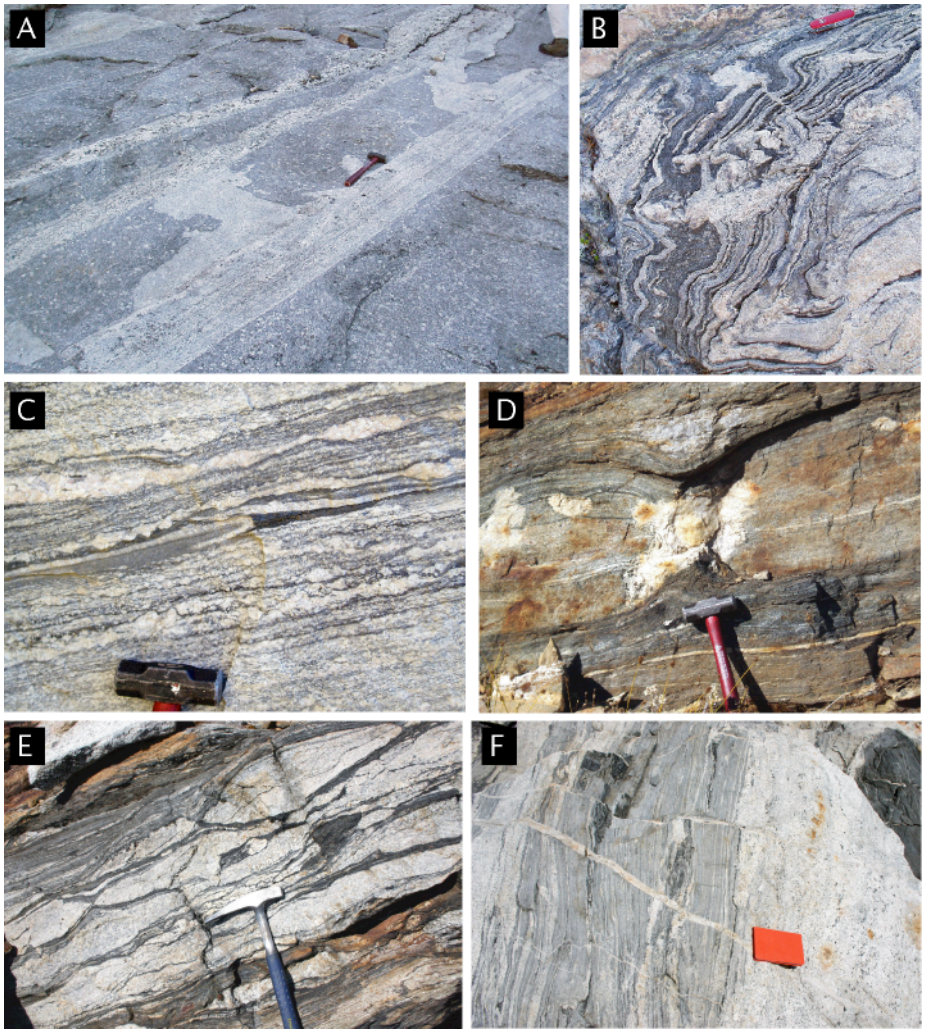

Figure 2.4: Photographs showing the different types of migmatites found in the Valhalla complex: (A) dikes intruding the orthogneiss unit; the dikes are connected by leucosome that interacts with the host orthogneiss; (B) folded stromatic leucosome; (C) mylonitic migmatite from along the Slocan Lake fault, illustrating small (~5 cm-scale) pinch and swell structures and biotite selvages forming around the leucosome; (D) leucosome crystallized in a boudin neck; (E) stromatic migmatite; and (F) an inclusion of a biotite gneiss within diatexite.

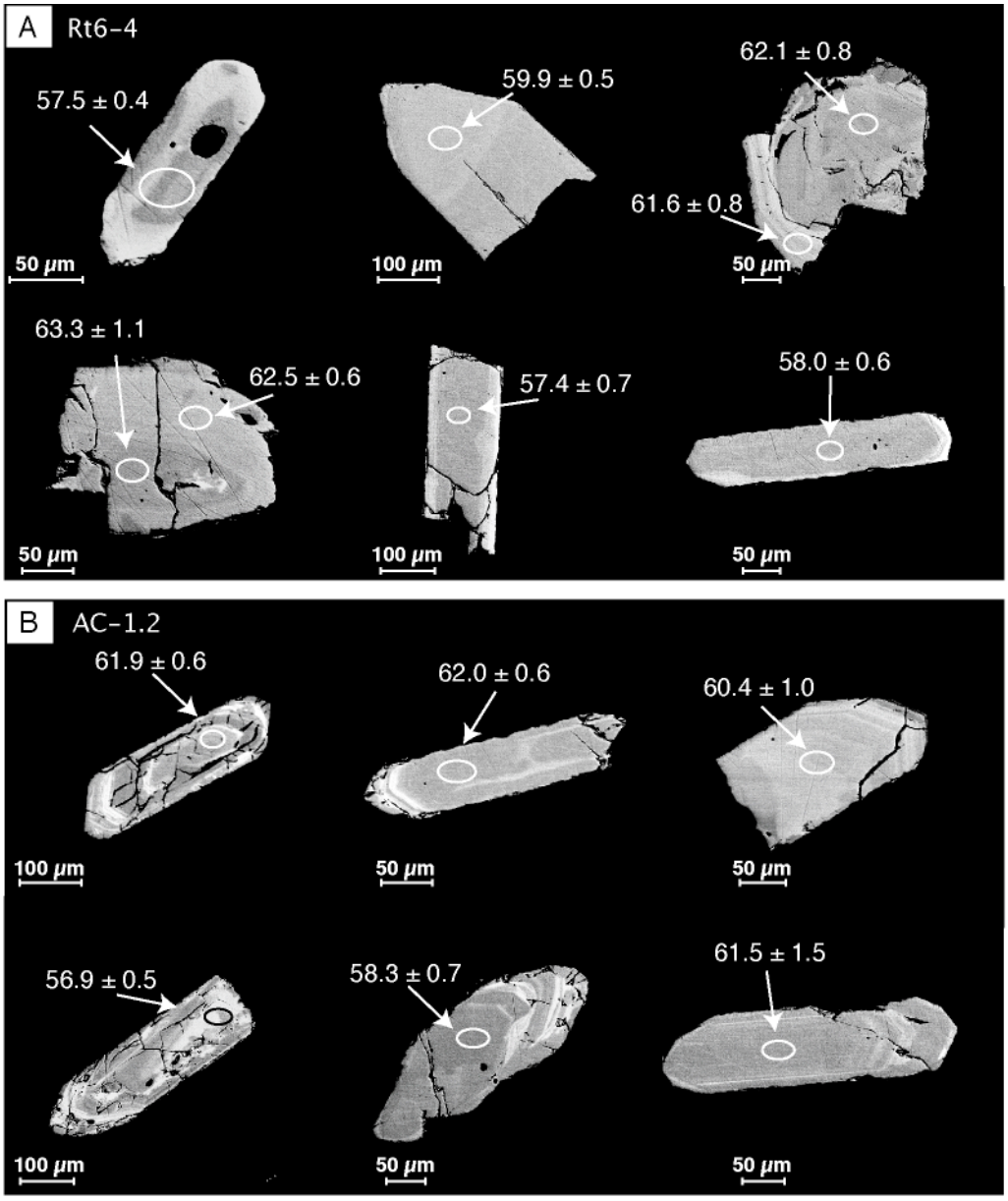

Figure 2.5: Representative BSE images of zircon with their respective $^{238}U/^{206}Pb$ isotopic results from (A) sample Rt6-4 and (B) AC-1.2. Note the variability in zoning.

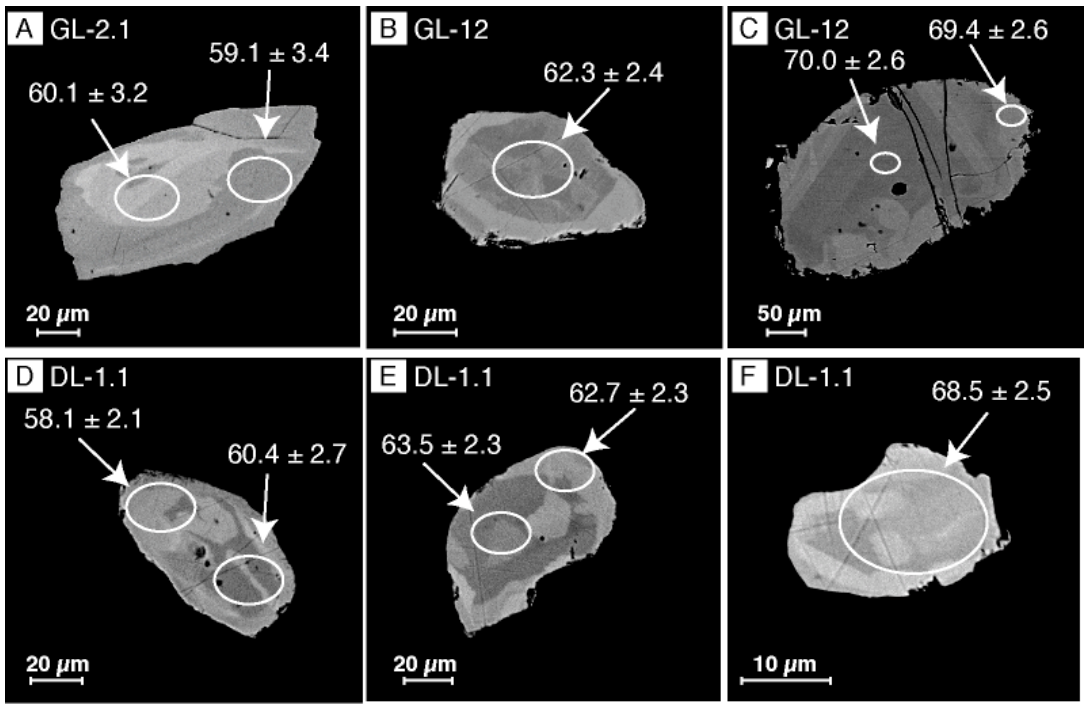

Figure 2.6: Representative BSE images showing patchy zoning in monazite from samples (A) GL-2.1; (B) and (C) GL-12; and (D), (E), and (F) DL-1.1. The $^{232}Th/^{208}Pb$ ages and location of the analyses are shown for each sample.

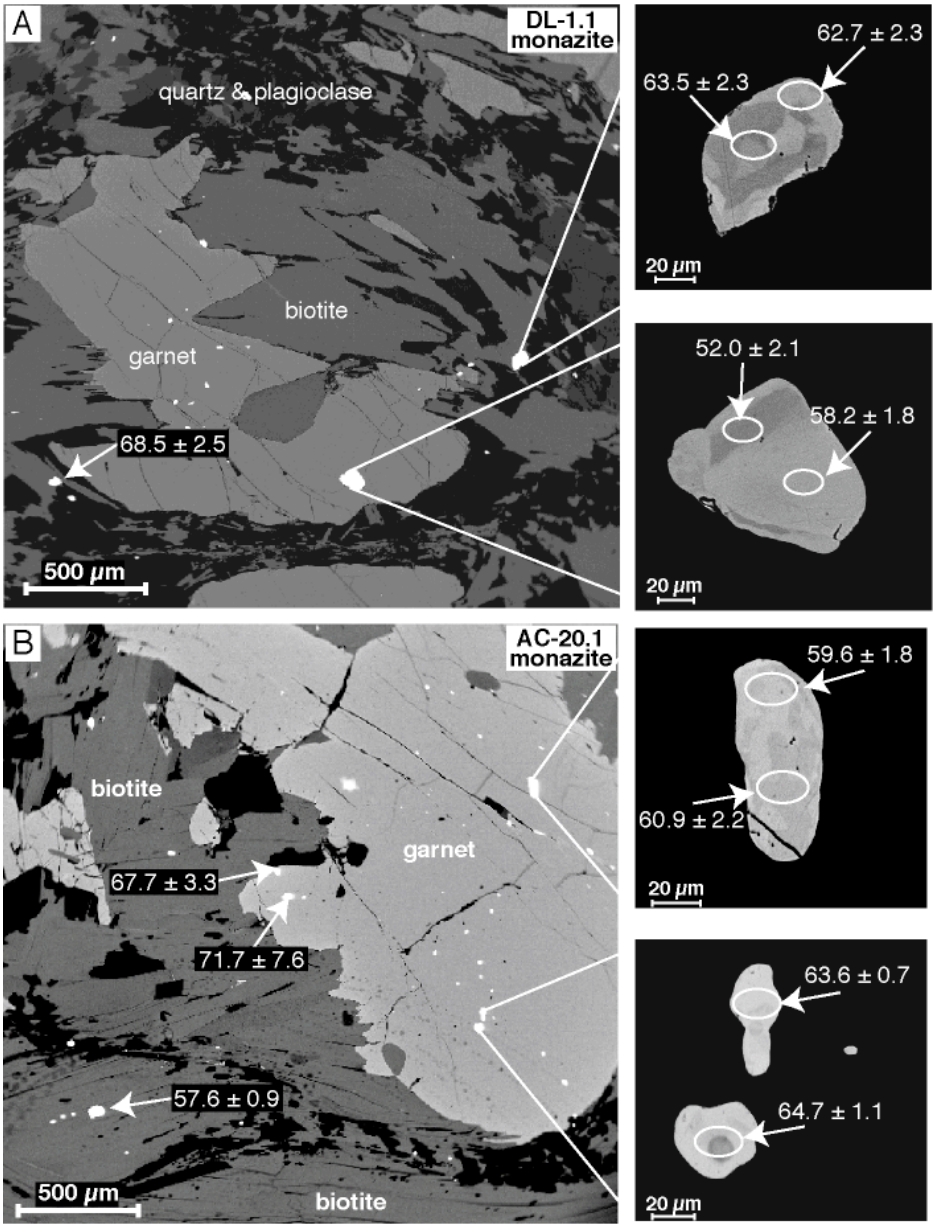

Figure 2.7: Representative BSE images of parts of a thin section showing the location of monazite grains within the rock matrix and also of individual monazite grains from (A) sample DL-1.1 and (B) sample AC-20.1. The zoning in the individual monazite grains is a primary function of the Y and U composition. The images also illustrate the *in situ* age(s) yielded by the individual monazite grains. Note that the ages are independent of location, i.e., there is not a systematic difference between grains included in garnet versus those in the matrix.

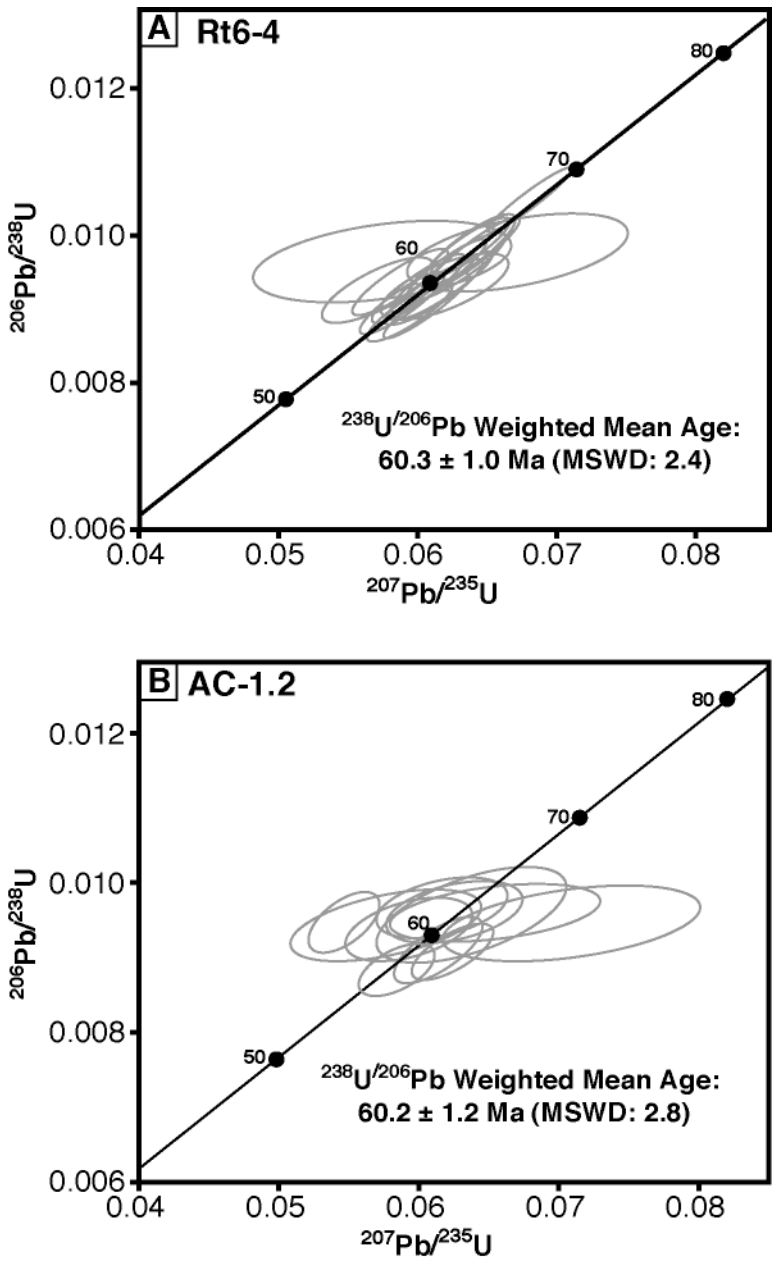

Figure 2.8: Zircon U-Pb results from the Valhalla complex. U-Pb concordia diagram for (A) sample Rt6-4.1 and (B) sample AC-1.2.

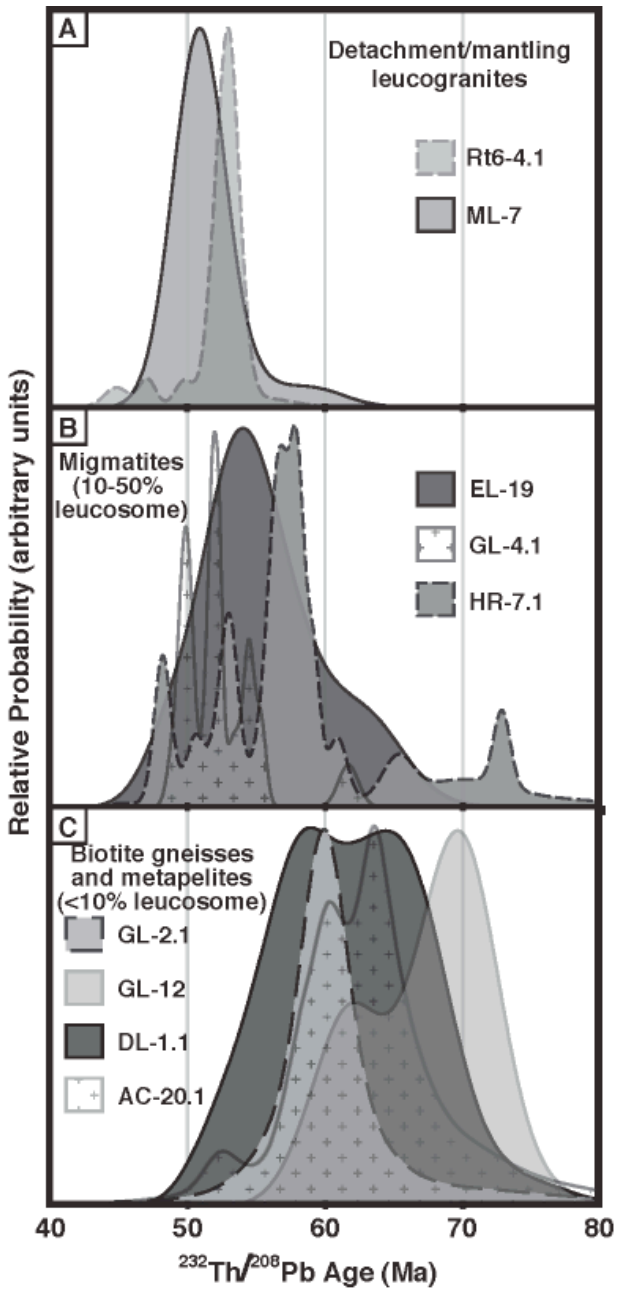

Figure 2.9: Monazite Th-Pb age results from the Valhalla complex. Cumulative probability plots for single-spot total Pb-ages of (A) a leucosome crystallized in a boudin neck (Rt6-4) from along the Slocan Lake fault and a mantling leucogranite (ML-7); (B) migmatitic quartzofeldspathic gneisses (EL-10, GL-4.1) and a migmatitic paragneiss (HR-7.1); (C) biotite gneisses (DL-1.1, GL-12) and metapelites (GL-2.1, AC-20.1).

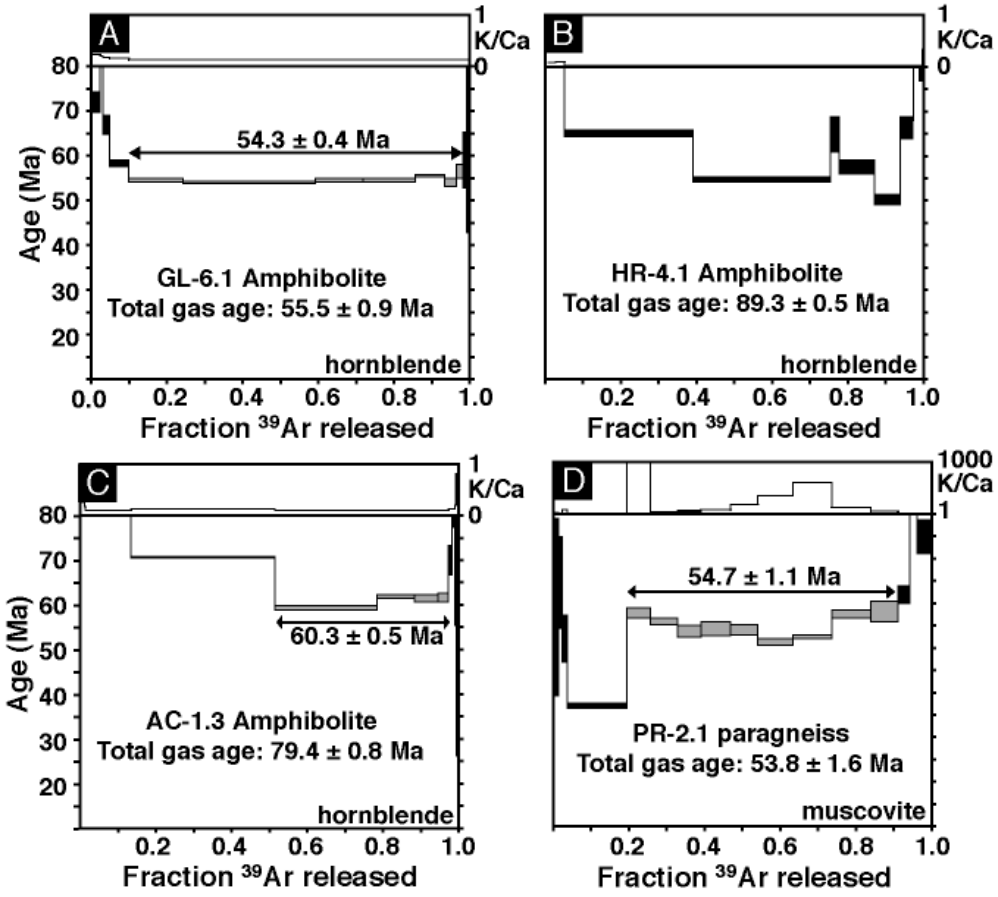

Figure 2.10: Hornblende $^{40}Ar/^{39}Ar$ age spectra for (A) sample GL-6.1; (B) sample HR-4.1; (C) sample AC-1.3; and muscovite $^{40}Ar/^{39}Ar$ age spectra for (D) sample PR-2.1. Shaded boxes indicate steps used in calculating preferred age. K/Ca ratios are shown on top of each respective spectra. Note difference on scale for K/Ca ratios between muscovite and hornblende.

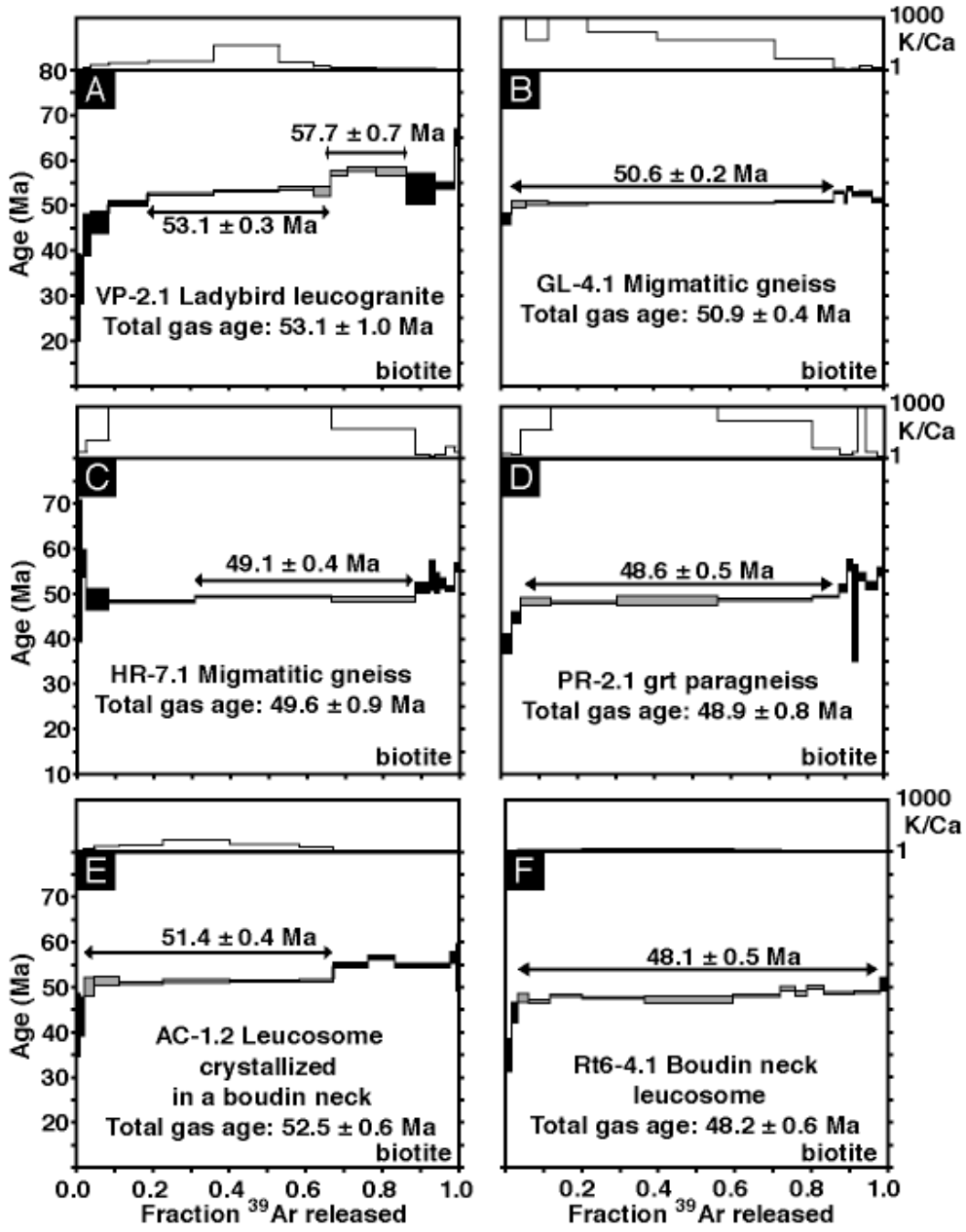

Figure 2.11: Biotite $^{40}Ar/^{39}Ar$ age spectra for (A) sample VP-2.1; (B) sample GL-4.1; (C) sample HR-7.1; (D) sample PR-2.1; (E) sample AC-1.2; and (F) sample Rt6-4.1. Shaded boxes indicate steps used in calculating preferred age. K/Ca ratios are shown on top of each respective spectra.

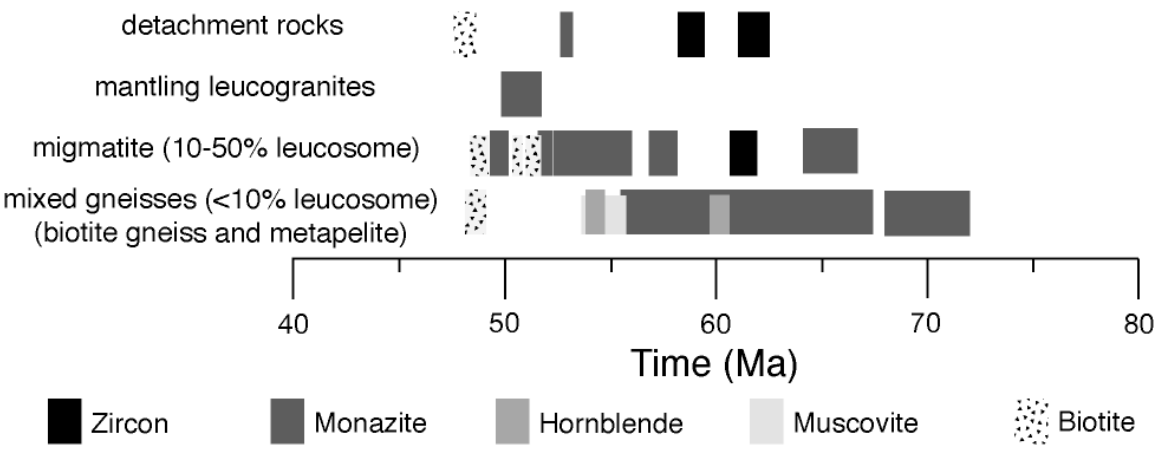

Figure 2.12: Timeline of tectonometamorphic events in the Valhalla complex recorded by U-Th-Pb and Ar-Ar geochronology from this study. The timeline is divided into the main lithologic units, by structural depth, and by isotopic system.

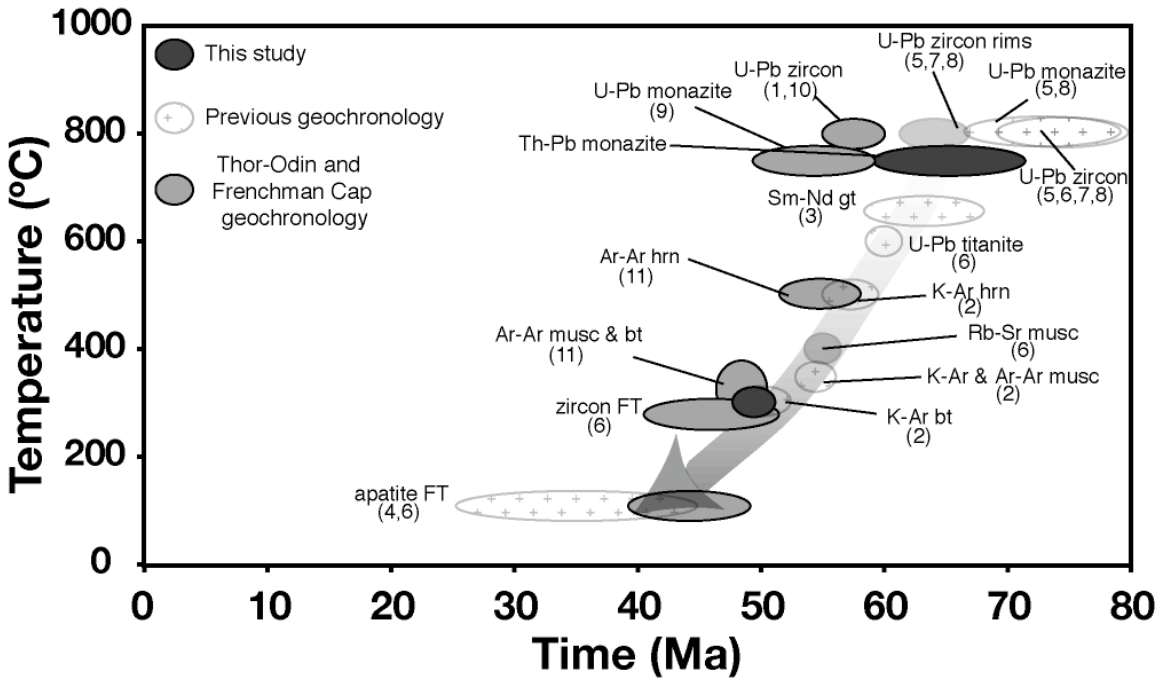

Figure 2.13: Temperature-time evolution of the Omineca domes, demonstrating the similarity in timing of tectonic events along the belt. A representative T-t path has been added, shown with the arrow. Numbers refer to published geochronometric results including: (1) *Carr* [1992]; (2) *Carr et al*. [1987]; (3) *Ducea et al*. [2000]; (4) *Lorencak et al.* [2001]; (5) *Parrish* [1990]; (6) *Parrish* [1995]; (7) *Spear* [2004]; (8) *Spear and Parrish* [1996]; (9) *Teyssier et al.* [2005]; (10) *Vanderhaeghe et al.* [1999b]; (11) *Vanderhaeghe et al*. [2003]. Monazite ages are shown at 800 ºC and 750 ºC to reflect uncertainty in the temperature corresponding to the monazite Th/Pb age. Only metamorphic monazite results are shown; the monazites from the migmatites that were affected by fluid-mediated recrystallization are not shown.

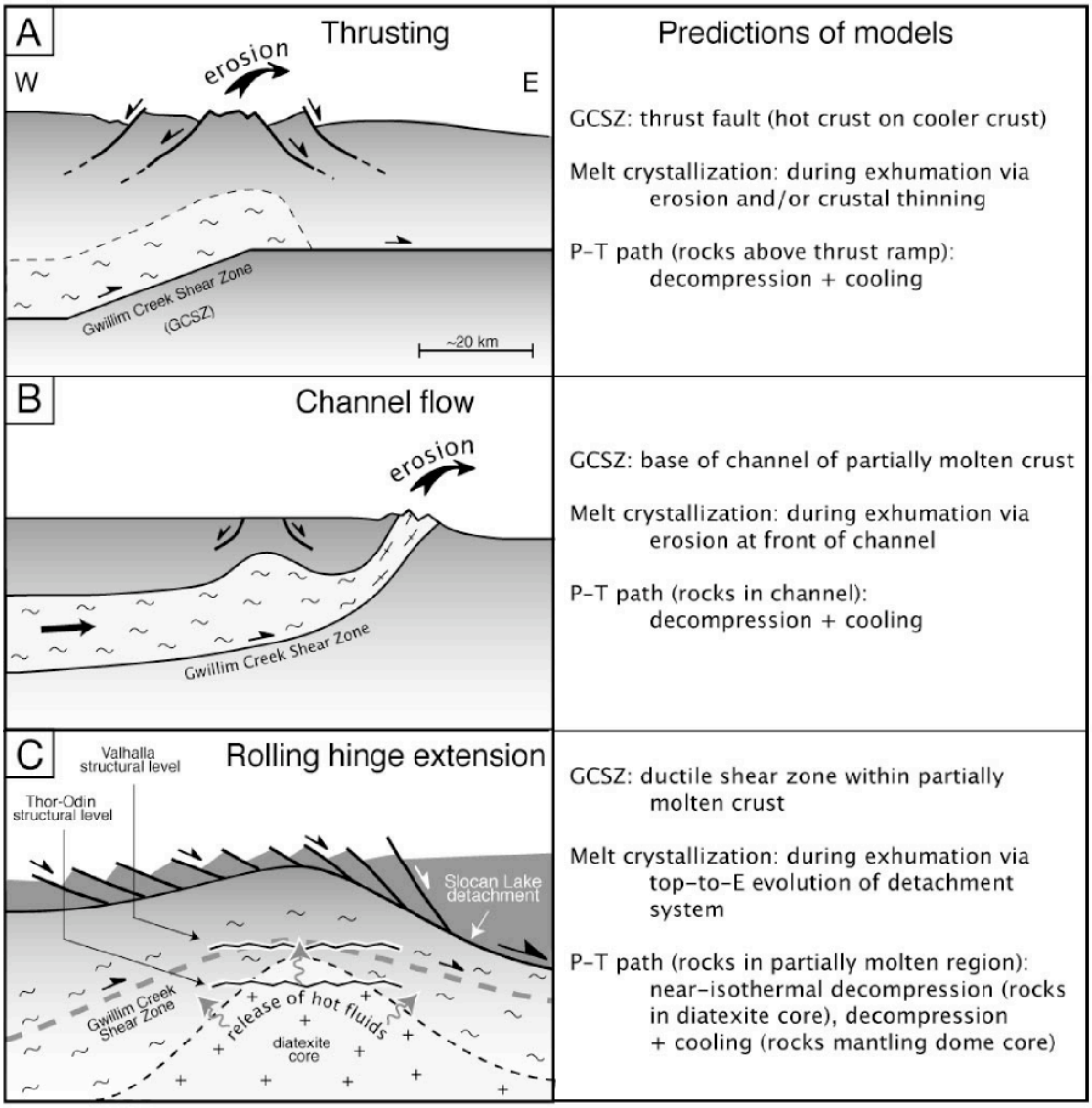

Figure 2.14: Schematic models for the exhumation of the Valhalla complex in the context of regional metamorphism and crustal melting: (A) thrusting, (B) channel flow, and (C) rolling hinge extension.

Table 2.1 Summary of Previously Published Geochronometric Studies of the Valhalla Complex

Rock	Location	Age (Ma)	Analyzed Mineral	Isotope System	Method	Reference
paragneiss	GCSZ, Passmore	85-75	monazite	Th-Pb	IMP	Spear, 2004
	GCSZ, Passmore	60 ± 2	monazite	Th-Pb	IMP	Spear, 2004
	GCSZ, Passmore, gt core	67.3 ± 2.3	garnet	Sm-Nd		Ducea et al., 2003
	GCSZ, Passmore, gt rim	59.8 ± 2	garnet	Sm-Nd		Ducea et al., 2003
	GCSZ, Passmore	75 ± 5	zircon	U-Pb lower intercept	ID-TIMS	Spear & Parrish, 1996
	GCSZ, Passmore	67.5	anatectic zircon	U-Pb	ID-TIMS	Parrish, 1990
	GCSZ, Passmore	74 to 65	monazite	U-Pb	ID-TIMS	Spear & Parrish, 1996
	GCSZ, Valhalla, bimodal distribution	80-79 Ma	monazite	U-Pb	ID-TIMS	Spear & Parrish, 1996
		60.1 ± 0.5	monazite	U-Pb	ID-TIMS	Spear & Parrish, 1996
orthogneiss		100 ± 5	zircon	U-Pb	ID-TIMS	Carr et al. 1987
	Gwillim Creek area, central Valhalla	110 +15-7	zircon	U-Pb	ID-TIMS	Parrish, 1995
	Gwillim Creek area, central Valhalla	116-110	zircon	Pb/Pb	ID-TIMS	Spear & Parrish, 1996
	Gwillim Creek area, central Valhalla	73-65	allanite	U-Pb	ID-TIMS	Spear & Parrish, 1996
	Gwillim Creek area, central Valhalla	61-56	titanite	U-Pb	ID-TIMS	Spear & Parrish, 1996
	southern part of unit	89 ± 3	zircon	U-Pb	ID-TIMS	Parrish, 1984
	southern part of unit	52.2 ± 2.5	biotite	K-Ar		Wanless et al., 1978, 1979
	southern part of unit	55.5 ± 2.9	hornblende	K-Ar		Wanless et al., 1978, 1979
Airy quartz monzonite		62 ± 1	zircon	U-Pb	ID-TIMS	Carr et al., 1987
	near Koch Creek	63.5 ± 1	zircon	U-Pb	ID-TIMS	Parrish, 1984
Ladybird granite		58 ± 1	zircon	U-Pb lower intercept	ID-TIMS	Parrish et al., 1988
	intrudes Valkyr shear zone	56.5 ± 1.5	zircon	U-Pb lower intercept	ID-TIMS	Parrish et al., 1988
	intrudes Valkyr shear zone	57 to 51.5	monazite	U-Pb	ID-TIMS	Parrish et al., 1988
	Slocan Lake fault	54.5 ± 1	muscovite	Rb-Sr	ID-mass spec.	Parrish et al., 1988
	Slocan Lake fault	49 to 47	muscovite	K-Ar	ID-mass spec.	Parrish et al., 1988
granitic veins	intrudes Mulvey gneiss	96-64	zircon	U-Pb	ID-TIMS	Parrish et al., 1988
	intrudes Mulvey gneiss	61-52	monazite	U-Pb	ID-TIMS	Parrish et al., 1990
pegmatite & aplite	footwall GCSZ, Valhalla	93-81	zircon	U-Pb	ID-TIMS	Parrish, 1995
	footwall GCSZ, Valhalla	90-60	monazite	U-Pb	ID-TIMS	Parrish, 1995
	intruding GCSZ, Valhalla	ca. 52	zircon & monazite	U-Pb	ID-TIMS	Parrish, 1995
	cross-cutting GCSZ, Valhalla	51 to 50	zircon & monazite	U-Pb	ID-TIMS	Parrish et al., 1988
	GCSZ, Passmore	72-57	zircon	U-Pb	ID-TIMS	Spear & Parrish, 1996
	GCSZ, Passmore	69.5-64.5	monazite	U-Pb	ID-TIMS	Spear & Parrish, 1996
Valhalla Range, encompassing Valhalla complex	Various other rocks of Valhalla complex	60 ± 2	titanite	U-Pb		S. Grist & R.R. Parrish, unpublished data or R.R. Parrish, unpublished data[a]
		58 ± 2	hornblende	K-Ar		
		47 ± 2	biotite	K-Ar		
		44-26	apatite	fission track		

[a]Reported in Parrish, 1995.

Table 2.2 Summary of Sample Lithology, Location, and U-Th-Pb Ages

Sample ID	Rock Type	Location	Analyzed Mineral	Isotope System	n[a]	Age (Ma)	MSWD
Rt6-4	leucosome crystallized in a boudin neck	49°48'26"N; 117°28'08"W	zircon	U-Pb	17	60.3 ± 2.0	2.40
Rt6-4	leucosome crystallized in a boudin neck	49°48'26"N; 117°28'08"W	monazite	Th-Pb	20	52.9 ± 1.5	0.61
ML-7	leucogranite	49°48'49"N; 117°49'17"W	monazite	Th-Pb	14	50.8 ± 2.3	0.25
EL-19	migmatitic quartzofeldspathic gneiss	49°51'02"N; 117°43'24"W	monazite	Th-Pb	16	54.0 ± 3.6	1.80
GL-4.1	migmatitic quartzofeldspathic gneiss	49°48'54"N; 117°44'40"W	monazite	Th-Pb	3	54.7 ± 3.1	1.80
GL-4.1	migmatitic quartzofeldspathic gneiss	49°48'54"N; 117°44'40"W	monazite	Th-Pb	6	51.9 ± 1.5	0.68
GL-4.1	migmatitic quartzofeldspathic gneiss	49°48'54"N; 117°44'40"W	monazite	Th-Pb	5	49.7 ± 1.6	1.02
HR-7.1	grt-bearing migmatitic paragneiss	49°40'50"N; 117°42'45"W	monazite	Th-Pb	22	73 to 48	
AC-1.2	leucosome crystallized in a boudin neck	49°32'49"N; 117°46'49"W	zircon	U-Pb	9	60.2 ± 3.0	2.80
GL-2.1	grt-sil metapelite	49°48'24"N; 117°44'20"W	monazite	Th-Pb	5	59.9 ± 4.2	0.09
GL-12	grt-bt gneiss	49°48'44"N; 117°44'35"W	monazite	Th-Pb	7	70.0 ± 4.5	0.22
DL-1.1	grt-bt gneiss	49°47'42"N; 117°44'17"W	monazite	Th-Pb	10	65.8 ± 3.8	0.89
DL-1.1	grt-bt gneiss	49°47'42"N; 117°44'17"W	monazite	Th-Pb	11	57.4 ± 4.2	1.60
AC-20.1	grt-sil-kfs metapelite	49°32'36"N; 117°43'51"W	monazite	Th-Pb	16	64.5 ± 2.4	1.05
AC-20.1	grt-sil-kfs metapelite	49°32'36"N; 117°43'51"W	monazite	Th-Pb	21	60.1 ± 2.4	1.40

[a]Represents number of analyses that were included in weighted average domain age.

Table 2.3 Analytical $^{232}Th/^{208}Pb$ monazite isotopic data

Grain[a]	Th/U	ThO_2/Th	$^{208}Pb^*/^{232}Th$	% Radiogenic ^{208}Pb	$^{208}Pb/^{232}Th$ Age (Ma)	1 s.e.
Rt6-4 Leucosome crystallized in a boudin neck						
1sp1	10.52	2.388	0.0026	99.05	53.4	0.6
2sp1	20.57	2.376	0.0026	85.69	52.6	0.9
2sp2	16.20	2.298	0.0026	99.08	53.4	0.6
3sp1	16.84	2.363	0.0026	99.03	53.3	0.6
3sp2	11.46	2.420	0.0026	99.01	53.0	0.5
4sp1	16.26	2.466	0.0026	99.03	52.8	0.6
4sp2	16.39	2.596	0.0026	99.01	53.3	0.6
5sp1	20.58	2.431	0.0025	98.16	49.8	0.5
6sp1	17.56	2.458	0.0026	99.11	52.2	0.6
7sp1	11.86	2.502	0.0026	99.01	53.1	0.6
7sp2	11.15	2.538	0.0027	99.05	53.9	0.6
8sp1	10.42	2.383	0.0026	99.04	52.6	0.6
9sp1	13.49	2.406	0.0026	99.03	51.9	0.6
9sp2	16.72	2.246	0.0022	99.03	44.9	0.5
10sp1	17.00	2.401	0.0026	99.02	53.1	0.6
11sp1	58.39	2.486	0.0023	98.58	47.1	0.6
12sp1	15.74	2.532	0.0026	99.11	53.1	0.6
13sp1	19.01	2.411	0.0026	99.03	52.5	0.6
14sp1	10.79	2.387	0.0028	99.08	55.6	2.0
15sp1	11.29	2.472	0.0026	98.95	52.9	0.5
15sp2	10.58	2.534	0.0026	98.78	52.0	0.5
16sp1	17.08	2.383	0.0026	99.03	52.9	0.6
17sp1	16.04	2.512	0.0026	99.16	52.9	0.6
ML-7 Leucogranite						
1sp1	23.50	2.870	0.0025	98.02	50.5	1.7
4sp1	11.14	2.981	0.0025	98.15	49.6	1.6
5sp1	40.90	2.755	0.0025	98.35	50.9	1.8
6sp1	29.87	2.964	0.0025	98.23	51.3	1.6
7sp1	20.05	2.944	0.0026	97.54	51.6	1.6
8sp1	78.96	2.753	0.0027	98.16	54.0	1.9
10sp1	16.35	2.936	0.0024	98.71	49.0	1.6
12sp1	19.69	2.840	0.0025	98.38	49.8	1.7
14sp1	169.60	3.020	0.0025	99.08	50.8	1.6
17sp1	147.90	3.022	0.0026	98.81	51.6	1.6
18sp1	33.52	2.794	0.0026	98.90	51.6	1.8
19sp1	10.89	2.849	0.0026	98.39	51.6	1.8
20sp1	21.20	2.879	0.0025	98.37	50.8	1.7
21sp1	47.92	2.809	0.0025	93.23	50.9	1.8
22sp1	32.35	2.956	0.0025	98.55	51.3	1.6
23sp1	38.97	2.494	0.0029	98.82	58.8	2.5
EL-19 Migmatitic quartzofeldspathic gneiss						
1sp1	27.50	2.621	0.0026	90.96	52.6	2.0
2sp1	24.24	2.711	0.0027	97.39	55.1	2.0
2sp2	34.88	2.327	0.0028	72.78	56.3	2.8
3sp1	38.88	2.684	0.0026	96.05	52.7	2.0
3sp2	26.74	2.074	0.0026	88.72	53.0	3.2
5sp1	41.56	2.567	0.0027	94.09	53.8	2.2
5sp2	38.68	2.639	0.0024	96.73	48.5	1.9
6sp1	13.12	2.606	0.0028	96.75	56.3	2.2
7sp1	24.94	2.314	0.0027	91.57	54.2	2.6
8sp1	22.72	2.162	0.0028	88.44	57.3	3.2
9sp1	8.44	2.402	0.0030	92.51	60.9	2.8
10sp1	26.20	2.623	0.0025	90.64	50.4	2.0
11sp1	14.84	2.517	0.0028	92.11	56.0	2.3
11sp2	8.43	2.510	0.0027	92.89	53.9	2.3
12sp1	13.34	2.613	0.0026	93.41	53.0	2.1
13sp1	6.55	2.674	0.0031	88.55	63.5	2.4
15sp1	11.80	2.574	0.0029	96.64	58.6	2.4
16sp1	8.28	2.342	0.0032	86.31	63.9	3.0
GL-4.1 Migmatitic quartzofeldspathic gneiss						
1sp1	34.57	2.874	0.0026	99.04	52.2	0.5

2sp1	25.50	2.786	0.0026	99.13	51.7	0.7
2sp2	17.27	2.808	0.0026	97.72	51.6	1.0
3sp1	28.27	2.792	0.0026	98.48	51.6	0.6
3sp2	6.54	2.749	0.0027	98.90	54.3	0.6
4sp1	52.22	2.733	0.0026	99.05	51.7	0.5
4sp2	45.21	2.862	0.0026	98.88	51.9	0.5
5sp1	12.10	2.734	0.0025	98.83	50.1	0.5
5sp2	12.12	2.685	0.0024	98.93	48.9	0.6
6sp1	33.91	2.859	0.0025	99.10	49.6	0.6
7sp1	15.31	2.767	0.0025	98.64	49.5	0.5
7sp2	18.31	2.768	0.0025	98.77	49.9	0.6
8sp1	34.34	2.683	0.0027	99.02	55.3	0.5
9sp1	31.67	2.798	0.0026	98.92	53.3	0.6
10sp1	34.50	2.817	0.0027	99.10	54.4	0.6
10sp2	23.81	2.712	0.0031	99.21	61.7	0.9
HR-7.1	**Grt-bearing migmatitic paragneiss**					
1sp1	49.67	2.472	0.0028	99.04	56.8	0.6
1sp2	32.74	2.277	0.0028	99.10	56.5	0.6
2sp1	51.24	2.435	0.0025	98.80	50.7	0.5
3sp1	44.64	2.567	0.0028	99.04	57.0	0.6
3sp2	37.52	2.716	0.0029	99.00	58.0	0.6
4sp1	10.75	2.626	0.0036	99.06	73.0	0.7
4sp2	10.45	2.364	0.0032	99.41	65.4	0.8
5sp1	94.19	2.473	0.0028	99.08	57.1	0.7
6sp1	52.40	2.410	0.0026	98.82	52.6	0.6
6sp2	52.41	2.518	0.0026	98.94	53.3	0.6
7sp1	58.11	2.540	0.0029	98.82	57.7	0.6
8sp1	41.53	2.491	0.0029	98.86	58.6	0.7
9sp1	83.49	2.496	0.0024	98.87	48.3	0.5
10sp1	51.90	2.556	0.0028	98.92	56.5	0.6
11sp1	71.72	2.444	0.0026	98.88	53.2	0.6
12sp1	93.11	2.516	0.0024	98.73	48.4	0.6
12sp2	48.53	2.617	0.0029	98.99	58.4	0.6
13sp1	188.90	1.437	0.0036	99.11	71.8	1.5
14sp1	42.19	1.830	0.0035	99.10	69.9	1.1
15sp1	32.54	2.686	0.0029	99.14	59.4	0.6
16sp1	35.13	2.363	0.0028	99.15	55.8	0.6
17sp1	31.26	2.485	0.0030	98.93	61.0	0.6
AC-1.2	**Leucosome crystallized in a boudin neck**				51.7	0.6
1sp1	85.18	2.803	0.0028	98.91	56.5	2.0
1sp2	85.68	2.496	0.0026	98.99	51.7	1.9
GL-2.1	**GRT-SIL metapelite**					
13sp1	18.68		0.0029	88.85	59.1	3.4
13sp2	18.64		0.0030	91.15	60.1	3.2
17sp1	12.75		0.0032	92.27	64.9	9.7
20sp1*	20.11		0.0030	98.02	59.7	1.5
20sp2*	20.79		0.0030	98.99	60.2	1.6
GL-12	**GRT-bearing biotite gneiss**					
1sp1*	17.63	2.226	0.0036	96.64	72.0	3.8
4sp1	12.36	2.619	0.0034	97.87	67.8	2.6
5sp1	12.49	2.660	0.0031	97.21	62.3	2.4
6sp1	12.37	2.644	0.0033	98.78	65.6	2.5
8sp1	12.10	3.101	0.0035	87.46	71.2	2.3
10sp1	13.88	2.627	0.0034	98.74	69.5	2.7
13sp1	14.58	2.653	0.0029	96.46	59.5	2.3
14sp2	8.91	1.772	0.0029	98.83	58.4	5.3
17sp1	12.38	2.932	0.0031	96.40	61.7	2.0
18sp1	13.82	2.648	0.0034	98.57	69.4	2.6
18sp2	6.83	2.714	0.0035	98.49	70.0	2.6
19sp1	9.93	2.717	0.0035	98.28	69.9	2.5
DL-1.1	**GRT-bearing biotite gneiss**					
1sp1	6.22	2.824	0.0030	97.04	60.9	2.1
1sp2	5.46	2.749	0.0028	93.68	55.9	2.0
4sp1*	0.06	1.582	0.3159	86.72	5549.0	629.0
5sp1*	12.36	3.044	0.0029	97.97	58.2	1.8

5sp2*	10.79	2.554	0.0026	97.46	52.0	2.1
6sp1	6.68	2.751	0.0031	95.19	63.5	2.3
6sp2	5.82	2.725	0.0031	98.09	62.7	2.3
8sp1	11.49	2.698	0.0034	98.06	68.5	2.5
9sp1*	8.84	2.740	0.0033	97.67	66.4	2.4
10sp1*	12.97	2.153	0.0030	85.06	60.1	3.4
12sp1	15.12	2.757	0.0029	98.11	58.1	2.1
12sp2	11.45	2.408	0.0030	96.78	60.4	2.7
13sp1	18.67	2.595	0.0027	95.64	54.4	2.2
13sp2	15.95	2.340	0.0029	89.74	58.8	2.8
14sp1	10.17	2.499	0.0030	94.32	60.0	2.5
14sp2	10.58	2.506	0.0028	98.48	56.4	2.4
15sp1	9.92	2.190	0.0036	88.77	73.2	3.9
16sp1	12.83	2.564	0.0033	98.05	66.5	2.7
16sp2	10.22	2.680	0.0032	97.83	64.7	2.4
17sp1	12.36	2.514	0.0033	95.79	65.7	2.7
18sp1*	6.87	2.505	0.0033	98.54	66.9	2.8
19sp1*	6.14	2.552	0.0033	97.30	66.2	2.7
AC-20.1	**GRT-SIL-KFS metapelite**					
2sp1	4.15		0.0028	94.56	56.6	8.0
9sp1	16.63		0.0030	94.98	59.8	0.8
10sp1*	12.46		0.0030	96.94	61.3	1.1
11sp1	7.83		0.0031	92.35	62.6	2.7
15sp1	4.71		0.0029	97.67	58.0	5.9
16sp1	6.96		0.0029	98.49	58.6	0.7
16bsp1	8.52		0.0031	98.24	62.8	1.6
17sp1	5.92		0.0030	92.44	61.3	5.5
17sp2	6.12		0.0031	95.80	62.4	4.6
18sp1*	9.85		0.0033	97.51	65.7	1.6
19sp1	10.49		0.0031	98.38	63.2	1.5
19sp2	10.23		0.0032	99.26	63.8	1.2
20sp1	6.36		0.0026	97.96	52.5	1.2
21sp1*	10.01		0.0030	97.84	59.6	1.8
21sp2*	10.12		0.0030	98.70	60.9	2.2
21bsp1*	11.12		0.0031	99.20	62.9	1.4
21bsp2*	11.27		0.0032	99.44	63.7	1.0
22asp1*	6.71		0.0036	98.54	71.7	7.6
22asp2*	6.67		0.0035	99.27	71.3	6.4
22bsp1*	13.29		0.0034	96.49	67.7	3.3
22bsp2*	13.19		0.0035	99.04	70.9	2.6
23sp1	6.77		0.0029	97.57	57.6	0.9
23sp2	7.01		0.0030	98.18	59.5	2.7
23bsp1	13.82		0.0036	98.63	72.2	8.3
23bsp2	14.15		0.0036	98.96	72.7	7.2
24sp1*	8.10		0.0031	99.21	63.6	0.7
24sp2*	8.14		0.0032	99.37	64.7	1.1
26sp1	10.16		0.0031	95.71	62.8	3.9
26sp2	7.20		0.0029	91.08	58.5	5.8
27sp1	9.77		0.0033	98.17	65.8	2.2
27sp2	10.41		0.0033	98.89	66.2	1.8
27bsp1	7.47		0.0031	98.98	62.8	4.3
27bsp2	7.53		0.0031	99.19	62.8	3.9
28sp1	8.50		0.0030	98.26	60.2	0.8
28sp2	8.59		0.0030	98.70	60.7	1.1
28bsp1	5.79		0.0033	91.38	66.8	9.9
28bsp2	5.74		0.0033	92.80	66.6	8.6
30sp1	10.18		0.0032	98.29	64.7	2.5

[a]Grain, spot number; * indicates that the grain was included in garnet.

[b]0 represents analyses in which the data did not yield reliable calculated dates.

Table 2.4 Analytical U-Pb zircon isotopic data

Grain[a]	Th (est. ppm)	U (est. ppm)	Th/U	$^{207}Pb/^{206}Pb$	$^{207}Pb/^{235}U$	$^{206}Pb/^{238}U$	% Radiogenic ^{207}Pb	% Radiogenic ^{206}Pb	$^{207}Pb/^{206}Pb$[b] Age (Ma)	1 s.e.	$^{207}Pb/^{235}U$ Age (Ma)	1 s.e.	$^{206}Pb/^{238}U$ Age (Ma)	1 s.e.
Rt6-4 Leucosome crystallized in a boudin neck														
1sp1	83.5	8932.7	0.009	0.047	0.064	0.010	98.10	99.90	76.8	19.9	63.0	1.3	62.6	1.3
1sp2	155.0	13609.2	0.011	0.047	0.068	0.010	99.60	100.00	51.7	13.8	66.8	1.2	67.2	1.2
2sp1	74.1	4970.3	0.014	0.047	0.063	0.010	99.10	99.90	74.3	27.1	61.8	1.4	61.4	1.2
2sp2	32.9	3719.4	0.008	0.044	0.059	0.009	98.90	99.90	0.0	0.0	58.0	1.4	60.1	1.2
3sp1	54.4	7284.4	0.007	0.046	0.064	0.010	99.60	100.00	53.2	26.6	62.7	1.3	63.0	1.2
3sp2	85.9	9408.5	0.009	0.047	0.064	0.010	99.20	100.00	45.4	21.4	62.6	1.2	63.1	1.1
4sp1	334.7	629.7	0.507	0.048	0.057	0.010	86.00	99.20	0.0	0.0	56.7	3.6	61.9	1.4
4sp2	373.1	672.4	0.530	0.049	0.067	0.010	89.40	99.30	187.7	97.1	66.0	3.1	62.7	1.4
5sp1	29.7	4163.8	0.007	0.048	0.059	0.009	99.50	100.00	102.1	24.6	58.6	1.2	57.6	1.1
6sp1	29.4	3967.1	0.007	0.047	0.059	0.009	98.80	99.90	49.3	23.9	58.1	1.2	58.3	1.1
7sp1	50.0	1566.6	0.030	0.043	0.057	0.009	97.00	99.80	0.0	0.0	56.4	1.6	59.4	1.1
12sp2	86.7	5256.5	0.016	0.047	0.062	0.009	99.80	100.00	109.4	20.4	61.1	1.3	59.9	1.2
13sp1	57.7	4762.8	0.012	0.046	0.062	0.009	85.60	99.00	110.7	52.0	61.0	1.8	59.7	1.2
14sp1	76.6	7713.5	0.009	0.047	0.061	0.009	93.90	99.60	101.7	26.0	60.3	1.4	59.3	1.2
15sp1	47.8	6225.6	0.007	0.047	0.061	0.009	97.10	99.80	127.4	19.6	59.8	1.2	58.1	1.2
16sp1	56.8	3501.9	0.015	0.043	0.060	0.009	99.40	100.00	44.4	24.1	59.2	1.3	59.6	1.2
19sp1	92.5	9041.0	0.010	0.047	0.061	0.009	100.00	100.00	57.3	20.8	60.6	1.4	60.7	1.3
AC-1.2 Leucosome crystallized in a boudin neck														
1sp1	185.6	1145.0	0.162	0.048	0.063	0.010	93.60	99.60	52.7	101.0	61.6	2.8	61.8	1.1
2sp1	11.5	371.9	0.031	0.047	0.059	0.009	87.40	99.20	0.0	0.0	58.4	2.6	60.3	1.1
3sp1	35.1	339.9	0.103	0.044	0.062	0.010	98.40	99.90	4.0	100.0	60.7	2.7	62.2	1.1
4sp1	31.0	2560.2	0.012	0.045	0.058	0.009	81.60	98.70	87.4	54.9	57.6	1.6	56.9	0.9
5sp1	9.8	134.4	0.073	0.047	0.071	0.009	93.30	99.50	378.2	157.0	69.5	5.1	60.9	1.3
7sp1	48.6	386.5	0.126	0.039	0.058	0.009	89.50	99.40	0.0	0.0	56.9	3.9	60.7	1.3
8sp1	14.2	677.8	0.021	0.041	0.055	0.009	99.10	100.00	0.0	0.0	54.0	1.6	60.9	1.1
9sp1	14.7	1085.3	0.014	0.047	0.062	0.009	98.80	99.90	181.2	55.6	61.4	1.9	58.4	1.0
10sp1	11.9	282.2	0.042	0.046	0.064	0.010	91.50	99.50	106.2	136.0	62.7	4.2	61.6	1.7
12sp1	83.8	643.3	0.130	0.046	0.065	0.010	104.00	100.00	162.3	146.0	64.3	4.2	61.7	1.0
13sp1	20.3	963.0	0.021	0.045	0.061	0.009	98.70	99.90	137.1	61.9	60.5	2.1	58.5	1.2

[a]Grain, spot number.

[b]0 represents analyses in which the data did not yield reliable calculated dates.

Table 2.5 Summary of Sample Lithology, Location, and $^{40}Ar/^{39}Ar$ Ages

Sample ID	Rock Type	Location	Analyzed Mineral	Integrated Age (Ma)	steps	% ^{39}Ar	Preferred Age (Ma)
Rt6-4	leucosome crystallized in a boudin neck	49° 48'26"N; 117°28'08"W	biotite	48.2 ± 0.6	3 - 13	91.4	48.1 ± 0.5
GL-4.1	migmatitic quartzofeldspathic gneiss	49° 48'54"N; 117°44'40"W	biotite	50.9 ± 0.4	2 - 7	79.9	50.6 ± 0.2
HR-7.1	grt-bearing migmatitic paragneiss	49° 40'50"N; 117°42'45"W	biotite	49.6 ± 0.9	4 - 6	57.4	48.8 ± 0.4
AC-1.2	leucosome crystallized in a boudin neck	49° 32'49"N; 117°46'49"W	biotite	52.5 ± 0.6	3 - 8	62.2	51.4 ± 0.4
VP-2.1	leucogranite	49° 42'59"N; 117°57'54"W	biotite	53.1 ± 1.0	10 - 12	15.2	57.7 ± 0.7
VP-2.1	leucogranite	49° 42'59"N; 117°57'54"W	biotite	53.1 ± 1.0	6 - 9	30.5	53.1 ± 0.3
PR-2.1	grt-bearing paragneiss	49° 34'29"N; 117°43'48"W	biotite	48.9 ± 0.8	3 - 7	74.6	48.6 ± 0.5
PR-2.1	grt-bearing paragneiss	49° 34'29"N; 117°43'48"W	muscovite	53.8 ± 1.6	5 - 13	65.3	54.7 ± 1.1
GL-6.1	amphibolite	49° 49'08"N; 117°44'45"W	hornblende	55.5 ± 0.9	5 - 11	71.9	54.3 ± 0.4
HR-4.1	amphibolite	49° 39'14"N; 117°42'36"W	hornblende	89.3 ± 0.5			
AC-1.3	amphibolite	49° 32'49"N; 117°46'49"W	hornblende	79.4 ± 0.8	7 - 10	19.1	60.3 ± 0.5

Table 2.6 Analytical $^{40}Ar/^{39}Ar$ isotopic data[a]

ID	Temp (ºC)	^{36}Ar (mol)	^{37}Ar (mol)	^{39}Ar (mol)	^{40}Ar (mol)	$^{40}Ar^*$ (%)	$^{40}Ar^*/^{39}Ar(K)$	Cumulate ^{39}Ar (%)	Calculated Age (Ma)	± 1 s.d. (Ma)	Ca/K
Rt6-4.1 biotite, leucosome crystallized in a boudin neck, J = 2.1880E-3, Lambda K40 = 5.5430E-10											
1	570	1.0090E-15	2.5970E-16	2.8960E-15	3.2420E-13	8.0	8.96	1.6	35.0	3.5	1.70E-01
2	600	4.9110E-16	2.5730E-16	3.0350E-15	1.7980E-13	19.3	11.42	3.2	44.5	2.3	1.61E-01
3	620	4.7230E-16	1.7990E-16	5.0480E-15	2.0160E-13	30.7	12.27	6.0	47.8	1.1	6.77E-02
4	650	3.6310E-16	2.2860E-16	9.9590E-15	2.2740E-13	52.7	12.03	11.4	46.9	0.5	4.36E-02
5	680	1.3640E-16	2.5190E-16	1.5640E-14	2.3410E-13	82.6	12.37	20.0	48.2	0.4	3.06E-02
6	720	4.8080E-17	3.6360E-16	2.9520E-14	3.7720E-13	96.0	12.27	36.1	47.8	0.2	2.34E-02
7	760	2.3730E-17	4.0900E-16	4.2520E-14	5.2560E-13	98.5	12.17	59.4	47.4	0.8	1.83E-02
8	800	1.8130E-17	4.0130E-16	2.2150E-14	2.8020E-13	97.9	12.39	71.5	48.2	0.2	3.44E-02
9	830	1.6800E-17	3.5020E-16	6.8860E-15	9.3040E-14	94.5	12.77	75.2	49.7	0.4	9.66E-02
10	870	2.2800E-17	3.8190E-16	5.8620E-15	8.0090E-14	91.4	12.49	78.4	48.7	0.6	1.24E-01
11	910	2.3430E-17	4.8800E-16	8.1370E-15	1.1180E-13	93.7	12.87	82.9	50.1	0.4	1.14E-01
12	960	3.2470E-17	6.8800E-16	1.4360E-14	1.8960E-13	94.8	12.51	90.7	48.7	0.3	9.10E-02
13	1010	3.1980E-17	7.9680E-16	1.2120E-14	1.6240E-13	94.0	12.60	97.4	49.1	0.3	1.25E-01
14	1060	3.7360E-17	1.1180E-15	3.8250E-15	6.0910E-14	81.9	13.04	99.5	50.8	1.4	5.55E-01
15	1120	5.2380E-17	2.0880E-15	4.9140E-16	2.4990E-14	38.9	19.82	99.7	76.6	5.6	8.10E+00
16	1350	2.5040E-16	2.4920E-15	5.2100E-16	8.8630E-14	16.8	28.65	100.0	109.7	12.9	9.12E+00
Total		3.0300E-15	1.0750E-14	1.8300E-13	3.1620E-12		12.37				
Integrated age ± 1 s.d.				*n* = 16					48.2	0.6	
Preferred aged ± 1 s.d.			steps 3-13	*n* = 11					48.1	0.5	
GL-4.1 biotite, migmatitic quartzofeldspathic gneiss, J = 2.1954E-3, Lambda K40 = 5.5430E-10											
1	570	1.1110E-15	4.6450E-19	7.6420E-15	4.2070E-13	21.9	12.08	2.7	47.2	1.4	1.15E-04
2	600	4.2680E-16	4.6480E-19	1.0720E-14	2.6430E-13	52.2	12.86	6.5	50.2	0.7	8.24E-05
3	620	2.4990E-16	1.4790E-17	1.6190E-14	2.8430E-13	73.9	12.98	12.3	50.7	0.5	1.74E-03
4	650	1.6960E-16	4.6530E-19	2.8780E-14	4.2280E-13	88.0	12.92	22.5	50.5	0.3	3.07E-05
5	680	7.9250E-17	3.7480E-17	5.0550E-14	6.7910E-13	96.4	12.95	40.4	50.6	0.2	1.41E-03
6	720	5.5470E-17	7.8450E-17	8.5850E-14	1.1320E-12	98.3	12.96	70.9	50.6	0.2	1.74E-03
7	760	6.6220E-17	1.0510E-16	4.3770E-14	5.9050E-13	96.5	13.02	86.4	50.8	0.2	4.56E-03
8	800	6.5850E-17	1.9480E-16	6.8300E-15	1.1230E-13	82.5	13.58	88.8	53.0	0.3	5.42E-02
9	830	6.1040E-17	1.9510E-16	2.7300E-15	5.4110E-14	66.6	13.19	89.8	51.5	0.9	1.36E-01
10	870	4.7060E-17	1.9670E-16	3.4930E-15	6.2040E-14	77.5	13.76	91.0	53.7	0.4	1.07E-01
11	910	4.2970E-17	1.1870E-16	5.6280E-15	8.8780E-14	85.5	13.49	93.0	52.7	0.4	4.01E-02
12	960	2.3960E-17	7.1200E-17	9.0700E-15	1.2980E-13	94.4	13.50	96.2	52.7	0.6	1.49E-02
13	1010	4.2750E-17	8.7140E-17	8.2220E-15	1.2070E-13	89.4	13.12	99.2	51.2	0.5	2.01E-02
14	1060	2.1310E-17	9.7720E-17	9.3310E-16	2.1890E-14	71.2	16.70	99.5	64.9	1.8	1.99E-01
15	1120	3.8390E-17	1.9200E-16	4.3330E-16	1.9020E-14	40.4	17.74	99.6	68.9	7.6	8.42E-01
16	1350	2.3500E-16	2.1190E-16	1.0070E-15	8.8170E-14	21.2	18.59	100.0	72.2	9.1	4.00E-01
Total		2.7360E-15	1.6030E-15	2.8180E-13	4.4900E-12		13.04				
Integrated age ± 1 s.d.				*n* = 16					50.9	0.4	
Preferred age ± 1 s.d.			steps 2-7	*n* = 6					50.6	0.2	
HR-7.1 biotite, migmatitic paragneiss, J = 2.1937E-3, Lambda K40 = 5.5430E-10											
1	570	1.6940E-15	8.1390E-18	2.0120E-15	5.2900E-13	5.4	14.13	1.2	55.1	15.8	7.69E-03
2	600	5.3830E-16	7.7720E-18	1.9090E-15	1.8690E-13	14.9	14.55	2.3	56.7	3.1	7.73E-03
3	640	5.5320E-16	1.4780E-17	9.8010E-15	2.8600E-13	42.8	12.48	8.1	48.7	2.4	2.87E-03
4	680	7.2800E-16	1.8990E-17	3.8100E-14	6.8660E-13	68.5	12.35	30.4	48.2	0.3	9.47E-04

5	720	1.8920E-16	2.4130E-17	6.0680E-14	8.2370E-13	93.0	12.63	66.0	49.3	0.3	7.56E-04
6	760	2.7450E-16	3.4270E-17	3.7120E-14	5.4510E-13	84.9	12.47	87.8	48.7	0.6	1.75E-03
7	800	2.7990E-16	5.0580E-17	6.2130E-15	1.6480E-13	49.7	13.19	91.4	51.5	1.1	1.55E-02
8	830	1.5360E-16	3.0210E-17	1.9380E-15	7.2320E-14	37.2	13.87	92.6	54.1	3.4	2.96E-02
9	870	1.1090E-16	1.6340E-17	2.0930E-15	6.0950E-14	46.1	13.44	93.8	52.4	2.2	1.48E-02
10	910	6.6330E-17	2.2900E-17	2.8030E-15	5.7260E-14	65.6	13.41	95.4	52.3	1.1	1.55E-02
11	960	4.2950E-17	9.8010E-18	4.0870E-15	6.6390E-14	80.7	13.11	97.8	51.2	0.6	4.56E-03
12	1010	3.5660E-17	9.3040E-18	2.2700E-15	4.3150E-14	75.4	14.34	99.2	55.9	1.0	7.79E-03
13	1060	2.7930E-17	5.7390E-17	5.8240E-16	1.8990E-14	56.5	18.42	99.5	71.5	4.9	1.87E-01
14	1120	3.2330E-17	7.0790E-17	1.5930E-16	1.7990E-14	46.9	52.97	99.6	198.3	29.2	8.45E-01
15	1350	2.5630E-16	6.4180E-17	6.8340E-16	8.5900E-14	11.8	14.85	100.0	57.8	7.4	1.78E-01
Total		4.9830E-15	4.3960E-16	1.7050E-13	3.6450E-12		12.72				
Integrated age ± 1 s.d.				*n* = 15					49.6	0.9	
Preferred age ± 1 s.d.			steps 5-6	*n* = 2					49.1	0.4	
AC-1.2 biotite, leucosome crystallized in a boudin neck, J = 2.1808E-3, Lambda K40 = 5.5430E-10											
1	570	5.4770E-16	2.2620E-16	1.6810E-15	1.8000E-13	10.1	10.78	1.1	41.9	6.9	2.56E-01
2	600	2.8500E-16	7.4110E-17	1.6370E-15	1.0260E-13	17.8	11.18	2.2	43.5	4.3	8.60E-02
3	640	6.0030E-16	4.3730E-17	4.1160E-15	2.3060E-13	23.0	12.91	4.9	50.1	2.0	2.02E-02
4	680	5.8410E-16	5.4050E-17	9.8670E-15	3.0390E-13	43.1	13.28	11.5	51.5	0.9	1.04E-02
5	720	2.3400E-16	6.5620E-17	1.6970E-14	2.9290E-13	76.2	13.16	22.7	51.1	0.3	7.35E-03
6	760	1.0030E-16	6.2760E-17	2.6470E-14	3.8160E-13	92.0	13.27	40.2	51.5	0.4	4.51E-03
7	800	7.3620E-17	8.8770E-17	2.7030E-14	3.8140E-13	94.1	13.28	58.1	51.5	0.2	6.24E-03
8	830	5.5150E-17	6.7610E-17	1.3620E-14	1.9840E-13	91.6	13.35	67.1	51.8	0.3	9.43E-03
9	870	3.7180E-17	1.2720E-16	7.9470E-15	1.2420E-13	91.0	14.22	72.4	55.1	0.6	3.04E-02
10	910	4.2990E-17	3.4630E-16	5.8440E-15	9.5770E-14	86.6	14.19	76.3	55.0	0.6	1.13E-01
11	960	6.4000E-17	9.2810E-16	1.0300E-14	1.7000E-13	88.8	14.65	83.1	56.7	0.5	1.71E-01
12	1010	7.7180E-17	1.0560E-15	1.2620E-14	2.0220E-13	88.6	14.20	91.5	55.0	0.4	1.59E-01
13	1060	7.9530E-17	2.7510E-15	9.0660E-15	1.5200E-13	84.6	14.18	97.5	55.0	0.4	5.77E-01
14	1120	4.8350E-17	1.4170E-15	2.5550E-15	5.1510E-14	72.4	14.61	99.2	56.6	1.3	1.05E+00
15	1350	1.9920E-16	1.2670E-15	1.2880E-15	7.6900E-14	23.6	14.08	100.0	54.6	5.1	1.87E+00
Total		3.0290E-15	8.5760E-15	1.5100E-13	2.9440E-12		13.55				
Integrated age ± 1 s.d.				*n* = 15					52.5	0.6	
Preferred age ± 1 s.d.			steps 3-8	*n* = 6					51.4	0.4	
VP-2.1 biotite, Ladybird granite, J = 2.1740E-3, Lambda K40 = 5.5430E-10											
1	570	7.6700E-16	6.3740E-17	1.1960E-15	2.3580E-13	3.9	7.60	0.9	29.6	9.7	1.01E-01
2	600	3.6290E-16	1.1170E-16	1.4980E-15	1.2020E-13	10.8	8.66	2.0	33.6	5.3	1.42E-01
3	640	8.5050E-16	6.7250E-17	2.6130E-15	2.8070E-13	10.5	11.24	3.9	43.6	4.6	4.89E-02
4	680	1.1880E-15	2.9810E-17	6.3640E-15	4.2730E-13	17.8	11.95	8.6	46.3	2.4	8.90E-03
5	720	6.1590E-16	6.4120E-17	1.4250E-14	3.6860E-13	50.5	13.08	19.0	50.6	0.6	8.55E-03
6	760	1.9470E-16	6.7580E-17	2.3260E-14	3.7490E-13	84.5	13.62	36.0	52.6	0.3	5.52E-03
7	800	5.9980E-17	2.6300E-17	2.3260E-14	3.3850E-13	94.6	13.77	53.1	53.2	0.2	2.15E-03
8	830	4.7620E-17	4.6000E-17	1.2080E-14	1.8260E-13	92.1	13.93	61.9	53.8	0.4	7.24E-03
9	870	6.4300E-17	4.1750E-17	6.3090E-15	1.0580E-13	81.9	13.73	66.5	53.1	1.1	1.26E-02
10	910	6.7240E-17	6.2890E-17	6.0050E-15	1.0880E-13	81.6	14.79	70.9	57.1	0.6	1.99E-02
11	960	9.4550E-17	1.0200E-16	1.0060E-14	1.7950E-13	84.3	15.05	78.3	58.1	0.5	1.93E-02
12	1010	7.7230E-17	1.6560E-16	1.0700E-14	1.8280E-13	87.4	14.92	86.1	57.6	0.9	2.94E-02
13	1060	7.7170E-17	3.0610E-16	1.0490E-14	1.6910E-13	86.4	13.93	93.8	53.8	3.5	5.54E-02
14	1120	7.0270E-17	1.8360E-15	6.8800E-15	1.1760E-13	82.4	14.09	98.9	54.4	0.7	5.07E-01

15	1350	1.6720E-16	8.5220E-16	1.5680E-15	7.5870E-14	34.9	16.92	100.0	65.2	1.9	1.03E+00
Total		4.7050E-15	3.8430E-15	1.3650E-13	3.2680E-12		13.73				
Integrated age ± 1 s.d.				*n* = 15					53.1	1.0	
Preferred age #1 ± 1 s.d.			steps 6-9	*n = 4*					53.1	0.3	
Preferred age #2 ± 1 s.d.			steps 10-12	*n = 3*					57.7	0.7	
PR-2.1 biotite, grt-bearing paragneiss, J = 2.1844E-3, Lambda K40 = 5.5430E-10											
1	570	5.6140E-16	2.4740E-17	4.3640E-15	2.0970E-13	20.9	10.02	2.6	39.1	2.3	1.08E-02
2	600	2.5230E-16	2.8350E-17	4.2010E-15	1.2320E-13	39.4	11.55	5.1	44.9	1.4	1.28E-02
3	640	2.7730E-16	1.3130E-17	1.3430E-14	2.4960E-13	67.0	12.46	13.0	48.4	0.8	1.86E-03
4	680	1.6030E-16	1.0540E-17	2.8520E-14	4.0190E-13	88.0	12.40	29.9	48.2	0.2	7.02E-04
5	720	6.9980E-17	1.6990E-17	4.4090E-14	5.7330E-13	96.2	12.51	56.0	48.6	1.1	7.32E-04
6	760	5.3660E-17	3.0320E-17	4.1320E-14	5.3540E-13	96.8	12.55	80.5	48.8	0.2	1.39E-03
7	800	5.0780E-17	3.0560E-17	1.2010E-14	1.6810E-13	90.9	12.71	87.6	49.4	0.2	4.83E-03
8	830	3.8220E-17	2.6220E-17	3.2060E-15	5.3720E-14	78.8	13.21	89.5	51.3	0.9	1.55E-02
9	870	2.8490E-17	2.0180E-17	2.6460E-15	4.7020E-14	81.9	14.56	91.1	56.5	1.3	1.45E-02
10	910	2.6490E-15	8.1890E-18	1.9710E-15	8.0590E-13	2.9	11.78	92.2	45.8	10.7	7.90E-03
11	960	5.1060E-17	4.8120E-19	3.6340E-15	6.5730E-14	76.9	13.91	94.4	54.0	1.0	2.52E-04
12	1010	3.8100E-17	2.1410E-17	5.2870E-15	8.2060E-14	86.1	13.37	97.5	51.9	0.8	7.69E-03
13	1060	2.4660E-17	4.2240E-17	2.8020E-15	4.7030E-14	84.4	14.16	99.2	55.0	0.9	2.86E-02
14	1120	3.4760E-17	1.9070E-16	7.6550E-16	2.2330E-14	54.0	15.75	99.6	61.0	3.0	4.73E-01
15	1350	2.1300E-16	1.2050E-16	6.0970E-16	7.3130E-14	13.9	16.69	100.0	64.6	3.4	3.76E-01
Total		4.5030E-15	5.8460E-16	1.6890E-13	3.4580E-12		12.57				
Integrated age ± 1 s.d.				*n* = 15					48.9	0.8	
Preferred age ± 1 s.d.			steps 3-7	*n* = 5					48.6	0.5	
PR-2.1 muscovite, grt-bearing paragneiss, J = 2.1671E-3, Lambda K40 = 5.5430E-10											
1	570	4.8130E-16	1.5620E-17	6.1740E-16	1.5170E-13	6.2	15.33	1.4	59.0	19.8	4.81E-02
2	600	9.5200E-17	2.1570E-17	4.3440E-16	3.5440E-14	20.6	16.81	2.5	64.5	10.2	9.44E-02
3	620	4.6350E-17	3.5160E-18	5.5190E-16	2.1160E-14	35.2	13.50	3.7	52.0	5.1	1.21E-02
4	650	1.1000E-16	2.7280E-16	6.7280E-15	9.6890E-14	66.3	9.55	19.4	37.0	0.7	7.70E-02
5	680	4.1260E-17	4.9390E-19	2.7160E-15	5.2950E-14	76.8	14.98	25.7	57.7	1.2	3.46E-04
6	720	4.2730E-17	5.1460E-17	3.0390E-15	5.6800E-14	77.6	14.51	32.8	55.9	0.8	3.22E-02
7	760	3.9740E-17	3.5490E-17	2.7630E-15	5.0280E-14	76.5	13.92	39.2	53.6	1.3	2.44E-02
8	800	4.5800E-17	2.5410E-17	3.3080E-15	6.0000E-14	77.3	14.02	46.9	54.0	1.6	1.46E-02
9	830	3.3760E-17	9.1610E-18	3.0650E-15	5.3020E-14	81.0	14.02	54.0	54.0	1.1	5.68E-03
10	870	3.8610E-17	6.2930E-18	4.0820E-15	6.5630E-14	82.4	13.26	63.5	51.1	0.7	2.93E-03
11	910	3.1100E-17	3.8540E-18	4.3270E-15	6.7990E-14	86.3	13.56	73.6	52.3	0.4	1.69E-03
12	960	4.0720E-17	1.8220E-17	4.3820E-15	7.7600E-14	84.3	14.94	83.8	57.5	0.9	7.90E-03
13	1010	3.8010E-17	4.2410E-17	3.1270E-15	5.8430E-14	80.6	15.07	91.1	58.0	2.3	2.58E-02
14	1060	3.3010E-17	2.4490E-16	1.2760E-15	3.0300E-14	67.8	16.09	94.0	61.8	2.1	3.65E-01
15	1120	2.3150E-17	2.2160E-16	9.0890E-16	2.8310E-14	75.8	23.62	96.1	90.1	2.9	4.63E-01
16	1350	1.6170E-16	1.6830E-16	1.6630E-15	8.0330E-14	40.5	19.56	100.0	74.9	3.8	1.92E-01
Total		1.3020E-15	1.1410E-15	4.2990E-14	9.8680E-13		13.98				
Integrated age ± 1 s.d.				*n* = 16					53.8	1.6	
Preferred aged ± 1 s.d.			steps 5-13	*n* = 9					54.7	1.1	
GL-6.1 hornblende, amphibolite, J = 2.1688E-3, Lambda K40 = 5.5430E-10											
1	860	1.7480E-16	4.5810E-15	2.1170E-15	9.0800E-14	43.6	18.73	2.2	71.8	2.2	4.12E+00

2	900	7.4790E-18	2.0900E-15	7.8160E-16	1.9610E-14	89.7	22.56	3.1	86.2	3.4	5.09E+00
3	950	1.7160E-17	4.6520E-15	1.6590E-15	3.3420E-14	86.1	17.39	4.8	66.8	2.1	5.34E+00
4	1000	2.0100E-17	1.6790E-14	4.7930E-15	7.6580E-14	94.3	15.12	9.9	58.2	0.8	6.68E+00
5	1030	3.1480E-17	5.2560E-14	1.3640E-14	1.9620E-13	97.8	14.12	24.2	54.4	0.3	7.34E+00
6	1060	5.6050E-17	1.2490E-13	3.3020E-14	4.6430E-13	99.0	13.97	59.0	53.8	0.3	7.21E+00
7	1090	3.3950E-17	4.8220E-14	1.2120E-14	1.7570E-13	96.9	14.10	71.7	54.4	0.5	7.59E+00
8	1120	3.5360E-17	5.2930E-14	1.2880E-14	1.8680E-13	97.2	14.13	85.3	54.5	0.4	7.83E+00
9	1150	3.7020E-17	3.0190E-14	7.2640E-15	1.1220E-13	92.9	14.39	93.0	55.4	0.4	7.92E+00
10	1180	4.5500E-17	1.2190E-14	3.0060E-15	5.4170E-14	77.4	13.99	96.1	53.9	1.0	7.73E+00
11	1210	4.8140E-17	6.3100E-15	1.5850E-15	3.6760E-14	63.0	14.65	97.8	56.4	1.6	7.59E+00
12	1240	6.0030E-17	4.6010E-15	1.1260E-15	3.4490E-14	49.9	15.32	99.0	59.0	6.2	7.79E+00
13	1280	7.6700E-17	2.1880E-15	5.4130E-16	3.1020E-14	27.6	15.88	99.5	61.1	18.4	7.70E+00
14	1320	1.2220E-16	9.7520E-16	2.7640E-16	4.0370E-14	10.8	15.83	99.8	60.9	22.7	6.72E+00
15	1420	3.2820E-16	3.1560E-16	1.6620E-16	1.0070E-13	3.7	22.39	100.0	85.6	66.9	3.61E+00
Total		1.0940E-15	3.6350E-13	9.4980E-14	1.6530E-12		14.41				
Integrated age ± 1 s.d.				*n* = 15					55.5	0.9	
Preferred age ± 1 s.d.			steps 5-10	*n* = 6					54.2	0.4	

HR-4.1 hornblende, amphibolite, J = 2.1674E-3, Lambda K40 = 5.5430E-10

1	600	7.2260E-16	5.4350E-16	2.3300E-16	2.3880E-13	10.6	108.84	0.8	382.1	137.4	4.44E+00
2	640	1.2920E-16	5.4200E-16	9.4920E-17	4.5940E-14	17.0	82.62	1.1	297.2	62.3	1.09E+01
3	680	9.6910E-17	6.9990E-16	9.3730E-17	3.7820E-14	24.5	99.27	1.4	351.6	75.4	1.43E+01
4	750	1.4640E-16	1.2010E-15	1.6980E-16	1.2010E-13	64.1	455.47	2.0	1238.9	52.3	1.35E+01
5	820	1.3060E-16	1.5170E-15	2.1400E-16	1.3210E-13	70.9	440.06	2.8	1208.3	22.1	1.35E+01
6	880	7.5980E-17	1.0360E-15	2.3330E-16	4.1480E-14	46.1	82.28	3.5	296.0	18.1	8.47E+00
7	950	7.5370E-17	2.1220E-15	4.5660E-16	3.3590E-14	34.3	25.34	5.1	96.4	7.0	8.86E+00
8	1020	1.8430E-16	1.4970E-13	9.9940E-15	2.0690E-13	81.0	16.98	38.9	65.2	0.8	2.88E+01
9	1050	1.1120E-16	1.6000E-13	1.0770E-14	1.6810E-13	90.1	14.24	75.4	54.8	0.6	2.86E+01
10	1080	2.6370E-17	8.5270E-15	6.5360E-16	1.7850E-14	61.2	16.88	77.6	64.8	4.0	2.50E+01
11	1120	5.9040E-17	4.2660E-14	2.7820E-15	5.4130E-14	75.8	14.93	87.0	57.4	1.6	2.95E+01
12	1160	7.1290E-17	3.0440E-14	2.0250E-15	4.4000E-14	59.2	13.01	93.9	50.2	1.3	2.89E+01
13	1200	6.5530E-17	1.5600E-14	1.0360E-15	3.5460E-14	49.9	17.27	97.4	66.3	2.5	2.90E+01
14	1250	7.5880E-17	7.7740E-15	5.1660E-16	3.3740E-14	35.9	23.72	99.1	90.5	9.0	2.89E+01
15	1320	1.3440E-16	1.8930E-15	1.4400E-16	4.3900E-14	10.0	30.70	99.6	116.2	39.3	2.52E+01
16	1420	3.7250E-16	1.8910E-16	1.1730E-16	1.1890E-13	7.4	75.14	100.0	272.2	273.8	3.07E+00
Total		2.4780E-15	4.2450E-13	2.9530E-14	1.3730E-12		23.42				
Integrated age ± 1 s.d.				*n* = 16					89.3	4.6	

AC-1.3 hornblende, amphibolite, J = 2.1697E-3, Lambda K40 = 5.5430E-10

1	860	8.6990E-16	1.8410E-15	8.7250E-16	5.0820E-13	49.5	288.57	0.9	877.1	11.2	4.01E+00
2	900	5.4850E-17	8.6230E-16	2.9690E-16	3.6420E-14	55.7	68.52	1.2	250.1	9.3	5.53E+00
3	950	6.0560E-17	3.5210E-15	6.6260E-16	4.4900E-14	60.9	41.45	1.9	155.4	5.8	1.01E+01
4	1000	7.5430E-17	1.5230E-14	2.9190E-15	1.1080E-13	81.2	30.94	4.9	117.2	1.3	9.95E+00
5	1030	6.8690E-17	3.5050E-14	7.9830E-15	2.0810E-13	91.9	24.03	13.2	91.7	0.5	8.37E+00
6	1060	1.5180E-16	1.5790E-13	3.6670E-14	7.0150E-13	95.8	18.39	51.3	70.6	0.2	8.21E+00
7	1090	8.3350E-17	1.1550E-13	2.6010E-14	4.1250E-13	96.8	15.40	78.3	59.3	0.4	8.47E+00
8	1120	4.6110E-17	4.5040E-14	9.7200E-15	1.6510E-13	94.4	16.09	88.4	61.9	0.4	8.84E+00
9	1150	3.7520E-17	2.7890E-14	6.0150E-15	1.0400E-13	92.0	15.95	94.7	61.4	0.9	8.84E+00
10	1180	3.6170E-17	1.2380E-14	2.6190E-15	5.1320E-14	81.5	16.04	97.4	61.7	1.0	9.02E+00
11	1210	4.1200E-17	3.7260E-15	8.9630E-16	2.8080E-14	57.9	18.21	98.3	69.9	3.3	7.92E+00

12	1240	4.6210E-17	2.1710E-15	6.0040E-16	2.6340E-14	49.0	21.54	98.9	82.4	5.0	6.89E+00
13	1280	7.5450E-17	1.0170E-15	4.1890E-16	2.9140E-14	23.8	16.59	99.4	63.8	8.5	4.62E+00
14	1320	1.1260E-16	1.8570E-16	2.8030E-16	3.6540E-14	8.9	11.66	99.7	45.1	18.7	1.26E+00
15	1420	2.8510E-16	2.9960E-17	3.2930E-16	9.1230E-14	7.6	21.16	100.0	81.0	39.1	1.73E-01
Total		2.0450E-15	4.2240E-13	9.6290E-14	2.5540E-12		20.75				
Integrated age ± 1 s.d.				*n* = 15					79.4	0.8	
Preferred aged ± 1 s.d.			steps 7-10	*n* = 4					60.3	0.5	

[a]Separates were irradiated for 96 hours in positions X33 or X34 of the HIFAR nuclear reactor at Lucas Heights, New South Wales. Cadmium shielding was used to reduce the thermal neutron dose rece by the samples. The minerals were irradiated with the fluence monitor GA1550 [intercalibrated K/Ar age of 98.5 Ma; *Spell and McDougall*, 2003].

Chapter 3: Fluid-rock Interaction in Orogenic Crust Tracked by Zircon Depth Profiling

Stacia Gordon*, Marty Grove, Donna Whitney*, Axel Schmitt***, Christian Teyssier***

*Department of Geology and Geophysics, University of Minnesota, Minneapolis, MN 55455
**Department of Geological and Environmental Sciences, Stanford University, Stanford, CA 94305
***Department of Earth and Space Sciences, University of California, Los Angeles, CA 90095

This chapter has been submitted to *Geology* and is currently in the review process.

ABSTRACT

Ion microprobe U-Pb, $\delta^{18}O$, and Ti depth profiling analyses of natural zircon rims permit unprecedented assessment of the relationship between timing, temperature, and geochemical environment during crystallization and cooling of deep orogenic crust. Zircon from migmatite in a deeply exhumed gneiss dome in the Valhalla metamorphic core complex, SE British Columbia, Canada, record the timing of melt crystallization and subsequent fluid-rock interaction before the final stages of extension and exhumation. Zircon interiors reveal a weighted mean age of 58 ± 2 Ma, interpreted as the timing of melt crystallization. Depth profiling U-Pb measurements of unpolished zircon rims yield an age of 51 Ma over 4 μm. Ti in zircon thermometry indicates 650 ºC for both rim and interior, confirming that the complex remained at high-temperature during zircon crystallization. Previous $\delta^{18}O$ measurements suggest that high temperature fluids with $\delta^{18}O$ of ca. 10 ‰ pervasively infiltrated the complex. The oxygen zircon results clearly resolve a $\delta^{18}O$ contrast between zircon interiors (7.2 ‰) and rims (8.4 ‰). The heavy interior $\delta^{18}O$ values indicate the timing of melt crystallization and equilibration of the rims with melt at 58 Ma. Alternatively, $\delta^{18}O$ values from the 51 Ma rims match the composition predicted (8.4 ‰) from fluid interaction based upon previous work. Integrating the age and $\delta^{18}O$ results reveal that amphibolite-facies fluid-rock interaction persisted until final rapid exhumation of the Valhalla complex. The results further indicate the potential power of coupling ion microprobe U-Pb, $\delta^{18}O$, and Ti depth profiling of natural zircon rims to assess crustal evolution.

INTRODUCTION

Fluid-rock interactions strongly influence partial melting, rock deformation and metamorphic processes during orogeny (e.g., Newton, 1989; Morrison and Anderson, 1998; Manning and Ingebritsen, 1999; Baxter, 2003). Fluids are especially important because their circulation may strongly influence the thermal and mechanical behavior of the system. The relative timing of fluid-rock interaction during metamorphism and magmatism is generally resolved from field-based relative timing relationships such as those involving veins or metasomatic zones (e.g., Bebout and Barton, 1989). The absolute timing can be determined if a geologic feature created by or affected by fluid-rock interaction can be directly dated by radiogenic isotope methods. However, this can be a challenging task in high-grade metamorphic terrains where robust geochronometers like zircon are generally highly resistant to recrystallization, even during melt-generating reactions (Harrison and Watson, 1983; Watson, 1996). Characteristically, new zircon crystallization during amphibolite facies metamorphism is minimal and expressed by μm-scale overgrowths (e.g., Corfu et al., 2003). Resolving such a record thus requires high spatial resolution (e.g., Zeitler and Williams, 1988; Mojzsis and Harrison, 2002). Previous studies have used the ion microprobe in depth profiling mode to achieve the submicrometer-scale spatial resolution required to analyze ultrathin zircon rims that crystallized in response to fluid interactions (e.g., Carson et al., 2002; Breeding et al., 2004). In this study, we go further by integrating U-Pb age, Ti geothermometry, and oxygen isotope depth profiling of zircon rims to better understand timing, metamorphic conditions, and geochemistry of fluid-rock interaction in orogenic crust during the final stages of extension and gneiss dome crystallization in a metamorphic core complex.

GEOLOGIC BACKGROUND

The Valhalla complex is a gneiss dome located within the Shuswap metamorphic core complex, SE British Columbia (Fig. 1; Reesor, 1965; Carr et al., 1987). The complex exposes migmatitic gneisses and granitoid that achieved conditions of 820 ºC and 8 kbar (Spear and Parrish, 1996). Metamorphism occurred from ca. 85 to 58 Ma and culminated in a 62-58 Ma episode of granitoid emplacement and partial melt crystallization (Parrish et al., 1988; Parrish, 1995; Spear and Parrish, 1996; Gordon et al., 2008). Between 58 and 47 Ma, the Valhalla gneiss dome was exhumed to upper crustal levels (T <300 ºC; Parrish et al., 1988; Gordon et al., 2008).

Monazite Th-Pb age results from the migmatites range from 58 to 50 Ma (Gordon et al., 2008). Backscattered electron imaging of the monazites typically reveal patchy zoning, a texture that has been attributed to fluid-mediated recrystallization (Townsend et al., 2000). The variability in Th-Pb dates and the complicated zoning patterns exhibited by monazite are consistent with recrystallization involving fluids (See Ayers et al., 2006). Fluid-mediated recrystallization could either reflect fluids associated with continued high-grade metamorphism or retrograde fluids related to early stage exhumation. Holk and Taylor (2007) concluded that two dominant modes of hydrothermal activity characterized the Valhalla complex: (1) an early system involving circulation of magmatic and/or metamorphic, heavy $\delta^{18}O$ waters at lithostatic pressures and low water/rock ratios within the high-grade rocks; and (2) overprinting shallow-level convective circulation of surface-derived, lighter $\delta^{18}O$ waters at hydrostatic pressures and at high water/rock ratios (see also Magaritz and Taylor, 1976, 1986).

To evaluate the timing, physiochemical conditions, and consequences of fluid-rock interaction in the migmatitic rocks of the gneiss dome, we measured U-Pb age, $\delta^{18}O$ compositions, and Ti in zircon paleotemperatures from the outer rims of zircons from a migmatitic biotite gneiss (sample EL-20) using secondary ionization mass spectrometry (SIMS) depth profiling methods (Mojzsis and Harrision, 2002; Carson et al., 2002; Breeding et al., 2004). Further details are presented in the data repository. Zircons selected from EL-20 were clear, euhedral, tabular crystals that do not reveal distinct rims in cathodoluminescence images (Fig. 2), but rather exhibit simple oscillatory zoning.

RESULTS

We performed SIMS U-Pb age depth profiling measurements into the natural (unpolished) outer surfaces of 13 zircons from EL-20 and obtained a consistent ^{238}U-^{206}Pb age of ca. 51 ± 2 Ma over sputter pits that varied in depth from 3.7 to 4.5 μm (Fig. 3, 4A; Table 3.1). The results do not show any evidence for discordance (see data repository). After depth profiling analyses, the grains were polished and reanalyzed in conventional spot analysis mode. Twelve of fourteen analyses from the zircon interiors yield a weighted average ^{238}U-^{206}Pb age of 57.5 ± 2.6 Ma (MSWD: 1.8; Fig. 3, 4A; Table 3.2). This is ca. 6 m.y. older than the rim values and is similar to the melt crystallization ages yielded by zircon from other migmatites throughout the gneiss dome (Gordon et al., 2008).

To better determine the conditions in which zircon rim growth/recrystallization occurred, we have applied the Ti in zircon thermometer (Watson et al., 2006; Ferry and Watson, 2007) to both the rim and interiors of EL-20 zircon crystals. Crystallization

temperatures calculated from the depth profiling data range from 620 - 795 ºC with the majority of the analyses clustering around 650 ºC (n = 25; Fig. 4B). The temperatures are equivalent to the results obtained from the conventionally sectioned and polished interiors from the same sample (644-725 ºC, n = 17; Fig. 4B).

The $\delta^{18}O$ values measured from the rims yield a weighted mean $\delta^{18}O$ average of 8.4 ± 0.2 ‰ (n = 46; MSWD: 2.0; Fig. 4C; Table 3.3) with values up to 9.5 ± 0.7 ‰. These values are significantly higher than the $\delta^{18}O$ results measured from the interiors of the zircon grains in spot analysis mode, which yield a weighted, mean $\delta^{18}O$ average of 7.2 ± 0.1 ‰ (n = 45; MSWD: 3.2; Fig. 2, 4C). Detailed spot mapping of $\delta^{18}O$ from one EL-20 zircon confirm that rims are heavier in $\delta^{18}O$ relative to the zircon interiors (Fig. 2), but even the highest rim values in spot mode falls ~ 0.3 ‰ short of the average rim values acquired in depth profiling mode. It is possible that $\delta^{18}O$ spot values of the grain are averaging over growth zones with different isotopic compositions.

INTERPRETATION

The zircon rims with the elevated $\delta^{18}O$ values formed in the presence of an external mobile phase (melt or aqueous fluid). Based on the Ti thermometry results, remelting or a continuous partially molten state for sample EL20 could not produce the observed contrast in $\delta^{18}O$ at the isothermal conditions present from 58 to 51 Ma. Holk and Taylor (2000, 2007) reported relatively uniform quartz $\delta^{18}O$ values of 11.2 ± 0.9 ‰ throughout the Valhalla complex, and they interpreted these results to reflect equilibration of the gneiss dome rocks with $\delta^{18}O$ = 10 ‰ fluids exsolved from

progressive crystallization of migmatites and metamorphic devolatilization. The 8 to 9 ‰ $\delta^{18}O$ values measured from the 51 Ma zircon rims match those predicted from the same pervasive fluids that produced the $\delta^{18}O$ quartz values. Equilibrium oxygen isotopic fractionation between quartz and zircon as a function of temperature (Valley et al., 2003) predict zircon $\delta^{18}O$ values of 8.4 ‰ based on the quartz oxygen data. Further measurements performed with additional samples yield equivalent results. Integration of U-Pb age, Ti thermometry, and $\delta^{18}O$ results from the outermost several micrometers of sample EL-20 zircons indicate that high-temperature (ca. 650°C) magmatic and/or metamorphic fluids continued to infiltrate the migmatitic rocks of the Valhalla complex as late as 51 Ma. The results thus confirm that upper amphibolite facies conditions persisted until the onset of rapid exhumation of the gneiss dome at 50 Ma (Parrish et al., 1988; Gordon et al., 2008) and are consistent with petrologic evidence from the Valhalla and other domes of the same tectonic belt that indicates nearly isothermal decompression from upper amphibolite facies conditions (Duncan, 1984; Norlander et al., 2002; Marshall and Simandl, 2006).

DISCUSSION

Understanding fluid-rock interactions in orogenic crust in the context of timing, variability in physicochemical conditions, and tectonic processes has long presented a great challenge (e.g., Parnell, 1988). Many studies of core complexes have addressed the role that meteoric waters play in the thermal regime of detachment systems and have investigated how far surface-derived fluids have penetrated and exchanged with lower-plate rocks (e.g., Morrison, 1994; Morrison and Anderson, 1998; Holk and Taylor, 2007;

Mulch et al., 2007; Person et al., 2007). Less is known about the thermal effects of the fluid regime (e.g., advective heat transport) at deeper levels of core complexes, and in particular migmatite-cored core complexes that characterize the northern North American Cordillera as well as the Variscan and many segments of the Alpine-Himalayan orogenic belt (Whitney et al., 2004).

In orogenic systems that have experienced a protracted high temperature thermal and deformation history, evidence for late-stage metamorphic events can be impossible to detect using conventional geochemical methods. In this study, the combination of U-Pb age, Ti in zircon thermometry, and oxygen isotope analyses applied to a single mineral provides a comprehensive time-temperature-fluid dataset for zircon crystallization and fluid-rock interaction in a core complex system. Depth profiling by SIMS is best suited for deciphering this record because of the minimal extent of recrystallization that takes place during high-grade metamorphism in largely stable, resistant phases such as zircon (e.g., Ayers et al., 2006). Previous studies employing SIMS U-Pb age depth profiling have demonstrated its value for understanding fluid infiltration during contact (Carson et al., 2002) and regional metamorphism (e.g., Breeding et al., 2004). Our study demonstrates the value of also undertaking Ti in zircon thermometry and $\delta^{18}O$ compositional measurements from the outer natural surfaces of zircon to elucidate otherwise unattainable records of fluid history during regional metamorphism.

The fluids responsible for new zircon growth/recrystallization in the Valhalla complex could have been sourced from either continued metamorphic devolatilization of the migmatitic host rocks or heretofore unrecognized post 58 Ma crystallization of intrusions and partial melt emplaced at depths greater than those presently exposed within

the complex. Other gneiss domes in the Shuswap metamorphic core complex record granitoid emplacement and partial melt crystallization as young as 50 Ma (Carr, 1992; Vanderhaeghe et al., 1999; Crowley et al., 2001; Hinchey et al., 2006; Kruckenberg et al., 2008). The absence of post- 58 Ma plutons within the Valhalla complex may be attributed to its comparatively shallow structural level and its proximity to the cold foreland (Gordon et al., 2008). However, our new results are consistent with fluid being derived from metamorphism as well as from melt crystallization and granitoid emplacement within the deep portions of the Valhalla complex as late as 51 Ma. This evidence for previously unrecognized melt activity is important in that it helps explain how anomalously high grade conditions (i.e., upper amphibolite facies conditions) could have persisted until rapid exhumation initiated at 50 Ma.

ACKNOWLEDGMENTS: This research was supported by NSF grant EAR-0409776 to D. Whitney and C. Teyssier and NSF grant EAR-0609911 to M. Grove. We thank J. Ayers and D. Foster for critical reviews of the paper. The ion microprobe facility at UCLA is partly supported by a grant from the NSF's Instrumentation and Facilities Program, Division of Earth Sciences.

REFERENCES

Ayers, J.D., Loflin, M., Miller, C.F., Barton, M.D., and Coath, C.D., 2006, In situ oxygen isotope analysis of monazite as a monitor of fluid infiltration during contact metamorphism: Birch Creek Pluton aureole, White Mountains, eastern California: Geology, v. 34, p. 653-656.

Baxter, E.F., 2003, Natural constraints on metamorphic reaction rates, *in* Vance, D., et al., eds., Geochronology: linking the isotopic record with petrology and textures, Volume 220, Geological Society of London, p. 183-202.

Bebout, G.E., and Barton, M.D., 1989, Fluid flow and metasomatism in a subduction zone hydrothermal system: Catalina Schist terrane, California: Geology, v. 17, p. 976-980.

Breeding, C.M., Ague, J.J., Grove, M., and Rupke, A.L., 2004, Isotopic and chemical alteration of zircon by metamorphic fluids: U-Pb age depth-profiling of zircon crystals from Barrow's garnet zone, northeast Scotland: American Mineralogist, v. 89, p. 1067-1077.

Carr, S.D, 1992, Tectonic setting and U-Pb geochronology of the early Tertiary Ladybird leucogranite suite, Thor-Odin-Pinnacles area, southern Omineca belt, British Colombia: Tectonics, v. 11, p. 258-278.

Carr, S.D., Parrish, R.R., and Brown, R.L., 1987, Eocene structural development of the Valhalla complex, southeastern British Columbia: Tectonics, v. 6, v. 175-196.

Carson, C.J., Ague, J.J., Grove, M., Coath, C.D., and Harrison, T.M., 2002, U-Pb isotopic behaviour of zircon during upper-amphibolite facies fluid infiltration in the Napier Complex, east Antarctica: Earth and Planetary Science Letters, v. 199, p. 287-310.

Corfu, F., Hanchar, J.M., Hoskin, P.W.O., and Kinny, P., 2003, Atlas of zircon textures, *in* Hanchar, J.M. and Hoskin, W.O., eds., Zircon, Volume 53: Reviews in Mineralogy and Geochemistry, Mineralogical Society of America, p. 468-500.

Crowley, J.L., Brown, R.L., and Parrish, R.R., 2001, Diachronous deformation and a strain gradient beneath the Selkirk allochthon, northern Monashee complex, southeastern Canadian Cordillera: Journal of Structural Geology, v. 23, p. 1103-1121.

Duncan, I.J., 1984, Structural evolution of the Thor-Odin gneiss dome: Tectonophysics, v. 101, p. 87-130.

Ferry, J.M., and Watson, E.B., 2007, New thermodynamic models and revised calibrations for the Ti-in-zircon and Zr-in-rutile thermometers: Contributions to Mineralogy and Petrology, v. 154, p. 429-437.

Gordon, S.M., Whitney, D.L., Teyssier, C., Grove, M., and Dunlap, W.J., 2008, Timescales of migmatization, melt crystallization, and cooling in a Cordilleran gneiss dome: the Valhalla complex, southeastern British Columbia: Tectonics, v. 27, TC4010, doi:10.1029/2007TC002103.

Harrison, T.M., and Watson, E.B., 1983, Kinetics of zircon dissolution and zirconium diffusion in granitic melts of variable water content: Contributions to Mineralogy and Petrology, v. 84, p. 67-72.

Hinchey, A.M., Carr, S.D., McNeill, P.D., and Rayner, N., 2006, Paleocene-Eocene high-grade metamorphism, anatexis, and deformation in the Thor-Odin dome, Monashee complex, southeastern British Columbia: Canadian. Journal of Earth Sciences, v. 43, p. 1341-1365.

Holk, G.J., and Taylor, H.P., Jr., 2000, Water as a petrologic catalyst driving homogenization of the middle crust in the metamorphic core complexes of British Columbia: International Geology Review, v. 42, p. 97-130.

Holk, G.J., and Taylor, H.P., Jr., 2007, $^{18}O/^{16}O$ evidence for contrasting hydrothermal regimes involving magmatic and meteoric-hydrothermal waters at the Valhalla metamorphic core complex, British Columbia: Economic Geology, v. 102, p. 1063-1078.

Kruckenberg, S.C., Whitney, D.L., Teyssier, C., Fanning, M., and Dunlap, W.J., 2008, Paleocene-Eocene migmatite crystallization, extension, and exhumation in the hinterland of the northern Cordillera: Okanogan dome, Washington USA, Geological Society of America Bulletin, v. 120, p. 912-929.

Magaritz, M., and Taylor, H.P., Jr., 1976, $^{18}O/^{16}O$ and D/H studies along a 500 km traverse across the Coast Range batholith and its country rocks, central British Columbia: Canadian Journal of Earth Sciences, v. 13, p. 1514-1536.

Magaritz, M., and Taylor, H.P., Jr., 1986, $^{18}O/^{16}O$ and D/H studies of plutonic granitic and metamorphic rocks across the Cordilleran batholiths of southern British Columbia: Journal of Geophysical Research, v. 91, p. 849-857.

Manning, C.E., and Ingebritsen, S.E., 1999, Permeability of the continental crust: Implications of geothermal data and metamorphic systems: Reviews of Geophysics, v. 37, p. 127-150.

Marshall, D., and Simandl, G., 2006, Phase relations and metamorphism in the sapphirine bearing granulites of the Valhalla complex, Slocan Valley, BC: GAC/MAC Annual Meeting, Abstracts, v. 31, p. 96.

Mojzsis, S.J., and Harrison, T.M., 2002, Establishment of a 3.83-Ga magamatic age for the Akilia tonalite (southern West Greenland): Earth and Planetary Science Letters, v. 202, p. 563-576.

Morrison, J., 1994, Meteoric water-rock interaction in the lower plate of the Whipple Mountain metamorphic core complex, California: Journal of Metamorphic Geology, v. 12, p. 827-840.

Morrison, J., and Anderson, J.L., 1998, Footwall refrigeration along a detachment fault: implications for the thermal evolution of core complexes: Science, v. 279, p. 63-66.

Mulch, A., Teyssier, C., Cosca, M.A., and Chamberlain, C.P., 2007, Stable isotope paleoaltimetry of Eocene core complexes in the North American Cordillera: Tectonics, v. 26, doi:10.1029/2006TC001995.

Newton, R.C., 1989, Metamorphic fluids in the deep crust: Annual Review of Earth and Planetary Sciences, v. 17, p. 385-410.

Norlander, B.N., Whitney, D.L., Teyssier, C., and Vanderhaeghe, O., 2002, Partial melting and decompression of the Thor-Odin dome, Shuswap metamorphic core complex, Canadian Cordillera: Lithos, v. 61, p. 103-125.

Parnell, J., 1998, Approaches to dating and duration of fluid flow and fluid-rock interaction, *in* Parnell, J., ed., Dating and duration of fluid flow and fluid-rock interaction: Geological Society of London Special Publication 144, p. 1-8.

Parrish, R.R., 1984, Slocan Lake fault: a low angle fault zone bounding the Valhalla gneiss complex, Nelson map area, southern British Columbia: Geological Survey of Canada, Paper, v. 84-1A, p. 323-330.

Parrish, R.R., 1995, Thermal evolution of the southeastern Canadian Cordillera: Canadian Journal of Earth Sciences, v. 32, p. 1618-1642.

Parrish, R.R., Carr, S.D., and Parkinson, D.L., 1988, Eocene extensional tectonics and geochronology of the southern Omineca belt, British Colombia and Washington: Tectonics, v. 7, p. 181-212.

Person, M.P., Mulch, A., Teyssier, C., and Gao, Y., 2007, Isotope transport and exchange during detachment tectonics, Shuswap metamorphic core complex, British Columbia: American Journal of Science, v. 307, p. 555-589.

Reesor, J.E., 1965, Structural evolution and plutonism in Valhalla gneiss complex, British Columbia: Geological Survey of Canada Bulletin, v. 129, p. 128.

Schaubs, P.M., Carr, S.D., and Berman, R.G., 2002, Structural and metamorphic constraints on ca. 70 Ma deformation of the northern Valhalla complex, British Columbia: Implications for the tectonic evolution of the southern Omineca belt: Journal of Structural Geology, v. 24, p. 1195-1214.

Spear, F.S., and Parrish, R.R., 1996, Petrology and cooling rates of the Valhalla Complex, British Columbia, Canada: Journal of Petrology, v. 37, p. 733-765.

Townsend, K.J., Miller, C.F., D'Andrea, J.L., Ayers, J.C., Harrison, T.M., and Coath, C.D., 2000, Low temperature replacement of monazite in the Iretaba granite, southern Nevada: geochronological implications: Chemical Geology, v. 172, p. 95-112.

Valley, J.W., Bindeman, I.B. and Peck, W.H., 2003, Empirical calibration of oxygen isotope fractionation in zircon: Geochimica et Cosmochimica Acta, v. 67, p. 3257-3266.

Vanderhaeghe, O., Teyssier, C., and Wysoczanski, R., 1999, Structural and geochronological constraints on the role of partial melting during the formation of the Shuswap metamorphic core complex at the latitude of the Thor-Odin Dome, British Columbia: Canadian Journal of Earth Sciences, v. 36, p. 917-943.

Vanderhaeghe, O., Teyssier, C., McDougall, I., and Dunlap, W.J., 2003, Cooling and exhumation of the Shuswap metamorphic core complex constrained by $^{40}Ar/^{39}Ar$ thermochronology: Geological Society of America Bulletin, v. 115, p. 200-216.

Watson, E.B., 1996,Dissolution, growth and survival of zircons during crustal fusion: kinetics principles, geologic models and implications for isotopic inheritance: Proceedings of the Royal Society of Edinburgh, v. 87, p. 43-56.

Watson, E.B., Wark, D.A., and Thomas, J.B., 2006, Crystallization thermometers for zircon and rutile: Contributions to Mineralogy and Petrology, v. 151, p. 413-433.

Whitney, D.L., Teyssier, C., and Vanderhaeghe, O., 2004, Gneiss domes and crustal flow, *in* Whitney, D.L. et al., eds., Gneiss domes and orogeny: Geological Society of America Special Paper 380, p. 15-33.

Zeitler, P.K., and Williams, I.S., 1988, U-Pb dating of metamorphic zircon overgrowths by means of depth profiling with an ion microprobe: EOS (Transactions American Geophysical Union), v. 69, p.464.

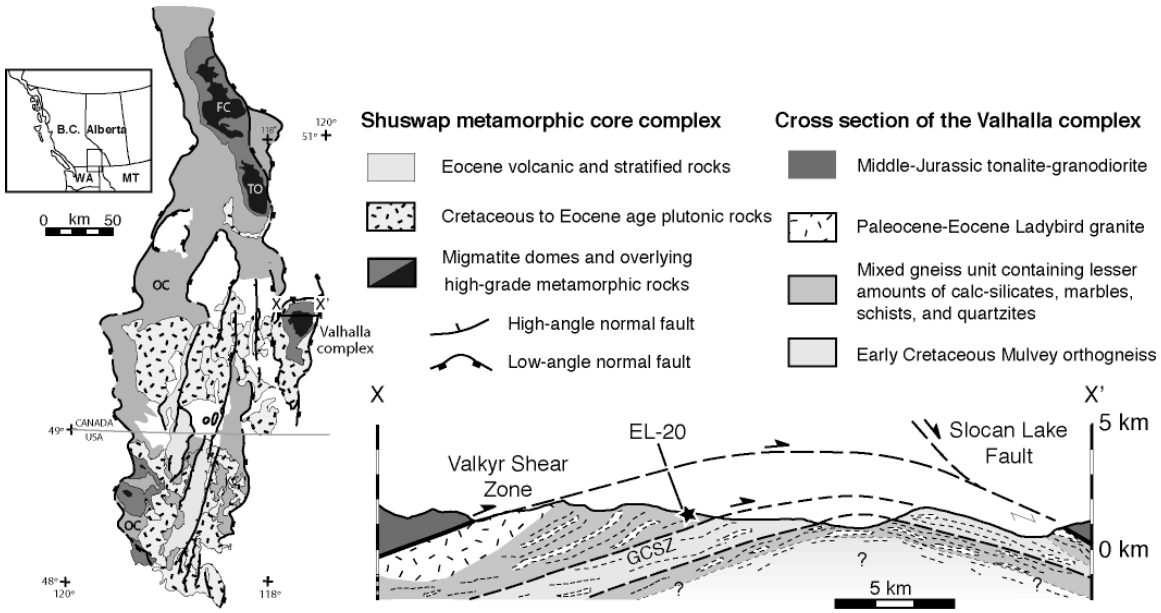

Figure 3.1: Simplified geologic map of the Shuswap metamorphic core complex, revealing the series of gneiss domes including Frenchman Cap (FC), Thor-Odin (TO), Valhalla complex, and Okanagan-Kettle (OC) (after Kruckenberg et al., 2008). A cross-section through the Valhalla complex is also shown, illustrating the main lithologic units and location of the studied sample; GCSZ: Gwillim Creek shear zone (after Schaubs et al., 2002).

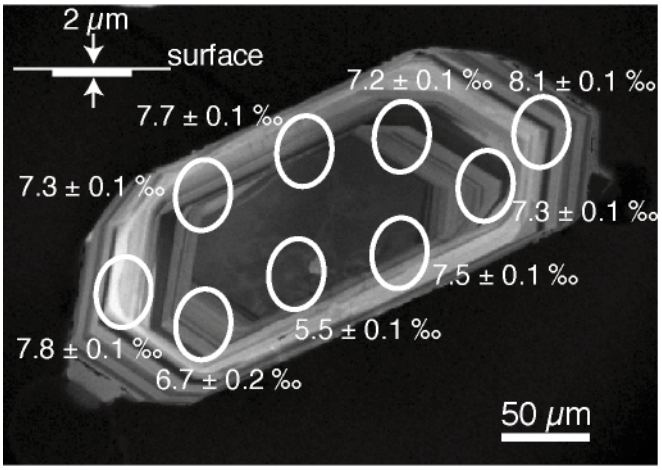

Figure 3.2: Cathodoluminescence image of a selected EL-20 zircon. The image shows individual $\delta^{18}O$ spot measurements made across the crystal. Inset shows sputter crater cross-section drawn to scale to illustrate spatial resolution in depth profiling mode parallel to zircon growth zones.

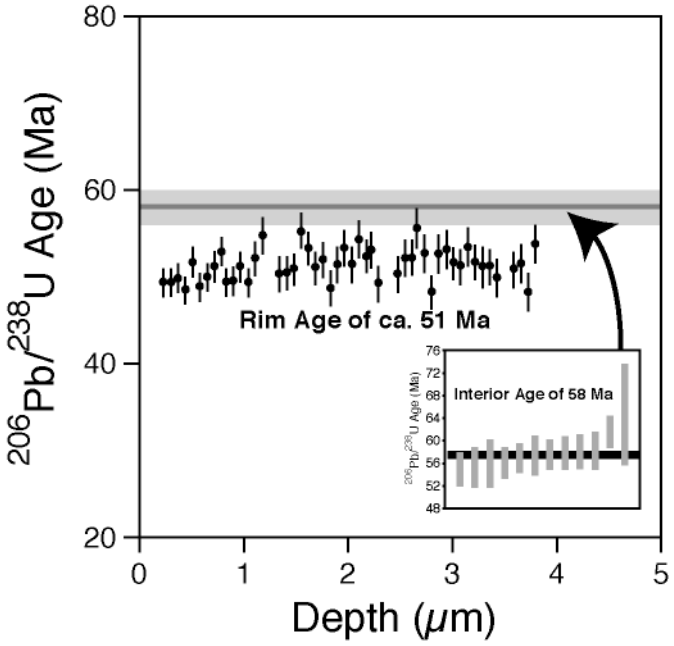

Figure 3.3: $^{238}U/^{206}Pb$ age versus depth plot for an EL-20 zircon revealing the variation in age as the ion probe beam sputtered into the crystal. The black bar surrounded by gray across the age versus depth plot represents the age and error obtained through conventional polished analyses. The inset is a weighted mean age figure for the conventional polished analyses.

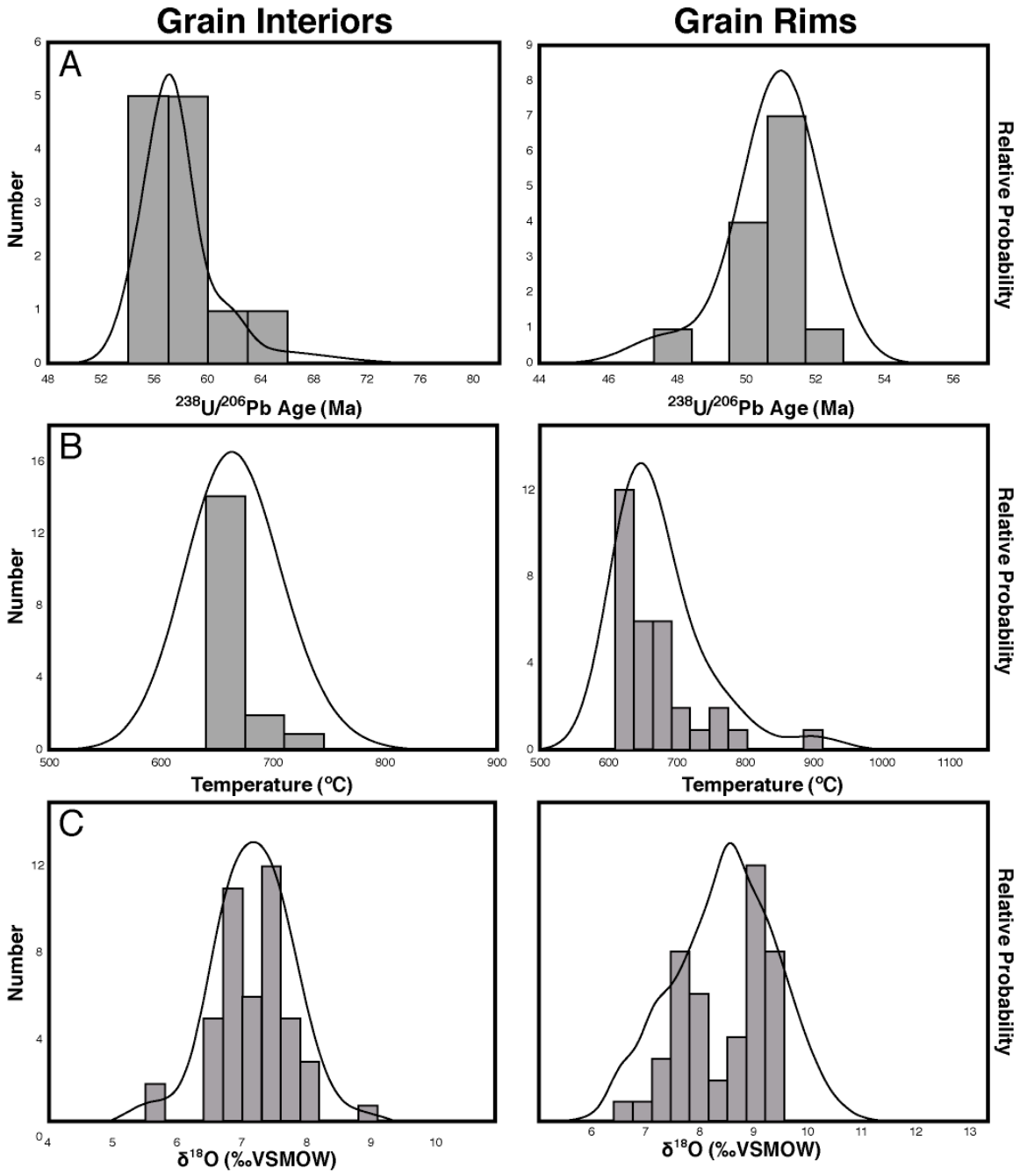

Figure 3.4: Relative probability diagrams for both the unpolished rims and the interiors of the grains. (A, B) U-Pb measurements; (C, D) Ti in zircon thermometry; and (E, F) $\delta^{18}O$ measurements.

Table 3.1: *Ion microprobe analytical U-Pb zircon isotopic data from depth profiling*

Grain*	Th (est. ppm)	U (est. ppm)	Th/U	$^{207}Pb/^{206}Pb$ value	1 s.e.	$^{207}Pb/^{235}U$ value	1 s.e.	$^{206}Pb/^{238}U$ value	1 s.e.	Correlation of Concordia Ellipses	% Radiogenic ^{207}Pb	% Radiogenic ^{206}Pb	Analysis Run Time (s)	$^{207}Pb/^{206}Pb^{\dagger}$ Age (Ma)	1 s.e.	$^{207}Pb/^{235}U$ Age (Ma)	1 s.e.	$^{206}Pb/^{238}U$ Age (Ma)	1 s.e.
EL-20 Migmatite																			
Grain 1	69.52	1013.82	0.069	0.0518	7.4190	0.0592	7.8220	0.0083	3.0620	0.3241	85.55	98.98	186.3	274.3	170.0	58.4	4.4	53.3	1.6
Cycle 2	73.68	1007.08	0.073	0.0462	7.8150	0.0503	8.1690	0.0079	2.9510	0.2979	65.51	97.86	235.9	5.7	188.0	49.8	4.0	50.8	1.5
Cycle 3	81.21	1054.37	0.077	0.0462	7.7320	0.0524	8.1150	0.0082	2.9800	0.3090	56.91	97.31	285.4	6.4	186.0	51.9	4.1	52.9	1.6
Cycle 4	73.63	996.97	0.074	0.0471	7.4010	0.0552	7.7460	0.0085	2.9250	0.3043	51.27	97.07	335.0	55.5	177.0	54.5	4.1	54.5	1.6
Cycle 5	83.80	989.09	0.085	0.0453	7.7980	0.0540	8.1840	0.0086	3.0310	0.3095	62.38	97.80	384.6	0.0	0.0	53.4	4.3	55.4	1.7
Cycle 6	76.26	972.66	0.078	0.0395	8.3300	0.0456	8.6670	0.0084	2.9540	0.2823	65.26	98.26	434.1	0.0	0.0	45.3	3.8	53.8	1.6
Cycle 7	72.74	973.46	0.075	0.0466	7.5490	0.0522	7.8840	0.0081	2.9090	0.2970	52.63	97.17	483.6	27.2	181.0	51.7	4.0	52.2	1.5
Cycle 8	83.40	996.34	0.084	0.0407	8.7390	0.0463	9.1270	0.0082	2.9890	0.2909	64.05	97.89	533.3	0.0	0.0	46.0	4.1	52.9	1.6
Cycle 9	75.58	987.94	0.077	0.0566	6.6510	0.0640	6.9680	0.0082	2.9150	0.3153	66.77	97.80	583.0	476.8	147.0	63.0	4.3	52.6	1.5
Cycle 10	79.35	998.24	0.079	0.0484	7.4710	0.0536	7.7880	0.0080	2.9250	0.2938	77.96	98.69	632.5	120.0	176.0	53.0	4.0	51.5	1.5
Cycle 11	81.08	955.18	0.085	0.0425	8.1250	0.0479	8.4480	0.0082	2.9180	0.2813	69.68	98.38	682.1	0.0	0.0	47.5	3.9	52.5	1.5
Cycle 12	74.08	945.38	0.078	0.0532	7.1450	0.0593	7.5000	0.0081	2.9630	0.3144	66.34	97.72	731.7	337.2	162.0	58.5	4.3	51.9	1.5
Cycle 13	79.75	978.97	0.081	0.0454	7.8410	0.0527	8.2060	0.0084	3.0490	0.3028	73.82	98.51	781.3	0.0	0.0	52.1	4.2	54.0	1.6
Cycle 14	76.30	987.71	0.077	0.0475	7.4200	0.0546	7.7470	0.0083	2.9900	0.3001	65.32	98.08	830.8	73.2	176.0	54.0	4.1	53.6	1.6
Cycle 15	77.43	982.44	0.079	0.0483	7.3710	0.0527	7.6770	0.0079	2.9020	0.2925	66.76	98.08	880.3	113.2	174.0	52.2	3.9	50.9	1.5
Cycle 16	79.91	986.21	0.081	0.0502	7.0740	0.0583	7.4140	0.0084	2.9650	0.3119	71.07	98.31	1005.0	202.0	164.0	57.5	4.1	54.1	1.6
Cycle 17	73.55	1002.05	0.073	0.0459	7.4550	0.0551	7.8330	0.0087	3.0050	0.3145	76.34	98.62	1055.0	0.0	0.0	54.5	4.2	55.9	1.7
Cycle 18	73.21	938.49	0.078	0.0550	6.8410	0.0648	7.1930	0.0085	3.0100	0.3234	75.50	98.40	1105.0	413.2	153.0	63.8	4.4	54.8	1.6
Cycle 19	62.96	903.19	0.070	0.0442	8.1110	0.0535	8.5130	0.0088	3.0950	0.3087	89.13	99.34	1154.0	0.0	0.0	52.9	4.4	56.3	1.7
Cycle 20	64.56	837.33	0.077	0.0440	7.9680	0.0476	8.2190	0.0078	2.8900	0.2615	79.48	98.97	1204.0	0.0	0.0	47.2	3.8	50.4	1.5
Cycle 21	64.88	789.14	0.082	0.0506	7.5270	0.0573	7.8300	0.0082	3.0100	0.2911	70.55	98.26	1253.0	220.8	174.0	56.5	4.3	52.7	1.6
Cycle 22	57.55	819.42	0.070	0.0472	7.8680	0.0531	8.1770	0.0082	3.0860	0.2869	86.95	99.27	1303.0	60.4	187.0	52.5	4.2	52.3	1.6
Cycle 23	70.85	810.68	0.087	0.0462	8.1610	0.0519	8.4770	0.0082	3.0020	0.2804	84.24	99.10	1352.0	5.3	197.0	51.3	4.2	52.3	1.6
Cycle 24	63.29	808.91	0.078	0.0442	8.3300	0.0525	8.6800	0.0086	3.1400	0.2901	80.44	98.93	1402.0	0.0	0.0	52.0	4.4	55.3	1.7
Cycle 25	68.12	796.04	0.086	0.0420	8.6350	0.0491	8.9630	0.0085	3.1130	0.2771	96.24	99.81	1451.0	0.0	0.0	48.7	4.3	54.5	1.7
Cycle 26	63.14	802.89	0.079	0.0500	7.6440	0.0571	7.9510	0.0083	3.0620	0.2910	90.86	99.47	1501.0	196.7	178.0	56.4	4.4	53.2	1.6
Cycle 27	69.82	820.69	0.085	0.0458	8.1490	0.0535	8.4750	0.0085	3.1320	0.2867	100.00	100.00	1550.0	0.0	0.0	53.0	4.4	54.4	1.7
Cycle 28	69.49	829.57	0.084	0.0518	7.5400	0.0591	7.8640	0.0083	3.0970	0.2993	100.00	100.00	1600.0	277.3	173.0	58.3	4.5	53.1	1.6
Cycle 29	71.31	830.64	0.086	0.0535	7.3670	0.0597	7.6780	0.0081	3.0010	0.2970	100.00	100.00	1649.0	349.1	167.0	58.8	4.4	52.0	1.6
Cycle 30	70.04	852.23	0.082	0.0501	7.6000	0.0581	7.9560	0.0084	3.0970	0.3070	97.62	99.86	1699.0	198.3	177.0	57.3	4.4	54.0	1.7
Cycle 31	67.23	779.29	0.086	0.0443	8.5350	0.0507	8.9090	0.0083	3.0820	0.2917	79.10	98.76	1824.0	0.0	0.0	50.2	4.4	53.3	1.6
Cycle 32	65.65	771.81	0.085	0.0482	7.9110	0.0574	8.2590	0.0086	3.1400	0.2984	87.39	99.28	1874.0	107.5	187.0	56.7	4.6	55.5	1.7
Cycle 33	66.10	760.40	0.087	0.0528	7.7320	0.0596	8.1000	0.0082	3.1470	0.3087	88.63	99.25	1923.0	318.6	176.0	58.8	4.6	52.6	1.7
Cycle 34	65.66	737.03	0.089	0.0506	8.0020	0.0583	8.3590	0.0084	3.2030	0.3007	87.30	99.23	1972.0	224.2	185.0	57.5	4.7	53.6	1.7
Cycle 35	68.81	736.91	0.093	0.0494	8.0450	0.0546	8.3440	0.0080	3.0430	0.2787	80.31	98.85	2022.0	165.6	188.0	54.0	4.4	51.5	1.6
Cycle 36	64.10	728.92	0.088	0.0484	8.2770	0.0544	8.6140	0.0081	3.1460	0.2876	67.54	98.07	2072.0	118.0	195.0	53.8	4.5	52.3	1.6
Cycle 37	68.67	738.66	0.093	0.0454	8.7120	0.0499	9.0320	0.0080	3.1140	0.2734	74.81	98.60	2121.0	0.0	0.0	49.4	4.4	51.2	1.6
Cycle 38	75.89	718.45	0.106	0.0501	8.2380	0.0564	8.5660	0.0082	3.1250	0.2852	47.25	96.89	2171.0	197.2	191.0	55.7	4.6	52.5	1.6
Cycle 39	71.16	700.56	0.102	0.0443	9.0700	0.0515	9.4630	0.0084	3.2280	0.2897	59.84	97.67	2220.0	0.0	0.0	51.0	4.7	54.1	1.7
Cycle 40	72.33	704.61	0.103	0.0506	8.3800	0.0563	8.7430	0.0081	3.1850	0.2937	100.00	100.00	2270.0	222.3	194.0	55.6	4.7	51.8	1.6
Cycle 41	76.04	710.40	0.107	0.0461	8.8390	0.0516	9.1880	0.0081	3.1540	0.2804	100.00	100.00	2319.0	3.2	213.0	51.1	4.6	52.2	1.6
Cycle 42	72.34	707.87	0.102	0.0461	8.9860	0.0496	9.3330	0.0078	3.1770	0.2775	96.30	99.79	2369.0	0.7	217.0	49.1	4.5	50.1	1.6
Cycle 43	69.83	686.58	0.102	0.0531	8.2080	0.0597	8.5680	0.0082	3.2620	0.2985	86.91	99.16	2418.0	334.8	186.0	58.9	4.9	52.3	1.7
Cycle 44	77.72	673.24	0.115	0.0473	8.9290	0.0523	9.2830	0.0080	3.1890	0.2806	82.15	98.96	2468.0	66.7	213.0	51.8	4.7	51.4	1.6
Cycle 45	70.70	654.80	0.108	0.0507	8.6310	0.0541	8.9690	0.0078	3.2340	0.2829	71.54	98.28	2517.0	225.0	200.0	53.5	4.7	49.8	1.6
Cycle 46	80.91	657.36	0.123	0.0518	8.5260	0.0597	8.8690	0.0084	3.2800	0.2876	67.05	98.10	2642.0	278.5	195.0	58.9	5.1	53.6	1.8
Cycle 47	76.23	645.39	0.118	0.0430	9.9250	0.0470	10.3100	0.0079	3.2580	0.2733	65.72	98.08	2692.0	0.0	0.0	46.6	4.7	51.0	1.7
Cycle 48	76.93	625.09	0.123	0.0504	9.1870	0.0536	9.5780	0.0077	3.3060	0.2886	96.35	99.76	2741.0	213.6	213.0	53.0	5.0	49.5	1.6

Cycle 49	76.22	628.33	0.121	0.0531	8.8470	0.0555	9.1930	0.0076	3.3300	0.2830	81.08	98.82	2791.0	331.7	201.0	54.8	4.9	48.7	1.6
Cycle 50	74.56	620.14	0.120	0.0433	9.9220	0.0482	10.3000	0.0081	3.3540	0.2730	60.75	97.92	2840.0	0.0	0.0	47.8	4.8	51.9	1.7
Cycle 51	78.33	631.78	0.124	0.0460	9.1900	0.0479	9.5090	0.0075	3.0710	0.2638	42.21	96.75	2962.0	0.0	0.0	47.5	4.4	48.5	1.5
Cycle 52	77.06	644.24	0.120	0.0470	9.1830	0.0484	9.5330	0.0075	3.1010	0.2733	86.37	99.17	3012.0	47.4	219.0	48.0	4.5	48.1	1.5
Cycle 53	85.57	631.05	0.136	0.0471	9.2950	0.0473	9.6270	0.0073	3.0750	0.2658	85.61	99.16	3061.0	54.7	222.0	47.0	4.4	46.8	1.4
Cycle 54	78.96	644.54	0.123	0.0406	9.8790	0.0427	10.2200	0.0076	3.1010	0.2585	75.68	98.78	3111.0	0.0	0.0	42.5	4.3	49.0	1.5
Cycle 55	82.38	634.13	0.130	0.0546	8.0680	0.0551	8.3360	0.0073	2.9860	0.2674	67.57	98.04	3160.0	394.2	181.0	54.4	4.4	47.0	1.4
Cycle 56	89.61	666.31	0.134	0.0525	8.2740	0.0544	8.5690	0.0075	3.0010	0.2715	76.75	98.61	3210.0	305.5	189.0	53.8	4.5	48.3	1.4
Cycle 57	86.41	667.76	0.129	0.0400	9.8790	0.0420	10.2300	0.0076	3.0120	0.2603	52.54	97.56	3259.0	0.0	0.0	41.8	4.2	48.9	1.5
Cycle 58	83.22	662.67	0.126	0.0449	8.9740	0.0456	9.2830	0.0074	2.9720	0.2623	85.95	99.24	3309.0	0.0	0.0	45.2	4.1	47.3	1.4
Cycle 59	88.26	693.60	0.127	0.0533	7.9920	0.0568	8.3480	0.0077	3.0280	0.2966	88.75	99.26	3359.0	340.8	181.0	56.1	4.6	49.7	1.5
Cycle 60	87.52	716.54	0.122	0.0422	8.9510	0.0429	9.2270	0.0074	2.8770	0.2503	85.37	99.29	3408.0	0.0	0.0	42.6	3.9	47.3	1.4
Cycle 61	90.40	765.23	0.118	0.0517	7.7970	0.0528	8.1180	0.0074	2.9400	0.2882	91.56	99.48	3533.0	270.7	179.0	52.2	4.1	47.6	1.4
Cycle 62	94.96	747.70	0.127	0.0492	7.9710	0.0511	8.2620	0.0075	2.8680	0.2733	96.84	99.82	3583.0	157.5	187.0	50.6	4.1	48.4	1.4
Cycle 63	96.12	774.00	0.124	0.0575	7.0990	0.0614	7.4230	0.0077	2.8820	0.3040	90.21	99.34	3632.0	510.8	156.0	60.5	4.4	49.7	1.4
Cycle 64	86.78	777.53	0.112	0.0487	8.0900	0.0497	8.4470	0.0074	2.9130	0.2926	86.68	99.14	3682.0	133.8	190.0	49.3	4.1	47.6	1.4
Cycle 65	82.41	762.11	0.108	0.0471	7.9740	0.0477	8.2570	0.0073	2.8380	0.2697	75.81	98.65	3731.0	55.3	190.0	47.3	3.8	47.1	1.3
Cycle 66	83.61	749.76	0.112	0.0448	8.4440	0.0455	8.7900	0.0074	2.8720	0.2814	80.54	98.84	3781.0	0.0	0.0	45.2	3.9	47.4	1.4
Cycle 67	89.78	764.62	0.117	0.0468	8.3200	0.0449	8.6480	0.0070	2.7890	0.2767	89.33	99.33	3831.0	37.9	199.0	44.6	3.8	44.8	1.2
Cycle 68	82.81	756.23	0.110	0.0468	7.8700	0.0472	8.1720	0.0073	2.7710	0.2766	89.13	99.36	3880.0	38.5	188.0	46.9	3.7	47.0	1.3
Cycle 69	87.66	757.62	0.116	0.0515	7.4200	0.0543	7.7400	0.0077	2.8430	0.2939	84.27	99.03	3930.0	261.9	170.0	53.7	4.1	49.1	1.4
Cycle 70	88.50	752.60	0.118	0.0469	7.9340	0.0479	8.2380	0.0074	2.8200	0.2768	74.46	98.57	3979.0	44.1	190.0	47.5	3.8	47.6	1.3
Cycle 71	91.40	747.44	0.122	0.0448	8.3740	0.0454	8.7190	0.0073	2.8190	0.2814	97.18	99.83	4029.0	0.0	0.0	45.1	3.9	47.2	1.3
Cycle 72	82.20	729.35	0.113	0.0502	7.3700	0.0511	7.6280	0.0074	2.7250	0.2717	83.37	99.06	4078.0	203.0	171.0	50.6	3.8	47.4	1.3
Cycle 73	84.76	747.71	0.113	0.0537	7.1440	0.0554	7.4610	0.0075	2.7900	0.2983	73.98	98.30	4128.0	357.2	161.0	54.8	4.0	48.1	1.3
Cycle 74	98.59	775.41	0.127	0.0515	7.3970	0.0524	7.7080	0.0074	2.7570	0.2892	82.69	98.93	4177.0	264.0	170.0	51.8	3.9	47.4	1.3
Grain 2	33.01	487.23	0.068	0.0512	11.9200	0.0527	12.4300	0.0075	3.8430	0.2858	25.40	93.56	178.8	249.7	274.0	52.1	6.3	47.9	1.8
Cycle 2	38.44	481.56	0.080	0.0494	11.5300	0.0555	12.0200	0.0082	4.0230	0.2871	38.67	95.52	228.4	167.8	269.0	54.9	6.4	52.3	2.1
Cycle 3	36.44	463.47	0.079	0.0488	11.3100	0.0540	11.7500	0.0080	3.9670	0.2785	64.17	97.53	277.9	137.0	266.0	53.4	6.1	51.6	2.0
Cycle 4	39.81	490.56	0.081	0.0412	13.0300	0.0455	13.5100	0.0080	3.8750	0.2665	25.67	95.09	327.4	0.0	0.0	45.1	6.0	51.4	2.0
Cycle 5	41.84	489.31	0.086	0.0563	10.2500	0.0629	10.6900	0.0081	4.0040	0.2953	53.94	96.57	376.8	462.4	227.0	62.0	6.4	52.1	2.1
Cycle 6	38.26	496.65	0.077	0.0502	11.0000	0.0542	11.4500	0.0078	3.9160	0.2833	71.35	97.95	426.4	203.6	255.0	53.6	6.0	50.3	2.0
Cycle 7	46.51	467.95	0.099	0.0456	11.6700	0.0511	12.0900	0.0081	3.9090	0.2666	39.01	96.31	475.9	0.0	0.0	50.6	6.0	52.2	2.0
Cycle 8	42.48	492.40	0.086	0.0588	10.1500	0.0648	10.6000	0.0080	4.0880	0.3008	72.31	97.87	525.4	561.3	221.0	63.7	6.6	51.3	2.1
Cycle 9	48.52	486.48	0.100	0.0395	14.3800	0.0447	14.9300	0.0082	4.0590	0.2693	88.89	99.27	574.8	0.0	0.0	44.4	6.5	52.7	2.1
Cycle 10	47.95	466.75	0.103	0.0530	10.8500	0.0569	11.2300	0.0078	3.9740	0.2700	49.98	96.74	624.3	328.3	246.0	56.2	6.1	50.0	2.0
Cycle 11	48.65	447.14	0.109	0.0530	11.0900	0.0630	11.5900	0.0086	4.1710	0.2979	49.29	96.45	673.8	329.4	252.0	62.1	7.0	55.3	2.3
Cycle 12	46.10	429.74	0.107	0.0507	11.3500	0.0597	11.7300	0.0085	4.2100	0.2683	73.55	98.49	723.3	227.6	262.0	58.8	6.7	54.8	2.3
Cycle 13	45.88	415.76	0.110	0.0434	12.7100	0.0502	13.1100	0.0084	4.1560	0.2555	71.57	98.49	772.8	0.0	0.0	49.8	6.4	53.9	2.2
Cycle 14	48.38	396.30	0.122	0.0487	12.5200	0.0542	13.0000	0.0081	4.1930	0.2738	69.50	98.01	822.3	132.3	294.0	53.6	6.8	51.9	2.2
Cycle 15	43.60	386.31	0.113	0.0450	12.9900	0.0492	13.4100	0.0079	4.2210	0.2555	45.43	96.91	871.9	0.0	0.0	48.8	6.4	50.9	2.1
Cycle 16	50.57	381.53	0.133	0.0569	11.8200	0.0613	12.1800	0.0078	4.3830	0.2609	78.73	98.69	996.8	487.1	261.0	60.4	7.1	50.2	2.2
Cycle 17	50.67	376.81	0.134	0.0511	12.3600	0.0567	12.7800	0.0080	4.2790	0.2627	92.74	99.56	1046.0	246.9	285.0	56.0	7.0	51.7	2.2
Cycle 18	53.46	371.71	0.144	0.0425	15.2200	0.0458	15.7700	0.0078	4.3620	0.2636	56.51	97.34	1096.0	0.0	0.0	45.5	7.0	50.2	2.2
Cycle 19	52.45	364.17	0.144	0.0512	12.7300	0.0556	13.0500	0.0079	4.2840	0.2381	26.87	96.13	1146.0	250.1	293.0	54.9	7.0	50.5	2.2
Cycle 20	54.90	368.09	0.149	0.0464	14.2700	0.0532	14.8500	0.0083	4.4580	0.2789	100.00	100.00	1195.0	16.2	343.0	52.6	7.6	53.5	2.4
Cycle 21	49.35	369.18	0.134	0.0492	13.6500	0.0584	14.2700	0.0086	4.5030	0.2913	100.00	100.00	1245.0	156.9	320.0	57.6	8.0	55.3	2.5
Cycle 22	57.62	365.08	0.158	0.0549	12.4600	0.0619	12.8600	0.0082	4.4290	0.2622	76.62	98.61	1294.0	409.9	279.0	61.0	7.6	52.5	2.3
Cycle 23	55.37	377.06	0.147	0.0601	11.7100	0.0790	12.3300	0.0095	4.8450	0.3217	44.84	96.02	1344.0	607.3	253.0	77.2	9.2	61.2	3.0
Cycle 24	54.90	361.49	0.152	0.0391	16.5200	0.0444	17.1100	0.0082	4.4200	0.2618	100.00	100.00	1393.0	0.0	0.0	44.1	7.4	52.9	2.3
Cycle 25	57.37	355.09	0.162	0.0559	12.3400	0.0695	12.8200	0.0090	4.6240	0.2810	100.00	100.00	1443.0	448.5	274.0	68.2	8.5	57.8	2.7
Cycle 26	53.26	352.52	0.151	0.0607	11.8100	0.0669	12.2700	0.0080	4.4510	0.2812	93.34	99.52	1492.0	627.1	255.0	65.8	7.8	51.4	2.3

Cycle 27	52.24	336.58	0.155	0.0359	19.5100	0.0392	20.1900	0.0079	4.5370	0.2596	62.25	97.65	1542.0	0.0	0.0	39.0	7.7	50.8	2.3
Cycle 28	61.16	341.35	0.179	0.0580	12.6900	0.0645	13.1000	0.0081	4.5360	0.2624	53.74	97.19	1591.0	530.7	278.0	63.4	8.1	51.7	2.3
Cycle 29	56.07	350.98	0.160	0.0369	17.8500	0.0399	18.4600	0.0078	4.5180	0.2538	82.15	99.03	1641.0	0.0	0.0	39.7	7.2	50.3	2.3
Cycle 30	48.68	325.65	0.149	0.0483	13.8600	0.0536	14.3300	0.0081	4.5310	0.2608	41.65	96.63	1690.0	113.6	327.0	53.1	7.4	51.7	2.3
Cycle 31	59.63	343.08	0.174	0.0559	12.9500	0.0616	13.3600	0.0080	4.5380	0.2595	74.81	98.51	1815.0	449.0	288.0	60.7	7.9	51.3	2.3
Cycle 32	55.76	360.76	0.155	0.0437	14.9700	0.0507	15.4300	0.0084	4.6790	0.2486	-20.18	94.26	1865.0	0.0	0.0	50.2	7.6	54.0	2.5
Cycle 33	57.94	342.70	0.169	0.0558	13.1800	0.0697	13.8600	0.0091	4.9030	0.3119	40.99	95.75	1914.0	442.8	293.0	68.4	9.2	58.2	2.8
Cycle 34	54.06	331.47	0.163	0.0371	16.9700	0.0396	17.4600	0.0077	4.4040	0.2355	100.00	100.00	1964.0	0.0	0.0	39.5	6.8	49.7	2.2
Cycle 35	57.77	335.87	0.172	0.0389	17.6700	0.0460	18.3400	0.0086	4.7850	0.2682	91.03	99.50	2013.0	0.0	0.0	45.7	8.2	55.1	2.6
Cycle 36	58.61	333.38	0.176	0.0593	12.4800	0.0661	12.9000	0.0081	4.5440	0.2669	69.87	98.09	2063.0	579.0	271.0	65.0	8.1	51.9	2.4
Cycle 37	52.78	329.25	0.160	0.0264	29.0500	0.0277	29.8200	0.0076	4.7750	0.2400	35.94	96.30	2113.0	0.0	0.0	27.7	8.2	48.9	2.3
Cycle 38	58.14	321.71	0.181	0.0578	13.1700	0.0619	13.7100	0.0078	4.6280	0.2821	8.41	93.54	2162.0	521.2	289.0	61.0	8.1	49.9	2.3
Cycle 39	54.44	317.28	0.172	0.0473	14.4300	0.0515	14.8500	0.0079	4.4700	0.2438	44.37	97.11	2212.0	64.1	344.0	51.0	7.4	50.7	2.3
Cycle 40	54.28	327.96	0.165	0.0559	13.4600	0.0617	14.0600	0.0080	4.7110	0.2917	18.02	93.99	2261.0	448.9	299.0	60.8	8.3	51.4	2.4
Cycle 41	52.89	331.48	0.160	0.0469	15.3600	0.0512	15.9600	0.0079	4.8290	0.2733	15.84	94.82	2311.0	43.1	367.0	50.7	7.9	50.9	2.5
Cycle 42	57.72	324.20	0.178	0.0626	12.8200	0.0658	13.3200	0.0076	4.7850	0.2813	69.89	97.84	2360.0	692.8	273.0	64.7	8.4	49.0	2.3
Cycle 43	56.50	317.80	0.178	0.0353	20.7400	0.0376	21.4500	0.0077	4.7600	0.2585	54.94	97.40	2410.0	0.0	0.0	37.4	7.9	49.6	2.4
Cycle 44	53.81	328.48	0.164	0.0326	21.8200	0.0357	22.5400	0.0079	4.9250	0.2522	40.71	96.84	2459.0	0.0	0.0	35.6	7.9	51.0	2.5
Cycle 45	60.32	335.55	0.180	0.0475	15.4800	0.0512	15.9500	0.0078	4.8640	0.2483	100.00	100.00	2509.0	72.7	368.0	50.7	7.9	50.2	2.4
Cycle 46	62.12	373.96	0.166	0.0580	12.7800	0.0651	13.3800	0.0081	4.7900	0.3032	85.94	98.99	2634.0	530.0	280.0	64.0	8.3	52.3	2.5
Cycle 47	71.40	428.90	0.166	0.0278	24.0600	0.0316	24.8000	0.0082	4.8030	0.2479	46.36	97.28	2683.0	0.0	0.0	31.6	7.7	53.0	2.5
Cycle 48	88.55	465.02	0.190	0.0632	11.5000	0.0657	11.9500	0.0075	4.3850	0.2835	93.30	99.55	2733.0	715.4	244.0	64.6	7.5	48.4	2.1
Cycle 49	94.09	515.04	0.183	0.0414	14.7800	0.0443	15.3700	0.0078	4.3650	0.2733	70.40	98.44	2782.0	0.0	0.0	44.0	6.6	49.8	2.2
Grain 3	106.37	1016.08	0.105	0.0537	8.0020	0.0570	8.3960	0.0077	3.2050	0.3111	59.02	97.23	178.8	358.6	181.0	56.3	4.6	49.5	1.6
Cycle 2	99.62	1098.01	0.091	0.0480	8.1960	0.0508	8.5850	0.0077	3.1170	0.3036	54.40	97.11	228.3	100.7	194.0	50.3	4.2	49.3	1.5
Cycle 3	115.80	1199.71	0.097	0.0471	8.1020	0.0505	8.5120	0.0078	3.0870	0.3109	80.62	98.79	277.8	52.2	193.0	50.0	4.2	49.9	1.5
Cycle 4	107.05	1171.13	0.091	0.0493	7.6660	0.0560	8.0880	0.0082	3.1220	0.3247	58.34	97.34	327.3	162.4	179.0	55.3	4.4	52.9	1.6
Cycle 5	106.95	1217.92	0.088	0.0405	9.2760	0.0441	9.7130	0.0079	3.1600	0.2980	62.55	97.75	376.9	0.0	0.0	43.8	4.2	50.7	1.6
Cycle 6	108.73	1242.60	0.088	0.0484	7.6770	0.0548	8.0920	0.0082	3.1100	0.3220	89.45	99.34	426.4	120.0	181.0	54.1	4.3	52.7	1.6
Cycle 7	118.06	1243.43	0.095	0.0488	7.5740	0.0554	7.9190	0.0082	3.0910	0.3046	87.62	99.34	475.9	135.6	178.0	54.7	4.2	52.9	1.6
Cycle 8	111.06	1242.14	0.089	0.0401	8.9870	0.0443	9.4200	0.0080	3.1020	0.3010	85.93	99.18	525.5	0.0	0.0	44.1	4.1	51.5	1.6
Cycle 9	123.87	1266.41	0.098	0.0447	7.9570	0.0486	8.3250	0.0079	3.0210	0.3005	67.20	98.22	575.1	0.0	0.0	48.2	3.9	50.6	1.5
Cycle 10	137.87	1332.93	0.103	0.0448	8.0070	0.0500	8.4250	0.0081	3.0600	0.3149	54.54	97.37	624.6	0.0	0.0	49.6	4.1	52.0	1.6
Cycle 11	133.13	1322.45	0.101	0.0486	7.4490	0.0550	7.8680	0.0082	3.1020	0.3287	78.76	98.76	674.2	126.5	175.0	54.3	4.2	52.7	1.6
Cycle 12	132.05	1332.55	0.099	0.0459	7.7540	0.0504	8.1710	0.0080	3.0210	0.3192	82.32	98.94	723.7	0.0	0.0	49.9	4.0	51.1	1.5
Cycle 13	134.85	1350.65	0.100	0.0489	7.1940	0.0572	7.6060	0.0085	3.0370	0.3316	84.75	99.11	773.3	144.7	169.0	56.5	4.2	54.4	1.7
Cycle 14	137.38	1380.35	0.100	0.0462	7.4210	0.0519	7.8010	0.0081	2.9650	0.3150	76.54	98.71	822.9	7.3	179.0	51.4	3.9	52.3	1.6
Cycle 15	138.50	1351.56	0.102	0.0556	6.6560	0.0645	7.0930	0.0084	3.0140	0.3532	99.13	99.94	872.4	436.0	148.0	63.5	4.4	54.1	1.6
Cycle 16	133.73	1389.76	0.096	0.0458	7.3830	0.0539	7.8090	0.0085	3.0280	0.3304	90.05	99.43	997.2	0.0	0.0	53.3	4.1	54.8	1.7
Cycle 17	142.30	1412.74	0.101	0.0466	7.3650	0.0514	7.7530	0.0080	2.9150	0.3178	87.72	99.28	1047.0	30.3	177.0	50.9	3.9	51.3	1.5
Cycle 18	156.42	1452.01	0.108	0.0546	6.6360	0.0616	7.0490	0.0082	2.9670	0.3456	82.42	98.88	1096.0	394.0	149.0	60.7	4.2	52.6	1.6
Cycle 19	163.11	1473.77	0.111	0.0437	7.6330	0.0492	8.0460	0.0082	2.9500	0.3195	74.71	98.62	1146.0	0.0	0.0	48.8	3.8	52.4	1.5
Cycle 20	171.20	1516.92	0.113	0.0482	7.0890	0.0543	7.5150	0.0082	2.9480	0.3366	65.96	97.99	1195.0	109.4	167.0	53.7	3.9	52.5	1.5
Cycle 21	178.80	1539.93	0.116	0.0423	7.6330	0.0463	8.0200	0.0079	2.8570	0.3105	77.60	98.84	1245.0	0.0	0.0	46.0	3.6	51.0	1.5
Cycle 22	188.12	1625.89	0.116	0.0530	6.4600	0.0632	6.9130	0.0087	2.9900	0.3630	97.79	99.87	1295.0	326.8	147.0	62.2	4.2	55.5	1.7
Cycle 23	192.26	1660.17	0.116	0.0477	6.8350	0.0551	7.2690	0.0084	2.8620	0.3439	89.73	99.39	1344.0	86.2	162.0	54.4	3.9	53.7	1.5
Cycle 24	199.58	1698.81	0.117	0.0486	6.7480	0.0557	7.1450	0.0083	2.8660	0.3350	84.18	99.14	1394.0	126.3	159.0	55.1	3.8	53.4	1.5
Cycle 25	184.10	1663.36	0.111	0.0495	6.8650	0.0540	7.3000	0.0079	2.8510	0.3433	92.22	99.49	1443.0	171.7	160.0	53.4	3.8	50.8	1.4
Cycle 26	182.05	1624.59	0.112	0.0532	6.4190	0.0577	6.8180	0.0079	2.8160	0.3440	92.03	99.50	1493.0	336.0	145.0	57.0	3.8	50.6	1.4
Cycle 27	181.63	1698.20	0.107	0.0457	7.2490	0.0515	7.7120	0.0082	2.9640	0.3437	91.52	99.49	1543.0	0.0	0.0	51.0	3.8	52.4	1.6
Cycle 28	176.56	1608.67	0.110	0.0503	6.6120	0.0544	6.9780	0.0079	2.7830	0.3276	91.31	99.50	1592.0	208.4	153.0	53.8	3.7	50.4	1.4
Cycle 29	178.89	1667.54	0.107	0.0408	7.6440	0.0469	8.0830	0.0083	2.9590	0.3271	85.24	99.23	1642.0	0.0	0.0	46.6	3.7	53.6	1.6

Cycle 30	177.11	1600.89	0.111	0.0482	6.8980	0.0534	7.3050	0.0080	2.8920	0.3348	74.77	98.56	1691.0	110.0	163.0	52.8	3.8	51.5	1.5
Cycle 31	160.61	1534.90	0.105	0.0519	6.6630	0.0535	7.0330	0.0075	2.7970	0.3274	84.87	99.05	1816.0	279.3	153.0	53.0	3.6	48.1	1.3
Cycle 32	166.66	1498.64	0.111	0.0480	7.0880	0.0539	7.5290	0.0081	2.9510	0.3410	71.81	98.30	1866.0	97.9	168.0	53.3	3.9	52.3	1.5
Cycle 33	144.01	1467.57	0.098	0.0428	7.5540	0.0463	7.9410	0.0079	2.8280	0.3114	85.77	99.20	1915.0	0.0	0.0	46.0	3.6	50.4	1.4
Cycle 34	148.34	1516.11	0.098	0.0487	6.9410	0.0563	7.3850	0.0084	3.0390	0.3475	74.41	98.51	1965.0	132.1	163.0	55.6	4.0	53.8	1.6
Cycle 35	152.32	1474.86	0.103	0.0497	6.9870	0.0518	7.3620	0.0076	2.8520	0.3218	86.46	99.18	2014.0	180.1	163.0	51.2	3.7	48.5	1.4
Cycle 36	151.35	1419.85	0.107	0.0493	6.9720	0.0548	7.3510	0.0081	2.9080	0.3246	97.48	99.86	2064.0	163.1	163.0	54.1	3.9	51.7	1.5
Cycle 37	145.49	1436.42	0.101	0.0420	7.9180	0.0449	8.3050	0.0077	2.9400	0.3055	89.16	99.43	2113.0	0.0	0.0	44.6	3.6	49.8	1.5
Cycle 38	143.11	1457.91	0.098	0.0508	6.9890	0.0561	7.3960	0.0080	2.9940	0.3346	90.49	99.42	2163.0	230.6	161.0	55.4	4.0	51.5	1.5
Cycle 39	129.17	1360.63	0.095	0.0470	7.4340	0.0529	7.8640	0.0082	3.0490	0.3311	92.70	99.56	2212.0	50.9	177.0	52.3	4.0	52.4	1.6
Cycle 40	128.07	1307.18	0.098	0.0517	7.1250	0.0548	7.5110	0.0077	2.9720	0.3245	94.97	99.68	2262.0	272.2	163.0	54.2	4.0	49.4	1.5
Cycle 41	135.16	1311.81	0.103	0.0479	7.4700	0.0526	7.8540	0.0080	3.0260	0.3163	80.97	98.93	2311.0	95.6	177.0	52.0	4.0	51.1	1.5
Cycle 42	112.11	1201.68	0.093	0.0522	7.0570	0.0572	7.4450	0.0079	3.0310	0.3282	92.56	99.54	2361.0	293.6	161.0	56.5	4.1	51.0	1.5
Cycle 43	112.24	1143.67	0.098	0.0531	7.1880	0.0561	7.5520	0.0077	3.0360	0.3179	94.46	99.66	2411.0	332.9	163.0	55.4	4.1	49.2	1.5
Cycle 44	115.44	1188.49	0.097	0.0406	8.7290	0.0434	9.1320	0.0078	3.0670	0.2964	79.16	98.87	2460.0	0.0	0.0	43.2	3.9	49.9	1.5
Cycle 45	112.64	1191.00	0.095	0.0459	7.8950	0.0485	8.2460	0.0077	3.0250	0.2969	84.14	99.13	2509.0	0.0	0.0	48.1	3.9	49.2	1.5
Cycle 46	114.89	1149.46	0.100	0.0492	7.8740	0.0515	8.2640	0.0076	3.1130	0.3107	63.02	97.75	2634.0	155.7	184.0	51.0	4.1	48.8	1.5
Cycle 47	109.45	1127.65	0.097	0.0461	8.0870	0.0498	8.4660	0.0078	3.1400	0.3034	80.81	98.94	2684.0	1.7	195.0	49.4	4.1	50.4	1.6
Cycle 48	110.32	1099.33	0.100	0.0543	7.5830	0.0548	7.9500	0.0073	3.1230	0.3111	68.85	97.98	2734.0	383.7	170.0	54.2	4.2	47.1	1.5
Cycle 49	104.73	1074.56	0.097	0.0448	8.6280	0.0476	9.0320	0.0077	3.3000	0.3026	75.51	98.68	2783.0	0.0	0.0	47.2	4.2	49.5	1.6
Grain 4	168.05	1570.63	0.107	0.0497	6.7610	0.0578	7.1690	0.0084	2.8530	0.3379	81.20	98.84	178.6	180.5	158.0	57.1	4.0	54.2	1.5
Cycle 2	159.89	1491.73	0.107	0.0448	7.3690	0.0455	7.6870	0.0074	2.6470	0.2899	76.94	98.69	228.2	0.0	0.0	45.2	3.4	47.3	1.3
Cycle 3	162.61	1552.32	0.105	0.0476	7.1070	0.0548	7.5120	0.0083	2.8660	0.3285	91.33	99.47	277.7	80.8	169.0	54.2	4.0	53.6	1.5
Cycle 4	159.01	1541.12	0.103	0.0486	6.9880	0.0516	7.3440	0.0077	2.7660	0.3140	86.57	99.19	327.3	129.8	164.0	51.1	3.7	49.5	1.4
Cycle 5	169.00	1609.42	0.105	0.0487	7.0640	0.0545	7.4870	0.0081	2.8680	0.3346	77.56	98.55	377.0	132.4	166.0	53.9	3.9	52.1	1.5
Cycle 6	196.83	1706.67	0.115	0.0451	7.2120	0.0499	7.5820	0.0080	2.7580	0.3129	81.93	98.99	426.5	0.0	0.0	49.4	3.7	51.5	1.4
Cycle 7	184.85	1664.95	0.111	0.0446	7.2510	0.0490	7.6230	0.0080	2.7890	0.3131	71.60	98.45	476.0	0.0	0.0	48.5	3.6	51.2	1.4
Cycle 8	191.07	1745.06	0.109	0.0399	7.7930	0.0433	8.1600	0.0079	2.7630	0.2993	53.69	97.64	525.6	0.0	0.0	43.1	3.4	50.6	1.4
Cycle 9	185.08	1678.12	0.110	0.0508	6.6330	0.0578	7.0050	0.0082	2.8240	0.3299	79.68	98.82	575.1	233.0	153.0	57.1	3.9	53.0	1.5
Cycle 10	165.12	1607.86	0.103	0.0503	6.8090	0.0563	7.2170	0.0081	2.8420	0.3365	64.07	97.68	624.6	208.9	158.0	55.7	3.9	52.2	1.5
Cycle 11	159.37	1552.95	0.103	0.0452	7.3310	0.0523	7.7530	0.0084	2.9020	0.3284	97.69	99.86	674.2	0.0	0.0	51.8	3.9	53.9	1.6
Cycle 12	172.46	1525.14	0.113	0.0459	7.3040	0.0501	7.6670	0.0079	2.7830	0.3087	88.18	99.33	723.7	0.0	0.0	49.6	3.7	50.9	1.4
Cycle 13	147.84	1509.02	0.098	0.0432	7.6090	0.0481	7.9990	0.0081	2.8760	0.3122	83.17	99.05	773.3	0.0	0.0	47.7	3.7	51.9	1.5
Cycle 14	154.32	1512.13	0.102	0.0368	8.6240	0.0419	9.0230	0.0082	2.8570	0.2949	82.06	99.06	822.8	0.0	0.0	41.7	3.7	52.9	1.5
Cycle 15	157.02	1474.68	0.106	0.0525	6.7240	0.0599	7.0990	0.0083	2.8810	0.3295	66.70	97.97	872.4	306.7	153.0	59.1	4.1	53.2	1.5
Cycle 16	185.17	1589.55	0.116	0.0486	7.0280	0.0516	7.3880	0.0077	2.7430	0.3136	88.98	99.34	997.6	129.6	165.0	51.0	3.7	49.4	1.4
Cycle 17	190.17	1696.22	0.112	0.0452	7.0450	0.0540	7.4650	0.0087	2.9040	0.3349	76.89	98.76	1047.0	0.0	0.0	53.4	3.9	55.6	1.6
Cycle 18	203.45	1758.51	0.116	0.0443	7.1290	0.0490	7.5050	0.0080	2.7260	0.3159	65.26	98.08	1097.0	0.0	0.0	48.6	3.6	51.5	1.4
Cycle 19	210.20	1815.71	0.116	0.0444	7.0770	0.0508	7.4950	0.0083	2.8290	0.3321	70.06	98.35	1146.0	0.0	0.0	50.3	3.7	53.3	1.5
Cycle 20	205.56	1749.87	0.117	0.0517	6.3960	0.0599	6.8080	0.0084	2.8320	0.3492	86.03	99.17	1196.0	270.7	147.0	59.1	3.9	54.0	1.5
Cycle 21	195.75	1687.41	0.116	0.0488	6.6960	0.0540	7.0750	0.0080	2.7530	0.3283	85.14	99.14	1245.0	139.2	157.0	53.4	3.7	51.5	1.4
Cycle 22	184.54	1598.28	0.115	0.0467	7.0970	0.0496	7.4660	0.0077	2.7310	0.3146	69.97	98.24	1295.0	33.0	170.0	49.1	3.6	49.5	1.4
Cycle 23	173.46	1625.12	0.107	0.0459	7.2460	0.0515	7.6770	0.0081	2.8820	0.3331	83.13	98.97	1345.0	0.0	0.0	51.0	3.8	52.2	1.5
Cycle 24	169.06	1602.51	0.105	0.0459	7.0690	0.0527	7.4670	0.0083	2.8540	0.3269	81.98	98.98	1394.0	0.0	0.0	52.2	3.8	53.5	1.5
Cycle 25	171.46	1573.84	0.109	0.0512	6.8030	0.0545	7.1920	0.0077	2.7970	0.3298	81.57	98.80	1444.0	248.8	157.0	53.9	3.8	49.6	1.4
Cycle 26	175.20	1596.70	0.110	0.0490	6.8560	0.0543	7.2140	0.0080	2.8210	0.3195	69.38	98.29	1493.0	146.8	161.0	53.6	3.8	51.6	1.5
Cycle 27	174.41	1604.96	0.109	0.0486	7.0340	0.0540	7.4170	0.0081	2.8840	0.3238	67.18	98.11	1543.0	126.8	166.0	53.4	3.9	51.8	1.5
Cycle 28	166.76	1524.28	0.109	0.0488	7.1480	0.0561	7.5570	0.0083	2.9350	0.3298	79.15	98.74	1592.0	138.3	168.0	55.4	4.1	53.5	1.6
Cycle 29	151.43	1441.90	0.105	0.0464	7.2600	0.0509	7.5950	0.0080	2.8130	0.3015	71.91	98.48	1642.0	19.2	174.0	50.4	3.7	51.1	1.4
Cycle 30	147.19	1346.78	0.109	0.0498	7.3120	0.0549	7.7190	0.0080	2.9520	0.3255	80.35	98.76	1692.0	187.3	170.0	54.2	4.1	51.3	1.5
Cycle 31	159.98	1364.59	0.117	0.0486	7.3660	0.0540	7.7210	0.0081	2.8910	0.3072	68.86	98.25	1816.0	126.8	173.0	53.4	4.0	51.7	1.5
Cycle 32	146.13	1345.98	0.109	0.0427	8.1240	0.0451	8.4710	0.0077	2.8880	0.2882	71.35	98.49	1865.0	0.0	0.0	44.8	3.7	49.2	1.4

Cycle 33	151.54	1306.98	0.116	0.0502	7.5230	0.0537	7.8930	0.0078	2.9520	0.3094	89.62	99.37	1915.0	204.2	175.0	53.1	4.1	49.8	1.5
Cycle 34	149.55	1289.17	0.116	0.0501	7.6070	0.0565	8.0230	0.0082	3.0260	0.3224	84.93	99.04	1964.0	200.3	177.0	55.8	4.4	52.5	1.6
Cycle 35	147.15	1252.10	0.118	0.0526	7.3890	0.0568	7.7490	0.0078	2.9820	0.3103	71.02	98.22	2014.0	311.3	168.0	56.1	4.2	50.3	1.5
Cycle 36	142.68	1160.57	0.123	0.0484	8.0150	0.0507	8.3790	0.0076	2.9270	0.2963	78.47	98.68	2063.0	118.4	189.0	50.2	4.1	48.8	1.4
Cycle 37	140.40	1192.61	0.118	0.0504	7.7520	0.0551	8.1150	0.0079	3.0450	0.3044	79.93	98.82	2113.0	213.5	180.0	54.4	4.3	50.9	1.5
Cycle 38	141.89	1130.09	0.126	0.0472	8.3040	0.0526	8.7010	0.0081	3.0800	0.3030	91.35	99.49	2163.0	58.0	198.0	52.1	4.4	51.9	1.6
Cycle 39	132.70	1116.46	0.119	0.0572	7.2990	0.0605	7.6650	0.0077	2.9860	0.3144	100.00	100.00	2212.0	498.6	161.0	59.6	4.4	49.2	1.5
Cycle 40	134.78	1132.83	0.119	0.0530	7.6380	0.0603	8.0340	0.0082	3.1430	0.3182	100.00	100.00	2262.0	329.6	173.0	59.4	4.6	52.9	1.7
Cycle 41	133.97	1068.04	0.125	0.0452	8.6300	0.0461	8.9730	0.0074	2.9050	0.2775	100.00	100.00	2311.0	0.0	0.0	45.8	4.0	47.5	1.4
Cycle 42	121.66	1041.89	0.117	0.0534	7.7730	0.0555	8.1210	0.0075	2.9910	0.2978	91.44	99.43	2361.0	347.0	176.0	54.9	4.3	48.4	1.4
Cycle 43	128.21	1026.17	0.125	0.0522	7.9350	0.0566	8.2760	0.0079	3.0790	0.2946	69.41	98.19	2411.0	293.8	181.0	55.9	4.5	50.5	1.6
Cycle 44	131.43	1014.32	0.130	0.0574	7.5110	0.0627	7.8500	0.0079	3.1070	0.3046	88.20	99.27	2460.0	504.9	165.0	61.8	4.7	50.9	1.6
Cycle 45	139.96	1000.46	0.140	0.0528	8.0890	0.0557	8.4330	0.0076	3.0800	0.2923	87.48	99.25	2510.0	320.4	184.0	55.0	4.5	49.1	1.5
Cycle 46	136.02	1006.76	0.135	0.0454	9.2370	0.0447	9.6030	0.0071	3.0660	0.2768	90.00	99.42	2635.0	0.0	0.0	44.4	4.2	45.8	1.4
Cycle 47	132.58	1025.87	0.129	0.0500	8.6240	0.0533	9.0450	0.0077	3.2230	0.3057	96.78	99.80	2685.0	193.5	201.0	52.7	4.6	49.6	1.6
Cycle 48	139.01	1031.87	0.135	0.0395	10.2300	0.0413	10.6200	0.0076	3.2390	0.2725	83.72	99.20	2734.0	0.0	0.0	41.1	4.3	48.8	1.6
Cycle 49	142.95	1044.75	0.137	0.0549	8.2760	0.0595	8.6900	0.0079	3.3440	0.3133	80.12	98.74	2784.0	408.9	185.0	58.7	5.0	50.5	1.7
Grain 5	91.31	965.92	0.095	0.0554	10.9600	0.0640	11.6300	0.0084	3.5340	0.3371	40.36	93.24	178.5	426.5	244.0	63.0	7.1	53.9	1.9
Cycle 2	91.41	1053.12	0.087	0.0502	9.6850	0.0561	10.2200	0.0081	3.2980	0.3198	63.87	96.81	228.0	203.6	225.0	55.4	5.5	52.0	1.7
Cycle 3	108.70	1202.49	0.090	0.0416	9.5670	0.0468	10.0400	0.0082	3.2130	0.3035	53.45	96.95	277.5	0.0	0.0	46.5	4.6	52.4	1.7
Cycle 4	135.03	1284.39	0.105	0.0535	7.5790	0.0603	8.0470	0.0082	3.0700	0.3389	64.21	97.28	327.1	348.1	171.0	59.5	4.7	52.5	1.6
Cycle 5	156.02	1420.10	0.110	0.0526	7.4650	0.0569	7.9140	0.0078	2.9910	0.3348	83.19	98.76	376.7	312.5	170.0	56.2	4.3	50.4	1.5
Cycle 6	189.28	1627.87	0.116	0.0379	8.9450	0.0423	9.3640	0.0081	2.9250	0.2962	81.92	99.02	426.3	0.0	0.0	42.1	3.9	51.9	1.5
Cycle 7	190.31	1694.16	0.112	0.0537	6.7000	0.0634	7.1630	0.0086	3.0470	0.3599	91.44	99.45	475.8	359.0	151.0	62.4	4.3	54.9	1.7
Cycle 8	193.77	1683.24	0.115	0.0475	7.3050	0.0536	7.7510	0.0082	2.9520	0.3374	84.54	99.04	525.3	75.9	174.0	53.0	4.0	52.5	1.5
Cycle 9	189.10	1660.45	0.114	0.0508	6.9070	0.0578	7.3350	0.0083	2.8880	0.3408	75.87	98.43	574.8	229.5	160.0	57.1	4.1	53.1	1.5
Cycle 10	170.74	1616.97	0.106	0.0472	7.2110	0.0542	7.6390	0.0083	2.9220	0.3337	93.18	99.58	624.4	58.8	172.0	53.6	4.0	53.5	1.6
Cycle 11	182.51	1636.15	0.112	0.0479	7.2010	0.0540	7.6220	0.0082	2.8900	0.3310	74.08	98.39	674.0	94.0	171.0	53.4	4.0	52.5	1.5
Cycle 12	169.33	1587.45	0.107	0.0483	6.9020	0.0538	7.2500	0.0081	2.8000	0.3145	74.01	98.56	723.6	112.3	163.0	53.2	3.8	51.9	1.5
Cycle 13	169.67	1583.99	0.107	0.0510	6.7110	0.0595	7.1160	0.0085	2.8730	0.3390	76.58	98.55	773.1	240.9	155.0	58.7	4.1	54.3	1.6
Cycle 14	184.42	1663.24	0.111	0.0447	7.4460	0.0487	7.8240	0.0079	2.8090	0.3108	60.50	97.76	822.6	0.0	0.0	48.3	3.7	50.8	1.4
Cycle 15	172.65	1706.81	0.101	0.0473	7.1890	0.0519	7.5830	0.0080	2.8420	0.3224	82.48	98.92	872.2	64.4	171.0	51.4	3.8	51.1	1.5
Cycle 16	174.60	1644.67	0.106	0.0464	7.3580	0.0530	7.7880	0.0083	2.9190	0.3307	80.27	98.78	997.4	19.0	177.0	52.4	4.0	53.2	1.6
Cycle 17	186.60	1693.01	0.110	0.0466	7.0960	0.0552	7.5000	0.0086	2.9010	0.3290	67.32	98.17	1047.0	31.0	170.0	54.6	4.0	55.1	1.6
Cycle 18	172.17	1664.53	0.103	0.0461	7.0670	0.0546	7.4700	0.0086	2.9220	0.3300	59.85	97.81	1097.0	2.9	170.0	54.0	3.9	55.1	1.6
Cycle 19	186.50	1658.47	0.112	0.0423	7.6770	0.0477	8.0860	0.0082	2.8870	0.3164	85.72	99.23	1146.0	0.0	0.0	47.3	3.7	52.5	1.5
Cycle 20	195.89	1741.60	0.112	0.0465	7.1340	0.0528	7.5570	0.0082	2.8730	0.3331	100.00	100.00	1196.0	24.4	171.0	52.3	3.9	52.9	1.5
Cycle 21	188.56	1712.74	0.110	0.0484	6.7390	0.0540	7.1110	0.0081	2.7980	0.3260	97.67	99.87	1245.0	116.4	159.0	53.4	3.7	52.0	1.5
Cycle 22	192.19	1680.69	0.114	0.0471	7.0690	0.0529	7.5040	0.0081	2.8360	0.3378	94.19	99.63	1295.0	56.4	169.0	52.4	3.8	52.3	1.5
Cycle 23	198.86	1753.74	0.113	0.0495	6.7040	0.0554	7.1220	0.0081	2.7930	0.3414	96.01	99.75	1344.0	169.6	157.0	54.8	3.8	52.2	1.5
Cycle 24	218.19	1821.04	0.120	0.0510	6.5970	0.0569	7.0250	0.0081	2.8100	0.3477	86.87	99.16	1394.0	239.9	152.0	56.2	3.8	52.0	1.5
Cycle 25	215.27	1864.73	0.115	0.0455	7.1560	0.0495	7.5580	0.0079	2.7420	0.3241	94.10	99.64	1443.0	0.0	0.0	49.1	3.6	50.7	1.4
Cycle 26	219.87	1832.00	0.120	0.0446	7.0370	0.0518	7.4400	0.0084	2.8000	0.3281	97.73	99.88	1493.0	0.0	0.0	51.3	3.7	54.2	1.5
Cycle 27	210.59	1864.02	0.113	0.0423	7.2970	0.0470	7.6860	0.0080	2.7710	0.3171	88.66	99.40	1542.0	0.0	0.0	46.6	3.5	51.7	1.4
Cycle 28	226.81	1920.17	0.118	0.0508	6.5250	0.0552	6.9090	0.0079	2.7440	0.3346	84.08	99.04	1592.0	229.3	151.0	54.5	3.7	50.6	1.4
Cycle 29	215.71	1821.37	0.118	0.0443	7.2840	0.0476	7.6800	0.0078	2.7270	0.3189	85.78	99.16	1641.0	0.0	0.0	47.2	3.6	50.1	1.4
Cycle 30	201.65	1759.51	0.115	0.0494	6.6410	0.0568	7.0720	0.0083	2.8410	0.3480	91.36	99.47	1691.0	166.7	155.0	56.1	3.9	53.5	1.5
Cycle 31	188.43	1671.49	0.113	0.0517	6.3970	0.0581	6.7960	0.0082	2.7600	0.3435	86.84	99.17	1816.0	272.0	147.0	57.4	3.8	52.4	1.4
Cycle 32	202.68	1721.24	0.118	0.0441	7.1990	0.0478	7.5640	0.0079	2.7400	0.3114	90.81	99.51	1866.0	0.0	0.0	47.4	3.5	50.4	1.4
Cycle 33	191.64	1714.50	0.112	0.0525	6.3680	0.0552	6.7160	0.0076	2.6750	0.3257	94.17	99.64	1915.0	306.9	145.0	54.6	3.6	49.0	1.3
Cycle 34	190.08	1700.00	0.112	0.0421	7.3620	0.0458	7.7300	0.0079	2.6860	0.3072	95.46	99.75	1965.0	0.0	0.0	45.5	3.4	50.7	1.4
Cycle 35	196.79	1727.50	0.114	0.0436	7.2020	0.0476	7.5790	0.0079	2.7190	0.3148	80.53	98.92	2015.0	0.0	0.0	47.2	3.5	50.9	1.4

Cycle 36	197.33	1726.10	0.114	0.0521	6.3160	0.0576	6.6820	0.0080	2.7080	0.3343	78.63	98.70	2064.0	291.6	144.0	56.8	3.7	51.4	1.4
Cycle 37	201.77	1757.67	0.115	0.0439	7.0050	0.0492	7.3680	0.0081	2.7120	0.3144	84.46	99.19	2114.0	0.0	0.0	48.8	3.5	52.2	1.4
Cycle 38	197.56	1730.88	0.114	0.0471	6.7950	0.0526	7.2000	0.0081	2.7900	0.3346	91.76	99.52	2163.0	54.0	162.0	52.0	3.7	52.0	1.4
Cycle 39	205.34	1733.09	0.118	0.0460	6.9740	0.0493	7.3610	0.0078	2.7140	0.3231	87.64	99.28	2213.0	0.0	0.0	48.8	3.5	49.9	1.4
Cycle 40	222.73	1850.52	0.120	0.0488	6.5850	0.0560	6.9880	0.0083	2.8060	0.3400	79.26	98.84	2262.0	136.4	155.0	55.3	3.8	53.4	1.5
Cycle 41	226.56	1897.48	0.119	0.0458	6.9400	0.0513	7.3590	0.0081	2.7650	0.3351	88.14	99.30	2312.0	0.0	0.0	50.7	3.6	52.1	1.4
Cycle 42	224.33	1899.38	0.118	0.0508	6.5330	0.0540	6.9490	0.0077	2.7290	0.3443	80.54	98.72	2361.0	232.9	151.0	53.4	3.6	49.5	1.4
Cycle 43	234.68	1937.89	0.121	0.0448	6.8990	0.0511	7.3190	0.0083	2.7990	0.3367	87.72	99.33	2411.0	0.0	0.0	50.6	3.6	53.1	1.5
Cycle 44	238.04	1907.10	0.125	0.0468	6.6610	0.0513	7.0480	0.0079	2.7050	0.3311	95.81	99.77	2460.0	40.7	159.0	50.8	3.5	51.0	1.4
Cycle 45	223.80	1824.56	0.123	0.0486	6.4150	0.0555	6.8340	0.0083	2.7230	0.3485	85.57	99.14	2510.0	128.3	151.0	54.8	3.7	53.2	1.4
Cycle 46	249.87	1897.27	0.132	0.0501	6.5070	0.0536	6.9380	0.0078	2.7330	0.3500	85.95	99.11	2635.0	201.6	151.0	53.0	3.6	49.8	1.4
Cycle 47	252.92	1952.68	0.130	0.0456	6.7750	0.0494	7.1720	0.0079	2.7020	0.3312	86.15	99.24	2685.0	0.0	0.0	48.9	3.4	50.5	1.4
Cycle 48	267.95	2028.84	0.132	0.0539	6.0260	0.0610	6.4830	0.0082	2.7690	0.3726	93.44	99.57	2734.0	365.5	136.0	60.2	3.8	52.8	1.5
Cycle 49	256.87	1998.78	0.129	0.0539	5.9500	0.0565	6.3370	0.0076	2.6160	0.3501	88.18	99.25	2784.0	367.7	134.0	55.8	3.4	48.8	1.3
Grain 6s1	36.13	590.64	0.061	0.0675	12.3200	0.0645	13.0000	0.0069	4.6330	0.3203	37.89	93.01	178.5	854.5	256.0	63.5	8.0	44.5	2.1
Cycle 2	40.66	590.18	0.069	0.0455	18.1100	0.0422	18.8400	0.0067	4.7630	0.2772	52.35	95.69	227.9	0.0	0.0	42.0	7.8	43.2	2.1
Cycle 3	38.42	583.13	0.066	0.0465	16.7000	0.0440	17.3800	0.0069	4.8790	0.2769	17.96	93.19	277.4	23.4	401.0	43.7	7.4	44.1	2.1
Cycle 4	36.52	527.94	0.069	0.0484	15.1300	0.0433	15.6600	0.0065	4.6410	0.2610	-43.49	88.96	326.9	119.9	357.0	43.0	6.6	41.7	1.9
Cycle 5	34.10	518.81	0.066	0.0367	21.2400	0.0358	21.9500	0.0071	5.0200	0.2544	2.84	92.85	376.4	0.0	0.0	35.7	7.7	45.5	2.3
Cycle 6	41.09	505.76	0.081	0.0518	15.5800	0.0560	16.3500	0.0078	5.3870	0.3045	-37.11	88.57	425.9	275.2	357.0	55.3	8.8	50.4	2.7
Cycle 7	42.38	495.58	0.086	0.0544	13.9700	0.0550	14.5200	0.0073	5.1000	0.2805	75.65	98.20	475.4	385.9	314.0	54.4	7.7	47.1	2.4
Cycle 8	43.04	484.31	0.089	0.0330	22.5100	0.0348	23.2400	0.0076	5.4120	0.2499	77.65	98.67	524.9	0.0	0.0	34.7	7.9	49.1	2.7
Cycle 9	49.09	447.64	0.110	0.0283	31.7800	0.0253	32.6100	0.0065	5.2100	0.2372	8.14	93.80	574.5	0.0	0.0	25.4	8.2	41.7	2.2
Grain 6s2	52.48	454.33	0.116	0.0452	17.6000	0.0434	18.2100	0.0070	5.3960	0.2591	88.25	99.26	179.9	0.0	0.0	43.2	7.7	44.8	2.4
Cycle 2	60.25	455.17	0.132	0.0592	13.8900	0.0578	14.2800	0.0071	5.1240	0.2539	70.16	98.08	229.4	576.0	302.0	57.1	7.9	45.5	2.3
Cycle 3	58.01	490.37	0.118	0.0569	14.5100	0.0596	15.2400	0.0076	5.3120	0.3071	84.35	98.72	279.0	489.4	320.0	58.8	8.7	48.8	2.6
Cycle 4	66.78	527.13	0.127	0.0514	14.2300	0.0558	14.7600	0.0079	5.1470	0.2754	23.37	95.41	328.5	257.8	327.0	55.1	7.9	50.6	2.6
Cycle 5	63.71	537.66	0.118	0.0303	23.8000	0.0313	24.5400	0.0075	5.2010	0.2461	26.67	95.95	378.0	0.0	0.0	31.3	7.6	48.0	2.5
Cycle 6	67.10	534.96	0.125	0.0451	15.4300	0.0453	15.9500	0.0073	4.9420	0.2582	60.00	97.76	427.5	0.0	0.0	45.0	7.0	46.8	2.3
Cycle 7	67.37	537.14	0.125	0.0363	18.0200	0.0408	18.6700	0.0081	5.2310	0.2621	43.66	97.23	477.0	0.0	0.0	40.6	7.4	52.3	2.7
Cycle 8	66.60	546.99	0.122	0.0400	16.8500	0.0434	17.5100	0.0079	5.0160	0.2726	47.13	96.91	526.6	0.0	0.0	43.1	7.4	50.5	2.5
Cycle 9	68.36	561.41	0.122	0.0307	26.5500	0.0296	27.3600	0.0070	5.0070	0.2513	91.60	99.42	576.2	0.0	0.0	29.6	8.0	45.0	2.3
Cycle 10	70.09	571.82	0.123	0.0673	11.5100	0.0715	11.9300	0.0077	4.9030	0.2894	78.11	98.44	625.6	848.3	239.0	70.1	8.1	49.5	2.4
Cycle 11	74.89	562.86	0.133	0.0452	15.5800	0.0435	16.1600	0.0070	4.6400	0.2662	100.00	100.00	675.1	0.0	0.0	43.3	6.8	44.9	2.1
Cycle 12	65.23	571.43	0.114	0.0451	14.5200	0.0510	15.1000	0.0082	4.9820	0.2792	81.65	98.95	724.6	0.0	0.0	50.5	7.4	52.6	2.6
Cycle 13	68.64	572.41	0.120	0.0533	13.4300	0.0609	14.0900	0.0083	5.1600	0.3073	38.23	95.78	774.2	341.3	304.0	60.0	8.2	53.2	2.7
Cycle 14	74.06	545.77	0.136	0.0489	15.0000	0.0490	15.5900	0.0073	4.9340	0.2752	13.55	94.39	823.7	143.4	352.0	48.6	7.4	46.7	2.3
Cycle 15	65.03	527.93	0.123	0.0489	14.6400	0.0481	15.0900	0.0071	4.9660	0.2539	-47.09	91.72	873.2	142.6	344.0	47.7	7.0	45.8	2.3
Cycle 16	72.62	518.72	0.140	0.0559	13.5700	0.0585	14.1300	0.0076	4.9950	0.2860	83.01	98.84	997.8	450.1	301.0	57.7	7.9	48.7	2.4
Cycle 17	72.90	484.81	0.150	0.0543	14.2200	0.0536	14.6500	0.0072	4.9740	0.2553	30.22	95.92	1047.0	384.6	320.0	53.0	7.6	45.9	2.3
Cycle 18	72.46	548.05	0.132	0.0425	17.4700	0.0439	18.1900	0.0075	5.0090	0.2781	76.05	98.38	1097.0	0.0	0.0	43.6	7.8	48.0	2.4
Cycle 19	73.99	529.88	0.140	0.0501	14.3000	0.0503	14.8200	0.0073	4.8300	0.2691	90.89	99.44	1147.0	200.7	332.0	49.8	7.2	46.7	2.3
Cycle 20	79.26	532.75	0.149	0.0358	19.1400	0.0373	19.8000	0.0076	4.9230	0.2574	60.47	97.88	1196.0	0.0	0.0	37.2	7.2	48.5	2.4
Cycle 21	81.17	556.48	0.146	0.0502	14.5900	0.0550	15.2700	0.0079	5.0860	0.2970	76.41	98.43	1246.0	204.6	339.0	54.4	8.1	51.0	2.6
Cycle 22	79.90	550.87	0.145	0.0361	19.7600	0.0357	20.4400	0.0072	4.8740	0.2566	80.32	98.87	1295.0	0.0	0.0	35.6	7.2	46.1	2.2
Cycle 23	77.14	549.40	0.140	0.0498	14.3800	0.0511	14.9400	0.0074	4.8430	0.2760	42.11	96.32	1345.0	184.4	335.0	50.6	7.4	47.8	2.3
Cycle 24	84.49	533.90	0.158	0.0464	15.1300	0.0506	15.5500	0.0079	4.8600	0.2426	66.72	98.46	1394.0	16.6	363.0	50.1	7.6	50.8	2.5
Cycle 25	80.46	550.18	0.146	0.0329	19.8600	0.0354	20.5100	0.0078	4.9020	0.2493	100.00	100.00	1444.0	0.0	0.0	35.4	7.1	50.1	2.5
Cycle 26	79.82	573.76	0.139	0.0455	15.5000	0.0473	16.1100	0.0075	4.9530	0.2747	90.80	99.45	1494.0	0.0	0.0	46.9	7.4	48.4	2.4
Cycle 27	85.19	532.24	0.160	0.0381	18.8000	0.0372	19.4700	0.0071	4.7130	0.2600	74.08	98.46	1543.0	0.0	0.0	37.1	7.1	45.4	2.1
Cycle 28	84.94	540.72	0.157	0.0462	15.2500	0.0484	15.8200	0.0076	4.8580	0.2688	90.48	99.46	1593.0	7.1	367.0	48.0	7.4	48.8	2.4
Cycle 29	83.40	561.71	0.148	0.0405	17.3900	0.0472	18.1600	0.0085	5.1930	0.2871	74.70	98.47	1642.0	0.0	0.0	46.9	8.3	54.4	2.8

Cycle 30	85.05	540.70	0.157	0.0534	14.1900	0.0557	14.8000	0.0076	5.0280	0.2885	96.54	99.77	1692.0	347.7	321.0	55.0	7.9	48.5	2.4
Cycle 31	76.14	518.59	0.147	0.0513	14.7600	0.0522	15.4000	0.0074	4.9420	0.2873	76.85	98.38	1816.0	253.6	340.0	51.7	7.8	47.4	2.3
Cycle 32	79.16	502.74	0.157	0.0568	13.4700	0.0575	13.9500	0.0073	4.8520	0.2705	91.08	99.43	1866.0	482.1	298.0	56.8	7.7	47.2	2.3
Cycle 33	83.88	526.97	0.159	0.0586	13.2500	0.0645	13.8500	0.0080	5.1140	0.2985	67.60	97.80	1916.0	551.5	289.0	63.4	8.5	51.3	2.6
Cycle 34	80.37	513.52	0.157	0.0290	24.2400	0.0290	24.9500	0.0073	4.9840	0.2397	65.60	98.34	1965.0	0.0	0.0	29.1	7.2	46.6	2.3
Cycle 35	90.77	515.54	0.176	0.0420	16.9900	0.0402	17.5100	0.0070	4.7480	0.2444	100.00	100.00	2015.0	0.0	0.0	40.1	6.9	44.7	2.1
Cycle 36	95.33	543.95	0.175	0.0441	16.4900	0.0438	17.0800	0.0072	4.8460	0.2606	89.73	99.43	2064.0	0.0	0.0	43.5	7.3	46.2	2.2
Cycle 37	87.90	516.84	0.170	0.0513	14.9000	0.0549	15.5700	0.0078	5.1200	0.2932	66.09	97.79	2113.0	254.2	343.0	54.3	8.2	49.9	2.5
Cycle 38	92.94	549.15	0.169	0.0559	13.5500	0.0644	14.2500	0.0084	5.1880	0.3129	60.91	97.36	2163.0	447.6	301.0	63.4	8.8	53.7	2.8
Cycle 39	99.20	582.49	0.170	0.0442	17.2100	0.0454	17.9600	0.0074	4.9830	0.2866	53.23	96.85	2212.0	0.0	0.0	45.1	7.9	47.8	2.4
Grain 7	51.40	810.64	0.063	0.0444	11.0600	0.0447	11.5000	0.0073	3.5540	0.2761	41.76	95.90	178.2	0.0	0.0	44.4	5.0	47.0	1.7
Cycle 2	54.95	777.98	0.071	0.0526	9.2700	0.0562	9.6580	0.0078	3.5160	0.2902	63.50	97.37	227.7	311.0	211.0	55.5	5.2	49.8	1.7
Cycle 3	48.01	796.92	0.060	0.0578	8.5410	0.0608	8.8890	0.0076	3.4800	0.2937	86.01	98.94	277.3	523.2	187.0	59.9	5.2	49.0	1.7
Cycle 4	46.58	758.73	0.061	0.0447	9.8000	0.0518	10.1600	0.0084	3.5790	0.2741	81.91	98.95	326.8	0.0	0.0	51.3	5.1	53.9	1.9
Cycle 5	46.33	712.85	0.065	0.0540	9.1350	0.0584	9.4810	0.0078	3.5950	0.2843	79.54	98.58	376.4	370.0	206.0	57.6	5.3	50.4	1.8
Cycle 6	57.16	708.38	0.081	0.0558	8.9160	0.0603	9.2150	0.0078	3.5360	0.2749	75.07	98.37	425.9	443.2	198.0	59.4	5.3	50.3	1.8
Cycle 7	47.45	717.93	0.066	0.0423	10.5200	0.0473	10.8800	0.0081	3.6060	0.2635	94.90	99.71	475.4	0.0	0.0	46.9	5.0	52.1	1.9
Cycle 8	48.57	638.64	0.076	0.0486	10.0700	0.0515	10.4200	0.0077	3.6130	0.2666	81.36	98.83	525.0	130.7	237.0	51.0	5.2	49.3	1.8
Cycle 9	44.71	613.47	0.073	0.0512	9.7210	0.0536	9.9820	0.0076	3.6210	0.2527	63.66	97.84	574.6	248.2	224.0	53.1	5.2	48.8	1.8
Cycle 10	43.76	638.48	0.069	0.0468	10.7100	0.0482	11.0500	0.0075	3.6900	0.2580	34.75	95.92	624.2	36.3	256.0	47.8	5.2	48.1	1.8
Cycle 11	42.58	597.26	0.071	0.0501	10.1000	0.0556	10.4500	0.0081	3.7640	0.2719	75.35	98.43	673.8	198.8	235.0	55.0	5.6	51.7	1.9
Cycle 12	41.12	579.40	0.071	0.0575	9.3010	0.0644	9.6080	0.0081	3.8020	0.2775	71.95	98.12	723.2	509.4	204.0	63.3	5.9	52.2	2.0
Cycle 13	43.61	590.25	0.074	0.0525	10.0200	0.0557	10.2900	0.0077	3.7950	0.2535	100.00	100.00	772.7	308.2	228.0	55.1	5.5	49.4	1.9
Cycle 14	42.16	597.73	0.071	0.0507	10.2000	0.0562	10.5300	0.0080	3.8760	0.2660	100.00	100.00	822.2	227.2	236.0	55.5	5.7	51.6	2.0
Cycle 15	40.54	584.19	0.069	0.0477	10.6300	0.0534	10.9900	0.0081	3.8760	0.2681	97.77	99.86	871.7	83.2	252.0	52.9	5.7	52.2	2.0
Cycle 16	42.37	534.86	0.079	0.0356	13.4100	0.0373	13.7700	0.0076	3.8180	0.2322	64.92	98.29	996.7	0.0	0.0	37.2	5.0	48.9	1.9
Cycle 17	45.41	547.51	0.083	0.0474	10.9800	0.0536	11.3300	0.0082	3.9520	0.2614	58.36	97.62	1046.0	71.6	261.0	53.0	5.9	52.6	2.1
Cycle 18	37.72	534.20	0.071	0.0374	13.5500	0.0413	13.9900	0.0080	3.9990	0.2511	81.42	98.96	1096.0	0.0	0.0	41.1	5.6	51.4	2.1
Cycle 19	44.60	536.41	0.083	0.0503	11.4000	0.0534	11.8400	0.0077	4.0220	0.2776	100.00	100.00	1146.0	209.7	264.0	52.8	6.1	49.4	2.0
Cycle 20	42.00	528.30	0.080	0.0567	10.3200	0.0568	10.6400	0.0073	3.9170	0.2643	88.99	99.22	1195.0	477.9	228.0	56.1	5.8	46.7	1.8
Cycle 21	41.77	549.67	0.076	0.0558	10.0900	0.0651	10.4700	0.0085	4.1410	0.2871	61.74	97.50	1245.0	444.4	224.0	64.1	6.5	54.4	2.2
Cycle 22	46.29	547.66	0.085	0.0407	12.3700	0.0464	12.7600	0.0083	4.0540	0.2536	65.39	98.22	1294.0	0.0	0.0	46.0	5.7	53.1	2.1
Cycle 23	39.00	518.92	0.075	0.0563	10.1100	0.0575	10.3800	0.0074	3.8440	0.2538	62.49	97.48	1344.0	464.6	224.0	56.7	5.7	47.5	1.8
Cycle 24	46.91	559.05	0.084	0.0619	9.6090	0.0715	9.9410	0.0084	4.0860	0.2855	79.13	98.56	1393.0	670.9	206.0	70.1	6.7	53.8	2.2
Cycle 25	50.16	561.96	0.089	0.0502	11.1800	0.0527	11.5300	0.0076	3.9890	0.2591	76.02	98.52	1443.0	204.3	259.0	52.1	5.9	48.9	1.9
Cycle 26	49.23	569.52	0.086	0.0437	11.8200	0.0488	12.1400	0.0081	4.0230	0.2456	71.53	98.57	1492.0	0.0	0.0	48.4	5.7	52.0	2.1
Cycle 27	43.01	552.64	0.078	0.0429	12.0800	0.0468	12.4200	0.0079	4.0820	0.2484	64.07	98.13	1542.0	0.0	0.0	46.5	5.6	50.9	2.1
Cycle 28	39.49	535.41	0.074	0.0442	11.7000	0.0482	12.0200	0.0079	4.0530	0.2469	51.02	97.43	1592.0	0.0	0.0	47.8	5.6	50.8	2.1
Cycle 29	42.28	534.84	0.079	0.0463	11.9000	0.0487	12.3100	0.0076	4.0560	0.2628	75.83	98.50	1641.0	11.3	286.0	48.3	5.8	49.0	2.0
Cycle 30	44.57	527.48	0.085	0.0619	9.6870	0.0664	9.9810	0.0078	3.9900	0.2726	81.22	98.69	1691.0	672.2	207.0	65.2	6.3	49.9	2.0
Cycle 31	49.90	550.72	0.091	0.0475	11.2100	0.0535	11.5700	0.0082	4.0060	0.2602	93.47	99.63	1815.0	76.4	266.0	53.0	6.0	52.4	2.1
Cycle 32	47.42	561.03	0.085	0.0488	11.0600	0.0539	11.3800	0.0080	4.0400	0.2553	67.06	98.17	1865.0	139.5	260.0	53.3	5.9	51.4	2.1
Cycle 33	50.17	558.26	0.090	0.0425	12.0000	0.0506	12.3700	0.0086	4.1640	0.2561	56.27	97.91	1914.0	0.0	0.0	50.1	6.0	55.4	2.3
Cycle 34	47.14	554.40	0.085	0.0518	10.5100	0.0579	10.8700	0.0081	3.9570	0.2712	94.27	99.64	1964.0	276.7	241.0	57.2	6.0	52.0	2.1
Cycle 35	51.57	586.54	0.088	0.0584	9.8960	0.0652	10.2800	0.0081	4.0140	0.2883	85.29	98.96	2013.0	546.0	216.0	64.2	6.4	52.0	2.1
Cycle 36	49.58	578.75	0.086	0.0387	12.9000	0.0433	13.3000	0.0081	4.1060	0.2497	100.00	100.00	2063.0	0.0	0.0	43.0	5.6	52.1	2.1
Cycle 37	46.29	568.02	0.081	0.0442	11.6900	0.0474	12.0300	0.0078	3.9740	0.2486	93.03	99.63	2112.0	0.0	0.0	47.1	5.5	50.0	2.0
Cycle 38	46.90	549.51	0.085	0.0444	11.7900	0.0470	12.1100	0.0077	4.0280	0.2448	71.43	98.54	2162.0	0.0	0.0	46.7	5.5	49.3	2.0
Cycle 39	49.70	517.83	0.096	0.0447	11.9800	0.0480	12.3400	0.0078	4.0090	0.2504	80.06	98.92	2211.0	0.0	0.0	47.6	5.7	50.1	2.0
Cycle 40	44.62	559.55	0.080	0.0516	10.6200	0.0568	10.9600	0.0080	4.0510	0.2666	100.00	100.00	2261.0	265.5	244.0	56.1	6.0	51.3	2.1
Cycle 41	47.15	548.80	0.086	0.0480	11.5100	0.0536	11.9100	0.0081	4.1760	0.2700	100.00	100.00	2311.0	100.4	272.0	53.0	6.2	52.0	2.2
Cycle 42	51.55	535.93	0.096	0.0424	12.6500	0.0423	13.0000	0.0072	3.9650	0.2387	92.51	99.61	2360.0	0.0	0.0	42.0	5.4	46.5	1.8

Cycle 43	47.15	550.58	0.086	0.0480	11.0800	0.0579	11.4800	0.0088	4.2190	0.2779	74.28	98.58	2410.0	97.6	262.0	57.2	6.4	56.2	2.4
Cycle 44	52.71	556.09	0.095	0.0466	11.3200	0.0508	11.6100	0.0079	3.9390	0.2424	79.61	98.97	2459.0	28.4	271.0	50.3	5.7	50.8	2.0
Cycle 45	52.30	575.41	0.091	0.0594	9.8520	0.0628	10.2000	0.0077	3.9810	0.2810	95.78	99.71	2509.0	580.8	214.0	61.9	6.1	49.3	2.0
Cycle 46	70.65	680.68	0.104	0.0524	10.1700	0.0520	10.5300	0.0072	3.7130	0.2717	61.08	97.50	2634.0	303.9	232.0	51.4	5.3	46.2	1.7
Cycle 47	80.57	739.11	0.109	0.0350	13.2800	0.0392	13.7700	0.0081	3.9340	0.2638	57.21	97.95	2683.0	0.0	0.0	39.0	5.3	52.2	2.1
Cycle 48	76.02	734.41	0.104	0.0519	9.8820	0.0529	10.2500	0.0074	3.6660	0.2774	81.44	98.83	2733.0	282.7	226.0	52.3	5.2	47.4	1.7
Cycle 49	85.24	771.28	0.111	0.0445	11.1600	0.0501	11.6600	0.0082	3.8890	0.2932	80.84	98.85	2782.0	0.0	0.0	49.6	5.6	52.4	2.0
Grain 8	51.99	383.39	0.136	0.0571	13.9900	0.0582	14.5800	0.0074	4.7690	0.2834	3.61	92.20	179.5	495.2	308.0	57.5	8.1	47.5	2.3
Cycle 2	48.91	361.17	0.135	0.0626	12.7100	0.0632	13.0900	0.0073	4.7340	0.2599	37.02	95.42	229.1	692.9	271.0	62.2	7.9	47.1	2.2
Cycle 3	56.95	381.17	0.149	0.0450	16.8300	0.0448	17.4100	0.0072	4.8640	0.2570	34.12	95.90	278.6	0.0	0.0	44.5	7.6	46.3	2.3
Cycle 4	63.93	380.98	0.168	0.0435	17.5500	0.0421	18.1200	0.0070	4.7960	0.2507	39.30	96.42	328.1	0.0	0.0	41.9	7.4	45.2	2.2
Cycle 5	51.35	376.43	0.136	0.0378	20.2600	0.0417	20.9900	0.0080	5.0130	0.2622	-5.44	93.16	377.6	0.0	0.0	41.5	8.5	51.4	2.6
Cycle 6	67.41	371.22	0.182	0.0483	17.0300	0.0522	17.7600	0.0078	5.0460	0.2829	26.06	94.78	427.2	112.1	402.0	51.7	9.0	50.4	2.5
Cycle 7	62.18	359.79	0.173	0.0604	13.0900	0.0702	13.5500	0.0084	4.8580	0.2727	82.85	98.87	476.8	618.4	283.0	68.9	9.0	54.1	2.6
Cycle 8	63.15	383.83	0.165	0.0548	13.7100	0.0622	14.1900	0.0082	4.8350	0.2683	39.74	96.30	526.3	403.8	307.0	61.3	8.4	52.9	2.6
Cycle 9	66.38	418.30	0.159	0.0412	17.6400	0.0439	18.3000	0.0077	4.7680	0.2659	66.25	97.91	575.8	0.0	0.0	43.6	7.8	49.6	2.4
Cycle 10	73.86	457.30	0.162	0.0466	14.3500	0.0549	14.8800	0.0086	4.6720	0.2670	74.60	98.61	625.4	26.1	344.0	54.3	7.9	54.9	2.6
Cycle 11	82.27	497.07	0.166	0.0507	13.9100	0.0513	14.4900	0.0073	4.3830	0.2802	100.00	100.00	674.9	225.2	322.0	50.8	7.2	47.2	2.1
Cycle 12	79.52	565.27	0.141	0.0475	13.0400	0.0552	13.5700	0.0084	4.5260	0.2823	92.49	99.57	724.4	76.3	310.0	54.6	7.2	54.1	2.4
Cycle 13	77.98	550.81	0.142	0.0509	12.2900	0.0591	12.8500	0.0084	4.3460	0.2954	82.90	98.85	773.9	234.6	284.0	58.3	7.3	54.1	2.3
Cycle 14	74.48	597.86	0.125	0.0513	11.4800	0.0639	12.0400	0.0090	4.4290	0.3071	87.88	99.23	823.4	255.7	264.0	62.9	7.3	57.9	2.6
Cycle 15	75.87	581.96	0.130	0.0316	18.4900	0.0352	19.1000	0.0081	4.1680	0.2528	52.03	97.26	873.0	0.0	0.0	35.1	6.6	51.8	2.2
Cycle 16	79.86	606.08	0.132	0.0435	12.3500	0.0520	12.8300	0.0087	4.1500	0.2751	74.12	98.64	997.8	0.0	0.0	51.4	6.4	55.7	2.3
Cycle 17	79.63	624.65	0.127	0.0460	11.8300	0.0554	12.3300	0.0087	4.1930	0.2858	69.21	98.29	1047.0	0.0	0.0	54.7	6.6	56.1	2.3
Cycle 18	81.34	617.79	0.132	0.0544	10.8400	0.0604	11.3200	0.0081	4.0740	0.2947	58.87	97.22	1097.0	388.5	243.0	59.6	6.6	51.7	2.1
Cycle 19	86.98	603.45	0.144	0.0401	13.6700	0.0474	14.2200	0.0086	4.0810	0.2757	59.22	97.69	1146.0	0.0	0.0	47.1	6.5	55.0	2.2
Cycle 20	93.25	678.29	0.137	0.0386	13.4600	0.0437	13.9400	0.0082	4.0110	0.2615	80.39	99.03	1196.0	0.0	0.0	43.4	5.9	52.7	2.1
Cycle 21	99.04	686.53	0.144	0.0602	9.8960	0.0658	10.2700	0.0079	3.9000	0.2849	100.00	100.00	1245.0	612.3	214.0	64.7	6.4	50.9	2.0
Cycle 22	93.08	709.39	0.131	0.0505	10.7800	0.0640	11.3300	0.0092	4.1790	0.3139	100.00	100.00	1295.0	216.5	250.0	63.0	6.9	59.0	2.5
Cycle 23	95.39	688.77	0.138	0.0421	12.4300	0.0468	12.9000	0.0081	3.9360	0.2685	100.00	100.00	1345.0	0.0	0.0	46.4	5.9	51.8	2.0
Cycle 24	93.77	677.38	0.138	0.0469	11.4600	0.0559	11.9700	0.0086	4.0370	0.2944	100.00	100.00	1394.0	46.0	274.0	55.3	6.4	55.5	2.2
Cycle 25	96.51	684.06	0.141	0.0356	14.3100	0.0409	14.8300	0.0083	4.0430	0.2625	100.00	100.00	1444.0	0.0	0.0	40.7	5.9	53.5	2.2
Cycle 26	104.93	705.83	0.149	0.0512	10.9400	0.0562	11.3400	0.0080	3.9020	0.2728	88.18	99.33	1493.0	249.7	252.0	55.6	6.1	51.2	2.0
Cycle 27	97.86	735.11	0.133	0.0560	10.1000	0.0675	10.6400	0.0087	4.0740	0.3210	69.12	97.84	1543.0	451.6	224.0	66.3	6.8	56.1	2.3
Cycle 28	100.86	744.10	0.136	0.0477	11.0700	0.0523	11.5200	0.0080	3.8060	0.2797	74.33	98.48	1592.0	83.2	263.0	51.8	5.8	51.1	1.9
Cycle 29	96.00	757.93	0.127	0.0542	10.1900	0.0586	10.6500	0.0078	3.8650	0.2971	72.91	98.18	1642.0	377.4	229.0	57.8	6.0	50.4	1.9
Cycle 30	97.98	751.12	0.130	0.0481	10.7500	0.0548	11.1800	0.0083	3.8750	0.2800	97.76	99.88	1691.0	105.3	254.0	54.1	5.9	53.0	2.0
Cycle 31	91.78	740.25	0.124	0.0487	10.8300	0.0531	11.2900	0.0079	3.8540	0.2880	80.42	98.79	1816.0	133.3	255.0	52.6	5.8	50.8	2.0
Cycle 32	85.62	746.42	0.115	0.0467	10.9500	0.0495	11.3700	0.0077	3.8180	0.2747	84.26	99.10	1866.0	31.3	262.0	49.0	5.4	49.4	1.9
Cycle 33	85.49	777.78	0.110	0.0457	11.0700	0.0554	11.6200	0.0088	4.0740	0.3054	100.00	100.00	1915.0	0.0	0.0	54.7	6.2	56.5	2.3
Cycle 34	93.97	762.77	0.123	0.0416	12.1700	0.0483	12.6900	0.0084	3.9290	0.2856	94.73	99.69	1965.0	0.0	0.0	47.9	5.9	54.2	2.1
Cycle 35	92.42	783.18	0.118	0.0513	10.2500	0.0576	10.7000	0.0081	3.9190	0.2947	85.33	99.10	2014.0	255.9	236.0	56.8	5.9	52.2	2.0
Cycle 36	84.00	709.98	0.118	0.0505	10.2400	0.0592	10.7000	0.0085	3.9040	0.2979	100.00	100.00	2064.0	218.3	237.0	58.4	6.1	54.6	2.1
Cycle 37	81.98	702.69	0.117	0.0443	11.2900	0.0500	11.7200	0.0082	3.9100	0.2770	100.00	100.00	2114.0	0.0	0.0	49.5	5.7	52.5	2.1
Cycle 38	92.65	737.49	0.126	0.0609	9.4210	0.0699	9.8950	0.0083	4.0040	0.3179	95.41	99.67	2163.0	634.6	203.0	68.6	6.6	53.5	2.1
Cycle 39	89.90	709.80	0.127	0.0491	11.1500	0.0520	11.6300	0.0077	3.8930	0.2885	80.44	98.74	2213.0	150.3	261.0	51.4	5.8	49.3	1.9
Cycle 40	87.37	688.92	0.127	0.0530	10.4400	0.0604	10.9400	0.0083	4.0100	0.3070	86.13	99.07	2262.0	329.9	237.0	59.6	6.3	53.1	2.1
Cycle 41	83.93	700.79	0.120	0.0468	11.3800	0.0497	11.8300	0.0077	3.8780	0.2791	100.00	100.00	2312.0	36.7	272.0	49.2	5.7	49.5	1.9
Cycle 42	86.98	681.28	0.128	0.0425	12.3300	0.0465	12.8300	0.0079	3.8910	0.2762	94.45	99.68	2361.0	0.0	0.0	46.1	5.8	50.9	2.0
Cycle 43	82.33	690.20	0.119	0.0468	11.2000	0.0539	11.6700	0.0083	4.0310	0.2867	83.48	99.06	2411.0	40.7	268.0	53.3	6.1	53.6	2.2
Cycle 44	85.77	701.82	0.122	0.0502	10.8900	0.0553	11.3500	0.0080	3.9870	0.2889	94.59	99.67	2461.0	203.5	253.0	54.7	6.0	51.3	2.0
Cycle 45	100.32	716.95	0.140	0.0500	11.0500	0.0550	11.4900	0.0080	3.9510	0.2802	77.83	98.71	2510.0	196.5	257.0	54.4	6.1	51.2	2.0

Cycle 46	97.85	679.52	0.144	0.0485	11.5500	0.0558	12.0100	0.0083	4.1650	0.2831	74.91	98.65	2635.0	122.2	272.0	55.1	6.5	53.6	2.2
Cycle 47	97.74	640.90	0.153	0.0518	11.3800	0.0547	11.7800	0.0077	4.0350	0.2673	81.31	98.96	2684.0	277.3	261.0	54.1	6.2	49.1	2.0
Cycle 48	94.04	659.33	0.143	0.0554	11.0000	0.0652	11.6400	0.0085	4.3510	0.3281	100.00	100.00	2734.0	430.1	245.0	64.2	7.2	54.8	2.4
Cycle 49	87.99	619.66	0.142	0.0512	11.1600	0.0572	11.6500	0.0081	4.0610	0.2925	100.00	100.00	2784.0	251.6	257.0	56.5	6.4	52.0	2.1
Grain 9	95.63	1020.83	0.094	0.0464	10.0100	0.0511	10.5000	0.0080	2.8860	0.3048	46.53	94.99	178.6	19.1	240.0	50.6	5.2	51.2	1.5
Cycle 2	102.01	1155.97	0.088	0.0541	7.3910	0.0588	7.8080	0.0079	2.7200	0.3232	39.78	94.72	228.2	373.1	166.0	58.1	4.4	50.7	1.4
Cycle 3	110.36	1160.14	0.095	0.0441	9.4310	0.0503	9.9030	0.0083	2.7980	0.3058	54.83	96.11	277.8	0.0	0.0	49.9	4.8	53.2	1.5
Cycle 4	104.24	1081.50	0.096	0.0519	7.4870	0.0594	7.9140	0.0083	2.7440	0.3248	28.73	94.06	327.3	278.8	171.0	58.6	4.5	53.3	1.5
Cycle 5	98.74	1037.52	0.095	0.0447	8.7120	0.0504	9.1410	0.0082	2.7540	0.3027	62.70	97.08	376.8	0.0	0.0	49.9	4.5	52.5	1.4
Cycle 6	98.82	1103.40	0.090	0.0442	8.5010	0.0499	8.9130	0.0082	2.7350	0.3004	57.97	96.84	426.3	0.0	0.0	49.4	4.3	52.6	1.4
Cycle 7	101.62	1088.62	0.093	0.0552	7.0070	0.0620	7.4030	0.0081	2.6920	0.3250	57.59	96.42	475.9	420.5	156.0	61.0	4.4	52.3	1.4
Cycle 8	98.05	1096.69	0.089	0.0534	7.0560	0.0615	7.4660	0.0084	2.7590	0.3292	37.57	94.98	525.5	344.7	160.0	60.6	4.4	53.6	1.5
Cycle 9	98.32	1088.97	0.090	0.0452	7.5530	0.0533	7.9210	0.0085	2.7400	0.3043	64.53	97.71	575.0	0.0	0.0	52.7	4.1	54.9	1.5
Cycle 10	97.82	1090.48	0.090	0.0511	7.1010	0.0612	7.5060	0.0087	2.7750	0.3269	71.63	97.87	624.5	247.1	163.0	60.3	4.4	55.7	1.5
Cycle 11	100.05	1104.37	0.091	0.0390	8.7690	0.0447	9.1460	0.0083	2.7210	0.2844	82.27	98.89	674.0	0.0	0.0	44.4	4.0	53.3	1.5
Cycle 12	108.60	1139.31	0.095	0.0483	7.5280	0.0561	7.9310	0.0084	2.7830	0.3165	61.71	97.25	723.5	112.3	178.0	55.5	4.3	54.2	1.5
Cycle 13	99.61	1115.49	0.089	0.0489	7.0300	0.0560	7.3790	0.0083	2.7030	0.3092	59.72	97.32	773.1	143.5	165.0	55.3	4.0	53.3	1.4
Cycle 14	100.62	1115.35	0.090	0.0511	6.9050	0.0570	7.2520	0.0081	2.6850	0.3113	61.31	97.29	822.7	244.9	159.0	56.2	4.0	51.9	1.4
Cycle 15	112.53	1135.08	0.099	0.0470	7.6550	0.0529	8.0380	0.0082	2.7250	0.3067	61.65	97.32	872.3	49.4	183.0	52.3	4.1	52.4	1.4
Cycle 16	95.54	1008.86	0.095	0.0518	7.1230	0.0603	7.5110	0.0084	2.8080	0.3214	66.46	97.57	997.7	275.5	163.0	59.5	4.3	54.2	1.5
Cycle 17	93.27	1006.67	0.093	0.0562	6.6110	0.0669	6.9770	0.0086	2.8260	0.3287	60.17	97.12	1047.0	460.8	147.0	65.7	4.4	55.4	1.6
Cycle 18	99.51	1017.88	0.098	0.0492	7.5080	0.0569	7.8900	0.0084	2.7740	0.3103	59.95	97.14	1097.0	159.5	176.0	56.2	4.3	53.8	1.5
Cycle 19	105.31	1053.09	0.100	0.0537	6.9940	0.0608	7.3500	0.0082	2.7690	0.3139	70.03	97.84	1146.0	356.8	158.0	59.9	4.3	52.8	1.5
Cycle 20	102.85	1047.13	0.098	0.0450	8.1410	0.0529	8.5510	0.0085	2.8780	0.3072	93.18	99.54	1196.0	0.0	0.0	52.3	4.4	54.7	1.6
Cycle 21	103.31	1036.10	0.100	0.0437	8.2760	0.0484	8.6390	0.0080	2.7280	0.2881	71.15	98.11	1246.0	0.0	0.0	48.0	4.1	51.6	1.4
Cycle 22	99.56	1039.86	0.096	0.0436	8.0270	0.0494	8.3790	0.0082	2.7660	0.2898	59.85	97.53	1295.0	0.0	0.0	49.0	4.0	52.7	1.5
Cycle 23	93.70	963.55	0.097	0.0517	7.2120	0.0588	7.5700	0.0083	2.7840	0.3095	64.63	97.51	1345.0	270.0	165.0	58.1	4.3	53.0	1.5
Cycle 24	100.93	982.51	0.103	0.0486	7.7570	0.0557	8.1480	0.0083	2.8140	0.3081	76.75	98.36	1394.0	126.2	183.0	55.0	4.4	53.4	1.5
Cycle 25	102.52	1021.30	0.100	0.0487	7.5390	0.0575	7.9250	0.0086	2.8670	0.3123	57.96	97.19	1444.0	132.1	177.0	56.8	4.4	55.0	1.6
Cycle 26	90.67	972.17	0.093	0.0512	7.5250	0.0592	7.9310	0.0084	2.8550	0.3188	74.52	98.07	1494.0	251.3	173.0	58.4	4.5	53.8	1.5
Cycle 27	98.57	978.32	0.101	0.0470	7.7600	0.0545	8.1320	0.0084	2.8180	0.3023	91.00	99.41	1543.0	49.8	185.0	53.9	4.3	54.0	1.5
Cycle 28	101.84	986.07	0.103	0.0487	7.5540	0.0562	7.9170	0.0084	2.8580	0.3044	85.58	99.08	1593.0	132.0	178.0	55.6	4.3	53.8	1.5
Cycle 29	105.91	990.87	0.107	0.0413	8.8940	0.0452	9.2640	0.0079	2.7890	0.2804	75.57	98.48	1642.0	-1.0	0.0	44.9	4.1	50.9	1.4
Cycle 30	98.30	1016.72	0.097	0.0454	8.1220	0.0499	8.4840	0.0080	2.8080	0.2919	87.68	99.20	1692.0	-1.0	0.0	49.5	4.1	51.2	1.4
Cycle 31	102.65	941.24	0.109	0.0541	7.0070	0.0611	7.3310	0.0082	2.7900	0.3039	70.81	98.05	1816.0	374.5	158.0	60.3	4.3	52.6	1.5
Cycle 32	99.17	943.11	0.105	0.0504	7.6450	0.0573	8.0330	0.0083	2.8690	0.3107	91.23	99.38	1866.0	211.1	177.0	56.6	4.4	53.0	1.5
Cycle 33	100.13	984.77	0.102	0.0572	6.8060	0.0664	7.1650	0.0084	2.8750	0.3224	89.22	99.22	1915.0	500.6	150.0	65.3	4.5	54.0	1.6
Cycle 34	97.81	979.34	0.100	0.0525	7.2070	0.0596	7.5650	0.0082	2.8370	0.3107	84.65	98.94	1965.0	305.5	164.0	58.8	4.3	52.9	1.5
Cycle 35	98.41	935.67	0.105	0.0444	8.4130	0.0509	8.8030	0.0083	2.9030	0.2961	84.96	99.04	2014.0	0.0	0.0	50.4	4.3	53.3	1.5
Cycle 36	96.56	951.90	0.101	0.0512	7.3870	0.0563	7.7230	0.0080	2.8120	0.2989	74.41	98.29	2064.0	250.8	170.0	55.7	4.2	51.2	1.4
Cycle 37	98.58	959.61	0.103	0.0448	8.0280	0.0495	8.3550	0.0080	2.8000	0.2823	78.99	98.76	2114.0	0.0	0.0	49.1	4.0	51.5	1.4
Cycle 38	94.04	969.27	0.097	0.0496	7.5520	0.0582	7.9430	0.0085	2.9360	0.3147	81.45	98.76	2163.0	175.9	176.0	57.5	4.4	54.6	1.6
Cycle 39	102.75	929.45	0.111	0.0465	7.9040	0.0514	8.2320	0.0080	2.8070	0.2852	79.16	98.75	2213.0	24.5	190.0	50.9	4.1	51.5	1.4
Cycle 40	98.60	920.93	0.107	0.0488	7.5070	0.0549	7.8330	0.0082	2.8040	0.2929	74.93	98.46	2262.0	137.3	176.0	54.3	4.1	52.4	1.5
Cycle 41	90.02	902.09	0.100	0.0402	9.0740	0.0450	9.4510	0.0081	2.8150	0.2801	70.76	98.19	2312.0	0.0	0.0	44.7	4.1	52.2	1.5
Cycle 42	95.02	934.41	0.102	0.0504	7.4790	0.0597	7.8580	0.0086	2.9420	0.3129	95.00	99.67	2361.0	212.3	173.0	58.9	4.5	55.2	1.6
Cycle 43	104.62	952.16	0.110	0.0522	7.3760	0.0575	7.7270	0.0080	2.8120	0.3040	75.00	98.27	2411.0	295.8	168.0	56.8	4.3	51.3	1.4
Cycle 44	93.90	929.63	0.101	0.0453	8.0300	0.0528	8.4110	0.0085	2.8830	0.3004	61.69	97.59	2460.0	0.0	0.0	52.3	4.3	54.3	1.6
Cycle 45	92.10	905.63	0.102	0.0381	8.9520	0.0453	9.3170	0.0086	2.8840	0.2787	86.20	99.27	2510.0	0.0	0.0	45.0	4.1	55.4	1.6
Cycle 46	89.98	877.25	0.103	0.0480	7.7680	0.0535	8.1190	0.0081	2.8250	0.2954	73.72	98.30	2635.0	100.1	184.0	52.9	4.2	51.9	1.5
Cycle 47	100.25	927.17	0.108	0.0505	7.5570	0.0545	7.8940	0.0078	2.8090	0.2954	78.41	98.58	2685.0	216.0	175.0	53.9	4.1	50.3	1.4
Cycle 48	92.71	919.62	0.101	0.0521	7.4200	0.0578	7.7800	0.0081	2.8610	0.3068	79.82	98.59	2734.0	290.1	170.0	57.1	4.3	51.7	1.5

Cycle 49	99.71	905.35	0.110	0.0502	7.6490	0.0548	7.9970	0.0079	2.8020	0.2966	83.06	98.85	2784.0	205.9	177.0	54.1	4.2	50.8	1.4
Grain 10	58.44	1215.33	0.048	0.0400	11.0600	0.0405	11.5100	0.0073	2.9420	0.2756	53.76	96.19	179.6	0.0	0.0	40.3	4.6	47.1	1.4
Cycle 2	60.44	1131.47	0.053	0.0396	10.8500	0.0379	11.2600	0.0069	2.9690	0.2678	59.71	96.99	229.1	0.0	0.0	37.8	4.2	44.6	1.3
Cycle 3	73.36	1183.12	0.062	0.0463	8.8750	0.0475	9.2810	0.0074	3.0810	0.2950	58.42	96.98	278.6	14.1	213.0	47.1	4.3	47.8	1.5
Cycle 4	68.29	1102.85	0.062	0.0494	8.8860	0.0507	9.3170	0.0074	3.1070	0.3022	63.92	97.10	328.1	167.0	208.0	50.2	4.6	47.8	1.5
Cycle 5	74.41	1101.83	0.068	0.0500	8.3080	0.0546	8.7250	0.0079	3.1750	0.3100	73.77	98.09	377.6	194.1	193.0	54.0	4.6	50.9	1.6
Cycle 6	75.58	1055.08	0.072	0.0521	8.5480	0.0538	8.9720	0.0075	3.1540	0.3071	84.65	98.78	427.2	287.7	195.0	53.2	4.7	48.2	1.5
Cycle 7	79.41	1104.14	0.072	0.0462	8.7680	0.0524	9.1970	0.0082	3.2910	0.3064	63.76	97.62	476.8	9.1	211.0	51.9	4.7	52.8	1.7
Cycle 8	76.95	1068.02	0.072	0.0502	8.8030	0.0528	9.2300	0.0076	3.2530	0.3046	75.00	98.14	526.3	201.7	204.0	52.2	4.7	49.0	1.6
Cycle 9	67.97	1067.47	0.064	0.0376	10.3900	0.0404	10.7900	0.0078	3.2370	0.2690	92.53	99.57	575.8	0.0	0.0	40.3	4.3	50.1	1.6
Cycle 10	79.49	982.57	0.081	0.0556	7.9670	0.0636	8.3920	0.0083	3.3660	0.3234	79.67	98.53	625.4	435.1	177.0	62.6	5.1	53.3	1.8
Cycle 11	67.41	969.44	0.070	0.0573	7.8630	0.0592	8.2220	0.0075	3.2210	0.3049	85.62	98.91	675.0	504.2	173.0	58.4	4.7	48.1	1.5
Cycle 12	68.88	1037.39	0.066	0.0378	10.0800	0.0417	10.4600	0.0080	3.3080	0.2710	68.40	98.31	724.6	0.0	0.0	41.5	4.3	51.3	1.7
Cycle 13	63.70	1051.15	0.061	0.0390	9.6140	0.0453	10.0100	0.0084	3.4070	0.2837	76.32	98.75	774.1	0.0	0.0	45.0	4.4	54.1	1.8
Cycle 14	62.30	986.18	0.063	0.0474	8.8380	0.0507	9.2280	0.0078	3.2780	0.2942	93.35	99.56	823.6	67.7	210.0	50.2	4.5	49.9	1.6
Cycle 15	57.44	964.99	0.060	0.0467	8.6470	0.0506	9.0120	0.0079	3.3120	0.2917	70.67	98.20	873.2	34.4	207.0	50.2	4.4	50.5	1.7
Cycle 16	52.76	985.82	0.054	0.0432	9.1790	0.0476	9.5700	0.0080	3.3680	0.2897	49.23	96.96	998.0	0.0	0.0	47.2	4.4	51.4	1.7
Cycle 17	52.96	1007.99	0.053	0.0521	8.1200	0.0561	8.4900	0.0078	3.3130	0.3044	47.07	96.34	1048.0	290.9	185.0	55.4	4.6	50.1	1.7
Cycle 18	52.30	1033.46	0.051	0.0440	8.9480	0.0506	9.3580	0.0083	3.4880	0.3014	70.03	98.25	1097.0	0.0	0.0	50.1	4.6	53.5	1.9
Cycle 19	51.45	1010.80	0.051	0.0466	8.3580	0.0509	8.6880	0.0079	3.2630	0.2870	71.68	98.33	1147.0	30.5	200.0	50.4	4.3	50.8	1.7
Cycle 20	50.61	1038.52	0.049	0.0443	8.7080	0.0525	9.1140	0.0086	3.4250	0.3039	75.42	98.54	1196.0	0.0	0.0	51.9	4.6	55.1	1.9
Cycle 21	47.87	973.02	0.049	0.0403	9.5200	0.0435	9.8670	0.0078	3.3590	0.2716	74.90	98.64	1246.0	0.0	0.0	43.2	4.2	50.2	1.7
Cycle 22	46.62	878.05	0.053	0.0470	9.2970	0.0521	9.7310	0.0080	3.5260	0.3014	50.21	96.65	1295.0	51.0	222.0	51.6	4.9	51.6	1.8
Cycle 23	44.22	856.82	0.052	0.0424	9.3900	0.0458	9.6920	0.0078	3.4260	0.2637	31.54	96.44	1345.0	0.0	0.0	45.5	4.3	50.3	1.7
Cycle 24	43.38	870.13	0.050	0.0448	9.6710	0.0507	10.0900	0.0082	3.6150	0.2938	100.00	100.00	1394.0	0.0	0.0	50.2	4.9	52.7	1.9
Cycle 25	46.99	820.75	0.057	0.0445	9.8340	0.0465	10.1800	0.0076	3.4770	0.2699	91.09	99.46	1444.0	0.0	0.0	46.2	4.6	48.6	1.7
Cycle 26	47.86	814.85	0.059	0.0546	8.6220	0.0618	9.0100	0.0082	3.5940	0.3052	78.28	98.48	1494.0	396.1	193.0	60.9	5.3	52.7	1.9
Cycle 27	49.55	802.72	0.062	0.0370	11.4500	0.0393	11.8200	0.0077	3.5830	0.2533	100.00	100.00	1543.0	0.0	0.0	39.1	4.5	49.5	1.8
Cycle 28	50.78	761.85	0.067	0.0481	9.5120	0.0515	9.8280	0.0078	3.5590	0.2684	90.32	99.43	1593.0	103.7	225.0	51.0	4.9	49.9	1.8
Cycle 29	49.47	770.84	0.064	0.0469	9.9420	0.0491	10.3000	0.0076	3.5650	0.2720	74.01	98.36	1642.0	42.3	238.0	48.6	4.9	48.8	1.7
Cycle 30	53.75	789.19	0.068	0.0630	8.5030	0.0711	8.9300	0.0082	3.8250	0.3232	100.00	100.00	1692.0	709.2	181.0	69.8	6.0	52.5	2.0
Cycle 31	51.09	689.36	0.074	0.0494	10.2700	0.0487	10.6400	0.0072	3.5550	0.2695	100.00	100.00	1817.0	165.5	240.0	48.3	5.0	45.9	1.6
Cycle 32	55.81	679.84	0.082	0.0418	11.0100	0.0471	11.3800	0.0082	3.7250	0.2614	82.88	99.09	1866.0	0.0	0.0	46.7	5.2	52.4	1.9
Cycle 33	54.11	698.25	0.077	0.0442	11.2300	0.0464	11.6300	0.0076	3.7990	0.2683	48.50	96.89	1916.0	0.0	0.0	46.0	5.2	48.9	1.9
Cycle 34	55.37	672.31	0.082	0.0500	10.1600	0.0538	10.5200	0.0078	3.7650	0.2732	80.15	98.76	1966.0	195.0	236.0	53.2	5.5	50.1	1.9
Cycle 35	54.94	665.83	0.083	0.0375	13.2200	0.0384	13.6500	0.0074	3.7650	0.2518	77.83	98.73	2015.0	0.0	0.0	38.3	5.1	47.8	1.8
Cycle 36	62.67	676.17	0.093	0.0546	9.7600	0.0598	10.1100	0.0079	3.8380	0.2796	74.84	98.41	2065.0	395.3	219.0	58.9	5.8	51.0	2.0
Cycle 37	55.26	646.81	0.085	0.0552	9.7530	0.0628	10.1500	0.0082	3.9790	0.2949	65.80	97.75	2114.0	421.7	218.0	61.8	6.1	52.9	2.1
Cycle 38	53.25	635.51	0.084	0.0408	11.9400	0.0415	12.3100	0.0074	3.6850	0.2470	77.30	98.74	2164.0	0.0	0.0	41.3	5.0	47.4	1.7
Cycle 39	58.73	640.46	0.092	0.0422	11.8000	0.0486	12.2400	0.0084	4.0350	0.2709	75.51	98.69	2213.0	0.0	0.0	48.2	5.8	53.7	2.2
Cycle 40	62.45	629.85	0.099	0.0568	9.7340	0.0671	10.1400	0.0086	4.0080	0.2967	85.36	99.04	2263.0	483.8	215.0	66.0	6.5	55.0	2.2
Cycle 41	61.06	590.85	0.103	0.0483	11.1300	0.0486	11.4700	0.0073	3.7660	0.2528	94.12	99.65	2312.0	111.8	263.0	48.1	5.4	46.9	1.8
Cycle 42	59.08	616.48	0.096	0.0500	10.9100	0.0569	11.3600	0.0083	4.0970	0.2892	72.66	98.27	2362.0	194.5	254.0	56.2	6.2	53.0	2.2
Cycle 43	55.94	619.63	0.090	0.0415	12.4500	0.0457	12.8900	0.0080	4.0880	0.2649	48.73	97.19	2411.0	0.0	0.0	45.3	5.7	51.2	2.1
Cycle 44	60.77	601.91	0.101	0.0573	10.0800	0.0630	10.4700	0.0080	4.0190	0.2868	58.78	97.21	2461.0	502.0	222.0	62.0	6.3	51.2	2.1
Cycle 45	64.08	630.53	0.102	0.0502	10.8900	0.0563	11.3000	0.0081	4.0330	0.2784	54.80	97.25	2510.0	205.3	253.0	55.6	6.1	52.2	2.1
Cycle 46	65.66	599.85	0.109	0.0461	11.6500	0.0509	12.1000	0.0080	3.9770	0.2756	49.68	96.97	2635.0	2.4	281.0	50.4	6.0	51.4	2.0
Cycle 47	65.46	611.42	0.107	0.0474	11.3800	0.0519	11.8300	0.0079	3.9680	0.2790	35.29	96.00	2685.0	68.2	271.0	51.4	5.9	51.0	2.0
Cycle 48	85.30	644.60	0.132	0.0576	10.2500	0.0612	10.6400	0.0077	3.9440	0.2827	32.54	95.57	2734.0	514.2	225.0	60.3	6.2	49.5	1.9
Cycle 49	71.98	653.73	0.110	0.0478	11.2800	0.0515	11.7400	0.0078	3.9370	0.2809	27.15	95.44	2784.0	91.1	267.0	50.9	5.8	50.1	2.0
Grain 11	156.25	1458.84	0.107	0.0475	7.6830	0.0496	8.0850	0.0076	2.7200	0.3123	75.60	98.24	178.6	74.2	183.0	49.1	3.9	48.6	1.3
Cycle 2	158.22	1433.77	0.110	0.0552	6.5950	0.0611	6.9910	0.0080	2.7500	0.3364	73.21	98.03	228.1	420.7	147.0	60.2	4.1	51.5	1.4

Cycle 3	158.17	1423.11	0.111	0.0481	7.0920	0.0537	7.4690	0.0081	2.7290	0.3172	73.57	98.32	277.7	105.1	168.0	53.1	3.9	52.0	1.4
Cycle 4	158.65	1496.30	0.106	0.0390	8.1930	0.0428	8.5690	0.0080	2.7420	0.2942	62.68	97.95	327.2	0.0	0.0	42.5	3.6	51.1	1.4
Cycle 5	178.02	1571.50	0.113	0.0469	7.0830	0.0494	7.4250	0.0076	2.6320	0.3043	69.09	98.12	376.6	45.3	169.0	49.0	3.6	49.1	1.3
Cycle 6	166.09	1555.75	0.107	0.0464	7.0810	0.0513	7.4580	0.0080	2.7150	0.3176	73.63	98.38	426.1	19.5	170.0	50.8	3.7	51.5	1.4
Cycle 7	170.84	1495.51	0.114	0.0476	6.9690	0.0525	7.3180	0.0080	2.6950	0.3105	72.31	98.37	475.6	79.1	166.0	51.9	3.7	51.3	1.4
Cycle 8	162.66	1545.52	0.105	0.0552	6.3490	0.0609	6.7190	0.0080	2.7410	0.3350	94.40	99.62	525.1	418.2	142.0	60.1	3.9	51.5	1.4
Cycle 9	165.20	1480.38	0.112	0.0512	6.7310	0.0558	7.0890	0.0079	2.6980	0.3197	100.00	100.00	574.7	251.2	155.0	55.2	3.8	50.7	1.4
Cycle 10	158.85	1479.92	0.107	0.0498	6.7020	0.0593	7.0850	0.0086	2.8380	0.3317	95.46	99.73	624.2	185.8	156.0	58.5	4.0	55.4	1.6
Cycle 11	157.84	1502.28	0.105	0.0499	6.8540	0.0571	7.2520	0.0083	2.8210	0.3317	81.52	98.82	673.8	190.9	159.0	56.3	4.0	53.2	1.5
Cycle 12	164.36	1515.30	0.108	0.0480	6.9870	0.0517	7.3150	0.0078	2.7300	0.3040	76.72	98.69	723.3	97.2	165.0	51.1	3.7	50.2	1.4
Cycle 13	144.12	1402.47	0.103	0.0393	8.1060	0.0429	8.4600	0.0079	2.7050	0.2880	87.95	99.35	772.8	0.0	0.0	42.7	3.5	50.9	1.4
Cycle 14	146.23	1413.42	0.103	0.0477	7.0160	0.0551	7.4060	0.0084	2.8090	0.3250	83.08	98.96	822.4	84.4	166.0	54.4	3.9	53.8	1.5
Cycle 15	160.89	1478.99	0.109	0.0481	7.0960	0.0535	7.4830	0.0081	2.7500	0.3207	84.77	99.02	871.8	105.6	168.0	52.9	3.9	51.7	1.4
Cycle 16	157.77	1457.35	0.108	0.0484	6.8520	0.0576	7.2540	0.0086	2.8420	0.3334	93.71	99.63	996.2	116.6	162.0	56.9	4.0	55.5	1.6
Cycle 17	161.05	1471.11	0.109	0.0448	7.1460	0.0510	7.5130	0.0083	2.7880	0.3140	97.56	99.87	1046.0	0.0	0.0	50.5	3.7	53.0	1.5
Cycle 18	166.22	1510.27	0.110	0.0488	6.8060	0.0536	7.1580	0.0080	2.7250	0.3162	91.38	99.49	1095.0	136.6	160.0	53.0	3.7	51.1	1.4
Cycle 19	167.86	1513.15	0.111	0.0459	7.0620	0.0500	7.4130	0.0079	2.6880	0.3086	91.32	99.50	1145.0	0.0	0.0	49.6	3.6	50.8	1.4
Cycle 20	168.31	1505.66	0.112	0.0511	6.5490	0.0584	6.9360	0.0083	2.7880	0.3360	91.87	99.50	1194.0	244.1	151.0	57.6	3.9	53.2	1.5
Cycle 21	168.37	1520.19	0.111	0.0435	7.1690	0.0500	7.5260	0.0083	2.7480	0.3094	85.65	99.26	1244.0	0.0	0.0	49.6	3.6	53.5	1.5
Cycle 22	172.89	1522.45	0.114	0.0518	6.4250	0.0573	6.7750	0.0080	2.6630	0.3245	78.72	98.68	1293.0	277.1	147.0	56.5	3.7	51.5	1.4
Cycle 23	173.73	1568.54	0.111	0.0509	6.4400	0.0577	6.8040	0.0082	2.7360	0.3306	85.77	99.16	1343.0	237.9	149.0	57.0	3.8	52.7	1.4
Cycle 24	208.66	1713.19	0.122	0.0484	6.7450	0.0541	7.1320	0.0081	2.7060	0.3289	84.08	99.04	1392.0	118.2	159.0	53.5	3.7	52.1	1.4
Cycle 25	209.04	1769.82	0.118	0.0444	7.0410	0.0492	7.4280	0.0080	2.6740	0.3208	66.89	98.08	1442.0	0.0	0.0	48.7	3.5	51.5	1.4
Cycle 26	215.32	1729.44	0.125	0.0502	6.3760	0.0588	6.8010	0.0085	2.7380	0.3517	87.71	99.24	1491.0	202.8	148.0	58.0	3.8	54.6	1.5
Cycle 27	220.82	1747.08	0.126	0.0438	6.8580	0.0490	7.2140	0.0081	2.6010	0.3138	93.98	99.68	1541.0	0.0	0.0	48.6	3.4	52.1	1.4
Cycle 28	246.59	1900.85	0.130	0.0438	6.9080	0.0500	7.3180	0.0083	2.6770	0.3317	98.05	99.89	1590.0	0.0	0.0	49.6	3.5	53.2	1.4
Cycle 29	252.14	1834.84	0.137	0.0530	5.9990	0.0581	6.3670	0.0080	2.5740	0.3411	93.20	99.59	1640.0	328.1	136.0	57.4	3.6	51.1	1.3
Cycle 30	258.64	1942.63	0.133	0.0435	6.7820	0.0489	7.1780	0.0081	2.6020	0.3291	92.04	99.56	1689.0	0.0	0.0	48.4	3.4	52.3	1.4
Cycle 31	245.53	1888.66	0.130	0.0523	5.8950	0.0594	6.3030	0.0082	2.6120	0.3584	87.39	99.21	1814.0	297.2	135.0	58.6	3.6	52.9	1.4
Cycle 32	234.67	1894.07	0.124	0.0466	6.3070	0.0532	6.7100	0.0083	2.6050	0.3442	84.85	99.12	1863.0	30.0	151.0	52.7	3.4	53.2	1.4
Cycle 33	260.07	1943.03	0.134	0.0448	6.6900	0.0482	7.0630	0.0078	2.5590	0.3230	79.97	98.88	1913.0	0.0	0.0	47.8	3.3	50.1	1.3
Cycle 34	229.45	1898.24	0.121	0.0476	6.2720	0.0528	6.6360	0.0080	2.5770	0.3319	85.55	99.19	1962.0	79.6	149.0	52.2	3.4	51.6	1.3
Cycle 35	239.08	1935.90	0.124	0.0446	6.5330	0.0514	6.9050	0.0084	2.6140	0.3278	82.52	99.09	2012.0	0.0	0.0	50.9	3.4	53.6	1.4
Cycle 36	228.45	1891.96	0.121	0.0463	6.5590	0.0501	6.9270	0.0079	2.5710	0.3249	83.99	99.07	2061.0	11.7	158.0	49.7	3.4	50.5	1.3
Cycle 37	205.31	1765.98	0.116	0.0478	6.4670	0.0541	6.8810	0.0082	2.7000	0.3449	98.15	99.89	2111.0	88.8	153.0	53.5	3.6	52.7	1.4
Cycle 38	201.30	1724.48	0.117	0.0503	6.2980	0.0555	6.6930	0.0080	2.6500	0.3427	89.53	99.34	2160.0	208.2	146.0	54.8	3.6	51.4	1.4
Cycle 39	209.16	1746.64	0.120	0.0475	6.6120	0.0514	6.9940	0.0079	2.6130	0.3290	84.21	99.03	2210.0	73.1	157.0	50.9	3.5	50.5	1.3
Cycle 40	203.20	1819.28	0.112	0.0475	6.4640	0.0523	6.8250	0.0080	2.6380	0.3265	97.97	99.88	2259.0	75.9	154.0	51.7	3.4	51.2	1.4
Cycle 41	211.81	1759.24	0.120	0.0442	6.9160	0.0490	7.3040	0.0080	2.6490	0.3239	94.36	99.68	2309.0	0.0	0.0	48.5	3.5	51.6	1.4
Cycle 42	203.82	1759.67	0.116	0.0505	6.2560	0.0558	6.6340	0.0080	2.6450	0.3382	96.25	99.77	2358.0	218.1	145.0	55.1	3.6	51.4	1.4
Cycle 43	196.95	1716.71	0.115	0.0427	7.0580	0.0469	7.4340	0.0080	2.6590	0.3166	83.67	99.11	2408.0	0.0	0.0	46.5	3.4	51.2	1.4
Cycle 44	201.88	1687.76	0.120	0.0432	7.1610	0.0482	7.5610	0.0081	2.6820	0.3228	84.63	99.11	2457.0	0.0	0.0	47.8	3.5	52.0	1.4
Cycle 45	194.10	1750.96	0.111	0.0491	6.3440	0.0539	6.7120	0.0080	2.6510	0.3324	85.66	99.16	2507.0	151.0	149.0	53.3	3.5	51.1	1.4
Cycle 46	169.92	1589.95	0.107	0.0459	6.8560	0.0480	7.2180	0.0076	2.6560	0.3169	91.96	99.53	2631.0	0.0	0.0	47.6	3.4	48.7	1.3
Cycle 47	168.29	1552.51	0.108	0.0437	7.1210	0.0479	7.5030	0.0080	2.7310	0.3183	91.48	99.53	2681.0	0.0	0.0	47.5	3.5	51.1	1.4
Cycle 48	178.98	1565.73	0.114	0.0460	6.9140	0.0510	7.2920	0.0080	2.7370	0.3222	89.28	99.40	2730.0	0.0	0.0	50.5	3.6	51.7	1.4
Cycle 49	170.69	1558.18	0.110	0.0504	6.5970	0.0555	6.9890	0.0080	2.7180	0.3346	87.09	99.16	2780.0	214.9	153.0	54.9	3.7	51.3	1.4
Grain 12	132.58	1429.29	0.093	0.0412	8.3170	0.0424	8.6720	0.0075	2.7210	0.2845	50.87	97.02	178.5	0.0	0.0	42.1	3.6	47.9	1.3
Cycle 2	138.42	1407.10	0.098	0.0552	6.5190	0.0648	6.9340	0.0085	2.8730	0.3473	64.14	97.46	228.0	421.0	146.0	63.8	4.3	54.7	1.6
Cycle 3	136.38	1405.22	0.097	0.0422	7.7790	0.0459	8.1340	0.0079	2.7200	0.2946	81.29	98.91	277.5	0.0	0.0	45.6	3.6	50.7	1.4
Cycle 4	144.96	1455.56	0.100	0.0562	6.3820	0.0616	6.7400	0.0079	2.7150	0.3298	64.91	97.49	327.0	458.8	142.0	60.7	4.0	51.0	1.4
Cycle 5	154.67	1513.12	0.102	0.0447	7.3440	0.0492	7.7050	0.0080	2.7370	0.3066	59.90	97.65	376.6	0.0	0.0	48.8	3.7	51.2	1.4

Cycle 6	156.33	1494.87	0.105	0.0476	7.0160	0.0529	7.4020	0.0081	2.7360	0.3222	62.80	97.63	426.2	78.1	167.0	52.3	3.8	51.8	1.4
Cycle 7	161.62	1552.40	0.104	0.0489	6.7250	0.0546	7.0940	0.0081	2.7260	0.3241	87.71	99.24	475.7	144.9	158.0	54.0	3.7	52.0	1.4
Cycle 8	178.52	1594.88	0.112	0.0417	7.4780	0.0458	7.8350	0.0080	2.6560	0.3009	78.39	98.81	525.3	0.0	0.0	45.5	3.5	51.2	1.4
Cycle 9	182.83	1578.51	0.116	0.0535	6.4690	0.0585	6.8520	0.0079	2.6870	0.3347	92.87	99.51	574.8	350.4	146.0	57.7	3.8	50.9	1.4
Cycle 10	172.75	1496.26	0.115	0.0397	7.9530	0.0454	8.3280	0.0083	2.7300	0.2981	90.72	99.50	624.4	0.0	0.0	45.1	3.7	53.2	1.4
Cycle 11	161.43	1487.51	0.109	0.0442	7.3430	0.0489	7.6870	0.0080	2.6400	0.2990	89.26	99.37	673.9	0.0	0.0	48.5	3.6	51.5	1.4
Cycle 12	154.15	1391.65	0.111	0.0539	6.4740	0.0609	6.8080	0.0082	2.7410	0.3201	80.78	98.82	723.4	367.1	146.0	60.1	4.0	52.6	1.4
Cycle 13	151.52	1407.82	0.108	0.0532	6.6960	0.0598	7.0890	0.0082	2.7930	0.3336	78.78	98.54	772.9	336.7	152.0	59.0	4.1	52.4	1.5
Cycle 14	150.99	1430.60	0.106	0.0463	7.1590	0.0530	7.5230	0.0083	2.7970	0.3130	83.96	99.08	822.4	13.8	172.0	52.4	3.9	53.3	1.5
Cycle 15	158.23	1412.58	0.112	0.0492	6.8280	0.0552	7.1790	0.0081	2.7030	0.3149	92.50	99.54	872.0	158.6	160.0	54.5	3.8	52.2	1.4
Cycle 16	175.50	1585.96	0.111	0.0437	7.2700	0.0487	7.6560	0.0081	2.6980	0.3157	97.90	99.88	996.7	0.0	0.0	48.3	3.6	51.9	1.4
Cycle 17	213.81	1630.47	0.131	0.0448	7.0940	0.0502	7.4630	0.0081	2.6630	0.3138	93.83	99.66	1046.0	0.0	0.0	49.8	3.6	52.3	1.4
Cycle 18	213.85	1717.74	0.124	0.0534	6.1400	0.0589	6.4990	0.0080	2.5930	0.3341	92.75	99.54	1096.0	343.5	139.0	58.1	3.7	51.4	1.3
Cycle 19	235.65	1821.26	0.129	0.0420	7.3150	0.0485	7.7210	0.0084	2.6990	0.3213	74.47	98.58	1145.0	0.0	0.0	48.1	3.6	53.7	1.4
Cycle 20	215.66	1748.49	0.123	0.0494	6.4410	0.0548	6.7960	0.0080	2.6330	0.3250	88.14	99.32	1195.0	167.3	150.0	54.1	3.6	51.6	1.4
Cycle 21	206.75	1693.72	0.122	0.0488	6.5530	0.0550	6.9320	0.0082	2.6700	0.3307	81.16	98.87	1244.0	140.3	154.0	54.4	3.7	52.5	1.4
Cycle 22	198.97	1658.50	0.120	0.0441	7.1280	0.0494	7.4910	0.0081	2.6710	0.3107	89.28	99.41	1294.0	0.0	0.0	49.0	3.6	52.1	1.4
Cycle 23	185.28	1576.06	0.118	0.0499	6.6300	0.0571	7.0010	0.0083	2.7060	0.3268	84.19	99.04	1344.0	188.5	154.0	56.4	3.8	53.3	1.4
Cycle 24	174.57	1425.07	0.122	0.0474	7.0820	0.0535	7.4430	0.0082	2.7260	0.3124	84.82	99.12	1393.0	68.2	169.0	52.9	3.8	52.6	1.4
Cycle 25	169.58	1365.59	0.124	0.0510	6.7910	0.0583	7.1410	0.0083	2.7550	0.3169	93.48	99.62	1443.0	242.1	156.0	57.6	4.0	53.2	1.5
Cycle 26	165.36	1321.13	0.125	0.0494	7.1530	0.0540	7.4890	0.0079	2.7380	0.3027	95.15	99.71	1492.0	164.9	167.0	53.4	3.9	50.9	1.4
Cycle 27	156.46	1305.67	0.120	0.0507	7.0990	0.0576	7.4630	0.0082	2.8310	0.3150	83.99	99.02	1542.0	227.6	164.0	56.9	4.1	52.9	1.5
Cycle 28	146.32	1281.82	0.114	0.0397	8.5980	0.0439	8.9590	0.0080	2.7980	0.2826	89.37	99.42	1591.0	0.0	0.0	43.7	3.8	51.6	1.4
Cycle 29	144.70	1190.71	0.122	0.0525	7.0160	0.0585	7.3370	0.0081	2.7640	0.3020	90.65	99.42	1641.0	307.3	160.0	57.7	4.1	51.9	1.4
Cycle 30	131.57	1116.10	0.118	0.0512	7.2780	0.0565	7.5970	0.0080	2.8260	0.2965	89.80	99.39	1690.0	248.2	168.0	55.8	4.1	51.5	1.5
Cycle 31	121.41	1076.96	0.113	0.0578	6.9760	0.0628	7.2780	0.0079	2.8950	0.3010	89.87	99.34	1815.0	522.9	153.0	61.8	4.4	50.6	1.5
Cycle 32	129.79	1058.44	0.123	0.0520	7.4990	0.0583	7.8280	0.0081	2.9000	0.2965	89.37	99.35	1864.0	283.4	172.0	57.5	4.4	52.3	1.5
Cycle 33	128.61	1036.20	0.124	0.0451	8.2050	0.0521	8.5120	0.0084	2.9040	0.2744	87.24	99.35	1914.0	0.0	0.0	51.6	4.3	53.8	1.6
Cycle 34	115.91	995.29	0.116	0.0470	8.4210	0.0534	8.8150	0.0082	3.0400	0.2992	91.77	99.49	1963.0	48.3	201.0	52.8	4.5	52.9	1.6
Cycle 35	107.16	1002.89	0.107	0.0532	7.6690	0.0567	8.0040	0.0077	2.9660	0.2959	100.00	100.00	2013.0	335.0	174.0	56.0	4.4	49.7	1.5
Cycle 36	111.60	954.80	0.117	0.0476	8.2340	0.0544	8.5750	0.0083	3.0610	0.2879	100.00	100.00	2062.0	81.6	195.0	53.8	4.5	53.1	1.6
Cycle 37	111.33	936.04	0.119	0.0455	8.6260	0.0504	8.9870	0.0080	3.0030	0.2849	93.69	99.63	2112.0	0.0	0.0	50.0	4.4	51.7	1.6
Cycle 38	112.55	954.87	0.118	0.0478	8.2500	0.0534	8.5700	0.0081	2.9980	0.2798	81.14	98.94	2161.0	89.9	196.0	52.8	4.4	52.0	1.6
Cycle 39	102.03	926.49	0.110	0.0424	8.9960	0.0469	9.3420	0.0080	3.0190	0.2741	96.52	99.81	2211.0	0.0	0.0	46.6	4.3	51.5	1.6
Cycle 40	112.18	915.40	0.123	0.0471	8.5630	0.0543	8.9150	0.0084	3.1380	0.2860	79.15	98.86	2260.0	52.6	204.0	53.7	4.7	53.7	1.7
Cycle 41	109.19	926.62	0.118	0.0504	8.3110	0.0565	8.6080	0.0081	3.1410	0.2756	63.94	98.07	2310.0	215.3	192.0	55.8	4.7	52.2	1.6
Cycle 42	106.10	841.85	0.126	0.0572	7.7150	0.0637	8.0620	0.0081	3.0470	0.3006	91.96	99.44	2359.0	498.0	170.0	62.7	4.9	51.9	1.6
Cycle 43	100.17	870.38	0.115	0.0538	8.0740	0.0591	8.3900	0.0080	3.1440	0.2860	89.71	99.37	2409.0	362.7	182.0	58.3	4.8	51.1	1.6
Cycle 44	104.59	848.59	0.123	0.0525	8.2890	0.0578	8.6000	0.0080	3.1280	0.2797	69.77	98.21	2458.0	307.2	189.0	57.1	4.8	51.3	1.6
Cycle 45	96.08	805.71	0.119	0.0418	10.0400	0.0434	10.4100	0.0075	3.1060	0.2648	98.49	99.91	2508.0	0.0	0.0	43.2	4.4	48.3	1.5
Cycle 46	95.27	804.20	0.118	0.0462	9.3980	0.0492	9.7520	0.0077	3.1730	0.2722	81.74	98.92	2632.0	7.9	226.0	48.8	4.6	49.6	1.6
Cycle 47	102.59	783.55	0.131	0.0537	8.6530	0.0579	8.9900	0.0078	3.2320	0.2821	75.46	98.46	2682.0	356.8	195.0	57.1	5.0	50.2	1.6
Cycle 48	91.38	729.97	0.125	0.0535	8.7550	0.0557	9.0860	0.0075	3.1870	0.2773	82.66	98.86	2731.0	350.0	198.0	55.0	4.9	48.5	1.5
Cycle 49	95.23	763.18	0.125	0.0490	9.1970	0.0513	9.4830	0.0076	3.1900	0.2565	67.14	98.19	2781.0	148.3	216.0	50.7	4.7	48.7	1.6
Grain 13	85.54	1078.70	0.079	0.0498	7.4000	0.0535	7.7660	0.0078	2.8080	0.3078	64.23	97.46	178.7	186.3	172.0	52.9	4.0	50.0	1.4
Cycle 2	85.48	998.25	0.086	0.0467	8.0780	0.0493	8.4410	0.0077	2.8040	0.2928	81.90	98.75	228.2	32.3	194.0	48.8	4.0	49.2	1.4
Cycle 3	94.38	1028.13	0.092	0.0439	8.0440	0.0474	8.3610	0.0078	2.8390	0.2793	77.49	98.73	277.7	0.0	0.0	47.0	3.8	50.3	1.4
Cycle 4	85.73	1010.90	0.085	0.0537	7.2650	0.0559	7.5970	0.0076	2.8240	0.3009	81.96	98.70	327.1	357.5	164.0	55.2	4.1	48.5	1.4
Cycle 5	83.68	966.56	0.087	0.0497	7.4190	0.0558	7.7410	0.0081	2.8840	0.2957	82.03	98.88	376.6	180.9	173.0	55.1	4.2	52.2	1.5
Cycle 6	73.72	879.58	0.084	0.0493	7.8180	0.0514	8.1260	0.0076	2.8730	0.2817	89.25	99.30	426.1	161.1	183.0	50.9	4.0	48.6	1.4
Cycle 7	69.21	836.94	0.083	0.0471	7.9670	0.0507	8.2560	0.0078	2.9060	0.2737	84.98	99.11	475.7	54.4	190.0	50.2	4.1	50.2	1.5
Cycle 8	67.27	822.77	0.082	0.0438	8.6620	0.0482	8.9990	0.0080	3.0030	0.2772	78.64	98.73	525.2	0.0	0.0	47.8	4.2	51.3	1.5

Cycle 9	66.64	752.51	0.089	0.0445	8.7740	0.0505	9.1170	0.0082	3.0640	0.2781	87.22	99.24	574.7	0.0	0.0	50.1	4.5	52.9	1.6
Cycle 10	65.67	700.46	0.094	0.0428	9.2450	0.0455	9.5320	0.0077	3.0500	0.2527	80.67	98.97	624.2	0.0	0.0	45.2	4.2	49.6	1.5
Cycle 11	73.16	696.99	0.105	0.0490	8.9900	0.0526	9.3210	0.0078	3.1820	0.2730	75.39	98.47	673.7	145.3	211.0	52.1	4.7	50.1	1.6
Cycle 12	64.04	664.49	0.096	0.0499	8.8090	0.0549	9.1260	0.0080	3.2070	0.2728	85.68	99.11	723.2	191.3	205.0	54.3	4.8	51.3	1.6
Cycle 13	65.94	622.77	0.106	0.0439	9.8370	0.0465	10.1500	0.0077	3.1480	0.2541	88.35	99.33	772.7	0.0	0.0	46.1	4.6	49.3	1.5
Cycle 14	59.33	640.12	0.093	0.0535	8.8230	0.0593	9.1970	0.0080	3.3400	0.2911	100.00	100.00	822.1	349.1	199.0	58.5	5.2	51.6	1.7
Cycle 15	59.45	610.79	0.097	0.0448	9.4980	0.0527	9.8150	0.0085	3.3250	0.2633	94.66	99.72	871.7	0.0	0.0	52.2	5.0	54.8	1.8
Cycle 16	57.38	594.01	0.097	0.0464	9.9330	0.0510	10.3000	0.0080	3.3700	0.2708	56.66	97.29	996.4	17.4	239.0	50.5	5.1	51.2	1.7
Cycle 17	57.67	575.35	0.100	0.0400	11.1200	0.0436	11.5000	0.0079	3.3300	0.2552	74.42	98.54	1046.0	0.0	0.0	43.3	4.9	50.7	1.7
Cycle 18	58.52	572.88	0.102	0.0468	9.6680	0.0511	9.9650	0.0079	3.3170	0.2546	95.42	99.74	1095.0	36.8	231.0	50.6	4.9	50.9	1.7
Cycle 19	52.44	550.81	0.095	0.0510	9.0120	0.0611	9.3400	0.0087	3.4440	0.2779	87.89	99.28	1145.0	241.5	208.0	60.2	5.5	55.8	1.9
Cycle 20	55.25	528.44	0.105	0.0521	9.3890	0.0591	9.7720	0.0082	3.4290	0.2849	96.16	99.74	1195.0	290.3	215.0	58.3	5.5	52.8	1.8
Cycle 21	57.04	543.74	0.105	0.0477	9.8510	0.0523	10.1800	0.0080	3.4150	0.2616	86.87	99.23	1244.0	83.2	234.0	51.8	5.1	51.1	1.7
Cycle 22	50.48	547.77	0.092	0.0538	9.2500	0.0603	9.6180	0.0081	3.5360	0.2859	87.72	99.16	1294.0	364.1	209.0	59.4	5.6	52.1	1.8
Cycle 23	55.26	530.17	0.104	0.0504	9.8430	0.0542	10.1700	0.0078	3.5140	0.2643	50.15	96.94	1343.0	214.9	228.0	53.6	5.3	50.0	1.8
Cycle 24	53.78	535.56	0.100	0.0461	10.0700	0.0515	10.3900	0.0081	3.4480	0.2565	72.15	98.44	1393.0	3.9	243.0	51.0	5.2	52.0	1.8
Cycle 25	59.26	551.30	0.107	0.0499	9.8440	0.0575	10.2300	0.0084	3.5590	0.2799	86.74	99.16	1442.0	191.2	229.0	56.7	5.6	53.6	1.9
Cycle 26	52.64	526.95	0.100	0.0537	9.2850	0.0608	9.6060	0.0082	3.5300	0.2730	61.80	97.58	1492.0	357.9	210.0	59.9	5.6	52.7	1.9
Cycle 27	58.11	542.81	0.107	0.0500	9.8600	0.0583	10.2200	0.0085	3.6380	0.2744	100.00	100.00	1541.0	194.2	229.0	57.5	5.7	54.3	2.0
Cycle 28	54.78	516.36	0.106	0.0449	10.6600	0.0504	10.9800	0.0082	3.6010	0.2530	100.00	100.00	1591.0	0.0	0.0	50.0	5.4	52.3	1.9
Cycle 29	55.73	511.37	0.109	0.0495	10.0300	0.0568	10.3700	0.0083	3.6240	0.2672	84.71	99.12	1640.0	171.4	234.0	56.1	5.7	53.4	1.9
Cycle 30	54.89	498.32	0.110	0.0517	9.7100	0.0566	9.9870	0.0079	3.4880	0.2531	44.48	96.76	1690.0	274.1	222.0	55.9	5.4	50.9	1.8
Cycle 31	50.55	496.65	0.102	0.0538	9.9000	0.0585	10.2900	0.0079	3.6340	0.2810	75.14	98.25	1814.0	362.2	223.0	57.7	5.8	50.6	1.8
Cycle 32	56.37	491.40	0.115	0.0478	10.4600	0.0537	10.7900	0.0082	3.6140	0.2562	94.54	99.70	1864.0	88.7	248.0	53.1	5.6	52.4	1.9
Cycle 33	49.25	474.38	0.104	0.0461	10.7400	0.0520	11.1200	0.0082	3.6330	0.2657	80.55	98.84	1913.0	1.3	259.0	51.5	5.6	52.6	1.9
Cycle 34	53.62	491.36	0.109	0.0408	11.7700	0.0488	12.2000	0.0087	3.7470	0.2662	78.79	98.85	1963.0	0.0	0.0	48.4	5.8	55.8	2.1
Cycle 35	53.24	498.48	0.107	0.0535	9.9520	0.0609	10.3400	0.0083	3.7370	0.2827	81.89	98.79	2012.0	351.1	225.0	60.0	6.0	53.0	2.0
Cycle 36	60.80	481.16	0.126	0.0498	10.6600	0.0521	10.9900	0.0076	3.5910	0.2545	74.27	98.46	2062.0	184.1	248.0	51.6	5.5	48.8	1.8
Cycle 37	56.77	480.52	0.118	0.0517	10.1700	0.0597	10.5400	0.0084	3.7400	0.2731	65.31	97.91	2111.0	271.4	233.0	58.8	6.0	53.8	2.0
Cycle 38	53.48	464.21	0.115	0.0401	12.0700	0.0460	12.4500	0.0083	3.7210	0.2505	82.28	99.11	2161.0	0.0	0.0	45.6	5.6	53.4	2.0
Cycle 39	54.68	444.17	0.123	0.0484	11.0300	0.0531	11.4500	0.0080	3.6390	0.2713	100.00	100.00	2210.0	120.0	260.0	52.6	5.9	51.1	1.9
Cycle 40	45.42	449.06	0.101	0.0460	11.1100	0.0504	11.4700	0.0079	3.7570	0.2579	94.24	99.67	2260.0	0.0	0.0	49.9	5.6	51.0	1.9
Cycle 41	54.61	456.99	0.120	0.0467	10.8800	0.0543	11.2000	0.0084	3.7220	0.2519	82.72	99.11	2310.0	33.2	261.0	53.7	5.9	54.2	2.0
Cycle 42	52.70	464.88	0.113	0.0429	11.7500	0.0479	12.1200	0.0081	3.7490	0.2524	81.62	99.02	2359.0	0.0	0.0	47.5	5.6	52.1	1.9
Cycle 43	51.39	460.46	0.112	0.0503	10.5700	0.0567	10.9300	0.0082	3.7940	0.2664	52.76	97.19	2409.0	208.1	245.0	56.0	6.0	52.5	2.0
Cycle 44	49.29	436.84	0.113	0.0502	10.9900	0.0549	11.4200	0.0079	3.7890	0.2752	89.98	99.33	2458.0	204.7	255.0	54.3	6.0	50.9	1.9
Cycle 45	56.67	456.09	0.124	0.0601	9.6320	0.0662	9.9560	0.0080	3.7630	0.2737	63.86	97.57	2508.0	606.4	208.0	65.1	6.3	51.3	1.9
Cycle 46	57.13	454.32	0.126	0.0427	12.3600	0.0466	12.7800	0.0079	3.7410	0.2569	83.59	99.06	2632.0	-1.0	0.0	46.3	5.8	50.9	1.9
Cycle 47	50.56	425.03	0.119	0.0554	10.3100	0.0620	10.7000	0.0081	3.8670	0.2776	84.39	98.96	2681.0	429.5	230.0	61.0	6.3	52.1	2.0
Cycle 48	45.91	418.33	0.110	0.0547	10.4100	0.0580	10.7800	0.0077	3.7670	0.2724	57.82	97.04	2731.0	401.5	233.0	57.2	6.0	49.3	1.9
Cycle 49	56.91	428.52	0.133	0.0478	11.5600	0.0551	11.9400	0.0084	3.9530	0.2619	100.00	100.00	2781.0	87.2	274.0	54.5	6.3	53.8	2.1

*grain, cycle represents the analyses measured as the beam sputters into the crystal

†0.0 represents analyses in which the data did not yield reliable calculated dates

Table 3.2 Analytical U-Pb zircon isotopic data from conventional polished analyses

	Th	U		$^{207}Pb/^{206}Pb$		$^{207}Pb/^{235}U$		$^{206}Pb/^{238}U$		Correlation of	% Radiogenic	% Radiogenic	$^{207}Pb/^{206}Pb$			$^{207}Pb/^{235}U$		$^{206}Pb/^{238}U$	
Grain	(est. ppm)	(est. ppm)	Th/U	value	1 s.e.	value	1 s.e.	value	1 s.e.	Concordia Ellipses	^{207}Pb	^{206}Pb	Age (Ma)	1 s.e.	ıge (Ma	1 s.e.	ıge (Ma	1 s.e.
EL-20 Migmatite																		
1sp1	171.3	591.8	0.289	0.053	9.166	0.067	9.483	0.009	2.214	0.258	74.88	97.98	340.9	208.0	65.4	6.0	58.1	1.3
2sp1	63.4	393.1	0.161	0.061	3.780	0.587	4.303	0.070	1.765	0.483	59.19	95.27	634.8	81.4	469.1	16.2	436.0	7.4
4sp1	101.9	901.1	0.113	0.032	7.021	0.095	7.511	0.022	2.065	0.367	37.42	94.08	-1.0	0.0	92.4	6.6	137.4	2.8
5sp1	183.1	726.2	0.252	0.054	7.376	0.066	7.564	0.009	1.812	0.222	78.56	98.31	373.9	166.0	64.9	4.8	56.8	1.0
6sp1	254.0	1013.1	0.251	0.055	5.055	0.073	5.431	0.010	1.855	0.367	83.75	98.77	408.0	113.0	71.1	3.7	61.5	1.1
7sp1	65.0	350.0	0.186	0.052	9.852	0.065	10.100	0.009	2.452	0.222	72.30	97.71	289.5	225.0	64.0	6.3	58.1	1.4
10sp1	206.3	956.4	0.216	0.048	6.073	0.059	6.533	0.009	1.826	0.383	80.51	98.67	92.2	144.0	58.3	3.7	57.4	1.0
11sp1	173.1	778.0	0.222	0.052	8.260	0.071	9.003	0.010	6.323	0.464	79.93	98.51	270.5	189.0	69.2	6.0	63.5	4.0
12sp1	134.9	602.0	0.224	0.052	6.535	0.065	7.142	0.009	2.115	0.423	81.96	98.67	307.0	149.0	64.0	4.4	57.7	1.2
13sp1	61.0	453.2	0.135	0.048	7.300	0.058	8.242	0.009	3.353	0.468	75.90	98.21	116.1	172.0	57.1	4.6	55.7	1.9
15sp1	36.1	378.8	0.095	0.050	15.860	0.058	16.380	0.009	2.281	0.293	59.27	96.12	174.7	370.0	57.4	9.1	54.7	1.2
16sp1	52.6	730.5	0.072	0.053	6.818	0.062	7.346	0.009	2.281	0.378	76.41	98.16	336.9	154.0	61.5	4.4	54.6	1.2
18sp1	201.3	724.5	0.278	0.050	14.620	0.060	15.200	0.009	2.009	0.347	63.11	96.75	184.0	341.0	59.0	8.7	56.0	1.1
19sp1	65.3	359.1	0.182	0.054	16.170	0.066	16.810	0.009	2.670	0.317	58.99	95.79	366.2	364.0	65.2	10.6	57.3	1.5

Table 3.3: Analytical oxygen isotope compositions of zircon

Grain	$^{18}O/^{16}O$ measured (x1000)	internal precision (1 SD x1000)	delta^{18}O V-SMOW (‰)*	delta^{18}O V-SMOW (1 SD ‰)*
EL20 Migmatite - unpolished rims				
EL20_m2_g1@1.ais	2.0200	0.000251	8.1	0.3
EL20_m2_g1@2.ais	2.0199	0.000131	8.1	0.3
EL20_m2_g2@1.ais	2.0215	0.000116	8.9	0.3
EL20_m2_g2@2.ais	2.0205	0.000217	8.4	0.3
EL20_m2_g3@1.ais	2.0217	0.000153	9.0	0.3
EL20_m3_s1_g1@1.ais	2.0195	0.000149	8.5	0.3
EL20_m3_s1_g2@1.ais	2.0194	0.000143	8.5	0.3
EL20_m3_s1_g3@1.ais	2.0154	0.000181	6.5	0.3
EL20_m3_s1_g4@1.ais	2.0166	0.000156	7.1	0.3
EL20_inM1_g1_s1.ais	2.0233	0.000137	9.2	0.7
EL20_inM1_g1_s2.ais	2.0229	0.000101	9.0	0.7
EL20_inM1_g2_s1.ais	2.0209	0.000184	8.0	0.7
EL20_inM1_g2_s2.ais	2.0203	0.000203	7.7	0.7
EL20_inM1_g3_s1.ais	2.0223	0.000112	8.7	0.7
EL20_inM1_g3_s2.ais	2.0231	0.000184	9.1	0.7
EL20_inM1_g4_s1.ais	2.0234	0.000156	9.2	0.7
EL20_inM1_g4_s2.ais	2.0235	0.000129	9.3	0.7
EL20_inM1_g5_s1.ais	2.0238	0.000146	9.4	0.7
EL20_inM1_g5_s2.ais	2.0234	0.000151	9.2	0.7
EL20_inM1_g6_s1.ais	2.0203	0.000125	7.7	0.7
EL20_inM1_g6_s2.ais	2.0203	0.000143	7.7	0.7
EL20_inM1_g7_s1.ais	2.0231	0.000175	9.1	0.7
EL20_inM1_g7_s2.ais	2.0230	0.000161	9.0	0.7
EL20_inM1_g8_s1.ais	2.0233	0.000127	9.2	0.7
EL20_inM1_g8_s2.ais	2.0235	0.000094	9.3	0.7
EL20_inM1_g9_s1.ais	2.0215	0.000162	8.3	0.7
EL20_inM1_g10_s1.ais	2.0203	0.000170	7.7	0.7
EL20_inM1_g10_s2.ais	2.0204	0.000125	7.7	0.7
EL20_inM1_g11_s1.ais	2.0229	0.000131	9.0	0.7
EL20_inM1_g11_s2.ais	2.0232	0.000195	9.1	0.7
EL20_inM1_g13_s2.ais	2.0234	0.000123	9.2	0.7
EL20_inM1_g14_s1.ais	2.0210	0.000102	8.1	0.7
EL20_inM1_g14_s2.ais	2.0202	0.000175	7.6	0.7
EL20_inM1_g12_s1.ais	2.0203	0.000180	7.7	0.7
EL20_inM1_g12_s2.ais	2.0208	0.000093	7.9	0.7
EL20_inM1_g13_s1.ais	2.0228	0.000117	9.0	0.7
EL20_inM1_g15_s1.ais	2.0212	0.000142	8.1	0.7
EL20_inM1_g16_s1.ais	2.0191	0.000185	7.1	0.7
EL20_inM1_g16_s2.ais	2.0196	0.000125	7.3	0.7
EL20_inM1_g17_s1.ais	2.0204	0.000123	7.7	0.7
EL20_inM1_g17_s2.ais	2.0198	0.000110	7.4	0.7
EL20_inM1_g19_s2.ais	2.0235	0.000129	9.3	0.7
EL20_inM1_g18_s1.ais	2.0229	0.000104	9.0	0.7
EL20_inM1_g18_s2.ais	2.0226	0.000092	8.8	0.7
EL20_inM1_g19_s1.ais	2.0240	0.000186	9.5	0.7
EL20 Migmatite - interior				
GM1_EL20_g24@1.ais	2.0166	0.000291	7.0	0.3
GM1_EL20_g24@2.ais	2.0169	0.000152	7.2	0.3
GM1_EL20_g23@1.ais	2.0182	0.000129	7.8	0.3
GM1_EL20_g23@2.ais	2.0154	0.000220	6.4	0.3
GM1_EL20_g22@1.ais	2.0162	0.000151	6.8	0.3
GM1_EL20_g22@2.ais	2.0138	0.000135	5.7	0.3
GM1_EL20_g21@1.ais	2.0161	0.000124	6.8	0.3
GM1_EL20_g21@2.ais	2.0163	0.000106	6.9	0.3

GM1_EL20_g20@1.ais	2.0175	0.000149	7.5	0.3
GM1_EL20_g20@2.ais	2.0161	0.000186	6.8	0.3
GM1_EL20_g19@1.ais	2.0159	0.000242	6.7	0.3
GM1_EL20_g19@2.ais	2.0160	0.000116	6.7	0.3
GM1_EL20_g18@1.ais	2.0185	0.000125	8.0	0.3
GM1_EL20_g18@2.ais	2.0172	0.000203	7.3	0.3
GM1_EL20_g17@1.ais	2.0164	0.000193	6.9	0.3
GM1_EL20_g17@2.ais	2.0159	0.000134	6.7	0.3
GM1_EL20_g16@1.ais	2.0057	0.000136	1.6	0.3
GM1_EL20_g16@2.ais	2.0066	0.000165	2.1	0.3
GM1_EL20_g15@1.ais	2.0159	0.000195	6.7	0.3
GM1_EL20_g15@2.ais	2.0167	0.000129	7.1	0.3
GM1_EL20_g14@1.ais	2.0162	0.000161	6.8	0.3
GM1_EL20_g14@2.ais	2.0157	0.000103	6.6	0.3
GM1_EL20_g13@1.ais	2.0168	0.000185	7.1	0.3
GM1_EL20_g13@2.ais	2.0164	0.000119	6.9	0.3
GM1_EL20_g12@1.ais	2.0186	0.000156	8.0	0.3
GM1_EL20_g12@2.ais	2.0178	0.000199	7.6	0.3
GM1_EL20_g11@1.ais	2.0157	0.000199	6.6	0.3
GM1_EL20_g11@2.ais	2.0172	0.000208	7.4	0.3
EL20_m2_s2@1.ais	2.0165	0.000220	7.8	0.3
EL20_m2_s2@2.ais	2.0144	0.000250	6.7	0.3
EL20_m2_s2@3.ais	2.0156	0.000193	7.3	0.3
EL20_m2_s2@4.ais	2.0164	0.000142	7.7	0.3
EL20_m2_s2@5.ais	2.0120	0.000198	5.5	0.3
EL20_m2_s2@6.ais	2.0160	0.000147	7.5	0.3
EL20_m2_s2@7.ais	2.0154	0.000128	7.2	0.3
EL20_m2_s2@8.ais	2.0155	0.000100	7.3	0.3
EL20_m2_s2@9.ais	2.0173	0.000165	8.2	0.3
EL20_m2_s2_g2@1.ais	2.0161	0.000228	7.6	0.3
EL20_m2_s2_g2@2.ais	2.0160	0.000238	7.5	0.3
EL20_m2_s2_g2@3.ais	2.0158	0.000154	7.4	0.3
EL20_m2_s2_g2@4.ais	2.0158	0.000152	7.4	0.3
EL20_m2_s2_g2@5.ais	2.0163	0.000174	7.6	0.3
EL20_m2_s2_g2@6.ais	2.0161	0.000179	7.5	0.3
EL20_m2_s2_g2@7.ais	2.0146	0.000108	6.8	0.3
EL20_m2_s2_g2@8.ais	2.0156	0.000125	7.3	0.3
EL20_m2_s2_g2@9.ais	2.0157	0.000109	7.4	0.3
EL20_m2_s2_g2@10.ais	2.0188	0.000189	8.9	0.3

*after correction for instrumental mass fractionation using Pacoima and AS3 zircon standard

DATA REPOSITORY

Zircon was separated from a sample of migmatitic biotite gneiss using standard techniques. The handpicked unpolished zircon grains were pressed into either prepolished aluminum or indium with a piston-press assembly. Standards AS3 (1099 ± 1 Ma; Paces and Miller, 1993) and Sri Lanka (SL-2) zircon (564 Ma ± 4 Ma; George Gehrels; personnel communication) were used for the U-Pb analyses. Measurements of standards NBS SRM 610 glass (70 % SiO_2; 434 ± 7 ppm Ti; Pearce et al., 1997) and SL13 zircon (15.3 % SiO_2; 6.32 ± 0.17 ppm Ti; Aikman, 2007) were interspersed for the Ti concentration analyses. Finally, for the oxygen isotope analyses, standards AS3 (+5.34‰; Trail et al., 2007) and Pacoima (+5.70‰; Booth et al., 2005) were used. Prior to depth profiling analyses, a MICROXAM surface profilometer was utilized to image the topography of each grain to identify those most favourable for analysis, i.e., those with flat crystal faces. All measurements were made using the Cameca ims1270 ion microprobe facility at the University of California, Los Angeles. Results are reported with 1σ errors, except for weighted mean ages that have 2σ errors. The U-Pb measurements were made with a negative ion oxygen beam according to the methods of Breeding et al. (2004) for the depth profiling of unpolished crystals and Schmitt et al. (2003) for analyses of polished grains. For the Ti measurements, we used instrumental conditions for spot analyses similar to those reported in Harrison and Schmitt (2007). In comparison, a Cs^+ beam and multicollection of $^{16}O^-$ and $^{18}O^-$ was utilized for oxygen isotope analyses. Analytical settings for oxygen isotope measurements are described in Trail et al. (2007).

U-Pb isotopic ratios and ages were calculated from measured ion intensities using

in-house software written by C.D. Coath (ZIPS v2.4). ISOPLOT v3 (Ludwig, 2003) was used to calculate $^{206}Pb/^{238}U$ - $^{207}Pb/^{235}U$ concordia diagrams (Fig. A1). Results from a single representative depth profile (grain 1; see table 1) are shown in Figure A1A. Statistically rigorous assessment of U-Pb concordance is hampered by low ion intensities of ^{207}Pb (typically 10-50 counts per second), and poor ^{207}Pb radiogenic yields (generally 50-90%) cause calculated $^{207}Pb/^{235}U$ ratios to be highly sensitive to correction for common Pb. Nevertheless, no obvious signs of U-Pb discordance are observed. Figure A1B shows a Concordia diagram containing the results from all of the depth profiling measurements (N=13). Each ellipse represents an integrated depth profiling analysis. Neither of the Concordia diagrams display convergence towards older ages and are thus inconsistent with U-Pb discordance.

REFERENCES

Aikman A.B., 2007, Tectonics of the eastern Tethyan Himalaya [Ph.D. thesis]: Australian National University.

Booth, A.L., Kolodny, Y., Chamberlain, C.P., McWilliams, M., Schmitt, A.K., and Wooden, J., 2005, Oxygen isotopic composition and U-Pb discordance in zircon: Geochimica et Cosmochimica Acta, v. 69, p. 4895-4905.

Breeding, C.M., Ague, J.J., Grove, M., and Rupke, A.L., 2004, Isotopic and chemical alteration of zircon by metamorphic fluids: U-Pb age depth-profiling of zircon crystals from Barrow's garnet zone, northeast Scotland: American Mineralogist, v. 89, p. 1067-1077.

Harrison, T.M., and Schmitt, A.K., 2007, High sensitivity mapping of Ti distributions in Hadean zircons: Earth and Planetary Science Letters, v. 261, p. 9-19.

Ludwig, K.R., 2003, Isoplot/Ex, v.3.0: Berkeley Geochronology Center Special Publication, v. 4, p. 70.

Paces, J.B., and Miller, J.D., 1993, Precise U-Pb age of Duluth Complex and related mafic intrusions, northeastern Minnesota: geochronological insights into physical, petrogenetic, paleomagnetic, and tectonomagmatic processes associated with the 1.1 Ga midcontinent rift system: Journal of Geophysical Research, v. 98, p. 13997-14013.

Pearce, N., Perkins, W., Westgate, J., Gorton, M., Jackson, S., Neal, C., and Chenery, S., 1997, A compilation of new and published major and trace element data for NIST SRM 610 and NIST SRM 612 glass reference materals: Geostandards Newsletter, v. 21, p. 115-144.

Schmitt, A.K., Grove, M., Harrison, T.M., Lovera, O.M., Hulen, J., and Waters, M. 2003, The Geysers – Cobb Mountain Magma System, California (Part 1): U-Pb zircon ages of volcanic rocks, conditions of zircon crystallization and magma residence times: Geochimica et. Cosmochimica. Acta, v. 67, p. 3423-3442.

Trail, D., Mojzsis, S.J., Harrison, T.M., Schmitt, A.K., Watson, E.B., and Young, E.D., 2007, Constraints on Hadean zircon protoliths from oxygen isotopes, Ti-thermometry, and rare earth elements: Geochemistry, Geophysics, and Geosystems, v. 8, p. 1-22.

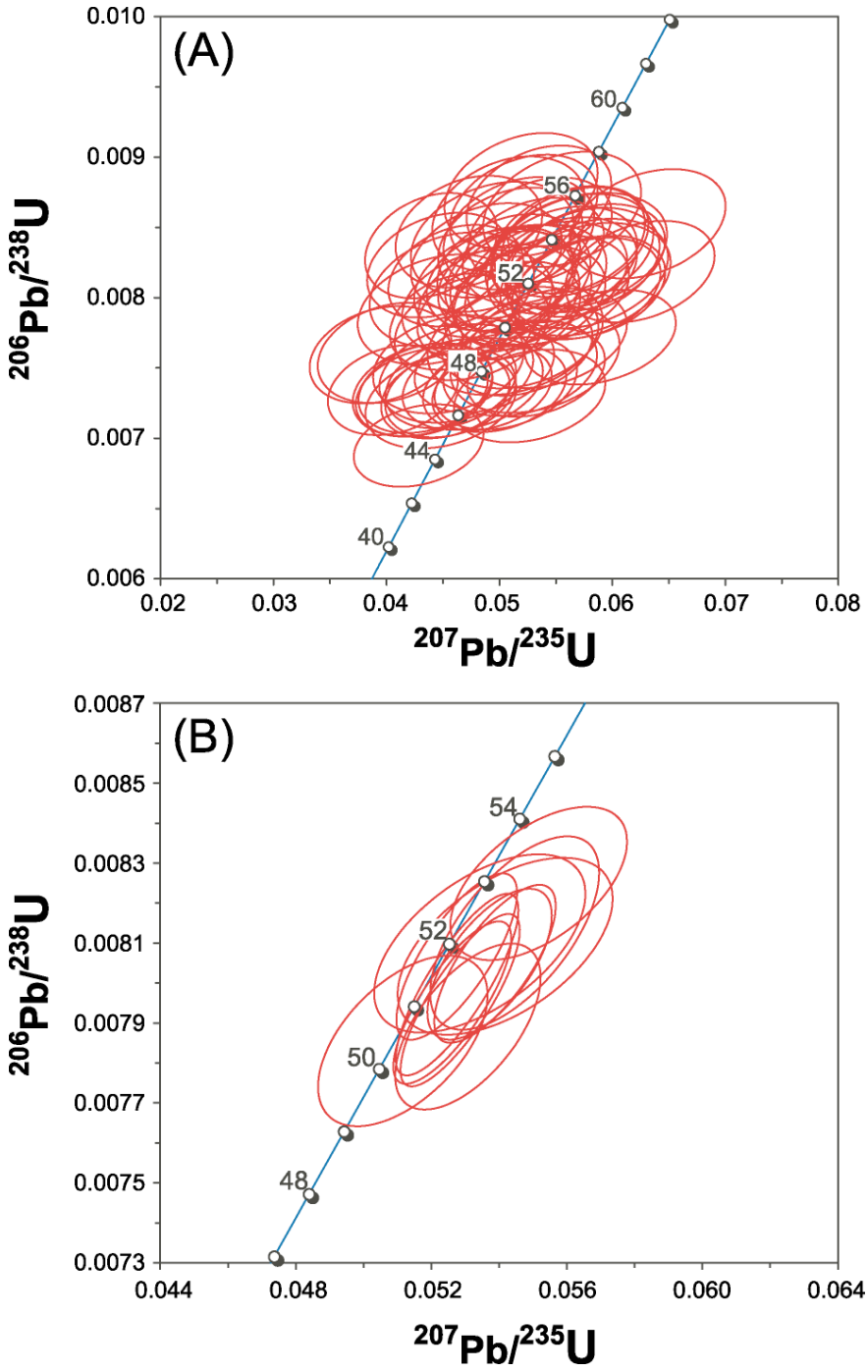

Figure 3.A1: $^{206}Pb/^{238}U$ vs. $^{207}Pb/^{235}U$ Concordia plots calculated using Isoplot v.3.0 software (see Ludwig, 2003). Error ellipses are 68.3 % confidence. (A) Representative depth profile run (EL20_g1). Error ellipses calculated for 75 individual cycles. (B) Results from all 13 depth profiles. Error ellipses calculated after integrating all data from respective depth profile runs. Detailed assessment of concordance is hampered by the high sensitivity of measured ^{207}Pb to common Pb correction.

Chapter 4: Time-temperature-fluid Evolution of Migmatite Dome Crystallization: Coupled U-Pb Age, Ti Thermometry, and O Isotopic Ion Microprobe Depth Profiling of Zircon and Monazite

Stacia Gordon*, Marty Grove, Donna Whitney*, Axel Schmitt***, Christian Teyssier***

*Department of Geology and Geophysics, University of Minnesota, Minneapolis, MN 55455
**Department of Geological and Environmental Sciences, Stanford University, Stanford, CA 94305
***Department of Earth and Space Sciences, University of California, Los Angeles, CA 90095

This chapter has been submitted to *Chemical Geology* and is currently in the review process.

ABSTRACT

The temporal fluid history of high-grade terranes is commonly difficult to track; however, the use of secondary ionization mass spectrometry (SIMS) depth profiling analysis of accessory minerals in high-grade metamorphic rocks can yield U-Pb geochronology, Ti in zircon thermometry, and oxygen isotope data that can be used to decipher temporal and physicochemical records of long-lived orogens. This investigation focuses on a migmatite dome in a Cordilleran metamorphic core complex that records a long history of partial melting during crustal thickening and/or orogenic collapse, and that had a dynamic history of metamorphism, deformation, and fluid flow. SIMS depth-profiling analyses of the outermost rims of zircon and monazite from samples representing a range of crustal levels elucidate the nature of the deep crustal environment during the final stages of extension and orogenic collapse between ca. 60 and 50 Ma, following a major episode of granitoid emplacement and partial melt crystallization. The results from ultrathin (0.25 to 5.00 μm) outer rims of zircon demonstrate that fluid infiltration driven by amphibolite facies metamorphic devolatilization and/or igneous crystallization persisted at deep crustal levels until just before the time that the rocks were rapidly exhumed to upper crustal levels. Collectively, the results indicate that metamorphic fluids continued to infiltrate the gneiss dome from ca. 58 to 50 Ma. The overlap in ages from the zircon rims and monazite with argon cooling ages suggest that the dome cooled rapidly from >650 ºC to 300 ºC from 51-47 Ma. The results further demonstrate that the evolution of high-grade terrains, including the fluid history, can be revealed in unprecedented detail through the combination of depth profiling analyses of U-Pb age, Ti thermometry, and O isotopes.

1. Introduction

The timing of high-temperature orogenic events such as metamorphism, crustal melting, and deformation is typically determined by U-Th-Pb analysis of accessory minerals such as zircon and monazite. Although growth and recrystallization of accessory minerals is being increasingly better understood in the context of the host rock petrogenesis (e.g., Kohn and Malloy, 2004; Kelsey et al., 2008), it remains a difficult task to relate ages measured from zircon and monazite to specific orogenic events. The length scales over which recrystallization and new growth occur are among the biggest difficulties that must be confronted during analyses of accessory minerals from high-grade metamorphic environments. It is well known that precursor zircon is very robust during metamorphic and melt-generating reactions (Harrison and Watson, 1983; Watson, 1996), which is both an advantage and a problem. Very slow diffusion rates for U, Th, Pb, O, and Ti (Watson and Cherniak, 1997; Cherniak and Watson, 2001, 2003, 2007) help ensure that both U-Pb age and stable isotopic and trace element compositions are preserved during subsequent deep crustal evolution. Conversely, new zircon growth associated with tectonic events post-dating the initial zircon growth typically occurs at very fine spatial scales (Corfu et al., 2003). Zircon is thus capable of preserving a long history of growth and modification that is not necessarily easily resolved, even when in situ spot measurements are performed using secondary ionization mass spectrometry (SIMS) methods with the ion microprobe. Monazite may also contain valuable chemical and textural information (e.g., Ayers et al., 2006), but monazite tends to recrystallize more readily than zircon (Teufel and Heinrich, 1997; Ayers et al., 2006; Harlov et al., 2007) and therefore may record age and stable isotopic information that is substantially

different than that yielded by coexisting zircon (e.g., Whitney et al., 2003; Kapp et al., 2005).

There has long been a disconnect between the minerals used in geochronology (e.g., zircon, monazite), the minerals used for determining the pressure-temperature conditions of metamorphic and magmatic events (e.g., garnet, plagioclase, mica, Al_2SiO_5), and the minerals used to track fluid-rock interactions (e.g., quartz, calcite, magnetite, graphite). Generally, the phases selected are chosen because they constitute the best-calibrated systems to yield the desired type of data. Unfortunately, use of different minerals and methods makes it difficult to integrate the diverse data in a meaningful way; however, this lack of integration may be overcome through the use of a versatile analytical tool like the ion microprobe that is capable of measuring U-Th-Pb age, $\delta^{18}O$ composition, and trace element concentrations from closely associated regions of a single phase such as zircon (e.g., Booth et al., 2005; Cavosie et al., 2005; Trail et al., 2007). When the SIMS depth profiling approach is employed, comprehensive age, metamorphic temperatures, and stable isotope datasets can be recovered from otherwise undecipherable submicron-scale records of metamorphic and magmatic events that are preserved on the outermost surface of zircon (Zeitler et al., 1989; Grove and Harrison, 1999; Mojzsis and Harrison, 2002; Carson et al., 2002; Breeding et al., 2004b). The depth profiling method has been employed previously for age determination using other techniques such as laser ablation inductively coupled plasma mass spectrometry (e.g., the rim-piercing method of Campbell et al., (2005); depth profiling of Hourigan et al., (2003)); however, the depth resolution of the laser ablation technique is much coarser so

that the results do not reveal the detail that may be obtained with ion microprobe measurements.

In this study, we employed both conventional SIMS analysis of sectioned zircon and monazite grains and SIMS depth-profiling analysis into natural zircon rims from high-grade metamorphic rocks, including migmatite. We integrated U-Th-Pb age, Ti thermometry, and oxygen isotope data from zircon and monazite to document the timing, temperature, and geochemistry of fluids during the evolution of the Valhalla complex, one of a series of migmatite domes located in the Omineca crystalline interior belt of the Canadian Cordillera (Fig. 1).

Gneiss domes are important features in collapsed orogens worldwide (Whitney et al., 2004a), and typically record evidence for complex interactions among crustal melting, fluid flow, and extension (e.g., Vanderhaeghe and Teyssier, 1997; Vanderhaeghe et al., 1999; Teyssier and Whitney, 2002). Elucidating these interactions requires integrated information about the timing and conditions of migmatite petrogenesis/crystallization and associated tectonic events. Although a general tectonic history of crustal thickening and exhumation has been established for the Valhalla complex, it has not been clear when, why, and rate at which the partially molten rocks of the complex crystallized and cooled, and how these events related to other tectonothermal processes such as extension and fluid flow. Furthermore, understanding the evolution of the deep crust in this region is of central importance for evaluating the hypothesis that this belt of migmatite domes represented the eastern exhumed margin of a regionally extensive orogenic plateau that also included the continental magmatic arc to the west (e.g., Whitney et al., 2004b).

2. Geologic overview

Regional convergence in the Mesozoic drove crustal thickening throughout the North American Cordillera (see references in Parrish et al., 1988). Within the Omineca belt, the southern Canadian segment of the Cordillera, Late Mesozoic-Early Cenozoic orogeny was associated with widespread high-temperature metamorphism and crustal melting (Brown et al., 1986; Carr, 1992; Vanderhaeghe and Teyssier, 1997), forming a series of migmatite domes that record conditions of 730 - 800ºC at 8-12 kbar (Fig. 1; Harvey, 1994; Spear and Parrish, 1996; Crowley and Parrish, 1999; Norlander et al., 2002).

Zircon and monazite U-Th-Pb geochronology have documented extensive granitoid emplacement and melt crystallization throughout the Omineca belt between 60 - 50 Ma (Carr et al., 1987; Parrish et al., 1988; Carr, 1992; Vanderhaeghe et al., 1999b; Crowley et al., 2001; Hinchey et al., 2006; Gordon et al., 2008; Kruckenberg et al., 2008). Migmatite is pervasive at all structural levels of the domes and provides evidence that a large region of the lower crust was partially molten. In most of the Omineca domes, evidence for melt crystallization spanned most, if not all, of the 60-50 Ma interval (Vanderhaeghe et al., 1999b; Crowley et al., 2001; Hinchey et al., 2006; Kruckenberg et al., 2008). The Valhalla complex is exceptional in the Omineca belt in that available U-Pb zircon evidence for pluton emplacement and melt crystallization indicates that this activity occurred over a more restricted interval (62-58 Ma; Carr et al., 1987; Parrish et al., 1988; Gordon et al., 2008). All of the domes record petrologic evidence for high-temperature decompression (e.g., Norlander et al., 2002; Marshall and Simandl, 2006). In

addition, all of the domes also yield biotite Ar cooling ages that indicate Ar closure below 300 ºC between 51-47 Ma (Wanless et al., 1978, 1979; Parrish et al., 1988; Vanderhaeghe et al., 2003; Gordon et al., 2008; Kruckenberg et al., 2008).

The Valhalla complex consists of three main units: 1) the 100 Ma K-feldspar megacrystic, granodioritic, Mulvey orthogneiss, 2) a metasedimentary unit consisting of migmatitic biotite and quartzofeldspathic paragneiss, and 3) leucocratic granitoid bodies, including the Airy Quartz Monzonite and the Ladybird Leucogranite (Fig. 1; Reesor, 1965; Carr et al., 1987). The migmatitic portions of the metasedimentary unit typically contain 10 to 50% leucosome, with small (~50 x 50 m) bodies of very high-melt fraction migmatite (diatexite). Leucosomes that crystallized in boudin necks contain neo-formed zircon that yield 60 ± 2 Ma ages that constrain the timing of migmatite crystallization (Gordon et al., 2008). Monazite from the migmatitic rocks yields a range of ages from 58 to 50 Ma (Gordon et al., 2008). However, because monazite is prone to fluid-mediated recrystallization (Teufel and Heinrich, 1997; Ayers et al., 2006), the Th-Pb age results obtained most likely reflect the timing of fluid flow rather than initial migmatite crystallization (Gordon et al., 2008).

The Valhalla complex is bounded by an Eocene fault system consisting of the ductile Valkyr shear zone on the west, north, and south and the brittle-ductile Slocan Lake fault to the east (Fig. 1; Carr et al., 1987). Based on oxygen isotope studies of quartz and feldspar, the Slocan Lake fault is thought to have served as a permeable boundary for two hydrothermal fluid regimes found in Valhalla (Holk and Taylor 2000, 2007). The two regimes consist of: 1) convective circulation of surface derived meteoric waters in the upper plate that descend into the lower plate; and 2) lower plate

metamorphic and magmatic waters at low water-rock ratios that move upward from deep to shallow structural levels. Near the Slocan Lake fault, there is evidence for mixing of the two hydrothermal regimes, and evidence also exists that meteoric fluids circulated to great depths along faults such as Slocan Lake (e.g., Magaritz and Taylor, 1986; Mulch et al., 2007; Person et al., 2007). In addition, lode deposits in the hanging wall of the Slocan Lake fault are thought to be associated with Valhalla fluids and movement along the fault system (Beaudoin et al., 1992; Holk and Taylor, 2007). Samples were collected from throughout the Valhalla complex to better understand the lower plate hydrothermal regime, and in particular, to obtain more evidence to understand the timing and physicochemical conditions in which fluid-rock interaction occurred.

3. Sample selection

Three samples were selected to represent the full range of exhumed structural levels within the Valhalla complex (Fig. 1). The structurally highest sample, Rt6-4, is a mylonitized leucosome that accumulated within a boudin neck directly below the Slocan Lake fault. It contains quartz, plagioclase, and lesser amounts of K-feldspar, with accessory biotite, apatite, zircon, and monazite. Zircons from this sample were previously dated by conventional ion microprobe techniques at 60 ± 2 Ma (Gordon et al., 2008). Sample EL-20 is a migmatitic quartzofeldspathic paragneiss with a similar mineralogy to the boudin neck leucosome from the metasedimentary unit. The gneiss occurs structurally beneath the mantling granitoid bodies (Ladybird leucogranite and Airy quartz monzonite) but overlies the core of the Valhalla dome (Fig. 1). The structurally deepest sample, UP-20, is a strongly deformed metapelite from the Gwillim Creek shear zone in the Passmore dome (Fig. 1), and is representative of the variably migmatized metapelite present

throughout the Valhalla complex. Biotite and sillimanite define a mylonitic fabric in the metapelite. The sample also contains quartz, plagioclase, and K-feldspar. Similar metapelite was used for thermobarometric analysis, and yields peak *P-T* conditions of 8 kbar at 820 ºC (Spear and Parrish, 1996).

4. Analytical methods

4.1. Sample preparation

Standard crushing, density, and magnetic methods were employed to extract zircons from the three samples. The recovered grains were generally clear, euhedral to subhedral, and ~100 to 250 μm in length. Zircons from Rt6-4 were pervasively fractured (Fig. 2). This condition may reflect mylonitic deformation associated with displacement on the Slocan Lake fault. In spite of this, a sufficient number of grains exhibited crack-free crystal faces for successful analyses. Sample EL-20, the migmatite, contained glassy zircons that had large, flat crystal faces (Fig. 2). Zircons from the metapelite, UP-20, show smaller crystal faces and more obviously rounded edges (Fig. 2). The rounded morphology could reflect abrasion during sedimentary transport or the existence of metamorphic overgrowths.

We tried a number of sample preparation methods for the depth profiling approach in an effort to optimize results. Three different mounting techniques were employed. In each, we selected only grains that preserved primary crystal faces. In the first mounting method, the {100} surfaces of selected grains were placed face down on a glass substrate that was coated with an ultrathin film of vacuum grease. These grains were potted in a 5 mm diameter drop of epoxy. We used a small drop to minimize grain

mobility and hence topography on the analysis surface. After curing, these mini mounts were removed from the glass and remounted together with prepolished standards to form a composite 1-inch diameter epoxy mount. No additional polishing was carried out. The mount was ultrasonically cleaned in 1 *N* HCl for several minutes, rinsed in pure H_2O, and coated in Au. The second method involved pressing grains into pre-polished indium with a piston-press assembly. Mounts prepared in this manner were cleaned as described above except that they were placed in 1 N HCL for only 30 seconds to minimize dissolution of the metal substrate. In our third approach, we used a piston-press assembly to press grains directly into a 1" polished aluminium disk. The Al mounts were cleaned in the same manner as the indium mounts.

A MICROXAM surface profilometer was utilized to image the topography of each grain to identify those most favourable for analysis (Fig. 3). The imaging revealed that mounting grains in indium or aluminium was superior to epoxy because of greater success in aligning zircon surfaces parallel to the mounting surface. We ultimately preferred indium over aluminium because use of the latter minimized the number of grains that were partially dislodged or plucked during grinding and polishing carried out in preparation for subsequent conventional SIMS analysis.

For conventional U-Pb spot analysis, the mounts prepared for depth-profiling analysis were sectioned, polished, and cleaned as previously described. Backscattered electron and cathodoluminescene (CL) images were taken to document internal compositional variation to guide the placement of spot analyses (Fig. 3). Monazite was mounted in the same manner, ultrasonically cleaned without HCl, and coated with Au.

Because the monazite from these samples does not typically display flat crystal faces, we did not attempt depth-profiling measurements.

Below we describe the methods used for the U-Pb, Ti, and oxygen isotope measurements. A more detailed discussion of the techniques is located in the electronic supplement.

4.2. U-Pb measurements

All measurements were made using the Cameca ims1270 ion microprobe facility at the University of California, Los Angeles. The analytical conditions used for U-Pb conventional spot measurements of sectioned and polished zircon are presented in Schmitt et al. (2003). The conditions used for depth-profiling measurements in this study were previously described by Breeding et al. (2004b). A 10 nA, 25 μm diameter, aperture-defined O^- ion beam was used for conventional analyses. A larger ~40 μm spot was used for depth profiling. We used a mechanical "field aperture" set at 25 μm to block signal derived from the periphery of the pit to exclude crater edge effects. The standard operating conditions used for the analyses involved a primary ion beam intensity of ~10 nA, mass resolving power of ~4500, and a 50 eV energy window. Typical sputtering rates were ~0.0015 μm/s. To increase Pb^+ yields, oxygen flooding of the sample surface at a pressure of 3.5×10^{-5} Torr was used (Schuhmacher et al., 1994).

Zircon ages were determined by comparison with a calibration curve defined by measurements of standards. At the start of the analyses, ~6 standards were run to identify whether the instrument was stable and to begin development of the calibration curve. Subsequently, standards were run every fourth analysis (i.e., three unknowns and then a

standard analysis). Both AS3 zircon (1099 ± 1 Ma; Paces and Miller, 1993) and Sri Lanka (SL-2) zircon (564 Ma ± 4 Ma; Gehrels; personnel communication) were used. Generally, the precision of the analysis is determined by the reproducibility of the standard calibration curve rather than counting statistics (Harrison et al., 1995). Standard reproducibility varied from 2-4% over the course of the measurements. To enhance the spatial record of U-Pb age vs. depth, the sputtering duration was longer for unpolished grains than it was for polished zircon (~30 minutes versus ~15 minutes).

The zircon ages and errors reported here were calculated using UCLA software [ZIPS v2.4 written by C.D. Coath and others]. Errors for individual analyses are plotted at the ± 1σ level. Ages calculated for individual cycles in depth profiling mode are also ± 1σ. We used ISOPLOT software (Ludwig, 2003) to calculate model concordia and weighted mean ages. The errors are reported at the ± 2σ level for the weighted mean and concordia ages. The depth profiling results are reported in Table 1. The results from the conventional analyses are reported in Table 2.

4.3 Ti concentrations

For the Ti measurements, we used instrumental conditions for spot analyses similar to those reported in Harrison and Schmitt (2007). A 6 nA primary O^- ion beam was focused to a ~ 25 μm spot. A mass resolving power of ~8500 was used in conjunction with a 30 eV energy window. Analysis was undertaken with Ti^+ and $^{30}SiO^+$ measured in multicollection mode using electron multipliers. We interspersed measurements of NBS SRM 610 glass (70 % SiO_2; 434 ± 7 ppm Ti; Pearce et al., 1997) and SL13 zircon (15.3 % SiO_2; 6.32 ± 0.17 ppm Ti; Aikman, 2007) throughout analyses of unknowns to monitor inter-element fractionation. Temperatures were calculated from

the Ti concentration measurements based on the calibration presented in Ferry and Watson (2007):

$$\log (\text{ppm Ti}) = 5.711 - 4800/T(K) - \log (a_{SiO2}) + \log (a_{TiO2}).$$

Because all of our samples contained both rutile and quartz, we set the activities of SiO_2 and TiO_2 to unity in these calculations. Possible systematic errors (e.g., mis-estimation of SiO_2 and TiO_2 activity) and possible contribution of Ti from non-zircon phases (e.g., inclusions) likely outweigh analytical errors by a wide margin. We have assigned uncertainties of ± 25°C for calculated temperatures. The Ti concentrations and calculated temperatures are shown in Table 3. Two different calculated temperatures, one based on the Watson and Harrison (2005) calibration and one based on the Ferry and Watson (2007) calibration, are shown.

4.4 Oxygen isotopes

Analytical settings for oxygen isotope measurements are described in Trail et al. (2007). In this study, a ~3 nA primary Cs^+ ion beam was focused to ~ 25 μm. Mass resolving power was set to ~3500 with a 30 eV energy window. A liquid nitrogen cold finger positioned near the sample was used to limit ^{18}O backgrounds. Multicollection of $^{16}O^-$ and $^{18}O^-$ involved use of Faraday detectors fitted with 10^{10} and 10^{11} Ohm resistors, respectively. Background corrections were performed with each analysis. We measured standards, AS3 (+5.34‰; Trail et al., 2007) and Pacoima (+5.70‰; Booth et al., 2005) for zircon and 554 (+7.54‰; Ayers et al., 2006) for monazite throughout the analyses in order to correct for instrumental mass fractionation. All $\delta^{18}O$ results are expressed relative to Vienna standard mean ocean water (V-SMOW). Uncertainties are reported at the ± 1σ level and are listed in Table 4 for zircon and Table 5 for monazite.

5. Results

5.1. U-Pb age

Thirteen zircons were analyzed in depth-profiling mode from the structurally highest sample (Rt6-4). In most of the depth profiles, U-Pb ages calculated from the first ~ 5 cycles of data rise progressively in a convex-up pattern from ca. 35 to 45 Ma to a plateau at 55 to 60 Ma (Fig. 4A). The end result of the profile is consistently within error of the results determined from the sectioned grains. While these resemble diffusion profiles, published Pb in zircon diffusion data (Cherniak and Watson, 2003) reveal that the observed length scales are much too long to be explained by volume diffusion given plausible ambient temperature-time histories (see Appendix 1). We attribute most of the observed age variation shown in Figure 4A to Pb loss due to radiation damage that is exacerbated in the near-rim environment, possibly due to fluid-grain interactions. This hypothesis is supported by the high U-contents prevalent through Rt6-4 zircons (ca. 3000 ppm). The 55 to 60 Ma age plateaus measured from the rims are little affected in that they are slightly younger than or equivalent to U-Pb ages previously reported for zircon interiors from Rt6-4. The latter yield a weighted mean $^{206}Pb/^{238}U$ age of 60 ± 2 Ma (MSWD = 2.4; Fig. 5A) based on seventeen spots obtained from thirteen grains, indicating the time at which the leucosome crystallized (Gordon et al., 2008).

Depth-profiling results from thirteen grains yield a consistent $^{206}Pb/^{238}U$ age of 51± 2 Ma from sputter pits that varied in depth from 3.7 to 4.5 μm for the structurally intermediate sample EL-20 (Fig. 4B). In contrast, 12 of 14 analyses from the zircon interiors define a weighted mean $^{206}Pb/^{238}U$ age of 58 ± 2 Ma (MSWD: 1.8; Fig. 5B). The

fact that interior U-Pb ages are readily resolved from the younger rim values confirms the existence of relatively thick (> 3.5 μm) rims on the EL-20 zircons. Moreover, the reproducibility of the rim ages leads us to believe that they are geologically meaningful. Our assessment is also based upon the fact that the uranium contents determined from the EL-20 rims are much lower (750-1000 ppm) than those yielded by Rt6-4. CL imaging of the EL-20 zircons do not show obvious evidence for the thick overgrowths; the euhedral textures and oscillatory zoning of the sectioned interiors of these grains suggest that the EL-20 zircon crystallized from melt. The zoning, however, can be complicated, and evidence for the overgrowths may be hidden in the zoning. The two older grains not included in the weighted mean age yield $^{206}Pb/^{238}U$ dates of 138 ± 3 Ma and 436 ± 9 Ma and appear to be inherited zircons.

Zircons from the structurally deepest sample, UP-20, exhibit rounded morphologies consistent with the grains being detrital or possibly having metamorphic overgrowths (cf. Corfu et al., 2003; Fig. 3C). A total of 39 unpolished grains were analyzed in depth-profiling mode. The extent of new zircon growth at the rim varied dramatically from grain to grain in this sample (Fig. 4C). Fourteen of the analyses lack evidence of a Cretaceous to Eocene overgrowth. Twelve of the analyses resolve $^{206}Pb/^{238}U$ ages of ca. 70 Ma before rapidly yielding older ages with progressive sputtering. The thin Late Cretaceous rims are consistent with zircon growth during the prograde metamorphic evolution of the Valhalla complex. In addition, $^{206}Pb/^{238}U$ ages associated with 8 rims cluster near 60 Ma. In the five remaining cases, $^{206}Pb/^{238}U$ ages yielded by zircons rims extend down to 50 Ma.

The U-Pb age results obtained from the sectioned UP-20 zircons are shown in Figure 5C. The interiors of three grains yield latest Cretaceous $^{206}Pb/^{238}U$ ages of 75 ± 1 Ma, 68 ± 1 Ma, and 68 ± 1 Ma (Fig. 5C) ages that we interpret to reflect prograde metamorphism because the ages reflect similar ages obtained from other nearby metapelites (Spear and Parrish, 1996; Ducea et al., 2003; Spear, 2004). The interiors of all other grains yield Proterozoic $^{207}Pb/^{206}Pb$ ages that range from ca. 1.3 Ga to 2.6 Ga. We interpret these as detrital ages and note that the metapelitic rocks of the Omineca belt formed from an amalgam of terranes that were partly derived from, and thrust eastward over, sedimentary sequences that had previously accumulated along the North American paleomargin (Brown et al., 1986; Price, 1986). CL images of the grains are complicated, and show cross-cutting zoning in the grains (Fig. 2C).

5.2. Ti in zircon geothermometry

To better determine the physical conditions of the 60-50 Ma zircon growth we applied the Ti in zircon thermometer (Watson et al., 2006; Ferry and Watson, 2007). Because the dates measured from the Rt6-4 rims are probably a result of radiation damage, no further measurements were performed with the sample. Crystallization temperatures calculated from depth profiling data into the EL-20 rims range from 620 - 795 ºC, with the majority of the analyses clustering around 650 ºC (n = 25; Fig. 6A). These are equivalent to the results obtained from the same sample from the conventionally sectioned and polished interiors that range from T = 644-725 ºC (n = 17; Fig. 6A) and cluster near 665°C. There was not a systematic correlation between the age and temperature, i.e., the higher temperatures (e.g., 795 ºC) did not systemically come from an older or younger rim or core. A similar temperature relationship is exhibited by

the structurally deepest (UP-20) sample; however, it yields higher overall temperatures. The unpolished rims range from T = 620-907 ºC (n = 41; Fig. 6B) and cluster near 700°C from all grains, including the Cretaceous-Eocene grains as well as Proterozoic grains. The polished interiors revealed a similar range of (580-850 ºC; n = 32; Fig. 6B) and also cluster near 700°C. Again, there is no correlation between the temperature and age in the metapelite.

5.3. Oxygen isotope analysis

We undertook oxygen depth profiling measurements of samples EL-20 and UP-20. In both cases, zircon rims yield $\delta^{18}O$ values that are consistently heavier than those measured from grain interiors. EL-20 rims yield a weighted mean $\delta^{18}O$ value of 8.4 ± 0.2 ‰ (n = 46; MSWD = 2.0; Fig. 7A) with values up to 9.5 ± 0.7 ‰. In comparison, EL-20 zircon interiors yield a weighted mean $\delta^{18}O$ value of 7.2 ± 0.1 ‰ (n = 45; MSWD = 3.2; Figs. 7A, 8). Elevated $\delta^{18}O$ occur in the near-rim environments, particularly near prismatic grain terminations. An even more dramatic contrast was observed for the metapelite sample (UP-20). Zircon rim compositions from UP-20 yield a weighted mean $\delta^{18}O$ value of 8.9 ± 0.2 ‰ (n = 37; MSWD: 1.6; Fig. 7B) with some results up to 10.3 ± 0.7 ‰. These are measurably heavier than the compositions recorded by the majority of the zircon interiors of the metapelite, which range from 4.0 ± 0.3 ‰ to 10.1 ± 0.3 ‰ (Fig. 7B). The 10.1 ‰ value came from a single analysis; the majority of the analyses from the interior yield lighter results (Fig. 7B). The variability in zircon interiors record the polygenetic origin of the grains.

We also measured oxygen isotopic compositions from monazite from UP-20, EL-20, and Rt6-4. Three additional monazite samples from two other migmatites and a leucogranite body were also analyzed. All of the monazites examined reveal $\delta^{18}O$ values that are very similar to those obtained from the zircon rims. Somewhat lighter weighted mean $\delta^{18}O$ value of 7.9 ± 0.2 ‰ (n = 21; MSWD: 0.6; Fig. 9A) was yielded by Rt6-4 monazite. In comparison, a weighted mean $\delta^{18}O$ value of 8.6 ± 0.3 ‰ (n = 13; MSWD: 2.1; Fig. 9B) was obtained from EL-20 monazites. Twenty-one monazites from UP-20 yield a weighted mean $\delta^{18}O$ value of 9.0 ± 0.3 ‰ (MSWD: 2.1; Fig. 9C)

Three additional samples with Th-Pb ages that range from 58 to 51 Ma (Gordon et al., 2008) were chosen for oxygen isotope analysis. Backscattered electron imaging of the monazite grains reveals that all display patchy zoning that may indicate that the grains experienced fluid-mediated recrystallization (e.g., Townsend et al., 2000). HR-7.1, a garnet-bearing migmatitic paragneiss, is comprised of ~ 10% leucosome and was collected from between the Valhalla and Passmore domes in the metasedimentary unit. Previous Th-Pb age measurements were heterogeneous, ranging from 73 to 48 Ma with multiple ages clustering near 58 Ma (Gordon et al., 2008). The same monazites also yield a heterogeneous range of $\delta^{18}O$ values from 10.7 ± 0.5 ‰ to 4.9 ± 0.5 ‰ based on sixteen analyses although all but four analyses are > 7 ‰ (Fig. 9B). Sample GL-4.1 is a deformed stromatic migmatite, and the monazite yielded weighted average Th-Pb age domains of 55 ± 3 Ma, 52 ± 2 Ma and 50 ± 2 Ma (Gordon et al., 2008). Twenty-two $\delta^{18}O$ analyses reveal a homogeneous distribution of values that yield a weighted mean of 9.4 ± 0.2 ‰ (MSWD: 0.7; Fig. 9B). Sample, ML-7, was collected to compare the monazite from the mantling Ladybird leucogranite to migmatites present at deeper levels. A

weighted mean $\delta^{18}O$ value of 9.0 ± 0.2 ‰ (n = 13; MSWD: 1.2; Fig. 9A) was determined for monazite from the leucogranite. The monazite from the leucogranite yielded a Th-Pb age of 51 ± 2 Ma (Gordon et al., 2008).

6. Discussion

6.1. Utilizing accessory minerals to track orogenic processes

The submicron-scale spatial resolution offered by SIMS depth profiling of zircon and other phases is an underutilized tool in the geosciences. The results of this and previous studies (e.g., Zeitler et al., 1989; Carson et al., 2002; Mozjsis and Harrison, 2002; Breeding et al., 2004b) have shown that zircons may preserve important isotopic information in sub-micron scale rims that can be analyzed to document thermal and fluid events in high-grade terranes. Depth profiling is thus a powerful tool for U-Th-Pb geochronology. When age information is integrated with geothermometry (i.e., Ti in zircon; Ferry and Watson, 2007) and tracer isotopic information (i.e., oxygen isotopes), recovery of previously inaccessible information concerning the physical and chemical environment of (re)crystallization of geochronologically important minerals is possible. Application of the approach to both zircon and monazite can reveal significant evidence for multiple thermal and fluid events in high-grade terranes; however, this study demonstrates that these accessory minerals can record different information because monazite can recrystallize readily in the presence of aqueous fluid and perhaps also in response to deformation. For example, Th-Pb age and the $\delta^{18}O$ measurements reveal that monazite is very susceptible to alteration even under low water-rock conditions (Ayers et al., 2006; this study). The Th-Pb age results are all younger than the zircon melt

crystallization results in this study, and the heavy $\delta^{18}O$ values are consistent with the monazites recrystallizing in the presence of metamorphic or magmatic fluids. Thus, interpretation of monazite U-Th-Pb age results may be difficult. In comparison, zircon is much more resistant in these high-grade conditions, and only seems to undergo minimal recrystallization.

The three samples analyzed reveal a range of alteration and degree of preservation of isotopic overgrowths on the rims of zircon. The depth profiling analyses of the leucosome crystallized in a boudin neck, Rt6-4, reveal very limited rim alteration or growth ($< 0.25\ \mu$m). Radiation damage in the near-rim environment probably resulted in the observed results and explains why initial U-Pb ages (ca. 35-45 Ma) from the outermost portions of the rims are younger than biotite $^{40}Ar/^{39}Ar$ ages (48 Ma) from the same sample (Gordon et al., 2008). In comparison, the migmatitic gneiss, EL-20, yields a plateau in the age versus depth plots with an age of 51 Ma for the outermost, $> 3.5\ \mu$m of the rims. The zircon rims of this sample have been significantly altered and contain a thick ($> 3.5\ \mu$m) overgrowth that is clearly distinguishable from the interior 57.5 Ma age. The final sample, the metapelite, contains a variety of grains that yield a range of ages, Proterozoic to Eocene, with variable rim alteration. The range in rim growth and alteration in the metapelite probably reflects the polygenetic origin of the grains. In particular, if some grains have undergone significant sedimentary transport, cracks and other surficial features may allow penetration of fluids deeper into the crystals.

In general, the three samples do reveal a variety of fluid alteration in the near-rim environment of the zircon. The differences are probably a consequence of a variety of factors, including: lithology of the overall rock, origin of the zircon (i.e., inherited versus

metamorphic/magmatic), degree of deformation, and structural location in the Valhalla complex. It is difficult to access which factor is most relevant; however, the structural level appears to be the most obvious factor in the results from the Valhalla complex: the structurally highest sample, Rt6-4, did not undergo significant fluid-alteration in comparison to the structurally deeper samples, UP-20 and EL-20. The structurally deeper migmatitic gneiss and metapelite were probably in contact with fluids fluxing through the system for a greater amount of time whereas Rt6-4 was probably primarily affected by meteoric fluids driven down along the Slocan Lake fault late in the deformation history of the Complex.

6.2. Fluid-rock interaction in orogeny: the Valhalla migmatite dome and core complex

The timing, extent, and conditions of fluid-rock interactions are important factors in the evolution of orogenic systems. Fluids mediate transfer of mass and thermal energy, weaken rocks, and trigger chemical reactions (e.g., Rye et al., 1976; Bebout and Barton, 1989; Baumgartner and Ferry, 1991; Ingebritsen and Manning, 1999; Manning and Ingebritsen, 1999; Breeding et al., 2004a). This is perhaps most obvious within subduction zones where fluids control elemental recycling from the subducted slab to the mantle wedge and strongly influence partial melting and the generation of new crust (e.g., Manning, 1997; Elliott et al., 1997; Breeding et al., 2004a). It is also widely recognized that fluid is intimately linked to partial melting, deformation, and extension in active orogenic settings (e.g., Manning and Ingebritsen, 1999; Santosh et al., 2004), but the record of fluid-rock interaction may not be well integrated with tectonic processes owing to lack of data about age/timing of fluid-related processes. Therefore, although fluid-rock

interactions can be evaluated from geochemical, petrologic, and/or physical observations (e.g., Nesbitt and Muehlenbachs, 1989; Beaudoin et al., 1991; Elliot et al., 1997; Manning, 2001; Holness and Watt, 2001), it is important to couple stable isotope data with age information (e.g., Ayers et al., 2006).

Previous studies of the Valhalla complex have suggested that the rocks underwent a protracted (40 m.y.) thermal evolution that terminated when the complex cooled below 300 ºC at 51-47 Ma (Wanless et al., 1978, 1979; Carr et al., 1987; Parrish, 1990; Parrish, 1995; Spear and Parrish, 1996; Spear, 2004; Gordon et al., 2008). During this history, partial melting played a major role in the evolution of the complex, culminating with melt crystallization from 60-58 Ma (Gordon et al., 2008; this study). Similar results from the other Omineca domes indicate that a large portion of orogenic crust was partially molten during the Paleocene-Eocene, as indicated by a spread in zircon U-Pb crystallization ages between 60 to 50 Ma. In contrast, zircon U-Pb crystallization ages from the Valhalla complex all cluster between 60-58 Ma. The paucity of younger zircon age results for the Valhalla complex has obscured important details of the evolution of the complex from 60 to 50 Ma. Although monazite Th-Pb ages from the migmatites range from 58 to 50 Ma (Gordon et al., 2008), CL imaging reveals patchy internal microstructures consistent with fluid-mediated recrystallization (cf. Townsend et al., 2000). The combination of U-Pb zircon age, Ti in zircon thermometry, and oxygen isotope depth profiling in zircon and monazite reveal that while the other Omineca domes still contained partially molten crust in the 60 to 50 Ma interval, the Valhalla complex also remained at high-temperature (> 650°C) and continued to be infiltrated by aqueous fluid derived from metamorphic devolatilization and possible undetected melt crystallization at depth. The overlap within

error in the rim ages from the zircon, the youngest monazite ages, and argon biotite cooling ages suggest that the Valhalla complex cooled rapidly from 51 to 47 Ma from temperature of > 650 ºC to 300 ºC.

Holk and Taylor (2000) analyzed the $\delta^{18}O$ from quartz and feldspar throughout the Valhalla complex and found uniform values of 11.2 ± 0.9 ‰ and 10.0 ± 0.2 ‰, respectively. The fractionation law relating equilibrium zircon, monazite, and quartz $\delta^{18}O$ values is given by:

$$\delta^{18}O_A - \delta^{18}O_B = A_{A-B}\ 10^6/T^2 \text{ (T in K)}$$

where A is 2.64 for zircon-quartz (Valley et al., 2003) and 2.20 for monazite-quartz (Breecker and Sharp, 2007). Based upon these relationships, the predicted $\delta^{18}O$ values for zircon and monazite in equilibrium with quartz are 8.4 ‰ and 8.9 ‰ respectively. The fact that the predicted values are so similar to those that we measured from the zircon rims and recrystallized monazites indicates that all likely equilibrated with the same fluids.

The $\delta^{18}O$ values (7.2 ‰) from the zircon interiors of the migmatitic sample, EL-20, reflect the oxygen isotopic composition of the melt-equilibrated zircon at 57.5 Ma. If the leucosome had stayed molten (or remelted) subsequently, no change in the $\delta^{18}O$ value would be expected on the rims of the zircons given the Ti thermometry results indicating constant temperature from 57.5 to 51 Ma. Therefore, the measurable contrast in $\delta^{18}O$ values between the interior and rims of the EL-20 zircons indicate that the external mobile component that helped to form the rims was not a melt phase.

Holk and Taylor (2000, 2007) found that the most $\delta^{18}O$ homogenized zones within the core complexes of the Omineca belt are closely associated with leucogranites

or migmatite-rich zones, indicating that hydrothermal fluids were exsolved from the melt when it crystallized or that the melts promoted oxygen isotope exchange with the surrounding host rock; therefore, the fluids in the Valhalla complex were probably derived from melt crystallization and metamorphic devolatilization. Fluids probably moved structurally up in the system to the bounding detachment faults and fractures in the upper plate (Holk and Taylor, 2007), which is supported by mineralization in the hanging wall adjacent to the Slocan Lake fault (Fig. 10; Beaudoin et al., 1992).

The bulk quartz, feldspar and whole rock $\delta^{18}O$ values reported by Holk and Taylor (2000, 2007) represent an integrated measure of fluid-rock interactions that require a predominately deep metamorphic or igneous source of fluids beneath the Slocan Lake fault. Conversely, hydrogen isotopic compositions reveal that infiltration of meteoric fluids did not exceed to depths well beneath the detachment fault (Holk and Taylor, 2000, 2007). While the shifted hydrogen isotopic compositions likely record a late overprint associated with detachment faulting along the Slocan Lake fault, our spatially and temporally resolved results clearly indicate that metamorphic or igneous source of fluids remained prevalent within the migmatite complex as late as 50 ± 2 Ma based on the 50 Ma age from the GL-4.1 monazites. It thus appears most probable that infiltration of late-stage meteoric fluids into the migmatite complex must have occurred subsequent to 51 Ma during greenschist-facies overprinting as the rocks cooled and were exhumed to the surface.

The quartz and feldspar $\delta^{18}O$ values from Holk and Taylor (2000, 2007) provide an estimation of the chemical signature of fluids present in the Valhalla complex; however, the previous $\delta^{18}O$ work lacks an understanding of the timing and physical

conditions in which the fluids were present. Thus, the combination of U-Pb age, $\delta^{18}O$, and Ti measurements all from zircon reveal that the fluids in Valhalla primarily affected the rocks late (< 60 Ma) in the protracted history of the Valhalla complex while the complex remained at high temperature.

7. Conclusions

We have demonstrated that integration of sub-micron-scale U-Pb geochronology, Ti in zircon thermometry, and oxygen isotope measurement from unpolished zircon rims constitutes a powerful approach for deciphering tectonic events recorded by high-grade metamorphic rocks, including migmatite. This approach permits assessment of the relationship between timing, physical conditions, and geochemical environment attending zircon recrystallization, information that is vital for interpreting accessory mineral analyses as well as understanding the late fluid-rich history of high-grade terrains. Our results for zircon and monazite reveal that the Valhalla complex, British Columbia, remained at high-temperatures (> 650 °C) for up to 6.5 ± 2 m.y. (from the interior EL-20 zircon age of 57.5 to the EL-20 zircon rim age of 51 Ma) after migmatite and associated granitoid bodies had crystallized. During this interval however, the complex continued to interact with metamorphic and magmatic fluids until rapid cooling, likely associated with exhumation, beginning at 51 Ma.

ACKNOWLEDGMENTS

This research was supported by the NSF grant EAR-0409776 to C. Teyssier and D. Whitney, the Department of Geology and Geophysics at the University of Minnesota, and

NSF grant EAR-0609911 to M. Grove. The ion microprobe facility at UCLA is partly supported by a grant from the Instrumentation and Facilities Program, Division of Earth Sciences, National Science Foundation.

Appendix 1 In order to test whether the $^{238}U/^{206}Pb$ age profiles created with the depth profiling represent Pb diffusion profiles, we undertook diffusion calculations to model age profiles measured for sample RT6-4 (see text). A single diffusion domain, episodic loss model was used with an activation energy (E) of 131 kcal/mol and a frequency factor (D_0) of 7.64 cm^2/s (Cherniak and Watson, 2003). Zircon was modeled as a sphere with an assumed effective diffusion radius (r_o) equal to 50 μm. The results show age profiles predicted for temperatures from 900 ºC to 700 ºC under two conditions: holding the grains at these temperatures for 1 m.y. or 10 m.y. (Fig. 11 in appendix). Based on the Ti-in-zircon results, we would expect the depth profiles to be similar to those predicted at 700 ºC. The diffusion model at 700 ºC shows that there would be an initial increase in the ages in the first 0.1 μm of the profile before an age plateau was attained. However, this is not the pattern seen in the Rt6-4 U-Pb age depth profiles. In the case of Rt6-4, the penetration depth is at least 0.25 μm and is normally greater. As explained in the text, the observed age profiles are geologically implausible and appear to reflect Pb loss from radiation-damaged high-uranium zircon in the near-rim environment.

REFERENCES

Aikman, A.B., 2007. Tectonics of the eastern Tethyan Himalaya, Ph.D. thesis, Australian National University.

Ayers, J.D., Loflin, M., Miller, C.F., Barton, M.D., Coath, C.D., 2006. In situ oxygen isotope analysis of monazite as a monitor of fluid infiltration during contact metamorphism: Birch Creek Pluton aureole, White Mountains, eastern California. Geology 34, 653-656.

Baumgartner, L.P., Ferry, J.M., 1991. A model for coupled fluid-flow and mixed-volatile mineral reactions with applications to regional metamorphism. Contributions to Mineralogy and Petrology 106, 273-285.

Beaudoin, G., Taylor, B.E., Sangster, D.F., 1991. Silver-lead-zinc veins, metamorphic core complexes, and hydrologic regimes during crustal extension. Geology 19, 1217-1220.

Beaudoin, G., Roddick, J.C., sangster, D.F., 1992. Eocene age for Ag-Pb-Zn-Au vein and replacement deposits of the Kokanee Range, southeastern British Columbia. Canadian Journal of Earth Sciences 29, 3-14.

Bebout, G.E., Barton, M.D., 1989. Fluid flow and metasomatism in a subduction zone hydrothermal system: Catalina Schist terrane, California. Geology 17, 976-980.

Booth, A.L., Kolodny, Y., Chamberlain, C.P., McWilliams, M., Schmitt, A.K., Wooden, J., 2005. Oxygen isotopic composition and U-Pb discordance in zircon. Geochimica et Cosmochimica Acta 69, 4895-4905.

Breecker, D.O., Sharp, Z.D., 2007. A monazite oxygen isotope thermometer. American Mineralogist 92, 1561-1572.

Breeding, C.M., Ague, J.J., Bröcker, M., 2004a. Fluid-metasedimentary rock interactions in subduction-zone mélange: Implications for the chemical composition of arc magmas. Geology 32, 1041-1044.

Breeding, C.M., Ague, J.J., Grove, M., Rupke, A.L., 2004b. Isotopic and chemical alteration of zircon by metamorphic fluids: U-Pb age depth-profiling of zircon crystals from Barrow's garnet zone, northeast Scotland. American Mineralogist 89, 1067-1077.

Brown, R.L., Journeay, J.M., Lane, L.S., Murphy, D.C., Rees, C.J., 1986. Obduction, backfolding and piggyback thrusting in the metamorphic hinterland of the southeastern Canadian Cordillera. Journal of Structural Geology 8, 255-268.

Campbell, I.H., Reiners, P.W., Allen, C.M., Nicolescu, S., Upadhyay, R., 2005. He-Pb double dating of detrital zircons from the Ganges and Indus Rivers: implications for quantifying sediment recycling and provenance studies. Earth and Planetary Science Letters 237, 402-432.

Carr, S.D., 1992. Tectonic setting and U-Pb geochronology of the early Tertiary Ladybird leucogranite suite, Thor-Odin-Pinnacles area, southern Omineca belt, British Colombia. Tectonics 11, 258-278.

Carr, S.D., Parrish, R.R., Brown, R.L., 1987. Eocene structural development of the Valhalla complex, southeastern British Columbia. Tectonics 6, 175-196.

Carson, C.J., Ague, J.J., Grove, M., Coath, C.D., Harrison, T.M., 2002. U-Pb isotopic behaviour of zircon during upper-amphibolite facies fluid infiltration in the Napier Complex, east Antarctica. Earth and Planetary Science Letters 199, 287-310.

Cavosie, A.J., Valley, J.W., Wilde, S.A., E.I.M.F., 2005. Magmatic $\delta^{18}O$ in 4400-3900 Ma detrital zircons: a record of the alteration and recycling of crust in the Early Archean. Earth and Plantary Science Letters 235, 663-681.

Cherniak, D.J., Watson, E.B., 2001. Pb diffusion in zircon. Chemical Geology 172, 5-24.

Cherniak, D.J., Watson, E.B., 2003. Diffusion in zircon. In: Hanchar, J.M., Hoskin, P.W.O. (Eds.), Zircon. Reviews in Mineralogy and Geochemistry, vol. 53, pp. 113-143.

Cherniak, D.J., Watson, E.B., 2007. Ti diffusion in zircon. Chemical Geology 242, 470-483.

Cook, F.A., Simony, P.S., Coflin, K.C., Green, A.G., Milkereit, B., Price, R.A., Parrish, R., Patenaude, C., Gordy, P.L., Brown, R.L., 1988. Lithoprobe southern Canadian Cordilleran transect: Rocky Mountain thrust belt to Valhalla gneiss complex: Geophysical Journal International 89, 91-98.

Crowley, J.L., Parrish, R.R., 1999. U-Pb isotopic constraints on diachronous metamorphism in the northern Monashee complex, southern Canadian Cordillera. Journal of Metamorphic Geology 17, 483-502.

Crowley, J.L., Brown, R.L., Parrish, R.R., 2001. Diachronous deformation and a strain gradient beneath the Selkirk allochthon, northern Monashee complex, southeastern Canadian Cordillera. Journal of Structural Geology 23, 1103-1121.

Elliott, T., Plank, T., Zindler, A., White, W., Bourdon, B., 1997. Element transport from slab to volcanic front at the Mariana arc. Journal of Geophysical Research 102, 14991-15019.

Ferry, J.M., Watson, E.B., 2007. New thermodynamic models and revised calibrations for the Ti-in-zircon and Zr-in-rutile thermometers. Contributions to Mineralogy and Petrology 154, 429-437.

Gordon, S.M., Whitney, D.L., Teyssier, C., Grove, M., Dunlap, W.J., 2008. Timescales of migmatization, melt crystallization, and cooling in a Cordilleran gneiss dome: the Valhalla complex, southeastern British Columbia. Tectonics 27, doi:10.1029/2007TC002103.

Grove, M., Harrison, T.M., 1999. Monazite Th-Pb age depth profiling. Geology 27, 487-490.

Harlov, D.E., Wirth, R., Hetherington, C.J., 2007. The relative stability of monazite and huttonite at 300-900 ºC and 200-1000 MPa: metasomatism and the propagation of metastable mineral phases. American Mineralogist 92, 1652-1664.

Harrison, T.M., Schmitt, A.K., 2007. High sensitivity mapping of Ti distributions in Hadean zircons. Earth and Planetary Science Letters 261, 9-19.

Harrison, T.M., Watson, E.B., 1983. Kinetics of zircon dissolution and zirconium diffusion in granitic melts of variable water content. Contributions to Mineralogy and Petrology 84, 67-72.

Harrison, T.M., McKeegan, K.D., Le Fort, P., 1995. Detection of inherited monazite in the Manaslu leucogranite by $^{208}Pb/^{232}Th$ ion microprobe dating: Crystallization age and tectonic significance. Earth and Planetary Science Letters 133, 271-282.

Harvey, J.L., 1994. Sapphirine-bearing amphibolites in the Okanogan complex, Washington: thermobarometry and tectonic implications. M.S. thesis, Northern Arizona University.

Hinchey, A.M., Carr, S.D., McNeill, P.D., Rayner, N., 2006. Paleocene-Eocene high-grade metamorphism, anatexis, and deformation in the Thor-Odin dome, Monashee complex, southeastern British Columbia. Canadian Journal of Earth Sciences 43, 1341-1365.

Holk, G.J., Taylor, H.P., Jr., 2000. Water as a petrologic catalyst driving homogenization of the middle crust in the metamorphic core complexes of British Columbia. International Geology Review 42, 97-130.

Holk, G.J., Taylor, H.P., Jr., 2007. $^{18}O/^{16}O$ evidence for contrasting hydrothermal regimes involving magmatic and meteoric-hydrothermal waters at the Valhalla metamorphic core complex, British Columbia. Economic Geology 102, 1063-1078.

Holness, M.B., Watt, G.R., 2001. Quartz recrystallization and fluid flow during contact metamorphism: a cathodoluminescence study. Geofluids 1, 215-228.

Hourigan, J.K., Reiners, P.W., Nicolescu, S., Plank, T., Kelley, K., 2003. Zonation-dependent alpha-ejection correction by laser ablation ICP-MS depth profiling: toward

improved precision and accuracy of (U-Th)/He ages. Eos Trans. AGU, Fall Meeting Supplement 84, V22G-04

Ickert, R.B., Hiess, J., Williams, I.S., Holden, P., Ireland, T.R., Lanc, P., Schram, N., Foster, J.J., Clement, S.W., 2008. Determining high precision, in situ, oxygen isotope ratios with a *SHRIMP II*: analyses of MPI-DING silicate-glass reference materials and zircon from contrasting granites. Chemical Geology 257, 114-128.

Ingebritsen, S.E., Manning, C.E., 1999. Geological implications of a permeability-depth curve for the continental crust. Geology 27, 1107-1110.

Kapp, J.L.D., Harrison, T.M., Kapp, P.A., Grove, M., Lovera, O.M., Lin, D., 2005. The Nyaingentanglha Shan: a window into the tectonic, thermal, and geochemical evolution of the Lhasa block, southern Tibet. Journal of Geophysical Research 110, B08413.

Kelsey, D.E., Clark, C., Hand, M., 2008. Thermobarometric modeling of zircon and monazite growth in melt-bearing systems: examples using model metapelitic and metapsammitic granulites. Journal of Metamorphic Geology 26, 199-212.

Kohn, M.J., Malloy, M.A., 2004. Formation of monazite via prograde metamorphic reactions among common silicates: implications for age determinations. Geochimica et Cosmochimica Acta 68, 101-113.

Kruckenberg, S.C., Whitney, D.L., Teyssier, C., Fanning, M., Dunlap, W.J., 2008. Paleocene-Eocene migmatite crystallization, extension, and exhumation in the hinterland of the northern Cordillera: Okanogan dome, Washington USA. Geological Society of America Bulletin 120, 912-929.

Ludwig, K.R., 2003. Isoplot/Ex, v3.00. Berkeley Geochronology Center Special Publication 4, 70.

Magaritz, M., Taylor, H.P., Jr., 1986. $^{18}O/^{16}O$ and D/H studies of plutonic granitic and metamorphic rocks across the Cordilleran batholiths of southern British Columbia. Journal of Geophysical Research 91, 2193-2217.

Manning, C.E., 1997. Coupled reaction and flow in subduction zones: Silica metasomatism in the mantle wedge. In: Jamtveit, B., Yardley, B.W.D. (Eds.) Fluid flow and transport in rocks; Mechanisms and Effects, pp. 139-148.

Manning, C.E., Ingebritsen, S.E., 1999. Permeability of the continental crust: Implications of geothermal data and metamorphic systems. Reviews of Geophysics 37, 127-150.

Marshall, D., Simandl, G., 2006. Phase relations and metamorphism in the sapphirine bearing granulites of the Valhalla complex, Slocan Valley, BC. GAC/MAC Annual Meeting Abstracts Program 31, 96.

Mojzsis, S.J., Harrison, T.M., 2002. Establishment of a 3.83-Ga magmatic age for the Akilia tonalite (southern West Greenland). Earth and Planetary Science Letters 202, 563-576.

Mulch, A., Teyssier, C., Cosca, M.A., Chamberlain, C.P., 2007. Stable isotope paleoaltimetry of Eocene core complexes in the North American Cordillera. Tectonics 26, doi:10.1029/2006TC001995.

Nesbitt, B.E., Muehlenbachs, K., 1989. Origins and movement of fluids during deformation and metamorphism in the Canadian Cordillera. Science 245, 733-736.

Norlander, B.N., Whitney, D.L., Teyssier, C., Vanderhaeghe, O., 2002. Partial melting and decompression of the Thor-Odin dome, Shuswap metamorphic core complex, Canadian Cordillera. Lithos 61, 103-125.

Paces, J.B., Miller, J.D., 1993. Precise U-Pb age of Duluth Complex and related mafic intrusions, northeastern Minnesota: geochronological insights into physical, petrogenetic, paleomagnetic, and tectonomagmatic processes associated with the 1.1 Ga midcontinent rift system. Journal of Geophysical Research 98, 13997-14013.

Parrish, R.R., 1990. U-Pb dating of monazite and its application to geological problems. Canadian Journal of Earth Sciences 27, 1431-1450.

Parrish, R.R., 1995. Thermal evolution of the southeastern Canadian Cordillera. Canadian Journal of Earth Sciences 32, 1618-1642.

Parrish, R.R., Carr, S.D., Parkinson, D.L., 1988. Eocene extensional tectonics and geochronology of the southern Omineca belt, British Colombia and Washington. Tectonics 7, 181-212.

Pearce, N., Perkins, W., Westgate, J., Gorton, M., Jackson, S., Neal, C., Chenery, S., 1997. A compilation of new and published major and trace element data for NIST SRM 610 and NIST SRM 612 glass reference materals. Geostandards Newsletter 21, 115-144.

Person, M.P., Mulch, A., Teyssier, C., Gao, Y., 2007. Isotope transport and exchange during detachment tectonics, Shuswap metamorphic core complex, British Columbia. American Journal of Science 307, 555-589.

Price, R.A., 1986. The southeastern Canadian Cordillera: Thrust faulting, tectonic wedging and delamination of the lithosphere. Journal of Structural Geology 8, 238-254.

Reesor, J.E., 1965. Structural evolution and plutonism in Valhalla gneiss complex, British Columbia. Geological Survey of Canada Bulletin 129, 128.

Rye, R.O., Schuiling, R.D., Rye, D.M., Jansen, J.B.H., 1976. Carbon, hydrogen, and oxygen isotope studies of the regional metamorphic complex at Naxos, Greece. Geochimica et Cosmochimica Acta 40, 1031-1049.

Santosh, M., Tsunogae, T., Yoshikura, S., 2004. "Ultrahigh density" carbonic fluids in ultrahigh-temperature crustal metamorphism. Journal of Mineralogical and Petrological Sciences 99, 164-179.

Schaubs, P.M., S.D. Carr, Berman, R.G., 2002. Structural and metamorphic constraints on ca. 70 Ma deformation of the northern Valhalla complex, British Columbia: Implications for the tectonic evolution of the southern Omineca belt. Journal of Structural Geology 24, 1195-1214.

Schmitt, A.K., Grove, M., Harrison, T.M., Lovera, O.M., Hulen, J.,Waters, M., 2003. The Geysers – Cobb Mountain Magma System, California (Part 1): U-Pb zircon ages of volcanic rocks, conditions of zircon crystallization and magma residence times. Geochimica et Cosmochimica Acta 67, 3423-3442.

Schuhmacher, M., de Chambost, E., McKeegan, K.D., Harrison, T.M., Migeon, H., 1994. Dating of zircon with the CAMECA IMS 1270. In: Benninghoven, A., Nihei, Y., Shimizu, R., Werner, H.W. (Eds.), Secondary Ion Mass Spectrometry SIMS IX. Wiley, New York, pp. 912-922.

Spear, F.S., Parrish, R.R., 1996. Petrology and cooling rates of the Valhalla Complex, British Columbia, Canada. Journal of Petrology 37, 733-765.

Spear, F.S., 2004. Fast cooling and exhumation of the Valhalla metamorphic core complex, southeastern British Columbia. International Geology Review 46, 193-209.

Teufel, S., Heinrich, W., 1997. Partial resetting of the U-Pb isotope system in monazite through hydrothermal experiments: An SEM and U-Pb isotope study. Chemical Geology 137, 273-281.

Teyssier, C., Whitney, D.L., 2002. Gneiss domes and orogeny. Geology 30, 1139-1142.

Teyssier, C., Ferré, E.C., Whitney, D.L., Norlander, B., Vanderhaeghe, O., Parkinson, D., 2005. Flow of partially molten crust and origin of detachments during collapse of the

Cordilleran orogen. In: Bruhn, D., Burlini, L. (Eds.), High-strain zones: Structure and physical properties, Geol. Soc.-Lon. Special Publications, vol. 245, pp. 39-64.

Townsend, K.J., Miller, C.F., D'Andrea, J.L., Ayers, J.C., Harrison, T.M., Coath, C.D., 2000. Low temperature replacement of monazite in the Iretaba granite, southern Nevada: geochronological implications. Chemical Geology 172, 95-112.

Trail, D., Mojzsis, S.J., Harrison, T.M., Schmitt, A.K., Watson, E.B., Young, E.D., 2007. Constraints on Hadean zircon protoliths from oxygen isotopes, Ti-thermometry, and rare earth elements. Geochemistry Geophysics Geosystems 8, 1-22.

Valley, J.W., Bindeman, I.B., Peck, W.H., 2003. Empirical calibration of oxygen isotope fractionation in zircon. Geochimica et Cosmochimica Acta 67, 3257-3266.

Vanderhaeghe, O., Teyssier, C., 1997. Formation of the Shuswap metamorphic complex during late-orogenic collapse of the Canadian Cordillera: role of ductile thinning and partial melting of the mid- to lower crust. Geodinamica Acta 10, 41-58.

Vanderhaeghe, O., Teyssier, C., Wysoczanski, R., 1999. Structural and geochronological constraints on the role of partial melting during the formation of the Shuswap metamorphic core complex at the latitude of the Thor-Odin Dome, British Columbia. Canadian Journal of Earth Sciences 36, 917-943.

Vanderhaeghe, O., Teyssier, C., McDougall, I., Dunlap, W.J., 2003. Cooling and exhumation of the Shuswap metamorphic core complex constrained by $^{40}Ar/^{39}Ar$ thermochronology. Geological Society of America Bulletin 115, 200-216.

Watson, E.B., 1996. Surface enrichment and trace-element uptake during crystal growth. Geochimica et Cosmochimica Acta 60, 5013-5020.

Watson, E.B., Cherniak, D.J., 1997. Oxygen diffusion in zircon. Earth and Planetary Science Letters 148, 527-544.

Watson, E.B., Wark, D.A., Thomas, J.B., 2006. Crystallization thermometers for zircon and rutile. Contributions to Mineralogy and Petrology 151, 413-433.

Wanless, R.K., Stevens, R.D., Lachance, G.R., Delabio, R.N., 1978. Age determinations and geological studies, K-Ar isotopic ages, report 13. Geological Survey of Canada Paper 77-2.

Wanless, R.K., Stevens, R.D., Lachance, G.R., Delabio, R.N., 1979. Age determinations and geological studies, K-Ar isotopic ages, report 14. Geological Survey of Canada Paper 79-2.

Wheeler, J.O., McFeely, P., 1991. Tectonic Assemblage Map of the Canadian Cordillera and Adjacent Parts of the United States of America, Geological Survey of Canada, Map 1712A.

Whitney, D.L., Teyssier, C., Fayon, A.K., Hamilton, M.A., Heizler, M., 2003. Tectonic controls on metamorphism, partial melting, and intrusion: timing of regional metamorphism and magmatism of the Nigde Massif, Turkey. Tectonophysics 376, 37-60.

Whitney, D.L., Teyssier, C., Fayon, A.K., 2004a. Isothermal decompression, partial melting and exhumation of deep continental crust. In: Grocott, J., McCaffrey, K.J.W., Taylor, G., Tikoff, B. (Eds.) Vertical Coupling and Decoupling in the Lithosphere, Geol. Soc.-Lon. Special Publications, vol. 227, 313-326.

Whitney, D.L., Paterson, S.R., Schmidt, K.L., Glazner, A.F., Kopf, C.F., 2004b. Growth and demise of continental arcs and orogenic plateaux in the North American Cordillera: from Baja to British Columbia. Grocott, J., McCaffrey, K.J.W., Taylor, G., Tikoff, B. (Eds.) Vertical Coupling and Decoupling in the Lithosphere, Geol. Soc.-Lon. Special Publications, vol. 227, pp. 167-176.

Zeitler, P.K., Sutter, J.F., Williams, I.S., Zartman, R., Tahirkheli, R.A.K., 1989. Geochronology and temperature history of the Nanga Parbat-Haramosh Massif, Pakistan. In: Malinconico, L.L., Jr., Lillie, R.J. (Eds.) Tectonics of the Western Himalayas. Geological Society of America Special Paper, vol. 232, pp. 1-22.

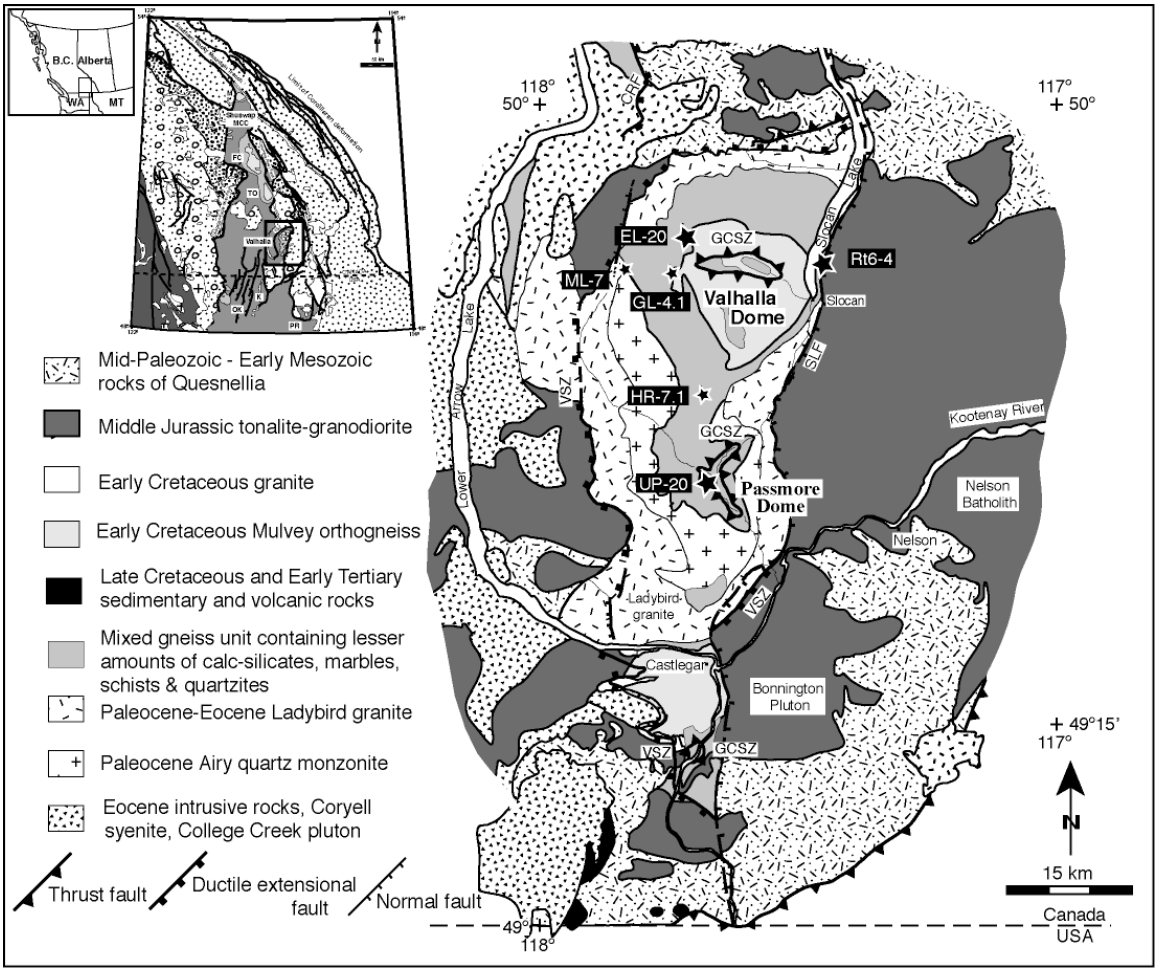

Figure 4.1: Simplified geologic map of the Valhalla complex, showing main lithological units, structural elements and sample locations. GCSZ, Gwillim Creek shear zone; SLF, Slocan Lake fault; VSZ, Valkyr shear zone (modified after Schaubs et al., 2002). Inset is a simplified geologic map of the Canadian Cordillera and the Omineca belt (modified after Wheeler and McFeely (1991) and Vanderhaeghe et al. (2003)).

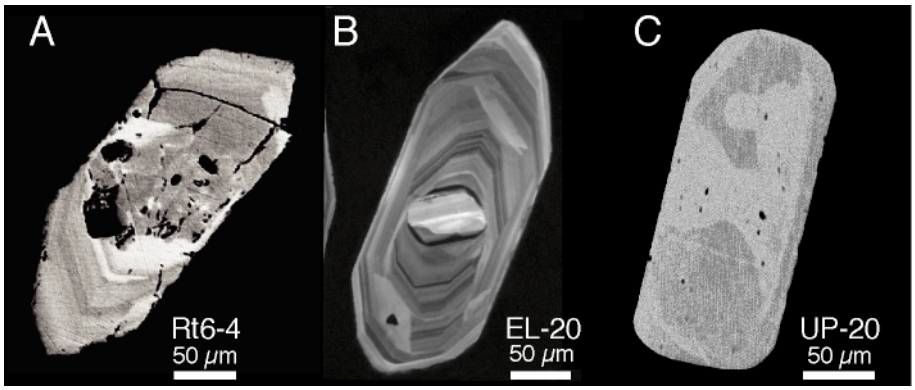

Figure 4.2: Representative cathodoluminescene and backscatter images for the three samples: (A) Rt6-4; (B) EL-20; and (C) UP-20. Note the lack of complex zoning in the grains.

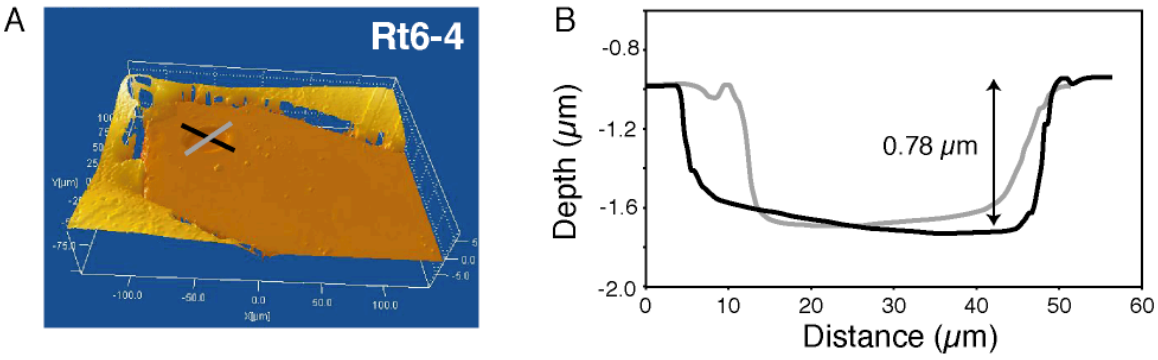

Figure 4.3: Representative images of a zircon grain analyzed in this study. (A) Microxam profilometer image illustrating that the zircon grains were flush with the epoxy. The image also shows the pit created during a U-Pb depth profiling analysis as the ion beam sputters into the grain. The lines shown across the pit represent the location of the cross sections shown in B. (B) Cross sections of a pit created during U-Pb depth profiling analysis. Note the vertical exaggeration.

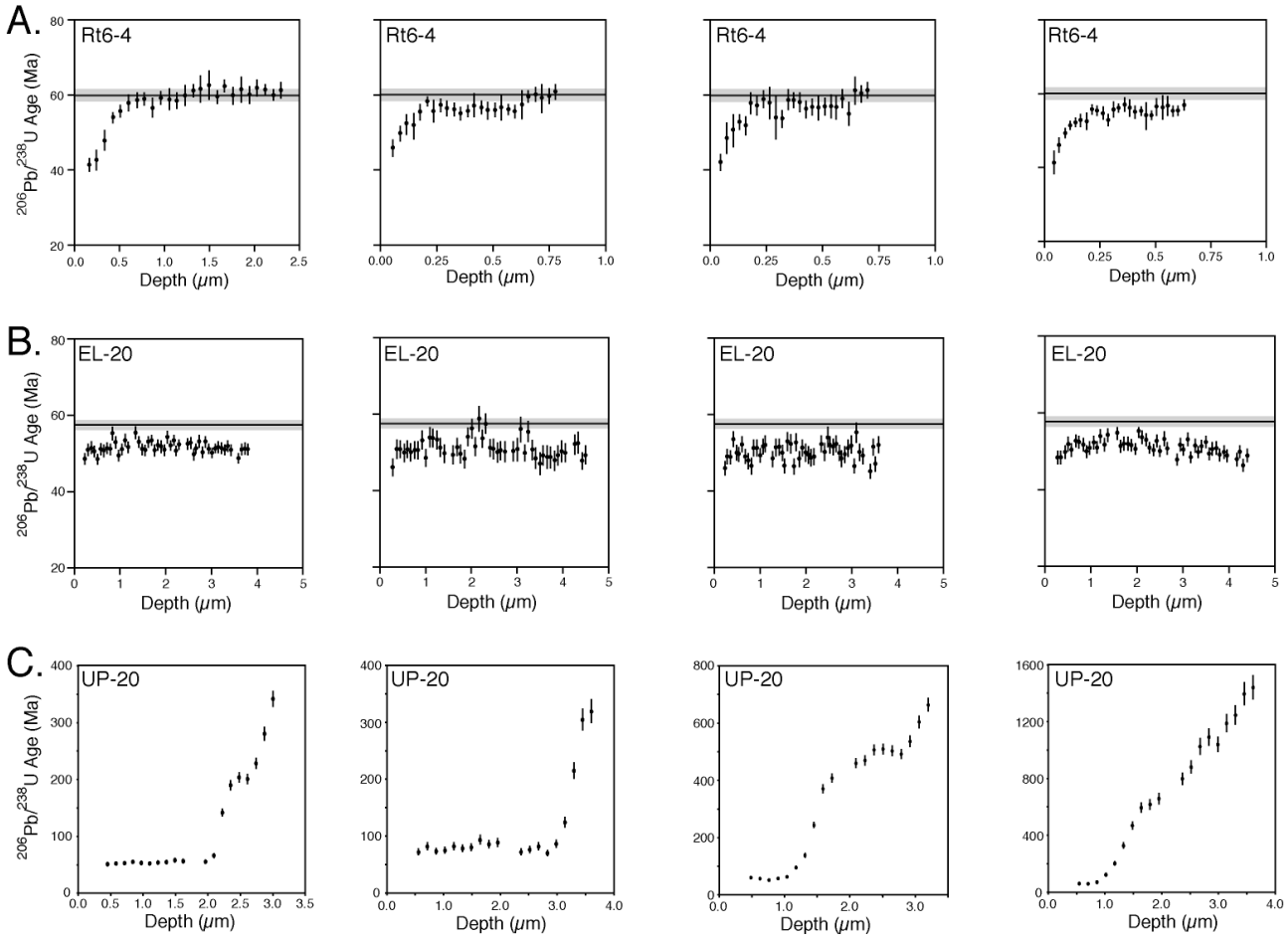

Figure 4.4: ^{238}U-^{206}Pb age versus depth diagrams for the three samples: (A) Rt6-4; (B) EL-20; and (C) UP-20. The depth represents the amount the ion beam sputtered into the crystal with 0 equaling the surface of the grain. Note the difference in scales for the samples.

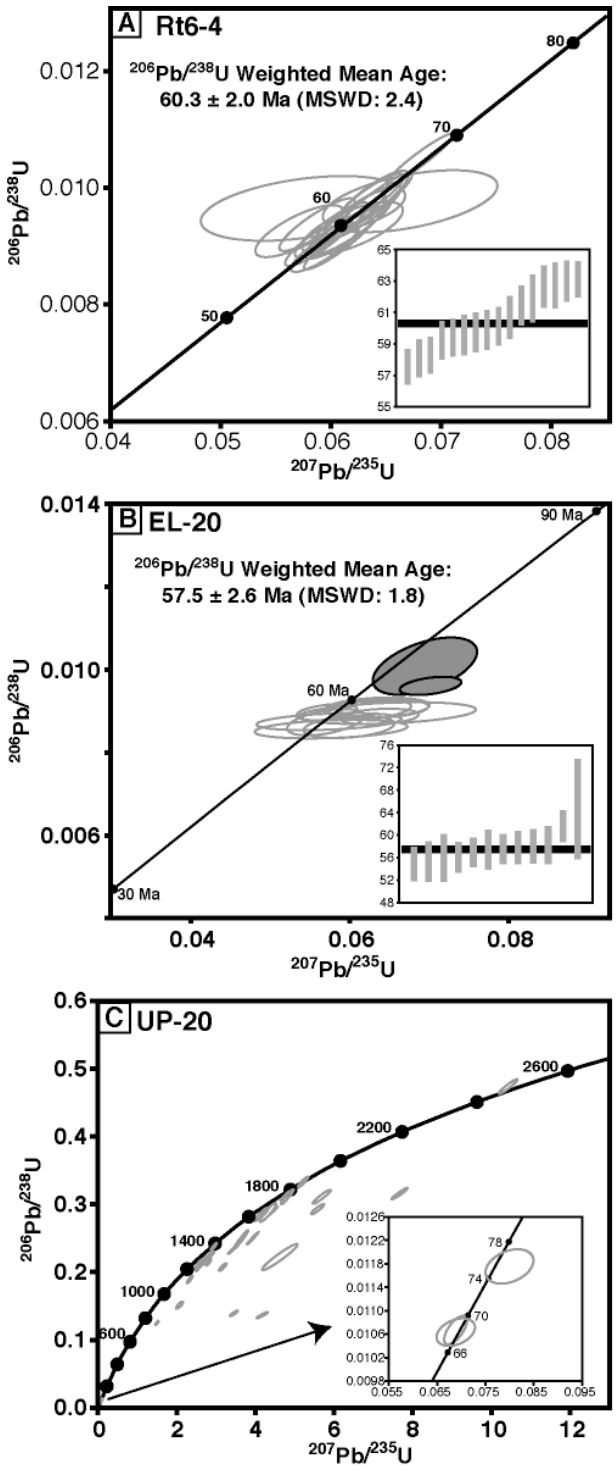

Figure 4.5: Zircon U-Pb results from the Valhalla complex. U-Pb concordia diagram for (A) Rt6-4.1; (B) EL-20; and (C) UP-20. The filled ellipses were not included in the calculation of the $^{238}U/^{206}Pb$ concordant ages. The inset for (A) and (B) illustrates the individual spot analyses used for the calculation of the weighted mean ages.

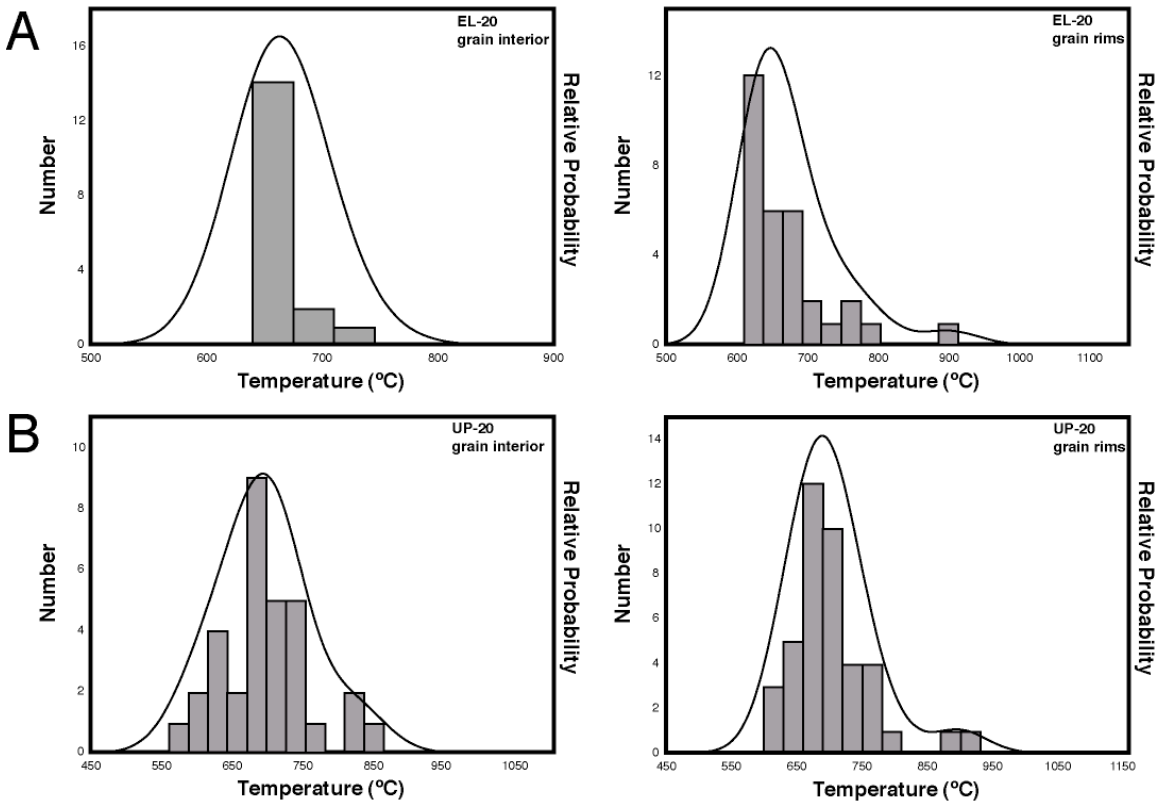

Figure 4.6: Ti in zircon thermometry results from the interior and rims of the zircons. Relative probability diagrams are shown including the histograms for samples (A) EL-20 and (B) UP-20.

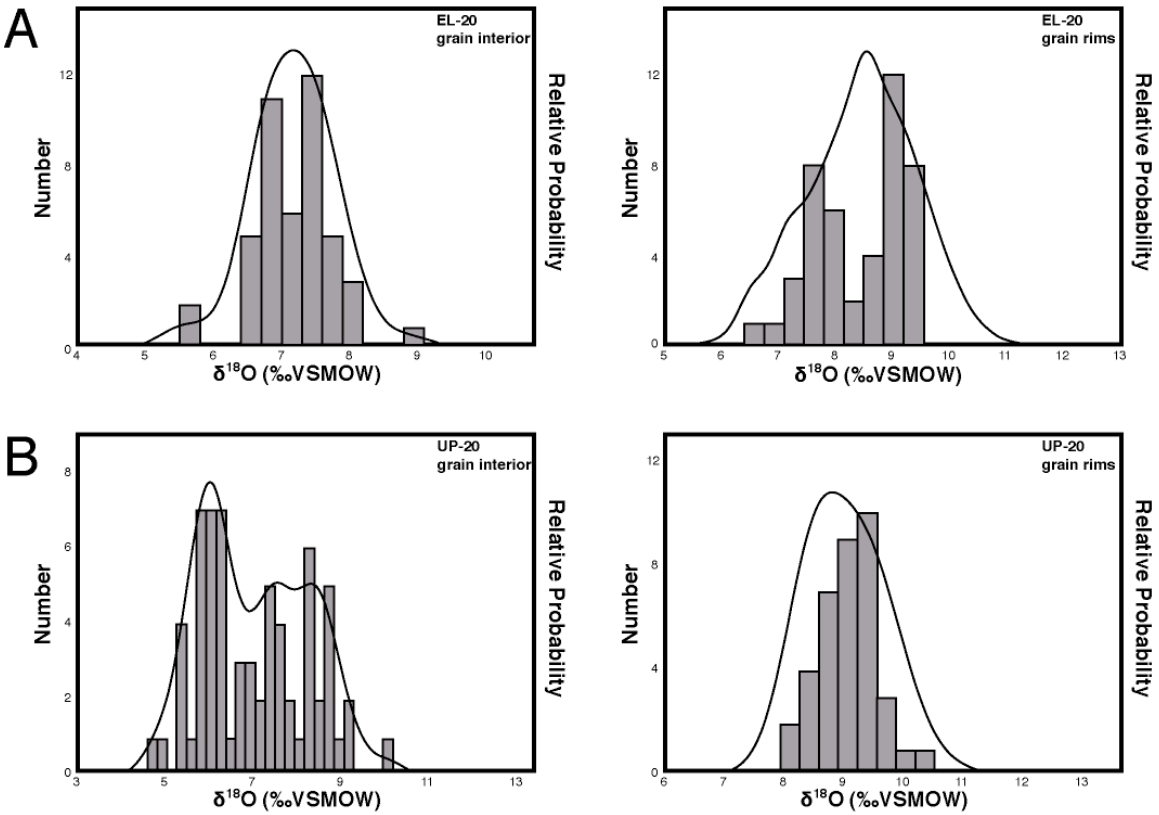

Figure 4.7: Oxygen isotope results from the interior and rims of the zircons. Relative probability diagrams are shown including the histograms for samples (A) EL-20 and (B) UP-20.

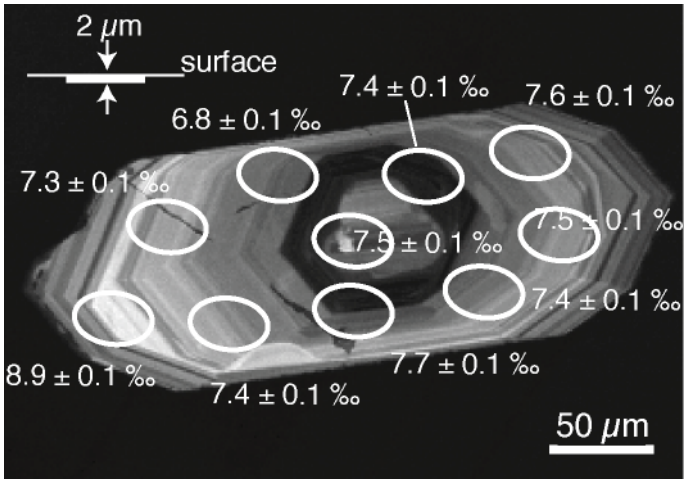

Figure 4.8: Cathodoluminescene image of a zircon grain from sample EL-20, illustrating the variation in oxygen isotope results across a single grain. Individual spot analyses are shown. Note the heaviest $\delta^{18}O$ values are from the rim of the zircon, and the lightest $\delta^{18}O$ values are from the interior of the grains. Inset shows sputter crater cross-section drawn to scale to illustrate spatial resolution in depth profiling mode parallel to zircon growth zones.

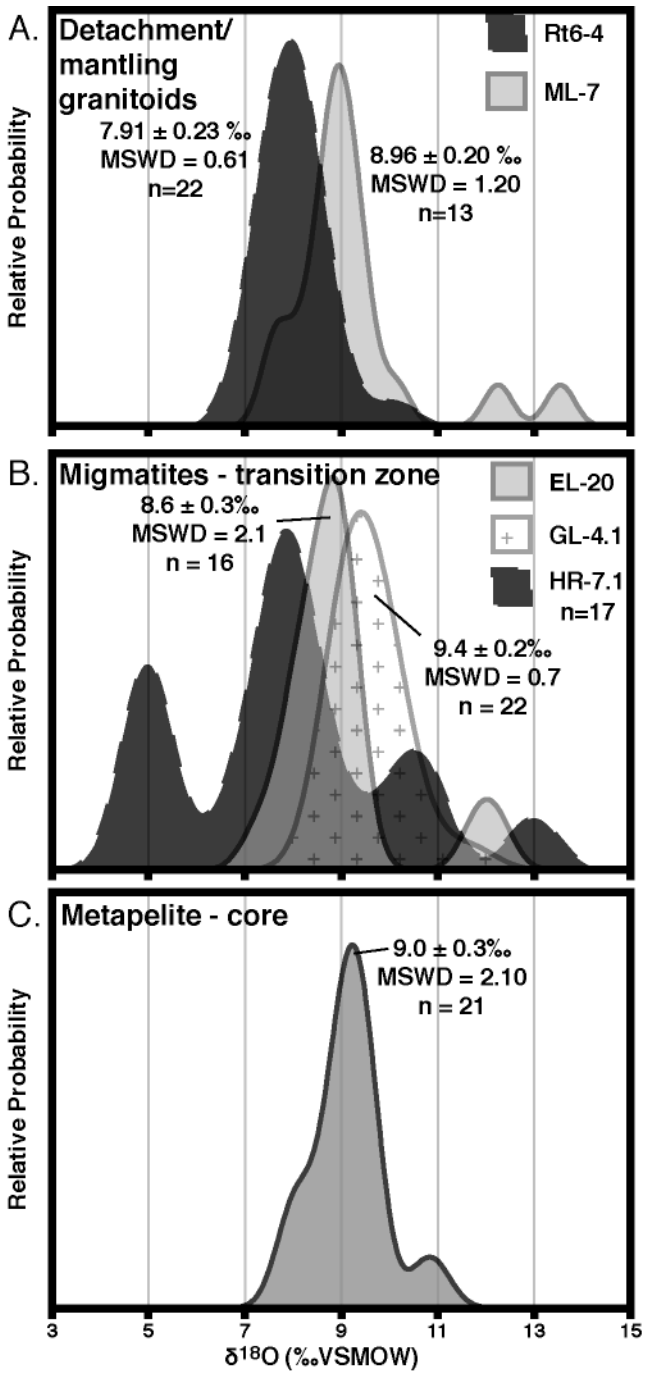

Figure 4.9: Oxygen isotope results from the monazite. Relative probability diagrams display the monazite results. Samples are divided by structural locality in the dome: (A) detachment/mantling granitoids including Rt-6 and ML-7; (B) migmatites from the transition zone including EL-20, GL-4.1, and HR-7.1; and (C) metapelite from the core, UP-20.

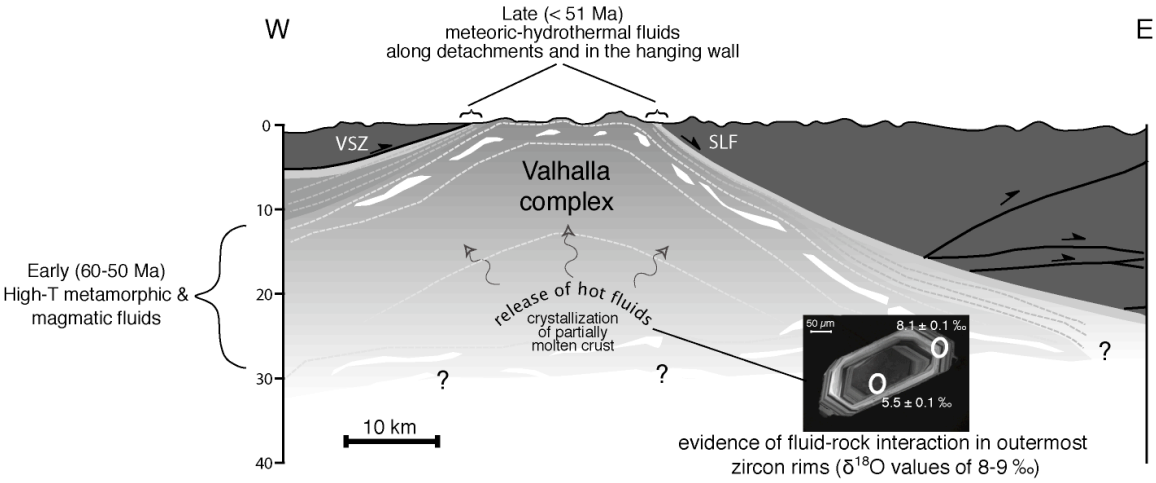

Figure 4.10: Simplified geologic cross section of the current location of the Valhalla complex revealing the position of the two early Tertiary hydrothermal regimes found in the complex: 1) meteoric waters, and 2) magmatic/metamorphic fluids (after Cook et al., 1988). White bodies are representative of the granitoids present in the Valhalla complex.

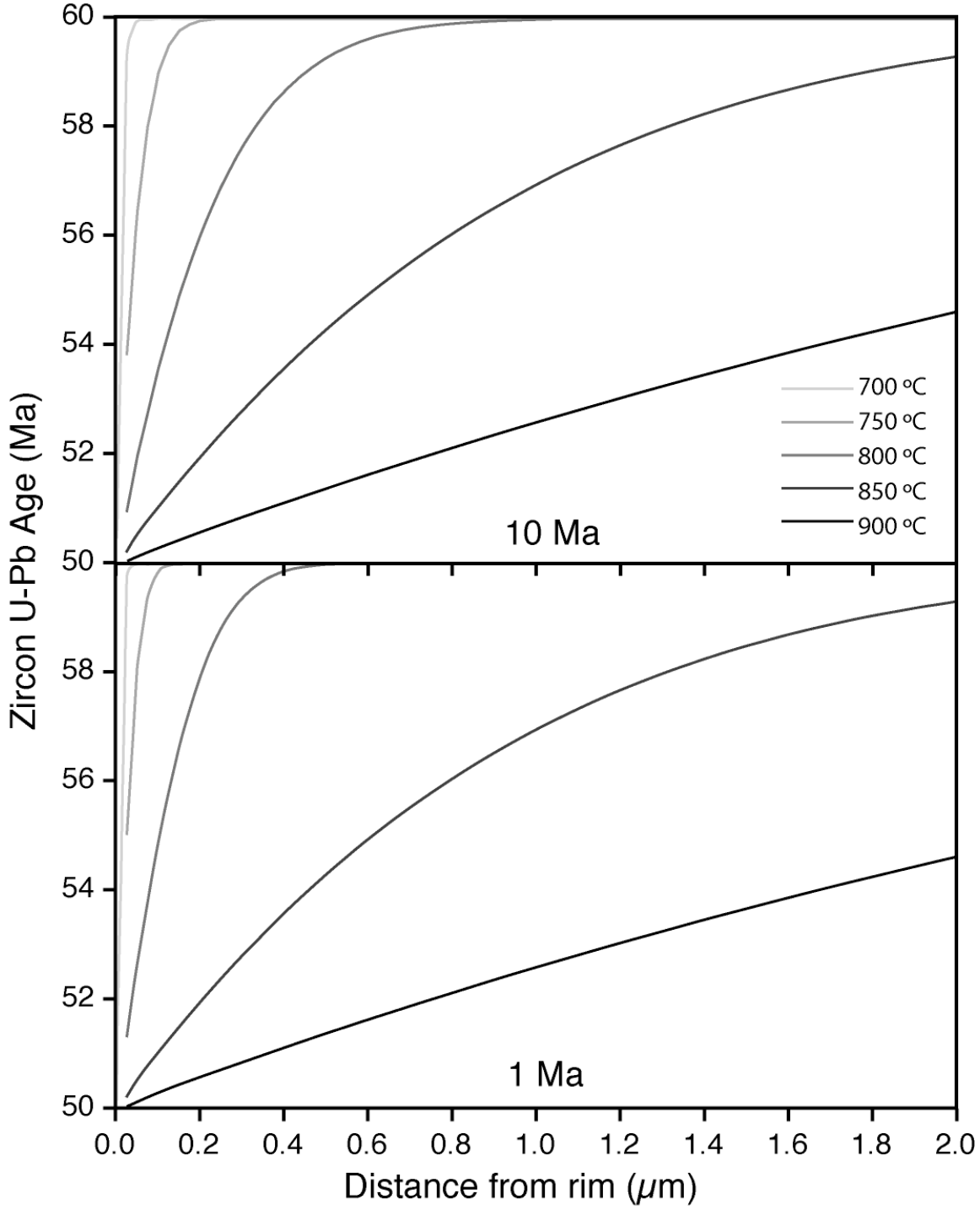

Figure 4.11: Diffusion calculation results that show age profiles predicted for temperatures from 900 ºC to 700 ºC under two conditions: holding the grains at these temperatures for 1 m.y. or 10 m.y.

Table 4.2: Analytical U-Pb zircon isotopic data from conventional polished analyses

Grain[a]	Th (est. ppm)	U (est. ppm)	Th/U	$^{207}Pb/^{206}Pb$	$^{207}Pb/^{235}U$	$^{206}Pb/^{238}U$	% Radiogenic ^{207}Pb	% Radiogenic ^{206}Pb	$^{207}Pb/^{206}Pb$[b] Age (Ma)	1 s.e.	$^{207}Pb/^{235}U$ Age (Ma)	1 s.e.	$^{206}Pb/^{238}U$ Age (Ma)	1 s.e.
Rt6-4 Leucosome crystallized in a boudin neck														
1sp1	83.5	8932.7	0.009	0.047	0.064	0.010	98.10	99.90	76.8	19.9	63.0	1.3	62.6	1.3
1sp2	155.0	13609.2	0.011	0.047	0.068	0.010	99.60	100.00	51.7	13.8	66.8	1.2	67.2	1.2
2sp1	74.1	4970.3	0.014	0.047	0.063	0.010	99.10	99.90	74.3	27.1	61.8	1.4	61.4	1.2
2sp2	32.9	3719.4	0.008	0.044	0.059	0.009	98.90	99.90	0.0	0.0	58.0	1.4	60.1	1.2
3sp1	54.4	7284.4	0.007	0.046	0.064	0.010	99.60	100.00	53.2	26.6	62.7	1.3	63.0	1.2
3sp2	85.9	9408.5	0.009	0.047	0.064	0.010	99.20	100.00	45.4	21.4	62.6	1.2	63.1	1.1
4sp1	334.7	629.7	0.507	0.048	0.057	0.010	86.00	99.20	0.0	0.0	56.7	3.6	61.9	1.4
4sp2	373.1	672.4	0.530	0.049	0.067	0.010	89.40	99.30	187.7	97.1	66.0	3.1	62.7	1.4
5sp1	29.7	4163.8	0.007	0.048	0.059	0.009	99.50	100.00	102.1	24.6	58.6	1.2	57.6	1.1
6sp1	29.4	3967.1	0.007	0.047	0.059	0.009	98.80	99.90	49.3	23.9	58.1	1.2	58.3	1.1
7sp1	50.0	1566.6	0.030	0.043	0.057	0.009	97.00	99.80	0.0	0.0	56.4	1.6	59.4	1.1
12sp2	86.7	5256.5	0.016	0.047	0.062	0.009	99.80	100.00	109.4	20.4	61.1	1.3	59.9	1.2
13sp1	57.7	4762.8	0.012	0.046	0.062	0.009	85.60	99.00	110.7	52.0	61.0	1.8	59.7	1.2
14sp1	76.6	7713.5	0.009	0.047	0.061	0.009	93.90	99.60	101.7	26.0	60.3	1.4	59.3	1.2
15sp1	47.8	6225.6	0.007	0.047	0.061	0.009	97.10	99.80	127.4	19.6	59.8	1.2	58.1	1.2
16sp1	56.8	3501.9	0.015	0.043	0.060	0.009	99.40	100.00	44.4	24.1	59.2	1.3	59.6	1.2
19sp1	92.5	9041.0	0.010	0.047	0.061	0.009	100.00	100.00	57.3	20.8	60.6	1.4	60.7	1.3
EL-20 Migmatite														
1sp1	171.3	591.8	0.289	0.051	0.064	0.009	74.88	97.98	243.6	218.0	62.7	6.0	58.1	1.4
2sp1	63.4	393.1	0.161	0.060	0.577	0.070	59.19	95.27	592.9	82.1	462.2	16.5	436.4	8.8
4sp1	101.9	901.1	0.113	0.031	0.093	0.022	37.42	94.08	-1.0	0.0	90.7	6.7	138.5	3.4
5sp1	183.1	726.2	0.252	0.052	0.064	0.009	78.56	98.31	292.0	172.0	62.7	4.7	56.9	1.2
6sp1	254.0	1013.1	0.251	0.053	0.070	0.010	83.75	98.77	328.5	116.0	68.9	3.7	61.6	1.3
7sp1	65.0	350.0	0.186	0.051	0.063	0.009	72.30	97.71	226.9	233.0	62.5	6.3	58.3	1.6
10sp1	206.3	956.4	0.216	0.046	0.057	0.009	80.51	98.67	8.9	148.0	56.4	3.7	57.6	1.2
11sp1	173.1	778.0	0.222	0.050	0.069	0.010	79.93	98.51	193.8	196.0	68.2	6.2	64.7	4.4
12sp1	134.9	602.0	0.224	0.051	0.063	0.009	81.96	98.67	231.7	153.0	62.1	4.4	57.8	1.4
13sp1	61.0	453.2	0.135	0.047	0.057	0.009	75.90	98.21	66.3	176.0	56.3	4.6	56.0	2.0
15sp1	36.1	378.8	0.095	0.049	0.058	0.009	59.27	96.12	141.0	378.0	56.9	9.2	54.9	1.4
16sp1	52.6	730.5	0.072	0.050	0.060	0.009	76.41	98.16	214.5	211.0	59.1	5.5	55.3	1.7
18sp1	201.3	724.5	0.278	0.048	0.057	0.009	63.11	96.75	81.1	361.0	56.7	8.7	56.1	1.3
19sp1	65.3	359.1	0.182	0.053	0.065	0.009	58.99	95.79	307.7	378.0	63.7	10.7	57.4	1.7
UP-20 Metapelite														
1sp1in	52.8	208.6	0.253	0.106	4.216	0.287	99.65	99.95	1739.0	11.4	1677.0	15.1	1628.0	25.9
4sp1in	34.6	178.2	0.194	0.105	4.099	0.284	99.54	99.94	1710.0	13.8	1654.0	16.8	1610.0	26.9

5sp1in	54.4	167.1	0.325	0.176	7.655	0.316	99.88	99.98	2615.0	9.1	2191.0	15.7	1768.0	26.6
6sp1in	9.5	781.8	0.012	0.047	0.069	0.011	95.97	99.76	46.5	85.4	67.6	2.5	68.2	1.0
7sp1in	190.0	179.6	1.058	0.112	4.765	0.308	99.88	99.98	1834.0	12.3	1779.0	14.9	1732.0	24.7
8sp1in	35.4	492.9	0.072	0.111	4.453	0.291	99.91	99.99	1817.0	5.3	1722.0	12.2	1645.0	20.7
9sp1in	36.3	477.1	0.076	0.179	3.452	0.140	99.93	99.99	2645.0	12.3	1516.0	15.2	843.3	15.3
10sp1in	9.2	602.4	0.015	0.049	0.080	0.012	95.37	99.71	164.8	90.0	78.2	3.1	75.3	1.2
11sp1in	22.3	350.1	0.064	0.221	4.169	0.137	99.83	99.96	2989.0	13.3	1668.0	18.3	826.2	17.2
12sp1in	5.5	759.7	0.007	0.086	1.495	0.126	99.99	100.00	1342.0	17.0	928.5	11.8	764.3	13.4
15sp1in	68.8	257.7	0.267	0.138	5.575	0.293	99.84	99.97	2201.0	13.5	1912.0	16.8	1657.0	25.6
18sp1in	9.0	1090.0	0.008	0.089	2.931	0.238	99.91	99.99	1411.0	9.8	1390.0	13.2	1376.0	21.3
19sp1in	300.4	659.0	0.456	0.110	4.753	0.313	99.92	99.99	1801.0	5.6	1777.0	13.7	1756.0	24.6
20sp1in	5.3	501.4	0.011	0.089	2.690	0.219	99.85	99.98	1404.0	10.4	1326.0	11.2	1278.0	16.7
21sp1in	164.8	504.9	0.326	0.160	10.420	0.474	99.93	99.99	2452.0	8.1	2473.0	14.1	2500.0	30.7
22sp1in	5.8	195.5	0.030	0.113	5.203	0.333	99.90	99.99	1854.0	10.4	1853.0	14.8	1852.0	26.3
23sp1in	9.4	933.4	0.010	0.089	2.543	0.207	99.95	99.99	1410.0	15.4	1284.0	13.7	1211.0	19.4
24sp1in	13.4	1486.8	0.009	0.047	0.069	0.011	98.48	99.91	37.1	41.3	67.6	1.5	68.4	1.0
g1sp1al	170.0	282.3	0.602	0.114	3.929	0.250	100.00	100.00	1862.0	8.5	1620.0	21.6	1440.0	32.5
g3sp1al	59.5	299.3	0.199	0.089	2.593	0.212	100.00	100.00	1395.0	14.0	1299.0	15.4	1241.0	20.5
g4sp1al	581.0	113.9	5.102	0.109	4.319	0.288	99.68	99.96	1776.0	21.5	1697.0	26.3	1634.0	46.0
g5sp1al	132.0	230.1	0.574	0.092	2.845	0.225	99.70	99.97	1461.0	16.8	1368.0	21.6	1308.0	31.5
g6sp1al	324.0	222.8	1.454	0.132	5.676	0.311	99.98	100.00	2130.0	17.0	1928.0	23.1	1746.0	33.4
g7sp1al	72.3	701.0	0.103	0.106	3.398	0.232	99.98	100.00	1733.0	8.8	1504.0	15.8	1347.0	21.7
g8sp1al	545.0	457.7	1.191	0.111	3.165	0.208	99.98	100.00	1810.0	17.0	1449.0	14.7	1215.0	18.6
g9sp1al	389.0	95.9	4.058	0.106	3.626	0.248	99.85	99.98	1729.0	14.7	1555.0	28.3	1430.0	49.8
g11sp1al	110.0	44.7	2.462	0.150	4.618	0.223	99.68	99.94	2351.0	30.8	1753.0	54.4	1296.0	67.5
g14sp1al	588.0	503.3	1.168	0.099	2.072	0.152	99.92	99.99	1602.0	24.3	1140.0	19.4	912.5	19.2
g15sp1al	448.0	619.7	0.723	0.095	2.803	0.215	100.00	100.00	1521.0	12.8	1356.0	13.3	1254.0	18.7
g17sp1al	203.0	728.3	0.279	0.089	2.327	0.190	99.95	99.99	1400.0	13.8	1221.0	15.7	1122.0	21.4

[a]Grain, spot number, in=indium mount, al=aluminum mount.

Table 4.3: Analytical oxygen isotope compositions of zircon

Grain	$^{18}O/^{16}O$ measured (x1000)	internal precision (1 SD x1000)	delta^{18}O V-SMOW (‰)*	delta^{18}O V-SMOW (1 SD ‰)*
EL20 Migmatite - unpolished rims				
EL20_m2_g1@1.ais	2.0200	0.000251	8.1	0.3
EL20_m2_g1@2.ais	2.0199	0.000131	8.1	0.3
EL20_m2_g2@1.ais	2.0215	0.000116	8.9	0.3
EL20_m2_g2@2.ais	2.0205	0.000217	8.4	0.3
EL20_m2_g3@1.ais	2.0217	0.000153	9.0	0.3
EL20_m3_s1_g1@1.ais	2.0195	0.000149	8.5	0.3
EL20_m3_s1_g2@1.ais	2.0194	0.000143	8.5	0.3
EL20_m3_s1_g3@1.ais	2.0154	0.000181	6.5	0.3
EL20_m3_s1_g4@1.ais	2.0166	0.000156	7.1	0.3
EL20_inM1_g1_s1.ais	2.0233	0.000137	9.2	0.7
EL20_inM1_g1_s2.ais	2.0229	0.000101	9.0	0.7
EL20_inM1_g2_s1.ais	2.0209	0.000184	8.0	0.7
EL20_inM1_g2_s2.ais	2.0203	0.000203	7.7	0.7
EL20_inM1_g3_s1.ais	2.0223	0.000112	8.7	0.7
EL20_inM1_g3_s2.ais	2.0231	0.000184	9.1	0.7
EL20_inM1_g4_s1.ais	2.0234	0.000156	9.2	0.7
EL20_inM1_g4_s2.ais	2.0235	0.000129	9.3	0.7
EL20_inM1_g5_s1.ais	2.0238	0.000146	9.4	0.7
EL20_inM1_g5_s2.ais	2.0234	0.000151	9.2	0.7
EL20_inM1_g6_s1.ais	2.0203	0.000125	7.7	0.7
EL20_inM1_g6_s2.ais	2.0203	0.000143	7.7	0.7
EL20_inM1_g7_s1.ais	2.0231	0.000175	9.1	0.7
EL20_inM1_g7_s2.ais	2.0230	0.000161	9.0	0.7
EL20_inM1_g8_s1.ais	2.0233	0.000127	9.2	0.7
EL20_inM1_g8_s2.ais	2.0235	0.000094	9.3	0.7
EL20_inM1_g9_s1.ais	2.0215	0.000162	8.3	0.7
EL20_inM1_g10_s1.ais	2.0203	0.000170	7.7	0.7
EL20_inM1_g10_s2.ais	2.0204	0.000125	7.7	0.7
EL20_inM1_g11_s1.ais	2.0229	0.000131	9.0	0.7
EL20_inM1_g11_s2.ais	2.0232	0.000195	9.1	0.7
EL20_inM1_g13_s2.ais	2.0234	0.000123	9.2	0.7
EL20_inM1_g14_s1.ais	2.0210	0.000102	8.1	0.7
EL20_inM1_g14_s2.ais	2.0202	0.000175	7.6	0.7
EL20_inM1_g12_s1.ais	2.0203	0.000180	7.7	0.7
EL20_inM1_g12_s2.ais	2.0208	0.000093	7.9	0.7
EL20_inM1_g13_s1.ais	2.0228	0.000117	9.0	0.7
EL20_inM1_g15_s1.ais	2.0212	0.000142	8.1	0.7
EL20_inM1_g16_s1.ais	2.0191	0.000185	7.1	0.7
EL20_inM1_g16_s2.ais	2.0196	0.000125	7.3	0.7
EL20_inM1_g17_s1.ais	2.0204	0.000123	7.7	0.7
EL20_inM1_g17_s2.ais	2.0198	0.000110	7.4	0.7
EL20_inM1_g19_s2.ais	2.0235	0.000129	9.3	0.7
EL20_inM1_g18_s1.ais	2.0229	0.000104	9.0	0.7
EL20_inM1_g18_s2.ais	2.0226	0.000092	8.8	0.7
EL20_inM1_g19_s1.ais	2.0240	0.000186	9.5	0.7
EL20 Migmatite - interior				
GM1_EL20_g24@1.ais	2.0166	0.000291	7.0	0.3
GM1_EL20_g24@2.ais	2.0169	0.000152	7.2	0.3
GM1_EL20_g23@1.ais	2.0182	0.000129	7.8	0.3
GM1_EL20_g23@2.ais	2.0154	0.000220	6.4	0.3
GM1_EL20_g22@1.ais	2.0162	0.000151	6.8	0.3
GM1_EL20_g22@2.ais	2.0138	0.000135	5.7	0.3
GM1_EL20_g21@1.ais	2.0161	0.000124	6.8	0.3

GM1_EL20_g21@2.ais	2.0163	0.000106	6.9	0.3
GM1_EL20_g20@1.ais	2.0175	0.000149	7.5	0.3
GM1_EL20_g20@2.ais	2.0161	0.000186	6.8	0.3
GM1_EL20_g19@1.ais	2.0159	0.000242	6.7	0.3
GM1_EL20_g19@2.ais	2.0160	0.000116	6.7	0.3
GM1_EL20_g18@1.ais	2.0185	0.000125	8.0	0.3
GM1_EL20_g18@2.ais	2.0172	0.000203	7.3	0.3
GM1_EL20_g17@1.ais	2.0164	0.000193	6.9	0.3
GM1_EL20_g17@2.ais	2.0159	0.000134	6.7	0.3
GM1_EL20_g16@1.ais	2.0057	0.000136	1.6	0.3
GM1_EL20_g16@2.ais	2.0066	0.000165	2.1	0.3
GM1_EL20_g15@1.ais	2.0159	0.000195	6.7	0.3
GM1_EL20_g15@2.ais	2.0167	0.000129	7.1	0.3
GM1_EL20_g14@1.ais	2.0162	0.000161	6.8	0.3
GM1_EL20_g14@2.ais	2.0157	0.000103	6.6	0.3
GM1_EL20_g13@1.ais	2.0168	0.000185	7.1	0.3
GM1_EL20_g13@2.ais	2.0164	0.000119	6.9	0.3
GM1_EL20_g12@1.ais	2.0186	0.000156	8.0	0.3
GM1_EL20_g12@2.ais	2.0178	0.000199	7.6	0.3
GM1_EL20_g11@1.ais	2.0157	0.000199	6.6	0.3
GM1_EL20_g11@2.ais	2.0172	0.000208	7.4	0.3
EL20_m2_s2@1.ais	2.0165	0.000220	7.8	0.3
EL20_m2_s2@2.ais	2.0144	0.000250	6.7	0.3
EL20_m2_s2@3.ais	2.0156	0.000193	7.3	0.3
EL20_m2_s2@4.ais	2.0164	0.000142	7.7	0.3
EL20_m2_s2@5.ais	2.0120	0.000198	5.5	0.3
EL20_m2_s2@6.ais	2.0160	0.000147	7.5	0.3
EL20_m2_s2@7.ais	2.0154	0.000128	7.2	0.3
EL20_m2_s2@8.ais	2.0155	0.000100	7.3	0.3
EL20_m2_s2@9.ais	2.0173	0.000165	8.2	0.3
EL20_m2_s2_g2@1.ais	2.0161	0.000228	7.6	0.3
EL20_m2_s2_g2@2.ais	2.0160	0.000238	7.5	0.3
EL20_m2_s2_g2@3.ais	2.0158	0.000154	7.4	0.3
EL20_m2_s2_g2@4.ais	2.0158	0.000152	7.4	0.3
EL20_m2_s2_g2@5.ais	2.0163	0.000174	7.6	0.3
EL20_m2_s2_g2@6.ais	2.0161	0.000179	7.5	0.3
EL20_m2_s2_g2@7.ais	2.0146	0.000108	6.8	0.3
EL20_m2_s2_g2@8.ais	2.0156	0.000125	7.3	0.3
EL20_m2_s2_g2@9.ais	2.0157	0.000109	7.4	0.3
EL20_m2_s2_g2@10.ais	2.0188	0.000189	8.9	0.3

*after correction for instrumental mass fractionation using Pacoima and AS3 zircon standard

Table 4.4: Analytical oxygen isotope compositions of monazite

Grain	$^{18}O/^{16}O$ measured (x1000)	internal precision (1 SD x1000)	delta^{18}O V-SMOW (‰)*	delta^{18}O V-SMOW (1 SD ‰)*
Rt6-4 Leucosome crystallized in a boudin neck				
Rt6_m06_g1@1.ais	2.015023	0.000104662	7.64672	0.53024
Rt6_m06_g2_s1.ais	2.014753	7.11413E-05	7.5117	0.53024
Rt6_m06_g3_s1.ais	2.015169	0.000105012	7.71973	0.53024
Rt6_m06_g4_s1.ais	2.015167	9.0496E-05	7.71873	0.53024
Rt6_m06_g5_s1.ais	2.014325	8.27201E-05	7.29767	0.53024
Rt6_m06_g6_s1.ais	2.014128	0.00014968	7.19916	0.53024
Rt6_m06_g7_s1.ais	2.015181	9.6082E-05	7.72573	0.53024
Rt6_m06_g9_s1.ais	2.015086	0.000106611	7.67822	0.53024
Rt6_m06_g10_s1.ais	2.016329	9.89404E-05	8.2998	0.53024
Rt6_m06_g11_s1.ais	2.015829	0.000113593	8.04977	0.53024
Rt6_m06_g12_s1.ais	2.014362	9.72928E-05	7.31617	0.53024
Rt6_m06_g13_s1.ais	2.015568	0.000131578	7.91925	0.53024
Rt6_m06_g14_s1.ais	2.015985	0.000118394	8.12778	0.53024
Rt6_m06_g15_s1.ais	2.015717	0.0001179	7.99376	0.53024
Rt6_m06_g16_s1.ais	2.014985	8.73008E-05	7.62771	0.53024
Rt6_m06_g17_s1.ais	2.017055	0.000108267	8.66285	0.53024
Rt6_m06_g18_s1.ais	2.016253	0.000134742	8.2618	0.53024
Rt6_m06_g19_s1.ais	2.01651	8.04891E-05	8.39032	0.53024
Rt6_m06_g20_s1.ais	2.016709	0.000131987	8.48983	0.53024
Rt6_m06_g21_s1.ais	2.016355	9.23025E-05	8.31281	0.53024
Rt6_m06_g22_s1.ais	2.016208	8.16611E-05	8.2393	0.53024
EL-20 Migmatite				
EL20mon_inM1_g1_s1.ais	2.023752	0.000206509	12.2134	0.37483
EL20mon_inM1_g1_s2.ais	2.022956	9.27093E-05	11.8152	0.37483
EL20mon_inM1_g2_s1.ais	2.016448	0.000163253	8.56015	0.37483
EL20mon_inM1_g3_s1.ais	2.01683	0.000160257	8.75122	0.37483
EL20mon_inM1_g4_s1.ais	2.016867	0.000144357	8.76972	0.37483
EL20mon_inM1_g5_s1.ais	2.017578	0.000112248	9.12534	0.37483
EL20mon_inM1_g6_s1.ais	2.017717	0.000158699	9.19487	0.37483
EL20mon_inM1_g7_s1.ais	2.017577	8.15252E-05	9.12484	0.37483
EL20mon_inM1_g8_s1.ais	2.016905	9.88981E-05	8.78873	0.37483
EL20mon_inM1_g9_s1.ais	2.016924	9.72203E-05	8.79823	0.37483
EL20mon_inM1_g10_s1.ais	2.016088	0.000204608	8.38009	0.37483
EL20mon_inM1_g11_s1.ais	2.016004	0.000190367	8.33808	0.37483
EL20mon_inM1_g11_s2.ais	2.015442	0.000150111	8.05699	0.37483
EL20mon_inM1_g13_s1.ais	2.015351	0.000134868	8.01147	0.37483
EL20mon_inM1_g14_s1.ais	2.013902	0.000139145	7.28673	0.37483
EL20mon_inM1_g15_s1.ais	2.015121	9.69482E-05	7.89643	0.37483
EL20mon_inM1_g16_s1.ais	2.017265	0.000135841	8.96879	0.37483
EL20mon_inM1_g17_s1.ais	2.017665	0.000110754	9.16886	0.37483
UP-20 Migmatite				
UP20mon_inM1_g3_s1.ais	2.017944	0.000227335	9.3084	0.37483
UP20mon_inM1_g4_s1.ais	2.016925	0.000121115	8.79873	0.37483
UP20mon_inM1_g4_s2.ais	2.017893	7.24636E-05	9.28289	0.37483
UP20mon_inM1_g6_s1.ais	2.017893	0.000103267	9.28289	0.37483
UP20mon_inM1_g7_s1.ais	2.01764	0.000146171	9.15635	0.37483
UP20mon_inM1_g7_s2.ais	2.018348	0.000118575	9.51047	0.37483
UP20mon_inM1_g8_s1.ais	2.015408	0.0001193	8.03998	0.37483
UP20mon_inM1_g9_s1.ais	2.017726	0.000147979	9.19937	0.37483
UP20mon_inM1_g10_s1.ais	2.015032	0.000172386	7.85192	0.37483
UP20mon_inM1_g11_s1.ais	2.018498	9.63712E-05	9.5855	0.37483
UP20mon_inM1_g11_s2.ais	2.018507	0.000129375	9.59	0.37483
UP20mon_inM1_g11_s3.ais	2.017368	0.000165163	9.02031	0.37483

UP20mon_inM1_g12_s1.ais	2.017924	0.00013019	9.2984	0.37483
UP20mon_inM1_g12_s2.ais	2.018508	0.00013037	9.5905	0.37483
UP20mon_inM1_g13_s1.ais	2.017229	0.000139184	8.95078	0.37483
UP20mon_inM1_g14_s1.ais	2.018288	0.000103077	9.48046	0.37483
UP20mon_inM1_g15_s1.ais	2.020764	0.000122848	10.7189	0.37483
UP20mon_inM1_g16_s1.ais	2.015717	0.000206372	8.19453	0.37483
UP20mon_inM1_g17_s1.ais	2.017157	0.00017233	8.91477	0.37483
UP20mon_inM1_g18_s1.ais	2.017074	0.000160588	8.87326	0.37483
UP20mon_inM1_g18_s2.ais	2.016658	0.000130918	8.66519	0.37483
UP20mon_inM1_g19_s1.ais	2.015311	0.000100303	7.99146	0.37483
UP20mon_inM1_g21_s1.ais	2.021364	9.51019E-05	11.019	0.37483
ML-7 Ladybird leucogranite				
ML7_gm06_g1_s1.ais	2.013247	8.37805E-05	7.61305	0.29933
ML7_gm06_g2_s1.ais	2.013263	0.000116389	7.62106	0.29933
ML7_gm06_g4_s1.ais	2.014115	9.93701E-05	8.04747	0.29933
ML7_gm06_g5_s1.ais	2.015587	0.000128882	8.7842	0.29933
ML7_gm06_g7_s1.ais	2.014832	7.04138E-05	8.40633	0.29933
ML7_gm06_g8_s1.ais	2.015449	9.20638E-05	8.71513	0.29933
ML7_gm06_g9_s1.ais	2.015894	0.00010735	8.93785	0.29933
ML7_gm06_g10_s1.ais	2.015904	8.55092E-05	8.94285	0.29933
ML7_gm06_g12_s1.ais	2.016894	0.000134609	9.43834	0.29933
ML7_gm06_g13_s1.ais	2.016945	0.000126858	9.46387	0.29933
ML7_gm06_g14_s1.ais	2.016275	0.000120461	9.12854	0.29933
ML7_gm06_g15_s1.ais	2.016219	0.00011915	9.10051	0.29933
ML7_gm06_g16_s1.ais	2.015913	7.80041E-05	8.94736	0.29933
ML7_gm06_g17_s1.ais	2.01496	8.65718E-05	8.47039	0.29933
ML7_gm06_g18_s1.ais	2.016621	0.000124766	9.30171	0.29933
ML7_gm06_g19_s1.ais	2.015617	0.000125324	8.79921	0.29933
GL-4.1 Migmatitic quartzofeldspathic gneiss				
GL4_m06_g1_s1.ais	2.019221	0.000124312	9.746	0.53024
GL4_m06_g1_s2.ais	2.018799	0.000088514	9.53497	0.53024
GL4_m06_g2_s1.ais	2.017642	5.98453E-05	8.95639	0.53024
GL4_m06_g2_s2.ais	2.017169	6.71804E-05	8.71986	0.53024
GL4_m06_g3_s1.ais	2.01788	0.000159708	9.07541	0.53024
GL4_m06_g3_s2.ais	2.018071	7.55087E-05	9.17092	0.53024
GL4_m06_g4_s1.ais	2.01778	8.54385E-05	9.0254	0.53024
GL4_m06_g5_s1.ais	2.018053	0.000129977	9.16192	0.53024
GL4_m06_g6_s1.ais	2.019803	9.50539E-05	10.037	0.53024
GL4_m06_g7_s1.ais	2.019315	0.000109136	9.793	0.53024
GL4_m06_g8_s1.ais	2.019771	0.000101031	10.021	0.53024
GL4_m06_g9_s1.ais	2.018698	0.000142407	9.48446	0.53024
GL4_m06_g12_s1.ais	2.019972	0.000137162	10.1215	0.53024
GL4_m06_g13_s1.ais	2.019491	0.000110245	9.88102	0.53024
GL4_m06_g14_s1.ais	2.01818	0.000125852	9.22543	0.53024
GL4_m06_g15_s1.ais	2.020051	0.000128866	10.1611	0.53024
GL4_m06_g16_s1.ais	2.018046	0.000106718	9.15842	0.53024
GL4_m06_g17_s1.ais	2.017786	9.85938E-05	9.0284	0.53024
GL4_m06_g18_s1.ais	2.017146	0.000104374	8.70836	0.53024
GL4_m06_g18_s2.ais	2.018439	9.57738E-05	9.35495	0.53024
GL4_m06_g19_s1.ais	2.018331	0.000134057	9.30094	0.53024
GL4_m06_g20_s1.ais	2.019068	0.000148625	9.66949	0.53024
HR-7.1 Grt-bearing migmatitic gneiss				
HR7_m06_g1_s1.ais	2.01552	0.000115782	7.89525	0.53024
HR7_m06_g2_s1.ais	2.013173	0.000150135	6.72159	0.53024
HR7_m06_g3_s1.ais	2.009609	6.67185E-05	4.93935	0.53024
HR7_m06_g4_s1.ais	2.015184	0.000100837	7.72723	0.53024
HR7_m06_g7_s1.ais	2.02571	0.000193066	12.9909	0.53024
HR7_m06_g8_s1.ais	2.019324	0.000184149	9.79751	0.53024

HR7_m06_g9_s1.ais	2.016741	0.000103952	8.50583	0.53024
HR7_m06_g10_s1.ais	2.015543	0.000108914	7.90675	0.53024
HR7_m06_g11_s1.ais	2.014526	0.000141179	7.39818	0.53024
HR7_m06_g12_s1.ais	2.01489	7.56783E-05	7.58021	0.53024
HR7_m06_g13_s1.ais	2.016901	0.000104299	8.58584	0.53024
HR7_m06_g14_s1.ais	2.020956	8.39394E-05	10.6136	0.53024
HR7_m06_g15_s1.ais	2.021247	0.000120185	10.7591	0.53024
HR7_m06_g16_s1.ais	2.009669	0.000124796	4.96936	0.53024
HR7_m06_g20_s1.ais	2.015691	0.000104185	7.98076	0.53024
HR7_m06_g21_s1.ais	2.009464	0.000101098	4.86684	0.53024
HR7_m06_g22_s1.ais	2.010033	9.80306E-05	5.15138	0.53024

*after correction for instrumental mass fractionation using 554 monazite standard

APPENDIX

In order to test whether the $^{238}U/^{206}Pb$ age profiles created with the depth profiling represent Pb diffusion profiles, we undertook diffusion calculations to model age profiles measured for sample RT6-4 (see text). A single diffusion domain, episodic loss model was used with an activation energy (E) of 131 kcal/mol and a frequency factor (D_0) of 7.64 cm^2/s (Cherniak and Watson, 2003). Zircon was modeled as a sphere with an assumed effective diffusion radius (r_o) equal to 50 μm. The results show age profiles predicted for temperatures from 900 ºC to 700 ºC under two conditions: holding the grains at these temperatures for 1 m.y. or 10 m.y. (Fig. 11 in appendix). Based on the Ti-in-zircon results, we would expect the depth profiles to be similar to those predicted at 700 ºC. The diffusion model at 700 ºC shows that there would be an initial increase in the ages in the first 0.1 μm of the profile before an age plateau was attained. However, this is not the pattern seen in the Rt6-4 U-Pb age depth profiles. In the case of Rt6-4, the penetration depth is at least 0.25 μm and is normally greater. As explained in the text, the observed age profiles are geologically implausible and appear to reflect Pb loss from radiation-damaged high-uranium zircon in the near-rim environment.

Chapter 5: High-precision Dating of Migmatites in an Exhumed Continental Arc

Stacia Gordon*, Sam Bowring, Donna Whitney*, Robert Miller***, Noah McLean****

*Department of Geology and Geophysics, University of Minnesota, Minneapolis, MN 55455
**Earth and Planetary Sciences, Massachusetts Institute of Technology, Cambridge, MA 02139
***Geology Department, San José State University, San José, CA 95192

This chapter will be submitted to *Lithos* in the near future.

Abstract

High-precision zircon and monazite U-Pb geochronology of deformed migmatites provides a record of the timing of partial melting, metamorphism, and deformation. The Skagit Gneiss of the exhumed North Cascades continental arc (Washington, USA) is mostly comprised of tonalitic orthogneiss and plutons that have crystallization ages ranging from 90 to 45 Ma. Zircon and monazite from different textural varieties of leucosomes (e.g., layer-parallel/discordant; fine-grained/pegmatitic) from three outcrops of metasedimentary and metaigneous migmatite were analyzed using the CA-TIMS technique. The overall results reveal two main pulses of melt crystallization, (I) 68 to 63 Ma, and II) 53 to 47 Ma, but within each outcrop, leucosomes record a narrow range of crystallization ages. Zircon in trondhjemitic leucosomes from the westernmost migmatite yields Group I dates; the mesosome (sillimanite-garnet-biotite) contains zircons as young as 61 Ma. Zircon in leucosomes from the easternmost outcrop yield only Group II dates, and a biotite gneiss from this outcrop contains 47 Ma zircon. The third outcrop gave dates from both groups: 65 Ma and 53 Ma, in addition to older, inherited dates (160 to 93 Ma) in a garnet-bearing gneiss, and younger dates (46 Ma) in a crosscutting granitic dike. Monazite from leucosomes and mesosomes also yields bimodal results, indicating the timing of prograde metamorphism (ca. 69 Ma) and deformation ±fluid-mediated growth and recrystallization (49-46 Ma). These results indicate that partial melting occurred during Late Cretaceous metamorphism and Eocene transtension and exhumation, suggesting that the crust must have been relatively weak during parts of the Late Cretaceous to Eocene. The similarity in U-Pb zircon and monazite dates in the

migmatites to Ar cooling dates and basin formation ages suggests a coupling between flow of the middle crust and brittle extension and basin formation.

1. Crustal Melting and Orogeny

Throughout the evolution of an orogen, from crustal thickening to orogenic collapse, the thermal history of the lithosphere changes (e.g., Karlstrom and Williams, 2006). During orogeny, processes related to magmatic and/or solid-state transfer of material and heat between structural levels affects the composition and rheology of the lithosphere. For example, mass transfer in the form of melt extraction, magma transport, and pluton emplacement affect the thermal structure and overall strength of orogenic crust. Of particular importance are processes such as crustal melting that may have significant consequences for the rheology, thermal evolution, and chemical differentiation of continental crust.

Partial melting is an important process in the orogenic middle crust because it influences the magnitude and style of crustal flow and enhances the rate of deformation/strain. Both processes are important in controlling the strength of the middle crust (e.g., Hollister and Crawford, 1986; Dell'Angelo et al., 1987; Hollister, 1993; Handy et al., 2001). The effects of partial melting are not, however, limited to the deep crust; for example, partially molten crust in addition to crustal thickening may be responsible for the high, uniform elevation and shape of the Tibetan Plateau (Fielding et al., 1994; Nelson et al., 1996; Clark and Royden, 2000). In addition, studies of exhumed (crystallized) partially molten crust (migmatite terrains) have suggested that partial melting may drive upper crustal extension in a feedback relationship between extension

and buoyant melt ascent, and that these combined processes may drive orogenic collapse (e.g., Dewey, 1988; Rey et al., 2001). The magnitude, mechanisms, and timing of partial melting are therefore major factors in dynamic linking of deep and shallow crustal processes during orogeny.

Studies that have examined partial melting in orogens have focused on migmatites and leucogranites exposed in the hinterland of the North American Cordillera fold-and-thrust belt (e.g., Vanderhaeghe et al., 1999; Gordon et al., 2008; Kruckenberg et al., 2008), the Aegean/eastern Mediterranean (Keay et al., 2001; Whitney et al., 2003), the Variscan (Brown, 2005; Gébelin et al., 2007), and the Himalaya (e.g., Inger and Harris, 1993; Walker et al., 1999; Zhang et al., 2004). In continental arc settings such as Fiordland, New Zealand (e.g., Waight et al., 1998; Klepeis et al., 2007) and the Coast Plutonic Belt – North Cascades Range, USA-Canada (e.g., Crawford et al., 1987; Paterson et al., 2004), studies have investigated the relationship between magmatism and extension, and some papers have investigated partial melting, but the studies have not utilized high-precision geochronology to understand the timing of melt crystallization and its link to other processes and the consequences for arc evolution.

The North Cascades, Washington, at the southern end of the Coast Belt (Fig. 1), is an exhumed Late Cretaceous continental arc. This orogen is an ideal locality to study the role of partial melting and the interaction between deep and shallow processes in continental crust because a range of crustal paleodepths from >40 km to the surface is exposed, including sedimentary basins that received detritus during exhumation. In addition, the North Cascades contain numerous plutons and abundant migmatites that can

be examined to understand the thermal history of orogenic crust in a continental magmatic arc.

In this study, we have analyzed leucosome and host gneiss (mesosome) from migmatites in the high-grade Skagit Gneiss Complex of the crystalline core of the North Cascades (Fig. 2). We selected localities for analysis that have previously been the focus of study and debate about the conditions and mechanisms of migmatization (Misch, 1968; Yardley, 1978; Whitney, 1992a; Whitney and Irving, 1994). In order to determine the timing of melt crystallization and deformation, leucosomes with different textures (i.e., pegmatitic and fine-grained; layer-parallel and discordant) were collected from each locality for zircon and monazite U-Pb geochronology and microstructural characterization (Table 1).

2. Geologic Overview of the North Cascades and Skagit Gneiss

2.1 North Cascades Range

The Northern Cascade Mountains represent the southernmost part of the Coast Plutonic Complex-North Cascades Range that runs for >1500 km from Alaska to Washington (Fig. 1A). The orogen initially formed in the mid-Cretaceous during final accretion of terranes along the North American paleomargin (e.g., Monger et al., 1982; Crawford et al., 1987; Rubin et al., 1990; Journeay and Friedman, 1993). Compressional deformation including folding and thrusting, accompanied by abundant granitoid plutons, resulted in crustal thicknesses estimated to be ≥ 60 km by ~90 Ma in the North Cascades (Miller and Paterson, 2001). Pluton emplacement ages range from ca. 96 to 45 Ma. Pressure-temperature estimates (>10 kbar and >650 ºC) for exhumed crust, combined

with paleobotanical and stable isotopic studies that suggest that the area of northern Washington to Idaho and southeastern British Columbia was ~1 to 2 km higher in the Eocene and Oligocene than at present (Wolfe et al., 1998; Mulch et al., 2004, 2007), may indicate that an orogenic plateau formed in the Late Mesozoic-Early Cenozoic, with the Coast Plutonic Complex-North Cascades orogen representing the exhumed western margin of the plateau (Whitney et al., 2004).

The North Cascades core is divided into the Wenatchee and Chelan blocks by the post-metamorphic, high-angle Entiat fault (Fig. 1B). The two blocks preserve different magamtic histories with the Wenatchee block recording arc magamatism from ca. 96 to 84 Ma (e.g., Tabor et al., 1989; Miller et al., 2003). In comparison, the Chelan block records magmatism down to ca. 45 Ma, and experienced Eocene orogen-parallel stretching, plutonism, and exhumation (e.g., Tabor et al., 1989; Hurlow, 1992; Paterson and Miller, 1998; Paterson et al., 2004; Miller et al., 2006).

Deformation in the North Cascades Range switched from dominantly dextral transpression to transtension at ca. 58-55 Ma (Tabor et al., 1989; Miller and Bowring, 1990; Umhoefer and Miller, 1996). During the Eocene, two deep crustal domains were exhumed and preserve the youngest cooling dates and ductile deformation in the North Cascades core: the non-migmatitic 11-12 kbar Swakane Gneiss and the migmatitic 9-10 kbar Skagit Gneiss (Whitney et al., 1992b, 1999; Valley et al., 2003; Matzel et al., 2004). In addition to the exhumation of the two domains, transtensional basins were formed during strike slip faulting.

2.2 Skagit Gneiss

The Skagit Gneiss (Fig. 1B) is predominately upper amphibolite-facies tonalitic orthogneiss with lesser amounts of amphibolite, biotite paragneiss, calc-silicate rocks and rare pelitic schist and gneiss, all of which are exposed in a northwest-southeast trending antiform (Fig. 3; Misch, 1966, 1968). In the north-central part of the Skagit Gneiss, both meta-igneous and metasedimentary rocks are migmatitic (Fig. 3; Misch, 1966; Whitney and Irving, 1994).

Information about the metamorphic *P-T* conditions is derived from metapelitic rocks and garnet amphibolite. Rocks from different structural levels of the Skagit Gneiss record maximum conditions of 8-10 kbar at 650 – 725 ºC (Whitney et al., 1992b). Cordierite rims on garnet and staurolite in some metapelitic rocks suggest that metamorphic reactions continued during decompression to $P < 5$ kbar. The thermobarometric results from the Skagit reveal that the migmatitic portion attained higher pressures and temperatures than other parts of the Skagit (Whitney, 1992b).

The high-grade Skagit Gneiss is bounded by the Late Cretaceous(?) – Eocene Ross Lake fault zone (RLFZ) in the east and the Straight Creek fault in the west (Fig. 1B, 3). Movement on the RLFZ was predominantly dextral strike-slip with components of reverse slip during the Paleocene and dextral-normal (down-to-E) shear in the Eocene (Misch, 1966; Miller and Bowring, 1990; Miller, 1994). On the western side, the Skagit Gneiss is bounded by the Marblemount orthogneiss and Napeequa units, and these units are separated from greenschist- and blueschist-facies rocks to the west by the Straight Creek fault. The fault zone has been largely obscured by the Chilliwack batholith (Misch, 1966; Tabor et al., 2003).

Previous geochronological studies have focused mainly on the timing of pluton emplacement and orthogneiss crystallization. Regional compressional deformation induced mid-Cretaceous (91-75 Ma) crustal thickening, suggesting that the high-*P* metamorphism had to have occurred by 75 Ma (Miller et al., 1993). The orthogneisses have yielded a variety of U-Pb zircon dates, from ca. 90 to 45 Ma (Mattinson, 1972; Miller et al., 1989; Miller and Bowring, 1990; Haugerud et al., 1991). Orthogneisses with the dominant Skagit metamorphic fabric (foliation striking NW-SE and lineations trending NW-SE or NNE-SSW) have a narrow range of crystallization ages (75-64 Ma) in the north-central part of the Skagit and are also cut by 46-45 Ma (whole rock Rb-Sr; U-Pb zircon, monazite, xenotime) granite bodies (Babcock et al., 1985; Haugerud et al., 1991; Tabor et al., 2003). Cooling ages ($^{40}Ar/^{39}Ar$ and K-Ar hornblende and biotite) range from 57-43 Ma and are the youngest cooling ages in the North Cascades crystalline core (Mattinson, 1972; Engels et al., 1976; Wernicke and Getty, 1997; Tabor et al., 2003). Because hornblende and biotite ages are very similar, it has been suggested that the Skagit Gneiss underwent rapid cooling (~100 ºC/m.y. or more) and possibly rapid exhumation (Wernicke and Getty, 1997).

2.3 Petrogenesis of the Skagit Migmatites

The north-central part of the Skagit Gneiss exposes abundant migmatites with low-K (trondhjemitic) leucosomes characterized by a variety of textures, from layer-parallel, fine-grained leucosomes (e.g., stromatic type of Mehnert, 1968) to discordant, coarse-grained pegmatite (Fig. 4). The origin of the migmatites has been the focus of numerous studies, with some investigations arguing for a subsolidus metamorphic

differentiation ± metasomatism origin (Misch, 1968; Yardley, 1978; Babcock and Misch, 1989) and other studies suggesting that partial melting occurred, in addition to the subsolidus processes (Whitney et al., 1992a; Whitney and Irving, 1994). The basis for the proposal that the leucosomes formed by subsolidus processes is that leucosome plagioclase has the same or similar composition as mesosome plagioclase; i.e., leucosome plagioclase is not as sodic as would be predicted based on melting experiments of simple granitic systems. Furthermore, the leucosomes are trondhjemitic, not granitic, despite having apparently formed from biotite-rich source rocks.

A partial melting origin for some Skagit leucosomes has been argued on the basis that low-K melts can be produced (typically at high water activity) from biotite-bearing source rocks (Conrad et al., 1988; Patiño Douce and Johnston, 1991) at the *P-T* conditions estimated for Skagit metamorphism (Whitney, 1992b). In addition, there are differences in the mineral assemblages, bulk rock major and trace element composition, fluid inclusion populations, and textural features of leucosome minerals (including accessory phases) that are consistent with a partial melting origin (Whitney, 1992a; Whitney and Irving, 1994). The leucosomes analyzed in the present study are from localities in which anatectic leucosomes have been interpreted using mineralogical, textural, and chemical criteria.

Although previous studies of the Skagit migmatites have investigated the origin of the migmatites and previous reconnaissance geochronology studies have provided information about the broad timing of high-grade metamorphism and magmatism (e.g., Misch, 1968; Mattinson, 1972; Yardley, 1978; Babcock and Misch, 1989; Miller et al., 1989; Haugerud et al., 1991; Miller and Bowring, 1992), studies of Skagit migmatite

petrogenesis and *P-T* conditions/paths have not been integrated with geochronology studies of the gneiss. In addition, the timing and conditions of leucosome crystallization and deformation in the Skagit Gneiss have not been determined and evaluated in the context of the role that crustal melting played in the tectonic history of the Skagit Gneiss. In the following sections, we describe the samples, methods, and results of a zircon and monazite U-Pb and microstructural study of Skagit migmatites.

3. Petrology and microstructural characteristics of the sample sites

Samples were collected from three outcrops in the north-central part of the Skagit Gneiss (Fig. 2; Table 1). From west to east, the outcrops are Gorge Lake (metapelite sample site SK-1 in Whitney, 1992b; Whitney and Irving, 1994), Sourdough Mountain (Yardley, 1978), and John Pierce Falls (Fig. 5; sample site SK-11 in Whitney, 1992b; Whitney and Irving, 1994). Sourdough Mountain represents the highest structural level of the three samples and is ~1.3-1.4 km structurally above John Pierce Falls and Gorge Lake. Only ~ 100 m of structural thickness separates John Pierce Falls and Gorge Lake, with John Pierce Falls slightly higher in structural level.

The analyzed leucosomes, including the pegmatite, are trondhjemitic, with the exception of a cross-cutting granitic dike at one locality. In addition, most of the leucosomes contain small (<0.8 mm), inclusion-free, Fe-rich peritectic garnet that are texturally and compositionally distinct from the larger (> 1 mm), inclusion-rich garnets in the adjacent mesosome.

Asymmetric structures (e.g., shear bands and rotated porphyroclasts) indicate dominant top-to-the-NW sense of shear. Quartz microstructures are commonly

characterized by subgrains, indicating recovery, probably due to low-temperature deformation during cooling and exhumation of the gneiss. In addition, the quartz has a strong crystallographic preferred orientation (CPO). Quartz typically wraps around larger plagioclase grains in both leucosome and mesosome, and preserves evidence in different types of deformation and recovery mechanisms for multiple deformation events (i.e., high-temperature and late, overprinting low-temperature events) in a single sample (Fig. 6). Plagioclase in these rocks does not typically display ductile deformation, such as deformation lamellae or deformation twins.

3.1 Gorge Lake metapelitic migmatite

The westernmost (Gorge Lake) locality consists of migmatitic garnet-sillimanite gneiss and is one of the few metapelite localities known within the Skagit Gneiss (Fig. 2). Thermobarometric analysis using exhange thermometers and net transfer equilibria barometers has revealed maximum recorded pressure-temperature conditions of 650-725 ºC at 8-10 kbar (Whitney, 1992b). The metapelitic gneiss is migmatitic and contains leucosomes exhibiting a variety of textures, from cm-scale pods to meter-scale pegmatitic veins. One mesosome and 5 leucosome samples were analyzed for U/Pb zircon and monazite geochronology.

The mesosome consists of quartz + biotite + plagioclase (An_{28}) + garnet + sillimanite + ilmenite ± texturally late cordierite rimming garnet. Accessory phases are Fe-sulfide, zircon, apatite, monazite, ± graphite. Relict staurolite, kyanite, and rutile are preserved as inclusions in some garnets. Garnet also contains crystallographically oriented needles of rutile. The mesosome and every textural variety of leucosome in the

outcrop are deformed; the mesosome and concordant leucosomes exhibit meter-scale upright folds. Biotite and ilmenite form an S-C fabric in the mesosome. Quartz and compositional layering also define S, and quartz is commonly recrystallized along the C plane. In addition, biotite along the shear bands is very fine-grained and appears to have taken up much of the strain. Throughout the sample, quartz ribbons have developed and contain subgrains, and larger (~1 mm) quartz grains contain deformation bands.

A ~10 cm wide lensoid leucosome (sample SK061DL) consists largely of quartz and plagioclase (An_{26}), with lesser amounts of biotite, garnet, apatite, zircon, and monazite. Throughout the sample, quartz is recrystallized and contains subgrains. In isolated domains, quartz is fine-grained and has a strong CPO based on microscopic petrographic observations. Small mm-scale shear zones cut across the sample. Some quartz grains preserve evidence of a higher-temperature fabric in the form of chessboard extinction, although lower-temperature bulging of grains to form new subgrains is the primary deformation mechanism in the sample. Plagioclase exhibits significant local sericitization, and most of the grains have corroded edges. A few small (<0.8 mm), inclusion-free peritectic garnets are present in the leucosome.

A 5-cm thick layer-parallel (stromatic) leucosome (SK061C) consists mainly of quartz with plagioclase (An_{27}) porphyroclasts and minor garnet, biotite, rutile, ilmenite, pyrite, zircon, and monazite. In the stromatic leucosome, quartz is highly deformed, wrapping around garnet and plagioclase porphyroblasts. The texture of the quartz suggests subgrain rotation and grain boundary migration recovery mechanisms. Plagioclase grains are large (~2-4 mm); some crystals contain deformation twins and show recrystallization along the grain boundaries.

A coarse-grained (~5-10 mm-size crystals) discordant leucosome (SK061A) contains quartz, plagioclase (An_{26}), biotite, ilmenite, rutile and zircon. Zircon grains occur throughout the sample as inclusions in quartz, plagioclase, biotite, and ilmenite, and along grain boundaries between quartz and plagioclase. Quartz has undergone significant grain size reduction and wraps around and is squeezed between larger (~6-10 mm) plagioclase grains. Most of the quartz has undulose extinction, but some contains subgrains. The larger plagioclase grains contain cracks that are filled with quartz. Some plagioclase shows undulatory extinction, kink bands, and deformation twins. Recrystallized plagioclase grains have developed along the edge of some crystals. Most of these textures suggest low-temperature deformation; however, SK061A also preserves evidence for a higher-temperature deformation in the form of weak chessboard extinction in some quartz.

A discordant ~ 0.5 m thick pegmatitic leucosome (SK061B) consists of quartz, plagioclase (An_{28}), biotite, and trace amounts of rutile, ilmenite, apatite, and zircon. Plagioclase typically forms large (~2 mm) metamorphic porphyroclasts; recrystallized quartz, biotite, and plagioclase occur in pressure shadows around the larger plagioclase grains. Some plagioclase grains show deformation twins, but more polygonal crystals meet at triple junctions and appear to have undergone recrystallization. Biotite forms a wispy foliation throughout the sample. Quartz ribbons contain deformation bands and show evidence for grain boundary migration. Rutile grains occur throughout the sample and have at least two textural forms: 1) small (~0.1 mm) square- to diamond-shaped grains in cross-section, and 2) larger (~0.4 – 1 mm), more irregularly shaped crystals. The smaller grains occur as inclusions in the larger plagioclase grains. The latter, larger grains

are generally associated with foliation-forming biotite. In addition, the larger grains appear to be more deformed than the small rutile grains and are elongated parallel to foliation.

A coarse-grained concordant leucosome (SK061F) was collected from within a m-scale folded mesosome-stromatic leucosome migmatite. The sample contains quartz, plagioclase, rutile, ilmenite, and zircon, and exhibits a distinct fabric in comparison to the other leucosomes at the metapelite locality: plagioclase dominates the matrix and has undergone significant sericitization and fracturing. The other leucosomes are more quartz-rich and not as altered. On a thin section scale, quartz in some regions of the leucosome shows intense recrystallization with a CPO, whereas other areas show strong chessboard extinction and deformation bands. Quartz is located in pockets within the dominant plagioclase matrix. Small (<0.8 mm) inclusion-free garnets are commonly associated with biotite and chlorite and are typically fractured and broken into smaller pieces.

3.2 John Pierce Falls migmatitic biotite gneiss

John Pierce Falls exposes a spectacular outcrop with a variety of leucosomes (Fig. 5). This outcrop represents the easternmost locality studied (Fig. 2). The outcrop consists of a large pegmatite body that envelops lenses of biotite gneiss containing layer-parallel leucosome. Part of the biotite gneiss has been interpreted as a metagraywacke based on the assemblage biotite + garnet + plagioclase + quartz + cummingtonite (Misch, 1968), but biotite gneiss lacking garnet and/or cummingtonite also occurs at this locality. The outcrop is intruded by a ~1 m thick late lineated granitic dike that crosscuts all lithologic

layering, gneissic fabrics, and other types of migmatite structures. Three samples were analyzed from John Pierce Falls: 1) pegmatite, 2) a layer-parallel leucosome from within a metagraywacke boudin, and 3) biotite gneiss (possible orthogneiss).

Pegmatite sample SK0620C is dominated by large (~3-5 mm) plagioclase (An_{19}) crystals that are wrapped by highly-recrystallized quartz, some of which occur in pressure shadows. Quartz shows evidence for grain boundary migration with amoeboid and lobate grain boundaries and forms foliation parallel ribbons. Recrystallization of plagioclase has occurred along the grain boundaries of some of the porphyroclasts, and plagioclase also shows evidence of brittle cracking with quartz filling the fractures. Biotite defines the foliation and wraps around plagioclase porphyroclasts.

A ~2-cm thick layer-parallel leucosome (SK0620B) is relatively coarse-grained with ~1-2 mm-scale plagioclase crystals (An_{29}). Several different quartz microstructures are preserved in the leucosome. Quartz wraps around and is located in pressure shadows of plagioclase grains. Larger (~0.25-0.50 mm) quartz crystals have irregular lobes along their grain boundaries suggesting that grain boundary migration was a recovery mechanism. The larger grains preserve some evidence for a higher-temperature fabric. Finally, narrow shear bands consisting of recrystallized quartz and biotite altered to chlorite cut across the section, preserving evidence for low-temperature deformation. Quartz grain size is reduced in these areas. The plagioclase appears ductilely deformed: some grains resemble sigma-structures. The majority of the plagioclase shows evidence for low-temperature deformation in the form of cracking, alteration along the grain boundary, recrystallization, and twinning.

The John Pierce Falls biotite gneiss (SK0620D) exhibits a strong lineation and foliation, but the sample preserves some igneous textures, such as oscillatory zoning in plagioclase. The tonalitic gneiss consists of plagioclase (An_{28}), quartz, K-feldspar, biotite, and trace amounts of apatite, ilmenite, zircon and monazite. Quartz ribbons contain deformation bands, suggesting low-temperature deformation. Plagioclase shows significant twinning and core/mantle structures, indicating at least moderate deformation temperatures (> 450 ºC).

3.3 Sourdough Mountain migmatitic garnet-biotite gneiss

Sourdough Mountain exposes a ridgeline of migmatitic garnet-biotite gneiss. In this study, a sample of garnet-biotite gneiss, 2 leucosomes, a pegmatite, and a granitic dike were analyzed for U/Pb zircon and monazite geochronology.

The garnet-biotite gneiss (SK06127E) consists of biotite, plagioclase, quartz, and garnet, with minor ilmenite, apatite, zircon, and monazite, and has a weak S-C fabric defined by biotite, recrystallized quartz, and compositional layering. Biotite is stable in both C and S and does not show any signs of retrogression, suggesting a high-temperature fabric. In addition, the biotite along with ilmenite encloses quartz ribbons. Garnets typically have few inclusions and have been altered to chlorite along fractures. Plagioclase (An_{35}) grains are on average equidimensional throughout the sample and show some evidence of alteration at grain boundaries. Quartz is recrystallized and typically forms equant, ~0.3 – 0.4 mm grains that meet in triple junctions; larger (>0.25 mm) quartz grains contain subgrains and deformation bands

A ~6 cm thick layer-parallel leucosome (SK06127A) consists of quartz, plagioclase (An_{33}), biotite, garnet, rutile, ilmenite and zircon. Abundant small, inclusion-free garnets occur throughout the leucosome, suggesting an anatectic origin for the leucosome. Biotite and ilmenite form a weak foliation. Quartz does not have a prominent alignment. Plagioclase varies in grain size but the majority is relatively coarse-grained (~0.5 - 3mm) in comparison to the quartz (<0.5 mm) and has corroded grain boundaries, presumably due to reactions with adjacent grains. Smaller plagioclase grains are equidimensional and form triple junctions in some spots. Quartz shows evidence for bulging, and is commonly interstitial between larger plagioclase grains. Quartz ribbons are aligned parallel to foliation. Subgrains within the ribbons contain deformation bands and show a strong CPO. The sample also contains shear bands oriented perpendicular to the foliation. The shear bands appear to be a late fabric and are defined by more intense quartz recrystallization.

A thick (~30 cm) layer-parallel leucosome (SK06127C) is moderately altered: plagioclase (An_{34}) is sericitized and fractured, and biotite has been partially replaced by chlorite. Smaller (~0.3 mm) recrystallized plagioclase grains form polygonal aggregates of mostly untwinned grains, suggesting at least moderate (> 450 ºC) temperature deformation. Quartz ribbons occur locally, and weak chessboard extinction occurs in some quartz aggregates.

A ~40 cm thick pegmatite sill (SK06127DL) is dominated by quartz and plagioclase, and also contains minor K-feldspar, biotite, chlorite (secondary), ilmenite, apatite and zircon. Plagioclase has been sericitized and occurs in a variety of grain sizes. The larger grains (~2-3 mm) of plagioclase typically reveal deformation twinning.

Numerous quartz ribbons cut the sample and consist of well-recrystallized equidimensional quartz that forms triple junctions. Quartz outside the ribbons contains subgrains and bulges into adjacent quartz grains.

A late, lineated granitic dike (SK06127F) that cuts across the outcrop, including the other gneiss and leucosome bodies analyzed, is similar to other such dikes that occur throughout the central and eastern parts of the Skagit Gneiss. The dike has a strong lineation but no foliation. The sample consists of quartz, plagioclase, K-feldspar, biotite, muscovite, small peritectic garnets, magnetite, zircon, and monazite. The cores of the K-feldspar grains have undergone significant sericitization; the rims are relatively unaltered. Plagioclase and K-feldspar both show deformation twinning. Subgrain formation and bulging dominate the recovery mechanisms in the quartz. Evidence for subgrain rotation is found in the form of new grains along the grain boundaries of larger quartz grains. Furthermore, the recrystallized quartz fills the space between larger plagioclase and K-feldspar grains in the matrix. A high-temperature fabric is indicated by chessboard extinction in some of the quartz grains.

4. U-Pb results

Zircon and monazite of varying sizes, shapes and clarity were recovered from the samples described in the previous section, and grains were analyzed according to the methods outlined in Appendix A. Geochronological data are reported at the 2σ uncertainty level (zircon: Table 2, Figs. 7, 8, 9, 10, 12, 13, 14; monazite: Table 3, Fig. 11).

4.1 Gorge Lake metapelitic migmatite

4.1.1 Mesosome (SK061DM). CL images of zircons selected for analysis from the mesosome of the migmatitic garnet-sillimanite gneiss (SK061DM) show relatively simple zoning patterns, although more complex patterns occur in a few grains (Fig. 8A). Two main populations of CL images are observed: 1) rounded grains that yield inherited $^{207}Pb/^{206}Pb$ results ranging from 1094.8 to 149.6 Ma; and 2) elongate grains that typically display oscillatory zoning and that reveal Late Cretaceous to Paleocene $^{206}Pb/^{238}U$ dates, ranging from 71.7 to 61.5 Ma (Fig. 7A).

To better understand the growth history of the zircons from the metapelitic mesosome, four zircons displaying complex zoning were chosen for more detailed analysis. The CL images were used as a guide for breaking each zircon into pieces, isolating different growth zones.

The CL image for zircon 26 reveals interior zoning that is truncated by possibly two different rims (Fig. 9A). The zircon is rounded and resembles a detrital grain. The crystal was broken into three pieces, so as to isolate the tips of the zircon (Fig. 9A). The interior of the grain shattered and was unrecoverable, but the two rim fragments were analyzed. These yielded $^{206}Pb/^{238}U$ dates of 160.23 ± 0.22 Ma and 197.31 ± 0.38, and are likely parts of a detrital grain. The results were discordant, suggesting that the dates are mixing ages. Any metamorphic zoning at the rim was too thin to isolate by this technique.

The other three mesosome zircons that were studied in detail all exhibit oscillatory zoning and all yielded similar rim dates (Fig. 9B, C, D, 10). Zircon 27 has a tabular morphology with slightly rounded edges (Fig. 9B). The grain has a small core that

appears to be truncated by a rim with oscillatory zoning. There is possibly a third zircon growth episode preserved on the outermost tips in a brighter, lower U zone. The zircon was broken into two pieces; the rim yielded a date of 65.56 ± 0.41 Ma, and the interior 106.47 ± 0.30 Ma. The Th/U ratio for the rim of the grain was lower (0.12) in comparison to the interior (0.25).

Zircon 29 also has a tabular morphology, and the grain is only rounded at the tips (Fig. 9C). A bright, low U rim cuts the oscillatory zoning in this crystal. Two pieces were extracted and gave dates of 65.04 ± 0.07 Ma and 88.35 ± 0.06 Ma (Fig. 10). The low U rim was included in the zircon piece that yielded the older 88 Ma date, suggesting that the dark, high U zoning seen in the CL image represents an older detrital core and the analysis reflects a mixture of rim and core. The oscillatory zoning at the opposite end of the grain preserves the young date of 65 Ma. For this grain, the Th/U ratio of the interior is lower than that of the rim: 0.11 versus 0.18, respectively.

Zircon 31 is comprised of a core surrounded by a rim with oscillatory zoning (Fig. 9D). The grain was broken into three pieces that yielded $^{206}Pb/^{238}U$ dates of 65.39 ± 0.15 Ma, 67.22 ± 0.49 Ma, and 152.99 ± 0.33 Ma (Fig. 10). The pieces yield Th/U ratios of 0.18, 0.14, and 0.27 from the rim to the interior of the grain. The rim and interior values are simiar to zircon 27. The core is likely detrital and the younger dates represent the timing of rim growth, although it is probable that the 67.22 Ma piece may represent a mixtures of core and rim zones and is therefore a mixed age.

Monazite in this sample occurs as inclusions in quartz, biotite, and garnet, and along grain boundaries between biotite and quartz. Analyses of thirteen monazite grains reveal two main $^{207}Pb/^{235}U$ date populations: 1) ca. 69 Ma (2 grains: 69.54 ± 0.15 Ma and

69.10 ± 0.11 Ma), and 2) ca. 49-46 Ma (10 grains, ranging from 49.02 ± 0.78 to 46.21 ± 0.32 Ma, with the majority of the dates clustering at ca. 48 Ma) (Fig. 11A). One monazite grain yielded a $^{207}Pb/^{235}U$ date of 63.80 ± 0.23 Ma. The monazite grains are unzoned, and there is no distinct textural difference between the two age groups.

*4.1.2. Lensoid leucosome (SK061DL)***.** In this cm-scale quartzofeldspathic lens, zircons are mostly located along grain boundaries between plagioclase and quartz, although zircon can be found throughout the thin section, including within garnet and biotite. Eleven zircon analyses reveal a range in $^{206}Pb/^{238}U$ dates from 68.97 ± 0.10 Ma to 65.30 ± 0.05 Ma, with most analyses clustering at ca. 68 Ma and one analysis of 90.06 ± 0.06 Ma (Fig. 7B). CL images of the zircons show oscillatory zoning and mostly euhedral crystals (Fig. 8B). The two grains that yielded ca. 65 Ma dates have a more rounded morphology and have a slightly higher Th/U ratio (0.21 to 0.10 versus 0.06 to 0.03).

4.1.3. Layer-parallel leucosome (SK061C). CL images of zircons from this ~5 cm thick concordant leucosome show oscillatory zoning (Fig. 8C). The $^{206}Pb/^{238}U$ dates range from 66.36 ± 0.04 Ma to 63.13 ± 0.05 Ma, and one older grain yielded a date of 84.30 ± 0.10 Ma (Fig. 7C). Five zircons from leucosome SK061C were broken into pieces to determine if there is variation in dates within a single grain or whether the spread in dates is caused by individual grains yielding different dates; two of the five grains are shown in Figure 12. In addition, Hf measurements were made using the MIT JEOL 733 Superprobe electron microprobe. The results reveal that there is no correlation of age with Hf concentration and that individual pieces of single grains yield the same date

within error (Fig 12); thus, it seems like the spread in dates represents different grains yielding different dates. Pale yellow monazite was also analyzed from this sample and reveals a similar distribution of $^{207}Pb/^{235}U$ dates to the metapelitic mesosome monazites: 1) dates from 69.28 ± 0.18 to 66.66 ± 0.28 Ma; and 2) 49.50 ± 0.54 to 48.64 ± 0.13 Ma (Fig. 11B). The older dates have lower Th/U ratios (12.9 to 6.2) in comparison to the younger dates (21.2 to 14.8). Furthermore, the Th/U ratios of the older grains are very similar to the Th/U ratio of the older monazite crystals from the mesosome.

4.1.4. Layer-parallel leucosome (SK061A). Eight zircons from this leucosome have $^{206}Pb/^{238}U$ dates ranging from 65.32 ± 0.04 Ma to 65.02 ± 0.04 Ma (Fig. 7D). These zircons are distinctly larger than in other leucosomes (> 100 μm), and all crystals have well-developed oscillatory zoning (Fig. 8D).

4.1.5. Layer-parallel leucosome (SK061F). This leucosome is from a folded mesosome-leucosome sequence, and contains oscillatory-zoned zircons that reveal a range in $^{206}Pb/^{238}U$ dates from 65.59 ± 0.04 Ma to 63.31 ± 0.04 Ma from 10 single crystal analyses with a clustering of dates at ca. 64.5 Ma (Fig. 7F, 8F). There is a slight inverse relationship between the date and Th/U ratio, with the oldest grain having a Th/U ratio of 0.10 and the youngest grain yielding a Th/U ratio of 0.21.

4.1.6. Pegmatitic leucosome (SK061B). Analyses of eight zircons yield $^{206}Pb/^{238}U$ dates that range from 64.78 ± 0.07 Ma to 63.75 ± 0.04 Ma (Fig. 7E). All of the grains analyzed have oscillatory zoning (Fig. 8E). The younger dates are from grains that have a more

elongate grain shape. U-Pb analyses of rutile were attempted; however, the grains are not radiogenic enough to obtain reliable analyses.

4.2. John Pierce Falls migmatitic biotite gneiss

Zircon and monazite from a pegmatite, a layer-parallel leucosome, and a biotite gneiss cut by the pegmatite were analyzed.

4.2.1. Pegmatite (SK0620C). Zircons occur throughout the matrix of the pegmatite and are pale pink. Zircons are typically >75 μm and most have oscillatory zoning (Fig. 8G). Fifteen analyses range from 53.99 ± 0.05 Ma to 52.62 ± 0.03 Ma (Fig. 13A). A CL image of one elongate zircon shows a core/rim relationship (Fig. 8G). This grain was broken into two pieces to assess the age difference between the core and rim. The grain yields the youngest dates with a core $^{206}Pb/^{238}U$ date of 47.56 ± 0.08 Ma and a rim date of 47.36 ± 0.05 Ma (Fig. 8G). The two analyses have the lowest Th/U ratio (0.05) of the grains analyzed (other zircons: 0.33 to 0.10). Monazites show weak near-rim oscillatory zoning in backscatter electron images. Six monazites reveal $^{207}Pb/^{235}U$ dates that cluster near ca. 47 Ma, with a range from 46.93 ± 0.07 Ma to 46.24 ± 0.13 Ma (Fig. 11C).

4.2.2. Layer-parallel leucosome (SK0620B). Zircon is rare; seven zircons were recovered, and these yielded a range of $^{206}Pb/^{238}U$ dates from 51.87 ± 0.04 Ma to 50.74 ± 0.16 Ma (Fig. 13B). Most of the zircons show complex zoning (Fig. 8H).

4.2.3. Biotite gneiss (SK0620D). In the gneiss, which is cut by the pegmatite, zircon and monazite occur in a variety of textural settings such as inclusions in plagioclase and along grain boundaries between quartz and plagioclase. Zircon grains have two main morphologies: 1) grains that are elongate and exhibit oscillatory zoning, and 2) grains that are equant and rounded and typically show more complex zoning, in some cases with a core/rim structure (Fig. 8I). The grains from group 2 yield inherited $^{207}Pb/^{206}Pb$ dates from 2551.8 Ma to 1306.6 Ma and low Th/U ratios (Fig. 13C). In comparison, the grains from group 1 have $^{206}Pb/^{238}U$ dates clustering near ca. 48 and 47 Ma. The Th/U ratios of the youngest grains vary from 0.38 to 0.27. $^{207}Pb/^{235}U$ monazite dates show a small spread from 48.20 ± 1.17 Ma to 46.14 ± 0.62 Ma, overlapping with the zircon results (Fig. 11D). The monazite results show the youngest U-Pb dates of this study.

4.3. Sourdough Mountain migmatitic garnet-biotite gneiss

A biotite gneiss, two layer-parallel leucosomes, a pegmatite, and a granitic dike were analyzed from this locality.

4.3.1. Biotite gneiss (SK06127E). CL images reveal very complex zoning in zircon (Fig. 8J), with most grains containing a oscillatory-zoned core. The oscillatory zoning is cut by either two or three rim domains. The outermost zone defined in the CL images is thin (~10-20 μm). Grains were broken in an attempt to isolate the different zones; however, the small size of the rim made it difficult to have enough radiogenic Pb for analysis. A combination of pieces of several grains as well as whole single grains reveal a range of $^{206}Pb/^{238}U$ dates from 161.12 ± 0.13 Ma to 93.13 ± 0.19 Ma (Fig. 14A). The pieces from

a single grain yield different ages from the interior of the grain versus the "rim," 119.34 ± 0.61 Ma and 93.13 ± 0.19 Ma, respectively (Fig. 8J).

4.3.2. Layer-parallel leucosome (SK06127A). CL images of the zircons show that many of the grains have a core that is surrounded by a ~50 μm rim (Fig. 8K). The grains were broken in order to analyze both zones. One grain revealed a ~3 m.y. difference in age, with the core yielding an $^{206}Pb/^{238}U$ date of 65.82 ± 0.04 Ma and the rim 62.33 ± 0.04 Ma (Fig. 14B). In comparison, another grain that was broken has a core age of 856.91 ± 0.52 Ma and a rim age of 63.59 ± 0.03 Ma. A whole grain with consistent concentric zoning shows the youngest $^{206}Pb/^{238}U$ date of 60.89 ± 0.03 Ma.

*4.3.3. Layer-parallel leucosome (SK06127C)***.** This leucosome is more altered than other leucosomes analyzed. Most of the zircon grains (n = 9) have simple zoning (Fig. 8L), and yield a $^{206}Pb/^{238}U$ date of ca. 65 Ma (Fig. 14C). The individual grains range from 65.37 ± 0.40 Ma to 64.64 ± 0.13 Ma, with a few older (inherited) ages. Monazite dates were all younger than the zircons: $^{207}Pb/^{235}U$ dates of 64.33 ± 0.41 Ma to 59.59 ± 1.97 Ma (Fig. 11E).

4.3.4. Pegmatite (SK06127D). Zircon grains are large (typically ~200 μm), euhedral, and have simple zoning patterns (Fig. 8M). The $^{206}Pb/^{238}U$ results cluster at ca. 53 Ma from 10 analyses, with a slight spread in dates from 53.69 ± 0.13 Ma to 52.98 ± 0.04 Ma (Fig. 14D).

4.3.5. Granitic dike (SK06127F). In the late lineated granitic dike, CL images show a range of zircon textures (Fig. 8N). Four grains that are more rounded and do not show obvious zoning reveal inherited $^{206}Pb/^{238}U$ dates from 176.33 to 109.72 Ma (Fig. 14E). In comparison, more elongate grains with oscillatory and concentric zoning yield the youngest $^{206}Pb/^{238}U$ dates of 55.01 ± 0.51 Ma and 46.35 ± 0.08 Ma. Two monazites were obtained and analyzed from the dike, and the monazite yield $^{207}Pb/^{235}U$ dates of 46.19 ± 0.20 Ma and 45.25 ± 1.22 Ma. A previous geochronometric study of the late-lineated granitic dike suite in the Skagit Gneiss determined a whole-rock Rb-Sr age of ca. 45 Ma, consistent with a xenotime date of 45.1 ± 0.4 Ma (Babcock et al., 1985; Haugerud et al., 1991); thus, the youngest zircon and monazite dates overlap within error of the Rb-Sr age of similar dikes.

5. Summary of geochronology results

The zircon and monazite results from leucosomes, biotite gneiss, and metapelitic gneiss yield a variety of Late Cretaceous to Eocene dates that document the timing of metamorphism, deformation, and melt crystallization in one of the structurally deepest exposed and highest grade parts of the North Cascades arc system. The three outcrops selected for sampling represent similar structural depths (Sourdough Mountain is ~1.4 km structurallly higher than Gorge Lake and John Pierce Falls) and the three sites are not separated by any major faults or any recognized ductile shear zones, but zircon grains from each outcrop has a distinct magmatic/metamorphic history: (1) At the westernmost locality, leucosomes yield only Late Cretaceous dates, and the metapelitic mesosome yields Late Cretaceous to Paleocene dates; (2) At the easternmost locality, all zircons are

Eocene, including a pegmatite dated at 53 Ma; and (3) At the intermediate locality, leucosome and pegmatite zircons record Late Cretaceous to Eocene dates, including a 53 Ma pegmatite, and the host gneiss records older dates (136-93 Ma) that probably represent detrital ages.

The geochronologic results from the John Pierce Falls outcrop are interesting because they contradict the geometric cross-cutting relations observed in the outcrop; i.e., the pegmatite yields older ages than the layer-parallel leucosomes that it cross-cuts. Possible explanations include (1) the pegmatite contains xenocrystic zircon entrained during intrusion of the pegmatite, and therefore these zircons do not record the age of the pegmatite; or (2) intrusion of the pegmatite and release of water-rich fluids during its crystallization triggered partial melting in the host gneiss, generating the layer-parallel leucosomes. The fact that the zircon data from the pegmatite cluster at ca. 53 Ma, the same age as the pegmatite on Sourdough Mountain, and have no evidence for an older age component, suggests that the zircons are probably not xenocrystic. A genetic link between pegmatite intrusion and layer-parallel leucosome generation is more likely, and is consistent with models for the generation of the trondhjemitic leucosomes in Skagit biotite gneiss. The young (ca. 47-46 Ma) dates from the biotite gneiss further support high-temperature conditions late in the history of the Skagit Gneiss.

Monazite results from the three outcrops are also complex. Monazite from one leucosome and the metapelitic mesosome from the western locality yield a bimodal population of Late Cretaceous and Eocene dates. In comparison, only Eocene dates were documented at John Pierce Falls, and monazite from a Sourdough leucosome yields 64-60 Ma dates. The presence of multiple populations of dates (e.g. 69 Ma vs. 49 Ma), some

of which are older and some of which are younger than dates of coexisting zircon, suggests that monazite may record evidence for crystallization and/or recrystallization events during metamorphism and deformation at different stages of the tectonic evolution of the migmatites. Using these new results, the timing of migmatization can now be considered in relation to thermal and tectonic events of the Skagit crystalline core.

6. Timing of Metamorphism

In the metapelite, both accessory zircon and monazite are present that may be used to determine the timing of metamorphism in the Skagit Gneiss. In addition, several generations of leucosome are present that cross-cut and/or are parallel to foliation. The composition and geochemistry of the leucosomes suggest that they are derived from melting of the metapelite (Whitney and Irving, 1994), and therefore, the crystallization age of the leucosomes yield a further estimate on the timing of metamorphism. The Late Cretaceous to Paleocene dates (71-61 Ma) recorded by zircon in the metapelitic mesosome at Gorge Lake likely indicate the timing of high-grade metamorphism, and the older dates (134, 284, and 825 Ma) likely indicate that some zircon was detrital, originating from the sedimentary protolith. The grains that record older ages have rounded edges, consistent with the interpretation of a detrital origin for these grains (Fig. 8A). In contrast, younger zircons have a more tabular morphology with sharp grain boundaries. The low Th/U ratios (0.01 to 0.07) of the zircons that yield dates of 71 to 61 Ma are consistent with a metamorphic origin (Rubatto, 2002; Hoskin and Schaltegger, 2003). In addition, CL images of the younger zircon grains show complex zoning with some parts of the grain revealing oscillatory zoning, other parts sector zoning, and

typically the different zones are cross-cutting. Yet, there is little evidence of older inherited radiogenic Pb (Fig. 7A), indicating that it is unlikely that these dates represent mixtures of detrital cores and metamorphic overgrowths. The CL images do not reveal any obvious textural differences between 71 and 61 m.y. zircon (Fig. 8A). Most likely the zircon grew incrementally over some or all of this interval and the complex internal structure reflects changing compositions of metamorphic fluids and/or melts.

Zircons from the leucosomes that are located in the metapelite yield dates from 68 to 63 Ma, similar dates to the younger zircon population from the metapelite. Because the leucosomes have probably not been derived from external sources, the 68 to 63 Ma dates give a further estimate on the timing of metamorphism in this region of the Skagit and are consistent with the metamorphic dates from the metapelite.

The older, Late Cretaceous (69-64 Ma) monazite results from the Gorge Lake and Sourdough localities likely record the timing of prograde metamorphism in the Skagit. The monazite dates are similar to those from zircons separated from the metapelite (mesosome). The older monazite occurs in both the metapelite and in leucosomes, suggesting that the monazite in the leucosomes was inherited during *in situ* melting or local transport of the leucosomes within the metapelitic host rock. The majority of the Th/U ratios of the 69 to 64 Ma monazites from both the mesosome and the leucosome are very similar, ~6.6 – 5.7 (Table 2). The similarity in Th/U ratios further suggests that the leucosome monazites were entrained into the melt from the mesosome.

The inferred timing of metamorphism based on zircon and monazite geochronology from migmatites is the same range recorded by plutons and dikes in the Skagit region, indicating that the North Cascades crystalline core experienced high-

temperature conditions throughout the Late Cretaceous to Eocene (Fig. 15). The presence of 65 Ma zircon and monazite in Skagit migmatite, the emplacement of the epidote-bearing Oval Peak batholith at 65 Ma, and the crystallization of orthogneiss bodies at 68 and 65 Ma (Miller et al., 1989; Miller and Bowring, 1990; Haugerud et al., 1991; Miller et al., 1993), suggest that a significant volume of granitoid melt was emplaced at this time. This interpretation is similar to that of Wernicke and Getty (1997), who proposed that peak Skagit metamorphism occurred between 68-60 Ma, based on the 68 Ma crystallization age of a metaquartz diorite body located between Gorge Lake and John Pierce Falls (Mattinson, 1972) and a 60 Ma Sm-Nd isochron age determined from analysis of zircon, apatite, hornblende and plagioclase. Regionally, the northwest Cordillera was still in a transpressional regime during the Late Cretaceous (e.g., Haeussler et al., 2003; Breitsprecher et al., 2003). Therefore, the zircons in the metapelite may record metamorphic growth at high-temperature conditions during thermal relaxation following major crustal thickening (≥ 60 km at ~90 Ma; Miller and Paterson, 2001). In addition, zircon and monazite metamorphic growth in the Skagit is probably highly influenced by the heat input generated during granitoid emplacement. The metapelite is surrounded by orthogneisses bodies that caused local heating and potential episodic metamorphic zircon growth.

This part of the Cordillera was affected by a change in plate motion at ~ 57 Ma, and the North Cascades arc became dominated by transtension (e.g., Miller and Bowring, 1990; Haugerud et al., 1989; Haeussler et al., 2003; Breitsprecher et al., 2003). The younger Paleocene-Eocene zircon and monazite ages from the Skagit Gneiss may be associated with metamorphism, partial melting, and deformation during isothermal

decompression from 8-10 kbar to 3-5 kbar at high-temperature conditions of > 650 ºC in a transtensional regime. Relative to zircon, monazite is more easily recrystallized during deformation, particularly in the presence of fluid at elevated temperature, and commonly records younger ages than zircon from the same rock (e.g., Teufel and Heinrich, 1997; Harlov et al., 2007). The younger monazite dates (49-46 Ma) from the Gorge Lake metapelitic mesosome and the John Pierce Falls samples may therefore reflect new monazite growth and/or fluid- and deformation-mediated recrystallization.

7. Anatectic Migmatite Crystallization

Anatectic leucosomes of the Skagit Gneiss yield different crystallization ages in each locality studied, and individual outcrops also record a variety of ages in texturally distinct leucosomes. For example, the oldest zircon crystallization age is 68 Ma at the westernmost locality, but the outcrop also contains leucosome with 64-63 Ma zircons. Leucosome mineral assemblages and composition are consistent with an origin by partial melting of the adjacent metapelitic gneiss composition (Whitney and Irving, 1994). The different zircon dates may indicate that the timing of melt crystallization varied on the scale of the outcrop due to different batches of melting. It is possible that some melt pods or bodies formed at different structural depths within the metapelite body and were subsequently injected or migrated to higher crustal levels and crystallized. Emplacement of nearby granitoid bodies could generate significant pulses of heating and melting in the metapelite.

The variation in crystallization ages on an outcrop-scale from leucosomes at Sourdough Mountain is probably a result of different melts intruding into the biotite

gneiss. All of the zircons from the host-biotite gneiss yield dates between 161 and 93 Ma. Although older zircons may be found in the gneiss, the currently-dated zircons all yield Jurassic to Cretaceous dates. The dates are consistent with detrital zircon results from sediments of the neighboring Methow basin (DeGraaff-Surpless et al., 2003). In comparison, the two concordant leucosomes from Sourdough yield mostly Late Cretaceous $^{206}Pb/^{238}U$ dates (65-61 Ma); however, both leucosomes contain detrital zircons with $^{207}Pb/^{206}Pb$ dates that range from 1343 to 2599 Ma, much older than the zircons dated from the biotite gneiss. The detrital zircon results indicate that the Sourdough leucosomes are probably not derived from local melting of the biotite gneiss, and instead, the melt must have been injected into the gneiss from an external source.

The zircon results reveal that migmatization of the Skagit Gneiss occurred over a significant time period (at least 20 m.y.) from the Latest Cretaceous to the Eocene. It is difficult to evaluate whether crustal melting occurred in pulses or whether it was a more continuous process. The low-K composition of the leucosomes may indicate that at least some of the partial melting was triggered by an influx of externally derived aqueous fluids from nearby syn-metamorphic crystallizing plutons (Whitney and Irving, 1994). A fluid inclusion study (Whitney, 1992a) documented evidence that a water-rich fluid was present in the Skagit during partial melting and metamorphism. Moreover, the CO_2-rich fluid inclusions are present in leucosomes in which textural and mineralogical features indicate an anatectic origin for the leucosome formation, suggesting that water-saturated melting was a primary mechanism for leucosome formation (Whitney and Irving, 1994). Various plutons with 68 to 65 Ma crystallization ages are located within ~ 1 km of the migmatite outcrops (Mattinson, 1972; Miller et al., 1989; Miller and Bowring, 1990;

Haugerud et al., 1991; Miller et al., 1993), and in addition, there are many undated deformed orthogneiss bodies that may have crystallized in the Cretaceous and Eocene, releasing fluids into the surrounding rocks. A possible scenario is that a second pulse of melting occurred during decompression as dehydration-melting reactions were crossed (Whitney, 1992b). Two partial melting mechanisms could explain the observed bimodal melt crystallization age results.

The leucosome zircon results show a small spread in individual dates on the m.y.- to 100,000-year time-scale from almost every sample. The spread in dates probably reflects continuous melting and re-melting over small time-scales. The Skagit Gneiss remained at high temperatures and was intruded by numerous plutonic bodies for over ~50 m.y., and therefore, the Skagit core was a high-temperature, fluid-rich environment ideal for continuous or episodic melting at local (outcrop) scales.

8. Partial Melting, Metamorphism and Deformation in the North Cascades Arc

The North Cascades and adjacent sedimentary basins provide an excellent locality to study the link between deep and shallow crust during orogenesis in continental magmatic arcs. The U-Pb zircon and monazite results from this study collectively show that metamorphism, partial melting, and deformation were major processes over a significant time from the Late Cretaceous to the Eocene. The ca. 53-46 Ma dates recorded in zircon from leucosomes are at the young end of the age spectrum for the North Cascades-Coast Plutonic belt complex (Fig.15). K-Ar and $^{40}Ar/^{39}Ar$ biotite and most hornblende cooling ages from the Skagit Gneiss range from 50 to 44 Ma (Engels et al., 1976; Tabor et al., 2003), showing that there is an overlap between high-grade

metamorphism and the argon cooling ages. Thus, the Skagit Gneiss must have undergone rapid cooling and presumably exhumation in the Eocene, soon after crystallization of the migmatites.

Non-marine sediments derived from external and local sources (primarily the Cascades core) were deposited in fault-bounded basins flanking the arc (Johnson, 1984, 1985; Tabor et al., 1984; Evans and Johnson, 1989; Evans, 1994; Vance, 2002) (Fig. 15). Zircon fission track dates from several of the basins, including the Swauk and Chumstick, range from ~54 to 48 Ma and 49-42 Ma, respectively (Gresens et al., 1981; Tabor et al., 1984) (Fig. 15). The young zircon and monazite dates from the leucosomes are the same or younger than the fission track dates from basin deposits, indicating that partial melt was still present in the high-grade Skagit Gneiss during transtensional extension and basin formation.

The microstructural results reveal that the leucosomes underwent significant post-melt crystallization deformation, with quartz fabrics recording both high-temperature and low-temperature deformation. Thus, deformation continued late into the thermal history of the Skagit Gneiss. This is consistent with the fact that the 46-44 Ma granitic dikes that intruded all parts of the Skagit are also deformed.

The results from the leucosomes, host-gneiss and metapelites show that metamorphism, deformation, and partial melting continued late in the history of the North Cascades arc, and furthermore, overlap with transtension. Based on the abundant migmatite in the crystalline core and the thermobarometric results that suggest high-grade conditions, the orogenic middle crust must have been relatively weak prior to and during extension. Moreover, the coincidence in dates between processes occurring in the deep

crust (i.e., partial melting and crustal flow) and processes occurring in the shallow crust (transtension and basin formation) may indicate a coupling between the crustal layers. For example, there may have been a positive feedback relationship between buoyant upward flow of melt and upper crustal transtension driving exhumation of the high-grade core, although extension outlasted partial melting as evidenced by the low-temperature overprint in the quartz microstructures of the leucosomes (Fig. 6). The results further suggest that the long-lived high temperature Skagit Gneiss cooled quickly, terminating flow of the weak middle crust at ca. 45 Ma. Collectively, the results indicate that deep and shallow processes are both spatially and temporarily related within continental magmatic arc systems and that the entire crustal package from the lower-crust to the surface must be examined in arcs in order to determine cooling and exhumation mechanisms.

ACKNOWLEDGEMENTS

This research was supported by NSF grant EAR-0510326 to D. Whitney, R. Miller, and S. Bowring, and the Department of Geology and Geophysics at the University of Minnesota. Thank you to Jahan Ramezani and Matt Rioux for their help in the TIMS lab. Thank you to Niki Wintzer for her help in the field and for discussions about the Hwy 20 Skagit corridor. We thank C. Teyssier for helpful discussions of the Skagit Gneiss.

REFERENCES

Babcock, R.S., Misch, P., 1989. Origin of the Skagit migmatites, North Cascades Range, Washington State. Contrib. Mineral. Petrol. 101, 485-495.

Babcock, R.S., Armstrong, R.L., Misch, P., 1985. Isotopic constraints on the age and origin of the Skagit Metamorphic Suite and related rocks. Abstracts with Programs-Geol. Soc. Am. 17, 339.

Breitsprecher, K., Thorkelson, D.J., Groome, W.G., Dostal, J., 2003. Geochemical confirmation of the Kula-Farallon slab window beneath the Pacific Northwest in Eocene time. Geology 31, 351-354.

Brown, M., 2005. Synergistic effects of melting and deformation: an example from the Variscan belt, western France. Geol. Soc. London 243, 205-226.

Clark, M.K., Royden, L.H., 2000. Topographic ooze: building the eastern margin of Tibet by lower crustal flow. Geology 28, 703-706.

Conrad, W.K., Nicholls, I.A., Wall, V.J., 1988. Water-saturated and undersaturated melting at 10 kbar: evidence for the origin of silicic magmas in the Taupo Volcanic Zone, New Zealand, and other occurrences. J. Petrol. 29, 765-803.

Crawford, M.L., Hollister, L.S., Woodsworth, G.J., 1987. Crustal deformation and regional metamorphism across a terrane boundary, Coast Plutonic Complex, British Columbia. Tectonics 6, 343-361.

DeGraaff-Surpless, K., Mahoney, J.B., Wooden, J.L., McWilliams, M.O., 2003. Lithofacies control in detrital zircon provenance studies: insights into the Cretaceous Methow basin, southern Canadian Cordillera. Geol. Soc. Am. Bull. 115, 899-915.

Dell'Angelo, L.N., Tullis, J., Yund, R.A., 1987. Transition from dislocation creep to melt-enhanced diffusion creep in fine-grained granitic aggregates. Tectonophysics 139, 325-332.

Dewey, J.F., 1988. Extensional collapse of orogens. Tectonics 7, 1123-1139.

Engels, J.C., Tabor, R.W., Miller, F.K., Obradovich, J.D., 1976. Summary of K-Ar, Rb-Sr, U-Pb, and fission track ages of rocks from Washington State prior to 1975 (exclusive of Columbia Plateau Basalts). U.S. Geological Survey, MF-710.

Evans, J.E., 1994. Depositional history of the Eocene Chumstick Formation: Implications of tectonic partitioning for the history of the Leavenworth and Entiat-Eagle Creek fault systems. Tectonics 13, 1425-1444.

Evans, J.E., Johnson, S.Y., 1989. Paleogene strike-slip basins of central Washington: Swauk Formation and Chumstick Formation. In: Joseph, N.L. et al. (Eds.), Geologic Guidebook for Washington and Adjacent Areas. Wash. Div. Geol. Earth Resources, Information Circular 86, 213-237.

Fielding, E., Isacks, B., Barazangi, M., Duncan, C.C., 1994. How flat is Tibet? Geology 22, 163-167.

Gébelin, A., Brunel, M., Monié, P., Faure, M., Arnaud, N., 2007. Relationships between Carboniferous magmatism and ductile shear zones in the Limousin (Massif Central, France). Tectonics 26, TC2008, doi:10.1029/2005TC001822.

Gresens, R.L., Naeser, C.W., Whetten, J.T., 1981. Stratigraphy and age of the Chumstick and Wenatchee Formations – Tertiary fluvial and lacustrine rocks, Chiwaukum Graben, Washington. Geol. Soc. Am. Bull. 92, 233-236.

Gordon, S.M., Whitney, D.L., Teyssier, C., Grove, M., Dunlap, W.J., 2008. Timescales of migmatization, melt crystallization, and cooling in a Cordilleran gneiss dome, the Valhalla complex, southeastern British Columbia. Tectonics 27, TC4010, doi:10.1029/2007TC002103.

Handy, M.R., Mulch, A., Rosenau, M., Rosenberg, C.L., 2001. The role of fault zones and melts as agents of weakening, hardening and differentiation of the continental crust: a synthesis. In: Holdworth, R.E., Strachan, R.A., Magloughlin, J.F., Knipe, R.J. (Eds.), The Nature and Tectonic Significance of Fault Zone Weakening. Geol. Soc. London, 186, pp. 305-332.

Haeussler, P.J., Bradley, D.C., Wells, R., Miller, M.L., 2003. Life and death of the Resurrection plate: evidence for an additional plate in the northeastern Pacific in Paleocene-Eocene time. Geol. Soc. Am. Bull. 115, 867-880.

Harlov, D.E., Wirth, R., Hetherington, C.J., 2007. The relative stabilitity of monazite and huttonite at 300-900 ºC and 200-1000 MPa: metasomatism and the propagation of metastable mineral phases. Am. Min. 92, 1652-1664.

Haugerud, R.A., van der Heyden, P., Tabor, R.W., Stacey, J.S., Zartman, R.E., 1991. Late Cretaceous and early Tertiary plutonism and deformation in the Skagit Gneiss Complex, North Cascades range, Washington and British Columbia. Geol. Soc. Am. Bull. 103, 1297-1307.

Hinchey, A.M., 2005. Thor-Odin dome: constraints on Paleocene-Eocene anatexis and deformation, leucogranite generation and the tectonic evolution of the southern Omineca belt, Canadian Cordillera. PhD thesis, Carleton University, Ottawa, Ontario, p. 258.

Hollister, L.S., 1993. The role of melt in the uplift and exhumation of orogenic belts. Chem. Geol. 108, 31-48.

Hollister, L.S., Crawford, M.L., 1986. Melt-enhanced deformation: A major tectonic process. Geology 14, 558-561.

Hoskin, P.W.O., Schaltegger, U., 2003. The composition of zircon and igneous and metamorphic petrogenesis. In: Hanchar, J.M., Hoskin, P.W.O. (Eds.), Zircon. Reviews Min. Geochem., 53, pp. 27-62.

Hurlow, H.A., 1992. Structural and U-Pb geochronologic studies of the Pasayten fault, Okanogan Range batholith, and southeastern Cascades crystalline core, Washington. PhD thesis, University of Washington, Seattle, WA.

Inger, S., Harris, N., 1993. Geochemical constraints on leucogranite magmatism in the Langtang Valley, Nepal Himalaya. J. Petrol. 34, 345-368.

Johnson, S.Y., 1984. Stratigraphy, age, and paleogeography of the Eocene Chuckanut Formation, northwest Washington. Can. J. Earth Sci. 21, 92-106.

Johnson, S.Y., 1985. Eocene strike-slip faulting and nonmarine basin formation in Washington. Soc. Econ. Paleontologists and Mineralogists Special Publication 37, 283-302.

Journeay, J.M., Friedman, R.M., 1993. The Coast Belt thrust system: Evidence of Late Cretaceous shortening in southwest British Columbia. Tectonics 12, 756-775.

Karlstrom, K.E., Williams, M.L., 2006. Nature of the middle-crust – heterogeneity of structure and process due to pluton-enhanced tectonism: an example from Proterozoic rocks of the North American Southwest. In: Brown, M., Rushmer, T. (Eds.), Evolution and differentiation of the continental crust. Cambridge, UK, Cambridge University Press, p. 268-295.

Keay, S., Lister, G., Buick, I., 2002. The timing of partial melting, Barrovian metamorphism and granite intrusion in the Naxos metamorphic core complex, Cyclades, Aegean sea, Greece. Tectonophysics 342, 275-312.

Klepeis, K.A., King, D., De Paoli, M., Clarke, G.L., Gehrels, G., 2007. Interaction of strong lower and weak middle crust during lithospheric extension in eastern New Zealand. Tectonics 26, TC4017, doi:10.1029/2006TC002003.

Kruckenberg, S.C., Whitney, D.L., Teyssier, C., Fanning, C.M., Dunlap, W.J., 2008. Paleocene-Eocene migmatite crystallization, extension, and exhumation in the hinterland of the northern Cordillera: Okanogan dome, Washington, USA. Geol. Soc. Am. Bull. 120, 912-929.

Mattinson, J.M., 1972. Ages of zircons from the northern Cascade Mountains, Washington. Geol. Soc. Am. Bull. 83, 3769-3784.

Matzel, J.E.P., Bowring, S.A., Miller, R.B., 2004. Protolith age of the Swakane Gneiss, North Cascades, Washington: Evidence of rapid underthrusting of sediments beneath an arc. Tectonics 23, TC6009, doi:10.1029/2003TC001577.

Miller, R.B., 1994. A mid-crustal contractional stepover zone in a major strike-slip system, North Cascades, Washington. J. Struct. Geol. 16, 47-60.

Miller, R.B., Bowring, S.A., 1990. Structure and chronology of the Oval Peak batholith and adjacent rocks: Implications for the Ross Lake fault zone, North Cascades, Washington. Geol. Soc. Am. Bull. 102, 1361-1377.

Miller, R.B., Paterson, S.R., 2001. Influence of lithological heterogeneity, mechanical anisotropy, and magmatism on the rheology of an arc, North Cascades, Washington. Tectonophysics, 342, 351-370.

Miller, R.B., Paterson, S.R., 1992. Tectonic implications of syn-emplacement and post-emplacement deformation of the Mount Stuart batholith for mid-Cretaceous orogenesis in the North Cascades. Can. J. Earth Sci. 29, 479-485.

Miller, R.B., Bowring, S.A., Hoppe, W.J., 1989. Paleocene plutonism and its tectonic implications, North Cascades, Washington. Geology 17, 846-849.

Miller, R.B., Brown, E.H., McShane, D.P., Whitney, D.L., 1993. Intra-arc crustal loading and its tectonic implications, North Cascades crystalline core, Washington and British Columbia. Geology 21, 255-258.

Miller, R.B., Paterson, S.R., Lebit, H., Alsleben, H., Lüneburg, C., 2006. Significance of composite lineations in the mid- to deep crust: a case study from the North Cascades, Washington. J. Struct. Geol. 28, 302-322.

Misch, P., 1966. Tectonic evolution of the northern Cascades of Washington State – a west Cordilleran case history. Can. Inst. Mining and Metallurgy 8, 101-148.

Misch, P., 1968. Plagioclase compositions and non-anatectic origin of migmatitic gneisses in Northern Cascade mountains of Washington State. Contrib. Mineral. Petrol. 17, 1-70.

Monger, J.W.H., Price, R.A., Tempelman-Kluit, D.J., 1982. Tectonic accretion and plutonic welts in the Canadian Cordillera. Geology 10, 70-75.

Mulch, A., Teyssier, C., Cosca, M.A., Vanderhaeghe, O., Vennemann, T.W., 2004. Reconstructing paleoelevation in eroded orogens. Geology 32, 525-528.

Mulch, A., Chamberlain, C.P., 2007. Stable isotope paleoaltimetry in orogenic belts – the silicate record in surface and crustal geological archives. Reviews Mineral. Geochemistry 66, 89-118.

Nelson, K.D., Wenjin Zhao, Brown, L.D., Kuo, J., Jinkai Che, Xianwen Liu, Klemperer, S.L., Makovsky, Y., Meissner, R., Mechie, J., Kind, R., Wenzel, F., Ni, J., Nabelek, J., Chen Leshou, Handong Tan, Wenbo Wei, Jones, A.G., Booker, J., Unsworth, M., Kidd, W.S.F., Hauck, M., Alsdorf, D., Ross, A., Cogan M., Changde Wu, Sandvol, E., Edwards, M., 1996. Partially molten middle crust beneath southern Tibet: Synthesis of project INDEPTH results. Science 274, 1684-1688.

Paterson, S.R., Miller, R.B., 1998. Magma emplacement during arc-perpendicular shortening; an example from the Cascades crystalline core, Washington. Tectonics 17, 571-586.

Paterson, S.R., Miller, R.B., Alsleben, H., Whitney, D.L., Valley, P.M., Hurlow, H., 2004. Driving mechanisms for > 40 km of exhumation during contraction and extension in a continental arc, Cascades core, Washington. Tectonics 23, TC3005, doi:10.1029/2002TC001440.

Patiño Douce, A.E., Johnston, A.D., 1991. Phase equilibria and melt productivity in the pelitic system: implications for the origin of peraluminous granitoids and aluminous granulites. Contrib. Min. Petrol. 107, 202-218.

Rey, P., Vanderhaeghe, O., Teyssier, C., 2001. Gravitational collapse of the continental crust: definition, regimes and modes. Tectonophysics 342, 435-449.

Rubatto, D., 2002. Zircon trace element geochemistry: partitioning with garnet and the link between U-Pb ages and metamorphism. Chem. Geol. 184, 123-138.

Rubin, C.M., Saleeby, J.B., Cowan, D.S., Brandon, M.T., McGroder, M.F., 1990. Regionally extensive mid-Cretaceous west-vergent thrust system in the northwestern Cordillera: Implications for continent-margin tectonism. Geology 18, 276-280.

Schilling, F.R., Partzsch, G.M., 2001. Quantifying partial melt fraction in the crust beneath the central Andes and the Tibetan Plateau. Physics Chem. Earth 26, 239-246.

Tabor, R., Haugerud, R., 1999. Geology of the North Cascades. The Mountaineers, Seattle, 143pp.

Tabor, R.W., Frizzell, V.A., Vance, J.A., Naeser, C.W., 1984. Ages and stratigraphy of lower and middle Tertiary sedimentary and volcanic rocks of the central Cascades,

Washington: application to the tectonic history of the Straight Creek fault. Geol. Soc. Am. Bull. 95, 26-44.

Tabor, R.W., Haugerud, R.A., Brown, E.H., Babcock, R.S., Miller, R.B., 1989. Accreted terranes of the North Cascades Range, Washington. 28th International Geological Congress, Field Trip Guidebook T307, 1-62.

Tabor, R.W., Haugerud, R.A., Hildreth, W., Brown, E.H., 2003. Geologic map of the Mount Baker 30- by 60 minute quadrangle, Washington, U.S. Geological Survey, Geologic Investigation Series, I-2660, with pamphlet, 70, scale 1:100,000.

Teufel, S., Heinrich, W., 1997. Partial resetting of the U-Pb isotope system in monazite through hydrothermal experiments: An SEM and U-Pb isotope study. Chem. Geol. 137, 273-281.

Teyssier, C., Whitney, D.L., 2002. Gneiss domes and orogeny. Geology 30, 1139-1142.

Umhoefer, P.J., Miller, R.B., 1996. Mid-Cretaceous thrusting in the southern Coast Belt, British Columbia and Washington, after strike-slip fault reconstruction. Tectonics 15, 545-565.

Valley, P.M., Whitney, D.L., Paterson, S.R., Miller, R.B., Alsleben, H., 2003. Metamorphism of deepest exposed arc rocks in the Cretaceous to Paleogene Cascades belt, Washington: evidence for large-scale vertical motion in a continental arc. J. Metamorph. Geol. 21, 203-220.

Vance, J.A., 2002. Age and provenance of nonmarine sandstones in the central and northwest Washington Cascades: Fission track evidence from detrital zircons. Geol. Soc. Am. Abstracts with Programs 34, 96.

Vanderhaeghe, O., Teyssier, C., 2001. Partial melting and flow of orogens, Tectonophysics 342, 451-472.

Vanderhaeghe, O., Teyssier, C., Wysoczanski, R., 1999. Structural and geochronological constraints on the role of partial melting during the formation of the Shuswap metamorphic core complex at the latitude of the Thor-Odin Dome, British Columbia. Can. J. Earth Sci. 36, 917-943.

Waight, T.E., Weaver, S.D., Muir, R.J., 1998. Mid-Cretaceous granitic magmatism during the transition from subduction to extension in southern New Zealand: a chemical and tectonic synthesis. Lithos, 45, 469-482.

Walker, J.D., Martin, M.W., Bowring, S.A., Searle, M.P., Waters, D.J., Hodges, K.V., 1999. Metamorphism, melting, and extension: Age constraints from the High Himalayan Slab of southeast Zanskar and northwest Lahaul. J. Geol. 107, 483-495.

Wernicke, B., Getty, S.R., 1997. Intracrustal subduction and gravity currents in the deep crust: Sm-Nd, Ar-Ar, and thermobarometric constraints from the Skagit Gneiss Complex, Washington. Geol. Soc. Am. Bull. 109, 1149-1166.

Whitney, D.L., 1992a. Origin of CO_2-rich fluid inclusions in leucosomes from the Skagit migmatites, North Cascades, Washington. J. Metamorph. Geol. 10, 715-725.

Whitney, D.L., 1992b. High pressure metamorphism in the western Cordillera of North America: an example from the Skagit Gneiss, North Cascades, Washington. J. Metamorph. Geol. 10, 71-85.

Whitney, D.L., Irving, A.J., 1994. Origin of K-poor leucosomes in a metasedimentary migmatite complex by ultrametamorphism, syn-metamorphic magmatism, and subsolidus processes. Lithos 32, 173-192.

Whitney, D.L., Miller, R.B., Paterson, S.R., 1999. P-T evidence for the magnitude of syn-metamorphic vertical tectonic motion in a contractional orogen: the North Cascades – Coast Mountains Belt, northern U.S. and Canadian Cordillera. J. Metamorph. Geol. 17, 73-88.

Whitney, D.L., Teyssier, C., Fayon, A.K., Hamilton, M.A., Heizler, M., 2003. Tectonic controls on metamorphism, partial melting, and intrusion: timing of regional metamorphism and magmatism of the Nigde Massif, Turkey. Tectonophysics 376, 37-60.

Whitney, D.L., Paterson, S.R., Schmidt, K.L., Glazner, A.F., Kopf, C.F., 2004. Growth and demise of continental arcs and orogenic plateaux in the North American Cordillera: from Baja to British Columbia. In: Grocott, J., McCaffrey, K.J.W., Taylor, G. & Tikoff, B. (Eds). Vertical Coupling and Decoupling in the Lithosphere. Geol. Soc., London, Special Publications, 227, 167-176.

Wolfe, J.A., Forest, C.E., Molnar, P., 1998. Paleobotanical evidence of Eocene and Oligocene paleoaltitudes in midlatitude western North America. Geol. Soc. Am. Bull. 110, 664-678.

Yardley, B.W.D., 1978. Genesis of the Skagit Gneiss migmatites, Washington, and the distinction between possible mechanisms of migmatization. Geol. Soc. Am. Bull. 89, 941-951.

Zhang, H.F., Harris, N., Parrish, R., Kelley, S., Zhang, L., Rogers, N., Argles, T., King, J., 2004. Causes and consequences of protracted melting of the mid-crust exposed in the North Himalayan antiform. Earth Planet. Sci. Lett. 228, 195-212.

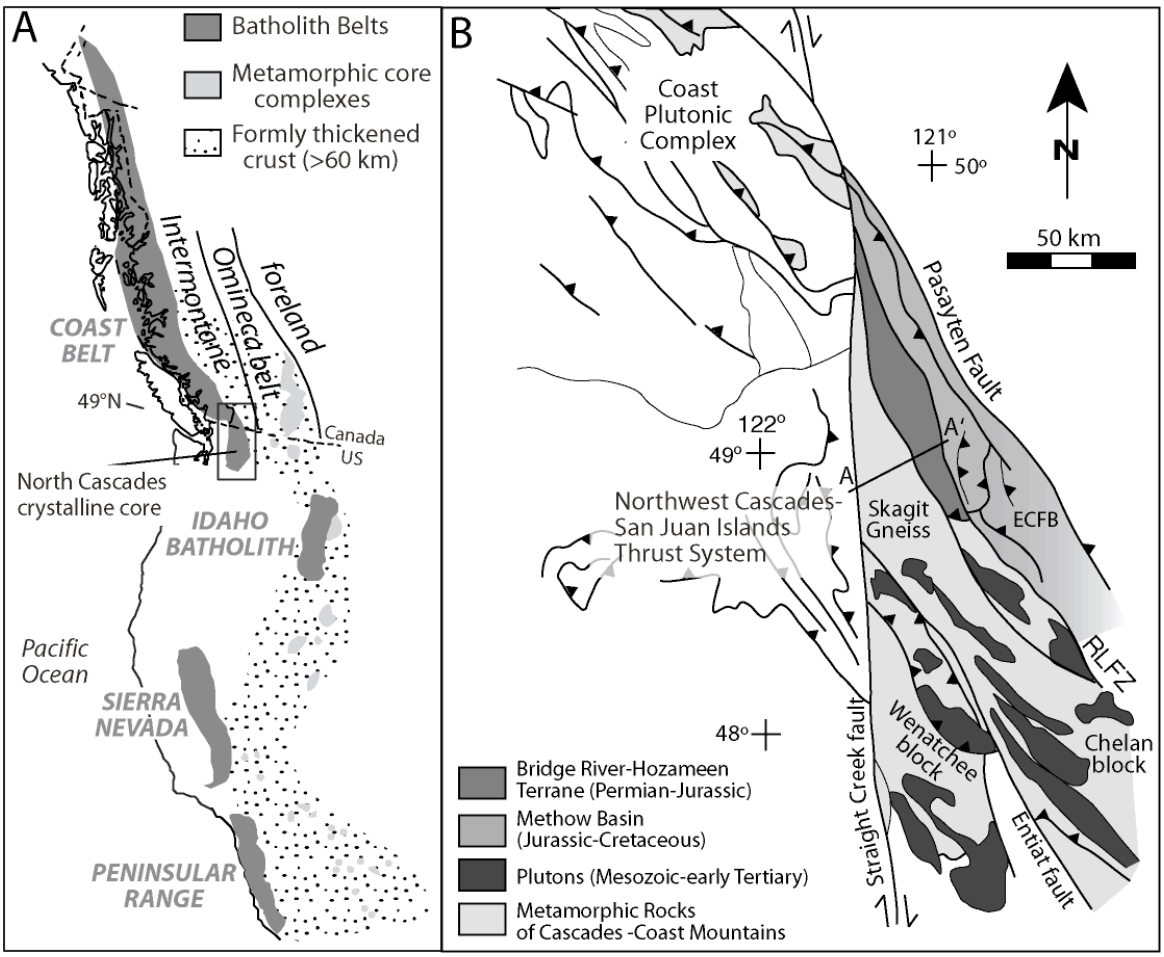

Figure 5.1: A) Simplified map of the North American Cordillera showing the location of the batholith belts, including the Coast Plutonic Complex-North Cascade Range, and the inboard interior belts, the Omineca-Sevier belt (after Whitney et al., 2004); B) Geologic map of the North Cascades, showing the location of the Skagit Gneiss and other tectonic elements of the orogen and adjacent terrains (after Miller et al., 2006). Line A to A' represents the cross section shown in Figure 3.

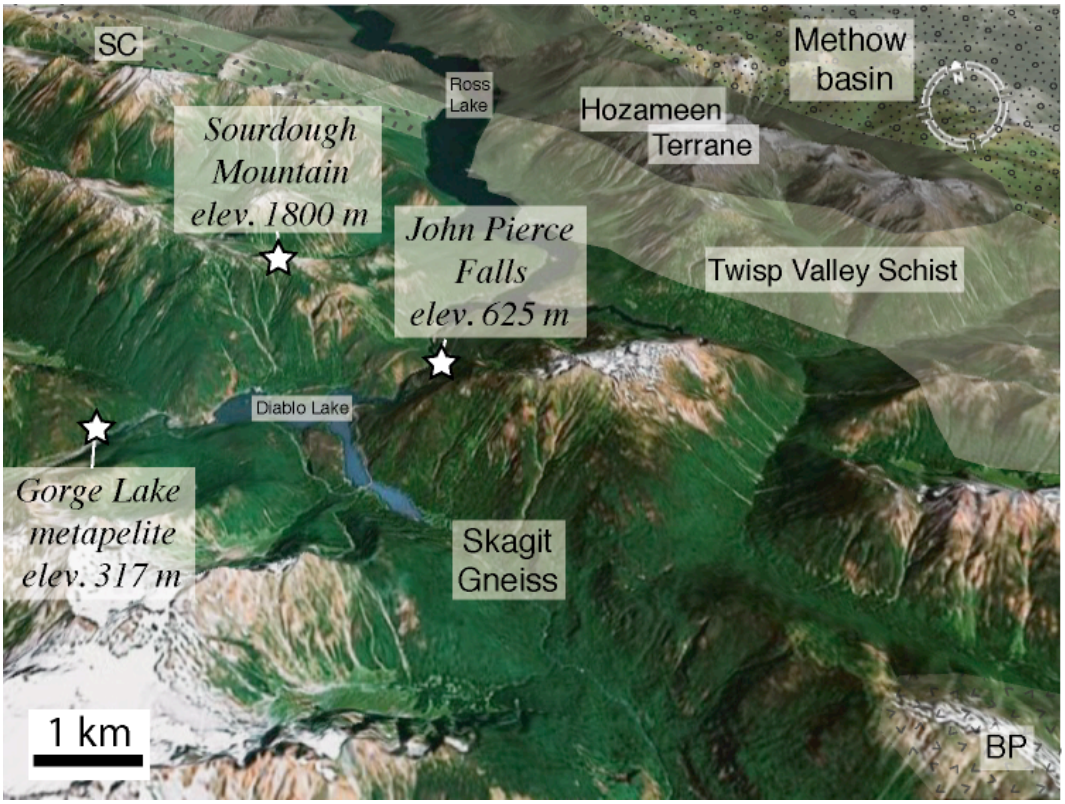

Figure 5.2: Oblique Google Earth map showing the location and elevation of the three outcrops in which leucosome, gneiss, and metapelite were collected. SC: Skymo Complex; BP: Black Peak batholith.

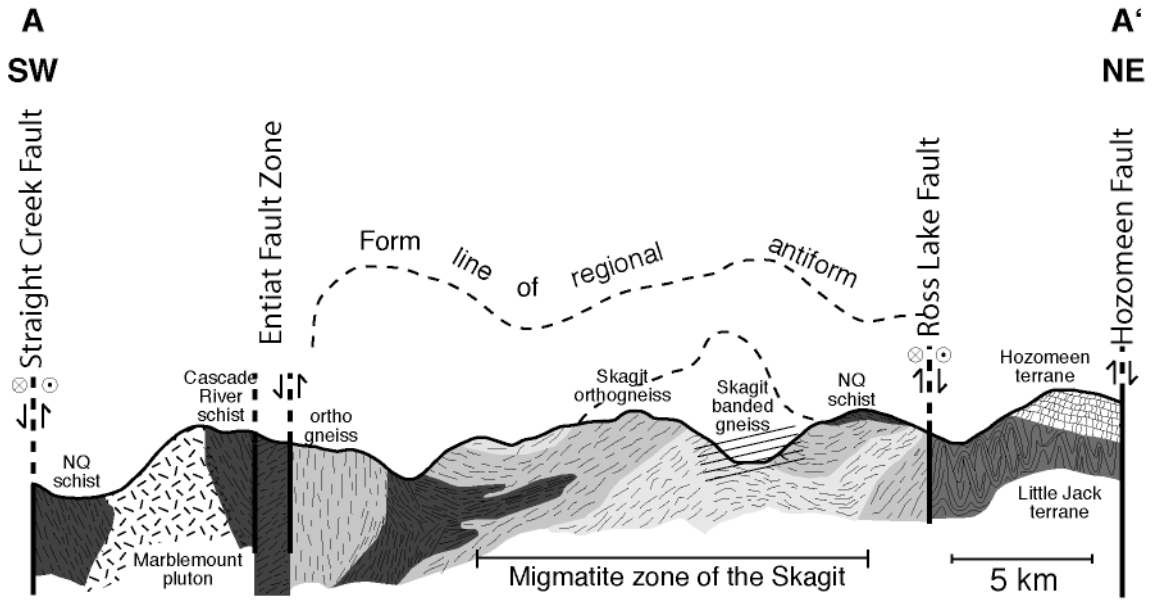

Figure 5.3: Simplified cross section through the Skagit Gneiss, showing the antiformal structure of the crystalline core. The line pattern indicates the approximate location of the sample collected for this study. Note the migmatites are exposed in the north-central portion of Skagit Gneiss (modified from Tabor and Haugerud, 1999).

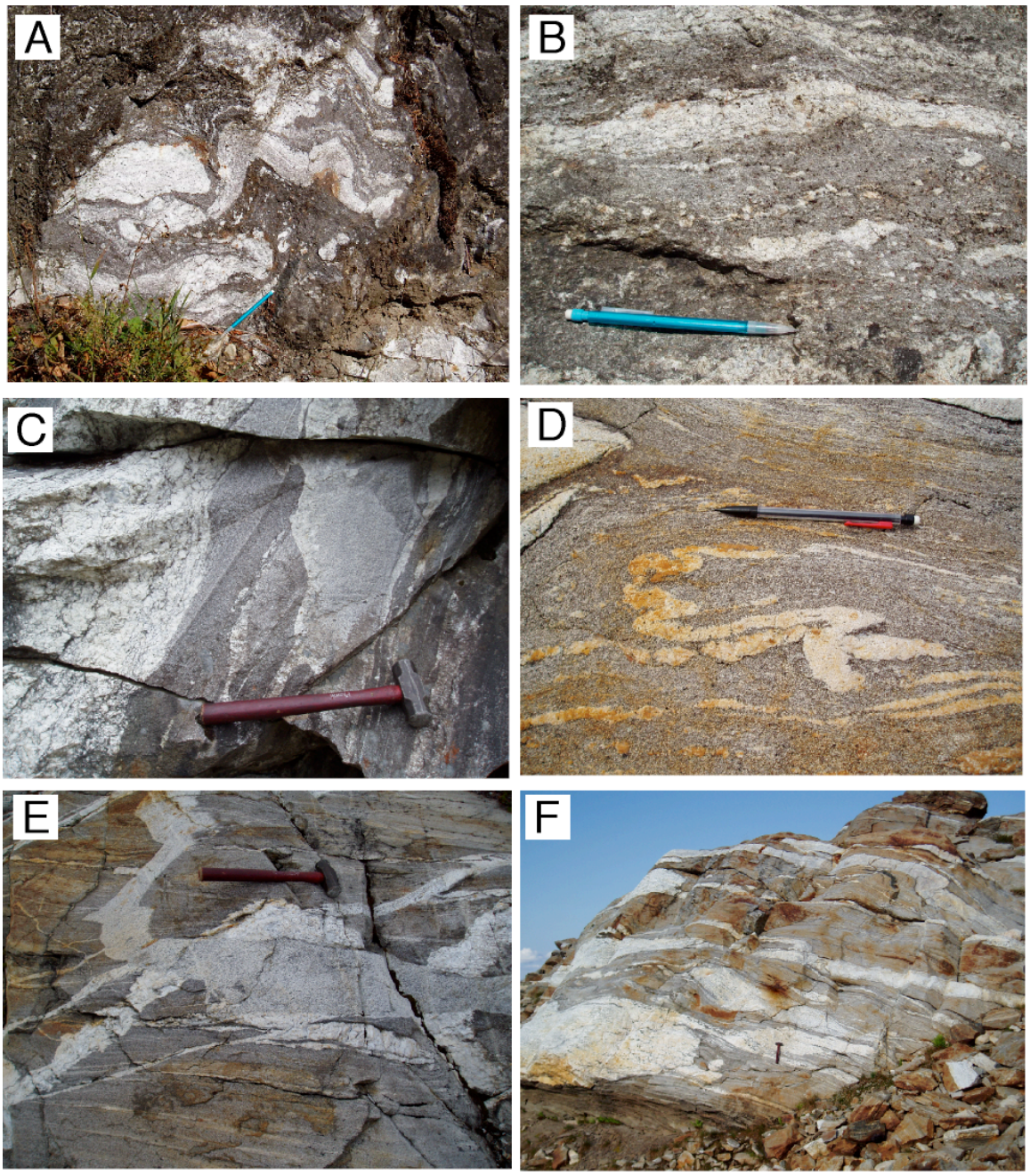

Figure 5.4: Photographs showing the different types of migmatites found in the Skagit Gneiss: A) folded leucosome within Gorge Lake metapelite; B) layer-parallel leucosome in the Gorge Lake metapelite; C) Discordant pegmatite (left in the photo) adjacent to the biotite gneiss at John Pierce Falls; D) folded leucosome in the garnet-biotite on Sourdough Mountain; E) several different textural types of leucosome cross-cutting layer-parallel leucosomes and foliation of the host-rock; and F) Pegmatite and layer-parallel leucosomes cutting the host garnet-biotite gneiss on Sourdough Mountain.

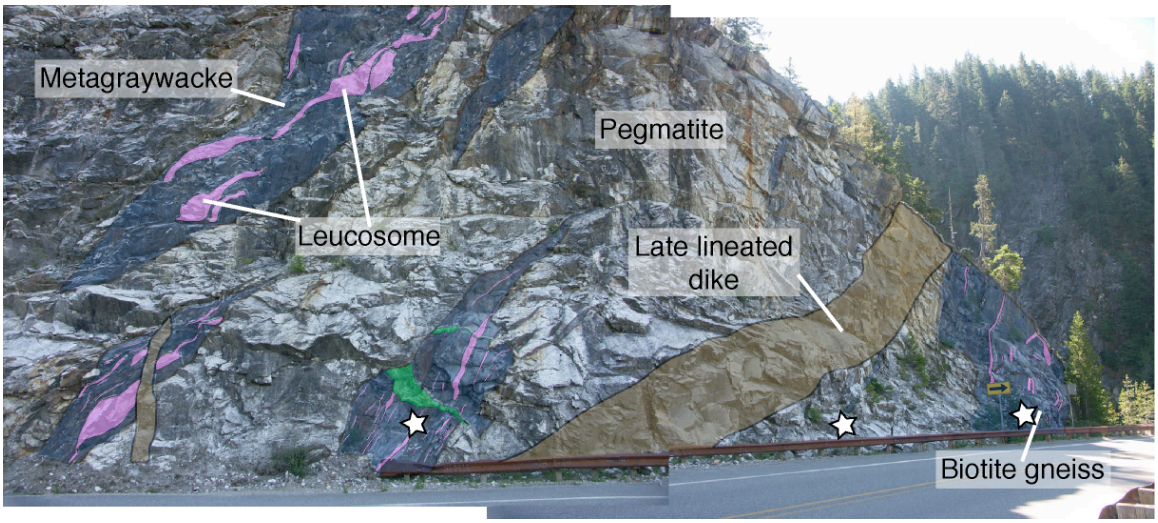

Figure 5.5: Annotated photograph of the John Pierce Falls outcrop. The unshaded rock represents the pegmatite, sample SK0620C. Within the pegmatite, lozenges of metagraywacke are shaded and contain layer-parallel leucosomes, including sample SK0620B. On the far right is the biotite gneiss body, sample SK0620D. The stars represent the exact spot in which the samples were collected.

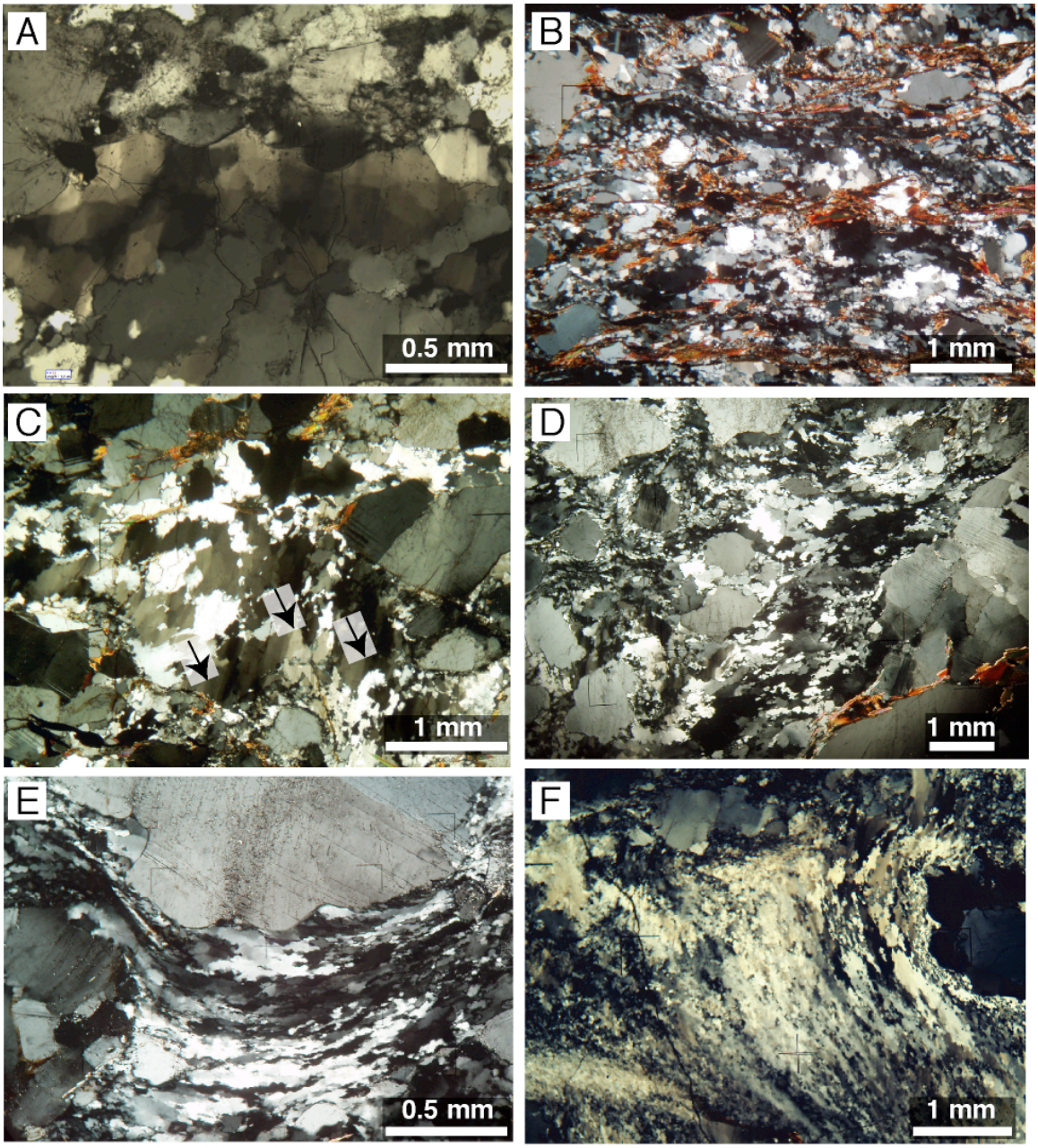

Figure 5.6: Photomicrographs showing some of the microstructural characteristics found in the Skagit Gneiss. (A) Chessboard extinction in quartz from sample SK061DL; (B) Biotite defines a S-C fabric and quartz is recrystallized in the metapelite, SK061DM; (C). Arrows point to deformation bands in some of the quartz grains of SK0620B. All of the quartz shows amoeboid grain edges; (D) Quartz is recrystallized along shear bands and plagioclase shows some recrystallization along the grain boundary and sericitization; (E) Quartz is recrystallized and elongated as it wraps around larger plagioclase crystals; (F) Extensive quartz recrystallization and a strong CPO in mylonitic fabrics of SK061C.

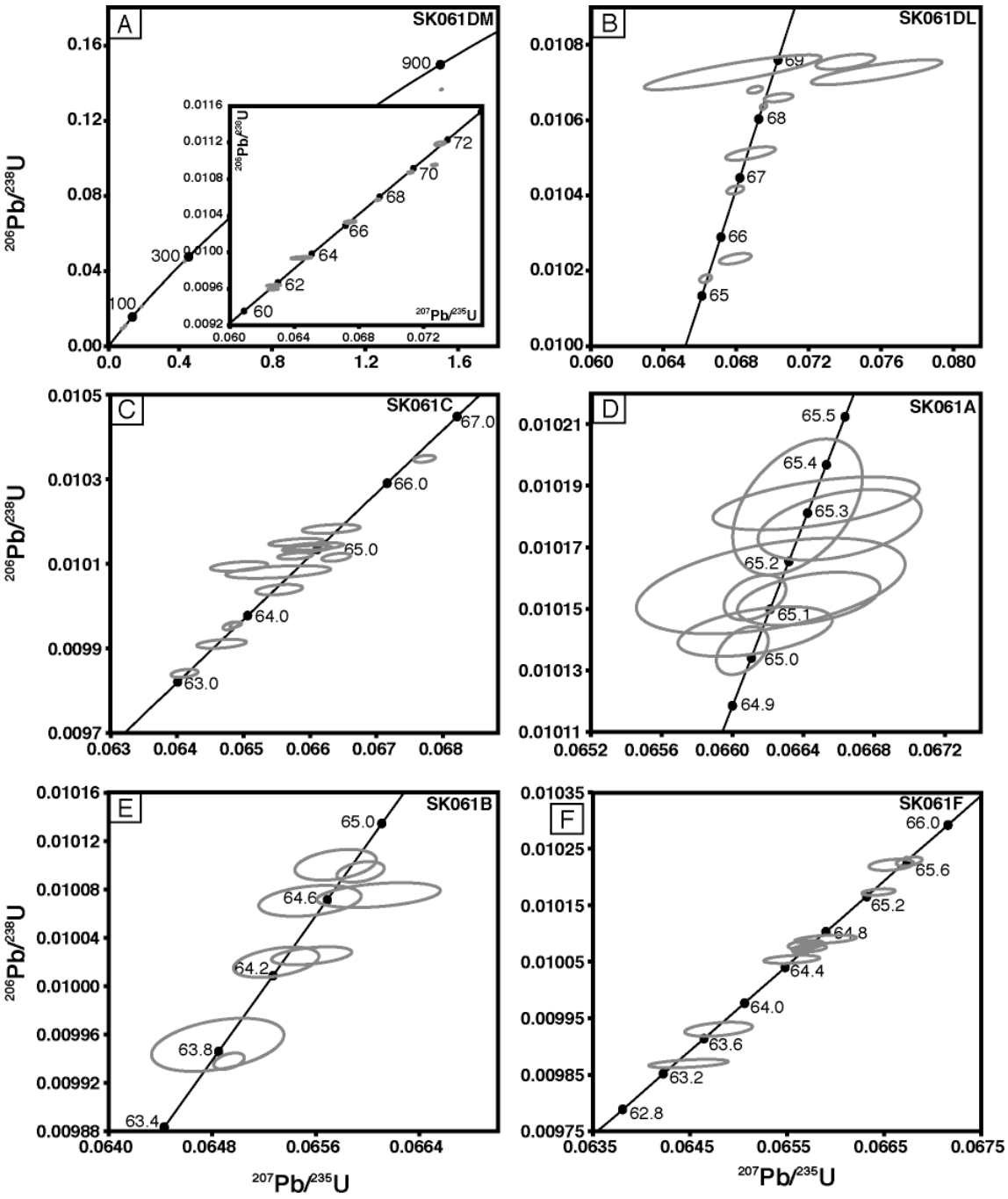

Figure 5.7: U-Pb concordia diagrams for zircon analyses from the Gorge Lake outcrop: (A) SK061DM; (B) SK061DL; (C) SK061C; (D) SK061A; (E) SK061B; and (F) SK061F.

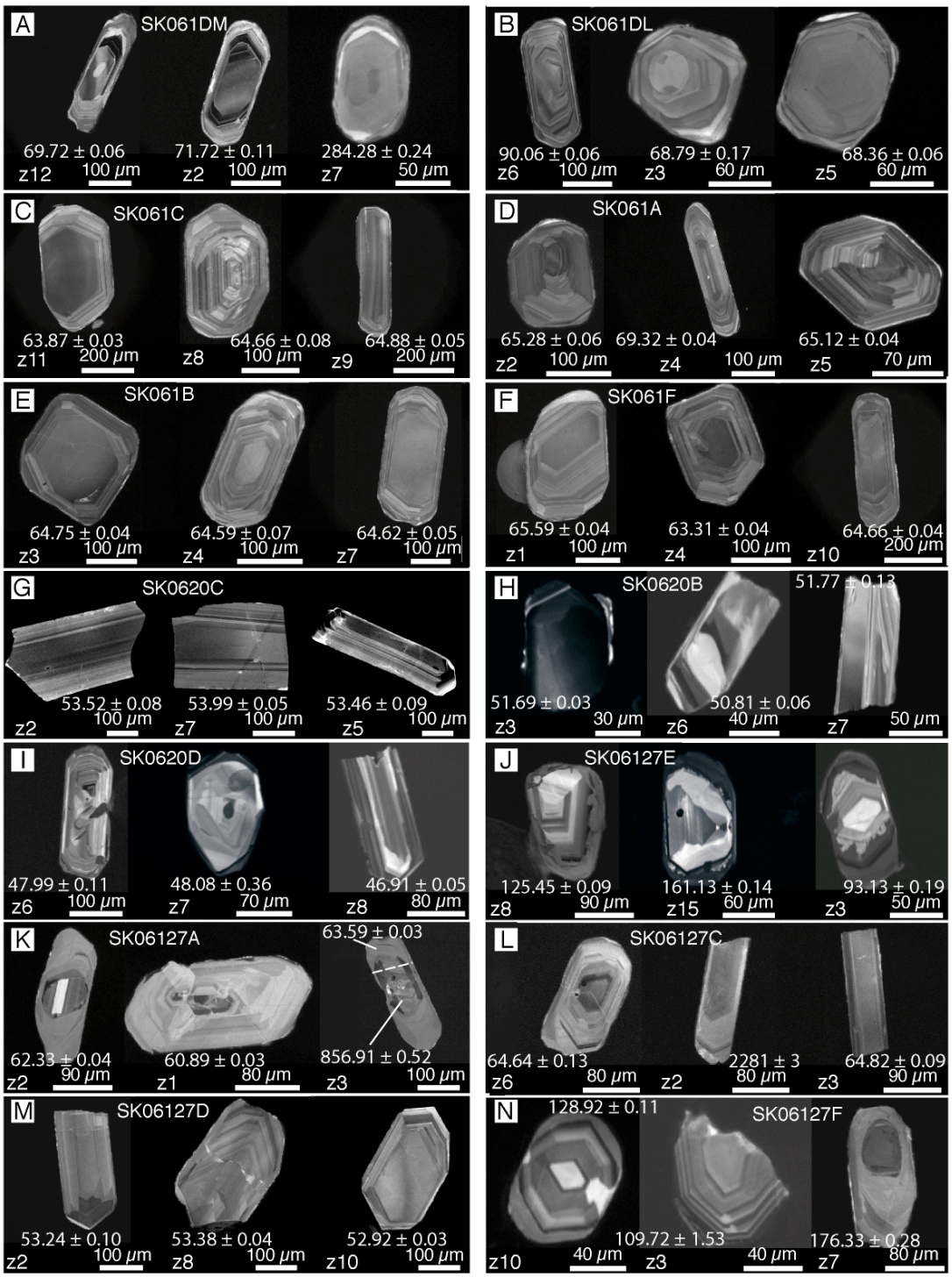

Figure 5.8: Cathodoluminescence images of zircon grains that were analyzed after imaging. The number corresponds to the fraction number in Table 2, and the U-Pb date is also shown for samples: (A) SK061DM; (B) SK061DL; (C) SK061C; (D) SK061A; (E) SK061B; (F) SK061F; (G) SK0620C; (H) SK0620B; (I) SK0620D; (J) SK06127E; (K) SK06127A; (L) SK06127C; (M) SK06127D; and (N) SK06127F.

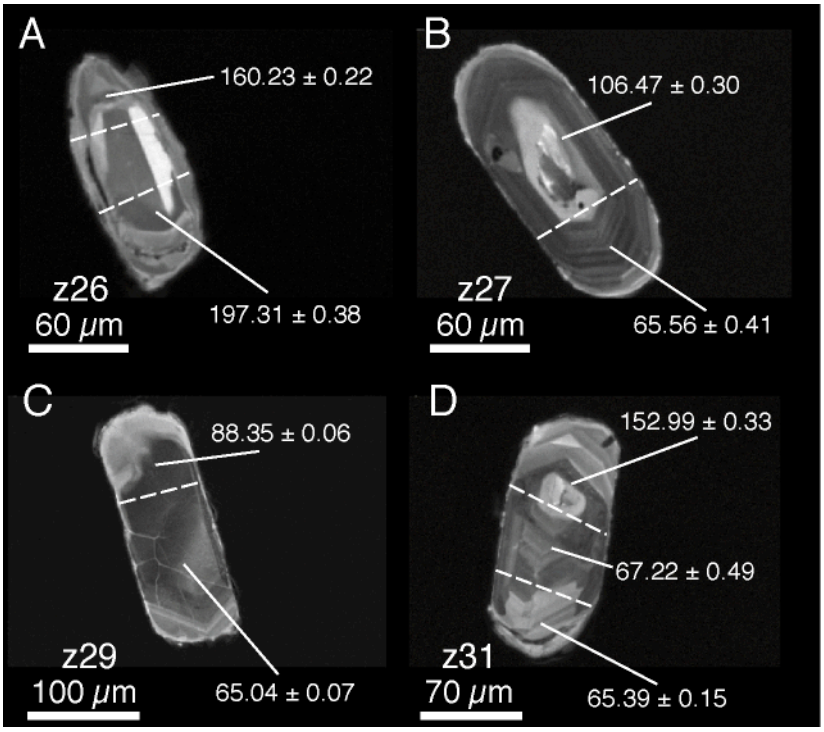

Figure 5.9: Cathodoluminescence images of zircon grains from sample SK061DM. The grains were broken into pieces along the dashed white lines and the individual pieces were analyzed and their respective dates are shown for grains: (A) z26; (B) z27; (C) z29; and (D) z31.

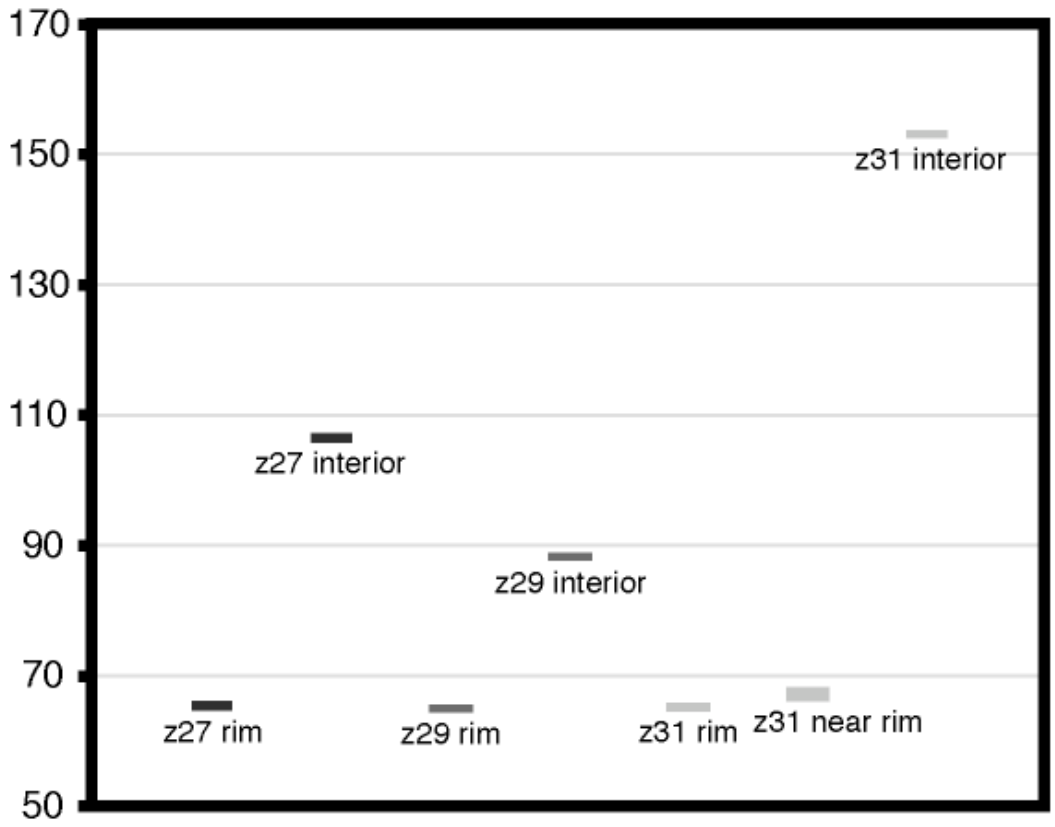

Figure 5.10: Weighted average diagram for the detailed zircon results, grains z27, z29, and z31. The weighted average diagram shows that the rim dates are consistently ca. 65 Ma, and the interior of the grains yield a variety of older dates.

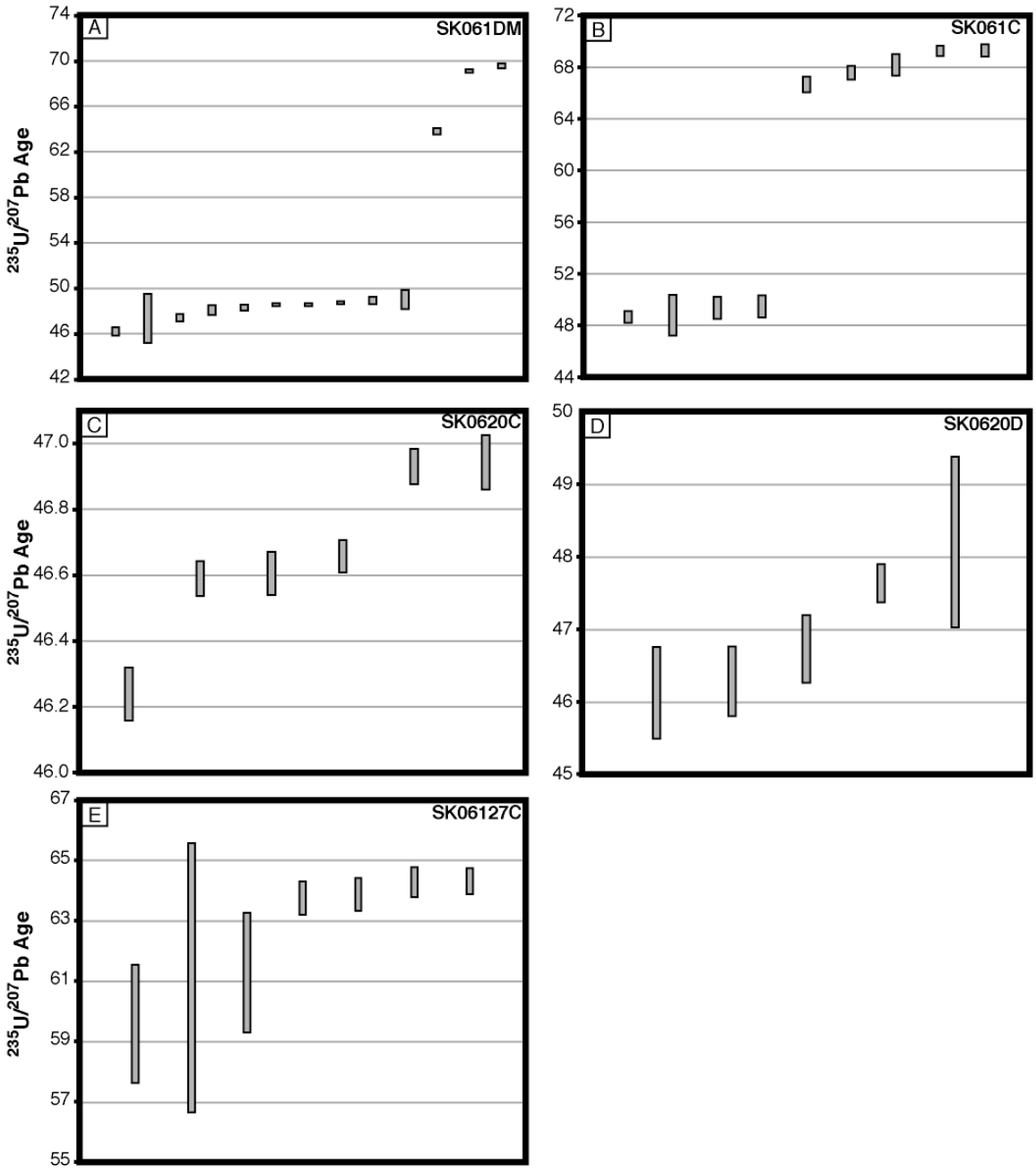

Figure 5.11: Monazite weighted average diagrams. Each bar represents a single monazite analysis. (A) SK061DM; (B) SK061C; (C) SK0620C; (D) SK0620D; and (E) SK06127C.

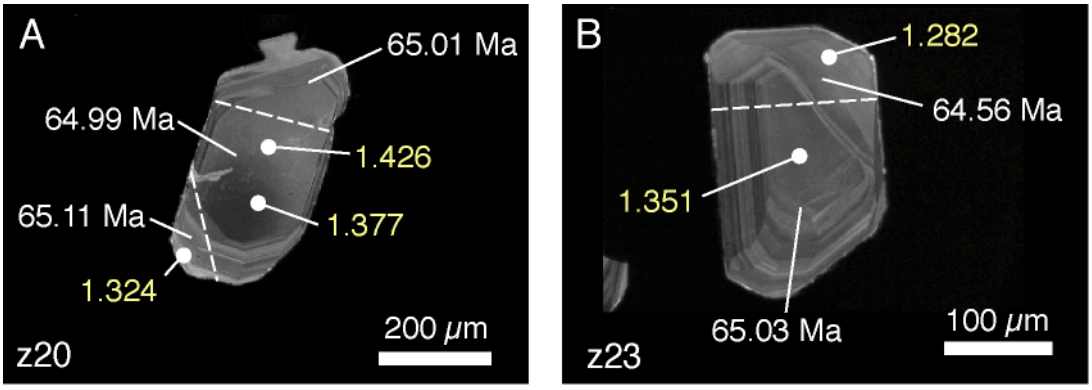

Figure 5.12: Cathodoluminescence images of zircon grains from sample SK061C. The grains were broken into pieces along the dashed white lines and the individual pieces were analyzed; their respective dates are shown. In addition, Hf measurements were obtained from the interior and the rim of the grain and marked by the small circles on the CL image. The results are shown in parts per million. The results are shown for grains: A) z20 and B) z23.

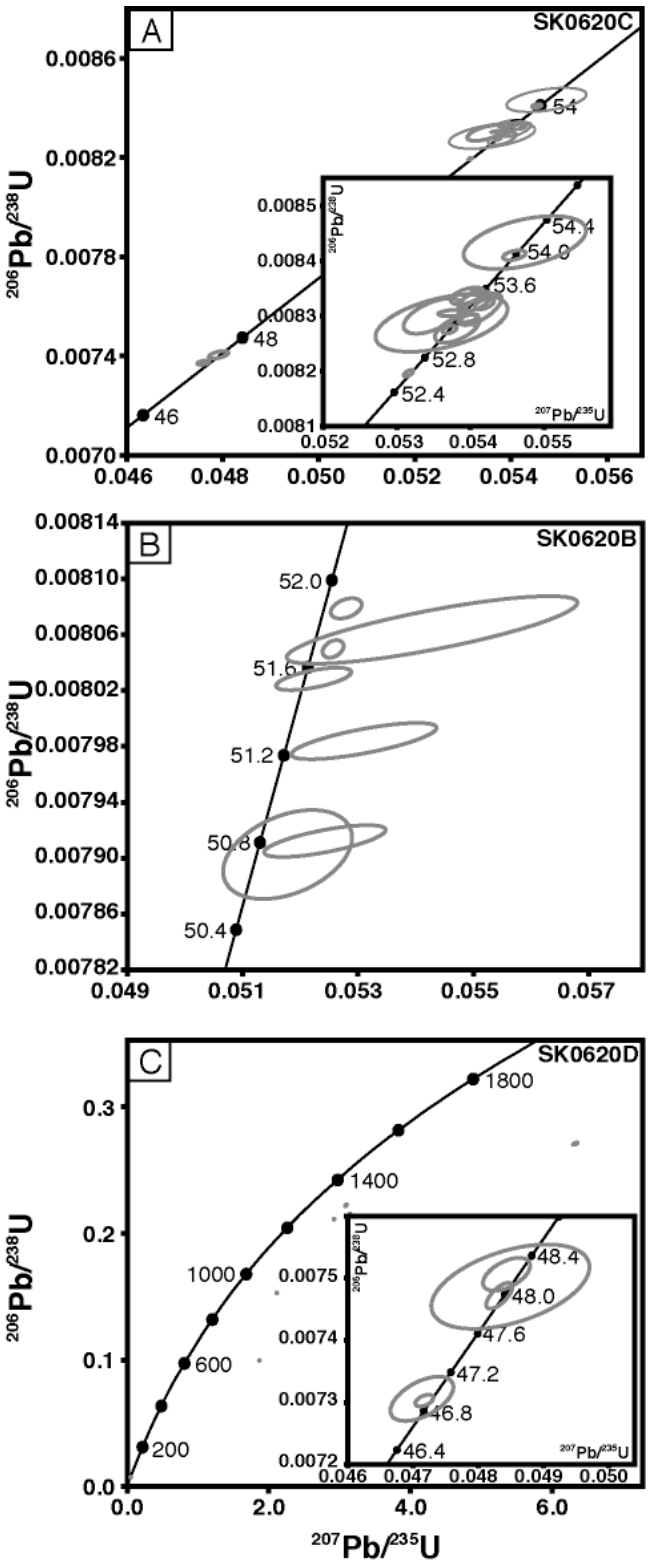

Figure 5.13: U-Pb concordia diagrams for zircon analyses from the John Pierce Falls outcrop: (A) SK0620C; (B) SK0620C; and (C) SK0620D.

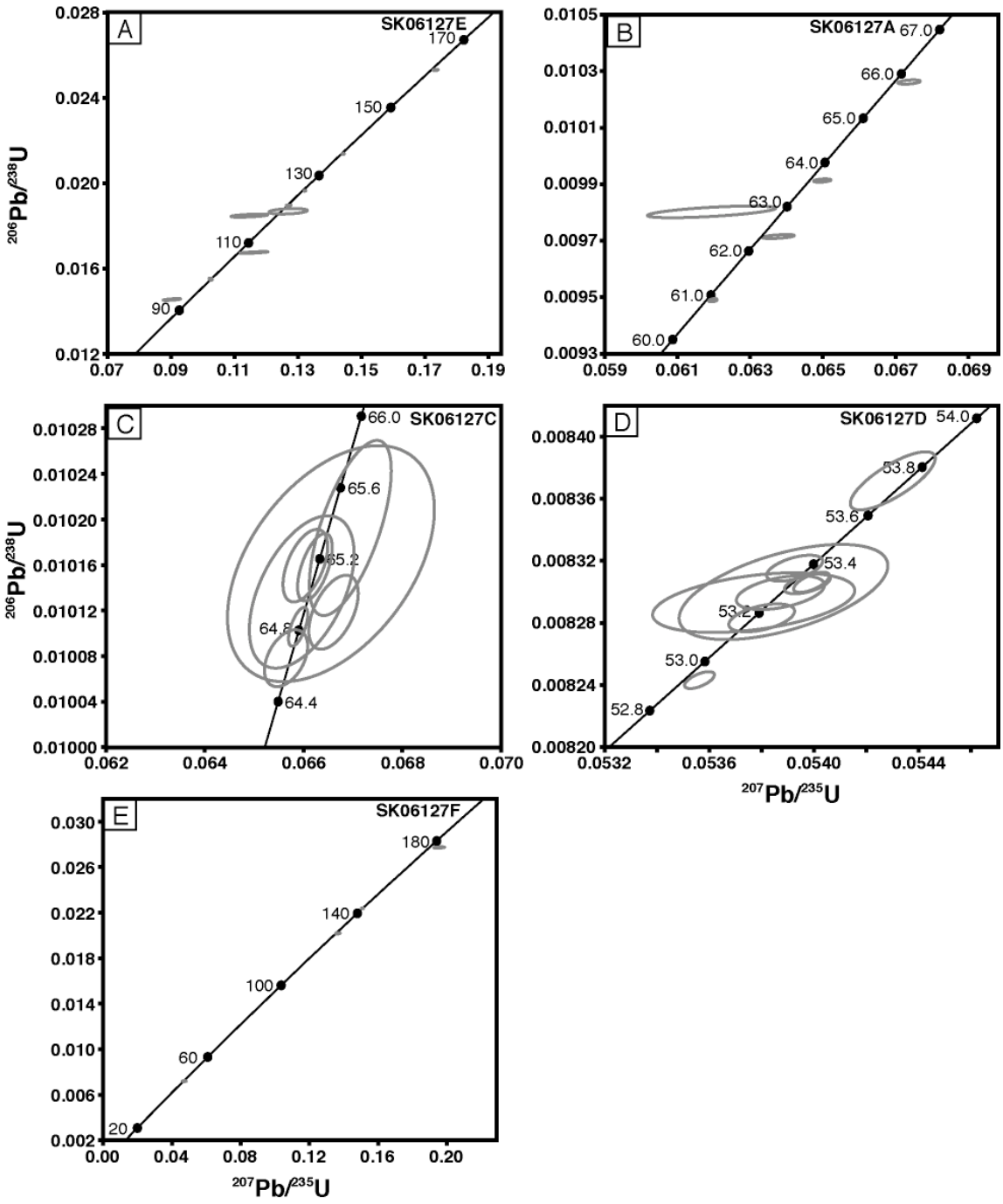

Figure 5.14: U-Pb concordia diagrams for zircon analyses from the Sourdough Mountain outcrop: (A) SK06127E; (B) SK06127A; (C) SK06127C; (D) SK06127D; and (E) SK06127F.

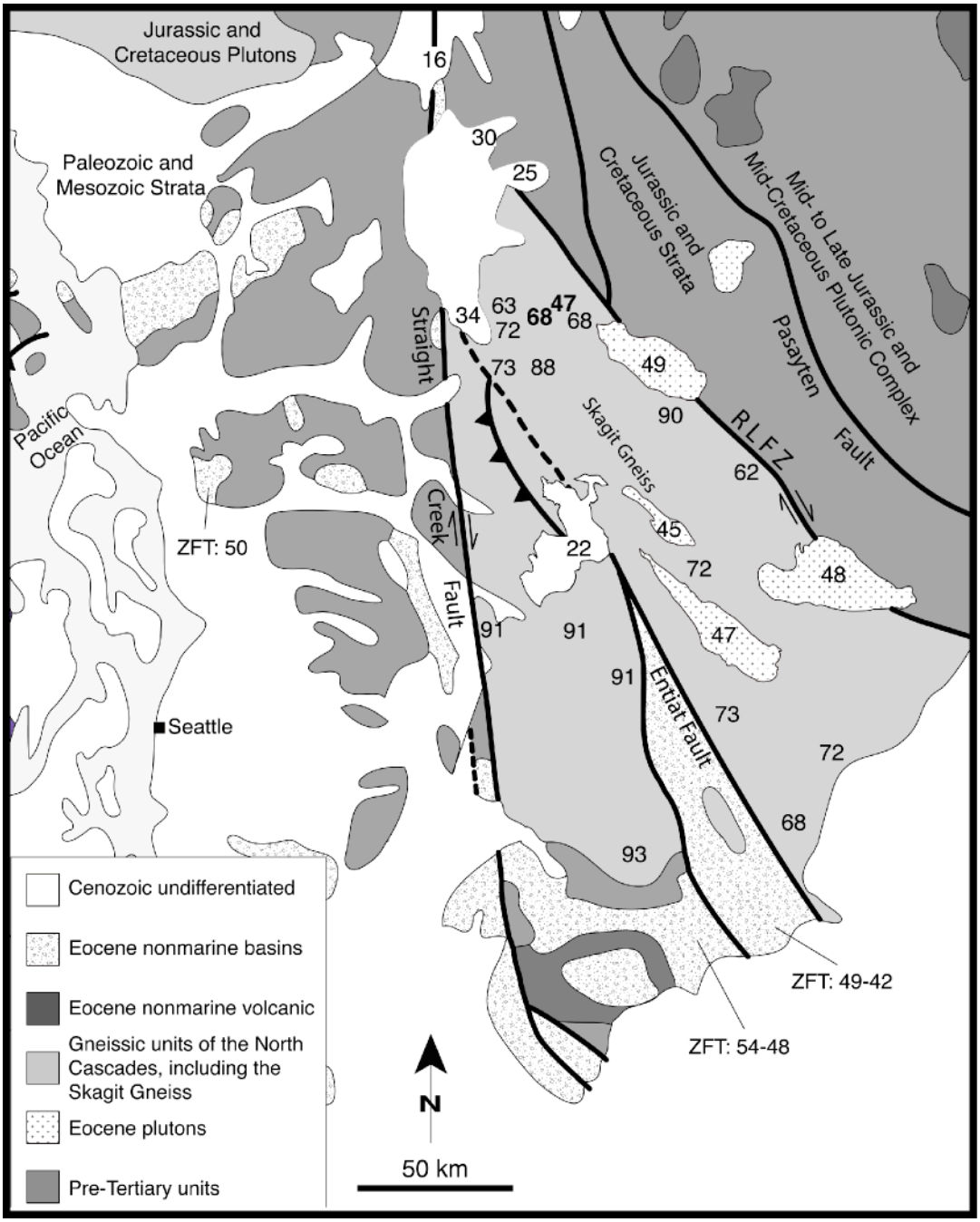

Figure 5.15: Regional geologic map of the Skagit Gneiss and adjacent terrains showing the emplacement ages of plutons in the region. Zircon fission track (ZFT on map) dates are also shown for comparison. Some of the results from this study are shown in bold.

Table 5.1: Summary of sample lithology, texture, location, and U-Pb dates

Sample name	Rock type	Leucosome thickness	Concordant/ discordant	U-Pb date(s) (Ma) zircon	monazite
Gorge Lake					
SK061DM	garnet-sillimanite gneiss			as young as 61	69; 49 to 46
SK061A	coarse-grained leucosome	50 cm	discordant	65	
SK061B	pegmatitic leucosome	0.5 m	discordant	65 to 64	
SK061C	fine-grained leucosome	5 cm	concordant	66 to 63	69 to 67; 49
SK061DL	fine-grained leucosome	10 cm	concordant	69 to 65	
SK061F	coarse-grained leucosome	30 cm	concordant	65 to 63	
John Pierce Falls					
SK0620B	medium-grained leucosome	2 cm	concordant	52 to 51	
SK0620C	pegmatite	5-10 m	discordant	54 to 53	47 to 46
SK0620D	biotite gneiss			48 to 47	48 to 46
Sourdough Mountain					
SK06127E	garnet-biotite gneiss			as young as 90	
SK06127A	fine-grained leucosome	6 cm	concordant	66 to 61	
SK06127C	medium-grained leucosome	30 cm	concordant	65	64 to 60
SK06127DL	pegmatite	40 cm	discordant/sub-parallel	54 to 53	
SK06127F	granitic dike	12 cm	discordant	as young as 46	46 to 45

Table 5.2: U-Pb isotopic data from zircon

	Composition			Isotopic ratios									Ages (Ma)						
Fraction[a]	Th/U	Pbc[b] (pg)	Pb*/ Pbc[c]	$^{206}Pb/^{204}Pb$[d]	$^{208}Pb/^{206}Pb$[e]	$^{206}Pb/^{238}U$[e]	% err[f]	$^{207}Pb/^{235}U$[e]	% err[f]	$^{207}Pb/^{206}Pb$[e]	% err[f]	Corr. Coeff.	$^{206}Pb/^{238}U$[g]	±[h]	$^{207}Pb/^{235}U$[g]	±[h]	$^{207}Pb/^{206}Pb$[g]	±[h]	Discordance %[i]
SK061DM - Mesosome																			
z1	0.379	0.51	27.5	1738.5	0.122	0.02112	0.09	0.14277	0.31	0.04904	0.29	0.394	134.71	0.12	135.51	0.39	149.64	6.69	11.2
z2	0.054	1.47	74.9	5184.3	0.017	0.01119	0.16	0.07301	0.37	0.04733	0.32	0.480	71.72	0.11	71.56	0.25	65.91	7.68	-3.1
z4	0.045	0.72	7.4	533.2	0.014	0.00993	0.12	0.06442	0.81	0.04703	0.77	0.400	63.73	0.08	63.39	0.50	50.54	18.42	-16.6
z5	0.159	1.82	61.4	3961.6	0.065	0.13662	0.16	1.43141	0.23	0.07599	0.15	0.734	825.49	1.27	902.14	1.35	1094.84	3.07	26.2
z6	0.012	0.63	199.9	13977.6	0.004	0.01057	0.08	0.06916	0.17	0.04745	0.15	0.493	67.79	0.06	67.90	0.11	71.83	3.53	10.5
z7	0.059	0.63	53.3	3665.4	0.021	0.04509	0.09	0.32722	0.19	0.05264	0.17	0.485	284.28	0.24	287.44	0.47	313.23	3.76	9.7
z8	0.022	0.62	29.4	2062.5	0.007	0.01096	0.07	0.07266	0.22	0.04810	0.21	0.370	70.24	0.05	71.22	0.15	104.23	4.93	35.2
z9	0.041	0.76	17.2	1208.9	0.013	0.01033	0.11	0.06744	0.44	0.04734	0.41	0.379	66.25	0.07	66.26	0.28	66.62	9.86	6.2
z11	0.050	0.99	13.8	968.9	0.016	0.00963	0.08	0.06270	0.58	0.04720	0.55	0.424	61.81	0.05	61.75	0.35	59.38	13.00	2.8
z12	0.025	0.69	67.8	4732.5	0.008	0.01087	0.08	0.07117	0.20	0.04747	0.17	0.463	69.72	0.06	69.81	0.13	73.09	74.84	9.3
z13	0.072	0.76	13.0	912.3	0.023	0.00959	0.06	0.06267	0.42	0.04739	0.41	0.366	61.53	0.04	61.72	0.25	69.03	9.65	16.1
z25A	0.217	1.08	1.7	131.0	0.070	0.01567	0.29	0.10406	3.37	0.04815	3.20	0.595	100.24	0.29	100.51	3.22	106.88	4.12	8.4
z26a	0.513	0.69	6.4	400.1	0.174	0.02517	0.14	0.18254	1.29	0.05260	1.21	0.596	160.23	0.22	170.24	2.02	311.72	75.71	49.5
z26c	0.281	0.92	4.9	318.0	0.150	0.03108	0.20	0.22708	1.23	0.05299	1.16	0.425	197.31	0.38	207.78	2.31	328.28	27.60	40.7
z27a	0.251	17.85	0.8	71.4	0.085	0.01665	0.28	0.11776	4.64	0.05129	4.39	0.883	106.47	0.30	113.04	4.96	253.72	26.35	58.9
z27b	0.123	0.42	1.4	113.3	0.039	0.01022	0.62	0.06665	10.62	0.04729	10.07	0.885	65.56	0.41	65.52	6.74	63.92	101.07	3.3
z29B	0.177	0.52	4.0	280.5	0.057	0.01014	0.10	0.06639	1.30	0.04749	1.24	0.619	65.04	0.07	65.27	0.82	73.69	241.28	16.3
z29A	0.111	0.29	15.8	1054.2	0.050	0.01380	0.07	0.12947	0.40	0.06804	0.37	0.513	88.35	0.06	123.62	0.47	869.90	29.40	90.5
z31a	0.182	0.60	2.9	210.4	0.059	0.01020	0.23	0.06683	3.07	0.04754	2.93	0.656	65.39	0.15	65.68	1.95	76.44	7.73	18.7
z31b	0.137	0.48	0.6	59.3	0.045	0.01048	0.73	0.06999	11.67	0.04843	11.10	0.791	67.22	0.49	68.69	7.75	120.18	69.54	46.0
z31c	0.270	0.83	3.5	240.3	0.106	0.02402	0.22	0.20452	2.04	0.06176	1.94	0.510	152.99	0.33	188.94	3.52	665.81	263.50	78.0
SK061DL - Lensoid leucosome																			
z2	0.041	0.64	23.5	1646.2	0.013	0.01064	0.05	0.06952	0.21	0.04740	0.20	0.351	68.21	0.04	68.24	0.14	69.31	4.72	6.8
z3	0.136	4.49	1.4	108.9	0.047	0.01073	0.25	0.07574	3.88	0.05120	3.68	0.790	68.79	0.17	74.13	2.77	249.93	84.76	73.3
z4	0.037	2.29	11.6	824.3	0.012	0.01068	0.07	0.06904	0.49	0.04688	0.47	0.384	68.49	0.05	67.79	0.32	43.04	11.27	-46.5
z5	0.130	3.87	5.7	400.8	0.042	0.01066	0.08	0.07034	0.93	0.04786	0.90	0.431	68.36	0.06	69.02	0.62	92.11	21.23	28.9
z6	0.098	1.86	19.0	1296.8	0.036	0.01407	0.07	0.10739	0.17	0.05536	0.15	0.481	90.06	0.06	103.58	0.17	426.96	3.35	79.6
z7	0.044	0.73	9.3	664.8	0.014	0.01042	0.09	0.06795	0.56	0.04732	0.54	0.385	66.80	0.06	66.76	0.36	65.31	12.78	3.5
z8	0.057	0.77	2.1	159.9	0.019	0.01076	0.15	0.07404	1.80	0.04992	1.72	0.548	68.97	0.11	72.52	1.26	191.47	39.99	65.0
z9	0.030	1.03	0.9	80.2	0.009	0.01073	0.35	0.06780	5.91	0.04584	5.61	0.862	68.79	0.24	66.61	3.81	-11.01	135.67	-1052.5
z10	0.106	1.74	2.5	190.2	0.034	0.01051	0.14	0.06880	1.64	0.04746	1.55	0.650	67.41	0.09	67.56	1.07	72.65	36.94	11.9
z12	0.165	0.75	6.9	477.6	0.054	0.01023	0.11	0.06796	1.07	0.04817	1.01	0.536	65.63	0.07	66.76	0.69	107.42	23.83	41.3
z13	0.207	0.55	21.4	1426.8	0.066	0.01018	0.08	0.06632	0.41	0.04724	0.39	0.339	65.30	0.05	65.20	0.26	61.59	9.30	0.2
SK061C - Layer-parallel leucosome																			
z1	0.124	1.19	56.7	3843.4	0.040	0.00995	0.08	0.06480	0.15	0.04722	0.12	0.543	63.85	0.05	63.76	0.09	60.43	2.93	1.0
z3	0.117	3.55	3.7	268.7	0.038	0.01316	0.12	0.08770	1.04	0.04832	0.98	0.475	84.31	0.10	85.36	0.85	114.95	23.21	28.8
z4	0.114	0.63	20.0	1375.1	0.037	0.00991	0.09	0.06467	0.47	0.04732	0.45	0.377	63.58	0.05	63.63	0.29	65.50	10.66	8.6
z5	0.182	0.74	54.8	3656.2	0.059	0.01035	0.06	0.06772	0.20	0.04746	0.19	0.361	66.37	0.04	66.53	0.13	72.62	4.46	13.2
z7	0.115	0.74	39.9	2718.2	0.037	0.00984	0.08	0.06411	0.26	0.04725	0.24	0.397	63.13	0.05	63.10	0.16	61.78	5.69	4.2
z8	0.134	0.88	9.1	628.1	0.043	0.01008	0.12	0.06552	0.98	0.04714	0.93	0.464	64.66	0.08	64.44	0.61	56.31	22.22	-7.3

z9	0.185	0.66	24.5	1639.2	0.060	0.01012	0.08	0.06639	0.27	0.04760	0.25	0.402	64.88	0.05	65.27	0.17	79.56	5.93	22.4
z10	0.127	1.04	17.3	1184.3	0.041	0.01004	0.10	0.06554	0.44	0.04735	0.41	0.393	64.39	0.06	64.46	0.28	66.82	9.82	9.1
z11	0.123	0.68	77.1	5222.6	0.040	0.00996	0.05	0.06488	0.11	0.04726	0.10	0.458	63.87	0.03	63.83	0.07	62.36	2.38	3.8
z20a	0.137	0.62	13.8	943.8	0.044	0.01015	0.07	0.06579	0.51	0.04701	0.48	0.434	65.11	0.05	64.70	0.32	49.57	11.44	-21.8
z20b	0.136	1.23	12.1	828.1	0.043	0.01014	0.06	0.06595	0.46	0.04719	0.43	0.451	65.01	0.04	64.85	0.29	58.95	10.27	-3.4
z20c	0.148	0.59	23.5	1584.7	0.047	0.01012	0.06	0.06578	0.33	0.04715	0.31	0.356	64.90	0.04	64.68	0.20	56.65	7.37	-7.1
z21b	0.169	0.60	1.3	102.7	0.054	0.01009	0.38	0.06608	5.94	0.04748	5.65	0.798	64.75	0.24	64.98	3.74	73.35	134.42	16.3
z23a	0.131	2.72	1.7	130.7	0.042	0.01006	0.16	0.06593	2.65	0.04751	2.52	0.806	64.56	0.10	64.83	1.66	74.91	59.84	18.3
z23c	0.200	2.11	0.5	54.1	0.065	0.01014	0.67	0.06678	11.74	0.04778	11.21	0.798	65.03	0.43	65.64	7.46	88.16	267.89	29.5
z25c	0.115	0.97	0.6	57.5	0.038	0.00993	0.43	0.06686	7.28	0.04882	6.93	0.825	63.71	0.27	65.71	4.63	139.39	163.15	55.9
z26	0.146	0.59	3.3	239.4	0.046	0.01008	0.19	0.06389	1.99	0.04596	1.90	0.533	64.67	0.12	62.89	1.22	-4.54	45.84	-10460.5
z26a	0.142	0.63	16.2	1101.9	0.046	0.01018	0.08	0.06632	0.54	0.04723	0.52	0.375	65.31	0.05	65.20	0.34	61.09	12.34	-0.5
z26c	-0.615	1.10	0.2	35.0	-0.074	0.00984	1.33	0.02350	60.56	0.01733	59.49	0.810	63.10	0.83	23.59	14.12	0.00	0.00	-102.4
z27a	0.142	0.69	13.3	905.5	0.045	0.01014	0.07	0.06606	0.56	0.04724	0.53	0.463	65.05	0.05	64.95	0.35	61.44	12.57	0.5
z27c	0.070	0.52	0.9	80.3	0.023	0.01005	0.40	0.06821	5.66	0.04920	5.39	0.714	64.49	0.25	67.00	3.67	157.52	126.20	60.4
z28a	0.132	0.43	14.8	1015.1	0.042	0.01009	0.09	0.06493	0.55	0.04665	0.52	0.386	64.75	0.06	63.88	0.34	31.60	12.43	-82.4
SK061A - Layer-parallel leucosome																			
z1	0.213	0.76	9.3	631.4	0.068	0.01015	0.07	0.06643	0.50	0.04745	0.47	0.406	65.12	0.04	65.30	0.31	71.94	11.27	14.2
z2	0.189	0.62	12.5	843.6	0.061	0.01018	0.09	0.06660	0.57	0.04746	0.54	0.397	65.28	0.06	65.47	0.36	72.63	12.76	14.7
z3	0.166	1.19	5.4	379.5	0.053	0.01016	0.12	0.06622	0.94	0.04728	0.89	0.447	65.15	0.08	65.10	0.59	63.38	21.19	3.3
z4	0.238	1.27	4.2	293.6	0.076	0.01018	0.07	0.06647	0.72	0.04734	0.68	0.531	65.32	0.04	65.34	0.45	66.24	16.28	6.8
z6	0.136	1.20	24.7	1683.0	0.044	0.01015	0.06	0.06613	0.22	0.04723	0.20	0.374	65.12	0.04	65.02	0.14	61.02	4.78	-0.3
z8	0.139	0.63	49.6	3352.0	0.045	0.01014	0.06	0.06605	0.18	0.04726	0.17	0.411	65.02	0.04	64.95	0.12	62.47	4.00	2.1
z9	0.174	0.60	10.5	719.5	0.056	0.01014	0.06	0.06612	0.54	0.04728	0.51	0.452	65.05	0.04	65.01	0.34	63.55	12.23	3.6
z10	0.198	0.74	26.0	1737.3	0.063	0.01018	0.18	0.06637	0.45	0.04727	0.41	0.437	65.31	0.11	65.24	0.28	62.73	9.65	1.9
SK061B - Pegmatitic leucosome																			
z1	0.189	0.70	17.1	1150.3	0.060	0.01010	0.10	0.06575	0.39	0.04722	0.37	0.326	64.78	0.07	64.66	0.25	60.13	8.86	-1.2
z2	0.170	0.57	43.6	2918.6	0.055	0.00994	0.06	0.06493	0.15	0.04739	0.14	0.418	63.75	0.03	63.88	0.09	68.67	3.25	12.3
z3	0.177	0.77	33.8	2263.8	0.057	0.01009	0.07	0.06594	0.23	0.04738	0.21	0.369	64.75	0.04	64.84	0.14	68.41	5.00	10.5
z4	0.191	0.55	19.8	1325.9	0.061	0.01007	0.10	0.06556	0.49	0.04721	0.47	0.298	64.59	0.07	64.47	0.31	60.02	11.25	-1.1
z6	2.926	1.05	21.5	808.4	0.940	0.01003	0.06	0.06557	0.39	0.04744	0.37	0.416	64.31	0.04	64.49	0.24	71.19	8.72	11.1
z7	0.182	1.78	13.1	887.4	0.059	0.01008	0.08	0.06608	0.59	0.04757	0.56	0.369	64.62	0.05	64.98	0.37	77.97	13.36	21.2
z8	0.160	1.33	12.7	867.8	0.051	0.00995	0.18	0.06484	0.65	0.04726	0.60	0.379	63.83	0.11	63.79	0.40	62.27	14.29	3.6
z9	0.221	0.80	18.6	1239.1	0.071	0.01002	0.10	0.06529	0.42	0.04726	0.39	0.373	64.27	0.06	64.22	0.26	62.46	9.26	3.1
SK061F - Layer-parallel leucosome																			
z1	0.101	0.67	58.7	4006.6	0.032	0.01023	0.06	0.06676	0.16	0.04734	0.15	0.447	65.59	0.04	65.62	0.10	66.57	3.50	7.0
z2	0.202	0.55	54.6	3619.2	0.065	0.01007	0.05	0.06567	0.13	0.04729	0.12	0.434	64.60	0.03	64.58	0.08	63.88	2.86	4.7
z3	0.193	0.58	29.3	1956.8	0.062	0.01017	0.05	0.06644	0.21	0.04737	0.20	0.354	65.25	0.03	65.32	0.13	67.77	4.72	9.0
z4	0.207	1.13	11.2	754.8	0.067	0.00987	0.06	0.06449	0.52	0.04739	0.50	0.456	63.31	0.04	63.45	0.32	68.71	11.81	13.0
z5	0.163	0.53	13.6	923.8	0.052	0.01009	0.06	0.06590	0.40	0.04737	0.38	0.405	64.72	0.04	64.80	0.25	67.80	8.96	9.8
z6	0.177	0.75	15.2	1029.4	0.057	0.01005	0.06	0.06555	0.36	0.04728	0.34	0.373	64.49	0.04	64.47	0.23	63.58	8.18	4.5
z7	0.185	0.55	33.1	2209.9	0.059	0.00993	0.10	0.06479	0.44	0.04732	0.41	0.370	63.70	0.07	63.75	0.27	65.46	9.87	8.3
z8	0.175	0.52	27.7	1863.3	0.056	0.01007	0.05	0.06573	0.22	0.04732	0.21	0.357	64.61	0.03	64.64	0.14	65.48	4.94	6.9
z9	0.130	0.53	46.7	3164.4	0.042	0.01022	0.08	0.06657	0.28	0.04724	0.27	0.317	65.56	0.05	65.44	0.18	61.31	6.44	-0.5
z10	0.162	0.57	28.8	1940.1	0.052	0.01008	0.06	0.06569	0.23	0.04727	0.21	0.358	64.66	0.04	64.60	0.14	62.65	5.08	2.9
SK0620B - Layer-parallel leucosome																			

z3	0.068	1.15	21.1	1458.9	0.022	0.00805	0.06	0.05257	0.28	0.04736	0.27	0.364	51.69	0.03	52.02	0.14	67.41	6.34	28.8
z4	0.050	1.91	17.2	1200.5	0.016	0.00808	0.07	0.05280	0.42	0.04740	0.40	0.372	51.87	0.04	52.24	0.21	69.29	9.43	30.3
z6	0.038	0.52	3.6	265.9	0.012	0.00791	0.12	0.05242	1.64	0.04805	1.56	0.712	50.81	0.06	51.88	0.83	101.86	36.94	52.8
z6B	0.040	0.95	4.3	316.5	0.013	0.00803	0.08	0.05223	1.02	0.04718	0.97	0.623	51.55	0.04	51.70	0.52	58.58	23.18	19.1
z7	0.115	4.43	1.2	100.8	0.038	0.00806	0.24	0.05428	3.80	0.04882	3.60	0.806	51.77	0.13	53.67	1.98	139.30	84.56	64.4
z12A	0.046	7.05	5.2	374.1	0.015	0.00790	0.33	0.05178	1.76	0.04752	1.67	0.371	50.75	0.17	51.26	0.88	75.41	39.67	37.2
z12b	0.073	1.73	2.3	176.6	0.024	0.00798	0.13	0.05310	1.94	0.04824	1.85	0.739	51.26	0.07	52.54	0.99	110.99	43.56	56.1
SK0620C - Pegmatite																			
z1	0.149	1.14	67.1	4512.9	0.048	0.00828	0.07	0.05371	0.15	0.04707	0.13	0.486	53.13	0.04	53.12	0.08	52.95	3.07	8.0
z2	0.175	0.83	20.9	1409.7	0.056	0.00834	0.14	0.05395	0.35	0.04694	0.31	0.489	53.52	0.08	53.36	0.18	46.14	7.29	-5.3
z4	0.268	0.90	3.6	250.7	0.085	0.00838	0.77	0.05375	1.58	0.04651	1.32	0.547	53.80	0.41	53.16	0.82	24.27	31.72	-87.3
z5	0.331	0.76	16.7	1080.1	0.106	0.00833	0.18	0.05406	0.34	0.04708	0.28	0.563	53.46	0.09	53.46	0.18	53.47	6.73	7.9
z7	0.165	0.76	37.5	2522.6	0.053	0.00841	0.09	0.05459	0.23	0.04708	0.20	0.445	53.99	0.05	53.97	0.12	53.28	4.87	6.9
z8	0.172	10.35	6.0	420.3	0.055	0.00843	0.47	0.05474	1.24	0.04708	1.11	0.456	54.14	0.25	54.11	0.65	53.05	26.43	6.3
z10	0.051	2.73	31.4	2185.8	0.016	0.00737	0.10	0.04760	0.22	0.04682	0.18	0.525	47.36	0.05	47.21	0.10	40.06	4.41	-4.0
z11	0.055	0.76	17.7	1238.2	0.018	0.00740	0.17	0.04791	0.35	0.04693	0.29	0.541	47.56	0.08	47.52	0.16	45.60	6.97	7.0
z13	0.209	0.46	8.7	588.7	0.067	0.00830	0.31	0.05349	0.61	0.04674	0.50	0.569	53.28	0.17	52.91	0.31	35.84	11.98	-31.6
z14	0.173	0.87	57.2	3823.1	0.056	0.00832	0.10	0.05419	0.20	0.04723	0.17	0.522	53.42	0.05	53.58	0.10	60.77	4.03	18.6
z15	0.092	1.04	88.2	6029.0	0.030	0.00820	0.06	0.05316	0.10	0.04704	0.07	0.625	52.62	0.03	52.59	0.05	51.13	1.79	6.1
z16	0.155	1.27	5.0	352.2	0.050	0.00829	0.51	0.05361	1.37	0.04691	1.21	0.481	53.20	0.27	53.02	0.71	44.82	28.88	-7.2
z17	0.118	0.95	10.1	703.3	0.038	0.00828	0.24	0.05382	0.46	0.04716	0.38	0.581	53.14	0.13	53.22	0.24	57.11	8.94	14.2
z18	0.101	0.82	9.5	666.7	0.032	0.00831	0.28	0.05412	0.45	0.04722	0.33	0.670	53.36	0.15	53.52	0.23	60.51	7.93	18.5
z22	0.196	0.63	102.3	6778.8	0.063	0.00834	0.06	0.05408	0.12	0.04701	0.10	0.512	53.56	0.03	53.48	0.06	49.73	2.45	1.6
z23	0.164	0.90	46.5	3118.6	0.053	0.00830	0.07	0.05398	0.19	0.04719	0.18	0.421	53.26	0.03	53.38	0.10	58.90	4.19	16.5
z24	0.217	0.76	20.9	1390.9	0.069	0.00831	0.06	0.05378	0.34	0.04697	0.33	0.332	53.32	0.03	53.19	0.18	47.59	7.79	-2.0
SK0620D - Biotite gneiss																			
z5A	0.080	0.51	42.4	2765.8	0.031	0.22261	0.31	3.09374	0.37	0.10080	0.20	0.844	1295.64	3.59	1431.14	2.81	1638.82	3.64	23.1
z6	0.384	1.50	34.0	2148.1	0.123	0.00747	0.23	0.04832	0.34	0.04691	0.25	0.687	47.99	0.11	47.92	0.16	44.51	5.93	3.0
z7	0.275	1.33	3.9	270.4	0.088	0.00749	0.74	0.04849	2.04	0.04698	1.82	0.462	48.08	0.36	48.08	0.96	48.02	43.47	9.5
z8	0.381	0.66	33.5	2121.6	0.122	0.00730	0.10	0.04718	0.24	0.04685	0.21	0.475	46.91	0.05	46.81	0.11	41.55	5.13	-0.6
z9A	0.007	0.85	1.4	115.1	0.002	0.20669	2.09	2.41124	2.82	0.08461	1.75	0.787	1211.14	23.07	1245.95	20.25	1306.64	33.88	8.0
z10	0.231	0.73	166.2	10235.5	0.092	0.21119	0.06	2.92238	0.09	0.10036	0.07	0.653	1235.15	0.66	1387.72	0.68	1630.78	1.27	26.6
z11	0.333	1.20	10.3	675.3	0.107	0.00751	0.29	0.04844	0.60	0.04680	0.51	0.529	48.21	0.14	48.03	0.28	38.91	12.29	-9.8
z12	0.341	0.66	127.5	6991.6	0.171	0.27113	0.29	6.33285	0.42	0.16940	0.31	0.684	1546.53	3.98	2023.01	3.71	2551.76	5.17	44.2
z13	0.304	0.57	7.2	482.7	0.097	0.00731	0.40	0.04714	0.83	0.04679	0.70	0.539	46.92	0.19	46.77	0.38	38.77	16.82	-6.8
z15	0.117	0.51	86.2	5492.6	0.049	0.21546	0.08	3.14877	0.12	0.10599	0.08	0.724	1257.84	0.92	1444.70	0.89	1731.59	1.46	30.1
z16	0.256	0.64	15.2	1002.3	0.082	0.00953	0.19	0.06230	0.35	0.04743	0.28	0.601	61.13	0.12	61.37	0.21	70.84	6.57	18.5
z17	0.069	2.86	11.4	708.5	0.079	0.09955	0.29	1.86571	0.33	0.13593	0.15	0.884	611.77	1.67	1069.01	2.19	2175.91	2.70	75.2
z20	0.063	1.38	67.2	4365.2	0.035	0.15340	0.09	2.11061	0.15	0.09979	0.12	0.601	920.02	0.73	1152.28	1.01	1620.09	2.17	46.3
SK06127E - Biotite gneiss																			
z3A	0.296	1.55	1.8	132.8	0.096	0.01869	0.52	0.12693	3.94	0.04927	3.80	0.327	119.34	0.61	121.33	4.50	160.52	88.96	26.9
z3C	0.183	0.64	1.5	121.2	0.055	0.01455	0.21	0.09020	2.61	0.04496	2.49	0.583	93.13	0.19	87.69	2.19	-57.94	60.80	-270.3
z8	0.358	1.25	75.7	4792.1	0.115	0.01965	0.07	0.13219	0.15	0.04879	0.13	0.486	125.45	0.09	126.06	0.18	137.53	3.11	10.1
z10	0.422	0.86	23.4	1465.9	0.135	0.02137	0.06	0.14423	0.25	0.04894	0.24	0.376	136.34	0.08	136.80	0.33	144.81	5.60	7.0
z11	0.297	3.05	1.8	133.3	0.088	0.01848	0.31	0.11470	4.16	0.04501	3.98	0.607	118.07	0.36	110.26	4.34	-55.26	97.00	-324.5
z12	0.323	1.07	6.9	460.7	0.103	0.01895	0.09	0.12662	0.78	0.04845	0.74	0.497	121.04	0.11	121.06	0.89	121.44	17.48	2.0

z13b	0.299	0.85	1.4	105.5	0.100	0.01676	0.23	0.11612	3.22	0.05026	3.05	0.753	107.12	0.25	111.55	3.40	207.19	70.74	49.3
z14	0.338	0.77	10.9	707.5	0.108	0.01554	0.07	0.10273	0.42	0.04794	0.40	0.363	99.41	0.07	99.29	0.40	96.36	9.49	-0.6
z15	0.203	1.37	17.6	1173.7	0.065	0.02531	0.09	0.17338	0.38	0.04968	0.36	0.379	161.13	0.14	162.35	0.57	180.18	8.30	11.5
SK06127A - Layer-parallel leucosome																			
z1	0.018	0.55	43.3	3023.0	0.006	0.00949	0.05	0.06198	0.15	0.04737	0.13	0.403	60.89	0.03	61.06	0.09	67.72	3.21	15.5
z2A	0.036	0.73	15.4	1083.3	0.012	0.01026	0.06	0.06737	0.37	0.04761	0.35	0.387	65.82	0.04	66.20	0.24	80.12	8.30	21.9
z2B1	0.007	0.54	7.4	530.9	0.002	0.00972	0.06	0.06378	0.57	0.04761	0.54	0.518	62.33	0.04	62.78	0.35	79.98	12.88	26.2
z2B2	-0.009	1.31	3.0	226.2	-0.003	0.00980	0.17	0.06193	2.34	0.04582	2.23	0.634	62.88	0.11	61.02	1.38	-11.68	53.82	-943.3
z3A	0.062	0.74	16.5	1144.3	0.020	0.00991	0.05	0.06498	0.31	0.04754	0.29	0.388	63.59	0.03	63.93	0.19	76.43	6.87	21.2
z3B	0.041	0.48	365.0	24121.1	0.020	0.14217	0.06	1.69031	0.09	0.08623	0.06	0.730	856.91	0.52	1004.88	0.56	1343.36	1.16	38.7
SK06127C - Layer-parallel leucosome																			
z1B	0.015	0.67	10.2	730.7	0.005	0.01012	0.26	0.06660	0.62	0.04774	0.53	0.511	64.90	0.17	65.47	0.39	86.26	12.60	28.3
z1C	0.168	1.83	37.7	2411.6	0.056	0.24775	0.09	3.38609	0.12	0.09912	0.07	0.794	1426.88	1.20	1501.18	0.94	1607.70	1.36	12.5
z2A	0.491	0.59	28.3	1572.6	0.160	0.42466	0.15	#######	0.17	0.17428	0.08	0.886	2281.59	2.90	2453.46	1.60	2599.14	1.34	14.5
z4	0.045	0.45	19.4	1358.9	0.014	0.01011	0.14	0.06589	0.24	0.04728	0.19	0.615	64.82	0.09	64.79	0.15	63.58	4.56	4.2
z5	0.036	0.70	11.3	804.6	0.011	0.01016	0.24	0.06622	0.44	0.04728	0.35	0.590	65.15	0.15	65.11	0.28	63.35	8.44	3.4
z6A	0.018	0.52	14.0	991.3	0.006	0.01008	0.20	0.06564	0.55	0.04723	0.50	0.423	64.64	0.13	64.55	0.34	61.12	11.84	0.9
z7A	0.230	2.12	0.8	70.5	0.075	0.01713	3.45	0.11572	4.68	0.04900	3.05	0.759	109.49	3.74	111.19	4.93	147.61	71.50	27.2
z7C	0.061	0.53	4.9	356.4	0.019	0.01014	0.54	0.06596	1.31	0.04719	1.14	0.498	65.01	0.35	64.85	0.82	58.97	27.24	-3.3
z11	0.060	0.79	3.6	269.2	0.019	0.01016	0.73	0.06451	1.69	0.04605	1.46	0.509	65.16	0.47	63.47	1.04	0.34	35.24	-1418.1
z12	0.226	1.20	3.4	238.4	0.073	0.01016	0.83	0.06655	2.57	0.04750	2.31	0.458	65.17	0.54	65.42	1.63	74.46	54.82	16.8
z13	0.070	0.68	4.3	310.9	0.023	0.01019	0.62	0.06694	1.01	0.04763	0.77	0.649	65.37	0.40	65.79	0.64	81.02	18.17	23.2
z14	0.069	0.60	10.8	756.8	0.022	0.01016	0.26	0.06603	0.56	0.04714	0.48	0.519	65.16	0.17	64.93	0.35	56.20	11.37	-8.3
SK06127D - Pegmatite																			
z1	0.173	0.91	32.5	2181.8	0.056	0.00830	0.11	0.05387	0.26	0.04745	0.23	0.452	53.28	0.06	53.28	0.13	0.05	5.46	7.8
z2	0.259	0.83	17.7	1170.0	0.083	0.00829	0.19	0.05377	0.59	0.04726	0.54	0.403	53.24	0.10	53.18	0.30	0.05	12.88	3.1
z4A	0.215	1.12	36.0	2388.3	0.069	0.00837	0.18	0.05430	0.24	0.04746	0.16	0.767	53.74	0.10	53.69	0.13	0.05	3.72	4.0
z5A	0.145	0.45	1.7	134.6	0.046	0.00839	1.53	0.05343	2.79	0.04728	2.23	0.605	53.83	0.82	52.85	1.44	0.05	53.54	-309.4
z5B	0.069	0.48	4.0	295.2	0.022	0.01015	0.69	0.06547	1.94	2.04727	1.74	0.460	65.10	0.44	64.39	1.21	0.05	41.61	-54.2
z6	0.183	0.47	66.3	4419.3	0.059	0.00831	0.06	0.05397	0.13	0.04734	0.11	0.527	53.32	0.03	53.38	0.07	0.05	2.67	12.2
z7	0.275	1.10	75.6	4904.2	0.088	0.00831	0.06	0.05399	0.10	0.04728	0.08	0.639	53.33	0.03	53.39	0.05	0.05	1.89	12.6
z8A	0.145	0.63	44.5	3002.9	0.046	0.00832	0.08	0.05393	0.16	0.04727	0.14	0.546	53.38	0.04	53.33	0.08	0.05	3.22	4.2
z8	0.209	0.54	9.3	628.0	0.067	0.00830	0.30	0.05388	0.61	1.04727	0.50	0.555	53.29	0.16	53.29	0.31	0.05	12.03	8.3
z9	0.136	0.69	41.5	2808.6	0.044	0.00828	0.09	0.05380	0.19	0.04723	0.17	0.490	53.18	0.05	53.21	0.10	0.05	4.01	10.4
z10	0.267	0.84	128.2	8316.9	0.086	0.00824	0.05	0.05356	0.09	3.04727	0.07	0.618	52.92	0.03	52.98	0.05	0.05	1.64	12.1
SK06127F - Granitic dike																			
z1	0.759	0.73	37.5	2136.0	0.242	0.02239	0.09	0.15083	0.33	0.04886	0.31	0.357	142.73	0.13	142.65	0.44	141.24	7.28	0.0
z3	0.911	0.60	0.6	54.6	0.116	0.01717	1.41	0.04397	38.92	0.01858	38.21	0.516	109.72	1.53	43.70	16.64	-2973.01	2374.11	-104.6
z4	0.462	0.51	0.6	57.1	0.073	0.00857	0.93	0.02690	34.32	0.02276	33.57	0.804	55.01	0.51	26.95	9.13	-2104.30	1492.17	-103.1
z7	0.403	0.73	4.5	298.1	0.132	0.02773	0.16	0.19543	1.40	0.05111	1.33	0.494	176.33	0.28	181.25	2.33	245.95	30.67	29.1
z8	0.304	0.60	2.0	148.6	0.099	0.00722	0.17	0.04715	2.42	0.04739	2.31	0.705	46.35	0.08	46.78	1.11	68.87	54.82	37.6
z10	0.448	0.62	6.8	435.4	0.144	0.02020	0.09	0.13660	0.78	0.04904	0.74	0.514	128.92	0.11	130.01	0.96	149.86	17.40	15.2

(a) Zircon fractions are composed of single grains.

(b) Total weight of common Pb.

(c) Ratio of radiogenic Pb to common Pb.

(d) Measured ratio corrected for spike and fractionation only. Mass fractionation correction of 0.25%/amu ± 0.04%/amu (atomic mass unit)

was applied to single-collector Daly analyses (based on daily analysis of NBS-981).

(e) Corrected for fractionation, spike, and blank. All common Pb in the analyses was assigned to procedural blank with a measured composition of 206Pb/204Pb = 18.271 ± 0.05, 207Pb/204Pb = 15.587 ± 0.05, 208Pb/204Pb = 38.119 ± 0.05 (2 sigma). U blanks were <0.1 pg.

(f) Errors are 2 sigma.

(g) Age calculations are based on the decay constants of Steiger and Jäger (1977).

(h) Error in the dates reported at 2 sigma.

(i) % discordance = 100 - (100 x (206Pb/238U age) / (207Pb/206Pb age)).

Table 5.3: U-Pb isotopic data from monazite

	Composition			Isotopic ratios									Ages (Ma)						
Fraction[a]	Th/U	Pbc[b] (pg)	Pb*/ Pbc[c]	$^{206}Pb/^{204}Pb$[d]	$^{208}Pb/^{206}Pb$[e]	$^{206}Pb/^{238}U$[e]	% err[f]	$^{207}Pb/^{235}U$[e]	% err[f]	$^{207}Pb/^{206}Pb$[e]	% err[f]	Corr. Coeff.	$^{206}Pb/^{238}U$[g]	±[h]	$^{207}Pb/^{235}U$[g]	±[h]	$^{207}Pb/^{206}Pb$[g]	±[h]	Discordance %[i]
SK061DM - Mesosome																			
m1	8.920	2.50	8.0	166.5	2.915	0.00748	0.13	0.04946	1.63	0.04793	1.55	0.628	48.06	0.06	49.02	0.78	95.93	36.63	50.1
m2	6.506	1.83	84.8	2017.4	2.073	0.01083	0.06	0.07042	0.16	0.04718	0.15	0.438	69.41	0.04	69.10	0.11	58.29	3.53	-19.1
m3	14.956	2.45	52.8	698.2	4.667	0.00758	0.06	0.04781	0.54	0.04573	0.51	0.499	48.69	0.03	47.42	0.25	-16.34	12.24	-399.4
m5A	12.760	2.39	46.3	688.3	4.032	0.00763	0.07	0.04872	0.41	0.04633	0.39	0.367	48.98	0.04	48.31	0.19	14.77	9.30	-232.2
m5B	10.814	2.49	114.3	1890.9	3.442	0.00761	0.06	0.04897	0.15	0.04668	0.14	0.449	48.86	0.03	48.55	0.07	32.78	3.31	-49.4
m5C	13.449	2.27	30.1	436.1	4.245	0.00760	0.09	0.04849	0.84	0.04628	0.80	0.544	48.80	0.04	48.08	0.39	12.10	19.19	-304.9
m11	8.904	4.45	35.3	692.2	2.808	0.01010	0.08	0.06485	0.37	0.04658	0.35	0.372	64.77	0.05	63.80	0.23	27.66	8.38	-134.9
m12A	10.973	0.83	57.5	962.2	3.413	0.00741	0.08	0.04657	0.72	0.04556	0.68	0.513	47.61	0.04	46.21	0.32	-25.41	16.45	-288.8
m13	15.764	0.93	80.6	983.5	5.064	0.00760	0.07	0.04936	0.57	0.04711	0.54	0.465	48.80	0.03	48.92	0.27	54.80	12.98	11.0
m14	11.878	0.43	6.1	112.4	3.684	0.00762	0.29	0.04775	4.51	0.04546	4.31	0.717	48.93	0.14	47.36	2.09	-31.14	104.66	-258.1
m15	6.926	1.34	87.7	1994.7	2.213	0.00761	0.06	0.04914	0.18	0.04686	0.17	0.394	48.84	0.03	48.71	0.09	42.34	3.96	-15.5
m16	9.895	2.15	240.3	4221.5	3.156	0.00759	0.09	0.04897	0.18	0.04677	0.15	0.520	48.77	0.04	48.55	0.09	37.27	3.69	-30.9
m17	6.620	1.56	108.5	2542.4	2.112	0.01088	0.06	0.07089	0.23	0.04724	0.22	0.351	69.79	0.04	69.55	0.15	61.21	5.14	-14.2
SK061C - Layer-parallel leucosome																			
m1A	12.876	1.87	60.2	887.2	0.011	0.01073	0.07	0.06881	0.34	0.04649	0.32	0.408	68.83	0.05	67.57	0.23	23.21	7.77	-197.9
m2A	5.664	6.97	92.1	2400.5	0.011	0.01086	0.06	0.07058	0.13	0.04712	0.11	0.511	69.65	0.04	69.25	0.09	55.38	2.65	-25.9
m2B	6.169	7.44	40.7	1015.4	0.011	0.01089	0.09	0.07061	0.26	0.04705	0.24	0.437	69.79	0.06	69.28	0.18	51.66	5.66	-35.3
m3	19.677	13.23	16.6	200.0	0.008	0.00758	0.30	0.04408	3.61	0.04217	3.45	0.584	48.69	0.15	43.80	1.55	-216.28	86.68	-123.0
m4A	21.208	12.58	15.0	159.9	0.008	0.00772	0.11	0.04982	1.11	0.04683	1.06	0.534	49.55	0.05	49.37	0.54	40.64	25.26	-22.1
m4B	19.977	6.54	11.9	136.5	0.008	0.00773	0.08	0.04996	1.11	0.04689	1.06	0.751	49.62	0.04	49.50	0.54	43.68	25.24	-13.6
m5A	14.768	7.99	51.0	678.9	0.008	0.00774	0.06	0.04907	0.28	0.04601	0.26	0.391	49.67	0.03	48.64	0.13	-1.98	6.22	-2675.6
m6A	6.191	1.35	24.8	631.5	0.011	0.01069	0.07	0.06785	0.44	0.04605	0.42	0.395	68.52	0.04	66.66	0.28	0.29	10.10	-22991.4
m6B	8.073	1.79	25.2	534.4	0.011	0.01080	0.09	0.06944	0.79	0.04663	0.76	0.487	69.25	0.06	68.16	0.52	30.17	18.11	-130.0
m7	17.626	1.54	13.6	169.3	0.008	0.00773	0.18	0.04922	2.66	0.04621	2.52	0.782	49.61	0.09	48.79	1.27	8.37	60.76	-493.3
SK0620C - Pegmatite																			
m2	29.864	30.17	136.1	998.3	9.173	0.00762	0.12	0.04732	0.30	0.04501	0.27	0.442	48.97	0.06	46.94	0.14	-55.33	6.46	-189.2
m3	27.261	38.28	33.6	283.1	8.303	0.00757	0.07	0.04659	0.29	0.04461	0.27	0.390	48.64	0.04	46.24	0.13	-76.69	6.52	-164.1
m4	16.930	3.36	135.6	1604.6	5.237	0.00752	0.07	0.04702	0.14	0.04532	0.12	0.534	48.33	0.03	46.66	0.06	-38.26	2.81	-227.0
m5	0.078	#####	6.4	458.3	0.025	0.00730	0.06	0.04730	0.16	0.04697	0.14	0.473	46.91	0.03	46.93	0.07	47.77	3.41	1.8
m6	7.943	32.77	18.0	393.3	2.487	0.00743	0.06	0.04697	0.21	0.04586	0.20	0.396	47.71	0.03	46.61	0.10	-9.67	4.81	-597.0
m7	24.166	4.40	140.5	1238.4	7.420	0.00757	0.06	0.04695	0.16	0.04499	0.14	0.423	48.61	0.03	46.59	0.07	-56.45	3.53	-186.8
SK0620D - Biotite gneiss																			
m1	95.909	4.28	180.0	474.5	27.919	0.00801	0.10	0.04711	0.99	0.04265	0.94	0.525	51.44	0.05	46.75	0.45	-188.04	23.50	-127.9
m2	66.895	1.97	59.6	226.9	19.890	0.00774	0.11	0.04648	1.38	0.04355	1.32	0.637	49.71	0.05	46.14	0.62	-136.00	32.66	-137.1
m3	19.474	1.55	64.0	687.8	5.943	0.00779	0.09	0.04804	0.54	0.04473	0.51	0.357	50.02	0.05	47.64	0.25	-70.30	12.54	-171.8
m4	63.294	1.43	65.2	249.4	19.566	0.00778	0.20	0.04861	2.48	0.04532	2.36	0.605	49.95	0.10	48.20	1.17	-38.26	57.42	-231.3
m6	57.427	3.06	101.2	423.5	17.281	0.00768	0.11	0.04666	1.05	0.04408	1.00	0.522	49.30	0.05	46.30	0.48	-106.24	24.68	-147.0

SK06127C - Layer-parallel leucosome																			
m1	23.693	1.12	49.7	448.0	7.428	0.01024	0.06	0.06540	0.66	0.04632	0.63	0.519	65.68	0.04	64.33	0.41	14.16	15.15	-365.4
m2	21.560	1.77	25.5	259.0	6.723	0.01022	0.08	0.06493	0.87	0.04606	0.83	0.548	65.57	0.05	63.88	0.54	0.68	19.90	-9541.0
m3	30.839	0.77	16.2	133.0	9.291	0.01015	0.21	0.06222	3.31	0.04444	3.16	0.697	65.13	0.14	61.29	1.97	-86.10	77.55	-176.6
m4	32.155	1.52	12.3	105.0	9.389	0.01019	0.20	0.06044	3.36	0.04304	3.22	0.730	65.33	0.13	59.59	1.95	-165.28	80.09	-140.2
m5	18.959	1.31	86.2	920.1	5.962	0.01020	0.10	0.06537	0.76	0.04646	0.72	0.505	65.44	0.06	64.29	0.48	21.64	17.26	-203.4
m6A	14.034	1.05	21.6	309.7	4.392	0.01017	0.10	0.06480	0.87	0.04622	0.83	0.446	65.22	0.06	63.76	0.53	9.06	19.89	-621.2
m6B	19.902	0.91	9.5	118.2	5.942	0.01022	0.42	0.06204	7.47	0.04404	7.10	0.884	65.53	0.28	61.12	4.43	-108.50	175.40	-161.2
SK06127F - Granitic dike																			
m2	50.499	4.29	12.7	77.6	14.825	0.00769	0.16	0.04557	2.76	0.04298	2.65	0.704	49.38	0.08	45.25	1.22	-168.73	66.01	-129.8
m3	4.625	8.01	15.5	470.9	1.473	0.00723	0.09	0.04654	0.43	0.04667	0.41	0.373	46.46	0.04	46.19	0.20	32.21	9.82	-44.4

(a) Monazite fractions are composed of single grains.
(b) Total weight of common Pb.
(c) Ratio of radiogenic Pb to common Pb.
(d) Measured ratio corrected for spike and fractionation only. Mass fractionation correction of 0.25%/amu ± 0.04%/amu (atomic mass unit) was applied to single-collector Daly analyses (based on daily analysis of NBS-981).
(e) Corrected for fractionation, spike, and blank. All common Pb in the analyses was assigned to procedural blank with a measured composition of 206Pb/204Pb = 18.271 ± 0.05, 207Pb/204Pb = 15.587 ± 0.05, 208Pb/204Pb = 38.119 ± 0.05 (2 sigma). U blanks were <0.1 pg.
(f) Errors are 2 sigma.
(g) Age calculations are based on the decay constants of Steiger and Jäger (1977).
(h) Error in the dates reported at 2 sigma.
(i) % discordance = 100 - (100 x (206Pb/238U age) / (207Pb/206Pb age)).

Chapter 6: Metamorphism and Deformation of High-Grade Gneiss and Adjacent Basin Material in a Strike-slip Fault Zone, Ross Lake Fault, North Cascades, USA

Stacia Gordon*, Donna L. Whitney*, Robert B. Miller*, Sam Bowring**, Noah McLean**, Nicholas Seaton***

*Department of Geology and Geophysics, University of Minnesota, Minneapolis, MN 55455
**Earth and Planetary Sciences, Massachusetts Institute of Technology, Cambridge, MA 02139
***Geology Department, San José State University, San José, CA 95192

This chapter will be submitted to the *Journal of Metamorphic Geology* in the near future.

ABSTRACT

Continental crust may be buried and exhumed in strike-slip fault zones through a combination of lateral and vertical movement. The relationship of metamorphism, exhumation, and strike-slip faulting can be examined by pressure-temperature-deformation (*P*-*T*-d) studies of orogenic crust exposed in transcurrent zones. The Skagit Gneiss, a migmatitic unit of the North Cascades, Washington (USA), was metamorphosed at depths of ~ 25-30 km in a transpressional continental arc. The long-lived, crustal-scale Ross Lake fault zone (RLFZ) bounds the eastern side of the Skagit Gneiss. The *P*-*T*-d conditions recorded by rocks on either side of the fault vary along the length of the fault zone, but most typically the fault separates high-grade gneiss from lower-grade rocks. In the vicinity of the RLFZ, the Ruby Mt-Elijah Ridge area at the eastern margin of the Skagit exposes several tectonic contacts between Skagit Gneiss and structurally overlying rocks; the latter rocks, including Methow basin deposits, record higher-grade metamorphism in this area than in correlative rocks to the north and south along the RLFZ. In this area, the Skagit Gneiss and overlying units all yield maximum *P*-*T* conditions of 8-10 kbar at >650 ºC, indicating that the basin rocks were buried to similar mid-crustal depths as the underlying gneiss unit. After exhumation to < 15 km depth, intrusion of late granitoid bodies drove local contact metamorphism in fault zone rocks, resulting in andalusite-cordierite in garnet schist. A high-temperature shear zone on Ruby Mt separates Skagit Gneiss from structurally overlying rocks and may have played a role in the exhumation of the Skagit and overlying units. An overlapping step-over in the Ross Lake fault zone facilitated burial and exhumation of the slice of the Methow basin. Oblique slip on the Ross Lake fault and the step-over in a transpressional

regime combined with buoyant vertical flow of migmatitic gneiss exhumed the high-grade Skagit Gneiss and the adjacent tectonic slice of metamorphosed Methow basin.

INTRODUCTION

Most orogens contain long-lived crustal- or lithosphere-scale strike-slip faults. Transcurrent motion may therefore affect orogenic processes at different crustal levels, and oblique tectonic regimes may influence the thermal and mechanical evolution of orogenic crust, including the exhumation history (mechanisms, rates) of metamorphic rocks. The evolution of crust in oblique orogens may be documented by modeling studies (e.g. Thompson *et al*., 1997) and/or field-based analysis of exhumed orogenic crust (e.g. Goscombe *et al.,* 2003).

The exhumation of mid- to lower-crustal rocks near strike-slip faults has been documented in a variety of orogenic settings, such as dominantly transpressional regimes (e.g. along the Alpine Fault, New Zealand; Little *et al*., 2005); Caribbean-South American plate boundary (e.g. Cruz *et al.*, 2007); the Appalachians (e.g. Snoke & Frost; 1990); and dominantly transtensional regimes (e.g. Walker Lane, western Basin and Range: Stewart, 1988; Unruh *et al*., 2003; Wesnousky, 2005); the Western Gneiss Region, Norway (e.g. Krabbendam & Dewey, 1998); and the Cordillera (e.g. Klepeis & Crawford, 1999; Foster *et al*., 2007). Some intracontinental strike-slip faults may show tectonic switches between transpression and transtension through time, leading to cycles of burial and exhumation (e.g. central Anatolia; Umhoefer *et al*., 2007).

Some strike-slip fault zones in ancient orogens, including arc systems, juxtapose exhumed orogenic crust with low-grade to unmetamorphosed rocks (e.g. the Ross Lake fault zone in the exhumed North Cascades arc (e.g. Misch, 1966; Haugerud, 1985; Kriens & Wernicke, 1990; Miller & Bowring, 1990; Miller *et al*., 1993; Miller, 1994); Walker Lane, northern Sierra Nevada (e.g., Stewart, 1988; Unruh *et al*., 2003; Wesnousky,

2005)). Although it is possible that lateral displacement may be responsible for juxtaposing terranes that formed at very different crustal levels, in some cases there is evidence for a component of vertical motion on the strike-slip fault system. In such cases, the role of strike-slip faults in the metamorphism and exhumation of orogenic crust can be investigated.

This paper focuses on the transcurrent Ross Lake fault zone (RLFZ) of the North Cascade Range, north-central Washington USA (Fig. 2). This fault zone marks the eastern boundary of high-grade rocks that formed in a continental arc during regional shortening (e.g., Monger *et al*., 1982; Crawford *et al*., 1987; Rubin *et al*, 1990; Journeay & Friedman, 1993). Exhumation of the high-grade rocks occurred after a switch to a dominantly transtensional regime (e.g., Tabor *et al.,* 1989; Miller & Bowring, 1990; Haugerud *et al.,* 1991; Umhoefer & Miller, 1996). The RLFZ is of interest for understanding the role of strike-slip fault systems in orogeny because the record of pressure-temperature-deformation relationships between rocks on either side varies along its length. For example, in some locations there is a major difference in thermal conditions recorded by rocks on either side of the fault, and in other locations, rocks from the basin side of the fault zone appear to have been metamorphosed, perhaps at similar conditions to the crystalline core side of the fault zone.

In this study, metapelitic gneiss and garnet amphibolite from the eastern margin of the Skagit Gneiss, in the vicinity of the Ross Lake fault zone, are used for *P-T* determination and microstructural analysis. Previous *P-T* studies (Whitney, 1991; Whitney, 1992b) were based on a few samples and were focused on determining the conditions of metamorphism of the migmatitic core of the gneiss unit. In this study,

samples were collected specifically from the eastern margin of the Skagit Gneiss and overlying units in and near the RLFZ to evaluate the role of transcurrent motion on the metamorphic and deformation processes.

GEOLOGIC OVERVIEW OF THE SKAGIT GNEISS AND ROSS LAKE FAULT

The Skagit Gneiss is exposed within the Northern Cascade Mountains in north-central Washington, a location that represents the southernmost extent of the Coast Plutonic Complex-North Cascades orogen that runs from Alaska to Washington (Fig. 1). The Skagit Gneiss (Misch, 1966; 1968) consists predominately of tonalitic orthogneiss with lesser amounts of biotite gneiss, amphibolite, calc-silicate, and metapelite exposed in a NW-SE trending antiform (Fig. 3A). In the north-central part of the Skagit Gneiss, both metasedimentary and metaigneous rocks are migmatitic and formed through a combination of subsolidus processes (metasomatism, metamorphic differentiation) (Misch, 1968; Yardley, 1978; Babcock & Misch, 1989) and partial melting (Whitney, 1992a; Whitney & Irving, 1994).

Results of previous geochronology and petrology studies suggest a long-lived, high-temperature history for the Skagit Gneiss, with magmatism ranging from ca. 90 to 45 Ma, and migmatite crystallization ages of 68-47 Ma (Mattinson, 1972; Miller *et al*., 1989; Miller & Bowring, 1990; Haugerud *et al.*, 1991; Gordon *et a*l., ms). Although early studies proposed a low-*P* metamorphic history for the Skagit Gneiss (Misch, 1966; 1968), thermobarometric estimates and reaction textures indicate higher-*P* conditions of 8-10 kbar at 650 – 725 ºC and near isothermal decompression to $P < 5$ kbar (Whitney, 1991; Whitney, 1992b).

The high-grade Skagit Gneiss is bounded by the Late Cretaceous(?) – Eocene Ross Lake fault zone (RLFZ) in the east and the Eocene, dextral Straight Creek fault in the west (Figs. 1, 2, 3A). The Straight Creek fault separates orthogneiss from low-grade Paleozoic and Mesozoic oceanic and arc rocks to the west, and has been largely obscured by the Chilliwack batholith (Misch, 1966; Tabor *et al*., 2003).

Eastern margin of the Skagit Gneiss

Ross Lake Fault Zone

Along most of its length, the high-angle RLFZ forms the boundary between the Skagit Gneiss and the Mesozoic Methow basin to the east. The RLFZ consists of a series of fault systems, including the Ross Lake fault proper (Misch, 1966); Hozameen-North Creek fault (Misch, 1966; McGroder, 1987), Foggy Dew fault (Barksdale, 1975; Miller & Bowring, 1990), Twisp River fault (Barksdale, 1975), and Gabriel Peak tectonic belt (Misch, 1977; Miller, 1987) (Fig. 2). Movement on the RLFZ was predominantly dextral strike-slip with components of reverse slip during the Paleocene and dextral-normal (down-to-E) shear in the Eocene (Misch, 1966; Haugerud, 1985; Miller & Bowring, 1990; Miller, 1994). In general, rocks on the west side of the fault are high-grade metamorphic rocks and magmatic complexes and rocks on the east are lower-grade units of the Methow basin or oceanic terranes, but the degree of difference in metamorphic grade across the fault varies along the strike of the fault.

At the NNE margin of the Skagit Gneiss, the RLFZ is a series of splays that separate structural blocks that consist of, from west to east, the Skagit Gneiss, the Skymo complex, the Little Jack terrane, and the Hozameen terrane (Haugerud, 1985; Baldwin *et*

al., 1997) (Fig. 2). The Skymo is a layered mafic complex of mantle-derived magma that was emplaced into mid- to shallow crustal levels in the mid-Eocene (Baldwin *et al.*, 1997; Whitney *et al.,* 2008). On the NE side of the fault in this region, the Little Jack terrane consists of graphitic phyllite. The Little Jack commonly preserves evidence of primary sedimentary features such as bedding (Tabor *et al*., 1994). The Little Jack terrane was affected by contact metamorphism (sillimanite zone) during emplacement of the Skymo mafic magma, but mineral assemblages and textures suggest low-temperature – low-pressure (andalusite zone) metamorphic conditions prior to contact metamorphism (Baldwin *et al.,* 1997). The RLFZ in this area is steeply dipping, has penetrative plastic and brittle deformation, and records Eocene dextral and reverse shear followed by normal slip movements (Baldwin *et al*., 1997). South of the Skymo-Little Jack contact, near Ross Lake, the RLFZ records a similar displacement history and separates Skagit orthogneiss from the Little Jack terrane (Fig. 2).

The southern segment of the RLFZ also consists of a series of fault splays that separate an oceanic pre-Upper Cretaceous assemblage, the Napeequa unit, on the southwest from Jurassic and Cretaceous shallow marine and subaerial clastic and volcanic Methow terrane rocks on the northeast (Fig. 2; Miller, 1994). There is a distinct break in metamorphic grade across the fault zone: Napeequa rocks were metamorphosed in the upper amphibolite facies, whereas the Methow rocks record sub-greenschist facies conditions (e.g., Miller et al., 1993; Miller, 1994).

Farther south, a left-stepping, dextral strike-slip step-over shear zone characterizes the RLFZ (Fig. 2; Miller & Bowring, 1990; Miller, 1994). Various strands of the RLFZ (Foggy Dew, Twisp River fault zones) juxtapose an oceanic assemblage on

the west side with pre-Upper Cretaceous North Creek arkose and volcanic rocks on the east. Previous studies have correlated the oceanic assemblage in this region with the Napeequa unit (Tabor *et al*., 1989; Miller *et al*., 1993). The North Creek unit has been metamorphosed to greenschist-facies, but, based on protolith lithology, is considered to be part of the Methow basin (Misch, 1966; Barksdale, 1975; Kriens & Wernicke, 1990; McGroder *et al.,* 1990; Miller *et al*., 1994). To the southwest of the Foggy Dew fault, the Gabriel Peak tectonic belt juxtaposes oceanic Napeequa and Skagit orthogneiss with the Black Peak batholith, a mid-Cretaceous (Hoppe, 1984) intrusion that was emplaced in the step-over zone between the two faults (Fig. 2; Miller, 1994).

The displacement history of the southern segment of the RLFZ includes dextral strike-slip (65-48 Ma) with reverse slip from 65 to 57 Ma, followed by 57 to 48 Ma oblique-slip (dextral strike plus a lesser component of normal slip) (Miller & Bowring, 1990; Miller, 1994). The Eocene slip history of the RLFZ is similar in both the northern and southern segments (Miller & Bowring, 1990; Miller, 1994; Baldwin *et al.,* 1997).

Some studies have suggested that the Coast Mountains-North Cascade orogen has been displaced northward during the middle to Late Cretaceous from a position at the latitude of present-day Baja California, Mexico, to its position today in Washington, British Columbia and southern Alaska (i.e. the Baja-BC hypothesis) (e.g. Beck, 1976; Irving, 1985; Umhoefer, 1987). According to the Baja-BC model, the North Cascades and associated terranes moved northward and became attached to North America between 66 and 56 Ma in a dextral-transpressive regime (Umhoefer, 1987). Thrusting followed by major dextral strike-slip faulting has been documented in the Coast Mountains-North Cascades (Umhoefer & Miller, 1996). The major slip on Ross Lake was

part of this latter faulting and was thus subsequent to the major terrane translation suggested by the Baja-BC hypothesis.

Ruby Mountain and Elijah Ridge

Along strike and between the two areas described in the previous section, extrapolation of the northern and southern segments of the RLFZ suggests that it should cut through the rocks exposed on and near Ruby Mountain and Elijah Ridge (Fig. 2). In both areas, the Napeequa unit lies structurally above the Skagit Gneiss (Fig. 3). The Napeequa unit is a heterogeneous, metamorphosed oceanic assemblage that contains amphibolite and quartzite (metachert) with subordinate marble, metaperidotite, and biotite schist (Tabor *et al*., 1987a, b; 1989). The unit is exposed in various places in the North Cascades, but in a particularly interesting area on Ruby Mountain, the Napeequa unit is preserved as a klippe(?) on Skagit Gneiss (Fig. 3). Below the Skagit-Napeequa contact, Ruby Mt consists almost entirely of a deformed hornblende-biotite tonalitic orthogneiss that has an intense, constrictional fabric near the contact.

Elijah Ridge exposes a more diverse set of rock types, but the majority have an intense mylonitic, constrictional fabric, similar to the fabrics along the contact on Ruby Mountain. The western side of Elijah Ridge consists of Napeequa amphibolite, metachert, and metapelite. The only previous *P-T* estimate from this area is from a kyanite-staurolite schist that yielded *P-T* conditions of 650 ºC and 8 kbar (Fig. 1B), slightly lower but similar to estimates from sillimanite gneiss in the structurally deepest exposed part of the Skagit Gneiss (Whitney, 1992b). Application of mass balance techniques (singular value

decomposition analysis) indicated that the Napeequa and Skagit metapelitic rocks formed from different protoliths (Whitney *et al*., 1995).

Eastern Elijah Ridge consists of various types of metasedimentary rocks including metaconglomerate, all of which are intruded by hornblende porphyry and hornblende gabbro, and late granitic dikes (Fig. 3C) (Misch, 1966; Kriens, 1988; Kriens & Wernicke, 1990; Miller *et al*., 1994). The east Elijah rocks have been interpreted as Methow terrane rocks (Kriens & Wernicke, 1990; Miller *et al*., 1994). The meta-Methow rocks are in contact with a small (~ 2 m wide) lens of metapelitic rock consisting of garnet-andalusite-cordierite schist and a staurolite-andalusite schist. Farther to the west, a large body of orthogneiss is exposed (Fig. 3C).

The rock types exposed on Ruby Mt and Elijah Ridge are similar to those described on either side of the RLFZ to the north and south, with Skagit orthogneiss and Napeequa generally found on the west and meta-Methow rocks to the east. In the study area, however, the Methow rocks record higher-grade metamorphism than the greenschist-facies Methow rocks to the north and south. In addition, questions remain about the location of the RLFZ zone in this area, the driving force for metamorphism of the Methow rocks, and the tectonic/metamorphic significance of the Skagit-Napeequa contact, including the origin of the constrictional fabrics near the contact in this region.

In order to evaluate these questions and to understand exhumation conditions and mechanisms of orogenic crust in continental arc systems, the eastern margin of the Skagit Gneiss has been examined for its petrologic and microstructural history. Samples with suitable assemblages were collected for thermobarometric analysis across the Skagit-

Napeequa contact and additional samples were collected for microstructural and electron backscatter diffraction (EBSD) analysis (Fig. 1).

ANALYTICAL METHODS

Microprobe analyses were obtained using a JEOL 8900 electron microprobe at the University of Minnesota. Natural standards were used for calibration and a ZAF matrix correction routine was used. Analyses were performed with a 20 nA beam current at 15 kV. A focused beam was used for most minerals with the exception of plagioclase and biotite; a slightly defocused beam was used to minimize K and Na loss. All minerals analyzed were checked for zoning on the thin-section and grain scale. Representative microprobe analyses for garnet, plagioclase, biotite, hornblende, clinopyroxene, cordierite and staurolite are given in Tables 1-7.

In addition to petrographic observations, fabric analysis of samples from Ruby Mt and Elijah Ridge were obtained using the electron backscattered diffraction technique (EBSD). A JEOL JSM FEG 6500F scanning electron microscope equipped with an EBSD detector was used for the analyses at the Characterization Facility, University of Minnesota, and operating conditions were a 10-15 nA beam current at 20 kV and a working distance of 15 to 25 mm. Step sizes of 4-20 μm were used depending on the quartz grain size in each individual sample. Oxford Instruments/HKL Channel 5 software was used for acquisition and data processing.

We measured $^{40}Ar/^{39}Ar$ cooling ages for muscovite from two samples along the contact between the Napeequa and Skagit orthogneiss on Ruby Mt. Pure mineral separates (~99%) were prepared using standard density and magnetic techniques.

Conventional step-heating was conducted at MIT using a double-vacuum, resistance furnace. Argon was purified in an all-metal extraction line and analyzed with a MAP 215-50 magnetic sector mass spectrometer. The heating schedule is shown with the results in Table 1. All ages are calculated with the decay constants recommended by *Steiger and Jäger* [1977]. Errors are reported at the 2σ confidence level. The $^{40}Ar/^{39}Ar$ results are presented as conventional age spectra. Preferred ages shown represent integrated weighted mean ages calculated for selected portions of each age spectrum (Figs. 18). The initial low-temperature increasing steps (typically the first 3-5) were not used in calculating the preferred ages. Similarly, the final high-temperature steps were commonly ignored due to elevated furnace blanks at very high temperature (~1673-1873 °C). The results are shown in Figure 18 and listed in Table 1.

PETROGRAPHY AND MINERAL CHEMISTRY

Rocks with suitable assemblages for unraveling the pressure-temperature history of the Skagit Gneiss are rare. A previous investigation (Whitney, 1992b) was limited to four metapelitic samples. In this study, four additional metapelitic rocks were discovered and used to determine *P-T* conditions, in addition to three garnet amphibolites (one in the Skagit Gneiss, two in the Napeequa unit) (Fig. 1).

Garnet amphibolite

Small bodies of amphibolite are associated with both the Skagit Gneiss and the Napeequa unit. On Ruby Mt, two garnet-bearing amphibolite samples were collected: one from ~ 0.5 km below the Napeequa contact (sample SK0626) and the other (SK0672) from

within the Napeequa unit at the top of Ruby Mt (Figs. 1; 3B). In addition, a garnet amphibolite (SK08273) was collected from the western end of Elijah Ridge.

The Skagit garnet amphibolite (SK0626) is migmatitic, with cm-scale foliation-parallel leucosomes, and the Ruby Napeequa amphibolite (SK0672) is migmatitic but finer-grained. The Napeequa amphibolite from Elijah (SK08273) is also fine-grained but is not migmatitic. All three samples are essentially bimineralic with hornblende and plagioclase forming a foliation and compositional banding. Minor amounts of titanite, quartz and ilmenite are present, and the Skagit amphibolite also contains texturally early clinopyroxene that has been partially replaced by hematite.

Garnets in the Skagit amphibolite (SK0626) are anhedral, ~4-5 mm, Ca-rich (Table 2) and contain hornblende, plagioclase, and clinopyroxene inclusions. Some garnets have a post-kinematic symplectitic corona consisting of a vermicular intergrowth of plagioclase and hornblende (cf. Misch & Onyeagocha, 1976). The garnets are unzoned, as is common for Skagit garnet.

Synkinematic garnets in the Ruby Napeequa amphibolite (SK0672) are typically euhedral, ~2–3 mm, and some contain sigmoidal inclusion trails of ilmenite. Garnets are Fe-rich with an almandine component of ~0.60 (Table 2). The garnets show minor growth zoning (i.e., slightly higher Mn in core).

Garnets from the Elijah Napeequa amphibolite (SK08273) are also euhedral and texturally and compositionally very similar to the Ruby Napeequa amphibolite. Garnets are Fe-rich (X_{Alm} = ~0.50), and the garnets have a slightly higher spessartine component in the core in comparison to the rim (core = 0.11; rim = 0.07).

Pargasitic hornblende combined with plagioclase forms the main foliation for the amphibolites and also typically is the lineation-forming mineral. The hornblende in the two Ruby samples is zoned: the edge of hornblende close to garnet tends to have a more blue-green color but is only slightly more Fe-rich and Ti-poor than the green hornblende in the matrix (Fig. 4) (Table 3). The Ruby Napeequa amphibolite (SK0672) contains minor biotite that seems to be a product of late breakdown of hornblende.

The pargasitic hornblende in the Elijah Napeequa amphibolite (SK08273) is unzoned in comparison to the Ruby amphibolites. The composition of the interior (X_{Fe} = 0.45-0.36) is very similar to the rims of the hornblende grains (X_{Fe} = 0.45-0.40). The only compositional difference is found in hornblende near garnets: the hornblende adjacent to the garnet has a X_{Fe} value of 0.50 from the crystal rims. Some of the hornblende near garnet is homogenous compositionally while other grains have an interior X_{Fe} value of 0.38, similar to the values from the matrix grains.

Plagioclase in all three amphibolites is zoned. Both normal and reverse concentric zoning are observed in the Ruby amphibolites, but reverse zoning is more common. Anorthite content of the plagioclase of normally zoned crystals changes from ~An_{45} to A_{36} from core to rim (Table 4). The reverse zoning is more variable, with core plagioclase values of An_{36-40} and rim values of An_{42-60}.

Reverse zoning dominates the plagioclase in the Elijah Napeequa amphibolite (SK08273). Commonly the core values of the plagioclase have compositions of An_{33-34} and the rim values have a higher anorthite content, An_{39-41} (Table 4). This pattern is found throughout the matrix plagioclase. However, the plagioclase near garnets tend to

have normal zoning with lower anorthite values, An_{31-36}, in the rims and more variable core values, An_{36-46}.

Clinopyroxene occurs in sample SK0626, the Skagit amphibolite, as a matrix phase and as inclusions in garnet. Grains are unzoned, with X_{Fe}= 0.29 (Table 5).

Metapelitic rocks

Two metapelitic schists were collected on Ruby Mountain: a migmatitic sillimanite-bearing schist (SK0691) and a migmatitic kyanite-bearing schist (SK0648) (Figs. 1, 5). Structurally, ~1200 m separates the Ruby schists. Two metapelitic samples were also collected from Elijah Ridge: a kyanite-staurolite schist (SK07240), and an andalusite-cordierite schist (SK07226), and structurally the Elijah schists are only 50 m apart, with SK07226 below SK07240. (Figs. 1, 6). The Elijah Ridge schists are ~ 2.75 km structurally higher than the Ruby Mt sample, SK0648.

Ruby Metapelite

The Ruby Mt schists both consist of quartz, biotite, plagioclase, garnet, ilmenite, cordierite, kyanite ± sillimanite, zircon, apatite and monazite (Fig. 5). In the sillimanite-bearing schist, tabular pseudomorph textures suggest the former presence of kyanite (Fig. 5D), and the kyanite-bearing schist contains fibrous sillimanite. As is typical of Skagit metapelitic rocks, the Ruby schists do not contain muscovite or K-feldspar.

Cordierite is an abundant matrix phase with biotite (Fig. 5), but also occurs as rims on garnet in SK0691 (Fig. 7) and Al_2SiO_5 phases in both samples (Fig. 5). In

particular, cordierite is associated with fibrolite in SK0648. Cordierite in both samples exhibits extensive hydrous alteration (pinitization).

Both samples are deformed and have strong S-C fabrics. In SK0691, sillimanite is found in the S and C planes, indicating that shear occurred at a relatively high-temperature (> 500 ºC). Chessboard extinction in matrix quartz in Ruby Mt sample, SK0648, further suggests high-temperature deformation (Kruhl, 1996; 1998). Both samples exhibit extensive quartz ribbon development, and the ribbons contain elongate subgrains and deformation bands. Sillimanite is present in the ribbons, suggesting a high-temperature origin for the ribbons, although they have been overprinted by a lower-temperature deformation. Plagioclase grains are deformed and elongated parallel to foliation.

In sample SK0691, the garnet-sillimanite-cordierite schist, garnets are typically subhedral, ~1 – 1.5 mm and Fe-rich (X_{Alm} = ~ 0.65 – 0.74) (Table 2). In addition, the garnets have inclusion-filled cores and inclusion-free rims. Inclusions are quartz, biotite, rutile, and zircon. Cordierite surrounds garnet and locally forms a symplectitic rim with quartz (Fig. 7). Zoning at the garnet rim suggests possible late (retrograde) reaction with adjacent cordierite and/or other minerals: near the cordierite, Mn and Fe in garnet increases and Mg decreases (Fig. 7) (Table 2). Plagioclase is commonly unzoned in sample SK0691, and its composition is typically ~An_{35} (Table 4). Biotite is homogeneous in the schist and the X_{Mg} values are generally ~ 0.40 to 0.50 with TiO_2 = 2.5 -3.0 wt % (Table 6). In sample SK0691, sillimanite forms well-developed prismatic crystals aligned in the foliation that is defined by compositional layering, biotite, and quartz ribbons (Fig.

5A). Textural evidence from SK0691 suggests that kyanite was probably once stable in this sample and has been replaced by sillimanite.

Garnets in SK0648, the garnet-kyanite-cordierite schist, have similar compositions to the garnets form SK0691: Fe-rich (X_{Alm} = ~ 0.65 – 0.74) (Table 2). They are generally euhedral and slightly larger, ~1.5 – 2 mm, and show similar resorption and retrograde zoning features, with Mn, Mg, and Ca significantly zoned around plagioclase inclusions and at garnet rims; Ca and Mg decrease near plagioclase, and Mn increases. Zoning around the plagioclase inclusions is interpreted to indicate post-entrapment net transfer reaction during decompression (Whitney, 1991). Plagioclase does not appear to be zoned; however, the composition of the plagioclase that is included in the garnet has a slightly lower An content: An_{36} for plagioclase inclusions versus An_{40} for matrix plagioclase (Table 4). Biotite from SK0648 is homogeneous and contains ~ 2 wt % TiO_2 and X_{Mg} values of 0.40 – 0.50 (Table 6). Kyanite forms tabular crystals in the SK0648 metapelite sample (Fig. 5B), and fibrous sillimanite is intergrown with biotite.

Elijah Metapelite

The Napeequa kyanite-staurolite schist from Elijah Ridge area, SK07240, (Figs. 1, 6) contains: quartz, biotite, plagioclase, muscovite, garnet, staurolite, kyanite, rutile, ilmenite, zircon, apatite and monazite. The andalusite-bearing schist (SK07226) occurs as a small (~ 2 m wide) lens on the eastern side of the Ridge near meta-Methow rocks, and contains quartz, biotite, plagioclase, garnet, andalusite, cordierite, muscovite, ilmenite, tourmaline, zircon, apatite and monazite. In contrast to Skagit metapelites, Elijah Ridge schists contain muscovite. Andalusite, cordierite, and muscovite represent a late, post-

tectonic assemblage; the minerals overprint the foliation (Fig. 6B). Tabular pseudomorphs containing cordierite may have formed after kyanite or staurolite (Fig. 6C).

Misch (1968) described the schist that is near the meta-Methow rocks and interpreted the andalusite to indicate a late-Buchan-style overprint. Rocks east of the Ross Lake fault also contain andalusite. These localities are ~1.5 km map distance from the Golden Horn batholith, which intruded at ca. 47-50 Ma (Miller *et al.*, 1989; Petro *et al.*, 2002).

Both samples are deformed. In the kyanite-staurolite schist, SK07240, garnets have extensively corroded and disaggregated. In addition, the garnets contain quartz inclusion trails that are at an angle to the matrix foliation, revealing an earlier deformation history. Staurolite and kyanite are elongate parallel to foliation and are typically disaggregated. Uniformly recrystallized quartz forms triple junction grain boundaries in some spots. Sample SK07226 is very micaceous and the micas show intense fabrics. Quartz, where present, is polygonal and contains deformation lamellae. The quartz is commonly found in small (~ 1-2 mm wide) pressure shadows around the garnet.

Garnets are rounded to ellipsoidal. Sample SK07240 contains growth-zoned garnets: Mn and Ca decrease from core to rim, and Mg and Fe increase. The X_{Mg} value decreases from core to rim (0.9 to 0.8). The garnets have overgrown an early foliation and are hence rich in quartz inclusions that are in trails oriented at an angle to the matrix foliation. The garnets are altered to chlorite and partially disaggregated.

The plagioclase in SK07240 has a different composition adjacent to garnet versus plagioclase in the matrix. Near garnet, the anorthite content is lower (An_{30-36}). The plagioclase is typically zoned near garnets as well, and has reverse and normal zoning, with An contents ranging from An_{31} (core) to An_{36} (rim) and other grains yielding An_{32} to An_{30} core to rim. There is not a systemic relationship of the normal versus reverse zoning. Away from the garnet, the anorthite content is typically An_{39-41} (Table 4).

In sample, SK07240, two generations of biotite are present: a fine-grained red-brown variety (Ti content of 0.3 to 0.6 wt % and X_{Mg} of 0.41-0.45) that forms the foliation, and a later generation of light brown porphyroblastic biotite (Ti content of 1.7 to 2.2 wt % and X_{Mg} of 0.38-0.39) that has a grain size of ~0.5 – 1 mm (Fig. 6A) (Table 6). Biotite porphyroblasts are wrapped by finer-grained biotite and muscovite.

In all schists examined for this study, the Al_2SiO_5 polymorphs (kyanite, sillimanite) have been partially replaced by cordierite or andalusite. In sample SK07240, kyanite has been deformed and is disaggregated into fragments that are elongated in the foliation plane.

Staurolite is not a common mineral in the Skagit Gneiss, but it occurs in metapelitic schists on Elijah Ridge. In previous studies, staurolite was described as inclusions in garnet in sillimanite gneiss, in the matrix of kyanite-bearing metapelite, and in the matrix of amphibolite (Whitney, 1992b). The coexistence of staurolite and hornblende suggests metamorphic $P > 6$ kbar (Selverstone *et al*., 1984; Arnold *et al.,* 2000). In this study, staurolite is present in SK06240, and typically occurs strung out along foliation layers (Fig. 6A). Staurolite in this sample has $X_{Mg} = 0.19$ and contains ~ 1 wt % ZnO (Table 8).

Garnets from sample SK07226 are more complex: garnets with different zoning patterns occur on the thin section scale. Smaller (~100 - 300 μm) garnets typically have homogeneous zoning with minor resorption (~2 μm-scale) and retrograde zoning near adjacent minerals such as cordierite. The smaller garnets are Fe-rich with almandine compositions of ~ 0.78 (Table 2). Other, typically larger (~ 2 - 3 mm) garnets have distinct discontinuous zoning (Fig. 8), with Ca-rich outer core regions (X_{Alm} = ~0.72 - 0.75) around a texturally and compositionally distinct core (X_{Alm} = ~0.69 – 0.70) (Table 2). In contrast, Mg is homogeneous throughout the garnet, and Fe and Mn show smooth, continuous growth zoning (Fig. 8). Similar garnets with distinct discontinuous zoning in Ca have been described from other areas along the eastern margin of the Skagit Gneiss (Miller *et al*., 1993). In some of SK07226 garnets that have texturally distinct core and rim regions, the interior of the garnet has been replaced by micas, tourmaline and in some cases cordierite during late probably retrograde metamorphic reactions.

The majority of the plagioclase is homogeneous in SK07226 and ranges in anorthite content from An_{30} to An_{41} (Table 4). However, plagioclase is zoned adjacent to garnet, the plagioclase has an anorthite composition of An_{33} (core) and An_{30} (rim), near the garnet.

Sample SK07226 is very micaceous, and contains homogeneous red-brown biotite (TiO_2 = 2.0 -2.4 wt % and X_{Mg} = ~0.25) (Table 6). The biotite forms small mm-scale folds in the sample, and it bends around the porphyroblasts of garnet, andalusite, and cordierite. In some places, cordierite has partially replaced biotite.

SK07226 lacks kyanite, but contains texturally late andalusite that overgrew the fabric. This sample has tabular pseudomorphs of cordierite that may once have been kyanite (or staurolite) (Fig. 6C).

The cordierite in sample SK07226 contains X_{Mg} = 0.45 – 0.47 in both the matrix and near garnet (Table 6), and the cordierite exhibits a variety of textures and degrees of alteration. In some areas of the thin section, the cordierite contains inclusion trails that mostly consist of ilmenite and apatite. Some cordierite contains subgrains, and some grains are twinned.

GEOTHERMOMETRY AND GEOBAROMETRY

Geothermometry

Metamorphic temperatures were obtained using garnet-biotite and garnet-hornblende geothermometry using the calibrations of Holdaway (2000) and Ravna (2000), respectively. In addition, AX (Thermocalc 3.26; Powell & Holland, 2001) was used to calculate temperatures. Unzoned garnet and matrix biotite composition were used in the garnet-biotite calculations. For garnet-hornblende thermometry, garnet core composition was paired with green matrix hornblende, and garnet rim with blue-green (near-garnet) hornblende.

For the Ruby Mt. samples, garnet-biotite geothermometry yields temperatures of ~ 700 – 800 ºC for the two schists. In comparison, garnet-hornblende thermometry from the amphibolites yields temperatures of ca. 675 – 730 ºC. The amphibolite results were within error of each other from above and below the contact between the Skagit orthogneiss and the Napeequa.

The two Elijah Ridge schist samples, the kyanite-staurolite schist and the andalusite-cordierite schist, both yield similar temperatures of 650 -700 º, and the Elijah amphibolite yields temperatures of 570 – 670 ºC. The temperatures from Elijah are slightly lower than temperatures obtained from Ruby Mt. Errors for the thermometers are on the order of 50 ºC; therefore, it is difficult to evaluate whether there is a difference in temperature between Elijah Ridge and Ruby Mountain. Results calculated for the andalusite-bearing schist likely indicate conditions prior to growth of andalusite, which is texturally late and likely not in equilibrium with the phases used in the temperature calculation.

Geobarometry

The garnet-plagioclase-quartz-hornblende geobarometer (Kohn & Spear, 1990) was applied to the garnet amphibolite samples, and the garnet-Al_2SiO_5-plagioclase-quartz (GASP) geobarometer (calibration of Holdaway, 2001) was used for metapelitic rocks. In addition, AX (Thermocalc 3.26; Powell & Holland, 2001) was employed for determining metamorphic pressure. Garnet core and matrix plagioclase compositions were used for calculating maximum pressures. For most of the samples, kyanite was assumed to be the stable Al_2SiO_5 polymorph, except for sample SK0691, in which sillimanite was chosen as the stable Al_2SiO_5 polymorph.

The majority of the samples from this study, including the Ruby amphibolites and the metapelites from Ruby and Elijah, yield very similar geobarometric results of 8-10 kbar. The pressure results from this study match with previous geobarometric investigations of metapelites in the north-central portion of the Skagit Gneiss (Whitney,

1992b). Slightly lower pressures, 7-8 kbar, were obtained from the amphibolite from Elijah Ridge.

Garnet zoning patterns in sample SK07226 may also yield information about the pressure history of the schist. Garnets that exhibit distinct discontinuous zoning in the grossular component (Fig. 8) may record the progressive reaction via net transfer between garnet and plagioclase. If the pressure-dependent reaction: 3 anorthite = grossular + 2 kyanite + quartz controlled the Ca components in coexisting garnet and plagioclase, the increase in Ca concentration towards the garnet rim indicates garnet growth during an increase in pressure. Within the Skagit, garnets with this distinctive zoning pattern have thus far only been found along the eastern margin near the Ross Lake fault zone (Miller *et al*., 1993; this study). Garnets from structurally deeper regions of the Skagit Gneiss to the west are generally homogeneous or have only thin retrograde zoning at garnet rims. Garnets from the eastern margin of the Skagit experienced slightly lower temperatures than the migmatitic core of the gneiss, so the garnets from the eastern margin may better record the prograde history. In addition, the eastern margin may have had a more complex later history owing to magmatism and faulting associated with the Ross Lake fault zone.

P-T **PATHS**

The metapelite samples and the garnet amphibolites from Ruby Mt and Elijah Ridge preserve evidence for multiple parts of the *P-T* path in their textures and mineral assemblages. Some of the garnets from the Elijah Ridge andalusite-cordierite schist record the earlier (pre-andalusite) metamorphic history, and the rims of these garnets

suggest a subsequent increase in pressure. The geobarometry results and textural evidence for the former presence of kyanite in all of the samples supports the inference that maximum metamorphic pressures were at kyanite zone conditions. Thermobarometric results for all of the samples in this study yield maximum conditions of 8-10 kbar at 650 to 750 ºC followed by near isothermal decompression to $P < 5$ kbar at high-temperatures (Fig. 9).

Evidence that metamorphic reactions continued during decompression include: 1) cordierite rimming the Al_2SiO_5 minerals and garnet (forming a wormy intergrowth of cordierite and quartz around garnet) in the metapelites, and 2) sympletitic rims of plagioclase and hornblende around Ca-rich garnets in the amphibolites. Whitney (1992b) found similar conditions and evidence that metamorphic reactions continued during isothermal decompression. In addition, Whitney (1992b) found relict kyanite inclusions in schists that also contain matrix sillimanite and cordierite, and documented a decrease in Ca at garnet rims linked with an increase in Ca at plagioclase inclusion rims. Based on these results, the sillimanite and cordierite found in the Ruby and Elijah samples likely grew during decompression at high temperature.

The *P-T* results from the eastern-side of Elijah Ridge reveal the metamorphic conditions present prior to a low-pressure metamorphic overprint (Buchan overprint of Misch, 1968). The 8-10 kbar results suggest that the eastern side of Elijah, near the bounding Ross Lake fault zone, was buried to depths of ca. 25-33 km; equivalent to samples farther west in the Skagit Gneiss.

MICROSTRUCTURAL ANALYSIS

For the purposes of microstructural analysis, samples were collected in a transect from Skagit Gneiss at the base of Ruby Mountain structurally up through the contact with the Napeequa (Fig. 1). In addition, a sample from the Napeequa on western Elijah Ridge, including a quartz-rich kyanite-staurolite schist, was analyzed to compare the deformation style between the two areas, and two samples used in previous *P*-*T*-t studies of the Skagit Gneiss migmatite were used to better understand the relationship of deformation and metamorphism (Fig. 1).

The microstructural analyses of Skagit orthogneiss and Napeequa tonalitic amphibolite and quartzite provide useful information for understanding the deformation history of the eastern margin of the Skagit and the nature of the Skagit-Napeequa contact (see below), but it is also useful to analyze the microstructures in rocks for which *P*-*T*-t information have been obtained. For this reason, a sample of leucosome and mesosome from a migmatitic garnet-sillimanite gneiss was selected for EBSD analysis (SK-1 from Whitney, 1992b and Whitney & Irving, 1994; SK061C and SK061DM from Gordon *et al*., ms) (Fig. 10). The mesosome (garnet-biotite-sillimanite gneiss) reveals moderate temperature fabrics with prism <a> slip dominating in quartz. An S-C fabric is also present in the sample, and sillimanite is found in both the S and C planes, indicating that this is a high-temperature fabric. The leucosome from this outcrop, however, has been completely overprinted. The leucosome quartz has undergone intense recrystallization and has a protomylonitic fabric. A strong CPO was produced by basal <a> slip and indicates top-to-north shear sense. The protomylonitic fabric of the leucosome quartz is very similar to the fabric found at the base of Ruby Mt, in the migmatite at John Pierce Falls. Although there are an insufficient number of samples analyzed to make a strong

interpretation of these data, it is possible that there is a late shear zone or distributed zone of shearing affecting the structurally deepest exposed rocks.

In order to evaluate the microstructures from along the eastern margin of the Skagit, samples were collected from a range of structural levels on Ruby Mt. Samples of Skagit Gneiss from near the base of Ruby Mt preserve a variety of microstructures that indicate a progressive sequence of deformation from high- to low-temperatures. A sample of a leucosome from migmatitic biotite gneiss at John Pierce Falls (Fig. 1) was selected for a detailed EBSD analysis. The sample has a melt crystallization age of ca. 51 Ma (sample SK0620B of Gordon *et al*., ms), which is younger than crystallization ages of Skagit leucosomes from other locations. The 51 Ma leucosome was significantly deformed after the melt crystallized. Quartz in some regions of the leucosome are coarse-grained and do not show evidence for recrystallization (Fig. 12A).

In order to evaluate the lower-temperature deformation, EBSD maps were created for two different parts of a single leucosome thin section: 1) an area in which the quartz is strung out, elongated and wraps around a porphyroblast of plagioclase, representing high strain zone and moderate to low-temperature deformation (Fig. 12A-C); and 2) an area with a shear zone that cuts ~60º from the foliation; the shear zone caused recrystallization in the quartz and contains biotite and chlorite, suggesting a relatively low-temperature feature (Fig. 12D-F).

The maps indicate a strong crystallographic preferred orientation (CPO) and prism <a> slip for quartz (Figs. 12). The EBSD map of the shear zone further reveals that quartz has undergone significant rotation and recrystallization (Fig. 12E). The large (0.3 – 0.5 mm) quartz grains do not show a preferred orientation. In comparison, in the shear

zone the grain size is much smaller (< 0.1 mm), and quartz and biotite are rotated ~ 60 º from the foliation plane.

An EBSD map of quartz wrapping plagioclase also reveals interesting quartz textures (Fig. 12B). The quartz has undergone significant recrystallization and grain size reduction in this area. However, directly beneath the large plagioclase grain in the analyzed area, there is a small pocket of quartz that is not as deformed. This is only visible in the EBSD map, and not via petrographic analysis. The quartz directly below the plagioclase appears to be more randomly oriented in comparison to the sheared quartz that has a strong CPO. Although it is difficult to evaluate textures in the third dimension, it appears that the quartz grains directly beneath the plagioclase were protected from recrystallization and that the strain was taken up further by grains farther from the plagioclase. The variety of quartz textures preserved in this single sample reveal evidence for continuous quartz deformation from high to low temperatures, potentially preserving evidence for deformation during cooling and exhumation of the Skagit Gneiss.

A variety of fabrics are also found in the orthogneiss that comprises most of Ruby Mt, structurally above the John Pierce Falls locality. For example, chessboard extinction in quartz may be evidence for high-temperature deformation (Kruhl, 1996; 1998). A tonalitic (biotite-hornblende) orthogneiss sample, SK0686, from the bottom of the Ruby transect was also selected for EBSD analysis. Plagioclase in this sample is coarse-grained (~1 mm), whereas quartz contains numerous subgrains and has been significantly recrystallized. The EBSD results reveal a strong CPO with basal <a> slip in quartz, indicating a low-temperature deformation fabric (Fig. 13). The asymmetric pattern of quartz *c* axes indicates top-to-north sense of shear. Relict coarser-grained quartz,

indicative of grains that have not undergone lower-temperature deformation, is located in isolated regions of the analyzed thin section. Compared to this coarser-grained quartz, the recrystallized quartz shown in the EBSD map and throughout the thin section is ~1/10 the original grain size.

This late, overprinting deformation is observed at the base of Ruby Mountain, but the majority of Ruby Mt orthogneiss, does not exhibit this deformation fabric. More common throughout the rest of Ruby Mt is the preservation of a high-temperature fabric; that is, quartz typically has not undergone much recrystallization, and is coarse-grained (Fig. 11A). Quartz ribbons are present and contain deformation bands. Shear bands do not contain low-temperature index minerals (e.g. chlorite) and appear also to be moderate- to high-temperature features.

In the structurally highest regions of Ruby Mountain, ~ 0.5 km below the Napeequa contact, the orthogneiss is strongly lineated, with constrictional fabrics (Fig. 14A). Pegmatites that intrude the orthogneiss are deformed and are typically L-tectonites. In orthogneiss from the entire transect, kinematic indicators are difficult to evaluate and in some areas indicate top-to-north, and in other areas top-to-south, without a consistent pattern. Orthogneiss near the contact with the Napeequa contains mrymekite, late muscovite that is found in S and C shear planes, and deformation lamellae in quartz (Fig. 11B). However, the similarity in pressure-temperature conditions across the shear zone suggests that the shear zone is a high-temperature feature.

The intense constrictional fabrics are continuous across the contact from the Skagit orthogneiss into the overlying Napeequa unit. EBSD analysis of a Napeequa quartzite, SK0671, shows that significant deformation bands are present in recrystallized

quartz, and that quartz has a strong CPO (Fig. 15). Grain boundary migration was probably a major deformation mechanism. The EBSD results indicate that basal <a> was the primary active slip system. In comparison, a garnet-bearing tonalitic amphibolite, sample SK0664, from the Napeequa was collected from near the contact with the Skagit orthogneiss. The sample contains compositional layers that consists of hornblende and quartz and plagioclase. Garnet is located throughout the layers and is typically sheared and elongated parallel to foliation. The EBSD results from a quartz-rich layer show a strong CPO in the quartz fabric and indicate that prism <a> was the primary active slip system (Fig. 16). The EBSD results suggest a lower-temperature deformational overprint in the amphibolite in comparison to the quartzite even though structurally the samples are at the same level.

Elijah Ridge consists of samples that have undergone similar deformation as the orthogneiss and Napeequa samples from Ruby. An intense, constrictional fabric is present on Elijah (Fig. 14B). A metapelite sample (SK-3 of Whitney, 1992b) was selected for analysis. The metapelite consists of kyanite, staurolite, garnet, biotite, plagioclase, quartz and ilmenite. Quartz ribbons are extensively developed in the sample, and quartz grains within the ribbons typically have deformation lamellae. Overall, the quartz is relatively coarse-grained with many crystals elongated parallel to foliation, forming grain sizes of ~ 1 mm. There is limited subgrain development in the metapelite, and the sample does not appear to have undergone much recrystallization. The EBSD results show the extensive ribbon development in the metapelite and reveal a weak girdle in the *c*-axis pole figure (Fig. 17), suggesting prism <a> slip was the dominant slip system in the quartz, similar to the results from Ruby Mt.

$^{40}Ar/^{39}Ar$ RESULTS

Two samples of pegmatite that intrude the Skagit orthogneiss and the Napeequa unit were collected from Ruby Mt near the contact between the Skagit and Napeequa. Sample SK0648B, a pegmatite that intrudes the Skagit Gneiss, yields consistent integrated, preferred, and isochron ages of 47.1 ± 0.3 Ma, 47.1 ± 0.3 Ma, and 47.0 ± 0.3 Ma, respectively (Fig. 18A). Slightly younger $^{40}Ar/^{39}Ar$ results were obtained from the pegmatite that intrudes the Napeequa amphibolite, sample SK0681, with integrated, preferred, and isochron ages of 46.9 ± 0.3 Ma, 46.8 ± 0.3 Ma, and 47.0 ± 0.3 Ma, respectively (Fig. 18B). However, the argon results from above and below the contact between the Skagit and Napeequa are the same within error.

DISCUSSION

Previous interpretations of Ruby-Elijah tectonic history

Several previous studies of the RLFZ have examined the rocks exposed on Ruby Mt and Elijah Ridge and have proposed very different interpretations of their tectonic significance:

(1) Whitney & McGroder (1989) interpreted the Skagit-Napeequa contact as the suture of the Insular and Intermontane belts because the contact juxtaposes oceanic rocks (above) with rocks formed in the deep parts of the continental arc (below).

(2) Kriens & Wernicke (1990) proposed that the Skagit and Napeequa rocks on the west side of Elijah Ridge are metamorphosed strata of the Methow terrane and that there is therefore no through-going strike-slip fault; i.e. the eastern Skagit-Methow region

is a tilted but largely intact crustal section. They interpreted the abrupt transition from higher-*P* rocks on west Elijah to lower-*P* rocks in the east as a result of a cryptic, pre-90 Ma normal fault that is unrelated to the RLFZ.

(3) Miller *et al.* (1994) argued that Elijah Ridge does represent a major tectonic boundary based on the imbrication of the Napeequa and meta-Methow rocks and the tectonic contact of units correlative with the Napeequa and Methow rocks farther SE and on a more regional scale (e.g. McGroder, 1989, 1991; Miller & Bowring, 1990). Mylonites are pervasive on Elijah Ridge, and the difference in metamorphic grade, specifically in pressure, between the Napeequa and the meta-Methow rocks further argues for a tectonic boundary.

An additional idea about the Skagit-Napeequa contact is that it represented the top of the flowing crust (Skagit) and that the Napeequa therefore represented the more rigid lid of a rheologically layered crust. This and previous models for the tectonic evolution of the region can be considered in light of the new *P-T* and microstructural data.

Re-evaluation of Ruby-Elijah tectono-metamorphic history

Field mapping of Ruby Mt and Elijah Ridge shows that the two areas consist of sheets of orthogneiss, with Napeequa on the far western end of Elijah Ridge, and Methow rocks lying structurally on top of the orthogneiss (Fig. 3). In addition, rocks on the far eastern side of Elijah Ridge are folded, but the rest of the Napeequa and orthogneiss sheets have planar fabrics that dip gently to moderately (~35-45 º) to the east.

Microstructural analyses show that at the base of Ruby Mt (i.e. the structurally deepest exposed part of the orthogneiss sheet), the rocks are overprinted by a low-

temperature deformation fabric (Figs. 11, 12). The majority of Ruby Mt (i.e. the orthogneiss body above the migmatites), however, has not been affected by this overprint, except for the tonalitic amphibolite from near the contact of the Skagit and Napeequa on Ruby Mt. Farther west in the core of the Skagit Gneiss, at the Gorge Lake metapelite locality, the leucosomes are mylonitic and have intense recrystallization fabrics, also revealing evidence for a low-temperature overprint (Fig. 15). This low-*T* event seems to have mostly been confined to the structurally deepest exposed, migmatitic part of the Skagit Gneiss.

A strain gradient is present near the summit of Ruby Mt and is characterized by an intensification of constrictional fabrics along the contact between the Skagit orthogneiss and the Napeequa unit. Both orthogneiss and Napeequa are deformed to L-tectonites and define a shear zone along the contact. Trondhjemitic pegmatite intruded both the orthogneiss and Napeequa and was subsequently deformed, but there is no evidence for melt accumulation along the contact itself. Instead, the continuity of fabrics across the contact, the similarity in Ar dates, and the similarity of thermobarometric results for garnet amphibolite above and below the contact suggests that the shear zone is a high-temperature feature, rather than a late, lower-temperature detachment zone related to exhumation of the gneiss. Some lower-temperature overprinting fabrics are found in the Napeequa amphibolite but the majority of the deformation is higher-temperature. The shear zone may have formed due to a rheologic contrast between the orthogneiss and Napeequa during emplacement of the orthogneiss. In addition, based on the similarities in *P-T* conditions across the shear zone, the zone probably represents an old contact that preserves an early, high-temperature deformation history that affected both the Skagit and

Napeequa units. The deformation could have developed along or transposing the intrusive contact.

In other areas where the Napeequa is exposed, the Napeequa typically forms small rafts within larger orthogneiss bodies. The Napeequa is commonly deformed, probably partly due to its composition (e.g. presence of metachert layers), and shear may have localized in the small, compositionally weak bodies of Napeequa relative to the larger orthogneiss bodies. Compared to all other major Skagit-Napeequa contacts in the region, however, the one on Ruby Mt reveals the most intense constrictional fabrics.

On Elijah Ridge, the Napeequa also exhibits constrictional fabrics, although the fabric is not quite as intense as on Ruby Mt. Thermobarometric results of Napeequa rocks on Elijah reveal slightly lower temperatures in comparison to Ruby (~650 ºC versus 750 ºC), although metapelites from both areas yield similar pressures (8-10 kbar) (Whitney, 1992b; this study). Prior to this study, evidence for high-*P* metamorphic conditions did not extend eastward past west Elijah; however, the andalusite-cordierite schist from east Elijah yields an early (pre-andalusite) high-*P* history of 8 kbar, consistent with results from west Elijah, Ruby Mt and even farther west in the antiformal core of the Skagit (Fig. 1).

East of the andalusite-cordierite schist, meta-Methow rocks and hornblende-bearing rocks, including porphyries, are exposed. West of the schist, the hornblende-bearing rocks occur as far as an exposure of Skagit orthogneiss on central Elijah Ridge. The high-*P* results from the schist suggest that part of the Methow terrane in this region was buried to mid-crustal depths. The late cordierite-andalusite overprint is probably related to contact metamorphism associated with emplacement of the Golden Horn

batholith and/or other Eocene plutonism (Fig. 2). Dikes of the Golden Horn cut across meta-Methow rocks on east Elijah.

Mapping did not identify the location of the RLFZ on Elijah or Ruby Mt because the fault has no obvious expression in this region, but, consistent with Miller *et al.* (1994), it is clear that a tectonic boundary almost certainly exists on Elijah Ridge between the oceanic Napeequa and the meta-Methow rocks. The contact between Skagit and/or Napeequa and Methow rocks is also tectonic, and in other areas to the north and south is steep (sub-vertical to ~70 º; Miller & Bowring, 1990). The tectonic boundary in the Elijah and Ruby field area, however, is more-gently dipping (~35-45º) (Figs. 3B, C) and may have formed early in the history of the Skagit Gneiss, before major activity on the RLFZ.

The *P*-*T*-d observations can be explained by an overlapping step-over zone that is present in the Ruby Mt-Elijah Ridge region, with the western fault zone potentially represented by the shear zone on Ruby Mt and the eastern part of the step-over fault zone located east of Elijah Ridge, obscured by the Golden Horn Batholith (Fig. 2). In map-view, the Napeequa, meta-Methow rocks and the intrusive units (e.g. the Golden Horn batholith and the Black Peak batholith), from the Ruby Mt-Elijah Ridge area to the Gabriel Peak Tectonic Belt-Foggy Dew fault zone intersection in the south (Figs. 2, 19A), define a duplex structure within the step-over zone, with meta-Methow rocks lying structurally above the Napeequa unit (Fig. 19A). Thus, the step-over zone in the Elijah Ridge-Ruby Mt area represents the northwestern end of the step-over previously defined in the southeastern RLFZ (Miller, 1994). The Golden Horn batholith obscures the link of the southern step-over zone with that of the Ruby Mt-Elijah Ridge area. The step-over

probably developed in a transpressional regime and was active during the Late Cretaceous to Eocene based on geochronology results from deformed batholiths found in the RLFZ further south of the Ruby Mt-Elijah Ridge area (Miller & Bowring, 1990).

Prior to major slip on the RLFZ (pre-65 Ma?), a package of rocks must have been present with the Napeequa tectonically in contact with and overlying the Skagit orthogneiss (Fig. 19B). The shear zone on Ruby Mt, between the Skagit orthogneiss and the Napeequa, preserves evidence for this tectonic boundary. The orthogneiss that overlies the Napeequa on Ruby Mt is thus potentially unrelated to the Skagit and probably intruded into the Napeequa prior to major RLFZ movement and was subsequently deformed with the Napeequa and underlying Skagit Gneiss (Fig. 3B). In addition, in the western Skagit, the Napeequa unit is also overlain by an orthogneiss body (Fig. 3A). The western Napeequa and orthogneiss may be correlative with the similar units in the east and are now on opposite limbs of the regional antiform. Skagit orthogneiss and migmatites are in the antiformal core (Fig. 19B). More geochronometric and geochemical studies need to be undertaken from the western and eastern limbs of the antiform to confirm whether the Napeequa and orthogneiss units from the west and east limb of the antiform are indeed correlated.

As movement on the RLFZ began, a step-over zone is inferred to have developed enveloping the Napeequa and a sliver of Methow terrane (Fig. 19A). Transtensional and associated compressional deformation along the step-over zone caused sliding and duplexing of the Napeequa and Methow units, with the Methow structurally higher than the oceanic unit. Compression and duplexing would drive further crustal thickening and burial of the Napeequa and Methow units. Thus, the Skagit Gneiss, the Napeequa, and

part of the Methow underwent similar burial and later exhumation, as confirmed by thermobarometry (Whitney, 1992a; this study). Furthermore, the gradient in metamorphic grade from the ca. 8 kbar pressures in the westernmost schist of the meta-Methow assemblage to lower-amphibolite-facies metasedimentary rocks on the eastern end of Elijah Ridge suggests that the Methow package was probably tilted so that the western end achieved greater pressures. The western end of the Methow was probably structurally relatively deep prior to duplexing. Thus, the strike-slip faulting was not necessarily causing burial of Methow rocks to ca. 25 km depth, but rather was aiding in further burial of deep Methow rocks, resulting in the 8 kbar pressures.

Another possible explanation for the structural relationship between the Napeequa and Skagit involves imbrication of an unconformable boundary (Miller *et al.,* 1994). In this model, the Napeequa did not form a sheet above the Skagit Gneiss. Instead, the Skagit orthogneisses (or their protolith magma) intruded the Napeequa. The imbrication model suggests that the orthogneiss located structurally above the Napeequa may also be part of the Skagit Gneiss Complex. In addition, according to this model, the Methow basin rocks would lie unconformably above the imbricated Skagit and Napeequa.

According to both the step-over and the imbrication models, the Ruby Mt-Elijah Ridge area preserves evidence for a tectonic boundary between the Methow basin and the Skagit Gneiss (Miller *et al*., 1994; this study). The relationship between these units is clearly related to activity along the RLFZ; therefore, the model of Kriens & Wernicke (1990) does not explain the deformational or metamorphic evidence for the tectonic juxtaposition of the Skagit Gneiss, Napeequa, and meta-Methow rocks.

The Skagit Gneiss rocks exposed directly below the Napeequa contact on Ruby Mt are orthogneiss, which may have at one time represented a 'channel' of crustal melt; that flowed beneath the more rigid (non-flowing) Napeequa unit. However, the Napeequa unit was not likely in the upper crust at this time based on the thermobarometric results. Although the timing of peak metamorphism has not been directly determined from the Ruby Mt rocks, the lack of metamorphic break or difference in Ar cooling dates across the contact indicates that the Napeequa and underlying Skagit rocks were metamorphosed, deformed, and exhumed together.

Exhumation of the Skagit Gneiss

The thermobarometric results from various locations in the Skagit Gneiss suggest significant crustal thickening (> 30 km) that was followed by near isothermal decompression. An overlap in melt crystallization ages, argon cooling ages, and timing of basin formation at ca. 50-47 Ma suggests rapid cooling and exhumation (Gordon *et al.*, ms). From ca. 57 to 45 Ma, the North Cascades was in a transtensional regime, and investigations of the RLFZ suggest that the slip history was dominated by dextral strike slip with significant components of normal and reverse slip during the late history of the Skagit (Miller & Bowring, 1990). Therefore, the Skagit Gneiss was rapidly exhumed at least in part due to the oblique strike-slip movements of the RLFZ and associated step-over zones in the Eocene.

The investigations of the bounding structures in the North Cascades, specifically in the Skagit Gneiss, demonstrate the complications of interpreting the role of strike-slip faulting in exhumation of mid- to lower-crustal rocks. Many studies of metamorphic

rocks adjacent to strike-slip faults have demonstrated that at least part of their exhumation history is coeval with strike-slip movement. In some strike-slip fault zones that separate high-grade crystalline rocks from basin rocks, the basin rocks may become involved in the burial history of the basement or adjacent exhumed high-grade crystalline rocks, and thus share a similar cooling and exhumation history to the crystalline rocks. Ross Lake fault zone studies demonstrate that along strike, the fault separates and incorporates different slices or sheets of high-grade Skagit/Napeequa and low-grade Methow basin terrane. In some sections, such as Ruby Mt-Elijah Ridge, the basin rocks are incorporated into the high-grade zone and undergo similar processes to the high-grade rocks, including metamorphism and deformation. The Elijah Ridge-Ruby Mt area of the RLFZ is directly east of the location of the majority of the migmatitic rocks in the Skagit Gneiss. Perhaps significant weakening of the middle crust due to abundant partial melting allowed the step-over zone to develop at this point in the RLFZ, thus allowing the dynamic relationship between the crystalline rocks and the basin to develop. The RLFZ in the Elijah Ridge-Ruby Mt area represents the diverse relationships and links between basins, basement, exhumation and strike-slip faulting that may develop in transtensional orogens.

ACKNOWLEDGMENTS

This research was supported by NSF grant EAR-0510326 to D. Whitney, R. Miller, and S. Bowring, the Doctoral Dissertation Fellowship from the University of Minnesota, and the Department of Geology and Geophysics at the University of Minnesota. Part of this work was carried out in the Institute of Technology Characterization Facility, University

of Minnesota, which receives partial support from NSF through the NNIN program. Thank you to N. Wintzer for her help in the field and for discussions about the Skagit Gneiss. Invaluable discussions with C. Teyssier about the Ross Lake fault zone greatly improved this manuscript.

REFERENCES

Arnold, J., Powell, R. & Sandiford, M., 2000. Amphibolites with staurolite and other aluminous minerals: calculated mineral equilibria in NCFMASH. *Journal of Metamorphic Geology*, **18**, 23-40.

Babcock, R.S., & Misch, P., 1989. Origin of the Skagit migmatites, North Cascades Range, Washington State. *Contributions to Mineralogy and Petrology*, **101**, 485-495.

Baldwin, J.A., Whitney, D.L. & Hurlow, H.A., 1997. Metamorphic and structural evidence for significant vertical displacement along the Ross Lake fault zone, a major orogen-parallel shear zone in the Cordillera of western North America. *Tectonics*, **16**, 662-681.

Barksdale, J.D., 1975. Geology of the Methow Valley, Okanogan County, Washington. *Washington Division of Geology and Earth Resources Bulletin*, **68**, 72.

Beck, M., 1976. Discordant paleomagnetic pole positions as evidence of regional shear in the western Cordillera of North America. *American Journal of Science*, **276**, 695-712.

Cruz, L., Fayon, A.K., Teyssier, C. & Weber, J., 2007. Exhumation and deformation processes in transpressional orogens: the Venezuelan Paria Peninsula, SE Caribbean-South American plate boundary. In: *Exhumation Associated with Continental Strike-slip Fault Systems* (eds. Till, A.B., Roeske, S.M., Sample, J.C. & Foster, D.A.), pp. 149-165. Geological Society of America Special Paper **434**.

Foster, D.A., Doughty, P.T., Kalakay, T.J., Fanning, C.M., Coyner, S., Grice, W.C. & Vogl, J., 2007. Kinematics and timing of exhumation of metamorphic core complexes along the Lewis and Clark fault zone, northern Rocky Mountains, USA. In: *Exhumation Associated with Continental Strike-slip Fault Systems* (eds. Till, A.B., Roeske, S.M., Sample, J.C. & Foster, D.A.), pp. 207-232. Geological Society of America Special Paper **434**.

Gordon, S.M., Bowring, S., Whitney, D.L., Miller, R.B. & McLean, N., in prep. High-precision dating of migmatites in an exhumed continental arc. *Lithos.*

Goscombe, B., Gray, D. & Hand, M., 2003. Variation in metamorphic style along the Northern Margin of the Damara Orogen, Namibia. *Journal of Petrology,* **45**, 1261-1295.

Haugerud, R.A., 1985. Geology of the Hozameen Group and the Ross Lake shear zone, Maselpanik area, North Cascades, southwestern British Columbia. Ph.D. thesis, University of Washington, Seattle, Washington, p. 263.

Haugerud, R.A., van der Heyden, P., Tabor, R.W., Stacey, J.S. & Zartman, R.E., 1991. Late Cretaceous and early Tertiary plutonism and deformation in the Skagit Gneiss Complex, North Cascades range, Washington and British Columbia. *Geological Society of America Bulletin*, **103**, 1297-1307.

Holdaway, M.J., 2000. Application of new experimental and garnet Margules data to the garnet-biotite geothermometer. *American Mineralogist*, **85**, 881-892.

Holdaway, M.J., 2001. Recalibration of the GASP geobarometer in light of recent garnet and plagioclase activity models and versions of the garnet-biotite geothermometer. *American Mineralogist*, **86**, 1117-1129.

Hoppe, W.J., 1984. Origin and age of the Gabriel Peak orthogneiss, North Cascades, Washington. M.Sc. thesis, University of Kansas, p. 79.

Irving, E., 1985. Whence British Columbia? *Nature*, **314**, 673-674.

Klepeis, K.A. & Crawford, M.L., 1999. High-temperature arc-parallel normal faulting and transtension at the roots of an obliquely convergent orogen. *Geology*, **27**, 7-10.

Kohn, M.J. & Spear, F.S., 1990. Two new geobarometers for garnet amphibolites, with applications to southeastern Vermont. *American Mineralogist*, **75**, 89-96.

Krabbendam, M. & Dewey, J.F., 1998. Exhumation of UHP rocks by transtension in the Western Gneiss Region, Scandinavian Caledonides. In: *Continental transpressional and transtensional tectonics* (eds. Holdsworth, R.E., Strachan, R.A. & Dewey, J.F.), pp. 159-181. Geological Society [London] Special Publication **135**.

Kriens, B., Tectonic evolution of the Ross Lake area, NW Washington-SW British Columbia. Ph.D. thesis, Harvard University, pp. 214.

Kriens, B. & Wernicke, B., 1990. Nature of the contact zone between the North Cascades crystalline core and the Methow sequence in the Ross Lake area, Washington: implications for Cordilleran tectonics. *Tectonics*, **9**, 953-981.

Kruhl, J.H., 1996. Prism- and basal-plane parallel subgrain boundaries in quartz: a microstructural geothermobarometer. *Journal of Metamorphic Geology*, **14**, 581-589.

Kruhl, J.H., 1998. Prism- and basal-plane parallel subgrain boundaries in quartz: a microstructural geothermobarometer: Reply. *Journal of Metamorphic Geology*, **16**, 142-146.

Little, T.A., Cox, S., Vry, J.K. & Batt, G., 2005. Variations in exhumation level and uplift rate along the oblique-slip Alpine fault, central Southern Alps, New Zealand. *Geological Society of America Bulletin*, **117**, 707-723.

Mattinson, J.M., 1972. Ages of zircons from the northern Cascade Mountains, Washington. *Geological Society of America Bulletin*, **83**, 3769-3784.

McGroder, M.F., 1987. Yalakom-Foggy Dew fault: a 500 (+) km long Late Cretaceous-Paleogene oblique-slip fault in Washington and British Columbia. *Geological Society of America Abstracts with Programs*, **19**, 430.

McGroder, M.F., 1989. Structural geometry and kinematic evolution of the eastern Cascades foldbelt, Washington and British Columbia. *Canadian Journal of Earth Sciences*, **26**, 1586-1602.

McGroder, M.F., 1991. Reconciliation of two-sided thrusting, burial metamorphism, and diachronous uplift in the Cascades of Washington and British Columbia. *Geological Society of America Bulletin*, **103**, 189-209.

McGroder, M.F., Garver, J.I. & Mallory, V.S., 1990. Bedrock geologic map, biostratigraphy, and structure sections of the Methow basin, Washington and British Columbia. *Washington Division of Geology and Earth Resources Open File Report*, **90-19**, 32.

Miller, R.B., 1987. Geology of the Twisp River – Chelan Divide region, North Cascades, Washington. *Washington, Division of Geology and Earth Resources,* Open-file report, **87-17**.

Miller, R.B., 1994. A mid-crustal contractional stepover zone in a major strike-slip system, North Cascades, Washington. *Journal of Structural Geology*, **16**, 47-60.

Miller, R.B. & Bowring, S.A., 1990. Structure and chronology of the Oval Peak batholith and adjacent rocks: Implications for the Ross Lake fault zone, North Cascades, Washington. *Geological Society of America Bulletin*, **102**, 1361-1377.

Miller, R.B., Bowring, S.A. & Hoppe, W.J., 1989. Paleocene plutonism and its tectonic implications, North Cascades, Washington. *Geology*, **17**, 846-849.

Miller, R.B., Whitney, D.L. & Geary, E.D., 1993. Tectono-stratigraphic terranes and the metamorphic history of the northeastern part of the crystalline core of the North Cascades: evidence from the Twisp Valley Schist. *Canadian Journal of Earth Sciences*, **30**, 1306-1323.

Miller, R.B., Haugerud, R.A., Murphy, F. & Nicholson, L.S., 1994. Tectonostratigraphic framework of the northeaster Cascades. *Bulletin of the Washington Division of Geology and Earth Resources*, **80**, 73-92.

Miller, R.B., Paterson, S.R., Labit, H., Alsleben, H. & Lüneburg, C., 2006. Significance of composite lineations in the mid- to deep crust: a case study from the North Cascades, Washington. *Journal of Structural Geology*, **28**, 302-322.

Misch, P., 1966. Tectonic evolution of the northern Cascades of Washington State – a west Cordilleran case history. *Canadian Institute of Mining and Metallurgy*, **8**, 101-148.

Misch, P., 1977. Bedrock geology of the North Cascades. In: *Centennial Field Trip Guidebook, Cordilleran Section*, pp. 393-398. Geological Society of America.

Misch, P., 1968. Plagioclase compositions and non-anatectic origin of migmatitic gneisses in Northern Cascade mountains of Washington State. *Contributions to Mineralogy and Petrology,* **17**, 1-70.

Misch, P. & Onyeagocha, A.C., 1976. Symplectite breakdown of Ca-rich almandines in upper-amphibolite facies, Skagit Gneiss, North Cascades, Washington. *Contributions to Mineralogy and Petrology*, **54**, 189-224.

Petro, G.T., Housen, B.A. & Iriondo, A., 2002. Tectonic significance of paleomagnetism of the Eocene Golden Horn batholith. *Geological Society of America Program with Abstracts,* **98**.

Powell, R. & Holland, T., 2001. Course notes for "THERMOCALC workshop 2001: Calculating metamorphic phase equilibria. CD-ROM.

Ravna, E.K., 2001. Distribution of Fe^{2+} and Mg between coexisting garnet and hornblende in synthetic and natural systems: an empirical calibration of the garnet-hornblende Fe-Mg geothermometer. *Lithos*, **53**, 265-277.

Selverstone, J., Spear, F.S., Franz, G. & Morteani, G., 1984. High-pressure metamorphism in the SW Tauern Window, Austria: P-T paths from hornblende-kyanite-staurolite schists. *Journal of Petrology*, **25**, 501-531.

Snoke, A.W. & Frost, B.R., 1990. Exhumation of high pressure pelitic schist, Lake Murray spillway, South Carolina: Evidence for crustal extension during Alleghenian strike-slip faulting. *American Journal of Science*, **290**, 853-881.

Stewart, J.H., 1988. Tectonics of the Walker Lane belt, western Great Basin: Mesozoic and Cenozoic deformation in a zone of shear. In: *Metamorphism and crustal evolution of the Western United States* (ed. Ernst, W.G.), pp. 683-713. Rubey Volume, **7**, Englewood Cliffs, New Jersey, Prentice Hall.

Tabor, R.W. & Haugerud, R.A., 1999. *Geology of the North Cascades*, The Mountaineers, Seattle, Washington.

Tabor, R.W., Frizzell Jr., V.A., Whetten, J.T., Waitt Jr., R.B., Swanson, D.A., Byerly, G.R., Booth, D.B., Hetherington, M.J. & Zartman, R.E., 1987a. Geologic map of the Chelan 30' by 60' Quadrangle, Washington. *U.S. Geological Survey Miscellaneous Investigation Map*, 33 pp., 1 sheet.

Tabor, R.W., Zartman, R.E. & Frizzell Jr., V.A., 1987b. Possible tectonostratigraphic terranes in the North Cascades crystalline core, Washington. In: *Selected Papers on the Geology of Washington* (ed. Schuster, J.E.), pp. 107-127. Washington Division of Geology and Earth Resources, Anaheim, California.

Tabor, R.W., Haugerud, R.A., Brown, E.H., Babcock, R.S. & Miller, R.B., 1989. *Accreted Terranes of the North Cascades Range, Washington, Field Trip Guidebook*, **T307**, 62 pp., AGU, Washington, D.C.

Tabor, R.W., Haugerud, R.A., Booth, D.B. & Brown, E.H., 1994. Preliminary geologic map of the Mount Baker 30- by 60-minute quadrangle, Washington. *US Geological Survey Open File Report*, **94-403**.

Tabor, R.W., Haugerud, R.A., Hildreth, W. & Brown, E.H., 2003. Geologic map of the Mount Baker 30- by 60 minute quadrangle. Washington, U.S. Geological Survey, Geologic Investigation Series, I-2660, with pamphlet, **70**, scale 1:100,000.

Thompson, A.B., Schulmann, K. & Jezek, J., 1997. Thermal evolution and exhumation in obliquely convergent (transpressive) orogens. *Tectonophysics*, **280**, 171-184.

Umhoefer, P.J., 1987. Northward translation of "Baja British Columbia" along the Late Cretaceous to Paleocene margin of western North America. *Tectonics*, **6**, 377-394.

Umhoefer, P.J. & Miller, R.B., 1996. Mid-Cretaceous thrusting in the southern Coast Belt, British Columbia and Washington, after strike-slip fault reconstruction. *Tectonics*, **15**, 545-565.

Umhoefer, P.J., Whitney, D.L., Teyssier, C., Fayon, A.K., Casale, G. & Heizler, M.T., 2007. Yo-yo tectonics in a wrench zone, Central Anatolian fault zone, Turkey. In: *Exhumation Associated with Continental Strike-slip Fault Systems* (eds. Till, A.B., Roeske, S.M., Sample, J.C. & Foster, D.A.), pp. 35-58. Geological Society of America Special Paper **434**.

Unruh, J., Humphrey, J. & Barron, A., 2003. Transtensional model for the Sierra Nevada frontal fault system, eastern California. *Geology*, **31**, 327-330.

Wesnousky, S.G., 2005. The San Andreas and Walker Lane fault systems, western North America: Transpression, transtension, cumulative slip, and the structural evolution of a major transform plate boundary. *Journal of Structural Geology*, **27**, 1505-1512.

Whitney, D.L., 1991. Calcium depletion halos and Fe-Mn-Mg zoning around faceted plagioclase inclusions in garnet from a high-grade pelitic gneiss. *American Mineralogist*, **76**, 493-500.

Whitney, D.L., 1992a. Origin of CO_2-rich fluid inclusions in leucosomes from the Skagit migmatites, North Cascades, Washington. *Journal of Metamorphic Geology*, **10**, 715-725.

Whitney, D.L., 1992b. High pressure metamorphism in the western Cordillera of North America: an example from the Skagit Gneiss, North Cascades, Washington. *Journal of Metamorphic Geology*, **10**, 71-85.

Whitney, D.L. & McGroder, M.F., 1989. Cretaceous crustal section through the proposed Insular-Intermontane suture, North Cascades, Washington. *Geology*, **17**, 555-558.

Whitney, D.L., & Irving, A.J., 1994. Origin of K-poor leucosomes in a metasedimentary migmatite complex by ultrametamorphism, syn-metamorphic magmatism, and subsolidus processes. *Lithos*, **32**, 173-192.

Whitney, D.L., Lang, H.M. & Ghent, E.D., 1995. Quantitative determination of metamorphic reaction history; mass balance relations between groundmass and mineral inclusion assemblages in metamorphic rocks. *Contributions to Mineralogy and Petrology*, **120**, 404-411.

Whitney, D.L., Tepper, J.H., Hirschmann, M.M. & Hurlow, H.A., 2008. Late-orogenic mafic magmatism in the North Cascades, Washington: petrology and tectonic setting of the Skymo layered intrusion. *Geological Society of America Bulletin*, **120**, 531-542.

Yardley, B.W.D., 1978. Genesis of the Skagit Gneiss migmatites, Washington, and the distinction between possible mechanisms of migmatization. *Geological Society of America Bulletin*, **89**, 941-951.

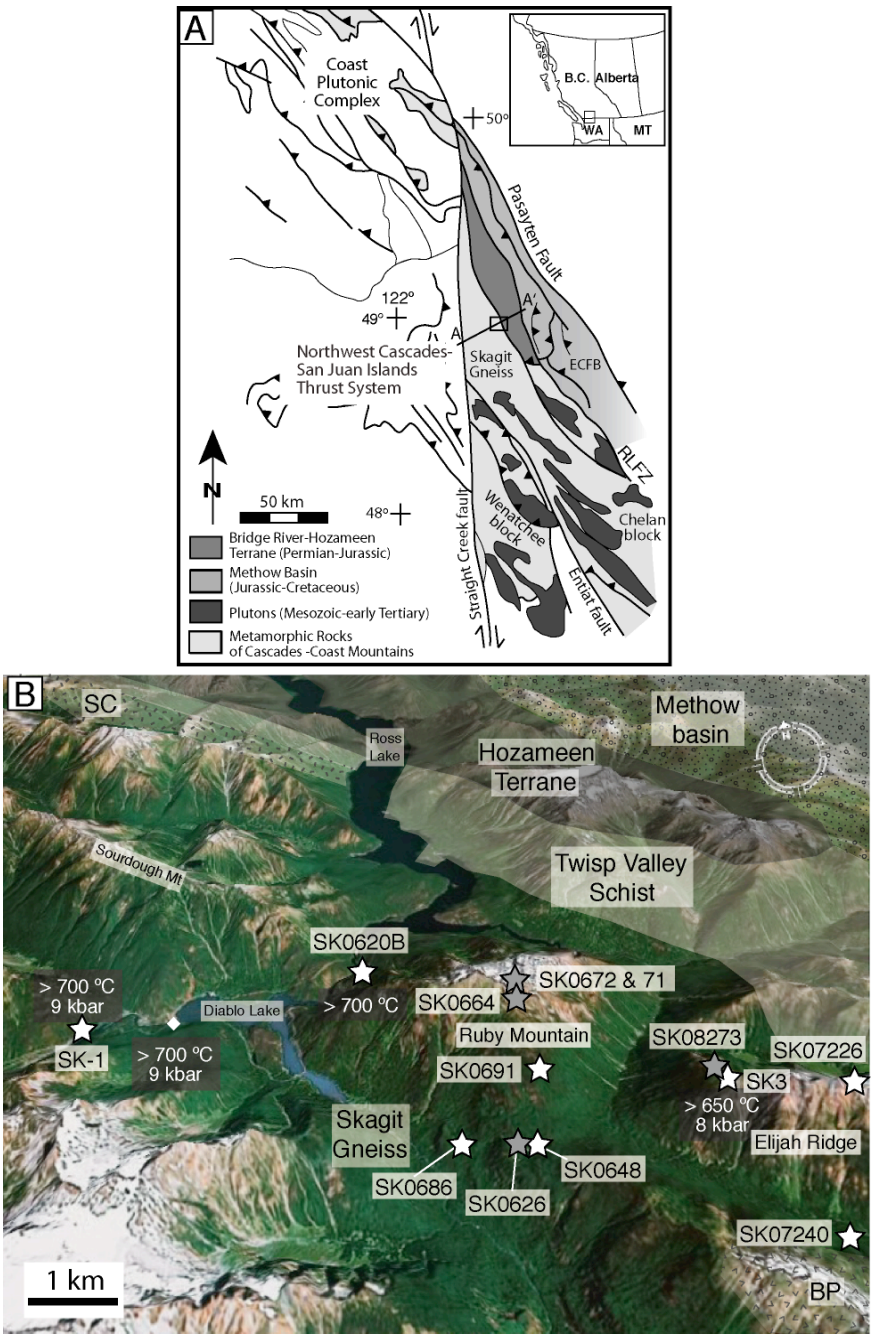

Figure 6.1: (A) Simplified geologic map of the North Cascades showing the location of the map in (B) and the cross section A-A' (Figure 3A) (modified after Miller *et al.*, 2006). The inset shows the location of the field area relative to the North American coast and Pacific Northwest. ECFB: Eastern Cascades fold-thrust belt; RLFZ: Ross Lake fault zone. (B) Google Earth image annotated with the geological units of the eastern Skagit Gneiss and adjacent terranes. The sample localities are shown from this study, and the sample localities and results are shown of a previous *P-T* investigation (Whitney, 1992b). SC: Skymo Complex; BP: Black Peak batholith.

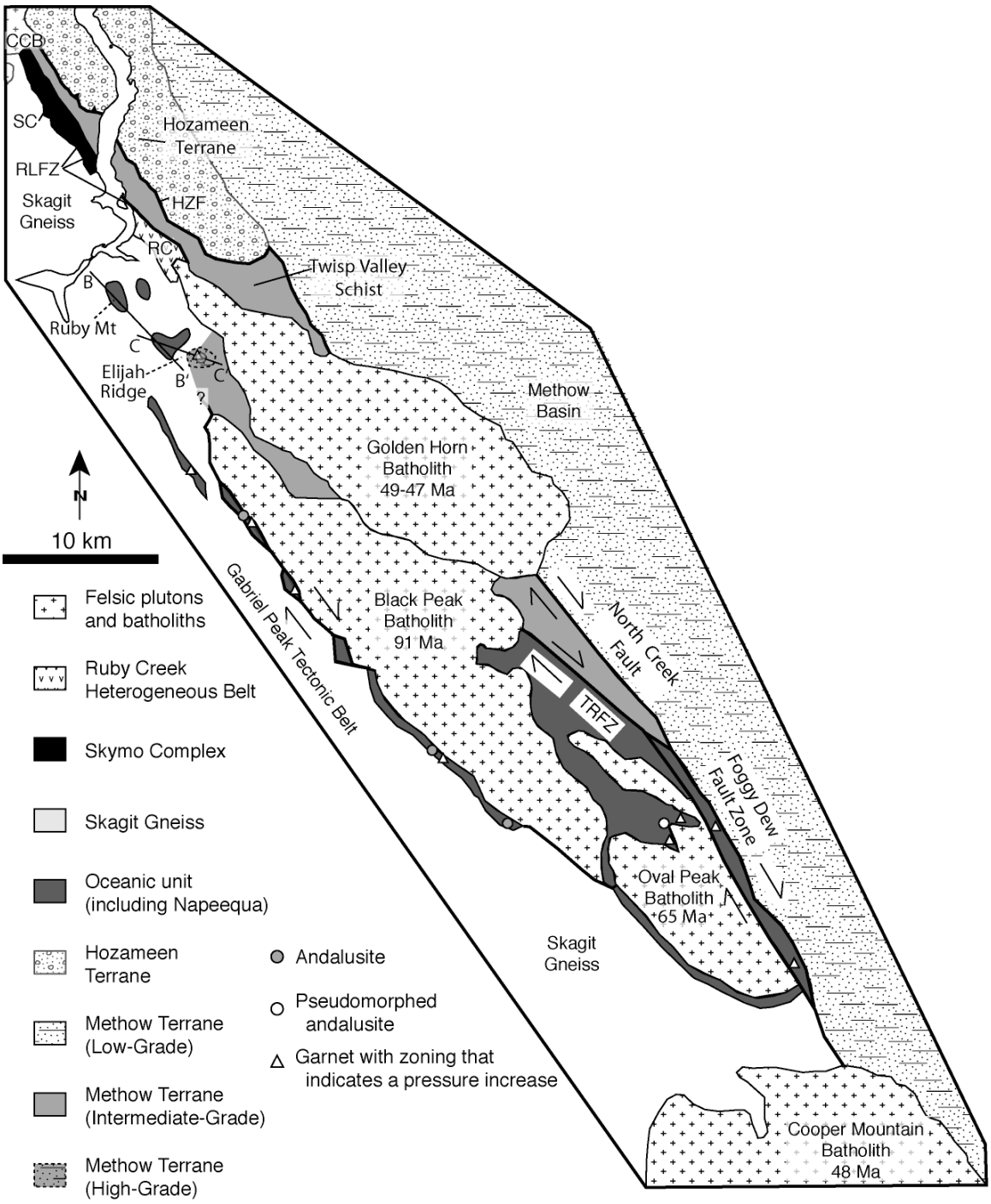

Figure 6.2: Geologic map of the Ross Lake fault zone region (modified from Miller, 1993; Baldwin *et al*., 1997). The dashed lines point to the location of Ruby Mt and Elijah Ridge. The location of cross sections B-B' and C-C' of Figure 3 are shown. CCB: Chilliwack composite batholith; SC: Skymo Complex; RC: Ruby Creek Heterogeneous Belt; TRFZ: Twisp River fault zone; HZF: Hozameen fault; RLFZ: Ross Lake fault zone.

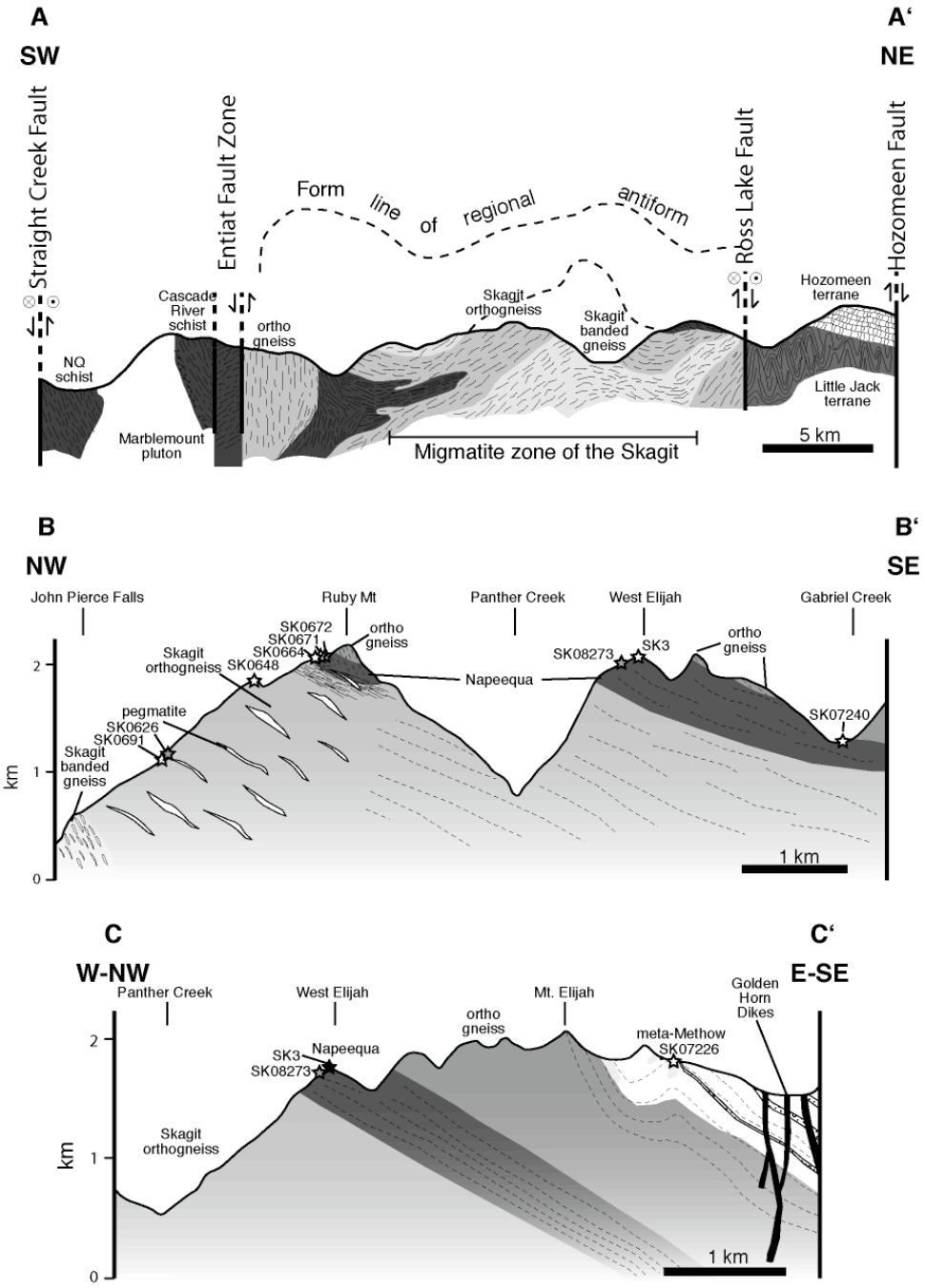

Figure 6.3: A series of cross sections from the Skagit Gneiss: (A) Regional cross section showing the major bounding fault structures (after Tabor & Haugerud, 1999); (B) A cross section through Ruby Mt and Elijah Ridge showing the gently dipping sheets of orthogneiss and Napeequa; and (C) A cross section of Elijah Ridge displaying the Napeequa on the western end of the Ridge, and orthogneiss, meta-Methow rocks, and Golden Horn dikes on the eastern end of the Ridge. Note the different scales and orientations for the cross sections. Where possible, the sample localities have been projected onto the cross sections.

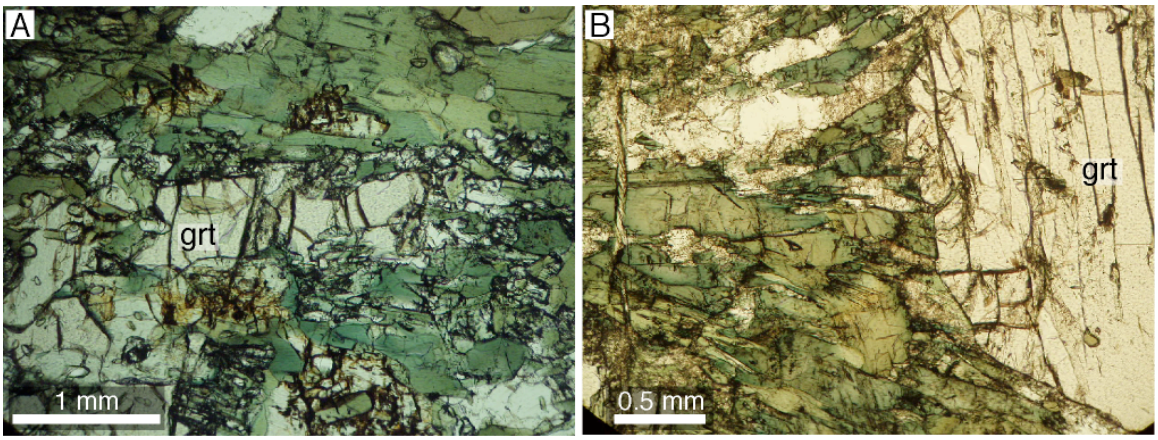

Figure 6.4: Photomicrographs showing the zoning in hornblende adjacent to garnet in samples (A) SK0626, and (B) SK0672.

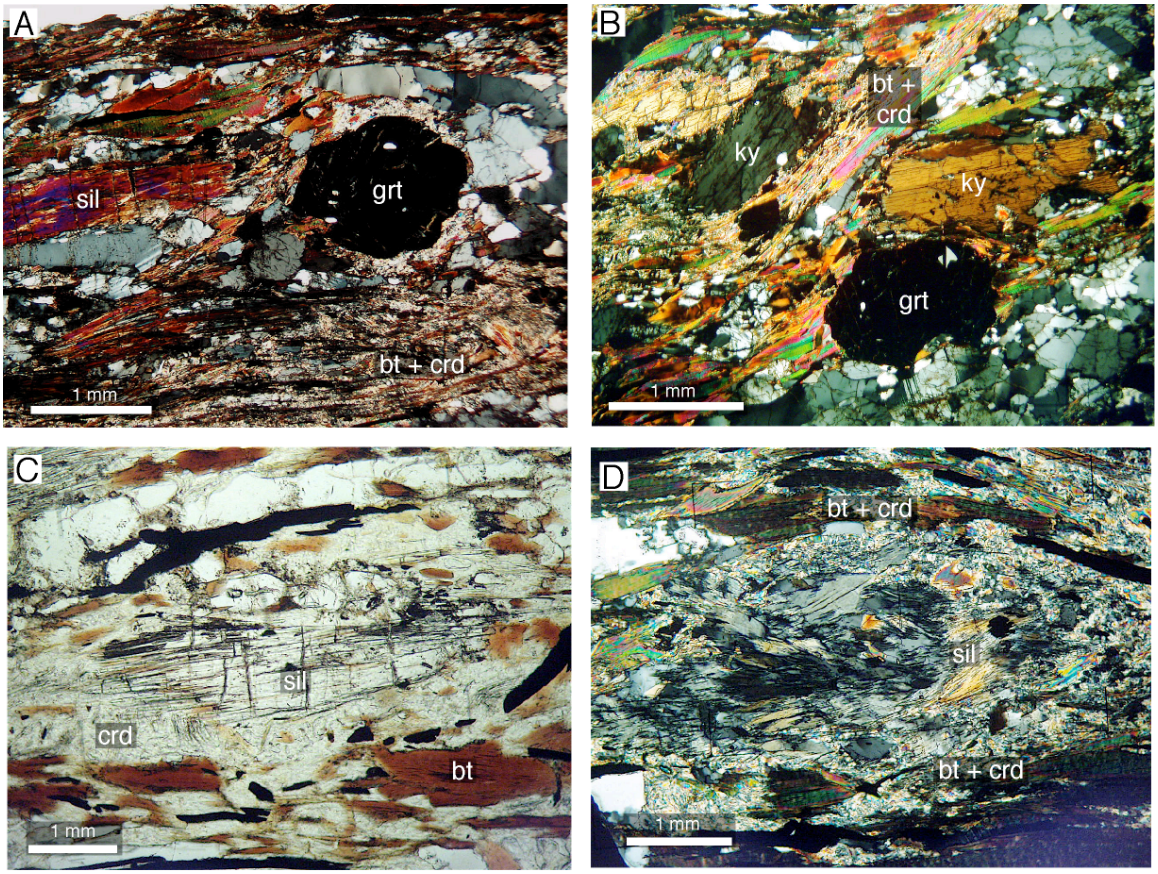

Figure 6.5: Photomicrographs showing the textural relationships of minerals in the Ruby Mt metapelites: (A) Sillimanite adjacent to garnet, and cordierite and biotite interlayered in the foliation in SK0691; (B) Prismatic kyanite, garnet, and cordierite in sample SK0648; (C) Cordierite replacing sillimanite in SK0691; and (D) Pseudomorph textures suggesting the former presence of kyanite, and fibrolite being replaced by cordierite.

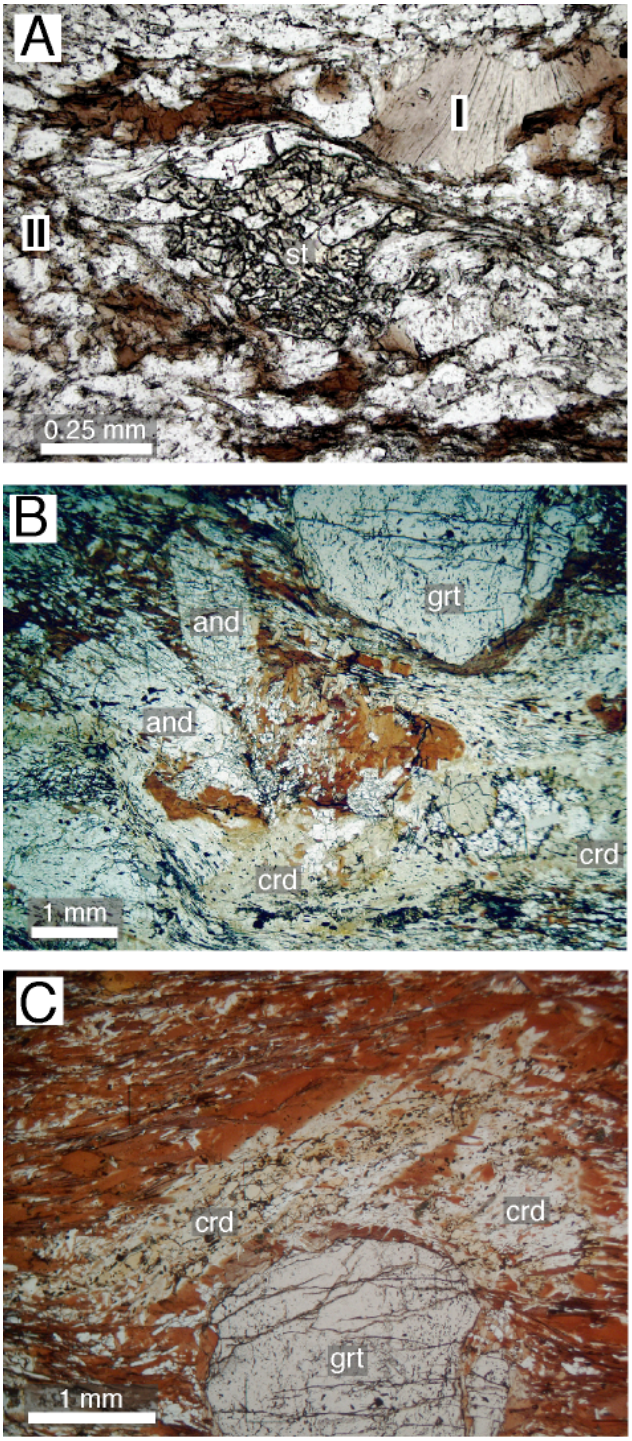

Figure 6.6: Photomicrographs showing the textural relationships of minerals in the Elijah Ridge metapelites: (A) Staurolite and two generations of biotite in sample SK07240; (B) Andalusite, cordierite, and garnet in schist sample SK07226; and (C) Tabular pseudomorph consisting of cordierite in sample SK07226.

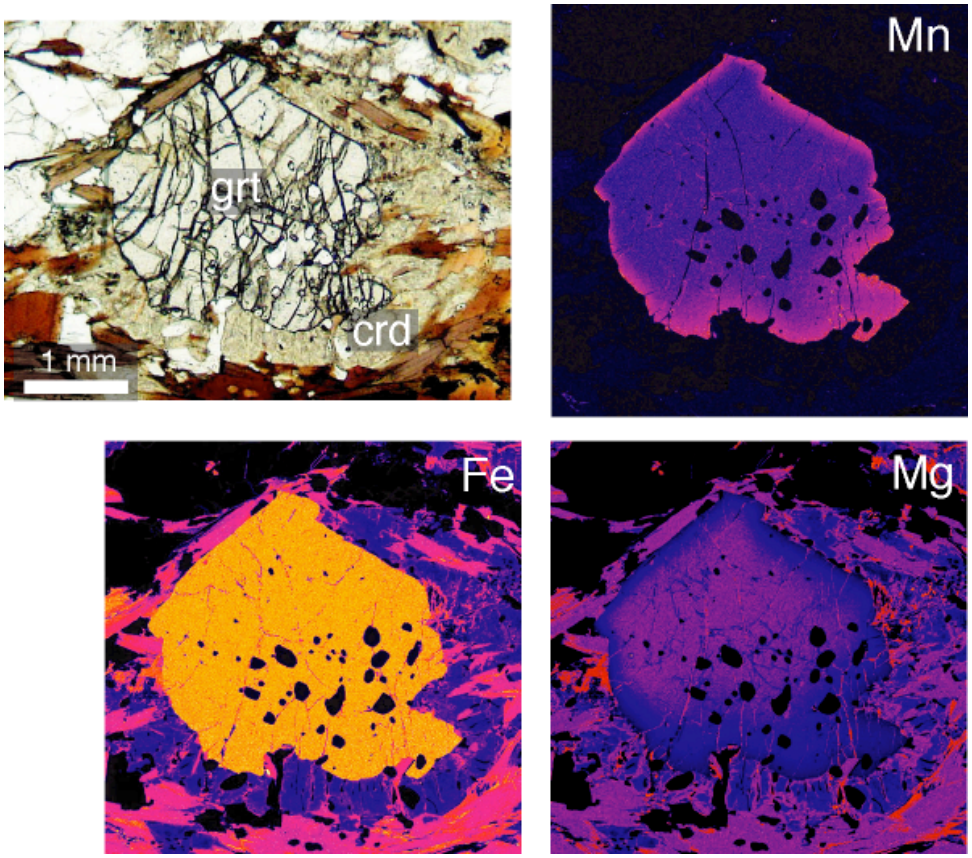

Figure 6.7: A photomicrograph and major element X-ray maps of a garnet from Ruby Mt sample SK0691, showing cordierite rimming garnet, and zoning in garnet near adjacent phases such as cordierite. Note that garnet is less resorbed where not rimmed by cordierite.

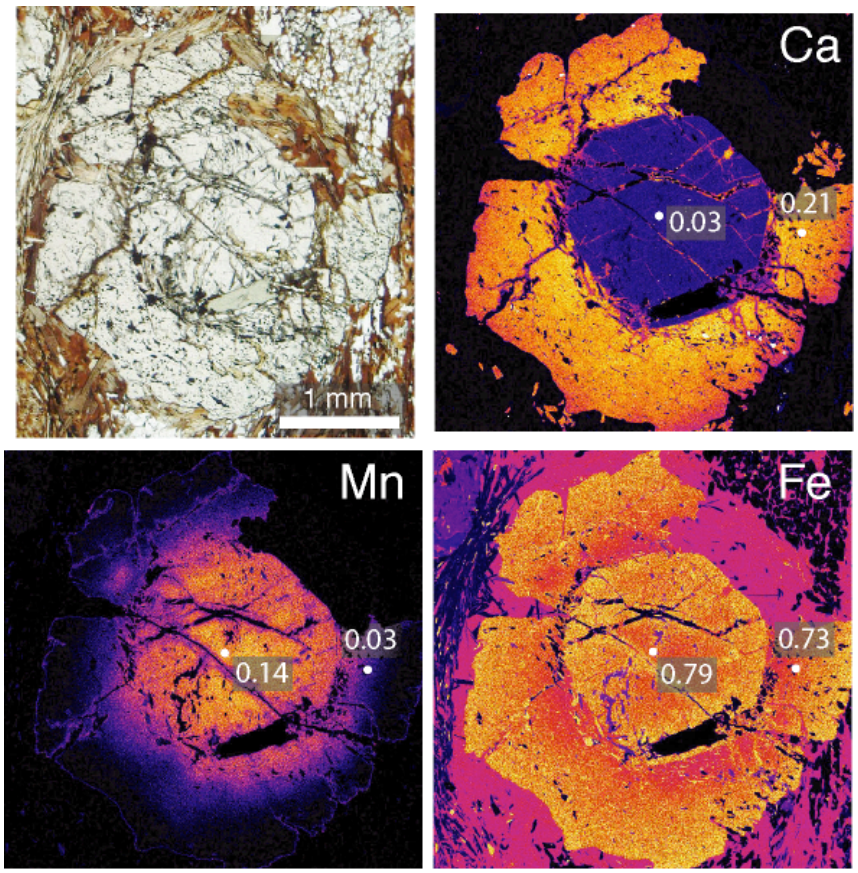

Figure 6.8: A photomicrograph and major element X-ray maps of a garnet from Elijah Ridge sample SK07226. The textural discontinuity between core and rim as seen in the photomicrograph corresponds to a discontinuity in Ca and Fe zoning, but Mn zoning shows a simple continuous pattern of decreasing Mn from core to rim. The maps have been annotated with the core and rim values of X_{Grs} on the Ca map, X_{Sps} on the Mn map, and X_{Alm} on the Fe map.

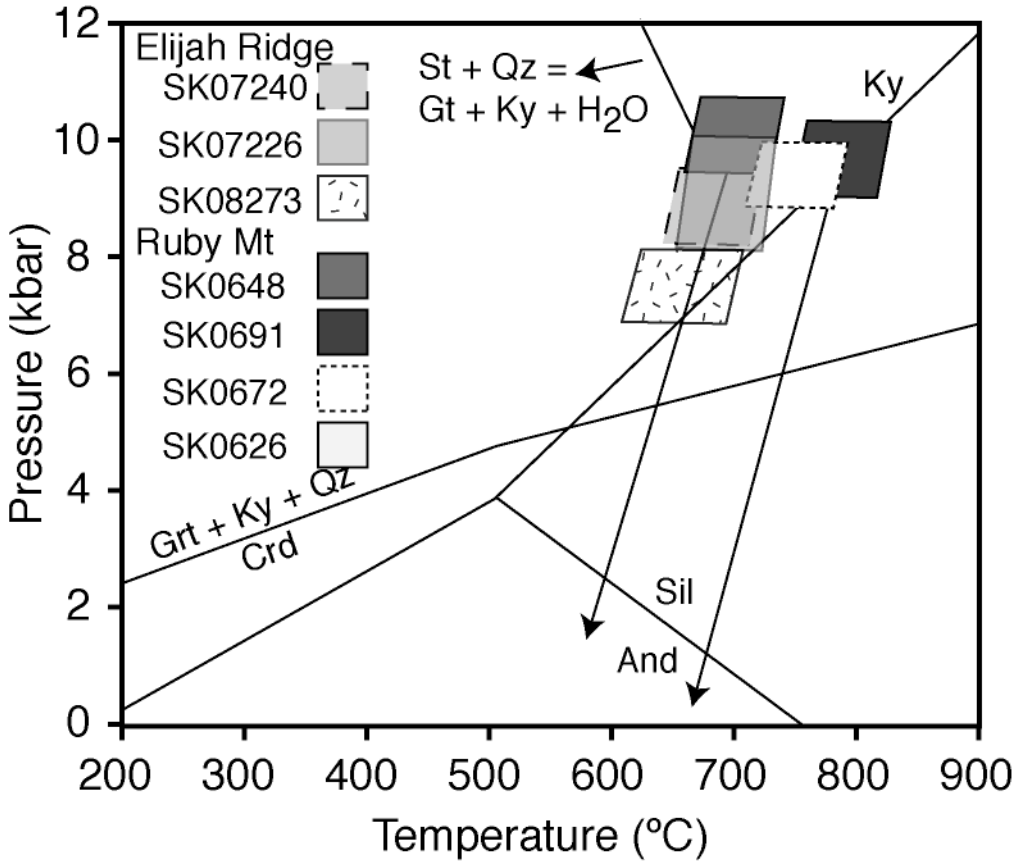

Figure 6.9: *P-T* diagram for metapelitic rocks from Ruby Mt. and Elijah Ridge. High metamorphic temperatures for the sillimanite schist are consistent with evidence for partial melting in the core of the Skagit. Note the near-isothermal decompression path determined form mineral assemblages and textures.

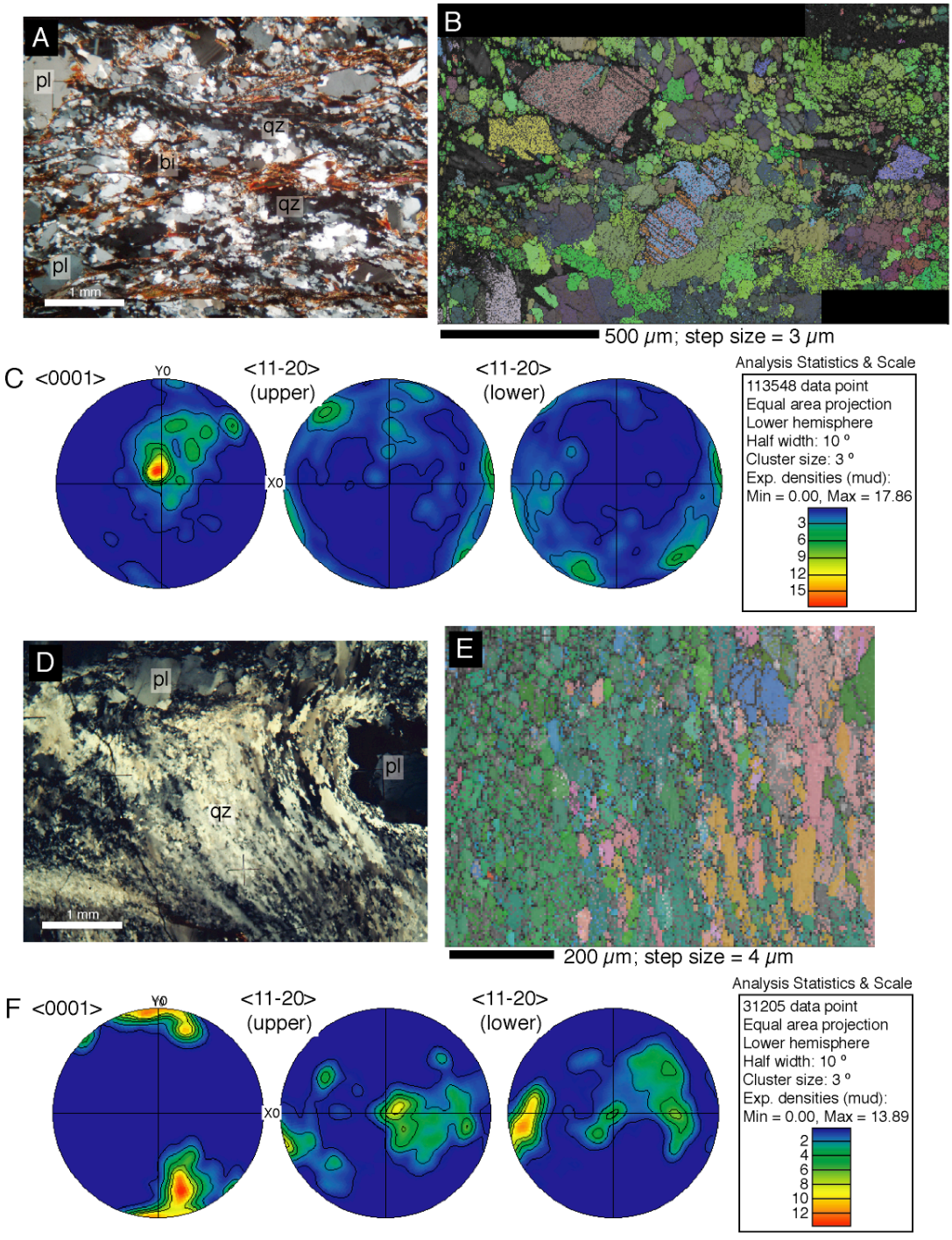

Figure 6.10: Electron backscattered diffraction results for a mesosome and leucosome sample from the Gorge Lake metapelite, SK-1. (A) Photomicrograph of the mesosome; the quartz was analyzed for EBSD analysis; (B) EBSD orientation map of quartz; (C) Contoured pole figure for the region shown in the map; (D) Photomicrograph of the leucosome; the quartz was analyzed for EBSD analysis; (E) EBSD orientation map of quartz; and (F) Contoured pole figure for the region shown in the map.

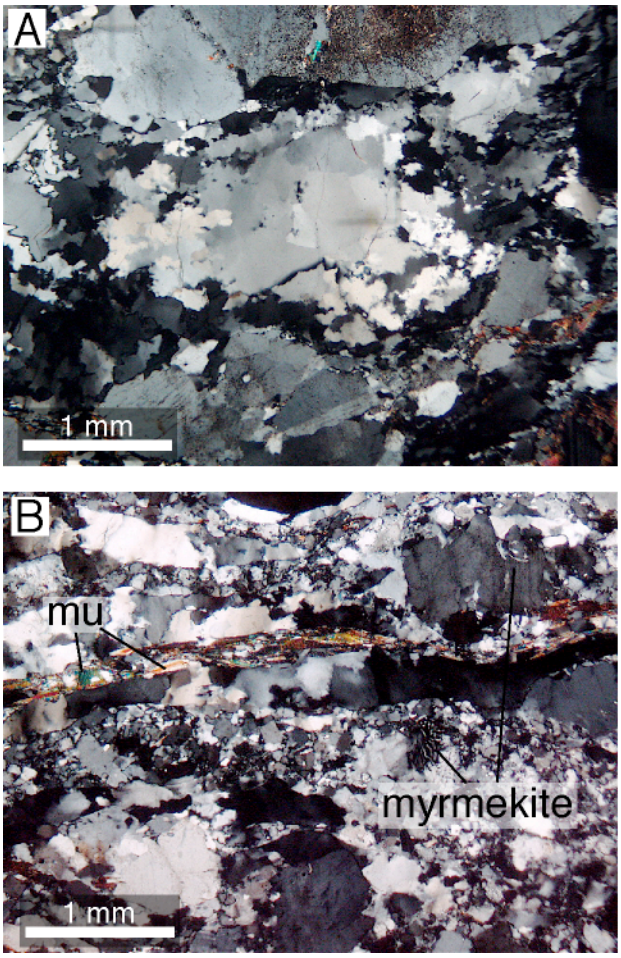

Figure 6.11: Photomicrographs of orthogneiss from Ruby Mt: (A) Large (~1 mm), quartz grain size, suggesting preservation of quartz that formed under higher temperature conditions; and (B) Evidence for a lower temperature overprint in the orthogneiss in the form of myrmekite, recrystallized quartz, and late muscovite present along foliation planes.

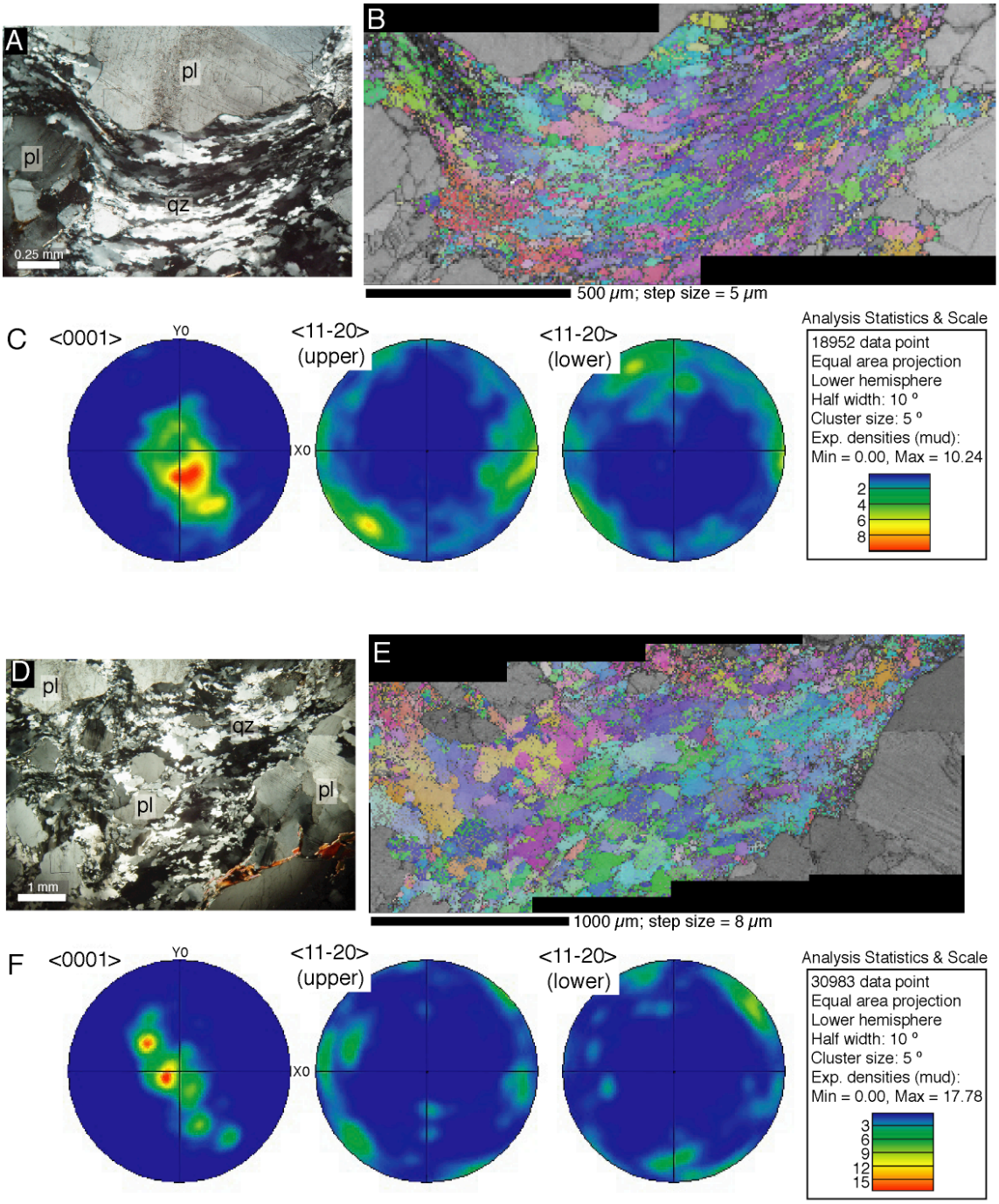

Figure 6.12: Electron backscattered diffraction results for layer-parallel leucosome SK0620B from the base of Ruby Mt. Two parts of the leucosome are shown. (A) Photomicrograph of quartz wrapping around a plagioclase grain; the quartz was analyzed for EBSD analysis; (B) EBSD orientation map of quartz; (C) Contoured pole figure for the region shown in the map; (D) Photomicrograph of a shear zone cutting at a ~45 º angle to the foliation plane; the quartz was analyzed for EBSD analysis; (E) EBSD orientation map of quartz; and (F) Contoured pole figure for the region shown in the map.

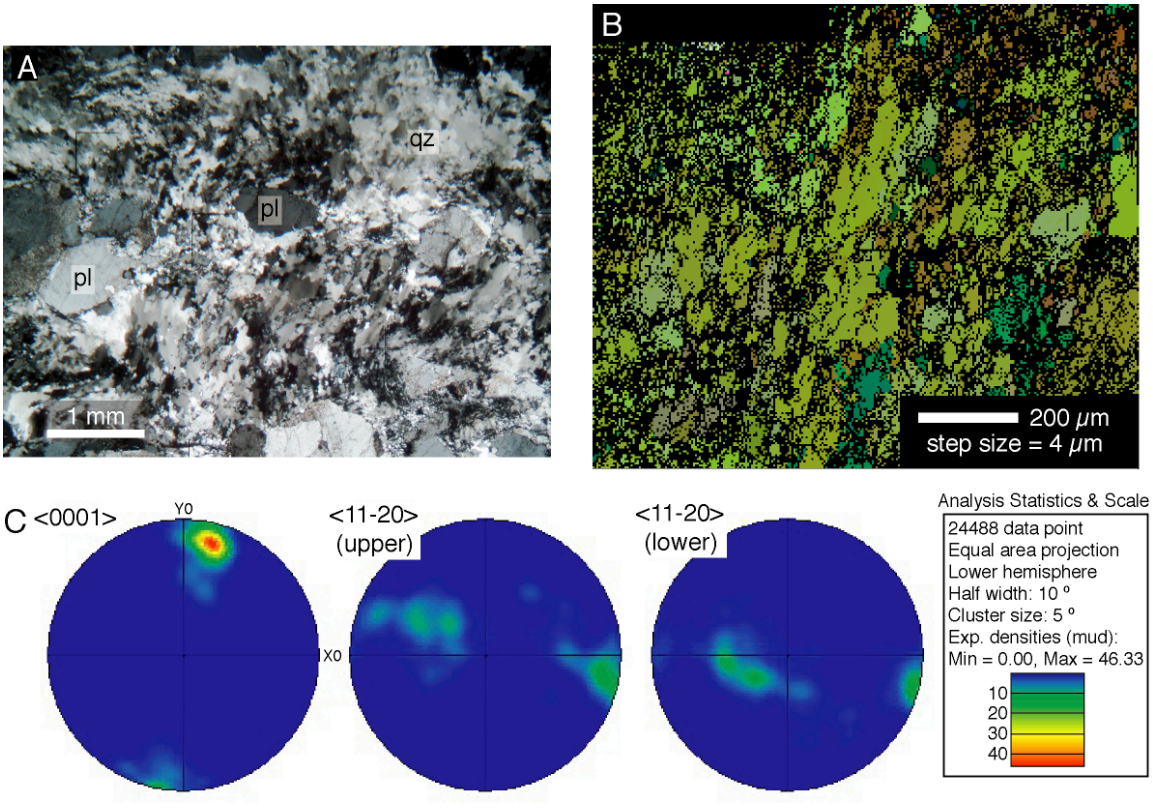

Figure 6.13: Electron backscattered diffraction results for a tonalitic orthogneiss SK0686 from Ruby Mt. (A) Photomicrograph of quartz; the quartz was analyzed for EBSD analysis; (B) EBSD orientation map of quartz; and (C) Contoured pole figure for the region shown in the map.

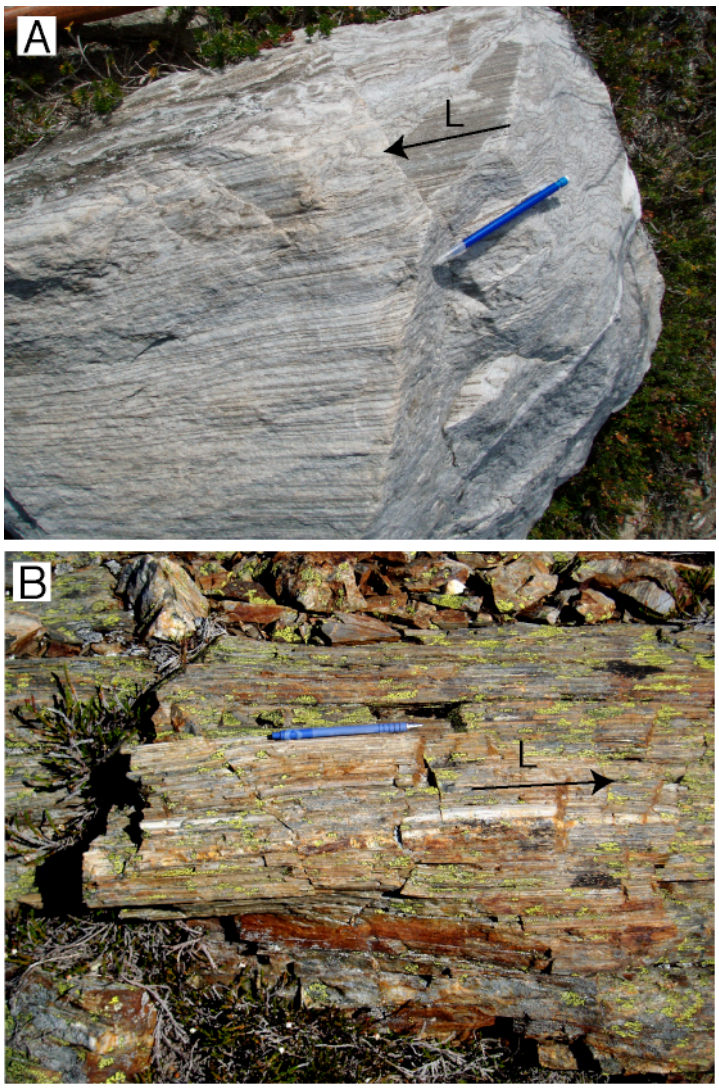

Figure 6.14: Field photographs showing the intense constrictional fabrics in (A) a Napeequa quartzite from Ruby Mt and (B) a metasiliceous gneiss of the Napeequa unit on West Elijah. The lineation (L) is shown in both photographs.

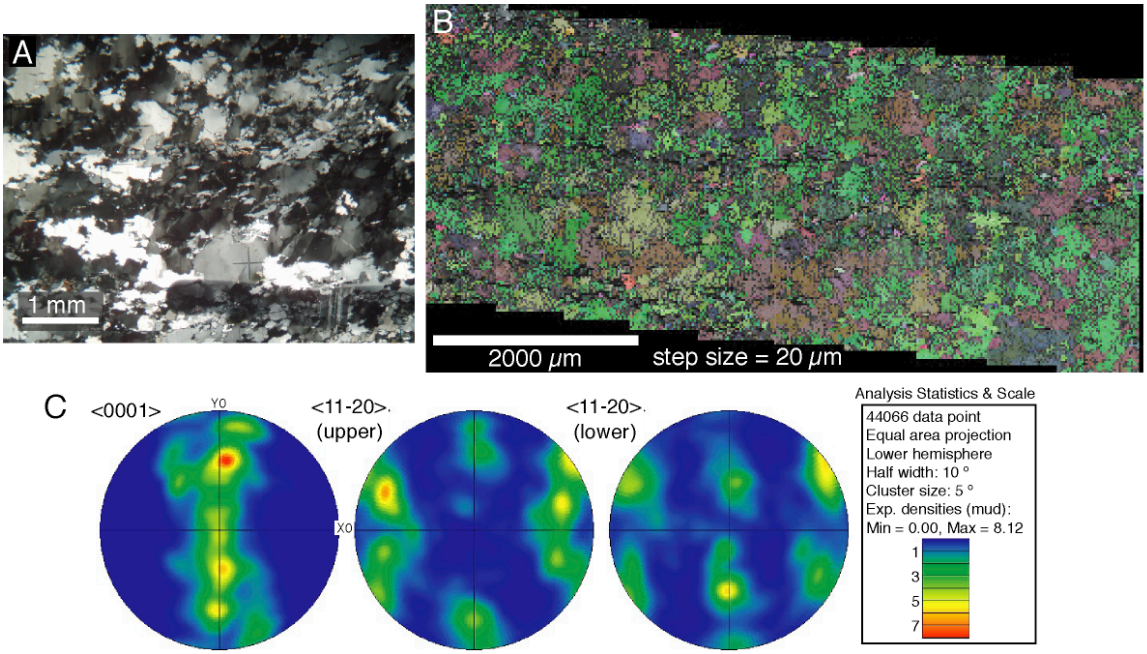

Figure 6.15: Electron backscattered diffraction results for a quartzite SK0671 from Ruby Mt. (A) Photomicrograph of quartz; the quartz was analyzed for EBSD analysis; (B) EBSD orientation map of quartz; and (C) Contoured pole figure for the region shown in the map.

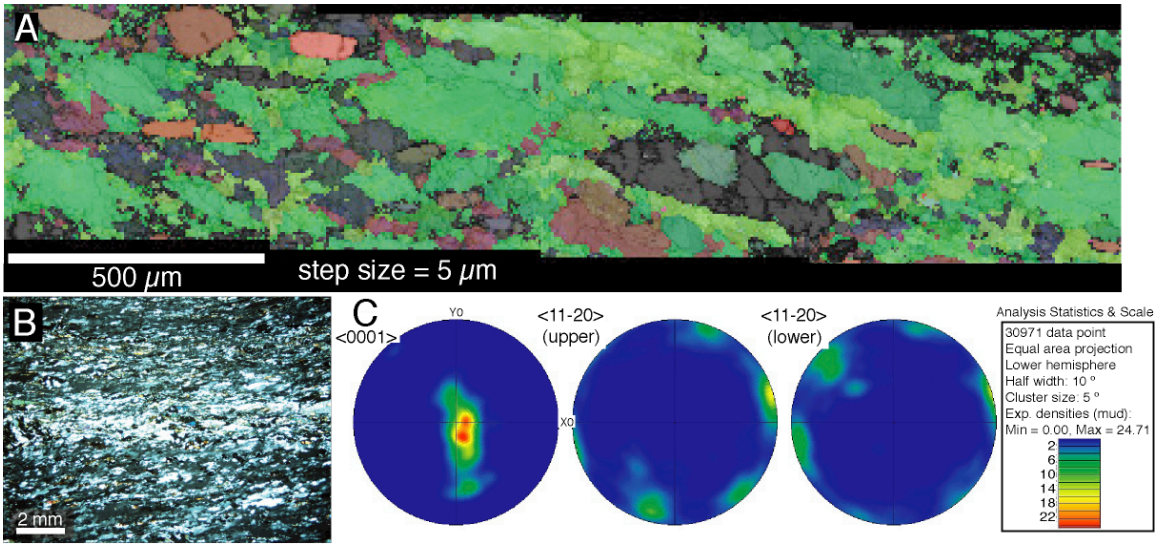

Figure 6.16: Electron backscattered diffraction results for a Ruby Mt Napeequa amphibolite, SK0664. (A) EBSD orientation map of quartz; (B) Photomicrograph of the quartz-rich layer of the amphibolite; and (C) Contoured pole figure for the region shown in the map.

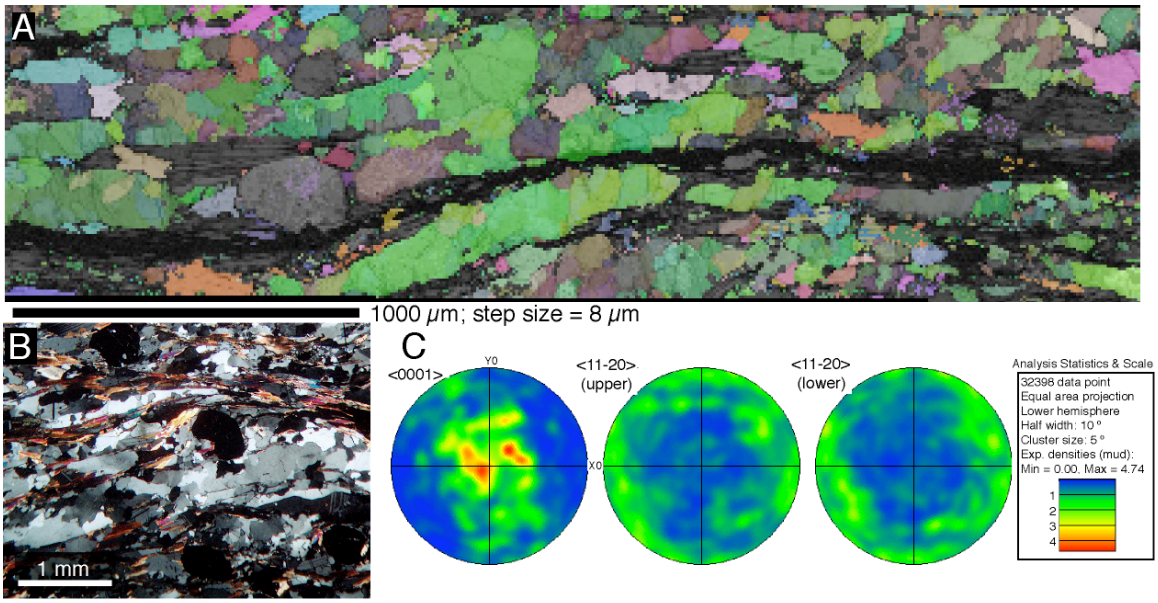

Figure 6.17: Electron backscattered diffraction results for a Elijah metapelite SK-3. (A) EBSD orientation map of quartz; (B) Photomicrograph of quartz ribbons; and (C) Contoured pole figure for the region shown in the map.

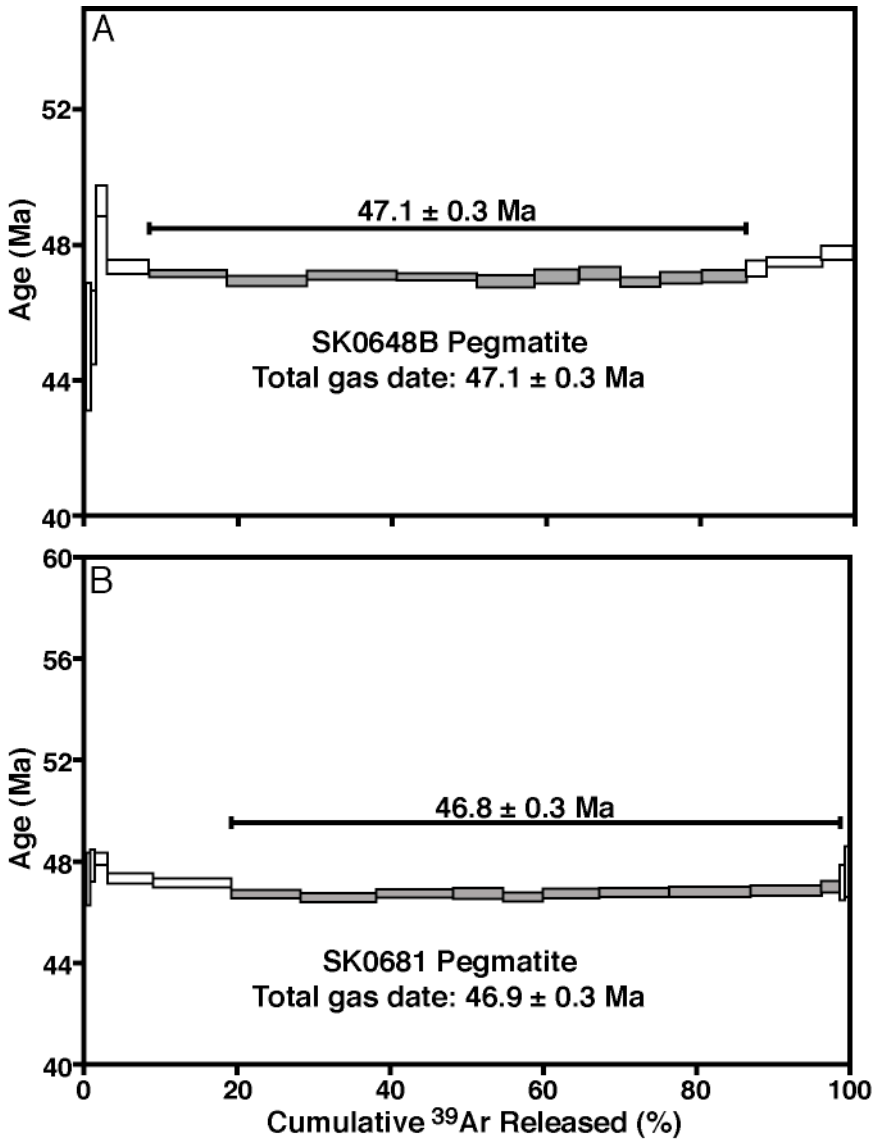

Figure 6.18: Muscovite $^{40}Ar/^{39}Ar$ age spectra for (A) sample SK0648B; and (B) sample SK0681. Shaded boxes indicate steps used in calculating preferred age.

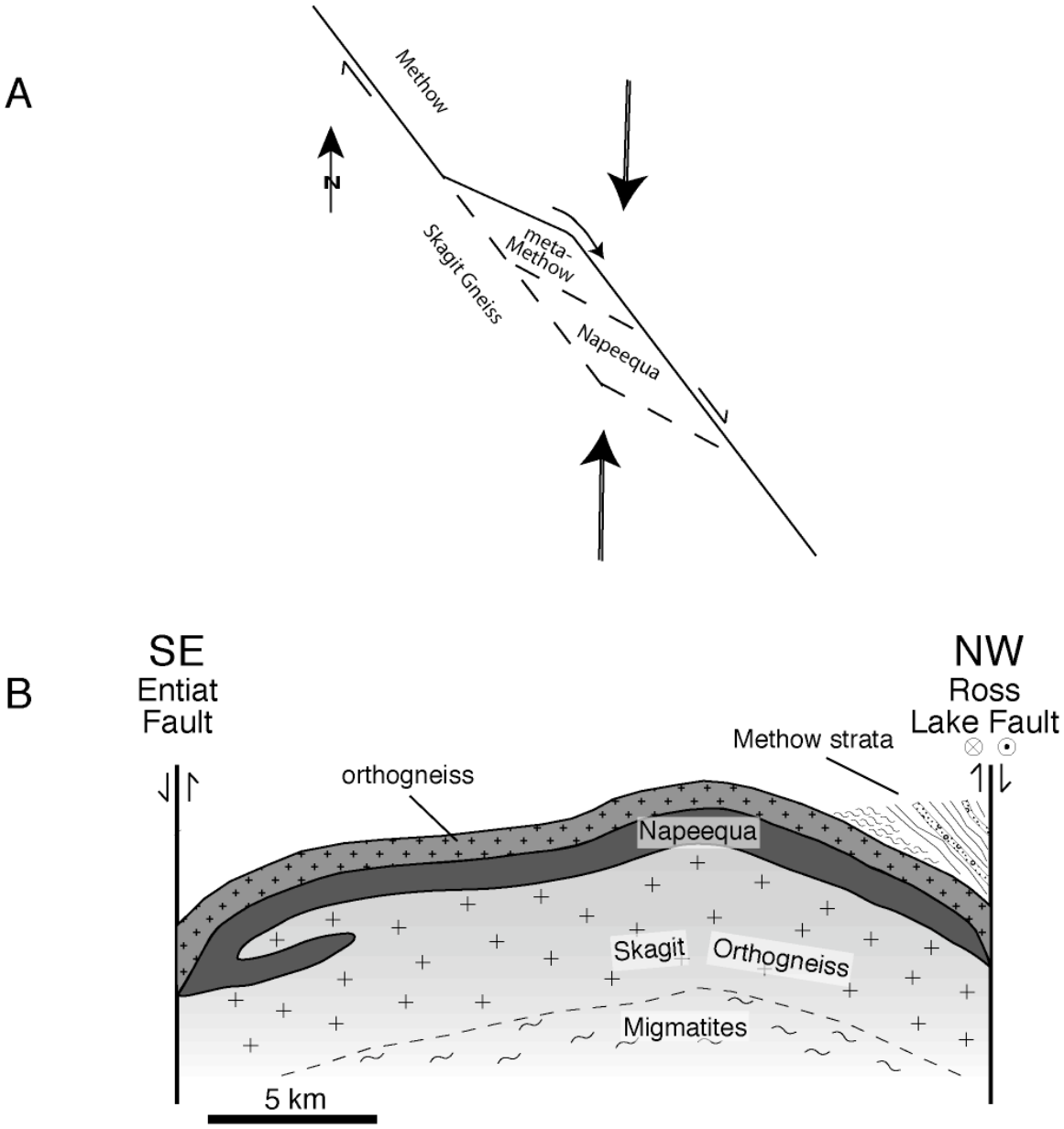

Figure 6.19: (A) Map view cartoon of the step-over zone in the Ross Lake fault zone and duplexing of the Napeequa and Methow units during regional transpression. (B) Simplified cross section of the Skagit Gneiss and overlying units showing the tectonic boundaries between the Skagit and the Napeequa, and between the Napeequa and Methow strata, prior to major movement on the Ross Lake fault zone.

Table 6.1: Analytical muscovite $^{40}Ar/^{39}Ar$ isotopic data

ID	Temp (ºC)	^{36}Ar	^{37}Ar	^{39}Ar	^{40}Ar	$^{40}Ar^*$ (%)	^{39}Ar (%)	K/Ca	Calculated Age (Ma)	± 2 sigma (Ma)
SK0648B, J = 3.0030E-3										
1	773	3.9264E-02	3.7019E-05	4.7761E-02	2.9512E-01	2.5	0.2	6.32E+02	33.2	6.9
2	873	3.6198E-03	6.1958E-06	7.6926E-02	6.4563E-01	37.6	0.4	6.08E+03	44.9	1.9
3	923	3.5066E-03	8.3157E-06	1.1590E-01	9.8204E-01	48.6	0.6	6.83E+03	45.3	0.9
4	973	6.8504E-03	-1.0579E-05	3.0823E-01	2.8434E+00	58.3	1.6	-1.43E+04	49.3	0.4
5	1023	3.2398E-03	4.8368E-05	1.0495E+00	9.2916E+00	90.4	5.5	1.06E+04	47.3	0.2
6	1048	1.5829E-03	3.9871E-05	1.9475E+00	1.7164E+01	97.0	10.1	2.39E+04	47.1	0.1
7	1073	7.4598E-04	7.9624E-05	1.9961E+00	1.7525E+01	98.4	10.4	1.23E+04	46.9	0.1
8	1098	7.1263E-04	3.8378E-05	2.2265E+00	1.9606E+01	98.6	11.6	2.84E+04	47.1	0.1
9	1123	6.2533E-04	-5.3636E-06	2.0258E+00	1.7829E+01	98.7	10.5	-1.85E+05	47.1	0.1
10	1148	6.3697E-04	5.5767E-05	1.4344E+00	1.2587E+01	98.2	7.5	1.26E+04	46.9	0.1
11	1173	5.8203E-04	5.7694E-05	1.0925E+00	9.6188E+00	97.9	5.7	9.28E+03	47.1	0.2
12	1223	6.6709E-04	6.3715E-05	1.0393E+00	9.1622E+00	97.6	5.4	7.99E+03	47.1	0.2
13	1273	7.8596E-04	4.7191E-05	9.7907E-01	8.5859E+00	97.1	5.1	1.02E+04	46.9	0.2
14	1323	6.6707E-04	3.5985E-05	1.0230E+00	8.9992E+00	97.5	5.3	1.39E+04	47.0	0.2
15	1373	5.9484E-04	5.5337E-05	1.1454E+00	1.0085E+01	98.0	6.0	1.01E+04	47.1	0.1
16	1473	2.8031E-04	1.9915E-05	4.7475E-01	4.1988E+00	97.8	2.5	1.17E+04	47.3	0.2
17	1673	9.4698E-04	4.7473E-05	1.3934E+00	1.2379E+01	97.5	7.2	1.44E+04	47.5	0.1
18	1873	1.6862E-03	4.8014E-05	8.4345E-01	7.5364E+00	93.5	4.4	8.61E+03	47.8	0.2
19	1873	6.1620E-04	6.6563E-07	2.4024E-03	3.4878E-02	16.1	0.0	1.77E+03	77.0	48.9
20	1073	4.9295E-04	2.0407E-05	1.6844E-04	-1.5798E-02	-12.2	0.0	4.04E+00	-596.8	858.3
21	673	7.9236E-05	6.3505E-06	-2.2901E-04	-1.7238E-02	-279.4	0.0	-1.77E+01	367.6	233.3
Total		6.8183E-02	7.0034E-04	6.8884E-02	1.6934E+02					
Integrated age ± 1 s.d.				*n* = 21					47.1	0.3
Preferred age ± 1 s.d.			steps 6-15	*n* = 10				MSWD = 1.41	47.1	0.3
SK0681, J = 3.0020E-3										
1	773	5.2948E-03	-3.5713E-06	4.0997E-02	2.3036E-01	12.8	0.2	-5.62E+03	30.2	2.2
2	873	3.3287E-03	2.0433E-06	1.0849E-01	9.5773E-01	49.3	0.5	2.60E+04	47.2	0.9
3	923	4.2164E-03	1.0832E-06	1.7457E-01	1.5609E+00	55.5	0.8	7.90E+04	47.8	0.6
4	973	3.6579E-03	1.5053E-07	3.8737E-01	3.4876E+00	76.2	1.7	1.26E+06	48.1	0.2
5	1023	3.2639E-03	4.1586E-05	1.3730E+00	1.2170E+01	92.4	5.9	1.62E+04	47.4	0.1
6	1048	1.4127E-03	2.3088E-05	2.3288E+00	2.0558E+01	97.7	10.0	4.94E+04	47.2	0.1
7	1073	8.0341E-04	1.3661E-04	2.0920E+00	1.8288E+01	98.4	9.0	7.50E+03	46.7	0.2
8	1098	7.2439E-04	8.8154E-05	2.2448E+00	1.9570E+01	98.6	9.7	1.25E+04	46.6	0.1
9	1123	7.4590E-04	3.9148E-05	2.3195E+00	2.0290E+01	98.6	10.0	2.90E+04	46.8	0.1
10	1148	6.6264E-04	5.4486E-05	1.5379E+00	1.3454E+01	98.2	6.6	1.38E+04	46.8	0.2
11	1173	6.9987E-04	3.8905E-05	1.1882E+00	1.0367E+01	97.7	5.1	1.50E+04	46.6	0.2
12	1223	8.8433E-04	5.4505E-05	1.7213E+00	1.5051E+01	98.0	7.4	1.55E+04	46.7	0.1
13	1273	8.1837E-04	9.1713E-05	2.0830E+00	1.8230E+01	98.4	9.0	1.11E+04	46.8	0.1
14	1323	4.2477E-04	9.9985E-05	2.4425E+00	2.1384E+01	99.1	10.5	1.20E+04	46.8	0.1
15	1373	2.7049E-04	1.4100E-04	2.1357E+00	1.8719E+01	99.2	9.2	7.42E+03	46.9	0.1
16	1473	-3.2224E-05	5.0392E-06	6.0873E-01	5.3515E+00	99.8	2.6	5.92E+04	47.0	0.2
17	1673	6.5788E-05	7.4786E-06	1.8067E-01	1.5976E+00	98.5	0.8	1.18E+04	47.3	0.7
18	1873	1.1494E-03	6.7080E-06	2.3711E-01	2.1331E+00	86.0	1.0	1.73E+04	48.1	0.6
19	1873	2.2706E-04	7.0608E-06	2.5063E-03	1.2524E-02	15.7	0.0	1.74E+02	26.9	52.7
20	1073	-7.5440E-05	2.7441E-05	-1.4503E-04	-5.7983E-03	20.6	0.0	-2.59E+00	204.5	526.6
21	673	-3.0002E-05	1.6576E-05	-2.2155E-04	-1.1694E-02	56.9	0.0	-6.55E+00	265.4	264.1
Total		2.8513E-02	8.7919E-04	2.9392E-02	2.0339E+02					
Integrated age ± 1 s.d.				*n* = 21					46.9	0.3
Preferred age ± 1 s.d.			steps 7-16	*n* = 10				MSWD = 1.90	46.8	0.3

Table 6.2: Representative microprobe analyses of garnet

	SK0672		SK0626		SK08273		SK0648		SK0691		SK07226 Large grt		SK07226 Small grt		SK07240	
	(c)[a]	(r)[a]	(c)	(r)	(c)	(r)	(c)	(r)	(c)	(r)	(c)	(r)	(c)	(r)	(c)	(r)
SiO_2	35.89	36.83	37.76	37.86	36.75	37.27	37.77	37.09	37.74	37.03	36.23	37.02	36.94	36.09	37.33	37.38
TiO_2	0.08	0.06	0.19	0.18	0.14	0.05	0.04	< d.l.**	< d.l.	< d.l.	0.08	0.12	0.11	0.10	0.08	0.05
Al_2O_3	20.91	21.55	21.72	21.95	21.47	21.77	22.34	21.69	22.40	21.87	21.24	21.61	21.22	20.62	21.24	21.58
FeO	27.83	28.54	22.18	22.12	23.15	23.88	29.92	32.78	30.13	32.46	33.63	31.96	35.02	34.92	29.93	32.23
MnO	4.89	1.87	2.15	2.36	4.78	3.10	1.35	3.62	1.49	4.22	5.73	1.24	0.21	0.23	2.95	0.73
MgO	1.83	2.61	2.87	2.85	2.66	2.90	5.10	3.37	5.78	2.43	0.99	0.60	0.91	0.91	1.92	3.80
CaO	7.52	8.34	13.76	13.62	9.45	9.93	4.05	2.15	2.51	2.78	1.10	7.32	6.31	6.32	7.17	4.64
Total	98.95	99.81	100.62	100.93	98.40	98.90	100.55	100.71	100.04	100.79	99.00	99.86	100.70	99.18	100.61	100.41
Cations per 12 oxygens																
Si	2.93	2.94	2.95	2.95	2.96	2.97	2.96	2.96	2.96	2.96	2.98	2.98	2.97	2.96	2.98	2.97
Ti	0.00	0.00	0.01	0.01	0.01	0.00	0.00	0.00	0.00	0.00	0.00	0.01	0.01	0.01	0.00	0.00
Al	2.01	2.03	2.00	2.01	2.04	2.04	2.04	2.02	2.05	2.04	2.06	2.05	2.01	1.99	2.00	2.02
Fe	1.90	1.91	1.45	1.44	1.56	1.59	1.96	2.19	1.98	2.17	2.32	2.15	2.36	2.39	2.00	2.14
Mn	0.34	0.13	0.14	0.16	0.33	0.21	0.09	0.24	0.10	0.29	0.40	0.08	0.01	0.02	0.20	0.05
Mg	0.22	0.31	0.33	0.33	0.32	0.34	0.60	0.40	0.68	0.29	0.12	0.07	0.11	0.11	0.23	0.45
Ca	0.66	0.71	1.15	1.14	0.81	0.85	0.34	0.18	0.21	0.24	0.10	0.63	0.54	0.56	0.61	0.39
Fe	0.61	0.62	0.47	0.47	0.52	0.53	0.66	0.73	0.67	0.73	0.79	0.73	0.78	0.78	0.66	0.71
Mn	0.11	0.04	0.05	0.05	0.11	0.07	0.03	0.08	0.03	0.10	0.14	0.03	0.00	0.01	0.07	0.02
Mg	0.07	0.10	0.11	0.11	0.11	0.12	0.20	0.13	0.23	0.10	0.04	0.02	0.04	0.04	0.08	0.15
Ca	0.21	0.23	0.37	0.37	0.27	0.28	0.11	0.06	0.07	0.08	0.03	0.21	0.18	0.18	0.20	0.13
X_{Fe}	0.90	0.86	0.81	0.81	0.83	0.82	0.77	0.84	0.75	0.88	0.95	0.97	0.96	0.96	0.90	0.83

[a] c = core; r = rim

** < d.l. = below the detection limit

Table 6.3: Representative microprobe analyses of hornblende

	SK0672		SK0626		SK08273	
	(c)[a]	(r)[a]	(c)	(r)	matrix	near garnet
SiO_2	38.58	39.49	43.09	41.37	45.78	44.63
TiO_2	0.06	0.00	0.71	0.70	0.71	0.69
Al_2O_3	20.13	17.13	14.46	15.14	11.74	11.20
FeO	21.88	21.02	16.13	19.18	15.06	17.31
MnO	0.18	0.13	0.40	0.57	0.35	0.56
MgO	5.59	7.03	9.88	7.82	11.21	9.82
CaO	11.22	11.19	12.04	11.80	11.86	11.68
Na_2O	1.90	1.87	1.43	1.46	1.04	1.02
K_2O	0.75	0.61	0.91	1.26	0.37	0.39
Total	100.29	98.46	99.05	99.28	98.12	97.30
Cations per 24 oxygens						
Si	5.76	5.99	6.34	6.19	7.00	6.97
Ti	0.01	0.00	0.08	0.08	0.08	0.08
Al	3.55	3.06	2.51	2.67	2.12	2.06
Fe	2.73	2.67	1.98	2.40	1.93	2.26
Mn	0.02	0.02	0.05	0.07	0.05	0.07
Mg	1.24	1.59	2.17	1.74	2.56	2.29
Ca	1.80	1.82	1.90	1.89	1.94	1.96
Na	0.55	0.55	0.41	0.42	0.31	0.31
K	0.14	0.12	0.17	0.24	0.07	0.08
X_{Fe}	0.69	0.63	0.48	0.58	0.43	0.50

[a] c = core; r = rim

Table 6.4: Representative microprobe analyses of plagioclase

	SK0672		SK0626		SK08273		SK0648	SK0691	SK07226 Large grt	SK07226 Small grt	SK07240A
	(c)[a]	(r)[a]	(c)	(r)	(c)	(r)					
SiO_2	57.62	53.23	58.13	55.92	59.49	57.94	59.01	59.55	58.83	59.30	58.07
Al_2O_3	27.28	30.27	26.96	27.62	25.89	27.24	26.36	26.05	25.72	25.45	25.98
Fe_2O_3	0.10	0.09	0.07	0.19	0.23	0.35	0.02	0.02	0.11	0.15	0.21
CaO	8.28	11.94	7.84	9.10	6.95	8.44	7.25	7.02	6.41	6.24	7.09
Na_2O	6.97	4.45	7.17	6.34	7.92	7.13	7.45	7.46	8.67	8.64	8.37
K_2O	0.11	0.07	0.13	0.27	0.08	0.09	0.12	0.10	0.16	0.20	0.12
Total	100.36	100.05	100.30	99.44	100.56	101.18	100.20	100.21	99.91	99.98	99.84
Si	2.57	2.40	2.59	2.53	2.64	2.57	2.64	2.67	2.63	2.65	2.61
Al	1.44	1.61	1.42	1.47	1.36	1.42	1.39	1.37	1.36	1.34	1.38
Fe	0.00	0.00	0.00	0.01	0.01	0.01	0.00	0.00	0.00	0.01	0.01
Ca	0.40	0.58	0.38	0.44	0.33	0.40	0.35	0.34	0.31	0.30	0.34
Na	0.60	0.39	0.62	0.56	0.68	0.61	0.65	0.65	0.75	0.75	0.73
K	0.01	0.00	0.01	0.02	0.00	0.00	0.01	0.01	0.01	0.01	0.01
mol% An	39.6	59.7	37.7	44.2	32.7	39.5	35.5	34.4	29.0	28.5	31.9

[a] c = core; r = rim

Table 6.5: Representative microprobe analysis of clinopyroxene

	SK0626
SiO_2	52.09
TiO_2	0.06
Al_2O_3	2.22
FeO	8.78
MnO	0.24
MgO	12.04
CaO	24.09
Na_2O	0.53
K_2O	0.03
Total	100.07
Cations per 6 oxygens	
Si	1.95
Ti	0.00
Al	0.10
Fe	0.28
Mn	0.01
Mg	0.67
Ca	0.97
Na	0.04
K	0.00
X_{Fe}	0.29

Table 6.6: Representative microprobe analyses of biotite

	SK0648	SK0691	SK07226	SK07240
SiO_2	35.62	34.09	32.35	34.09
TiO_2	1.99	2.73	2.24	1.05
Al_2O_3	21.59	21.53	22.47	23.52
FeO	18.06	19.46	24.96	21.00
MnO	0.08	0.08	0.07	0.04
MgO	10.01	8.90	4.96	8.16
CaO	< d.l.*	0.03	< d.l.	0.06
Na_2O	0.30	0.11	0.36	0.12
K_2O	8.89	8.21	9.02	8.65
F	0.02	0.02	< d.l.	< d.l.
Total	96.56	95.13	96.43	96.67
Cations per 22 oxygens				
Si	5.40	5.17	5.01	5.28
Ti	0.23	0.31	0.26	0.12
Al	3.86	3.84	4.10	4.30
Fe	2.29	2.47	3.24	2.72
Mn	0.01	0.01	0.01	0.01
Mg	2.26	2.01	1.14	1.88
Ca	0.00	0.00	0.00	0.01
Na	0.09	0.03	0.11	0.03
K	1.72	1.59	1.78	1.71
F	0.00	0.00	0.00	0.00
X_{Mg}	0.50	0.45	0.26	0.41

*< d.l. = below detection limit

Table 6.7: Representative microprobe analysis of cordierite

	SK06226
SiO_2	46.45
TiO_2	0.02
Al_2O_3	32.56
FeO	12.07
MnO	0.23
MgO	5.64
CaO	0.04
Na_2O	0.17
K_2O	0.02
Total	97.20
Si	4.94
Ti	0.00
Al	4.08
Fe	1.07
Mn	0.02
Mg	0.89
Ca	0.00
Na	0.03
K	0.00
X_{Fe}	0.54

Table 6.8: Representative microprobe analysis of staurolite

	SK06240
SiO_2	27.55
TiO_2	0.64
Al_2O_3	54.09
FeO	12.76
MnO	0.09
MgO	1.70
CaO	< d.l.*
ZnO	1.14
Total	97.95
Cations per 48 oxygens	
Si	7.97
Ti	0.14
Al	18.46
Fe	3.09
Mn	0.02
Mg	0.73
Ca	0.00
Zn	0.24
X_{Fe}	0.80

*< d.l. = below detection limit

Chapter 7: Conclusion to the Thesis

Orogenic Plateaux

Orogenic plateaux represent first-order expressions of crustal shortening and thickening at convergent plate margins. Geophysical, petrophysical, and petrologic studies of modern plateaux, including the Altiplano-Puna and the Tibetan plateaux, have suggested that a layer of partially molten crust is located in the mid- to lower-crust of the plateaux (e.g., Nelson et al., 1996; Schilling and Partzsch, 2001; Schilling et al., 2006). The melt flows laterally and is partially responsible for the uniformly high elevation and the shape of the plateaux (Fielding et al., 1994; Nelson et al., 1996; Clark and Royden, 2000). In addition, the presence of the melt (deduced to be ~20 vol. %) and its ability to flow probably has lead to strong crustal weakening in these plateau systems.

During the Late Mesozoic-Early Cenozoic, the North American Cordillera may have consisted of an orogenic plateau or series of plateaux that were created by crustal thickening, magmatism, partial melting, and flow of the mid- to lower-crust (e.g., Coney and Harms, 1984; England and Thompson, 1986; Molnar and Lyon-Caen, 1988; Wernicke et al., 1996; Wolfe et al., 1988; Dilek and Moores, 1999; Whitney et al., 2004). In the northeastern U.S. and southern British Columbia, the location of the two field areas from this dissertation, the proposed plateau extended from the North Cascades magmatic arc to the inboard crystalline belt consisting of the Shuswap metamorphic core complex (MCC), which contains the Valhalla complex. Today, a flat moho at depths of ca. 35 km depth is present from the North Cascades to the Shuswap MCC (e.g., Cook et al., 1988). Flow of partially molten crust could produce a flat moho within a plateau system (McKenzie et al., 2000), and partial melt was probably present in the proposed plateau for ca. 40 m.y. (from the timing of peak crustal thicknesses of ca. 60 km at 90 Ma in the

North Cascades (Miller and Bowring, 1990) to the timing of final melt crystallization at ca. 47 Ma (Chapter 5 of this dissertation)). Previous studies of these exhumed crystalline belts and the series of papers from this dissertation reveal three different types of evidence for a plateau: 1) evidence for thickened crust; 2) evidence for higher-elevations during the Late Mesozoic-Early Cenozoic; and 3) evidence for similar timescales of crustal thickening, extension and collapse over a broad region of the North American Cordillera.

Evidence for a paleoplateau

Geobarometry and geochemistry suggest evidence for crustal thicknesses of > 60 km in the Late Cretaceous. Upper amphibolite-facies migmatites and other non-migmatitic rocks have been exhumed to the surface in both the North Cascades and the Shuswap MCC. These rocks yield pressures of 8-12 kbar and 8-10 kbar in the North Cascades and the Shuswap MCC, respectively, suggesting paleodepths of > 30 km (Whitney, 1992; Spear and Parrish, 1996; Norlander et al., 2002; Valley et al., 2003; Chapter Six of this dissertation). Although these rocks were metamorphosed at high pressure, the lack of granulite facies assemblages indicates that these rocks were not in the lower crust of the orogen and were likely underlain by ≥ 10 km of additional orogenic crust.

Further evidence for a thick crust comes from geochemistry of calc-alkaline plutons in the North Cascades. The studies indicate that partial melting of garnet-bearing mafic crust occurred at depths of ~60 km (De Bari et al., 1998). Crustal thicknesses of the Altiplano-Puna, the modern analogue to the North American plateau, vary along strike

but range between ~50 – 70 km (Zandt et al., 1994), similar to the geobarometry and geochemistry paleodepth results estimated for the North American Cordillera plateau.

Paleoaltimetry studies suggest early to mid-Eocene paleoelevations that were 1-2 km higher than today. The studies are based on fossil plant assemblages from northeast Washington and southern British Columbia (Wolfe et al., 1998), and hydrogen isotope geochemistry from muscovite extracted from mylonitic quartzites within the crustal-scale extensional detachment of the Shuswap MCC (Mulch et al., 2004; 2007).

Geochronologic results from both the Shuswap MCC and the North Cascades, in particular the Skagit Gneiss, yield remarkably similar results even though the two terrains are separated by ~ 300 km (modern day map distance). Results from zircon and monazite geochronology of metapelites and other gneisses reveal prograde metamorphic and magmatic ages that range from ca. 90 to 60 Ma from both areas (Mattinson, 1972; Parrish et al., 1988; Miller et al., 1989; Miller and Bowring, 1990; Haugerud et al., 1991; Parrish, 1995; Spear and Parrish, 1996; Gordon et al., 2008; Chapters 2 and 5 of this dissertation). In addition, crystallization of partial melts and the timing of late fluid-infiltration overlap in time between the western and eastern boundaries of the plateau: 68-47 Ma in the Skagit Gneiss (Chapter 5 of this dissertation) and 60-50 Ma in the Shuswap MCC (Vanderhaeghe et al., 1999b; Crowley et al., 2001; Hinchey et al., 2006; Gordon et al., 2008; Kruckenberg et al., 2008; Chapters 2, 3, 4 of this dissertation). Finally, $^{40}Ar/^{39}Ar$ cooling ages are ca. 57-43 Ma in the Skagit Gneiss (Mattinson, 1972; Engels et al., 1976; Wernicke and Getty, 1997; Tabor et al., 2003) and 49-47 Ma in the Shuswap MCC (Wanless et al., 1978, 1979; Vanderhaeghe et al., 2003; Gordon et al., 2008; Chapter 2 of this dissertation), and the similarity in dates between melt crystallization and cooling has

suggested coeval rapid cooling and exhumation for both areas. Thus, the two field areas have a similar temporal record for crustal thickening and for extension and collapse of the overthickened crust.

Exhumation at plateau margins

Studies of the migmatites from both the North Cascades and the Shuswap MCC have suggested a strong link between lateral and vertical flow of melt and upper crustal extension and exhumation of the high-grade rocks in both areas. The role of partial melting in helping to trigger extension and exhumation may be extended to the demise of the orogenic plateau in the Eocene. Both field areas strongly suggest that there was probably a layer of partially molten crust within the paleoplateau in North America analogous to the layer imaged by geophysical studies in the Tibetan and Altiplano plateaux (Nelson et al., 1996; Schilling et al., 2006). The presence and flow of the melt created a strongly weakened crust during the Late Cretaceous to Eocene. Gravitational instability, a weakened crust, the flow of partial melt, and external plate reorganization may have triggered the collapse of the plateau.

Between the North Cascades and the Shuswap MCC, mostly low-grade sedimentary rocks and volcanic rocks are exposed; thus, most of the exhumation of the plateau was confined to the margins. Numerical modeling of plateau systems, in particular the Tibetan plateau, have suggested that there must be a viscosity contrast between the center and the margins of the plateau (e.g., Clark and Royden, 2000). In order to maintain no significant regional topographic slope, the central portion of the plateau must have a low viscosity in comparison to the margins. This viscosity contrast

was probably present in the proposed North American plateau. In addition, in the Cordillera, the central portion of the plateau was very weak whereas the margins are bordered by relatively strong, cold crust of the Rocky Mountain fold and thrust belt on the east and the subduction zone along the paleo-North American margin in the west. The viscosity and rheologic contrasts between the central portion of the plateau and the margins combined with excess potential energy may have driven crustal flow away from the center of the plateau; thus, once gravitational collapse began, the plateau would have collapsed at the margins first and the central portion of the plateau would have sunk down.

Additional analytical models further suggest that crustal deformation at the margins of the plateau may be coupled to mantle motion whereas the central part of the plateau is decoupled from the mantle (Royden, 1996). Thus, crustal convection is strongly tied to mantle motion, and the model suggests that channelized flow in the lower crust is much more rapid near the plateau margins and that surface extension will be concentrated at the transition from the plateau flanks to the central portion of the plateau, further supporting the concentration of exhumation at the plateau margins.

Additional reasons that are specific to the exhumation of orogenic crust at the eastern and western margins of the northern Cordillera exist for why the exhumation was concentrated in these localities. The eastern margin is bordered by the Rocky Mountain fold and thrust belt. The thrust belt serves as a fixed boundary to the eastern side of the plateau and to the flowing mid- to lower-crust. Modeling of fixed boundary gravitational collapse suggests that there will be an excess of potential energy that drives flow of the partially molten crust from the thickened crust to the adjacent regions; in this case, the

fold and thrust belt. The cold and strong fold and thrust belt would serve as a major barrier, similar to the basins described in the Tibetan plateau (Royden et al., 1997; Clark and Royden, 2000), potentially aiding in vertical flow of the melt. In addition, the precursor to the exhumed Shuswap MCC was probably thick (50-60 km), weak crust that evolved during allocthonous terrane accretion onto sedimentary sequences that had previously accumulated along the North American paleomargin during the Mesozoic (Coney, 1980; Brown et al., 1986; Price, 1986). The presence of weak, thick crust prior to the formation of the plateau may have caused a topographic stress and aided in the exhumation being concentrated along this eastern margin (Bird, 1991).

The western margin, consisting of the present day North Cascades, also had several reasons to be the focus of the exhumation. The western margin of the plateau may have been greatly affected by erosion owing to high rainfall associated with its location relative to Pacific weather patterns. Significant erosion and denudation has been shown to drive exhumation of ductile mid- to lower-crustal rocks to the surface (e.g., Beaumont et al., 2001; Zeitler et al., 2001). In addition, initiation of collapse is due to a change in the balance of forces that support the significant crustal thicknesses of orogens and plateaux during convergence (England and Houseman, 1988). Ridge subduction occurred outboard of the North Cascades at ca. 50 Ma (e.g., Cowan, 2003; Haeussler et al., 2003; Breitsprecher et al. 2003), and a slab window may have formed beneath the North Cascades. The change in plate motion and development of the slab window may have driven collapse of the plateau and exhumation along the western margin.

Differences in exhumation styles

Although exhumation timing and overall mechanism was the same in both areas, the structures associated with exhumation vary at the western and eastern margins. Exhumation in the western margin took place in a transtensional regime within a continental magmatic arc system. Oblique strike-slip faulting combined with buoyant, upward flow of melt drove extension of the Skagit Gneiss (Chapters 5, 6 of this dissertation). In comparison, the gneiss domes of the Shuswap MCC, including the Valhalla complex, represent a large-scale extensional system in which boudinage of the crust exhumed a north-south trending series of gneiss domes. Within each dome, vertical flow of melt combined with a rolling hinge detachment probably drove the decompression, partial melting, exhumation, and rapid cooling of the high-grade gneisses. In general, the two areas have slightly different exhumation mechanisms based on the dominantly oblique transtensional regime in the North Cascades and the purely extensional regime of the Shuswap MCC.

The evidence for thickened crust over a 300 km width of the North American Cordillera, the paleoaltimetry results that suggest paleoelevations that were 1-2 km higher than present elevations, and the similarity in timing of crustal thickening, deformation, and exhumation in the North Cascades and the Shuswap MCC all suggest that a plateau analogous to the Altiplano was present in western North American during the Cretaceous to Eocene. The position of the margins (e.g., above a slab window; at the boundary between the hot hinterland and cold foreland) combined with overall viscosity and rheologic contrasts and evidence for abundant crustal melting suggest evidence for collapse of the proposed plateau and concentration of exhumation at the plateau flanks. Collectively, the results from this thesis have outlined the mechanisms, timing, and

conditions of collapse of the plateau as recorded in orogenic crust exhumed at the western and eastern margins.

REFERENCES

Beaumont, C., Jamieson, R.A., Nguyen, M.H. & Lee, B., 2001. Himalayan tectonics explained by extrusion of a low-viscosity crustal channel coupled to focused surface denudation. *Nature*, **414**, 738-742.

Bird, P., 1991. Lateral extrusion of lower crust from under high topography, in the isostatic limit. *Journal of Geophysical Research*, **96**, 10275-10286.

Breitsprecher, K., Thorkelson, D.J., Groome, W.G. & Dostal, J., 2003. Geochemical confirmation of the Kula-Farallon slab window beneath the Pacific Northwest in Eocene time. *Geology*, **31**, 351-354.

Brown, R.L., Journeay, J.M., Lane, L.S., Murphy, D.C. & Rees, C.J., 1986. Obduction, backfolding and piggyback thrusting in the metamorphic hinterland of the southeastern Canadian Cordillera. *Journal of Structural Geology*, **8**, 255-268.

Clark, M.K. & Royden, L.H., 2000. Topographic ooze: Building the eastern margin of Tibet by lower crustal flow. *Geology*, **28**, 703-706.

Coney, P.J., 1980. Cordilleran metamorphic core complexes; an overview. *In*: Crittenden, M.D., Coney, P.J. & Davis, G.H. (Eds.), *Cordilleran metamorphic core complexes*. Boulder, Colorado, Geological Society of America Memoir, **153**, 7-34.

Coney, P.J. & Harms, T.A., 1984. Cordilleran metamorphic core complexes: Cenozoic extensional relics of Mesozoic compression. *Geology*, **12**, 550-554.

Cook, F.A., Simony, P.S., Coflin, K.C., Green, A.G., Milkereit, B., Price, R.A., Parrish, R., Patenaude, C., Gordy, P.L. & Brown, R.L., 1987. Lithoprobe southern Canadian Cordilleran transect: Rocky Mountain thrust belt to Valhalla gneiss complex. *Geophysical Journal of the Royal Astronomical Society*, **89**, 91-98.

Cowan, D.S., 2003. Revisiting the Baranof-Leech River hypothesis for early Tertiary coastwise transport of the Chugach-Prince William terrane. *Earth and Planetary Science Letters*, **213**, 463-475.

Crowley, J.L., Brown, R.L. & Parrish, R.R., 2001. Diachronous deformation and a strain gradient beneath the Selkirk allochthon, northern Monashee complex, southeastern Canadian Cordillera. *Journal of Structural Geology*, **23**, 1103-1121.

De Bari, S.M., Miller, R.B. & Paterson, S.R., 1998. Genesis of tonalitic plutons in the Cretaceous magmatic arc of the North Cascades: mixing of mantle derived magmas and melting of garnet-bearing lower crust. *Geological Society of America Abstracts with Programs*, **30**, 257-258.

Dilek, Y. & Moores, E.M., 1999. A Tibetan model for the Early Tertiary western United States. *Journal of the Geological Society, London*, **156**, 929-941.

England, P.C. & Thompson, A.B., 1986. Some thermal and tectonic models for crustal melting in continental collision zones. *In*: Coward, M.P. & Ries, A.C. (Eds.), *Collision Tectonics*. Geological Society, London, Special Publications, **19**, 83-94.

Engels, J.C., Tabor, R.W., Miller, F.K. & Obradovich, J.D., 1976. Summary of K-Ar, Rb-Sr, U-Pb, and fission track ages of rocks from Washington State prior to 1975 (exclusive of Columbia Plateau Basalts). *U.S. Geological Survey*, MF-710.

England, P.C. & Houseman, G.A., 1988. The mechanics of the Tibetan Plateau. *Philosophical Transactions of the Royal Society of London*, **A326**, 301-320.

Fielding, E., Isacks, B., Barazangi, M. & Duncan, C.C., 1994. How flat is Tibet? *Geology*, **22**, 163-167.

Gordon, S.M., Whitney, D.L., Teyssier, C., Grove, M. & Dunlap, W.J., 2008. Timescales of migmatization, melt crystallization, and cooling in a Cordilleran gneiss dome, the Valhalla complex, southeastern British Columbia. *Tectonics*, **27**, TC4010, doi:10.1029/2007TC002103.

Haeussler, P.J., Bradley, D.C., Wells, R. & Miller, M.L., 2003. Life and death of the Resurrection plate: evidence for an additional plate in the northeastern Pacific in Paleocene-Eocene time. *Geological Society of America Bulletin*, **115**, 867-880.

Haugerud, R.A., van der Heyden, P., Tabor, R.W., Stacey, J.S. & Zartman, R.E., 1991. Late Cretaceous and early Tertiary plutonism and deformation in the Skagit Gneiss Complex, North Cascades range, Washington and British Columbia. *Geological Society of America Bulletin*, **103**, 1297-1307.

Hinchey, A.M., Carr, S.D., McNeill, P.D. & Rayner, N., 2006. Paleocene-Eocene high-grade metamorphism, anatexis, and deformation in the Thor-Odin dome, Monashee complex, southeastern British Columbia. *Canadian Journal of Earth Sci*ences, **43**, 1341-1365.

Kruckenberg, S.C., Whitney, D.L., Teyssier, C., Fanning, C.M. & Dunlap, W.J., 2008. Paleocene-Eocene migmatite crystallization, extension, and exhumation in the hinterland of the northern Cordillera: Okanogan dome, Washington, USA. *Geological Society of America Bulletin*, **120**, 912-929.

Mattinson, J.M., 1972. Ages of zircons from the northern Cascade Mountains, Washington. *Geological Society of America Bulletin*, **83**, 3769-3784.

McKenzie, D., Nimmo, F., Jackson, J.A., Gans, P.B. & Miller, E.L., 2000. Characteristics and consequences of flow in the lower crust. *Journal of Geophysical Research*, **105**, 11029-11046.

Miller, R.B. & Bowring, S.A., 1990. Structure and chronology of the Oval Peak batholith and adjacent rocks: Implications for the Ross Lake fault zone, North Cascades, Washington. *Geological Society of America Bulletin*, **102**, 1361-1377.

Miller, R.B., Bowring, S.A. & Hoppe, W.J., 1989. Paleocene plutonism and its tectonic implications, North Cascades, Washington. *Geology*, **17**, 846-849.

Molnar, P. & Lyon-Caen, H., 1988. Some simple physical aspects of the support, structure, and evolution of mountain belts. *In*: Clark, S.P., Jr., Burchfiel, B.C. & Suppe, J. (Eds.), *Processes in Continental Lithospheric Deformation*. Geological Society of America Special Paper, **218**, 179-207.

Mulch, A., Teyssier, C., Cosca, M.A., Vanderhaeghe, O. & Vennemann, T.W., 2004, Reconstructing paleoelevation in eroded orogens. *Geology*, **32**, 525-528.

Mulch, A. & Chamberlain, C.P., 2007. Stable isotope paleoaltimetry in orogenic belts – the silicate record in surface and crustal geological archives. *Reviews in Mineralogy and Geochemistry*, **66**, p. 89-118.

Nelson, K.D., Wenjin Zhao, Brown, L.D., Kuo, J., Jinkai Che, Xianwen Liu, Klemperer, S.L., Makovsky, Y., Meissner, R., Mechie, J., Kind, R., Wenzel, F., Ni, J., Nabelek, J., Chen Leshou, Handong Tan, Wenbo Wei, Jones, A.G., Booker, J., Unsworth, M., Kidd, W.S.F., Hauck, M., Alsdorf, D., Ross, A., Cogan M., Changde Wu, Sandvol, E. & Edwards, M., 1996. Partially molten middle crust beneath southern Tibet: Synthesis of project INDEPTH results. *Science*, **274**, 1684-1688.

Norlander, B.N., Whitney, D.L., Teyssier, C. & Vanderhaeghe, O., 2002. Partial melting and decompression of the Thor-Odin dome, Shuswap metamorphic core complex, Canadian Cordillera. *Lithos*, **61**, 103-125.

Parrish, R.R., 1995. Thermal evolution of the southeastern Canadian Cordillera. *Canadian Journal of Earth Science*, **32**, 1618-1642.

Parrish, R.R., Carr, S.D. & Parkinson, D.L., 1988. Eocene extensional tectonics and geochronology of the southern Omineca belt, British Colombia and Washington. *Tectonics*, **7**, 181-212.

Price, R.A., 1986. The southeastern Canadian Cordillera: Thrust faulting, tectonic wedging and delamination of the lithosphere. *Journal of Structural Geology*, **8**, 238-254.

Rey, P., Vanderhaeghe, O. & Teyssier, C., 2001. Gravitational collapse of the continental crust: definition, regimes and modes. *Tectonophysics*, **342**, 435-449.

Royden, L., 1996. Coupling and decoupling of crust and mantle in convergent orogens: Implications for strain partitioning in the crust. *Journal of Geophyiscal Research*, **1996**, 17679-17705.

Royden, L.H., Burchfiel, B.C., King, R.W., Wang, E., Chen Zhiliang, Shen Feng & Liu Yuping., 1997. Surface deformation and lower crustal flow in eastern Tibet. *Science*, **276**, 788-790.

Schilling, F.R. & Partzsch, G.M., 2001. Quantifying partial melt fraction in the crust beneath the central Andes and the Tibetan Plateau. *Physics and Chemistry of the Earth*, **26**, 239-246.

Schilling, F.R., Trumbull, R.B., Brasse, H., Haberland, C., Asch, G., Bruhn, D., Mai, K., Haak, V., Giese, P., Muñoz, M., Ramelow, J., Rietbrock, A., Ricaldi, E. & Vietor, T., 2006. Partial melting in the Central Andean crust: a review of geophysical, petrophysical, and petrologic evidence. *In*: Oncken, O., Chong, G., Franz, G., Giese, P., Götze, H., Ramos, V.A., Strecker, M.R. & Wigger, P. (Eds.). *The Andes active subduction orogeny*, Springer, Berlin, pp. 459-474.

Spear, F.S. & Parrish, R.R.,1996. Petrology and cooling rates of the Valhalla Complex, British Columbia, Canada. Journal of Petrology, **37**, 733-765.

Tabor, R.W., Haugerud, R.A., Hildreth, W. & Brown, E.H., 2003. Geologic map of the Mount Baker 30- by 60 minute quadrangle, Washington. *U.S. Geological Survey, Geologic Investigation Series, I-2660, with pamphlet*, **70**, scale 1:100,000.

Valley, P.M., Whitney, D.L., Paterson, S.R., Miller, R.B. & Alsleben, H., 2003, Metamorphism of deepest exposed arc rocks in the Cretaceous to Paleogene Cascades belt, Washington: evidence for large-scale vertical motion in a continental arc. *Journal of Metamorphic Geology*, **21**, p. 203-220.

Vanderhaeghe, O., Teyssier, C. & Wysoczanski, R., 1999b. Structural and geochronological constraints on the role of partial melting during the formation of the Shuswap metamorphic core complex at the latitude of the Thor-Odin Dome, British Columbia. *Canadian Journal of Earth Sciences,* **36**, 917-943.

Vanderhaeghe, O., Teyssier, C., McDougall, I. & Dunlap, W.J., 2003. Cooling and exhumation of the Shuswap metamorphic core complex constrained by $^{40}Ar/^{39}Ar$ thermochronology. *Geological Society of America Bulletin*, **115**, 200-216.

Wernicke, B. & Getty, S.R., 1997. Intracrustal subduction and gravity currents in the deep crust: Sm-Nd, Ar-Ar, and thermobarometric constraints from the Skagit Gneiss Complex, Washington. *Geological Society of America Bulletin*, **109**, 1149-1166.

Wanless, R.K., Stevens, R.D., Lachance, G.R. & Delabio, R.N., 1978. Age determinations and geological studies, K-Ar isotopic ages, report 13. *Geological Survey of Canada, Paper*, **77-2**.

Wanless, R.K., Stevens, R.D., Lachance, G.R. & Delabio, R.N., (1979), Age determinations and geological studies, K-Ar isotopic ages, report 14, *Geological Survey of Canada, Paper*, **79-2.**

Wernicke, B., Clayton, R.W., Ducea, M., Jones, C.H., Park, S., Ruppert, S., Saleeby, J., Snow, J.K., Squires, L., Fliedner, M., Jiracek, G., Keller, R., Klemperer, S., Luetgert, J., Malin, P., Miller, K., Mooney, W., Oliver, H. & Phinney, R., 1996. Origin of high mountains in the continents: the southern Sierra Nevada. *Science*, **71**, 190-193.

Whitney, D.L., 1992. High pressure metamorphism in the western Cordillera of North America: an example from the Skagit Gneiss, North Cascades, Washington. *Journal of Metamorphic Geology*, **10**, 71-85.

Whitney, D.L., Paterson, S.R., Schmidt, K.L., Glazner, A.F. & Kopf, C.F., 2004. Growth and demise of continental arcs and orogenic plateaux in the North American Cordillera: from Baja to British Columbia. *In*: Grocott, J., McCaffrey, K.J.W., Taylor, G. & Tikoff, B. (Eds). *Vertical Coupling and Decoupling in the Lithosphere*, Geological Society, London, Special Publications, **227**, 167-176.

Wolfe, J.A., Forest, C.E. & Molnar, P., 1998. Paleobotanical evidence of Eocene and Oligocene paleoaltitudes in midlatitude western North America. *Geological Society of America Bulletin*, **110**, 664-678.

Zandt, G., Velasco, A.A. & Beck, S.L., 1994. Composition and thickness of the southern Altiplano crust, Bolivia. *Geology*, **22**, 1003-1006.

Zeitler, P.K., Koons, P.O., Bishop, M.P., Chamberlain, C.P., Craw, D., Edwards, M.A., Hamidullah, S., Qasim Jan, M., Asif Khan, M., Umar Khan Khattak, M., Kidd, W.S.F., Mackie, R.L., Meltzer, A.S., Park, S.K., Pecher, A., Poage, M.A., Sarker, G., Schneider, D.A., Seeber, L. & Shroder, J.F., 2001. Crustal reworking at Nanga Parbat, Pakistan: Metamorphic consequences of thermal-mechanical coupling facilitated by erosion. *Tectonics*, **20**, 712-728.

Complete Bibliography

Aikman, A.B., 2007. Tectonics of the eastern Tethyan Himalaya. Ph.D. thesis, Australian National University.

Archibald, D.A., Glover, J.K., Price, R.A., Farrar, E. & Carmichael, D.M., 1983. Geochronology and tectonic implications of magmatism and metamorphism, southern Kootenay arc and neighboring regions, southeastern British Columbia. Part I: Jurassic to mid-Cretaceous. *Canadian Journal of Earth Sciences,* **20**, 1891-1913.

Armstrong, R.L., 1982. Cordilleran metamorphic core complexes – From Arizona to southern Canada. *Annual Reviews of Earth and Planetary Sciences,* **10**, 129-154.

Armstrong, R.L. & Ward, P.L., 1991. Evolving geographic patterns of Cenozoic magmatism in the North American Cordillera; the temporal and spatial association of magmatism and metamorphic core. *Journal of Geophyical. Research,* **96**, 13201-13224.

Arnold, J., Powell, R. & Sandiford, M., 2000. Amphibolites with staurolite and other aluminous minerals: calculated mineral equilibria in NCFMASH. *Journal of Metamorphic Geology*, **18**, 23-40.

Ayers, J.C., Miller, C., Gorisch, B. & Milleman, J., 1999. Textural development of monazite during high-grade metamorphism: hydrothermal growth kinetics, with implications for U-Th-Pb geochronology. *American Mineralogist,* **84**, 1766-1780.

Ayers, J.D., Loflin, M., Miller, C.F., Barton, M.D. & Coath, C.D., 2006. In situ oxygen isotope analysis of monazite as a monitor of fluid infiltration during contact metamorphism: Birch Creek Pluton aureole, White Mountains, eastern California. *Geology,* **34**, 653-656.

Babcock, R.S. & Misch, P., 1989. Origin of the Skagit migmatites, North Cascades Range, Washington State. *Contributions to Mineralogy and Petrology*, **101**, 485-495.

Babcock, R.S., Armstrong, R.L. & Misch, P., 1985. Isotopic constraints on the age and origin of the Skagit Metamorphic Suite and related rocks. *Geological Society of America Programs with Abstracts*, **17**, 339.

Baldwin, J.A., Whitney, D.L. & Hurlow, H.A., 1997. Metamorphic and structural evidence for significant vertical displacement along the Ross Lake fault zone, a major orogen-parallel shear zone in the Cordillera of western North America. *Tectonics*, **16**, 662-681.

Barksdale, J.D., 1975. Geology of the Methow Valley, Okanogan County, Washington. *Washington Division of Geology and Earth Resources Bulletin*, **68**, 72.

Baumgartner, L.P. & Ferry, J.M., 1991. A model for coupled fluid-flow and mixed-volatile mineral reactions with applications to regional metamorphism. *Contributions to Mineralogy and Petrology,* **106**, 273-285.

Baxter, E.F., 2003. Natural constraints on metamorphic reaction rates. *In:* Vance, D., Müller, W. & Villa, I.M. (Eds*.), Geochronology: linking the isotopic record with petrology and textures*, **220**, Geological Society of London, p. 183-202.

Beaudoin, G., Taylor, B.E. & Sangster, D.F., 1991. Silver-lead-zinc veins, metamorphic core complexes, and hydrologic regimes during crustal extension. *Geology,* **19**, 1217-1220.

Beaudoin, G., Roddick, J.C. & Sangster, D.F., 1992. Eocene age for Ag-Pb-Zn-Au vein and replacement deposits of the Kokanee Range, southeastern British Columbia. *Canadian Journal of Earth Sciences,* **29**, 3-14.

Beaumont, C., Jamieson, R.A., Nguyen, M.H. & Lee, B., 2001. Himalayan tectonics explained by extrusion of a low-viscosity crustal channel coupled to focused surface denudation. *Nature*, **414**, 738-742.

Bebout, G.E. & Barton, M.D., 1989. Fluid flow and metasomatism in a subduction zone hydrothermal system: Catalina Schist terrane, California. *Geology,* **17**, 976-980.

Beck, M., 1976. Discordant paleomagnetic pole positions as evidence of regional shear in the western Cordillera of North America. *American Journal of Science*, **276**, 695-712.

Bird, P., 1991. Lateral extrusion of lower crust from under high topography, in the isostatic limit. *Journal of Geophysical Research*, **96**, 10275-10286.

Block, L. & Royden, L.H., 1990. Core complex geometries and regional scale flow in the lower crust. *Tectonics*, **9**, 557-567.

Booth, A.L., Kolodny, Y., Chamberlain, C.P., McWilliams, M., Schmitt, A.K. & Wooden, J., 2005. Oxygen isotopic composition and U-Pb discordance in zircon. *Geochimica et Cosmochimica Acta,* **69**, 4895-4905.

Brace, W.F. & Kohlstedt, D.L., 1980. Limits on lithospheric stress imposed by laboratory experiments. *Journal of Geophysical Research*, **85**, 6248-6252.

Breecker, D.O. & Sharp, Z.D., 2007. A monazite oxygen isotope thermometer. *American Mineralogist*, **92**, 1561-1572.

Breeding, C.M., Ague, J.J. & Bröcker, M., 2004a. Fluid-metasedimentary rock interactions in subduction-zone mélange: Implications for the chemical composition of arc magmas. *Geology*, **32**, 1041-1044.

Breeding, C.M., Ague, J.J., Grove, M. & Rupke, A.L., 2004b. Isotopic and chemical alteration of zircon by metamorphic fluids: U-Pb age depth-profiling of zircon crystals from Barrow's garnet zone, northeast Scotland. *American Mineralogist*, **89**, 1067-1077.

Breitsprecher, K., Thorkelson, D.J., Groome, W.G. & Dostal, J., 2003. Geochemical confirmation of the Kula-Farallon slab window beneath the Pacific Northwest in Eocene time. *Geology*, **31**, 351-354.

Brown, M., 2005. Synergistic effects of melting and deformation: an example from the Variscan belt, western France. *Geological Society of London*, **243**, 205-226.

Brown, R.L. & Read, P.B., 1983. Shuswap terrane of British Columbia: A Mesozoic "core complex." *Geology*, **11**, 164-168.

Brown, R.L., Journeay, J.M., Lane, L.S., Murphy, D.C. & Rees, C.J., 1986. Obduction, backfolding and piggyback thrusting in the metamorphic hinterland of the southeastern Canadian Cordillera. *Journal of Structural Geology*, **8**, 255-268.

Brown, R.L., Carr, S.D., Johnson, B.J., Coleman, V.J., Cook, F.A. & Varsek, J.L., 1992. The Monashee decollement of the southern Canadian Cordillera: A crustal scale shear zone linking the Rocky Mountain foreland to the lower crust beneath accreted terranes. *In*: McClay, K.R. (Ed.) *Thrust tectonics*, Geological Society of London, Special Publication, pp. 357-364.

Buck, W.R., 1988. Flexural rotation of normal faults. *Tectonics,* **7**, 959-973.

Buck, W.R., 1991. Mode of continental lithospheric extension, *Journal of Geophysical Research,* **96**, 20161-20178.

Carr, S.D., 1985. Ductile shearing and brittle faulting in Valhalla gneiss complex, southeastern British Columbia. *Geological Survey of Canada Papers*, **85-1A**, 89-96.

Carr, S.D., 1986. The Valkyr shear zone and the Slocan Lake fault zone: Eocene structures that bound the Valhalla gneiss complex, southeastern British Columbia, M.S. thesis, 106 pp., Carleton University, Ottawa.

Carr, S.D., 1991. U-Pb zircon and titanite ages of three Mesozoic igneous rocks south of the Thor-Odin-Pinnacles area, southern Omineca Belt, British Columbia, *Canandian Journal of Earth Sciences,* **28**, 1877-1882.

Carr, S.D., 1992. Tectonic setting and U-Pb geochronology of the early Tertiary Ladybird leucogranite suite, Thor-Odin-Pinnacles area, southern Omineca belt, British Colombia. *Tectonics,* **11**, 258-278.

Carr, S.D. & Simony, P.S., 2006. Ductile thrusting versus channel flow in the southeastern Canadian Cordillera: evolution of a coherent crystalline thrust sheet. *In*: Law, R.D., Searle, M.P. & Gobin, L. (Eds.), *Channel flow, Extrusion, and Exhumation in Continental Collision Zones, Special Publications*, Geological Society of London, vol. 268, pp. 561-587.

Carr, S.D., Parrish, R.R. & Brown, R.L., 1987. Eocene structural development of the Valhalla complex, southeastern British Columbia. *Tectonics,* **6**, 175-196.

Carson, C.J., Ague, J.J., Grove, M., Coath, C.D. & Harrison, T.M., 2002. U-Pb isotopic behaviour of zircon during upper-amphibolite facies fluid infiltration in the Napier Complex, east Antarctica. *Earth and Planetary Science Letters*, **199**, 287-310.

Carson, C.J., Berman, R.G., Stern, R.A., Sanborn-Barrie, M., Skulski, T. & Sandeman, H.A.I., 2004. Age constraints on the Paleoproterozoic tectonometamorphic history of the Committee Bay region, western Churchill Province, Canada: evidence from zircon and in situ monazite SHRIMP geochronology. *Canadian Journal of Earth Sciences,* **41**, 1049-1076.

Catlos, E.J., Gilley, L.D. & Harrison, T.M., 2002. Interpretation of monazite ages obtained via in situ analysis. *Chemical Geology*, **188**, 193-215.

Cherniak, D.J. & Watson, E.B., 2000. Pb diffusion in zircon. *Chemical Geology*, **172**, 5-24.

Cherniak, D.J. & Watson, E.B., 2001. Pb diffusion in zircon. *Chemical Geology,* **172**, 5-24.

Cherniak, D.J. & Watson, E.B., 2003. Diffusion in zircon. *In*: Hanchar, J.M., Hoskin, P.W.O. (Eds.), Zircon. Reviews in Mineralogy and Geochemistry, vol. 53, pp. 113-143.

Cherniak, D.J. & Watson, E.B., 2007. Ti diffusion in zircon. *Chemical Geology,* **242**, 470-483.

Cherniak, D.J., Watson, E.B., Grove, M. & Harrison, T.M., 2004. Pb diffusion in monazite: A combined RBS/SIMS study. *Geochimica Cosmochimica Acta*, **68**, 829-840.

Clark, M.K. & Royden, L.H., 2000. Topographic ooze: Building the eastern margin of Tibet by lower crustal flow. *Geology*, **28**, 703-706.

Coney, P.J., 1980. Cordilleran metamorphic core complexes; an overview. *In*: Crittenden, M.D., Coney, P.J. & Davis, G.H. (Eds.), *Cordilleran metamorphic core complexes*. Boulder, Colorado, Geological Society of America Memoir, **153**, 7-34.

Coney, P.J. & Harms, T.A., 1984. Cordilleran metamorphic core complexes: Cenozoic extensional relics of Mesozoic compression. *Geology*, **12**, 550-554.

Conrad, W.K., Nicholls, I.A. & Wall, V.J., 1988. Water-saturated and undersaturated melting at 10 kbar: evidence for the origin of silicic magmas in the Taupo Volcanic Zone, New Zealand, and other occurrences. *Journal of Petrology*, **29**, 765-803.

Cook, F.A., Simony, P.S., Coflin, K.C., Green, A.G., Milkereit, B., Price, R.A., Parrish, R., Patenaude, C., Gordy, P.L. & Brown, R.L., 1988. Lithoprobe southern Canadian Cordilleran transect: Rocky Mountain thrust belt to Valhalla gneiss complex. *Geophysical Journal of the Royal Astronomical Society*, **89**, 91-98.

Corfu, F., Hanchar, J.M., Hoskin, P.W.O. & Kinny, P., 2003. Atlas of zircon textures. *In:* Hanchar, J.M. & Hoskin, W.O. (Eds.), *Zircon*, v. 53: Reviews in Mineralogy and Geochemistry, Mineralogical Society of America, p. 468-500.

Cowan, D.S., 2003. Revisiting the Baranof-Leech River hypothesis for early Tertiary coastwise transport of the Chugach-Prince William terrane. *Earth and Planetary Science Letters*, **213**, 463-475.

Crawford, M.L., Hollister, L.S. & Woodsworth, G.J., 1987. Crustal deformation and regional metamorphism across a terrane boundary, Coast Plutonic Complex, British Columbia. *Tectonics,* **6**, 343-361.

Crittenden, M.D., Coney, P.J. & Davis, G.H., 1980. Cordilleran metamorphic core complexes. *Geological Society of America Memoir*, **153**, 496.

Crowley, J., 1997a. U-Pb geochronologic constraints on the cover sequence of the Monashee complex, Canadian Cordillera: Paleoproterozoic deposition on basement, *Canadian Journal of Earth Sciences,* **34**, 1008-1022.

Crowley, J., 1997b. U-Pb geochronology in Frenchman Cap dome of the Monashee Complex, Southern Canadian Cordillera: Early Tertiary tectonic overprint of a Proterozoic history, Ph.D. thesis, 219 pp., Carleton University, Ottawa.

Crowley, J.L. & Parrish, R.R., 1999. U-Pb isotopic constraints on diachronous metamorphism in the northern Monashee complex, southern Canadian Cordillera. *Journal of Metamorphic Geology,* **17**, 483-502.

Crowley, J.L., Brown, R.L. & Parrish, R.R., 2001. Diachronous deformation and a strain gradient beneath the Selkirk allochthon, northern Monashee complex, southeastern Canadian Cordillera. *Journal of Structural Geology*, **23**, 1103-1121.

Cruz, L., Fayon, A.K., Teyssier, C. & Weber, J., 2007. Exhumation and deformation processes in transpressional orogens: the Venezuelan Paria Peninsula, SE Caribbean-South American plate boundary. In: Till, A.B., Roeske, S.M., Sample, J.C. & Foster, D.A (Eds.) *Exhumation Associated with Continental Strike-slip Fault Systems.* Geological Society of America Special Paper, **434,** pp. 149-165..

De Bari, S.M., Miller, R.B. & Paterson, S.R., 1998. Genesis of tonalitic plutons in the Cretaceous magmatic arc of the North Cascades: mixing of mantle derived magmas and melting of garnet-bearing lower crust. *Geological Society of America Abstracts with Programs*, **30**, 257-258.

Dell'Angelo, L.N., Tullis, J. & Yund, R.A., 1987. Transition from dislocation creep to melt-enhanced diffusion creep in fine-grained granitic aggregates. *Tectonophysics,* **139**, 325-332.

Dewey, J.F., 1988. Extensional collapse of orogens. *Tectonics*, **7**, 1123-1139.

DeWolf, C.P., Belshaw, N. & O'Nions, R.K., 1993. A metamorphic history from micron-scale $^{207}Pb/^{206}Pb$ chronometry of Archean monazite. *Earth and Planetary Science Letters,* **120**, 207-220.

Dilek, Y. & Moores, E.M., 1999. A Tibetan model for the Early Tertiary western United States. *Journal of the Geological Society, London*, **156**, 929-941.

Ducea, M.N., Ganguly, J., Rosenberg, E.J., Patchett, P.J., Cheng, W. & Isachsen, C., 2003. Sm-Nd dating of spatially controlled domains of garnet single crystals: a new method of high-temperature thermochronology. *Earth and Planetary Science Letters*, **213**, 31-42.

Duncan, I.J., 1984. Structural evolution of the Thor-Odin gneiss dome. *Tectonophysics*, **101**, p. 87-130.

Elliott, T., Plank, T., Zindler, A., White, W. & Bourdon, B., 1997. Element transport from slab to volcanic front at the Mariana arc. *Journal of Geophysical Research,* **102**, 14991-15019.

England, P.C. & Thompson, A.B., 1986. Some thermal and tectonic models for crustal melting in continental collision zones. *In*: Coward, M.P. & Ries, A.C. (Eds.), *Collision Tectonics*. Geological Society, London, Special Publications, **19**, 83-94.

Engels, J.C., Tabor, R.W., Miller, F.K. & Obradovich, J.D., 1976. Summary of K-Ar, Rb-Sr, U-Pb, and fission track ages of rocks from Washington State prior to 1975 (exclusive of Columbia Plateau Basalts). *U.S. Geological Survey*, MF-710.

England, P.C. & Houseman, G.A., 1988. The mechanics of the Tibetan Plateau. *Philosophical Transactions of the Royal Society of London*, **A326**, 301-320.

Evans, J.E., 1994. Depositional history of the Eocene Chumstick Formation: Implications of tectonic partitioning for the history of the Leavenworth and Entiat-Eagle Creek fault systems. *Tectonics,* **13**, 1425-1444.

Evans, J.E. & Johnson, S.Y., 1989. Paleogene strike-slip basins of central Washington: Swauk Formation and Chumstick Formation. In: Joseph, N.L. et al. (Eds.), Geologic Guidebook for Washington and Adjacent Areas. Wash. Div. Geol. Earth Resources, Information Circular 86, 213-237.

Ferry, J.M. & Watson, E.B., 2007. New thermodynamic models and revised calibrations for the Ti-in-zircon and Zr-in-rutile thermometers. *Contributions to Mineralogy and Petrology*, **154**, 429-437.

Fielding, E., Isacks, B., Barazangi, M. & Duncan, C.C., 1994. How flat is Tibet? *Geology*, **22**, 163-167.

Foster, D.A., Doughty, P.T., Kalakay, T.J., Fanning, C.M., Coyner, S., Grice, W.C. & Vogl, J., 2007. Kinematics and timing of exhumation of metamorphic core complexes along the Lewis and Clark fault zone, northern Rocky Mountains, USA. *In*: Till, A.B., Roeske, S.M., Sample, J.C. & Foster, D.A. (Eds.), *Exhumation Associated with Continental Strike-slip Fault Systems*, Geological Society of America Special Paper **434**, pp. 207-232.

Gébelin, A., Brunel, M., Monié, P., Faure, M. & Arnaud, N., 2007. Relationships between Carboniferous magmatism and ductile shear zones in the Limousin (Massif Central, France). *Tectonics,* **26**, TC2008, doi:10.1029/2005TC001822.

Goetze, C. & Evans, B., 1979. Stress and temperature in the bending lithosphere as constrained by experimental rock mechanics. *Geophysical Journal of the Royal Astronomical Society*, **59**, 463-478.

Gresens, R.L., Naeser, C.W. & Whetten, J.T., 1981. Stratigraphy and age of the Chumstick and Wenatchee Formations – Tertiary fluvial and lacustrine rocks, Chiwaukum Graben, Washington. *Geological Society of America Bulletin*, **92**, 233-236.

Gordon, S.M., Whitney, D.L., Teyssier, C., Grove, M. & Dunlap, W.J., 2008. Timescales of migmatization, melt crystallization, and cooling in a Cordilleran gneiss dome, the

Valhalla complex, southeastern British Columbia. *Tectonics*, **27**, TC4010, doi:10.1029/2007TC002103.

Goscombe, B., Gray, D. & Hand, M., 2003. Variation in metamorphic style along the Northern Margin of the Damara Orogen, Namibia. *Journal of Petrology,* **45**, 1261-1295.

Grove, M. & Harrison, T.M., 1999. Monazite Th-Pb age depth profiling. *Geology*, **27**, 487-490.

Haeussler, P.J., Bradley, D.C., Wells, R. & Miller, M.L., 2003. Life and death of the Resurrection plate: evidence for an additional plate in the northeastern Pacific in Paleocene-Eocene time. *Geological Society of America Bulletin*, **115**, 867-880.

Handy, M.R., Mulch, A., Rosenau, M. & Rosenberg, C.L., 2001. The role of fault zones and melts as agents of weakening, hardening and differentiation of the continental crust: a synthesis. *In*: Holdworth, R.E., Strachan, R.A., Magloughlin, J.F., Knipe, R.J. (Eds.), *The Nature and Tectonic Significance of Fault Zone Weakening*. Geological Society of London, **186**, pp. 305-332.

Harlov, D.E., Wirth, R. & Hetherington, C.J., 2007. The relative stability of monazite and huttonite at 300-900 ºC and 200-1000 MPa: metasomatism and the propagation of metastable mineral phases. *American Mineralogist*, **92**, 1652-1664.

Harrison, T.M. & Watson, E.B., 1983. Kinetics of zircon dissolution and zirconium diffusion in granitic melts of variable water content. *Contributions to Mineralogy and Petrology*, **84**, 67-72.

Harrison, T.M. & Schmitt, A.K., 2007. High sensitivity mapping of Ti distributions in Hadean zircons. *Earth and Planetary Science Letters*, **261**, 9-19.

Harrison, T.M., McKeegan, K.D. & Le Fort, P., 1995. Detection of inherited monazite in the Manaslu leucogranite by $^{208}Pb/^{232}Th$ ion microprobe dating: Crystallization age and tectonic significance. *Earth and Planetary Science Letters*, **133**, 271-282.

Harrison, T.M., Grove, M., McKeegan, K.D., Coath, C.D., Lovera, O.M. & Le Fort, P., 1999. Origin and episodic emplacement of the Manaslu Intrusive Complex, Central Himalaya. *Journal of Petrology*, **40**, 3-19.

Harvey, J.L., 1994. Sapphirine-bearing amphibolites in the Okanogan complex, Washington: thermobarometry and tectonic implications. M.S. thesis, Northern Arizona University.

Haugerud, R.A., 1985. Geology of the Hozameen Group and the Ross Lake shear zone, Maselpanik area, North Cascades, southwestern British Columbia. Ph.D. thesis, University of Washington, Seattle, Washington, p. 263.

Haugerud, R.A., van der Heyden, P., Tabor, R.W., Stacey, J.S. & Zartman, R.E., 1991. Late Cretaceous and early Tertiary plutonism and deformation in the Skagit Gneiss Complex, North Cascades range, Washington and British Columbia. *Geological Society of America Bulletin*, **103**, 1297-1307.

Hawkins, D.P. & Bowring, S.A., 1997. U-Pb systematics of monazite and xenotime: case studies from the Paleoproterozoic of the Grand Canyon, Arizona. *Contribution to Mineralogy and Petrology,* **127**, 87-103.

Heaman, L. & Parrish, R.R., 1991. U-Pb geochronology of accessory minerals, *In:* Heaman, L. & Ludden, J.N. (Eds.), *Short course handbook on applications of radiogenic isotope systems to problems in geology*, Mineralogical Association of Canada, Toronto, pp. 59-100.

Hinchey, A.M., 2005. Thor-Odin dome: constraints on Paleocene-Eocene anatexis and deformation, leucogranite generation and the tectonic evolution of the southern Omineca belt, Canadian Cordillera. PhD thesis, Carleton University, Ottawa, Ontario, p. 258.

Hinchey, A.M., Carr, S.D., McNeill, P.D. & Rayner, N., 2006. Paleocene-Eocene high-grade metamorphism, anatexis, and deformation in the Thor-Odin dome, Monashee complex, southeastern British Columbia. *Canadian Journal of Earth Sci*ences, **43**, 1341-1365.

Holdaway, M.J., 2000. Application of new experimental and garnet Margules data to the garnet-biotite geothermometer. *American Mineralogist*, **85**, 881-892.

Holdaway, M.J., 2001. Recalibration of the GASP geobarometer in light of recent garnet and plagioclase activity models and versions of the garnet-biotite geothermometer. *American Mineralogist*, **86**, 1117-1129.

Holk, G.J. & Taylor, H.P., Jr., 2000. Water as a petrologic catalyst driving homogenization of the middle crust in the metamorphic core complexes of British Columbia. *International Geology Review,* **42**, 97-130.

Holk, G.J. & Taylor, H.P., Jr., 2007. $^{18}O/^{16}O$ evidence for contrasting hydrothermal regimes involving magmatic and meteoric-hydrothermal waters at the Valhalla metamorphic core complex, British Columbia. *Economic Geology*, **102**, 1063-1078.

Hollister, L.S., 1993. The role of melt in the uplift and exhumation of orogenic belts. *Chemical Geology*, **108**, 31-48.

Hollister, L.S. & Crawford, M.L., 1986. Melt-enhanced deformation: A major tectonic process. *Geology*, **14**, 558-561.

Holness, M.B. & Watt, G.R., 2001. Quartz recrystallization and fluid flow during contact metamorphism: a cathodoluminescence study. *Geofluids*, **1**, 215-228.

Hoppe, W.J., 1984. Origin and age of the Gabriel Peak orthogneiss, North Cascades, Washington. M.Sc. thesis, University of Kansas, p. 79.

Hurlow, H.A., 1992. Structural and U-Pb geochronologic studies of the Pasayten fault, Okanogan Range batholith, and southeastern Cascades crystalline core, Washington. PhD thesis, University of Washington, Seattle, WA.

Ingebritsen, S.E. & Manning, C.E., 1999. Geological implications of a permeability-depth curve for the continental crust. *Geology*, **27**, 1107-1110.

Inger, S. & Harris, N., 1993. Geochemical constraints on leucogranite magmatism in the Langtang Valley, Nepal Himalaya. *Journal of Petrology*, **34**, 345-368.

Irving, E., 1985. Whence British Columbia? *Nature*, **314**, 673-674.

Johnson, S.Y., 1984. Stratigraphy, age, and paleogeography of the Eocene Chuckanut Formation, northwest Washington. *Canadian Journal of Earth Sciences*, **21**, 92-106.

Johnson, S.Y., 1985. Eocene strike-slip faulting and nonmarine basin formation in Washington. *Society of Econ. Paleontologists and Mineralogists Special Publication,* **37**, 283-302.

Johnston, D.H., 1998. Structural and thermal evolution of northwest Thor-Odin dome, Monashee complex, southeast British Columbia, Ph.D. thesis, University of New Brunswick, Fredericton, New Brunswick, pp. 321.

Journeay, J.M. & Friedman, R.M., 1993. The Coast Belt thrust system: Evidence of Late Cretaceous shortening in southwest British Columbia. *Tectonics*, **12**, 756-775.

Kapp, J.L.D., Harrison, T.M., Kapp, P.A., Grove, M., Lovera, O.M. & Lin, D., 2005. The Nyaingentanglha Shan: a window into the tectonic, thermal, and geochemical evolution of the Lhasa block, southern Tibet. *Journal of Geophysical Research*, **110**, B08413.

Karlstrom, K.E. & Williams, M.L., 2006. Nature of the middle-crust – heterogeneity of structure and process due to pluton-enhanced tectonism: an example from Proterozoic rocks of the North American Southwest. *In*: Brown, M. & Rushmer, T. (Eds.),

Evolution and differentiation of the continental crust. Cambridge, UK, Cambridge University Press, p. 268-295.

Keay, S., Lister, G. & Buick, I., 2002. The timing of partial melting, Barrovian metamorphism and granite intrusion in the Naxos metamorphic core complex, Cyclades, Aegean Sea, Greece. *Tectonophysics*, **342**, 275-312.

Kelsey, D.E., Clark, C. & Hand, M., 2008. Thermobarometric modeling of zircon and monazite growth in melt-bearing systems: examples using model metapelitic and metapsammitic granulites. *Journal of Metamorphic Geology*, **26**, 199-212.

Klepeis, K.A. & Crawford, M.L., 1999. High-temperature arc-parallel normal faulting and transtension at the roots of an obliquely convergent orogen. *Geology*, **27**, 7-10.

Klepeis, K.A., King, D., De Paoli, M., Clarke, G.L. & Gehrels, G., 2007. Interaction of strong lower and weak middle crust during lithospheric extension in eastern New Zealand. *Tectonics*, **26**, TC4017, doi:10.1029/2006TC002003.

Kohn, M.J. & Malloy, M.A., 2004. Formation of monazite via prograde metamorphic reactions among common silicates: implications for age determinations. *Geochimica et Cosmochimica Acta*, **68**, 101-113.

Kohn, M.J. & Spear, F.S., 1990. Two new geobarometers for garnet amphibolites, with applications to southeastern Vermont. *American Mineralogist*, **75**, 89-96.

Krabbendam, M. & Dewey, J.F., 1998. Exhumation of UHP rocks by transtension in the Western Gneiss Region, Scandinavian Caledonides. In: *Continental transpressional and transtensional tectonics* (eds. Holdsworth, R.E., Strachan, R.A. & Dewey, J.F.), pp. 159-181. Geological Society [London] Special Publication **135**.

Kretz, R., 1983. Symbols for rock-forming minerals. *American Mineralogist*, **68**, 277-279.

Kriens, B., Tectonic evolution of the Ross Lake area, NW Washington-SW British Columbia. Ph.D. thesis, Harvard University, pp. 214.

Kriens, B. & Wernicke, B., 1990. Nature of the contact zone between the North Cascades crystalline core and the Methow sequence in the Ross Lake area, Washington: implications for Cordilleran tectonics. *Tectonics*, **9**, 953-981.

Kruhl, J.H., 1996. Prism- and basal-plane parallel subgrain boundaries in quartz: a microstructural geothermobarometer. *Journal of Metamorphic Geology*, **14**, 581-589.

Kruhl, J.H., 1998. Prism- and basal-plane parallel subgrain boundaries in quartz: a microstructural geothermobarometer: Reply. *Journal of Metamorphic Geology*, **16**, 142-146.

Kruckenberg, S.C., Whitney, D.L., Teyssier, C., Fanning, C.M. & Dunlap, W.J., 2008. Paleocene-Eocene migmatite crystallization, extension, and exhumation in the hinterland of the northern Cordillera: Okanogan dome, Washington, USA. *Geological Society of America Bulletin*, **120**, 912-929.

Kruse, S., McNutt, M.K., Phipps-Morgan, J., Royden, L. & Wernicke, B.P., 1991. Lithospheric extension near Lake Mead, Nevada: A model for ductile flow in the lower crust. *Journal of Geophysical Research*, **96**, 4435-4456.

Lambert, I.B. & Heier, K.S., 1968. Geochemical investigations of deep-seated rocks in the Australian Shield. *Lithos*, **1**, 30-53.

Little, T.A., Cox, S., Vry, J.K. & Batt, G., 2005. Variations in exhumation level and uplift rate along the oblique-slip Alpine fault, central Southern Alps, New Zealand. *Geological Society of America Bulletin*, **117**, 707-723.

Lorencak, M., Seward, D., Vanderhaeghe, O., Teyssier, C. & Burg, J.P., 2001. Low-temperature cooling history of the Shuswap metamorphic core complex, British Columbia: Constraints from apatite and zircon fission-track ages. *Canadian Journal of Earth Sciences*, **38**, 1615-1625.

Ludwig, K.R., 2003. Isoplot/Ex, v3.00. Berkeley Geochronology Center Special Publication, **4**, 70.

Magaritz, M. & Taylor, H.P., Jr., 1976. $^{18}O/^{16}O$ and D/H studies along a 500 km traverse across the Coast Range batholith and its country rocks, central British Columbia. *Canadian Journal of Earth Sciences*, **13**, 1514-1536.

Magaritz, M. & Taylor, H.P., Jr., 1986. $^{18}O/^{16}O$ and D/H studies of plutonic granitic and metamorphic rocks across the Cordilleran batholiths of southern British Columbia. *Journal of Geophysical Research*, **91**, 2193-2217.

Manning, C.E., 1997. Coupled reaction and flow in subduction zones: Silica metasomatism in the mantle wedge. *In*: Jamtveit, B. & Yardley, B.W.D. (Eds.) *Fluid flow and transport in rocks; Mechanisms and Effects*, pp. 139-148.

Manning, C.E. & Ingebritsen, S.E., 1999. Permeability of the continental crust: Implications of geothermal data and metamorphic systems. *Reviews of Geophysics*, **37**, 127-150.

Marshall, D. & Simandl, G., 2006. Phase relations and metamorphism in the sapphirine bearing granulites of the Valhalla complex, Slocan Valley, BC. *GAC/MAC Annual Meeting Abstracts Program*, **31**, 96.

Mattinson, J.M., 1972. Ages of zircons from the northern Cascade Mountains, Washington. *Geological Society of America Bulletin*, **83**, 3769-3784.

Matzel, J.E.P., Bowring, S.A. & Miller, R.B., 2004. Protolith age of the Swakane Gneiss, North Cascades, Washington: Evidence of rapid underthrusting of sediments beneath an arc. *Tectonics*, **23**, TC6009, doi:10.1029/2003TC001577.

McGroder, M.F., 1987. Yalakom-Foggy Dew fault: a 500 (+) km long Late Cretaceous-Paleogene oblique-slip fault in Washington and British Columbia. *Geological Society of America Abstracts with Programs*, **19**, 430.

McGroder, M.F., 1989. Structural geometry and kinematic evolution of the eastern Cascades foldbelt, Washington and British Columbia. *Canadian Journal of Earth Sciences*, **26**, 1586-1602.

McGroder, M.F., 1991. Reconciliation of two-sided thrusting, burial metamorphism, and diachronous uplift in the Cascades of Washington and British Columbia. *Geological Society of America Bulletin*, **103**, 189-209.

McGroder, M.F., Garver, J.I. & Mallory, V.S., 1990. Bedrock geologic map, biostratigraphy, and structure sections of the Methow basin, Washington and British Columbia. *Washington Division of Geology and Earth Resources Open File Report*, **90-19**, 32.

McKenzie, D., Nimmo, F., Jackson, J.A., Gans, P.B. & Miller, E.L., 2000. Characteristics and consequences of flow in the lower crust. *Journal of Geophysical Research*, **105**, 11029-11046.

Miller, R.B., 1987. Geology of the Twisp River – Chelan Divide region, North Cascades, Washington. *Washington, Division of Geology and Earth Resources,* Open-file report, **87-17**.

Miller, R.B., 1994. A mid-crustal contractional stepover zone in a major strike-slip system, North Cascades, Washington. *Journal of Structural Geology*, **16**, 47-60.

Miller, R.B. & Bowring, S.A., 1990. Structure and chronology of the Oval Peak batholith and adjacent rocks: Implications for the Ross Lake fault zone, North Cascades, Washington. *Geological Society of America Bulletin*, **102**, 1361-1377.

Miller, R.B. & Paterson, S.R., 1992. Tectonic implications of syn-emplacement and post-emplacement deformation of the Mount Stuart batholith for mid-Cretaceous orogenesis in the North Cascades. *Canadian Journal of Earth Science*, **29**, 479-485.

Miller, R.B. & Paterson, S.R., 2001. Influence of lithological heterogeneity, mechanical anisotropy, and magmatism on the rheology of an arc, North Cascades, Washington. *Tectonophysics*, **342**, 351-370.

Miller, R.B., Bowring, S.A. & Hoppe, W.J., 1989. Paleocene plutonism and its tectonic implications, North Cascades, Washington. *Geology*, **17**, 846-849.

Miller, R.B., Whitney, D.L. & Geary, E.D., 1993. Tectono-stratigraphic terranes and the metamorphic history of the northeastern part of the crystalline core of the North Cascades: evidence from the Twisp Valley Schist. *Canadian Journal of Earth Sciences*, **30**, 1306-1323.

Miller, R.B., Haugerud, R.A., Murphy, F. & Nicholson, L.S., 1994. Tectonostratigraphic framework of the northeaster Cascades. *Bulletin of the Washington Division of Geology and Earth Resources*, **80**, 73-92.

Miller, R.B., Paterson, S.R., Labit, H., Alsleben, H. & Lüneburg, C., 2006. Significance of composite lineations in the mid- to deep crust: a case study from the North Cascades, Washington. *Journal of Structural Geology*, **28**, 302-322.

Misch, P., 1966. Tectonic evolution of the northern Cascades of Washington State – a west Cordilleran case history. *Canadian Institute of Mining and Metallurgy*, **8**, 101-148.

Misch, P., 1977. Bedrock geology of the North Cascades. In: *Centennial Field Trip Guidebook, Cordilleran Section,* Geological Society of America, pp. 393-398..

Misch, P., 1968. Plagioclase compositions and non-anatectic origin of migmatitic gneisses in Northern Cascade mountains of Washington State. *Contributions to Mineralogy and Petrology,* **17**, 1-70.

Misch, P. & Onyeagocha, A.C., 1976. Symplectite breakdown of Ca-rich almandines in upper-amphibolite facies, Skagit Gneiss, North Cascades, Washington. *Contributions to Mineralogy and Petrology*, **54**, 189-224.

Mojzsis, S.J. & Harrison, T.M., 2002. Establishment of a 3.83-Ga magmatic age for the Akilia tonalite (southern West Greenland). *Earth and Planetary Science Letters*, **202**, 563-576.

Molnar, P. & Lyon-Caen, H., 1988. Some simple physical aspects of the support, structure, and evolution of mountain belts. *In*: Clark, S.P., Jr., Burchfiel, B.C. &

Suppe, J. (Eds.), *Processes in Continental Lithospheric Deformation*. Geological Society of America Special Paper, **218**, 179-207.

Monger, J.W.H., Souther, J.G. & Gabrielse, H., 1972. Evolution of the Canadian Cordillera; a plate-tectonic model. *American Journal of Science*, **272**, 577-602.

Monger, J.W.H., Price, R.A. & Tempelman-Kluit, D.J., 1982. Tectonic accretion and plutonic welts in the Canadian Cordillera. *Geology*, **10**, 70-75.

Montel, J.-M., Kornprobst, J. & Vielzeuf, D., 2000. Preservation of old U-Th-Pb ages in shielded monazite: example from the Beni Bousera Hercynian kinzigites (Morocco). *Journal of Metamorphic Geology,* **18***,* 335-342.

Morris, G.A., Larson, P.B. & Hooper, P.R., 2000. 'Subduction style' magmatism in a non-subduction setting: the Colville Igneous Complex, NE Washington state, USA. *Journal of Petrology*, **41**, 43-67.

Morrison, J., 1994. Meteoric water-rock interaction in the lower plate of the Whipple Mountain metamorphic core complex, California. *Journal of Metamorphic Geology*, **12**, 827-840.

Morrison, J. & Anderson, J.L., 1998. Footwall refrigeration along a detachment fault: implications for the thermal evolution of core complexes. *Science*, **279**, 63-66.

Mulch, A., Teyssier, C., Cosca, M.A., Vanderhaeghe, O. & Vennemann, T.W., 2004, Reconstructing paleoelevation in eroded orogens. *Geology*, **32**, 525-528.

Mulch, A. & Chamberlain, C.P., 2007. Stable isotope paleoaltimetry in orogenic belts – the silicate record in surface and crustal geological archives. *Reviews in Mineralogy and Geochemistry*, **66**, p. 89-118.

Nelson, K.D., Wenjin Zhao, Brown, L.D., Kuo, J., Jinkai Che, Xianwen Liu, Klemperer, S.L., Makovsky, Y., Meissner, R., Mechie, J., Kind, R., Wenzel, F., Ni, J., Nabelek, J., Chen Leshou, Handong Tan, Wenbo Wei, Jones, A.G., Booker, J., Unsworth, M., Kidd, W.S.F., Hauck, M., Alsdorf, D., Ross, A., Cogan M., Changde Wu, Sandvol, E. & Edwards, M., 1996. Partially molten middle crust beneath southern Tibet: Synthesis of project INDEPTH results. *Science*, **274**, 1684-1688.

Nesbitt, B.E. & Muehlenbachs, K., 1989. Origins and movement of fluids during deformation and metamorphism in the Canadian Cordillera. *Science*, **245**, 733-736.

Newton, R.C., 1989. Metamorphic fluids in the deep crust. *Annual Review of Earth and Planetary Sciences*, **17**, 385-410.

Norlander, B.N., Whitney, D.L., Teyssier, C. & Vanderhaeghe, O., 2002. Partial melting and decompression of the Thor-Odin dome, Shuswap metamorphic core complex, Canadian Cordillera. *Lithos*, **61**, 103-125.

Nyman, M.W., Pattison, D.R.M. & Ghent, E.D., 1995. Melt extraction during formation of K-feldspar-sillimanite migmatites, west of Revelstoke, British Columbia. *Journal of Petrology*, **36**, 351-372.

Nyström, A.I. & Kriegsman, L.M., 2003. Prograde and retrograde reactions, garnet zoning patterns, and accessory phase behaviour in SW Finland migmatites, with implications for geochronology. *In:* Vance, D., Müller, W. & Villa, I.M. (Eds.). *Geochronology: Linking the Isotopic Record with Petrology and Textures, Special Publications,* Geological Society of London, **220**, pp. 213-230.

Okulitch, A.V., 1984. The role of the Shuswap metamorphic complex in Cordilleran tectonism: a review. *Canadian Journal of Earth Sciences*, **21**, 1171-1193.

Paces, J.B. & Miller, J.D., 1993. Precise U-Pb age of Duluth Complex and related mafic intrusions, northeastern Minnesota: geochronological insights into physical, petrogenetic, paleomagnetic, and tectonomagmatic processes associated with the 1.1 Ga midcontinent rift system. *Journal of Geophysical Research,* **98**, 13997-14013.

Parkinson, D.L., 1991. Age and isotopic character of Early Proterozoic basement gneisses in the southern Monashee Complex, southeastern British Columbia. *Canadian Journal of Earth Sciences*, **28**, 1159-1168.

Parkinson, D.L., 1992. Age and tectonic evolution of the southern Monashee complex, southeastern British Columbia: A window into the deep crust, Ph.D. thesis, University of California, Santa Barbara, pp. 197.

Parnell, J., 1998. Approaches to dating and duration of fluid flow and fluid-rock interaction. *In:* Parnell, J. (Ed.), *Dating and duration of fluid flow and fluid-rock interaction*. Geological Society of London Special Publication, **144**, p. 1-8.

Parrish, R.R., 1984. Slocan Lake fault: a low angle fault zone bounding the Valhalla gneiss complex, Nelson map area, southern British Columbia. *Geological Survey of Canada Paper*, **84-1A**, 323-330.

Parrish, R.R., 1990. U-Pb dating of monazite and its application to geological problems. *Canadian Journal of Earth Sciences*, **27**, 1431-1450.

Parrish, R.R., 1995. Thermal evolution of the southeastern Canadian Cordillera. *Canadian Journal of Earth Science*, **32**, 1618-1642.

Parrish, R.R., and R.L. Armstrong, 1987. The ca. 162 Ma Galena Bay stock and its relationship to the Columbia River fault zone, southeast British Columbia. In: *Radiogenic age and isotopic studies: Report 1*, Geological Survey of Canada Paper, **87-2**, pp. 25-32.

Parrish, R., Carr, S.D. & Brown, R.L., 1985. Valhalla gneiss complex, southeast British Columbia: 1984 fieldwork. *Geological Survey of Canada Paper*, **85-1A**, 81-87.

Parrish, R.R., Carr, S.D. & Parkinson, D.L., 1988. Eocene extensional tectonics and geochronology of the southern Omineca belt, British Colombia and Washington. *Tectonics*, **7**, 181-212.

Paterson, S.R. & Miller, R.B., 1998. Magma emplacement during arc-perpendicular shortening; an example from the Cascades crystalline core, Washington. *Tectonics*, **17**, 571-586.

Paterson, S.R., Miller, R.B., Alsleben, H., Whitney, D.L., Valley, P.M. & Hurlow, H., 2004. Driving mechanisms for > 40 km of exhumation during contraction and extension in a continental arc, Cascades core, Washington. *Tectonics*, **23**, TC3005, doi:10.1029/2002TC001440.

Patiño Douce, A.E. & Johnston, A.D., 1991. Phase equilibria and melt productivity in the pelitic system: implications for the origin of peraluminous granitoids and aluminous granulites. *Contributions to Mineralogy and Petrology*, **107**, 202-218.

Pearce, N., Perkins, W., Westgate, J., Gorton, M., Jackson, S., Neal, C. & Chenery, S., 1997. A compilation of new and published major and trace element data for NIST SRM 610 and NIST SRM 612 glass reference materals. *Geostandards Newsletter*, **21**, 115-144.

Person, M.P., Mulch, A., Teyssier, C., & Gao, Y., 2007. Isotope transport and exchange during detachment tectonics, Shuswap metamorphic core complex, British Columbia. *American Journal of Science*, **307**, 555-589.

Petro, G.T., Housen, B.A. & Iriondo, A., 2002. Tectonic significance of paleomagnetism of the Eocene Golden Horn batholith. *Geological Society of America Program with Abstracts,* **98**.

Powell, R. & Holland, T., 2001. Course notes for "THERMOCALC workshop 2001: Calculating metamorphic phase equilibria. CD-ROM.

Price, R.A., 1986. The southeastern Canadian Cordillera: Thrust faulting, tectonic wedging and delamination of the lithosphere. *Journal of Structural Geology*, **8**, 238-254.

Raia, F. & Spera, F.J., 1997. Simulations of crustal anatexis: Implications for the growth and differentiation of the continental crust. *Journal of Geophysical Research*, **102**, 22629-22648.

Ravna, E.K., 2001. Distribution of Fe^{2+} and Mg between coexisting garnet and hornblende in synthetic and natural systems: an empirical calibration of the garnet-hornblende Fe-Mg geothermometer. *Lithos*, **53**, 265-277.

Reesor, J.E., 1965. Structural evolution and plutonism in Valhalla gneiss complex, British Columbia. *Geological Survey of Canada Bulletin*, **129**, 128.

Rey, P., Vanderhaeghe, O. & Teyssier, C., 2001. Gravitational collapse of the continental crust: definition, regimes and modes. *Tectonophysics*, **342**, 435-449.

Royden, L., 1996. Coupling and decoupling of crust and mantle in convergent orogens: Implications for strain partitioning in the crust. *Journal of Geophyiscal Research*, **1996**, 17679-17705.

Royden, L.H., Burchfiel, B.C., King, R.W., Wang, E., Chen Zhiliang, Shen Feng & Liu Yuping., 1997. Surface deformation and lower crustal flow in eastern Tibet. *Science*, **276**, 788-790.

Rubin, C.M., Saleeby, J.B., Cowan, D.S., Brandon, M.T. & McGroder, M.F., 1990. Regionally extensive mid-Cretaceous west-vergent thrust system in the northwestern Cordillera: Implications for continent-margin tectonism. *Geology*, **18**, 276-280.

Rusmore, M.E., Woodsworth, G.J. & Gehrels, G.E., 2005. Two-stage exhumation of midcrustal arc rocks, Coast Mountains, British Columbia. *Tectonics*, **24**, TC5013.

Rye, R.O., Schuiling, R.D., Rye, D.M. & Jansen, J.B.H., 1976. Carbon, hydrogen, and oxygen isotope studies of the regional metamorphic complex at Naxos, Greece. *Geochimica et Cosmochimica Acta*, **40**, 1031-1049.

Santosh, M., Tsunogae, T. & Yoshikura, S., 2004. "Ultrahigh density" carbonic fluids in ultrahigh-temperature crustal metamorphism. *Journal of Mineralogical and Petrological Sciences*, **99**, 164-179.

Schaubs, P. & Carr, S., 1998. Geology of metasedimentary rocks and late Cretaceous deformation history, in the Northern Valhalla complex, British Columbia. *Canadian Journal of Earth Sciences*, **38**, 1018-1036.

Schaubs, P.M., Carr, S.D. & Berman, R.G., 2002. Structural and metamorphic constraints on ca. 70 Ma deformation of the northern Valhalla complex, British Columbia: Implications for the tectonic evolution of the southern Omineca belt. *Journal of Structural Geology*, **24**, 1195-1214.

Schilling, F.R. & Partzsch, G.M., 2001. Quantifying partial melt fraction in the crust beneath the central Andes and the Tibetan Plateau. *Physics and Chemistry of the Earth*, **26**, 239-246.

Schilling, F.R., Trumbull, R.B., Brasse, H., Haberland, C., Asch, G., Bruhn, D., Mai, K., Haak, V., Giese, P., Muñoz, M., Ramelow, J., Rietbrock, A., Ricaldi, E. & Vietor, T., 2006. Partial melting in the Central Andean crust: a review of geophysical, petrophysical, and petrologic evidence. *In*: Oncken, O., Chong, G., Franz, G., Giese, P., Götze, H., Ramos, V.A., Strecker, M.R. & Wigger, P. (Eds.). *The Andes active subduction orogeny*, Springer, Berlin, pp. 459-474.

Schmitt, A.K., Grove, M., Harrison, T.M., Lovera, O.M., Hulen, J. & Waters, M., 2003. The Geysers – Cobb Mountain Magma System, California (Part 1): U-Pb zircon ages of volcanic rocks, conditions of zircon crystallization and magma residence times. *Geochimica et Cosmochimica Acta*, **67**, 3423-3442.

Schuhmacher, M., de Chambost, E., McKeegan, K.D., Harrison, T.M., Migeon, H., 1994. Dating of zircon with the CAMECA IMS 1270. In: Benninghoven, A., Nihei, Y., Shimizu, R., Werner, H.W. (Eds.), *Secondary Ion Mass Spectrometry SIMS IX*. Wiley, New York, pp. 912-922.

Selverstone, J., Spear, F.S., Franz, G. & Morteani, G., 1984. High-pressure metamorphism in the SW Tauern Window, Austria: P-T paths from hornblende-kyanite-staurolite schists. *Journal of Petrology*, **25**, 501-531.

Sevigny, J.H., Parrish, R.R. & Ghent, E.D., 1989. Petrogenesis of peraluminous granites, Monashee Mountains, southeastern Canadian Cordillera. *Journal of Petrology*, **30**, 557-581.

Snoke, A.W. & Frost, B.R., 1990. Exhumation of high pressure pelitic schist, Lake Murray spillway, South Carolina: Evidence for crustal extension during Alleghenian strike-slip faulting. *American Journal of Science*, **290**, 853-881.

Spear, F.S., 2004. Fast cooling and exhumation of the Valhalla metamorphic core complex, southeastern British Columbia. *International Geology Review*, **46**, 193-209.

Spear, F.S. & Parrish, R.R.,1996. Petrology and cooling rates of the Valhalla Complex, British Columbia, Canada. Journal of Petrology, **37**, 733-765.

Spell, T.L. & McDougall, I., 2003. Characterization and calibration of $^{40}Ar/^{39}Ar$ dating standards. *Chemical Geology Isotope Geoscience Section,* **198**, 189-211.

Steiger, R. & Jaeger, E., 1977. Subcommission on geochronology: Convention on the use of decay constants in geo and cosmochronology. *Earth and Planetary Science Letters*, **36**, 359-362.

Stewart, J.H., 1988. Tectonics of the Walker Lane belt, western Great Basin: Mesozoic and Cenozoic deformation in a zone of shear. In: Ernst (Ed.), *Metamorphism and crustal evolution of the Western United States*, Englewood Cliffs, New Jersey, Prentice Hall, **7**, pp. 683-713.

Struik, B. & Anderson, R.G., 2003. Paleogene pull-apart core- and rind-complexes, Canadian Cordillera. *Geological Society of America Abstracts with Programs*, **35**, 473.

Tabor, R.W. & Haugerud, R.A., 1999. *Geology of the North Cascades*, The Mountaineers, Seattle, Washington.

Tabor, R.W., Frizzell, V.A., Vance, J.A. & Naeser, C.W., 1984. Ages and stratigraphy of lower and middle Tertiary sedimentary and volcanic rocks of the central Cascades, Washington: application to the tectonic history of the Straight Creek fault. *Geological Society of America Bulletin*, **95**, 26-44.

Tabor, R.W., Frizzell Jr., V.A., Whetten, J.T., Waitt Jr., R.B., Swanson, D.A., Byerly, G.R., Booth, D.B., Hetherington, M.J. & Zartman, R.E., 1987a. Geologic map of the Chelan 30' by 60' Quadrangle, Washington. *U.S. Geological Survey Miscellaneous Investigation Map*, 33 pp., 1 sheet.

Tabor, R.W., Zartman, R.E. & Frizzell Jr., V.A., 1987b. Possible tectonostratigraphic terranes in the North Cascades crystalline core, Washington. In: Schuster, J.E. (Ed.), *Selected Papers on the Geology of Washington*, Washington Division of Geology and Earth Resources, Anaheim, California, pp. 107-127.

Tabor, R.W., Haugerud, R.A., Brown, E.H., Babcock, R.S. & Miller, R.B., 1989. *Accreted Terranes of the North Cascades Range, Washington, Field Trip Guidebook*, **T307**, 62 pp., AGU, Washington, D.C.

Tabor, R.W., Haugerud, R.A., Booth, D.B. & Brown, E.H., 1994. Preliminary geologic map of the Mount Baker 30- by 60-minute quadrangle, Washington. *US Geological Survey Open File Report*, **94-403**.

Tabor, R.W., Haugerud, R.A., Hildreth, W. & Brown, E.H., 2003. Geologic map of the Mount Baker 30- by 60 minute quadrangle, Washington. *U.S. Geological Survey, Geologic Investigation Series, I-2660, with pamphlet*, **70**, scale 1:100,000.

Teufel, S. & Heinrich, W., 1997. Partial resetting of the U-Pb isotope system in monazite through hydrothermal experiments: An SEM and U-Pb isotope study. *Chemical Geology*, **137**, 273-281.

Teyssier, C. & Whitney, D.L., 2002. Gneiss domes and orogeny. *Geology*, **30**, 1139-1142.

Teyssier, C., Ferré, E.C., Whitney, D.L., Norlander, B., Vanderhaeghe, O. & Parkinson, D., 2005. Flow of partially molten crust and origin of detachments during collapse of the Cordilleran orogen. In: Bruhn, D., Burlini, L. (Eds.), *High-strain zones: Structure and physical properties,* Geological Society of London Special Publications, **245**, pp. 39-64.

Townsend, K.J., Miller, C.F., D'Andrea, J.L., Ayers, J.C., Harrison, T.M. & Coath, C.D., 2000. Low temperature replacement of monazite in the Iretaba granite, southern Nevada: geochronological implications. *Chemical Geology*, **172**, 95-112.

Trail, D., Mojzsis, S.J., Harrison, T.M., Schmitt, A.K., Watson, E.B. & Young, E.D., 2007. Constraints on Hadean zircon protoliths from oxygen isotopes, Ti-thermometry, and rare earth elements. *Geochemistry Geophysics Geosystems*, **8**, 1-22.

Thompson, A.B., Schulmann, K. & Jezek, J., 1997. Thermal evolution and exhumation in obliquely convergent (transpressive) orogens. *Tectonophysics*, **280**, 171-184.

Umhoefer, P.J., 1987. Northward translation of "Baja British Columbia" along the Late Cretaceous to Paleocene margin of western North America. *Tectonics*, **6**, 377-394.

Umhoefer, P.J. & Miller, R.B., 1996. Mid-Cretaceous thrusting in the southern Coast Belt, British Columbia and Washington, after strike-slip fault reconstruction. *Tectonics*, **15**, 545-565.

Umhoefer, P.J., Whitney, D.L., Teyssier, C., Fayon, A.K., Casale, G. & Heizler, M.T., 2007. Yo-yo tectonics in a wrench zone, Central Anatolian fault zone, Turkey. In: Till, A.B., Roeske, S.M., Sample, J.C. & Foster, D.A. (Eds.) *Exhumation Associated with Continental Strike-slip Fault Systems*, Geological Society of America Special Paper, **434**, pp. 35-58.

Unruh, J., Humphrey, J. & Barron, A., 2003. Transtensional model for the Sierra Nevada frontal fault system, eastern California. *Geology*, **31**, 327-330.

Valley, P.M., Whitney, D.L., Paterson, S.R., Miller, R.B. & Alsleben, H., 2003, Metamorphism of deepest exposed arc rocks in the Cretaceous to Paleogene Cascades belt, Washington: evidence for large-scale vertical motion in a continental arc. *Journal of Metamorphic Geology*, **21**, p. 203-220.

Vance, J.A., 2002. Age and provenance of nonmarine sandstones in the central and northwest Washington Cascades: Fission track evidence from detrital zircons. *Geological Society of America Abstracts with Programs*, **34**, 96.

Vanderhaeghe, O. & Teyssier, C., 1997. Formation of the Shuswap metamorphic complex during late-orogenic collapse of the Canadian Cordillera: role of ductile thinning and partial melting of the mid- to lower crust. *Geodinamica Acta*, **10**, 41-58.

Vanderhaeghe, O. & Teyssier, C., 2001. Partial melting and flow of orogens, *Tectonophysics*, **342**, 451-472.

Vanderhaeghe, O., Teyssier, C. & Wysoczanski, R., 1999a. Structural and geochronological constraints on the role of partial melting during the formation of the Shuswap metamorphic core complex at the latitude of the Thor-Odin Dome, British Columbia. *Canadian Journal of Earth Sciences*, **36**, 917-943.

Vanderhaeghe, O., Teyssier, C. & Wysoczanski, R., 1999b. Structural and geochronological constraints on the role of partial melting during the formation of the Shuswap metamorphic core complex at the latitude of the Thor-Odin Dome, British Columbia. *Canadian Journal of Earth Sciences,* **36**, 917-943.

Vanderhaeghe, O., Teyssier, C., McDougall, I. & Dunlap, W.J., 2003. Cooling and exhumation of the Shuswap metamorphic core complex constrained by $^{40}Ar/^{39}Ar$ thermochronology. *Geological Society of America Bulletin*, **115**, 200-216.

Varsek, J.L. & Cook, F.A., 1994. Three-dimensional crustal structure of the Eastern Cordillera, southwestern Canada and northwestern United States, *Geological Society of America Bulletin*, **106**, 803-823.

Waight, T.E., Weaver, S.D. & Muir, R.J., 1998. Mid-Cretaceous granitic magmatism during the transition from subduction to extension in southern New Zealand: a chemical and tectonic synthesis. *Lithos*, **45**, 469-482.

Walker, J.D., Martin, M.W., Bowring, S.A., Searle, M.P., Waters, D.J. & Hodges, K.V., 1999. Metamorphism, melting, and extension: Age constraints from the High Himalayan Slab of southeast Zanskar and northwest Lahaul. *Journal of Geology*, **107**, 483-495.

Wanless, R.K., Stevens, R.D., Lachance, G.R. & Delabio, R.N., 1978. Age determinations and geological studies, K-Ar isotopic ages, report 13. *Geological Survey of Canada, Paper*, **77-2**.

Wanless, R.K., Stevens, R.D., Lachance, G.R. & Delabio, R.N., (1979), Age determinations and geological studies, K-Ar isotopic ages, report 14, *Geological Survey of Canada, Paper*, **79-2.**

Watson, E.B., 1996. Surface enrichment and trace-element uptake during crystal growth. *Geochimica et Cosmochimica Acta*, **60**, 5013-5020.

Watson, E.B. & Cherniak, D.J., 1997. Oxygen diffusion in zircon. *Earth and Planetary Science Letters*, **148**, 527-544.

Watson, E.B., Wark, D.A. & Thomas, J.B., 2006. Crystallization thermometers for zircon and rutile. *Contributions to Mineralogy and Petrology*, **151**, 413-433.

Wdowinski, S. & Axen, G.J., 1992. Isostatic rebound due to tectonic denudation: A viscous flow model of a layered lithosphere. *Tectonics*, **11**, 303-315.

Wernicke, B.P., 1990. The fluid crustal layer and its implications for continental dynamics. *In*: Salisbury, M.H. & Fountain, D.M., (Eds.), *Exposed cross sections of the continental crust*, Kluwer Academic Publishers, Dordrecht, Netherlands, pp. 509-544.

Wernicke, B. & Getty, S.R., 1997. Intracrustal subduction and gravity currents in the deep crust: Sm-Nd, Ar-Ar, and thermobarometric constraints from the Skagit Gneiss Complex, Washington. *Geological Society of America Bulletin*, **109**, 1149-1166.

Wernicke, B., Clayton, R.W., Ducea, M., Jones, C.H., Park, S., Ruppert, S., Saleeby, J., Snow, J.K., Squires, L., Fliedner, M., Jiracek, G., Keller, R., Klemperer, S., Luetgert, J., Malin, P., Miller, K., Mooney, W., Oliver, H. & Phinney, R., 1996. Origin of high mountains in the continents: the southern Sierra Nevada. *Science*, **71**, 190-193.

Wesnousky, S.G., 2005. The San Andreas and Walker Lane fault systems, western North America: Transpression, transtension, cumulative slip, and the structural evolution of a major transform plate boundary. *Journal of Structural Geology*, **27**, 1505-1512.

Wheeler, J.O. & McFeely, P., 1991. Tectonic Assemblage Map of the Canadian Cordillera and Adjacent Parts of the United States of America. *Geological Survey of Canada*, Map 1712A.

Whitney, D.L., 1991. Calcium depletion halos and Fe-Mn-Mg zoning around faceted plagioclase inclusions in garnet from a high-grade pelitic gneiss. *American Mineralogist*, **76**, 493-500.

Whitney, D.L., 1992a. Origin of CO_2-rich fluid inclusions in leucosomes from the Skagit migmatites, North Cascades, Washington. *Journal of Metamorphic Geology*, **10**, 715-725.

Whitney, D.L., 1992b. High pressure metamorphism in the western Cordillera of North America: an example from the Skagit Gneiss, North Cascades, Washington. *Journal of Metamorphic Geology*, **10**, 71-85.

Whitney, D.L. & McGroder, M.F., 1989. Cretaceous crustal section through the proposed Insular-Intermontane suture, North Cascades, Washington. *Geology*, **17**, 555-558.

Whitney, D.L., & Irving, A.J., 1994. Origin of K-poor leucosomes in a metasedimentary migmatite complex by ultrametamorphism, syn-metamorphic magmatism, and subsolidus processes. *Lithos*, **32**, 173-192.

Whitney, D.L., Lang, H.M. & Ghent, E.D., 1995. Quantitative determination of metamorphic reaction history; mass balance relations between groundmass and mineral inclusion assemblages in metamorphic rocks. *Contributions to Mineralogy and Petrology*, **120**, 404-411.

Whitney, D.L., Miller, R.B. & Paterson, S.R., 1999. P-T evidence for the magnitude of syn-metamorphic vertical tectonic motion in a contractional orogen: the North Cascades – Coast Mountains Belt, northern U.S. and Canadian Cordillera. *Journal of Metamorphic Geology*, **17**, 73-88.

Whitney, D.L., Teyssier, C., Fayon, A.K., Hamilton, M.A. & Heizler, M., 2003. Tectonic controls on metamorphism, partial melting, and intrusion: timing of regional metamorphism and magmatism of the Nigde Massif, Turkey. *Tectonophysics*, **376**, 37-60.

Whitney, D.L., Teyssier, C., Fayon, A.K., 2004a. Isothermal decompression, partial melting and exhumation of deep continental crust. In: Grocott, J., McCaffrey, K.J.W., Taylor, G., Tikoff, B. (Eds.) Vertical Coupling and Decoupling in the Lithosphere, Geol. Soc.-Lon. Special Publications, vol. 227, 313-326.

Whitney, D.L., Paterson, S.R., Schmidt, K.L., Glazner, A.F. & Kopf, C.F., 2004b. Growth and demise of continental arcs and orogenic plateaux in the North American Cordillera: from Baja to British Columbia. *In*: Grocott, J., McCaffrey, K.J.W., Taylor, G. & Tikoff, B. (Eds). *Vertical Coupling and Decoupling in the Lithosphere*, Geological Society, London, Special Publications, **227**, 167-176.

Whitney, D.L., Teyssier, C., and Vanderhaeghe, O., 2004c, Gneiss domes and crustal flow, *in* Whitney, D.L., Teyssier, C. & Siddoway, C. (Eds.), *Gneiss domes and orogeny*. Geological Society of America Special Paper, **380**, p. 15-33.

Whitney, D.L., Tepper, J.H., Hirschmann, M.M. & Hurlow, H.A., 2008. Late-orogenic mafic magmatism in the North Cascades, Washington: petrology and tectonic setting of the Skymo layered intrusion. *Geological Society of America Bulletin*, **120**, 531-542.

Wolfe, J.A., Forest, C.E. & Molnar, P., 1998. Paleobotanical evidence of Eocene and Oligocene paleoaltitudes in midlatitude western North America. *Geological Society of America Bulletin*, **110**, 664-678.

Yardley, B.W.D., 1978. Genesis of the Skagit Gneiss migmatites, Washington, and the distinction between possible mechanisms of migmatization. *Geological Society of America Bulletin*, **89**, 941-951.

Zandt, G., Velasco, A.A. & Beck, S.L., 1994. Composition and thickness of the southern Altiplano crust, Bolivia. *Geology*, **22**, 1003-1006.

Zhang, H.F., Harris, N., Parrish, R., Kelley, S., Zhang, L., Rogers, N., Argles, T. & King, J., 2004. Causes and consequences of protracted melting of the mid-crust exposed in the North Himalayan antiform. *Earth and Planetary Science Letters*, **228**, 195-212.

Zeitler, P.K. & Williams, I.S., 1988. U-Pb dating of metamorphic zircon overgrowths by means of depth profiling with an ion microprobe. *EOS (Transactions American Geophysical Union)*, **69**, 464.

Zeitler, P.K., Sutter, J.F., Williams, I.S., Zartman, R. & Tahirkheli, R.A.K., 1989. Geochronology and temperature history of the Nanga Parbat-Haramosh Massif, Pakistan. *In*: Malinconico, L.L., Jr. & Lillie, R.J. (Eds.) *Tectonics of the Western Himalayas*. Geological Society of America Special Paper, **232**, pp. 1-22.

Zeitler, P.K., Koons, P.O., Bishop, M.P., Chamberlain, C.P., Craw, D., Edwards, M.A., Hamidullah, S., Qasim Jan, M., Asif Khan, M., Umar Khan Khattak, M., Kidd, W.S.F., Mackie, R.L., Meltzer, A.S., Park, S.K., Pecher, A., Poage, M.A., Sarker, G., Schneider, D.A., Seeber, L. & Shroder, J.F., 2001. Crustal reworking at Nanga Parbat, Pakistan: Metamorphic consequences of thermal-mechanical coupling facilitated by erosion. *Tectonics*, **20**, 712-728.